Tucholke, B.E., Sibuet, J.-C., Klaus, A., et al., 2004
Proceedings of the Ocean Drilling Program, Initial Reports Volume 210

3. Site 1276[1]

Shipboard Scientific Party[2]

SITE SUMMARY

Hole: 1276A
Latitude: 45°24.3198′N
Longitude: 44°47.1496′W
Time on site: 1158.77 hr (0844 hr, 16 Jul–1530 hr, 2 Sep 2003)
Seafloor (drill pipe measurement from rig floor, mbrf): 4560
Distance between rig floor and sea level (m): 10.9
Water depth (drill pipe measurement from sea level, m): 4549.1
Total depth (from rig floor, mbrf): 6296.9
Total penetration (m): 1736.9
Total length of cored section (m): 936.9 (800.0–1736.9 mbsf)
Total core recovered (m): 790.35 (not including 6.37 m from wash Core 210-1276A-1W)
Core recovery (%): 85
Total number of cores: 103
Total number of drilled intervals: 3 (0–106.9, 106.9–753.0, and 753.0–800.0 mbsf)
Total length of drilled intervals without coring (m): 800

The prime drilling objectives of Leg 210 were to sample basement and the facies corresponding to the overlying U reflection in the Newfoundland Basin, both of which were deep targets. Additional objectives included investigation of the Cretaceous paleoceanography of the Newfoundland–Iberia rift and the record of how abyssal circulation developed in Paleogene time through this gateway to the sub-Arctic and Arctic seas.

At Site 1276, basement was estimated to be at 2080 meters below seafloor (mbsf) and the depth of U was estimated to be 1866 mbsf. Drilling and coring to these depths presented considerable engineering and operational challenges, both expected and unexpected. We were able to

[1]Examples of how to reference the whole or part of this volume.
[2]Shipboard Scientific Party addresses.

Ms 210IR-103

follow our operational plan to case the hole at Site 1276 with both 20- and 16-in casing as planned (Fig. F15, p. 58, in the "Leg 210 Summary" chapter), but very tight hole conditions prevented us from installing liners to greater depths. Ultimately, these hole conditions also prevented us from logging the hole.

Despite these difficulties, drilling at Site 1276 was an outstanding success. We cored from 800 to 1736.9 mbsf with a remarkable average core recovery of 85%, and we obtained a detailed record of sedimentation from the time that the Newfoundland–Iberia rift was a very narrow ocean basin (latest Aptian[?]–earliest Albian) up to the early Oligocene. This record captures an extensive series of major oceanographic events that affected the expanding North Atlantic Ocean during this time period, and it allowed us to accomplish virtually all of our major paleoceanographic objectives.

Site 1276 bottomed in diabase sills that appear to have been intruded into uppermost Aptian(?)–lower Albian sediments at very shallow subseafloor depths. These sills are estimated to lie only 100–200 m above basement, and it appears completely feasible that future drilling at this site can core to, and into, basement. Two sills were drilled, one at 1613–1623 mbsf and a second from 1719 mbsf to the bottom of the hole at 1737 mbsf (the sill base was not reached or recovered). These sills are diabases that are probably alkaline; they exhibit chilled margins and developed striking hydrothermal metamorphic effects in the enclosing sediments. The upper sill may have formed a seal, preventing the underlying sediments from becoming normally compacted and isolating fluids (including methane) in the section. Preliminary shipboard synthetic-seismogram modeling and velocity-depth analyses indicate that the top of the upper sill is at or near the basinwide U reflection. The sill lies in a unit of extensive uppermost Aptian(?)–lower Albian sedimentary gravity flows (lithologic Subunit 5C), and we interpret the U reflection to be created by a combination of the gravity flows and sills. Seismic signal reflection from the strong impedance contrasts, created by these interbedded igneous and sedimentary rocks, appears to explain the poor seismic signal penetration through U and thus the typically poor seismic definition of underlying basement.

The source of magmatism that created the sills is presently unknown, and such magmatism is certainly unexpected considering the nonvolcanic nature of the conjugate transition zone crust off Iberia. A source (mantle plume?) associated with development of the Newfoundland seamounts ~180 km to the south seems to be unlikely considering the basinwide distribution of the U reflection. However, some kind of regional postrift magmatic effect could help to explain the marked asymmetry of basement depth and roughness between the Newfoundland and Iberia conjugate margins (Fig. F4, p. 43, in the "Leg 210 Summary" chapter). Shore-based analyses of the Newfoundland Basin reflection data, together with synthetic-seismogram modeling based on the Site 1276 physical property data, age dating, and geochemical analyses, are expected to provide significant insights into this issue.

At Site 1276, we cored a greatly expanded Cretaceous sedimentary sequence, including black shales equivalent to the Hatteras Formation in the western North Atlantic. The black shale sequence extends from the lowermost Albian, or possibly the uppermost Aptian, upward through the Cenomanian/Turonian boundary. It reflects deposition under relatively low oxygen conditions in the deep basin, probably punctuated by intervals of total anoxia. Discrete black organic carbon–rich layers contain either terrestrial or marine carbon, or both, indicating that in-

put from both sources intermittently created reducing conditions at and below the seafloor. The geochemical and sedimentological data indicate a terrigenous input throughout the entire succession.

At Site 1276 we recovered sediments that may include five Oceanic Anoxic Events (OAEs). These are the latest Cenomanian–earliest Turonian(?) OAE 2 ("Bonarelli" event); the mid-Cenomanian event (MCE); and OAE 1b ("Paquier" event), OAE 1c, and OAE 1d in the Albian. In addition, one other, possibly new, Albian event is recognized from its characteristic black color coupled with high total organic carbon (TOC) and related geochemical indicators (see **"Oceanic Anoxic Events,"** p. 97, in "Geochemistry" and **"Biostratigraphy,"** p. 73). Analysis of these sediments will provide a rich data set to examine the paleoceanography of the Cretaceous North Atlantic Ocean as it expanded northward through the Newfoundland–Iberia rift.

Interestingly, similar dark sediments with locally black layers were recovered in parts of the uppermost Cretaceous and Paleocene section. This kind of occurrence has also been observed on the southern Bermuda Rise at Site 387 (Tucholke and Vogt, 1979), suggesting that low-oxygen conditions intermittently affected the North Atlantic at times well after the main episodes of anoxia that are documented in OAEs.

Most upper Turonian and younger sediments are facies characterized by reddish color and brown, green-gray, and other light colors that indicate a well-oxygenated basin, which is in marked contrast to the underlying section with its black shales. This change is well documented farther south in the North Atlantic Basin, where the multicolored sediments form the Plantagenet Formation (Jansa et al., 1979). The paleoceanographic change is thought to be associated with development of longitudinal deep circulation between the North and South Atlantic oceans when these two oceans first became fully connected at abyssal depths near the end of Cenomanian time (Tucholke and Vogt, 1979). Documentation of this oceanographic change off Newfoundland indicates that the widening rift was probably connected to the main North Atlantic Ocean over full ocean depth.

We recovered one of the few nearly complete upper Maastrichtian to lower Danian abyssal sedimentary sections across the Cretaceous/Tertiary (K/T) boundary at Site 1276. Extensive reworking and commonly carbonate free sediments prevent this section from being suitable for analyzing processes of biotic extinction, but the succession of biotic changes is obvious. High sedimentation rates in the lower Paleocene section will facilitate high-resolution study of biotic recovery following the Chicxulub (Yucatan) impact event at the K/T boundary.

The Paleocene/Eocene boundary interval is characterized worldwide by an abrupt warming event referred to as the Paleocene/Eocene Thermal Maximum (PETM), which is recorded by clay-rich precursor beds and followed by a sharp negative $\delta^{13}C$ excursion and a benthic foraminiferal extinction event. We cored this sequence at Site 1276. Although the specific boundary clay layer appears to be missing in our cores, a complete succession of the calcareous nannofossil events occurring immediately above the boundary clay layer was recognized and will provide important information on biotic recovery after this event.

Sedimentation patterns in the North and South Atlantic oceans have been profoundly affected by bottom currents since the initiation of strong abyssal circulation in Paleogene time. Determining when this initiation occurred, however, has been problematic because the currents created major unconformities (e.g., Horizon A^u in the central North Atlantic Basin) and thus left little lithologic or biostratigraphic

record to establish the timing of the event. Current interpretations are that the abyssal circulation developed near the Eocene/Oligocene boundary (Miller and Tucholke, 1983; Davies et al., 2001).

At Site 1276 we cored through a seismic marker that appears to coincide with this Paleogene circulation event. It matches an unconformity between lithologic Units 1 and 2 and a middle Eocene hiatus identified from preliminary biostratigraphy. The hiatus seems to represent a limited length of geologic time compared to other places where the unconformity has been cored, probably because gravity flows were flooding the Newfoundland deepwater margin with abundant sediment at the time. If our preliminary shipboard conclusions about the age of the hiatus are correct, then the age of this major paleoceanographic event may be 4–7 m.y. older than previously supposed. Shore-based analyses are planned to investigate this phenomenon in detail.

OPERATIONS

Bermuda Port Call

Leg 210 began at 1712 hr on Sunday, 6 July 2003, when the ship arrived in St. Georges, Bermuda. The ship arrived 1 day early, so the planned berth at the Royal Naval Dockyard (RND) on the west end of the island was not yet available. Immigration and custom clearance was completed that day. Because of the change in berth location, only one Ocean Drilling Program (ODP) container and freight could be loaded on Monday, 7 July. The drilling crew worked on replacing the drill line; unfortunately, the new drill line reel was larger, necessitating significant reworking of the mounting structure before it could be installed.

On Tuesday, 8 July, the ship moved to the RND at the west end of Bermuda. After the pilot boarded (0745 hr), all lines were released (0824 hr), the tug pulled the ship clear of the harbor (0831 hr), and the ship began the transit to the RND. The first line was ashore at the RND at 1035 hr. The early arrival in Bermuda and berth change resulted in port call activities not effectively starting until 8 July.

The ODP crew change was completed at 1430 hr on 8 July. This crew change was extended so that the technical staff could be informed about the status of the Integrated Ocean Drilling Program and changes in medical and retirement benefits. The Lawrence Berkley National Laboratory X-ray computed tomography (CT) scanner was installed in the core-entry area, and testing, calibration, and training began. Three containers of fresh groceries were loaded on Tuesday. Although the reefers had been left without power by dockworkers for ~24 hr, no spoilage occurred. ODP offloaded three 20-ft containers of supplies. We began loading 1400 metric tons of fuel on 8 July. Because of the small size of the transfer hose, this took 2 days; it also shut down all drill floor work on drill line replacement because of welding restrictions. Potable water was delivered to the ship by small truck on an hourly basis.

Other activities on 8 July included the following:

- A laboratory tour for staff from the Bermuda Underwater Exploration Institute was conducted.
- Vendor engineers installed an antivibration bracket for the active heave compensator (AHC) motion reference unit (MRU).
- The ODP operations engineer uncrated the Advanced Product Support Technology Drilling Sensor Sub (DSS), spare parts, tools,

and batteries and began testing the system with the Remote Memory Module (RMM).

Installation and testing of the electronics and firmware for the weight-on-bit (WOB) filter continued.

Activities related to troubleshooting the AHC problems continued on Wednesday, 9 July, including a technical review meeting with the Leg 209 ODP electronics technician, the Transocean operations manager, and the vendor service engineers in attendance. The rental MRU was mounted, and the existing MRU was diagnosed to have severe calibration problems.

On 9 July, the ship had to shift down the dock to make way for another arriving ship. The pilot was on board at 0915 hr, and the lines were cleared at 0950 hr; a tug was tied to the stern, and we started shifting along the pier. At 1020 hr, the vessel was secured to the wharf two ship lengths down the pier. Testing continued on the DSS and the RMM as well as on the WOB filter. The departing ODP dry ice and foreign freight shipments were sent out, and all departing ODP surface freight was staged on the dock. One of the drill collar (DC) racks was cleared out and then loaded with eight DCs and three tapered drill collars (TDCs). Delivery to the ship of the 30-ft DCs was difficult because of the very narrow roads in Bermuda. Two flats of DCs were placed on the dock in preparation for loading. American Bureau of Shipping surveyors were on board, carrying out various required ship inspections. More tours were conducted for Bermuda Biological Station staff and Texas A&M University Research Foundation representatives.

The Transocean crew crossover occurred on Thursday, 10 July. The new drill crew reorganized the DC rack and loaded the remaining 16 DCs. The reentry cone was spotted in the moonpool for assembly. The drill line installation was completed at 2100 hr. The AHC vendor engineers began testing and calibrating the AHC and then provided training for the drillers regarding setup and operating procedures for the AHC. The remaining ODP freight arrived on the dock late on Thursday evening, and the departing ODP containers were sealed for shipment.

On Friday, 11 July, the Leg 210 freight was loaded. The pilot and tug were ordered for a 1500 hr departure. A comprehensive safety equipment and lifeboat orientation was held for oncoming personnel and the science party.

Transit to Site 1276 (Proposed Site NNB-01A)

The pilot boarded at 1631 hr on Friday, 11 July, the tug boats were secured to the ship at 1638 hr, and the last line was released at 1648 hr. Once the tugs were clear of the ship (1655 hr), we transited to the pilot station with beautiful blue skies and calm seas. The pilot departed the ship, and we began the transit to Site 1276 (proposed Site NNB-01A) at 1813 hr. The Schlumberger logging engineer boarded the ship via the pilot boat.

During the transit from Bermuda, we assembled the reentry cone, picked up and determined the space-out of the bottom-hole assembly (BHA) for drilling in the 20-in casing, and performed general rig maintenance. On 14 July, we crossed the Gulf Stream and entered dense fog and cooler weather. That evening, we slowed to 9.5 nmi/hr as we entered marked fishing grounds in fog. During the final approach to Site 1276, we had to change heading slightly to avoid some research vessels

that were towing gear. After a transit of 1227 nmi at an average speed of 11 nmi/hr, we arrived at Site 1276 at 0800 hr on Wednesday, 16 July.

Site 1276

Once we arrived at the Global Positioning System (GPS) coordinates of Site 1276 (45°24.23′N, 44°47.15′W), the thrusters were lowered and switched to dynamic positioning (DP) mode at 0815 hr on 16 July. A seafloor positioning beacon was deployed at 0844 hr. The precision depth recorder indicated a water depth of 4564.5 m or 4575.4 meters below rig floor (mbrf).

Hole 1276A

Figure F1 shows a diagram of drilling, casing, and coring in Hole 1276A, and Table T1 gives a coring summary for the site.

F1. Site 1276 installation and cored intervals, p. 122.

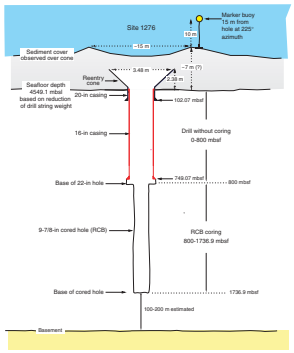

T1. Coring Summary, Site 1276, p. 314.

Installation of Reentry Cone and 20-in Casing

During the transit we had prepared the 20-in casing running tools (CRTs), BHA components, pilot bit, underreamer, centralizer, casing shoe, and reentry cone. The underreamer arms were set at 22 in. After the ship was on location in DP mode, we assembled DCs into five stands and stored them in the derrick. The upper guide horn was removed and stored in the DC rack so that the reentry cone could be centered over the moonpool.

A DC was attached to the top of the CRTs, and the CRTs were attached to the 20-in casing hanger and secured in the derrick. At 1430 hr on 16 July, we started rigging up for the assembly of eight joints of 20-in casing (total length = 102.07 m below the reentry cone mud skirt). The casing shoe joint was positioned in the rotary table, and the casing was assembled; the lowest three casing connections were spot welded. Once the casing hanger was attached to the top, we lowered the 20-in casing through the reentry cone and latched the hanger into it. We lifted the entire casing and reentry cone assembly to ensure that it was securely attached and to determine its weight (casing = 24,000 lb; casing + reentry cone = 38,000 lb). We then disconnected the CRTs from the casing hanger and welded the casing to the reentry cone. The CRTs, with two joints of DCs attached to the top, were stored in the derrick.

Our next step was to assemble the drill-in BHA. At 1930 hr, the drill crew started assembling a BHA consisting of the following: 18-in bit, bit sub with float, underreamer, crossover sub, mud motor, 14-in stabilizer, and 10 DCs to allow the bit to extend 4.83 m below the bottom of the casing. Once the mud motor was attached above the bit and underreamer, we flow tested this setup to ensure that the mud motor and underreamer were functioning properly.

The drill-in BHA (total length = 106.73 m below reentry cone mud skirt) was lowered through the reentry cone and 20-in casing, and the CRTs were attached to the top and latched into the reentry cone at 0105 hr on 17 July. After visually inspecting the latching of the casing to the reentry cone and the CRTs to the casing hanger, the entire assembly was raised to confirm that it was securely attached and to obtain a total weight (casing = 25,000 lb; casing + reentry cone = 40,000 lb; drill-in BHA below the CRTs = 40,000 lb; BHA above the CRTs = 10,000 lb). We lowered the reentry assembly through the moonpool (0205 hr) and prepared the rig floor for running the assembly to the seafloor. As the

assembly was lowered to 2701 mbrf, we filled the drill pipe with seawater every 10 stands.

Because of the deep water at Site 1276 and the planned deep penetration, we had to use some drill pipe that had not been used for a year. This required some extra time to remove pipe thread protectors that were stuck and to clean the threads. Because of rust inside the drill string, each time we picked up a stand we also had to run a rabbit through the pipe; we used a rabbit with a smaller outside diameter than normal to ensure that the inside of the drill string was open.

To minimize the risk that a large quantity of rust particles might be flushed down the drill string, potentially damaging the mud motor, we circulated a complete drill string volume of seawater through the drill pipe when the bit was at 2701 and 3621 mbrf. We deployed the vibration-isolated television camera system and continued to lower the drill string. We then picked up the top drive, spaced out the drill string, and established circulation; mud-motor circulation rates were recorded just off bottom.

Based on a reduction in drill string weight, the driller tagged seafloor at 2045 hr on 17 July, initiating Hole 1276A. The seafloor depth as felt by the drill bit was 4563 mbrf (4552.1 meters below sea level [mbsl]), but this was later corrected to 4560 mbrf (4549.1 mbsl) because the reentry cone could not be lowered past this depth when it landed. It took a total of 28 hr to drill the 20-in casing to 4662.0 mbrf (102.0 mbsf).

The highly variable penetration rates we experienced were due to the presence of several hard layers and, at times, what appeared to be a plugged jet in the bit. Drilling rates were mostly between 2 and 40 min/m, except for some very hard layers at 16, 56, and 62 mbsf drilled at 150, 80, and 210 min/m, respectively. We infer that these were intervals containing glacial dropstones. In general, the driller was using 100–140 strokes per minute (spm) (500–700 gallons per minute) while drilling, with a resulting torque of 5000 ft·lb at the bit with a bit rotation of ~70 rpm. Penetration slowed again while the last few meters were drilled, and the reentry cone landed on the seafloor 3 m shallower than expected.

After drilling in the casing (completed at 0045 hr on 19 July), our next step was to activate the CRTs to release the drill string from the 20-in casing and reentry cone. The driller reduced the string weight by 40,000 lb (the neutral point for the casing at the CRTs) and then attempted to release the CRTs at 0230 hr. Although they should have released relatively quickly, the CRTs finally released at 0500 hr, when the driller rapidly increased the WOB. Even then, it still required repeated raising and lowering of the drill string to fully release the BHA from the casing. This sticking may have been caused by the underreamer arms not being completely retracted or because the CRTs were sticking in the casing hanger. Using the subsea camera system, we observed that sediment was completely covering the reentry cone. To better visualize the cone and seafloor, we retrieved the camera to change the guide funnel so it could pass over the CRTs and reach down to the bit. During camera retrieval, we circulated seawater to attempt to wash away some of the sediment in the cone. When the camera was redeployed and had passed over the CRTs, we reconfirmed that the reentry cone was covered by sediment (see, e.g., Figs. **F2, F3, F4**), although a shallow "crater" in the sediment was clearly imaged on the sonar (see, e.g., Fig. **F5**). It appeared that we may have set the reentry cone base slightly below the seafloor. We raised the bit until it was just inside the reentry cone and

F2. Reentry 3, p. 123.

F3. Reentry 6, p. 124.

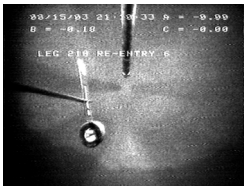

F4. Reentry 8, p. 125.

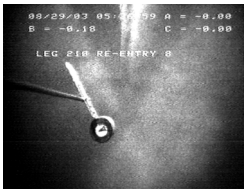

F5. Sonar image of reentry, p. 126.

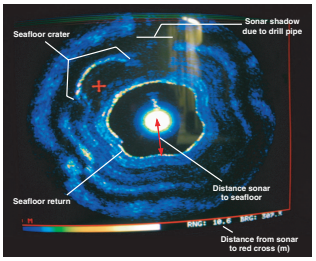

jetted with seawater to try to clear the sediments from the cone. The bit cleared the seafloor at 1000 hr.

Next, we retrieved the camera system and then pulled the drill string out of the hole. The drilling assembly was disassembled (DC stands stored in the derrick, CRTs detorqued, and mud motor and underreamer flow tested and then flushed with freshwater). The bit cleared the rotary table at 2300 hr.

Once the underreamer and bit were back on the rig floor, we observed that the underreamer's nozzles were damaged. The damage was likely due to plugging of the nozzles and the presence of glacial dropstones that were packed inside the bit and underreamer. Sediment (late Pliocene age, uppermost part of fan deposits) and rocks taken from the bit and underreamer were passed to the scientific party. The underreamer was subsequently repaired for drilling in the 16-in casing.

Installation of 16-in Casing to 800 mbsf

Our next operation was to install 16-in casing to 750 mbsf. The first step was to drill a 21-in hole to 800 mbsf. We started assembling the BHA at 0115 hr on 20 July. The BHA consisted of the following: $9^{7}/_{8}$-in wobble (pilot) bit, bit stabilizer, 21-in bicenter reamer, float sub, 8 DCs, DSS (which measures downhole WOB, torque, and pressure), 10 DCs, and TDC. The 174-m-long BHA weighed 50,000 lb, allowing a maximum WOB of 35,000 lb. The bicenter reamer could pass through the 20-in casing and was capable of drilling a 21-in hole beneath the casing.

While the BHA was lowered to the seafloor, the subsea camera system was deployed. At 1245 hr (with the bit at 4539 mbsl), the drill string length was adjusted in preparation to reenter Hole 1276A. The bit reentered the hole at 1300 hr. The reentry cone was buried in the sediment and was only visible as a dark conical depression in the seafloor; the sonar could clearly image this sedimentary crater above the cone.

The top drive was picked up, and we tagged the bottom of the hole at 4666.9 mbrf (106.9 mbsf). We alternated between passive and active heave compensation while drilling to check recent AHC calibrations and drilling procedures (a detailed engineering report is available from ODP).

The rate of penetration (ROP) varied from 21 to 3 m/hr, generally decreasing downhole. Substantial reductions in ROP occurred at 503 mbsf (from 13 to 7 m/hr) and at 685 mbsf (from 7 to 3–4 m/hr). A failed connection in the top drive circulation system interrupted drilling for 3 hr when the bit was at 666 mbsf (0915 hr on 23 July). The bit was raised off the bottom (to 5165 mbrf [605 mbsf]) to repair the top drive. After the repair, we drilled back to the bottom of the hole (609–666 mbsf), encountering 10–15 m of soft fill.

The wobble bit with bicenter reamer drilled smoothly with no indication of drag along the borehole walls. We circulated sepiolite mud (20 barrels [bbl]) every 50 m while drilling. The bit reached 800 mbsf at 2330 hr on 24 July.

We circulated 50 bbl of sepiolite mud to clean the hole and then raised the bit back up to the bottom of the 20-in casing shoe (102 mbsf). No tight sections of hole were encountered on the way up. While we lowered the bit back down, it encountered some resistance from 615 to 634 mbsf. We washed from there down to 800 mbsf and had to wash 15 m of soft fill from the bottom of the hole. We circulated another 40 bbl of mud to clean out the hole and then put 375 bbl of mud in the bottom of the hole so that mud would cover the tight interval at 615–634 mbsf. As the drill string was raised, additional tight spots

were found at 576–432, 423–412, and 288–103 mbsf that required use of the top drive. Once the bit was at the reentry cone and before we pulled completely out of the cone, we circulated seawater to clean sediments from the cone and make the next entry easier. The bit cleared the seafloor at 2100 hr on 25 July.

The BHA was taken apart and the bit was on the rig floor at 0640 hr on 26 July. The DSS was moved near the downhole laboratory so that the data could be downloaded. The wobble bit and bicenter reamer had experienced 84 hr of rotation with 25,000–35,000 lb WOB (70–75 rpm), and they could not be reused because of loose bearings.

Another problem with the top drive's seawater-circulation system was observed while we were tripping pipe out of the hole: water was leaking between the swivel and top drive shaft while circulating. At 0645 hr on 26 July, we started troubleshooting the top drive and swivel. The top drive was repaired, and pressure was tested to 1000 psi; it was put back in service by 1330 hr. Finally, preventative maintenance had to be done on the drill line (slip and cut).

We started preparing the rig floor for assembling the 16-in casing at 1515 hr. Once we were finished assembling the casing (749.11 m; 0200 hr on 27 July), the CRTs were attached to the casing hanger and the casing was lowered below the rig floor and hung on the moonpool doors. The CRTs were disconnected, and we started assembling the 16-in drilling BHA through the 16-in casing. The BHA consisted of the following: 14-in tricone bit, underreamer (arms set to 20 in), mud motor, 14-in centralizer/stabilizer, 12 DCs, and 21 stands plus a double of drill pipe. The BHA length was 753.90 m, and the pilot bit extended 4.83 m below the 16-in casing shoe.

We attached the CRTs to the top of the BHA (1115 hr), lowered them to the moonpool, and attached them to the 16-in casing hanger. We picked up the entire drilling/casing assembly (1245 hr) and deployed the camera system to inspect the casing and to confirm the spacing of the bit and underreamer below the casing.

At 1415 hr we began lowering the assembly to the seafloor. The bit was at the seafloor and ready for reentry at 0000 hr on 28 July. After only 10 min (0010 hr), we reentered Hole 1276A. When the bit was at 4649 mbrf (89 mbsf; 0100 hr), we attached the top drive. The bit passed through the base of the 20-in casing (102.07 mbsf) at 0200 hr.

From the 20-in casing shoe to 4930.79 mbrf (370.79 mbsf), the drilling time for each 9.6-m interval was 3 to 12 min. The drilling parameters for this section were WOB = 4,000–14,000 lb, circulation rate = 80–110 spm, and pump pressure = 650–1200 psi. We started circulating 30 bbl of mud every stand starting at 284 mbsf. We continued drilling in the casing from 5017 to 5050 mbrf (457–490 mbsf; WOB = 20,000–30,000 lb, circulation = 150 spm, and pressure = 2100 psi) until 0715 hr on July 29; at this time, it became apparent that the mud motor was not working properly. As we pumped 30 bbl of mud, the pump pressure increased by 700 psi. Although this was not typical for a mud-motor stall, we could not restart the mud motor despite repeated attempts at lifting off bottom or varying the circulating rate and WOB. At 1000 hr, we decided to retrieve the drill string to replace the mud motor.

The bit cleared the seafloor at 1415 hr, and the entire drilling/casing assembly was raised back to the ship. We hung the 16-in casing on the moonpool doors (2300 hr) and then began to take apart the BHA (2330 hr). Before taking apart the mud motor, underreamer, and bit, we tested the equipment by pumping seawater through it. The mud motor had seized up and would not rotate. Furthermore, the underreamer arms

would not open and the underreamer was packed off with sand (including sand under the piston that actuates the arms). Later, we found pieces of rubber jammed in the nozzles of the underreamer; these were from inside the mud motor, further documenting the failure of its internal mechanism.

The underreamer had to be completely taken apart, and nearly all moving parts were replaced. At 0430 hr on 30 July, we assembled the pilot bit, the rebuilt underreamer, and a new mud motor. Once this was tested, we started to reassemble the drilling BHA (0900 hr). The BHA was latched into the 16-in casing hanger at 1130 hr, and we started lowering the drilling BHA and casing back down to the seafloor.

Once the bit was near the seafloor (2000 hr), it took 45 min to reenter Hole 1276A (Fig. F2). The bit was lowered into the hole to 92 mbsf when we picked up the top drive to prepare for drilling. We began drilling the 16-in casing into the hole at 2200 hr. Drilling in the casing went quite quickly and smoothly down to 389.87 mbsf (drilling time = 2–14 min/9.6 m, WOB = 2,000–12,000 lb, and circulation = 145–155 spm; pressure = 1900– 2200 psi). We encountered what appeared to be a series of ledges at 392, 394, and 396 mbsf. It took 120 min to drill the interval from 389.87 to 399.47 mbsf. After each ledge was drilled, we had to apply 20,000 lb to work the casing past the ledge. While passing through this interval, the mud motor appeared to be experiencing torque, indicating that the underreamer arms were cutting hole. It is also possible that the underreamer arms were exposed to shock loads (perhaps as high as the full casing/BHA weight) when the casing would finally break through a ledge. From 389.87 to 754.05 mbsf, drilling time was 25–120 min/9.6 m, circulation was 155–160 spm, and pump pressure was 2150–2300 psi. Several hard intervals were encountered at 698, 703, and 743 mbsf. The casing hanger landed in the reentry cone at 1115 hr on 2 August with the bottom of the 16-in casing at 749.07 mbsf.

The 16-in casing landed 2.8 m higher than expected. We interpret that this was due to stretching of the drill pipe under the very heavy weight of the casing and drilling BHA; this is consistent with drill pipe stretch calculations. When we had deployed the 20-in casing and reentry cone, we calculated a drill pipe stretch of ~9.6 m. With the longer, much heavier 16-in casing string and drilling BHA, the calculated stretch was 12.4 m.

After we landed the casing, it took only 30 min to release the CRTs (1145 hr). We then reduced the circulation rate, pulled the bit and underreamer back into the casing, and started pulling out of the hole. The bit cleared the seafloor at 1440 hr. Before we could retrieve the drill string, we conducted routine preventative maintenance on the drill line (slip and cut). After the mud motor, underreamer, and pilot bit were retrieved and flushed out with freshwater in the moonpool, the bit arrived back on the rig floor at 0340 hr on 3 August.

We observed that the underreamer was missing its three outer cones (cutting structure on the arms) as well as two sets of pins that control how far the arms extend. These were lost in the hole. The body of the underreamer and bit exhibited some deep gouges, suggesting that the cones had been caught between these and the formation. We also observed water leaking from the hard covering over the top of the underreamer's bottom connection. Even after losing their cones, the underreamer arms appear to have continued cutting the formation because the outer parts of the arms had been worn back.

Attempted Cementing of the 16-in Casing

Our next operation was to cement the casing in place. We had originally planned to use a cement retainer. Because this would have required an extra pipe trip, we decided to use a 16-in Cameron cup tester (CCT) for the cementing operation instead.

At 0345 hr on 3 August, we tested the rig floor cementing equipment and then assembled the cementing BHA. The BHA consisted of a short piece of drill pipe, the CCT, an 8-in DC, a three-blade stabilizer, four DCs, a TDC, and five joints of 5½-in drill pipe (length = 110.09 m; weight = 27,000 lb).

We lowered the BHA and were ready for reentry at 1400 hr. The ship was positioned precisely at the same location where we had efficiently reentered before and where each time the bit was directly over the hole. However, this time there was no indication of the location of the hole on either the camera or sonar images.

After spending 1 hr searching for the hole with no success and with the ship directly over the previous reentry coordinates, we decided to probe the seafloor with the drill string in an attempt to locate the hole. The camera imaged a circular shadow, and we lowered into it at 1455 hr. It appeared that we had entered the hole because there was no reduction in drill string weight, and the drill string was lowered to 4643 mbrf (83 mbsf). At this point, we observed on the camera image that the drill string did not appear to be moving down into the seafloor. We immediately stopped lowering and raised it back up to 4569 mbrf (9.4 mbsf). We slowly lowered the drill string again, and it started meeting resistance at 13.4 mbsf. At this point, we decided to circulate seawater to attempt to clear sediment from the area. We also decided to raise the camera and inspect the drill string for damage. Unfortunately, we observed that the TDC was severely bent, so we had to retrieve the drill string before continuing. First, we conducted a sonar search of the area. We saw a sonar return ~60 m from the bit location, but we did not move closer to investigate. At 1900 hr, we began retrieving the drill string. When the end of the drill string was at 107 mbrf (0230 hr on 4 August), we had to cut off the connection from the last joint of 5½-in drill pipe and we removed the bent (~20°) TDC.

We replaced the TDC and started lowering the BHA back to the seafloor at 0400 hr. This time we attached a transponder to the camera/sonar system frame so that its position (and the end of the drill string) could be accurately monitored.

When the drill pipe was ready for reentry (1230 hr; 4554 mbrf, or 6 m above seafloor), we observed that the end of the drill string was offset 55–70 m from the moonpool. This was caused by a significant increase in bottom-current strength since the previous reentries. Moving the drill pipe to the location where it had just previously been lowered into the seafloor, we observed in the camera image a ~1-m-diameter hole in the seafloor together with an adjacent smaller hole. After discussion, we decided that this marked the previous attempted reentry and that it was not the location of the Hole 1276A cone. At this time, we began seeing plumes of sediment-laden water flowing from the southwest. We decided to trace these to their source, where we found a depression in the seafloor that turned out to be the sedimentary crater above Hole 1276A. The rim of the depression was visible on the sonar. Sediment-laden water was streaming from the seafloor around this depression, which was ~15 m in diameter. The next challenge was to lower the drill string into the 3.5-m-diameter cone that was buried in sediment, obscured by

flowing muddy water, and had a 75-m offset between the moonpool and the bit position.

During our first reentry attempt (1920 hr), the CCT appeared to hang up on the throat of the reentry cone (4563 mbrf; 3 mbsf). We slowly lowered the drill string to 4589 mbrf (29 mbsf), where it encountered an obstruction. We started circulating seawater to wash down from 4589 mbrf (29 mbsf) but tagged something hard at 4594 mbrf (34 mbsf; 0200 hr on 5 August). It was clear that the CCT was hanging up in the reentry cone, so we pulled out of the seafloor at 0325 hr.

After ~1 hr of repositioning the drill pipe directly over the hole, we attempted another reentry (0522 hr). Once again, we could not lower past 4564.5 mbrf (4.5 mbsf) in the cone. After 2 hr of trying, we decided to pull the pipe clear of the reentry cone (0730 hr) and cease attempts to use the CCT for cementing. The CCT reached the rig floor at 1630 hr. A total of 61 hr was expended while attempting reentry for the cementing job.

We decided to abandon attempts to cement the casing, as we felt that by now the formation had likely collapsed around the outside of the 16-in casing and taking additional time to cement would create even more risk to achieving any of the deep, primary leg objectives. We felt that it was important to verify that reentering Hole 1276A was possible and that the smaller $9^{7}/_{8}$-in rotary core barrel (RCB) bit was the best tool to use. Furthermore, we still did not know what impact the pieces of the underreamer previously lost in the hole would have on our ability to advance the hole.

RCB Coring from 800 mbsf

After preparing the rig floor (1830 hr on 5 August), we started assembling the BHA. The BHA consisted of an RCB bit (C3), a mechanical bit release (MBR) (so we could log after coring), one DC, the DSS (to measure downhole WOB, torque, and pressure), thirteen DCs, a TDC, and six joints of 5½-in drill pipe (length = 202.08 m; weight = 60,000 lb). When the bit was at 4550 mbrf (0500 hr on 6 August), we had to do drill line maintenance (slip and cut) before we started the coring operations. At 0630 hr, we started reentry attempts in Hole 1276A, where sediment-laden fluid was still billowing out of the seafloor around the hole. After almost 5 hr, we succeeded reentering the hole on our fourth attempt (1125 hr).

We lowered the drill pipe to 4.7 m below the 16-in casing (5313 mbrf; 754 mbsf), where the bit encountered some resistance. A core barrel (wash core) was deployed, and we drilled down to 5360 mbrf (800 mbsf, WOB = 10,000 lb, bit rotation = 70 rpm, circulation = 85 spm at 1100 psi, and torque = 150 A). After recovering the wash core (Core 210-1276A-1W; 2355 hr), we began RCB coring at 5360 mbrf (800 mbsf). By 0025 hr on 10 August, we had cored from 800 to 1059.7 mbsf and recovered 210 m of core (recovery = 81%). The time to cut each core varied primarily from 22 to 95 min (average = 50 min) except for Core 9R (876.8–886.4 mbsf), which took 120 min. Hole conditions remained good throughout the cored interval.

Coring parameters started at WOB = 12,000 lb, bit rotation = 70 rpm, and circulation = 85 spm at 1100 psi, but by Core 28R they were WOB = 20,000–25,000 lb, bit rotation = 60–70 rpm, and circulation = 115 spm at 1800 psi. Thirty barrels of sepiolite mud was circulated after every core. Particulate tracers for microbiological experiments were deployed while Cores 8R, 18R, 19R, and 28R were cut. The RMM was run on top of the core barrel while taking Cores 4R, 7R, 13R, and 24R to download

data from the DSS. The AHC was used while Cores 14R, 15R, 16R, 18R, 20R, and 22R were cut. While Core 22R was cut, the AHC developed a hydraulic leak, which was subsequently repaired.

RCB coring continued from 1059.7 to 1338.1 mbsf. Cores 29R to 57R penetrated 278.4 m of section and recovered 245.75 m (recovery = 88%). Coring parameters for Cores 29R through 32R were WOB = 20,000 lb, bit rotation = 70 rpm, circulation = 110 spm at 1600 psi, and torque = 175–200 A. During a wiper trip after Core 32R, we encountered no drag from the base of the hole (1098.2 mbsf) up to the 16-in casing at 749 mbsf. On the way back down to the bottom of the hole, tight spots had to be reamed out at 803, 864, and 874 mbsf. After 10 m of soft fill at the bottom of the hole had been cleaned out, we pumped 50 bbl of sepiolite mud to clean cuttings from the hole. After the 6.5-hr wiper trip, we resumed coring. From 1615 hr on 10 August to 0605 hr on 13 August, we cut Cores 33R through 57R (1098.2–1338.1 mbsf) and recovered 212.15 m (recovery = 88%). ROP varied from 19 to 6.4 m/hr and generally decreased downhole. Sepiolite mud (30 bbl) was circulated after each core. Coring parameters were WOB = 20,000 lb, bit rotation = 70 rpm, torque = 175 A, and circulation = 110 spm at 1600–1700 psi until the lower part of this section, where WOB, torque, and pump rates started to increase (WOB = 25,000 lb, torque = 200–300 A, and circulation = 130 spm at 2300 psi, respectively). Particulate tracers for microbiological studies were deployed on Core 48R.

There was a significant decrease in recovery in Cores 55R through 57R. Recovery had been averaging 93% in Cores 33R through 54R, but it dropped to 30%–60% in Cores 55R through 57R. Torque and pump pressure also increased while cutting Core 57R (torque = 400 A and pressure = 2600 psi, respectively). When Core 57R was recovered, we immediately noticed that its diameter was significantly reduced. Although the bit had only 44.8 cutting hr, the sudden change in core quality indicated that one or more of the core guides may have been bent inward or perhaps a single cone on the bit was not rotating properly. We decided to stop coring because we wanted to minimize chances that a bit failure might junk the hole, and we prepared to log the hole.

Attempted Logging of Hole 1276A

Before we conducted a wiper trip to prepare for logging, we circulated 60 bbl of sepiolite mud to clean cuttings from the hole and we then raised the bit up into the 16-in casing (0730–1030 hr on 13 August). We lowered the bit into the hole to 5626 mbrf (1066.8 mbsf; 1030–1215 hr), where we used the top drive to drill some tight spots down to 1095.6 mbsf. Once this section was clean, we removed the top drive and we were able to freely lower the bit to 1297 mbsf. At 1530 hr, we had to use the top drive again to drill from 1297 to 1338 mbsf. The bit was back at the bottom of the hole at 1630 hr. We circulated 50 bbl of mud and then displaced the hole with 185 bbl of mud before starting to pull out of the hole to drop the bit.

We raised the bit with the top drive in place up to 1297 mbsf, where the top drive was racked back. While we continued to pull out of the hole, the subsea camera/sonar system was deployed at 2015 hr so we could observe bit release and reentry for logging. The bit cleared the seafloor at 2210 hr, the ship was offset 50 m to the south, and at 2245 hr we lowered the rotary shifting tool (RST) on the wireline to release the bit. The bit did not release, and we lowered the RST again to close the MBR ports. When the sleeve was shifted back in place over the ports, at 0020 hr on August 14, we observed the bit falling off onto the

seafloor. At 0130 hr, the drill pipe was adjusted for reentry at 4553 mbrf (7 m above the seafloor).

At 0130 hr the DP operators began positioning the vessel for reentry. The offset between the beacon on the camera/sonar frame and the moonpool was 25–40 m. When the end of the pipe passed over the hole, we observed sediment-laden fluid still coming from the hole and obscuring it. The sedimentary crater was ~15 m in diameter. After an initial failed stab at the hole, we successfully reentered Hole 1276A at 0400 hr.

The end of the pipe (EOP) was lowered to 186.6 mbsf, and we retrieved the camera/sonar system. At 0445 hr, we started preparing the rig floor to run the wireline logging tools. The camera system was back on deck at 0630 hr, and we started assembling the triple combination (triple combo) tool string. Unfortunately, once the logging tools were deployed, they would not pass an obstruction ~5 m below the base of the 16-in casing (749 mbsf). We retrieved the logging tool and decided to try lowering the open EOP past the obstruction. We lowered the EOP to 821 mbsf (~21 m into the $9^{7}/_{8}$-in RCB hole) and deployed the triple combo a second time. Once again, the tool did not pass more than 3 m beyond the EOP. It was now clear that the logging tools would not enter the open hole, so we abandoned attempts to log and started to pull out of the hole to resume RCB coring. The triple combo tool was back on the rig floor at 2020 hr, and we began retrieving the drill string at 2230 hr. The EOP cleared the seafloor at 0020 hr on 15 August and was back on the rig floor at 0840 hr.

RCB Coring from 1338.1 mbsf

After attaching a new RCB bit, a new MBR, and removing a damaged piece of 5½-in drill pipe, we lowered the coring BHA down to the seafloor. The subsea camera/sonar system was deployed at 1730 hr when the bit was at 4517 mbrf (42 m above seafloor). Before we could reenter, we conducted preventative maintenance on the drill line (slip and cut) between 1800 and 1930 hr.

At 1930 hr, we began positioning for reentry with the bit at 4553 mbrf. We could clearly see the rim of the sediment crater above Hole 1276A on the camera image (Fig. **F3**), but this time the hole was not shrouded by sediment-laden water. We reentered Hole 1276A on the second attempt at 2145 hr and lowered the bit to 736 mbsf. After retrieving the subsea camera/sonar system, we started lowering the bit into the open hole below the 16-in casing (0015 hr on 16 August). The bit encountered as much as 25,000 lb of drag, so we installed the top drive to drill and circulate back to the bottom of the hole at 1338.1 mbsf. Tight spots in the hole had to be worked at 825, 834–839, 877–882, 904, 1005, 1053, 1085, 1148, 1170, 1236, and 1254 mbsf. These zones required WOB = as much as 10,000 lb, bit rotation = 75 rpm, torque = 175–300 A, and circulation = 100 spm at 1100 psi. Thirty barrels of mud were circulated at 1120 mbsf. Fill had to be drilled and washed from the hole at 1264.6–1338.1 mbsf. Before coring, we circulated 50 bbl of mud at 1338 mbsf.

We started coring at 1330 hr on August 16. Cores 58R through 61R were taken from 1338.1 to 1372.9 mbsf, and we recovered 32.66 m (recovery = 93%). ROP was 10.2 m/hr, and coring parameters were WOB = 15,000–20,000 lb, bit rotation = 70 rpm, circulation = 120 spm at 2300 psi, and torque = 200–300 A. After each core was cut, 30 bbl of mud was circulated.

Cores 62R through 80R were cut from 1372.9 to 1555.4 mbsf (0225 hr on 17 August to 1450 hr on 19 August), and we recovered 170.27 m (recovery = 93%). Drilling parameters remained relatively constant in this interval: WOB = 20,000–25,000 lb, bit rotation = 70 rpm, torque = 200–250 A, and circulation = 120–130 spm at 2300–2500 psi. The ROP decreased downhole from 9.3 m/hr (Cores 62R through 70R) to 6.2 m/hr (Cores 71R through 77R) to 3.8 m/hr (Cores 78R through 80R). The AHC was used while Core 64R was cut and then was used for all odd-numbered cores starting with Core 67R.

A full-length nonmagnetic RCB core barrel was deployed for all odd-numbered cores beginning with Core 59R, but we continued to use a standard barrel for even-numbered cores. Particulate tracers for microbiological contamination testing were deployed every tenth core starting with Core 69R.

The bit encountered a hard interval at 1412.4 mbsf. A substantial reduction in penetration rate occurred between Core 75R (85 min to cut 9.6 m; ROP = 6.7 m/hr) and Core 76R (170 min to cut 9.6 m; ROP = ~3.3 m/hr). This slow rate of penetration persisted while cutting Cores 77R through 80R. These cores also had slightly lower recovery. The recovered cores showed no obvious reason for the substantial change in penetration rate.

Because of the slow ROP and consistent torque, we decided to conduct a wiper trip up to the 16-in casing. At 1600 hr on 19 August, we circulated 50 bbl of sepiolite mud and then started raising the bit. The top drive was used to rotate and circulate as the bit was raised to 1284 mbsf. At 1830 hr, the top drive was removed and the bit was raised the rest of the way up to the 16-in casing. The wiper trip to this point lasted 5.75 hr.

We began lowering the bit back into the hole at 2045 hr. The bit immediately ran into a tight area at 851.5 mbsf, and we had to install the top drive in order to drill through it. Drilling did not start until 0000 hr on 20 August because we first had to replace a damaged 20-ft piece of drill pipe ("knobby") at the rig floor.

It took 13.5 hr to drill back to the bottom of the hole at 1555.4 mbsf. On the way back to bottom, tight sections of hole had to be drilled through and reamed up and down (864–875, 885–887, 992, 1000, 1005–1024, 1093, 1285–1351, and 1365 mbsf). Torque of 400–500 A and pump pressures as much as 1700 psi were recorded while drilling out the upper two intervals. Increased torque and pump pressures also occurred from 1285 to 1351 mbsf. The typical drilling parameters while reaming back to the bottom of the hole were WOB = 5,000–12,000 lb, bit rotation = 80 rpm, torque = 175–200 A, and circulation = 120 spm at 1200 psi. Sepiolite mud was circulated at 1300 mbsf (30 bbl) and 1514 mbsf (50 bbl).

Coring resumed at 1330 hr. Cores 81R through 84R were taken from 1555.4 to 1587.7 mbsf, and we recovered 17.85 m (recovery = 55%). Coring parameters were WOB = 20,000–35,000 lb, bit rotation = 65–70 rpm, torque = 200–300 A, and circulation = 120 spm at 2000–2200 psi. We circulated 30 bbl of mud after every core. The AHC was used while Core 82R was cut. Recovery for this core was very low (0.94 m), due to a mechanical problem with the check ball that allowed the full pump pressure to pass through the core barrel.

Because of the slow and apparently decreasing ROP (ROP = ~3 m/hr for Cores 81R through 83R and 1.8 m/hr for Core 84R), we decided to retrieve the drill string so that we could change the bit to one better suited to hard formations.

Top Drive Failure

We deployed the wireline sinker bar to retrieve Core 84R at 0715 hr on 21 August. While lowering the sinker bar, the driller noticed that the top drive was leaking while he was circulating seawater (similar to the failure that occurred on 24 July). The situation changed drastically when the leak turned into a deluge. The driller immediately landed and secured the drill string on the rig floor elevators. Fortunately, the bit was off the bottom of the hole when this occurred, thus allowing the driller to have access to the tool joint on the 5.5-in drill pipe.

Once the drill pipe had been secured, our next concerns were to make sure the pipe did not get stuck in the hole and to start retrieving the drill string as soon as possible. We needed to retrieve Core 84R, reestablish circulation, get the top drive out of the way, and then start pulling out of the hole.

Core 84R was pulled from the pipe and recovered on the rig floor at 0830 hr on 21 August. The circulating head was then attached to the top of the drill pipe so that we could pump seawater to prevent the pipe from becoming stuck in the hole. The knobby drill pipe attached to the bottom of the top drive had to be removed before the top drive could be pulled out of the way. At 0830 hr, the 30-ft knobby was removed but the other 20-ft knobby had to be cut off because we could not reach the connection to loosen it. Once the knobbies were removed from the top drive, the top drive was rotated back away from the rig floor.

At 0930 hr, we started raising the drill pipe out of the hole. The drill string encountered 50,000 lb of overpull and 25,000 lb of drag when the pipe was raised and lowered through 1312 mbsf. Based on previous hole conditions during wiper trips or pulling out of the hole, we were certain that circulation would be required to get out of the hole. Thus, we reinstalled the circulating head on the top of each stand of drill pipe. The pipe had to be worked up and down for ~2 hr before we could get through the interval from 1312 to 1323 mbsf. Tight hole conditions were encountered throughout the open hole, and the pipe had to be worked up and down during circulation (pump rate = 30 spm at 300 psi). At 1930 hr, after 7.5 hr, the bit was raised back up inside the 16-in casing. We continued retrieving the drill string, which cleared the seafloor at 2055 hr and was back on the rig floor at 0455 hr on 22 August.

Top Drive Repair

At 0500 hr, we began to disassemble the top drive to evaluate what had broken. A severe crack was found in the swivel-shaft box connection. The swivel shaft bears the entire weight of the 6147-m-long drill string (~680,000 lb). The crack extended ~60% around the circumference of the shaft. It was a major miracle that we did not lose the drill string and the hole and severely damage the derrick. We replaced the swivel shaft and then reassembled and tested the top drive. The top drive was fully repaired at 1530 hr.

RCB Coring from 1587.7 mbsf

We attached a new bit (CC-4) to the BHA and lowered it to the seafloor. The subsea camera system was launched at 0000 hr on 23 August. Before we could reenter Hole 1276A, we performed routine preventative maintenance on the drill line (slip and cut; 0045–0215 hr) and we picked up 10 new stands of 5-in drill pipe, measured lengths, and checked interior diameters.

We began searching for Hole 1276A at 0245 hr, and we reentered it on the second attempt at 0355 hr. The end of the drill string still had a

25 m offset from the moonpool due to currents, and there was 3 m of heave.

By 0545 hr, the bit was near the base of the 16-in casing. The bit was lowered to 1006 mbsf without using the top drive to rotate or circulate; this was the first time it entered so freely. The top drive was installed when the bit encountered drag (20,000–30,000 lb) at 1006 mbsf. The hole was redrilled from 1006 to 1587.7 mbsf (0930 hr on 22 August to 2045 hr on 23 August). Tight spots were encountered at 865, 990, 1006, 1070, and 1110 mbsf.

The RCB was dropped to start Core 85R at 2045 hr. While the core barrel was dropping to the bottom of the pipe, we continued to rotate and ream out the lowermost 8.5 m of hole.

Cores 85R and 86R were taken from 1587.7 to 1604.5 mbsf and recovered 14.59 m (recovery = 86%). We varied the coring parameters (WOB = 30,000 lb, bit rotation = 60 rpm, torque = 275 A, and circulation = 120 spm at 2300 psi) in an attempt to improve the rate of penetration (ROP = 2.3–2.7 m/hr), but there was no apparent improvement. Although the cores recovered alternating claystone and sandstone, there was no apparent change in drilling characteristics throughout the cored interval.

On 24 August, we cut Cores 85R to 90R from 6152.8 to 6200.8 mbrf (1592.8–1640.8 mbsf). Core recovery was 90%, and ROP was 3.0 m/hr. Coring parameters were WOB = 25,000–30,000 lb, bit rotation = 60 rpm, torque = 225–275 A, and circulation = 120 spm at 2300 psi. A sill was encountered at the bottom of Core 87R and in most of the upper part of Core 88R. Core 88R recovery was 97.1%, and ROP was 3.8 m/hr. The AHC was run on Cores 87R and 89R. Particulate tracers were deployed while Core 89R was cut. We continued to run full nonmagnetic core barrels on all odd-numbered cores.

On 25 August, we cut Cores 90R to 95R from 6200.8 to 6242.9 mbsf (1640.8–1682.9 mbsf). Coring parameters were consistent: WOB = 25,000 lb, bit rotation = 60 rpm, torque = 225–275 A, and circulation = 120 spm at 2300 psi. Core recovery was 86.8%, and ROP was 3.2 m/hr. The AHC was run while Core 91R was cut, but it then had to be shut down because of a hydraulic leak.

By midnight on 25 August, sea conditions had deteriorated and we encountered maximum heave of nearly 3 m. Throughout 26 August, we continued to experience heave of 1.5–2.0 m.

On 26 August, we cut Cores 95R to 100R from 6242.9 to 6290.8 mbsf (1682.9–1730.8 mbsf). Particulate tracers were deployed while Core 99R was cut. Coring parameters were WOB = 20,000–30,000 lb, bit rotation = 60– 70 rpm, circulation = 120 spm at 2200 psi, and torque = 225–350 A. Core recovery dropped from 80% for Core 96R to only 39% for Core 99R. For Cores 95R through 98R, ROP was 3–5 m/hr but then it dropped to 2.5 m/hr for Core 99R. We had to replace the lower 5-ft section of the nonmagnetic core barrel because of a cracked thread. This may have been damaged when we experienced the high heave late on 25 August or early on 26 August. Although we held a constant WOB of 25,000 lb, WOB could have ranged from 12,000 to 37,000 lb because of the heave.

While we cut Core 100R, the circulating pressures dropped from 2200 to 1700–1800 psi and the torque increased to 400–500 A. After advancing only 2 m in 4 hr, we decided to retrieve the core to see if we could tell why the penetration rate had dropped so dramatically. When we recovered Core 100R, it was empty. We deployed another core barrel and it did not appear to latch in properly, so it was immediately retrieved. When it was back on the rig floor, we noticed that the core

catcher fingers inside the core barrel were damaged, as if something had poked through the middle of the core barrel when it landed. At this point we believed that the bit must have been jammed with rocks, so we ran a bit deplugger down on the end of a core barrel. This did not appear to land properly, so we ran in again with another type of deplugger.

At this point we felt that whatever was jamming the bit might have been dislodged, so we deployed the barrel for Core 101R at 1200 hr on 27 August. While cutting this core, we observed relatively smooth torque of ~300 A during the first hour. After this, the torque became very erratic (200–500 A). After a 1-m advance (1731.1–1732.1 mbsf), we retrieved Core 101R at 1730 hr and it was empty.

It appeared that the bit was still jammed, so we decided to retrieve the drill string to replace the bit. We began raising the drill string at 1735 hr. The top drive was removed at 2245 hr when the bit was at 929 mbsf, but the circulating head had to be used from 865 to 813 mbsf to work through a section that had 30,000–40,000 lb of drag.

The bit cleared the seafloor at 0155 hr on August 28 and was back on the rig floor at 1005 hr. Pieces of diabase (~1.5 m total length) were jammed into the flapper valve. From all of the operations described above (especially the damaged core catcher fingers), we inferred that this 1.5 m of diabase most likely fell out of the core barrel while we retrieved Core 99R. In addition, the bit was severely damaged, with one cone missing and one cone completely seized up; the remaining two cones could be moved up and down nearly 1 in on the bit. The three remaining cones also had missing buttons and severe gouging, and the core guides were damaged.

Once the damaged bit and pieces of core were removed, we assembled a new C-7 bit to a boot basket sub (designed to catch broken pieces of metal in cavities along the outside of the sub) and then lowered the pipe back to the seafloor. We changed the bit in order to minimize damage to the cutting structure that could be caused by any remnants of the lost bit cone. We did not want to use conventional fishing tools or a magnet because of the poor hole conditions (it was taking 10–20 hr to drill back to bottom of hole each time) and because we wanted to continue coring if possible. Before we reentered the hole, we performed preventative maintenance on the drill line (slip and cut).

We positioned the drill pipe at 4553 mbrf and started to maneuver the ship for reentering Hole 1276A at 2115 hr on 28 August. Once again we had significant difficulties reentering the hole because of currents (surface and deep), a completely sediment-covered reentry cone (Fig. F4), and significant offset of the moonpool from the bit (~75 m). After 24 hr and 15 attempts, we reentered Hole 1276A at 2110 hr on 29 August. On this last and successful attempt, it at first appeared that we had missed the hole yet again because of difficulty in lowering the drill pipe. However, when we offset the ship back over the hole, the bit slipped in. It may be that we had actually stabbed the hole on previous attempts, but it seems that the offset had caused the bit to stick in the throat of the reentry cone.

When we lowered the bit into the hole, we encountered 30,000 lb of drag at 800 mbsf and had to raise the bit to 784 mbsf and install the top drive. It took ~28 hr to drill back down to the bottom of the hole at 1732.1 mbsf. We encountered tight spots at 800–900, 1030, 1075, 1285, 1320, 1354, and 1410 mbsf. It took ~5 hr to ream out and clean up a tight spot at 1688 mbsf using a WOB of 20,000 lb and torque of 300–400 A. Another difficult section of hole was encountered between 1720

and 1726.8 mbsf, where we needed to use a WOB of 20,000 lb and torque of 300–450 A.

We dropped the barrel for Core 102R at 0045 hr on 31 August and starting coring at 1732.1 mbsf. Because the cone that had broken off the previous bit was in the bottom of the hole, we used a low WOB and a slow rotation rate while lowering the bit 0.8 m to 1732.9 mbsf. It took 2 hr to advance this distance. Core 102R was recovered with only a single 2-cm-long piece of diabase. After cutting Core 103R from 1732.9 to 1734.9 mbsf (3 hr), it was retrieved and it was empty.

At 1030 hr on 31 August, we deployed a center bit to try to dislodge anything that might be jammed in the bit and preventing core recovery and to help break up any debris from the missing cone. At 1115 hr, when we were ready to lower the sinker bars to retrieve the center bit, torque increased to 400 A and pump pressure increased to 2750 psi. We did not deploy the sinker bars, and we reamed the tight hole from 1726.8 to 1693.8 mbsf. While reaming, we encountered drag of 40,000 lb, torque of 600 A, and pump pressures of 2750 psi.

At 1315 hr on 31 August, we retrieved the center bit and then lowered the bit back to the bottom of the hole (1693.8–1734.9 mbsf) and started cutting Core 104R. We took 4 hr to advance 2 m using WOB = 20,000 lb, bit rotation = 55 rpm, and circulation = 100 spm at 1750 psi. When Core 104R was recovered, it was empty.

At 2215 hr, we dropped another center bit in a further attempt to dislodge anything that might be jammed in the bit and to help break up any debris from the missing cone. The center bit was recovered at 0115 hr on 1 September, and it showed significant damage, indicating that it had been grinding on the lost cone in the bottom of the hole. We deployed another center bit at 0115 hr; it was retrieved at 0400 hr, and it showed significant damage to the cutting structure, also indicating that it had been grinding on metal in the bottom of the hole.

At 0400 hr, we deployed yet another center bit. When the bit had been lowered back down to 1734.9 mbsf (2 m above the bottom of the hole), we lost our ability to rotate the drill string (even with torque of >550 A) and pump pressures climbed to 2600 psi. We started to try to work the pipe up and down with overpull of 130,000 lb and pump pressures as much as 3000 psi. Rotation could not be reestablished even with torque of 600 A. By 0930 hr, we were able to remove only two singles of drill pipe and to raise the bit up to 1707.5 mbsf.

At 0930 hr, we lowered the wireline to remove the center bit. At 1045 hr, we removed the 30-ft knobby drill pipe below the top drive so that we would have more space in the rig to work the pipe up and down. We attempted to work the drill string from 1045 to 1230 hr with maximum overpulls of 160,000 lb, torque of 650 A, and pump pressures to 3000 psi, but we were unable to raise, lower, or rotate the drill string. At this time we decided to prepare for severing the drill string while we continued trying to free it.

At 1600 hr, the drill string began to move ever so slowly with WOB = 150,000 lb overpull and pump = 100 spm and 3000 psi. The hole problems seemed to be associated with a relatively unconsolidated sediment section recovered in Core 97R. This was the section of hole where we had problems on the previous day. By 1715 hr, we were able to remove another 9.6-m section of drill pipe. At this point, we could slowly raise the drill string with progressively less overpull. We were able to raise the drill string from 1698.1 to 1678.9 mbsf and remove two more singles of drill pipe with 80,000 lb overpull and pressures of 3000 psi.

We then raised the bit from 1678.9 to 1131.2 mbsf with WOB overpulls = 20,000–25,000 lb, torque = 400–500 A, and pump pressures = 2000 psi. We continued to raise the bit up into the base of the 16-in casing using the top drive. This required overpull of 10,000–25,000 lb and torque of 400 A from 950 to 750 mbsf.

By this time, it was clear that Hole 1276A could not be deepened without casing the open hole above total depth, so we decided to terminate operations at the site. Before we pulled out of the hole, we wanted to identify the location of Hole 1276A with a marker buoy deployed from the subsea camera/sonar system. The bit cleared the seafloor at 0600 hr on 2 September. At 0615 hr we released the marker buoy onto the seafloor 15 m from Hole 1276A at an azimuth of 225°. We then continued to retrieve the drill string and subsea camera/sonar. At 0910 hr, we released the seafloor positioning beacon and it was back on deck at 1015 hr. Once the bit was back on the rig floor (1530 hr), we began the transit to proposed Site NNB-04A (Site 1277).

LITHOSTRATIGRAPHY

The entire Neogene section and part of the Paleogene succession at Site 1276 was cased and not cored. Coring started at 800 mbsf following the retrieval of a wash core taken through the interval 753–800 mbsf. Beneath this wash core, recovery was excellent, approaching 100% for many cores. Five lithologic units are recognized (Fig. **F6;** Table **T2**), based primarily on proportions of sediment types, mineralogy of detrital and biogenic components, and bedding style. No attempt is made to define lithologic units that might correspond directly to units defined on the conjugate Iberia margin (Legs 149 and 173), but we do attempt in the concluding section of this chapter to compare and contrast the results from Site 1276 with those obtained from the Iberia sites (Deep Sea Drilling Project [DSDP] Site 398; ODP Legs 103, 149, and 173) and other North Atlantic drilling (DSDP Legs 43 and 76). The reader should be aware that Hole 1276A penetrated a succession that, in its lower part (e.g., in the Cretaceous interval), dips regionally oceanward at ~5° based on interpretation of seismic reflection data (see the **"Leg 210 Summary"** chapter). Cores preserve dips as high as ~12° relative to the core axis (see **"Structural Geology,"** p. 70). Also, a hole deviation of 7.4° in an unknown direction was measured at ~1650 mbsf using the Tensor tool. Thus, the reported stratigraphic thicknesses in the lower part of Hole 1276A (Table **T2**) must exceed true thicknesses.

The description of each unit includes a detailed account of the lithologies, grouped where appropriate according to whether these are essentially background hemipelagic sediments as opposed to redeposited units. Emphasis is placed on description of the various facies, taking advantage of the potential to illustrate many features in color. Information is integrated from visual study of the split cores, smear slides (see **"Site 1276 Smear Slides"**), thin section microscopy (see **"Site 1276 Thin Sections"**), X-ray diffraction (XRD) (see Table **T3**), CT scans, total organic carbon (TOC) (Tables **T17, T18**), and inductively coupled plasma–atomic emission spectroscopy (ICP-AES) analyses (see Table **T4**). Smear slide data are most useful for the study of fine-grained sediments, whereas thin sections were used to study sandstones and grainstones. XRD analysis was conducted mainly on fine-grained sediments that were systematically sampled (one per core), together with a small number of unusual lithologies. The CT scanner was used particularly to in-

F6. Lithostratigraphic summary, p. 127.

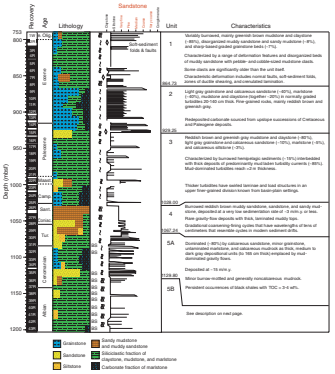

T2. Lithostratigraphic units, Hole 1276A, p. 316.

T3. XRD data, Hole 1276A, p. 318.

T4. ICP-AES major and trace element analyses, p. 323.

vestigate depositional and diagenetic structures in whole cores, and some examples of the results are included in this report. In addition, fine-grained sediments were analyzed by ICP-AES on a routine basis (at least one per core).

The descriptive sections are followed by an interpretation section that addresses depositional processes, paleoceanography, and sediment provenance and diagenesis as appropriate. In many cases the suggested interpretations are provisional, bearing in mind the difficulty of interpreting a sedimentary basin using only a single linear stratigraphic section. Reference is also made, where useful, to structural features that are treated more fully in **"Structural Geology,"** p. 70. Details regarding individual cores are available in **"Site 1276 Visual Core Descriptions."**

In the initial overview of each unit, colloquial names for rock colors are used because of the large variation in the cored succession. Readers interested in quantitative color data can obtain digital imaging system (DIS) information from the Janus database, captured from the scans of individual core sections that were acquired using the DIS (**www-odp.tamu.edu/database**). Many sediments have borderline textures between claystone and mudstone (see **"Lithostratigraphy,"** p. 4, in the "Explanatory Notes" chapter). This sometimes makes classification a matter of personal preference, especially because the silt content cannot be easily quantified from smear slide analyses. Therefore, the informal name "mudrock" was commonly used for undifferentiated claystone and mudstone to emphasize the general similarities in the spectrum of the fine-grained facies. However, different facies of mudrocks were described separately where possible. Also, the carbonate content, as assessed using HCl and/or smear slides and reflected in the terms calcareous, marlstone, and limestone, might not be entirely faithful to $CaCO_3$ percentages reported in **"Carbonate and Organic Carbon,"** p. 96, in "Geochemistry" because of the typical coarse sampling interval of one carbonate analysis per core.

"Black shales" were found in lithologic Subunits 5A and 5B and, rarely, in Subunit 5C. They are recognized by their very thin lamination (<1 mm), nannofossil abundance, and high organic carbon content (>1 wt% TOC) as estimated in smear slides and inferred from the dark sediment color. These descriptions are largely corroborated by TOC analyses in the range of 2–4 wt% for this facies. However, the identification of many of the black shales was based solely on visual inspection and smear slide analysis because of the relatively small number of shipboard TOC determinations.

Unit 1

Interval: 210-1276A-1W, 50 cm, to 8R-5, 113 cm
Depth: top: 753.00–794.13 mbsf; base: 864.73 mbsf
Age: middle Eocene–early Oligocene
Lithology: mainly greenish brown mudstone, claystone, and grainstone, with subordinate muddy sandstone and sandy mudstone

Unit 1 consists of ~85% mudstone and claystone (hereafter referred to as mudrock), ~8% muddy sandstone and sandy mudstone, and ~7% sharp-based, graded grainstone beds. The unit is mainly a drab brownish color with shades of green and gray. The defining characteristics of Unit 1 are a high proportion of mudrock; disorganized deposits of muddy sandstone and sandy mudstone with pebble- and cobble-sized mudstone clasts; and a range of deformation features including normal faults, soft-

sediment folds, zones of ductile shearing, and crenulated lamination (see "Structural Geology," p. 70).

The top of Unit 1 is placed at Section 210-1276A-1W-1, 50 cm, although presumably it extends uphole through the interval that was drilled but not cored. ODP convention places the top of Unit 1 at 753.00 mbsf because this wash core was nominally collected in previously drilled material over the depth range 753.0–800.0 mbsf. However, except for 50 cm of drilling breccia at the top of Section 210-1276A-1W-1 (including inferred glacial dropstones), all of Core 1W consists of only slightly fractured lithified sediments indistinguishable in facies from those recovered in Core 2R (cored interval 800.0–809.5 mbsf). Therefore, it is believed that the 580-cm-long interval recovered in Core 210-1276A-1W originated at the base of the "washed" interval, probably below 790.0 mbsf. This sediment is uppermost Eocene to lower Oligocene, whereas Core 210-1276A-2R is upper Eocene. The base of Unit 1 is placed at a sharp color and lithologic boundary with Unit 2, at Section 210-1276A-8R-5, 113 cm. This location correlates with a middle Eocene hiatus (see "Biostratigraphy," p. 73).

The mudrocks of Unit 1 are variably burrowed and represent slowly deposited hemipelagic sediments. The grainstones are normally graded and have planar lamination; they are interpreted as turbidites. The muddy sandstones and sandy mudstones form disorganized, ungraded beds with scattered floating clasts of mudrock and marlstone, and they are interpreted as debris flow deposits. Grainstones in Unit 1 include a variety of carbonate and siliciclastic grains derived from shelf depths and deeper.

The proportion of $CaCO_3$ determined from samples taken from Unit 1 is mostly <10 wt% (see "Carbonate and Organic Carbon," p. 96, in "Geochemistry"). Point values of ~30–50 wt% are present in thin intervals of more calcareous claystone and grainstone, some of which may actually be large, transported clasts in mass-flow deposits. TOC is mostly <1 wt%, although one claystone has a TOC value of 2.35 wt% (Sample 210-1276A-5R-4, 20–21 cm).

Lithologies

Mudstone and Claystone (Mudrock)

The dominant lithology is mudrock; it is the "background" lithology. Mudstones are intergradational with claystones. The colors of the mudstones vary, by gradational boundaries, between greenish gray (5GY 6/1), dark greenish gray (5GY 4/1), olive gray (5Y 3/2), grayish olive (10Y 4/2), and pale brown (5YR 5/2), although the general impression is of a drab brownish color overall. Burrowing varies from absent to slight to common (e.g., Core 210-1276A-6R). Where present, the burrowing includes *Chondrites*. Unusual fernlike burrows (?*Helicodromites*) were noted in Section 210-1276A-8R-2. The mudstones are locally interburrowed with sandstone or carbonate grainstone, producing complex textures (Fig. F7). The mudstone commonly contains sand-sized carbonate and mud clasts (e.g., Section 210-1276A-1W-3). The carbonate grains in the mudstones are mainly bioclasts, including benthic and planktonic foraminifers, sponge spicules, and fragments of echinoderms, red algae, mollusks, ostracodes, and fecal pellets. Millimeter-sized mud rip-up clasts are present locally. Several small (<3 cm) carbonate concretions were noted in Section 210-1276A-6R-5.

F7. Laminated sandstone with mud-filled burrows, Unit 1, p. 130.

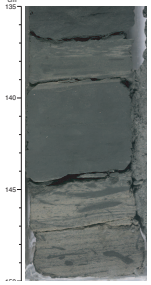

The dominant colors of the claystones are greenish gray (5GY 6/1) to dark greenish gray (5GY 4/1). The claystone ranges from homogeneous to mottled and commonly contains white carbonate sand and silt grains. It is only weakly calcareous, except where it is associated with carbonate concretions. Where present, thin planar lamination is defined by pale silt grains.

XRD analysis of the mudrocks (mudstones and claystones) reveals abundant quartz. Plagioclase is present throughout as a minor constituent, whereas potassium feldspar is found only locally in trace amounts. Opal-A is widespread, whereas zeolites are rare. Clay minerals are mainly illite and chlorite, and they are common throughout.

The major and trace element composition of the mudrocks, as determined by ICP-AES analysis (Table T4), is within the expected range for sediments derived from mixed continental and biogenic sources. Some samples are enriched in TiO_2, Zr, Cr, and V, compared to average hemipelagic sediments. This reflects a significant terrigenous-silt input. Minor relative enrichments in SiO_2 and MnO are also observed. $CaCO_3$ values of the background mudrocks are <1.5 wt%, and TOC values are <1 wt%. A few samples are relatively carbon rich (as much as 2.35 wt% TOC).

Grainstone

Calcareous grainstones are a secondary component of Unit 1. The well-graded, silt-, sand-, and commonly granule-sized grainstones (e.g., Section 210-1276A-6R-3) range from olive gray (5Y 4/1) to light olive gray (5Y 5/2). Most are present as thin to medium beds (5–20 cm) with sharp, typically scoured bases; only very rarely does a grainstone grade in grain size downward into the underlying unit (e.g., Section 210-1276A-6R-5). Most grainstones are medium to fine grained. Structures are planar lamination at the base (Fig. F8), passing upward into gently inclined lamination and then to rare current-ripple cross lamination. The inclined lamination occurs in the upper parts of some graded beds. Many bed tops are penetrated by burrows that extend downward from overlying fine-grained sediments. The grainstones contain occasional <1-cm subrounded mudstone rip-up clasts (Fig. F9).

The grainstones are dominated by reworked carbonate and some biosiliceous grains, including benthic and planktonic foraminifers, sponge spicules, echinoderms, red algae, radiolarians, and ostracodes, together with occasional micritic grains and fecal pellets (Fig. F10). They also contain as much as 20% siliciclastic components, mainly quartz, feldspar, mica, and heavy minerals.

Some grainstones are unusually coarse or contain unusual structures. One bed in Section 210-1276A-6R-4 is ~95 cm thick, has a sharp scoured base, and grades from coarse sand at the base to fine sand at the top. The lower part contains abundant, small (<1 mm), elongate, flattened rip-up clasts of mudstone, claystone, and micrite. Unusual wavy lamination in some grainstones is composed of anastomosing darker and lighter seams (e.g., interval 210-1276A-1R-3, 58–65 cm). Close inspection shows that the grain size decreases smoothly across these intervals. Smear slide analysis shows that the darker laminae are mainly mudstone grains, suggesting that carbonate grains and mud particles (e.g., grain aggregates and fecal pellets) were hydrodynamically sorted during deposition.

F8. Graded grainstone turbidite, Unit 1, p. 131.

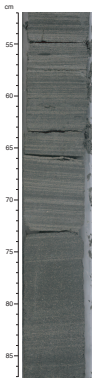

F9. Redeposited graded grainstone with mudstone rip-up clasts, Unit 1, p. 132.

F10. Grainstone, Unit 1, p. 133.

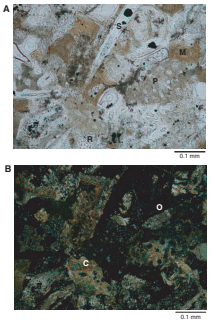

Muddy Sandstone and Sandy Mudstone

Muddy sandstone and sandy mudstone also form a secondary component of Unit 1. Two spectacular intervals of highly disorganized muddy sandstone and sandy mudstone are present near the top and near the base of Unit 1. Sections 210-1276A-2R-1 through 2R-4, 9 cm, consist of pale yellowish brown (10YR 6/2), highly disorganized muddy sandstone and sandy mudstone (>2 m thick) containing ubiquitous biogenic clasts and large plastically deformed claystone clasts. The individual clasts exhibit subtle inferred shear laminae. Some of these clasts are larger than the core diameter; thus, some "interbeds" of mudstone in this interval could be parts of large mud clasts. The biogenic clasts include abundant benthic foraminifers. In addition, a clast of nannofossil chalk of Valanginian age, presumably transported in a gravity flow or slump, was identified in interval 210-1276A-3R-1, 13–16 cm. In Sections 210-1276A-7R-1 through 7R-4 there is a 3.5-m-thick disorganized unit that probably represents a single debris flow deposit. The matrix is structureless, poorly sorted sandy mudstone with large benthic foraminifers dispersed throughout (Fig. **F11**).

Diagenesis

A common form of diagenesis is color mottling and reduction halos. Precipitation of authigenic carbonate is widespread, especially in the more calcareous intervals and in some clasts. In addition, small carbonate concretions are rarely present (e.g., interval 210-1276A-8R-2, 100–110 cm).

Weathering conditions on land during the Eocene–Oligocene in the North Atlantic region favored delivery of eroded material with little chemical alteration (Chamley, 1989). The predominantly illite and chlorite composition of the clay minerals is consistent with a continental source such as the adjacent North American continent under a regime of dominantly mechanical weathering.

Some of the grainstones are partly silicified, involving precipitation of both interparticle cement and grain replacement (e.g., interval 210-1276A-3R-4, 47–49 cm). Early opaline cements and opal-CT lepispheres are present, together with later-stage replacement of some grains by finely crystalline chalcedonic quartz (Fig. **F10**). Opaline silica is also widespread in the mudrocks, showing that silicification is widespread throughout Unit 1. The opal-bearing sediments in Cores 210-1276A-6R and 7R contain appreciable amounts of zeolites, which reflect the availability of dissolved silica during diagenesis.

Soft-Sediment Deformation

Syndepositional deformational structures are present in the upper part of Unit 1 and are best developed in the muddy sandstone and sandy mudstone (Fig. **F12**). These structures include normal faults, soft-sediment folds, ductile shear zones (Fig. **F13**), and crenulated convolute lamination (Fig. **F14**). These features are common down to Section 210-1276A-3R-4 but are rare beneath this section. Small conjugate faults and reverse faults (Fig. **F15**) also occur rarely (see **"Structural Geology,"** p. 70). In addition, many of the large clasts are internally deformed. For example, a small shear fold with a subhorizontal axial plane is present in mudstone in a large inferred clast in Section 210-1276A-2R-CC, together with small-scale crenulation lamination. These features resulted from deformation in a semilithified state. It is not always possible to

F11. Sandy mudstone with carbonate granules and mudstone rip-up clasts, Unit 1, p. 134.

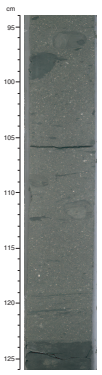

F12. Sandy mudstone with swirled texture, Unit 1, p. 135.

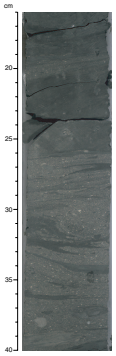

F13. Inferred shear band or deformed clast, Unit 1, p. 136.

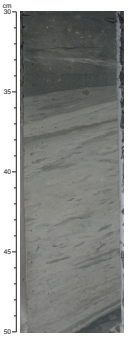

F14. Soft-sediment deformation in the upper part of Unit 1, p. 137.

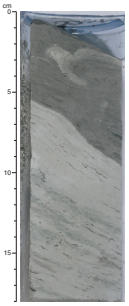

distinguish the deformation affecting clasts from that affecting the matrix of debris flow deposits because some of the apparent interbeds in the cores might be parts of larger mud clasts.

F15. Small reverse fault in graded grainstone, Unit 1, p. 138.

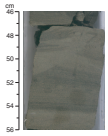

Depositional Processes and Paleoceanography

Unit 1 accumulated in a deepwater setting below the calcite compensation depth (CCD). This setting is inferred from the noncalcareous nature of Unit 1 mudrocks, particularly the dominant burrowed mudstones that are interpreted as hemipelagic sediments (Pickering et al., 1989). The sediments show no obvious evidence of modification by bottom currents (i.e., they lack diagnostic features such as coarsening–fining cycles in bioturbated intervals [Gonthier et al., 1984] or sorted laminae or ripple lenses rich in detrital heavy minerals [Heezen and Hollister, 1971]).

The slow accumulation of hemipelagic sediments was interrupted episodically by turbidity currents that carried mostly carbonate detritus. These gravity flows deposited organized beds containing laminations typical of the Bouma (1962) sequence. Infrequently, more disorganized gravity flows (i.e., debris flows) deposited structureless muddy sands containing large and diverse mudstone clasts and biogenic grains including benthic foraminifers. The mudstone clasts were probably derived from Paleogene and Cretaceous submarine outcrops (e.g., the walls of gullies and canyons in the adjacent continental slope).

Gravity-induced deformation of interlayered muds and unconsolidated debris flow deposits took place after shallow burial. The cause of this postdepositional soft-sediment deformation possibly was rapid downslope gravity emplacement of younger, unsampled deposits. Seismic profiles are consistent with the presence of deformed and redeposited strata ~200 m above the depth at which coring commenced (see the **"Leg 210 Summary"** chapter).

Gentle-slope rather than base-of-slope setting is suggested by the paucity of contractional structures such as reverse faults (cf. Barnes and Lewis, 1991). Little oversteepening at the time of deposition could have occurred because turbidity currents are supercritical on slopes >0.5° (Komar, 1971) and under those conditions cannot form the current ripples so commonly observed in Unit 1.

Unit 2

Interval: 210-1276A-8R-5, 113 cm, through 15R-3, 125 cm
Depth: 864.73–929.25 mbsf
Age: late Paleocene–middle Eocene
Lithology: carbonate grainstone and marlstone with subordinate mudrock; finer-grained facies are reddish brown to greenish gray

Unit 2 contains a higher proportion of carbonate-rich lithologies than Unit 1. It consists of ~40% grainstone and calcareous sandstone, ~40% marlstone, and ~20% mudrock (claystone and mudstone). At the top, fine-grained sediments are greenish gray, whereas reddish, brownish, and greenish gray colors predominate for much of the rest of the unit. The contact between Units 1 and 2 is marked by a sharp downhole change in facies and color from the drab greenish gray to brown mudrocks of Unit 1 to light-colored (pale greenish/grayish) grainstone-dominated intervals in Unit 2. The base of Unit 2 is defined at Section 210-1276A-15R-3, 125 cm, at the base of a grainstone bed. Below this, no

more grainstones are present until Section 210-1276A-18R-5, which is well within the underlying Unit 3.

Cores in Unit 2 show a high contrast between very light gray to greenish gray grainstones and much darker mudrocks that are shades of greenish gray (5GY 6/1 and 5GY 4/1) (e.g., Core 210-1276A-9R) (Fig. F16) to a variable reddish brown that appears in Core 10R and persists downhole (5YR 4/4 and 10R 4/6) (e.g., Cores 10R and 15R). Associated marlstones are darker than grainstones but lighter than mudrocks.

Graded, sharp-based beds of grainstone → marlstone are dominant in Unit 2. These beds are 20–140 cm thick and are overlain by darker-colored burrowed mudrocks. Some beds have a graded but otherwise structureless base. Sedimentary structures above the base are predominantly planar and have cross lamination. Burrows rarely cut the laminated grainstones. Instead, traces of deposit feeders are restricted to bed tops in marlstone or mudrock. Physical sedimentary structures are arranged into partial Bouma sequences, supporting the interpretation of these graded beds as turbidites. However, not all sequences of sedimentary structures follow the pattern reported by Bouma (1962). Specifically, some beds show reversals and repetitions of planar-laminated and ripple-laminated divisions. The proportion of Unit 2 formed by carbonate turbidites varies from ~70% at the top (Core 210-1276A-9R) to ~25% in the middle (Core 11R) to ~65% near the base (Core 14R). Large-scale trends in bed thickness or grain size appear to be absent.

Values of $CaCO_3$ in Unit 2 are <5–10 wt% in dark-colored mudrocks and >30 wt% in grainstones (see **"Carbonate and Organic Carbon,"** p. 96, in "Geochemistry"). Several grainstone samples exceed 60 wt% $CaCO_3$, with a maximum value of ~90 wt% in cemented grainstones. TOC is mostly <1 wt%, but two samples contain significantly higher amounts: 2.42 wt% in a burrowed claystone (Sample 210-1276A-11R-6, 0–5 cm) and 4.06 wt% in a coarse grainstone that has locally visible plant debris (Sample 14R-2, 0–1 cm). Carbonate detritus in the grainstones includes foraminifers, red algae, bryozoans, echinoderms, ostracodes, and mollusks.

Lithologies

Grainstone, Calcareous Sandstone, and Minor Carbonate Granule Conglomerate → Marlstone

Graded beds of grainstone (or calcareous sandstone) → marlstone dominate Unit 2. Greenish to grayish (5GY 6/1–5GY 4/1) calcareous grainstones are fine and medium grained to rarely coarse grained throughout Unit 2 (Fig. F17). The thickness of individual beds ranges from several centimeters to as much as ~1 m. Most of the grainstones begin with a sharp, scoured base (Fig. F18), ornamented in one case by possible flute casts. Above the basal scours are coarse to medium, mainly carbonate grains in a rock with a minor amount of mud matrix (Fig. F19). Scattered larger grains, several millimeters in size, commonly include micritic carbonate, green glauconite, flattened claystone rip-up clasts, and benthic foraminifers. The grainstone beds grade upward from medium to fine sand, through mud-supported silt-sized carbonate, and finally into marlstone or calcareous claystone at the top (e.g., Section 210-1276A-9R-1, 30 cm, through 9R-2, 72 cm). The critical observation is that these normally graded units (grainstone → marlstone → calcareous mudrock) are single-event deposits that were subsequently burrowed when organisms recolonized the seabed.

F16. Repeated graded intervals, Unit 2, p. 139.

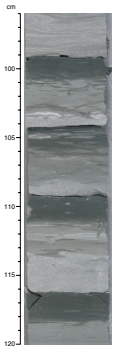

F17. Typical normally graded intervals, Unit 2, p. 140.

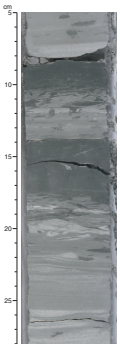

F18. Typical graded grainstone, Unit 2, p. 141.

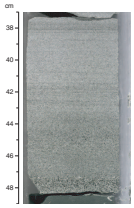

F19. Medium- to fine-grained, graded carbonate grainstone, Unit 2, p. 142.

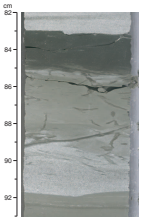

The graded intervals of sand-sized sediment exhibit planar and small-scale cross lamination (Fig. F20). Typically, the cross lamination is present toward the tops of individual graded units. By contrast, especially near the base of Unit 2, some grainstones exhibit relatively sharp tops as well as bases or they are essentially ungraded (e.g., Core 210-1276A-14R). In addition, the lower part of Unit 2 includes rare sets of inclined laminae and cross laminae that are contorted and folded (interval 210-1276A-14R-2, 10–30 cm). Near the top of Unit 2, there is a compacted and therefore folded grainstone dike (Fig. F21). Other small injections are present in the unit. These cannot be confused with burrows because they extend back into the core face as now-folded, but originally planar, sheets of grainstone.

Several of the grainstones exhibit unusual features. In one instance, a single amalgamated bed of grainstone is interpreted as 10 separate depositional events (interval 210-1276A-9R-1, 30 cm, through 9R-2, 104 cm). The thickest grainstone deposited during one event in this interval is inversely graded in its lowest 7 cm from coarse sand to granules. Scattered well-rounded granules and centimeter-sized rounded to subrounded pebbles are present in its coarsest sediments. These include shale clasts, sandstone clasts, pebbles of algal limestone, rare bivalve fragments, and metamorphic fragments (Fig. F22). From the top of the inversely graded sediment, the deposit grades normally upward to very fine sand at the top, just beneath the next surface in this multievent depositional unit.

An interesting deposit of calcareous sandstones and granule-sized calcareous conglomerates is present near the base of Unit 2 in Core 210-1276A-15R. The calcareous sandstones are fine grained to very coarse grained, moderately to poorly sorted, and range from structureless to planar and current-ripple laminated. This interval represents another amalgamated bed formed of separate depositional units that range from graded stratified beds to disorganized deposits with large deformed mud clasts (Fig. F23). These deposits contain "swirled" laminae and "shear" laminae indicative of syndepositional deformation of near-fluid, water-rich sediment (Figs. F24, F25). The thinner-bedded calcareous sandstones in Core 210-1276A-15R are graded and interbedded with burrowed mudstones.

Petrographic analysis shows that the clasts in the grainstones are dominantly fragmented to whole benthic and planktonic foraminifers with lesser (and variable) amounts of red algae, sponge spicules, radiolarians, ostracodes, phosphatic grains, and fragments of mollusks, bryozoans, and echinoderms (Figs. F26, F27, F28). The bioclasts have undergone some compaction and pressure solution, and they are locally cemented by interparticle and intraparticle carbonate. There is minor replacement of carbonate grains by chert. Noncalcareous, nonbiogenic components (<20%) are dominantly quartz with rare to trace amounts of pelletal glauconite, feldspar, mica, heavy minerals, and rock fragments including metamorphic, sedimentary, and volcanic varieties. The quartz grains range in shape from rounded to angular.

The calcareous sandstones contain a diverse suite of metamorphic and sedimentary lithic fragments and bioclastic debris. These mixed sediments also contain a significant proportion of biogenic carbonate grains, including benthic and planktonic foraminifers as well as other bioclasts. The calcareous sandstones in Core 210-1276A-15R were partly derived from felsic to mafic volcanic rocks, as inferred from the presence of large numbers of euhedral crystals that are likely to be volcanic quartz, unstrained tabular biotite, and altered

F20. Cross lamination with dark laminae, Unit 2, p. 143.

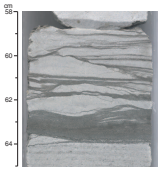

F21. Middle Eocene unconformity and sedimentary dike, top of Unit 2, p. 144.

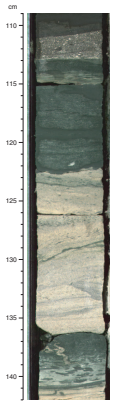

F22. Scattered granules and pebbles in grainstone, Unit 2, p. 145.

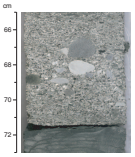

F23. Graded conglomerate → grainstone → sandstone, base of Unit 2, p. 146.

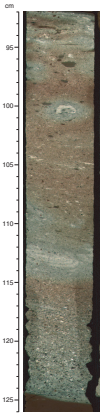

volcanic glass of felsic to intermediate composition (Fig. F29). Nannofossils were extracted from small micritic carbonate clasts in the coarsest-grained calcareous sandstones. Some of these clasts were found to be contemporaneous with the Paleogene age of Unit 2, whereas other clasts were derived from Upper Cretaceous carbonate rocks.

Marlstone

Marlstones are the second most abundant component of Unit 2. The marlstones are dominantly reddish to brownish; however, moderate reddish brown (10R 4/6), brownish gray (5YR 4/1) to grayish red (10R 4/2), olive gray (5Y 4/1), light olive gray (5Y 5/2), and greenish gray (5GY 6/1) hues were recorded. The main calcareous components are nannofossils, bioclastic debris, and micrite. Noncalcareous components are mainly clay minerals plus silt- to sand-sized minerals and rock fragments similar to those in the mudrocks and grainstones.

Locally, the marlstones are moderate reddish brown (10R 4/6), contain thin laminae of grainstone (e.g., Section 210-1276A-12R-4), and exhibit a vague planar lamination defined by silt grains (e.g., Core 13R). This variety of marlstone is moderately burrowed, with local greenish burrow mottling attributed to diagenetic reduction processes. A few intervals of marlstone are strongly burrowed, with grainstone filling the burrows (e.g., interval 210-1276A-13R-1, 120–130 cm). In places (e.g., Core 210-1276A-13R), very thin bedded (<5 cm) claystones and grainstones are interbedded with the marlstone. Marlstone from interval 210-1276A-12R-1, 13–16 cm, yields nannofossils indicating an Early Cretaceous (Valanginian) age, and it must be a sedimentary clast rather than in situ sediment.

Mudrocks (Mudstone and Claystone)

Mudrocks form ~20% of the unit. They are interbedded with other lithologies on a scale of tens of centimeters or are present as longer massive or planar-laminated intervals with gradational changes to other lithologies above and below (Core 210-1276A-10R). There is considerable variation in the intensity of burrowing, from rare to common (Fig. F30). Mudrocks are dominantly greenish gray down to Core 210-1276A-9R but are mainly reddish brown below. Some mudstones contain scattered plant debris (e.g., interval 210-1276A-14R-2, 45–60 cm). Burrows filled with claystone penetrate downward into the tops of several mudstone intervals.

Claystones in Unit 2 are slightly calcareous and greenish gray (5GY 6/1). They are mostly massive to slightly burrowed with scattered white silt grains composed mainly of carbonate (e.g., Core 210-1276A-10R). In Core 210-1276A-12R, indistinct planar lamination is visible where the sediment is not too bioturbated; in Section 12R-2, there is a marked downhole change to varicolored claystone ranging from moderate reddish brown (10R 4/6) to light olive gray (5Y 6/1), with subtle color variations. Thin section examination reveals biogenic components (e.g., nannofossils), quartz, and authigenic zeolites in addition to terrigenous clay.

XRD studies of the mudrocks (mudstones, claystones, and some marlstones) reveal mainly quartz plus a variable, generally minor contribution of plagioclase and alkali feldspar. Opal-A and opal-CT are locally abundant, together with zeolite (clinoptilolite). The clay minerals comprise abundant smectite; subordinate kaolinite, chlorite, and

F24. Deformed clastic sediments near the base of Unit 2, p. 147.

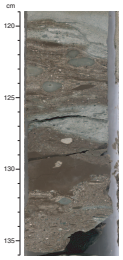

F25. Synsedimentary folding and shearing, base of Unit 2, p. 148.

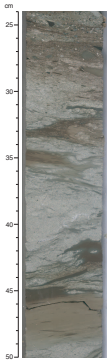

F26. Grainstones near the top of Unit 2, p. 149.

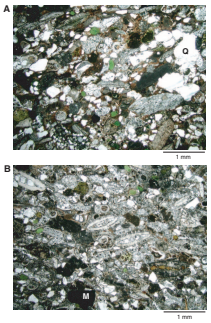

F27. Grainstones, Unit 2, p. 150.

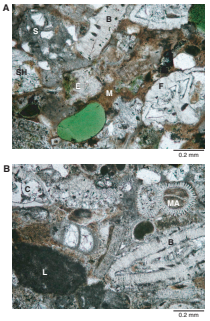

mixed-layer clays; rare illite; and a single occurrence of possible palygorskite.

Chemical analysis of the mudrocks from Unit 2, including some marlstones and silty mudstones (Table T4), shows that most are within the compositional range expected for variably calcareous hemipelagic sediments. However, about half of the samples from the lower part of the unit are relatively enriched in Al_2O_3 (to 15.72 wt%), TiO_2 (to 1.96 wt%), MgO (to 3.26 wt%), Ni (to 125 ppm), Cr (to 107 ppm), and Zr (to 745 ppm) compared with the average composition of hemipelagic sediments. Smear slides indicate the presence of abundant silt and quartz in these intervals, whereas XRD analysis of the same levels (e.g., Sample 210-1276A-12R-3, 30–32 cm) reveals the presence of zeolite, goethite, quartz, alkali feldspar, plagioclase, and calcite, plus the clay minerals listed above. SiO_2 values reach 71.10 wt% in Sample 210-1276A-14R-1, 39–42 cm. $CaCO_3$ in the mudrocks is mostly >1 wt%, and the marlstones contain as much as 44.4 wt% $CaCO_3$. TOC values are uniformly low (<0.25 wt%) in the fine-grained sediments analyzed.

Diagenesis

Both physical and chemical diagenetic effects are present. Burrows and small shale clasts are markedly flattened as a result of compaction (Fig. F31). The coarser grainstones contain a fine calcite-spar cement (Fig. F28). Other than cementation, chemical diagenesis is mainly reflected in oxidation-reduction effects. In pale greenish gray grainstones in Core 210-1276A-13R, there are several examples of subhorizontal or anastomosing dark greenish gray (5GY 4/1) seams (several millimeters thick) defined by colors indicative of clay or reduced iron (Fig. F32). These anastomosing greenish seams can be interpreted as protostylolites that are precursors to better-developed stylolites lower in the succession. The reddish marlstones are locally reduced to a greenish color where they are in contact with grainstone (e.g., Core 210-1276A-12R). Elsewhere, in Core 210-1276A-9R, brownish claystones have been chemically reduced in irregular fashion to a greenish color. Also, two brownish black layers that may represent strong oxidation are present in interval 210-1276A-15R-5, 38–90 cm.

Structure

Unit 2 contains rare soft-sediment faults with small offsets plus other postlithification brittle structures. For example, an extensional normal fault with ~2-cm displacement is present in interval 210-1276A-9R, 96–105 cm. Rare examples of soft-sediment folding were noted in the coarser-grained facies (Fig. F33). An unusual coarse-grained calcareous sandstone to granule conglomerate exhibits small, relatively low angle (30°) normal and antithetic faults in addition to soft-sediment folding (Fig. F34).

Depositional Processes, Paleoceanography, and Sediment Provenance

Unit 2 is characterized by deepwater hemipelagic deposition below the CCD, interrupted by abundant displaced calcareous and siliciclastic sediments. Calcareous turbidites dominate the upper part of the unit, whereas siliciclastic turbidites are more common in the lower part. Marlstones are interpreted as fine-grained sediment that was deposited

F28. Carbonate-cemented grainstone, Unit 2, p. 151.

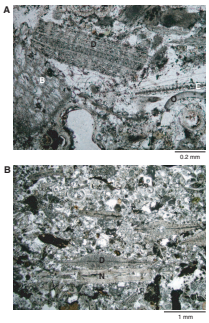

F29. Volcaniclastic sediment, base of Unit 2, p. 152.

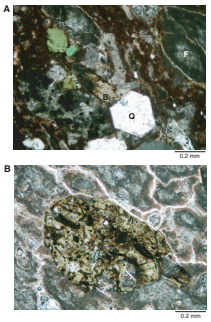

F30. Burrowed, lenticular sandstones, Unit 2, p. 153.

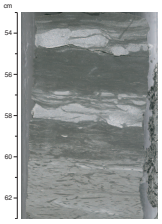

F31. Differential compaction of burrows, Unit 2, p. 154.

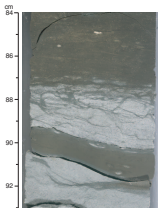

by low-density gravity flows or from low-density tails of turbidity currents that were also carrying carbonate sand. Most of the beds in the lower part of the unit were also deposited from discrete turbidity currents, but composite units, such as those in Core 210-1276A-15R, are interpreted as a succession of deposits from repeated pulses of high-density turbidity currents. Local reverse grading indicates grain interaction during deposition as a consequence of high suspended-sediment concentrations (Middleton and Southard, 1984). Liquefaction in one case induced grainstone injection downward into underlying fine-grained sediments (interval 210-1276A-8R-5, 133–141 cm) (Fig. F21).

The bioturbated calcareous claystone tops of the turbidites formed during times of slow deposition between gravity flows. Marked variations in the color of these claystones (grayish and greenish to reddish) might indicate differences in the extent of seafloor oxidation. Occasional thin to medium beds of massive claystone are interpreted as deposits from discrete mud-laden turbidity currents. These are comparable to the "unifites" originally described by Stanley (1981) from the Mediterranean Sea.

The main sources of redeposited sediments were weakly lithified siliciclastic and carbonate sediments of late Mesozoic and contemporaneous Paleogene age, located upslope on the continental margin. Dispersed Mesozoic and Paleogene microfossils appear to have been reworked from poorly lithified intervals of the original successions. In the lower part of Unit 2, siliciclastic detritus in the turbidites is relatively more abundant than carbonate detritus. The siliciclastic components in the turbidites were derived mainly from a basement terrain, probably composed of Precambrian to Paleozoic igneous and metamorphic rocks from Newfoundland or the adjacent Atlantic continental margin (Grant and McAlpine, 1990). However, other potential source areas to the north or east cannot be ruled out. The smectite mineralogy of the fine-grained sediments as determined by XRD is consistent with derivation from the adjacent Atlantic margin at a time during the Paleocene–Eocene when the climate was relatively warm and humid (Chamley, 1989). The major and trace element composition, with relatively abundant Al, Ti, Mg, Cr, and Ni, indicates the presence of a significant terrigenous input. The local co-occurrence of opal-A, opal-CT, and zeolite (clinoptilolite), together with relative enrichment in silica, is indicative of a reactive setting of silica diagenesis and the potential onset of chert formation.

The calcareous sandstones also contain rare felsic and mafic volcanic detritus. The most likely source is the nearby continental margin, including the Cretaceous Newfoundland seamounts. The known volcanism in these seamounts is mafic (Pe-Piper et al., 1990), whereas the volcanic detritus at Site 1276 includes material of silicic composition. A possible alternate source, albeit one that would require long-distance transport, could be the Greenland-Scotland margin, which was then rifting (Saunders et al., 1997). It is also possible that an as-yet-undiscovered source of bimodal volcanism exists on the adjacent Newfoundland continental margin.

Unit 3

Interval: 210-1276A-15R-3, 125 cm, through 25R-5, 80 cm
Depth: 929.25–1028.00 mbsf
Age: earliest Campanian–late Paleocene

F32. Alternating darker and lighter seams in a grainstone turbidite, Unit 2, p. 155.

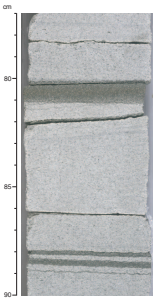

F33. Soft-sediment folding in a coarse grainstone, Unit 2, p. 156.

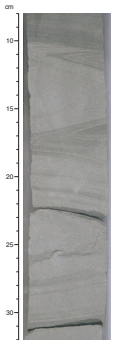

F34. Strongly deformed interval, base of Unit 2, p. 157.

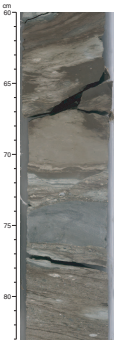

Lithology: mainly reddish mudstone and claystone with subordinate light gray grainstone and calcareous sandstone

Unit 3 is dominated by reddish mudstone and claystone (mudrocks), which together account for ~80% of the succession. Mainly grayish grainstone and calcareous sandstone, taken together, form ~10% of the unit, much less than in Unit 2. The remainder consists of minor amounts of marlstone (~5%), calcareous siltstone (~3%), and sandy mudstone (~2%). From the top to the base of Unit 3, the proportion of grainstone and marlstone increases at the expense of mudrock (Fig. F6). Grainstone constitutes ~20% of the lower part of the unit. The upper contact of Unit 3 is placed at a sharp downhole change from coarser-grained sediments above (Unit 2) into much finer-grained and muddy rocks. The lower contact of Unit 3 is placed at the base of a thick grainstone bed at Section 210-1276A-25R-5, 80 cm (Fig. F6). Below are reddish brown sandy mudstones of Unit 4.

Mudrocks in Unit 3 are predominantly reddish brown (Geological Society of America Rock Color Chart color codes and details are given in "Lithologies," p. 32) (see "Site 1276 Visual Core Descriptions"). Cores 210-1276A-15R, 22R, and 23R are entirely reddish brown. Cores 210-1276A-19R, 20R, 24R, and 25R contain gray mudrocks with a definite reddish cast or a mixture of light gray and reddish brown. Cores 210-1276A-16R through 18R and 21R are the only cores that do not have a reddish hue.

Only ~15% of Unit 3 is moderately to strongly burrowed. Some mudrocks and all of the muddy sandstones are burrowed. They accumulated slowly and were effectively reworked by deposit-feeding organisms. The remainder of Unit 3 is predominantly mudrock and consists of a wide variety of graded, mud-dominated gravity-flow deposits. Most of these deposits (~75%) begin with a grainstone or calcareous sandstone base that is generally planar laminated and rests sharply or erosively on underlying mudrock. The other gravity-flow deposits (~25%) have a similar laminated basal division that is composed of coarse calcareous siltstone.

Both types of gravity-flow deposit, whether grainy or silty at the base, grade upward into a generally thick mudstone to marlstone top and, in some cases, into claystone at the very top. These graded units can be as thick as ~2 m. The thickest examples are characterized by syndepositional deformation produced by rapid accumulation, differential loading in undercompacted sediments, and shearing (see below for details). Burrowing is restricted to the uppermost few tens of centimeters of these deposits, confirming their emplacement as single, large gravity-flow deposits. Grading and tractional structures indicate that they are mud-dominated turbidites. Clearly, the thick, mud-dominated turbidites accumulated at much higher short-term rates than the intervening burrowed mudrocks. Nevertheless, the overall sedimentation rate of the unit is low (~4–6 m/m.y.) (see "Biostratigraphy," p. 73). There is an interval of very slow sedimentation in Core 210-1276A-22R (perhaps <1 m/m.y.) that is discussed separately below.

Values of $CaCO_3$ in Unit 3 are mostly <15 wt% (see "Carbonate and Organic Carbon," p. 96, in "Geochemistry"). Peak values of 25–30 wt% occur above 970 mbsf, whereas three values in the range of 35–85 wt% occur from that point to the base of the unit. The highest values are found in marlstone and grainstone. TOC is mostly <1 wt%. The only anomalous sample, from the marlstone top of a >1-m-thick gravity-flow deposit, has 6.65 wt% TOC (interval 210-1276A-21R-2, 123–124 cm).

Calcareous detritus in the grainstones and calcareous sandstones includes foraminifers, carbonate lithoclasts, and fragments of echinoderms, ostracodes, and mollusks. The terrigenous fraction includes quartz, feldspar, micas, glauconite, and heavy minerals.

Lithologies

Mudrocks

Mudrocks, estimated at 80% of the total recovery, are predominantly mudstone. There are only minor amounts of claystone, calcareous claystone, marlstone, and sandy mudstone, which are treated in this section for the sake of brevity.

The mudstone is dominantly reddish but ranges from olive black (5Y 2/1) to grayish yellow green (5GY 7/2), dark greenish gray (5GY 4/1), light olive gray (5Y 6/1), light brown (5YR 5/4), and moderate brown (5YR 3/4) (Fig. **F35**). It has calcareous components that are mainly nannofossils, with minor foraminifers and micrite. The silt fraction is dominated by quartz, with lesser mica, feldspar, glauconite, organic (plant) matter, rock fragments, heavy minerals, and fish debris. The brownish mudstones have rare iron oxides.

The mudstones are devoid of lamination apart from occasional pale silty stringers. A common pattern is a sharp-based olive-gray (5Y 4/1) or light gray (N7) calcareous siltstone, grading upward into dark greenish gray (5GY 4/1) burrowed mudstone, which is topped by pale olive (10Y 6/2) calcareous mudstone or marlstone.

In the lower part of Unit 3, as seen in Core 210-1276A-21R, the mudstones form subtly graded intervals as much as 10 cm thick, each overlying a thin basal set of sand or silt laminae. Burrowing is restricted to the upper parts of the muddy tops of these units. In Cores 210-1276A-22R and 23R, minor intervals of mudstone are planar laminated, with little or no burrowing. In places, as in Core 210-1276A-23R, the mudstones are marked by greenish gray (5GY 6/1) bands that are ~1 cm thick, inferred to be chemically reduced during diagenesis. In Cores 210-1276A-23R through 25R, massive or parallel-laminated mudstone includes numerous siltstone laminations.

Burrowing ranges from occasional mud-filled burrows to intense bioturbation. Throughout Core 210-1276A-22R, many intervals are spectacularly burrowed by *Zoophycos* (Figs. **F36, F37**). This core is unusual relative to the rest of Unit 3 both for its *Zoophycos* traces and because it contains a significant proportion of sandy mudstone. Careful micropaleontological work has subsequently indicated that the sedimentation rate in this core is very low. Core 210-1276A-22R likely includes the entire Maastrichtian interval (see **"Biostratigraphy,"** p. 73).

The subordinate claystones and calcareous claystones of Unit 3 are dominantly reddish, although strictly they range from moderate brown (5YR 4/4), olive black (5Y 1/2), grayish yellow green (5GY 7/2), and grayish green (5G 5/2) to light olive gray (5Y 5/2). They form a subordinate but variable part of the unit (e.g., Fig. **F38**). The reddish to brownish colors reflect the presence of minor iron oxides. Beneath Core 210-1276A-18R, only minor claystone is present (e.g., in Core 24R).

There are minor amounts of weakly to (locally) strongly burrowed marlstone throughout Unit 3, ranging from pale green (10G 6/2) to light brown (5YR 6/4). These sediments are typically present in the normally graded depositional units described above (Figs. **F39, F40**).

XRD analysis of the fine-grained sediments reveals abundant quartz and calcite, together with rare but locally abundant plagioclase and po-

F35. Dark silty mudstone with *Chondrites* traces, Unit 3, p. 158.

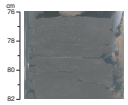

F36. *Zoophycos* burrows overprinted by diagenetic color banding, Unit 3, p. 159.

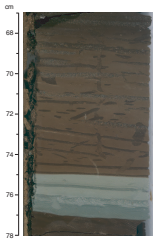

F37. *Zoophycos* burrow system in calcareous mudstone, Unit 3, p. 160.

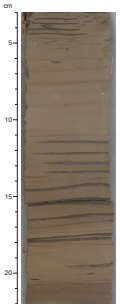

F38. *Chondrites* burrows in calcareous claystone, Unit 3, p. 161.

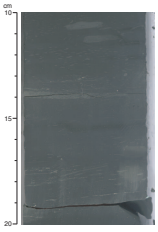

F39. Color-banded marlstone with *Chondrites* burrows, Unit 3, p. 162.

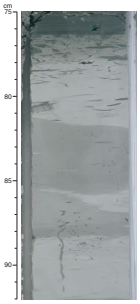

tassium feldspar (including sanidine). Sanidine is found in Core 210-1276A-23R. As in Unit 2, smectite is the dominant clay mineral, but illite and kaolinite increase in relative abundance below Core 210-1276A-20R. Opal was also detected.

ICP-AES analysis (Table T4) reveals major and trace element compositions of the mudrocks that are within the range expected for variably calcareous hemipelagic sediments. However, a few samples of claystones are relatively enriched in TiO_2 (to 1.54 wt%), Fe_2O_3 (to 9.79 wt%), MnO (to 0.29 wt%), Zr (to 586 ppm), and Cr (to 104 ppm) (e.g., Sample 210-1276A-22R-3, 91–93 cm). Smear slides of these sediments are rich in quartz, alkali feldspar, plagioclase, and calcite; thus, a correlation of this enrichment to terrigenous source rocks is likely. Several other samples exhibit relatively high values of SiO_2 (to 89.90 wt%) (e.g., Sample 210-1276A-17R-7, 24–28 cm) that may indicate silica diagenesis in these rocks, which is consistent with the XRD results. The "background" fine-grained sediments exhibit low values of $CaCO_3$ (<1 wt%) and low values of TOC (<1 wt%), although TOC is 1.10 wt% in one sample.

Grainstone, Calcareous Sandstone, and Calcareous Siltstone

Grainstone has a variety of colors: yellowish gray (5Y 8/1), light greenish gray (5GY 8/1), olive gray (5Y 4/1), light olive gray (5Y 6/1), white (N9), pale olive (10Y 6/2), and light brown (5YR 6/4). It forms ~10% of Unit 3. Beds of grainstone vary in abundance, thickness, and grain size from core to core. The beds are typically tens of centimeters thick, exhibit sharp scoured bases, and grade upward through planar-, cross-, or wavy-laminated divisions into mudstone (or occasionally marlstone) tops (Figs. F40, F41, F42, F43). Most grainstones are devoid of burrowing, but a few contain large cylindrical burrows that may represent the traces of organisms that attempted to escape from the turbidite immediately after its deposition (Fig. F44). Some of the grainstones are as much as several meters thick and contain unusual soft-sediment deformation and load structures. The thickest such graded bed is in Sections 210-1276A-25R-2 through 25R-4 (Fig. F45). In a thick graded bed in Sections 210-1277A-18R-5 through 18R-6, the bed grades rapidly from a sandy lower part to a thick silty/muddy top (Fig. F46). The sandy basal part of the bed is succeeded upcore by contorted laminae and zones of soft-sediment deformation ("load balls") (Fig. F47).

Based on thin section examination, the grainstones contain mainly carbonate clasts, commonly accompanied by glauconite. There is a variable siliciclastic component, especially near the base of the coarser-grained units (e.g., in Core 210-1276A-21R). Exceptionally, small rip-up clasts are present (e.g., at Section 210-1276A-24R-2, 67 cm). Carbonate components include reworked Maastrichtian (globorotalid) foraminifers (Fig. F48A) along with other mainly planktonic forms. Additional bioclasts are fragments of echinoderms, ostracodes, mollusks, sponge spicules, radiolarians, and fish debris (Fig. F48B). The percentage of reworked vs. contemporaneous bioclastic debris could not be determined. Fecal pellets and transported carbonate clasts (intraclasts) are concentrated locally. Rock fragments, where present, are mainly sedimentary (e.g., micritic limestone and claystone), with only minor metamorphic and volcanic varieties. Authigenic cements and grain replacements include carbonate, chert, and pyrite.

Throughout Unit 3, the siliciclastic component is sufficiently high (to >50%) that the coarser beds can be classified as calcareous sandstone. The calcareous sandstones are mainly gray (yellowish gray [5Y 8/

F40. Carbonate grainstone → marlstone turbidite, Unit 3, p. 163.

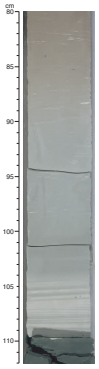

F41. Base of a granule-grade turbidite, Unit 3, p. 164.

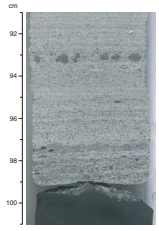

F42. Grainstone turbidite, Unit 3, p. 165.

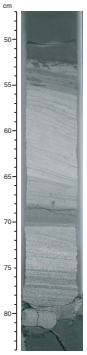

F43. Core photograph and CT scan of grainstone, Unit 3, p. 166.

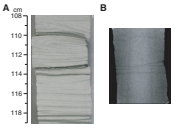

1], light greenish gray [5GY 8/1], olive gray [5Y 4/1], and light olive gray [5Y 6/1]) to greenish gray (5GY 6/1), similar to the grainstones of Unit 3. Individual sandstones exhibit scoured bases and grade from medium- to fine-grained sandstone with a mudstone top (Figs. **F49, F50**). Most of the sandstones are unburrowed, but a few are moderately burrowed. Where present, the burrows are filled with fine-grained mudstone or fine siltstone. The medium-grained to fine-grained sandstones contain scattered coarser grains, commonly white mica or glauconite. The siliciclastic components are subrounded to angular quartz, feldspar, mica, pelletal glauconite, and heavy minerals. In addition, physical property measurements highlighted a thin interval in Section 210-1276A-15R-4 that is characterized by high magnetic susceptibility. This was found in thin section to be caused by an enrichment in magnetite grains (Fig. **F51B**). Volcaniclastic detritus was identified in the same interval (Fig. **F51A**) and in one siltstone near the base of Unit 3 (Fig. **F52**).

Siltstone and calcareous siltstone form a minor part (<5%) of Unit 3, especially toward the base. Calcareous siltstones are most commonly light olive gray (5Y 5/2) to light brown (5YR 5/4), in contrast to the slightly paler colors of the grainstones. The siltstones occur in two main forms. First, they form the middle to upper parts of discrete graded beds, confined between intervals of fine-grained, graded grainstones and sandstones beneath and calcareous mudstone above. Occasionally, the siltstone divisions of thick, graded grainstones show anastomosing laminae interpreted to have been formed by soft-sediment shearing coupled with compaction effects (Fig. **F53**). Second, some calcareous siltstones form discrete thin beds or laminae at the base of graded siltstone–mudstone couplets as thick as several centimeters. The thicker siltstone interbeds mainly exhibit sharp bases (e.g., Core 210-1276A-20R). Laminae are sharp based; some grade upward, typically into mudstone (e.g., Core 210-1276A-23R). Down to Core 210-1276A-20R, siltstones compose only a few percent of the succession but are relatively more abundant beneath this. In addition, there are several thin (<20 cm) intervals of sandy siltstone (e.g., Core 210-1276A-16R) to massive siltstone (e.g., Core 20R). These are mainly devoid of burrowing, especially where they form parts of graded, inferred gravity-flow deposits (see below). Some otherwise structureless siltstones and muddy siltstones contain *Chondrites* burrows.

Cretaceous/Tertiary Boundary Interval

From detailed micropaleontological study, the K/T boundary was identified in Section 210-1276A-21R-4, between 41 and 49 cm (see **"Biostratigraphy,"** p. 73) (Fig. **F54**). From a sedimentological point of view, Section 210-1276A-21R-4 is fairly typical of Unit 3 above and below. It is characterized by interbedded mudstones, marls, and graded fine-grained sandstones with planar and cross lamination, interpreted as turbidites. However, in the intervals 210-1276A-21R-4, 41–47 cm, and 57–75 cm, there are two anomalous silty mudstone intervals that coarsen upward to a sandy top. The upper interval contains scattered sand and granule grains at 41 cm, including opaline silica granules that apparently replace biogenic carbonate. Such distinctive upward-coarsening mudstones are out of sedimentary context with the adjacent rhythmically bedded hemipelagic and normally graded redeposited sediments. We are presently unable to provide a satisfactory explanation for these inversely graded units. The upper one could be related to a K/T boundary event, but the lower one seems too far removed to be

F44. Grainstone turbidite with large cylindrical burrows, Unit 3, p. 167.

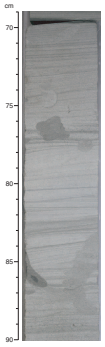

F45. Upper silt- to mud-grade divisions of beds, with wet-sediment features, Unit 3, p. 168.

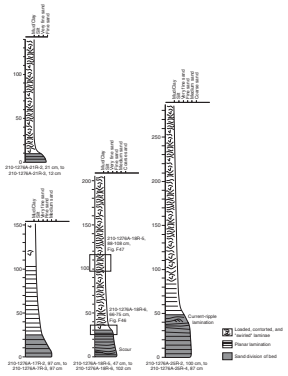

F46. Planar-laminated lower part of grainstone → mudstone turbidite, Unit 3, p. 169.

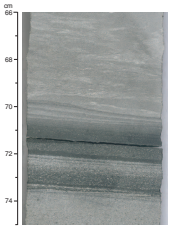

F47. Soft-sediment deformation in a very thick turbidite, Unit 3, p. 170.

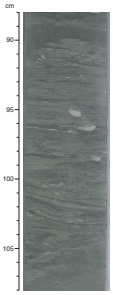

related unless sedimentation rates of the intervening mudrocks were unusually fast.

Diagenesis

An obvious diagenetic feature is the local occurrence of chemically reduced zones and mottles that produce subdued greenish and grayish colors. Diagenetically formed nodules of pyrite are locally present in the black claystone of Core 210-1276A-22R. Several of the graded grainstones exhibit anastomosing, several-millimeter-thick, darker seams of reduced iron or clay minerals (e.g., Fig. F55). These seams are interpreted to partly reflect size sorting of clay-rich aggregates that were later differentially compacted. However, some of the clay-rich seams cut across the primary lamination, showing that some degree of diagenetic dissolution/precipitation of carbonate and clay minerals is likely to be involved. In addition to minor cementation by microspar, some of the grainstones of Unit 3 are characterized by incipient silicification, indicated by the occurrence of chalcedonic quartz and opal-CT lepispheres.

Structure

Rare microfaults are discussed in "Structural Geology," p. 70. In addition, several examples of syndepositional folding, on a centimeter to millimeter scale, are present (Fig. F56).

Depositional Processes, Paleoceanography, and Sediment Provenance

Unit 3 is dominated by burrowed hemipelagic sediments deposited on an oxygenated seafloor below the CCD, interbedded with redeposited carbonate intervals, with an average overall sedimentation rate of ~5 m/m.y. (see "Biostratigraphy," p. 73). The presence of smectite and kaolinite indicates derivation from a warm, humid, deeply weathered landmass (Chamley, 1989). Kaolinite is known to be abundant around the K/T boundary elsewhere in the North Atlantic (Chamley et al., 1988).

Redeposited carbonate bioclasts are abundant in the upper part of the unit and are likely to represent a mixture of contemporaneous and reworked material that is partly of Cretaceous age. The bioclasts are found as isolated grains rather than in lithoclasts; thus, their most likely source was poorly consolidated granular carbonates that were originally deposited in a shelf to upper slope setting. Siliciclastic detritus is more abundant toward the base of the unit and was likely derived mainly from older sedimentary deposits, with a small contribution from igneous and metamorphic rocks. Relative enrichment in Fe, Ti, Mn, Zr, and Cr compared to average hemipelagic sediments may indicate a terrigenous or volcanogenic input, especially near the base of the unit.

The thick, graded beds are interpreted as turbidites with a silty or sandy basal division grading upward into a more calcareous or muddy upper part. Turbulent flow accounts for the grading and the organized divisions of planar and cross lamination. The restriction of burrows to the tops of graded depositional units suggests rapid emplacement. After initial deposition from turbidity currents, the top of each deposit was burrowed in an oxygenated setting. These mud-dominated deposits, particularly those with swirled laminae and load structures in an upper,

F48. Examples of foraminifers, Unit 3, p. 171.

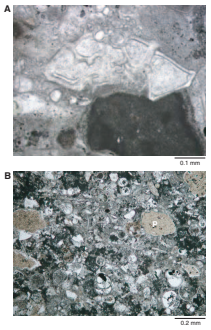

F49. Calcareous sandstone with finely laminated, muddy top, Unit 3, p. 172.

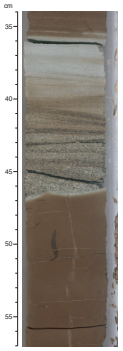

F50. Sandstone turbidite cut by *Zoophycos* burrows, Unit 3, p. 173.

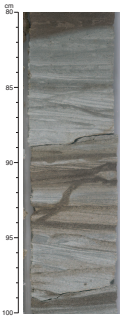

F51. Interval with high magnetic susceptibility, Unit 3, p. 174.

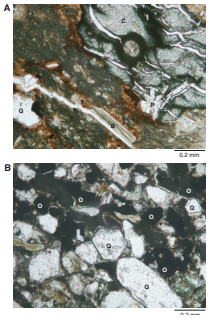

finer-grained division, resemble basin-plain turbidites described by several authors (Skipper and Middleton, 1975; Pickering and Hiscott, 1985; Weaver et al., 1986). Seismic profiles show that the seafloor at Site 1276 during deposition of Unit 3 was relatively flat (see "Seismic-Borehole Correlation," p. 107). We infer, therefore, an essentially featureless basin-plain setting for the deposition of this unit in which mud-laden turbidity currents spread widely and deposited sheetlike, graded units with muddy tops. Between turbidity currents, hemipelagic deposits accumulated slowly on the basin floor.

Unit 4

Interval: 210-1276A-25R-5, 80 cm, through 29R-6, 62 cm
Depth: 1028.00–1067.24 mbsf
Age: Turonian–latest Santonian
Lithology: reddish brown bioturbated muddy sandstone and sandstone

Unit 4 is dominantly siliciclastic, consisting of ~40% muddy sandstone, ~25% sandstone, ~20% mudstone, ~10% sandy mudstone, and ~5% siltstone. Grainstones and marlstones are rarely present. The characteristic sediment color is reddish brown. The coarser-grained rocks—muddy sandstones, sandstones, and sandy mudstones—are thoroughly bioturbated. This characteristic alone distinguishes Unit 4 from all other sediments recovered at Site 1276. Pervasive bioturbation is attributed to favorable environmental conditions (e.g., oxygenation and food supply) and the very slow sedimentation rate of this unit, ~2 m/m.y. or less (see "Biostratigraphy," p. 73). The only unburrowed sediments are infrequent graded beds of siltstone with mudstone tops. Only the uppermost part of each mudstone is penetrated by burrows that originated from the overlying coarser deposits. The lower contact of Unit 4 is defined at the base of the lowest muddy sandstone at Section 210-1276A-29R-6, 62 cm. This contact correlates with an unconformity in seismic profiles (see "Seismic-Borehole Correlation," p. 107).

Values of $CaCO_3$ in Unit 4 are <5 wt% above 1055 mbsf, but they are higher below that depth, with several values in the range of 25–40 wt% in rare grainstones and calcareous mudstones (see "Carbonate and Organic Carbon," p. 96, in "Geochemistry"). TOC is very low, from 0 to <0.4 wt%. The siliciclastic sediments of Unit 4 were derived from terrigenous sources and include clasts of a variety of metamorphic and igneous rocks.

Lithologies

Burrowed Sandstone, Muddy Sandstone, and Sandy Mudstone

Unit 4 is predominantly strongly burrowed, fine- to medium-grained, reddish brown (5YR 4/4, 5YR 5/6, and 5YR 5/2) to grayish (N4 and N6) sandstone, muddy sandstone, and sandy mudstone. Remnants of primary lamination are only locally preserved (Fig. F57). Typically, these sediments exhibit repetitions of well-burrowed and only sparsely burrowed sediment on a decimeter scale. There are also coarsening–fining cycles of similar scale that were not observed in other units recovered in Hole 1276A. Burrow types are diverse in the sandy sediments. The muddy sandstone occasionally exhibits dewatering features (e.g.,

F52. Tuffaceous siltstone, Unit 3, p. 175.

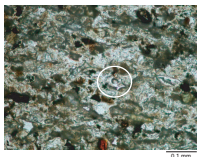

F53. Unusual wavy or wispy lamination in grainstone, Unit 3, p. 176.

F54. Inferred location of the K/T boundary, Unit 3, p. 177.

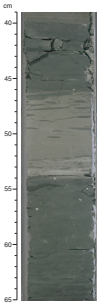

F55. Stylolites in graded grainstones, Unit 3, p. 178.

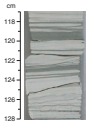

F56. Deformed siltstone laminae, Unit 3, p. 179.

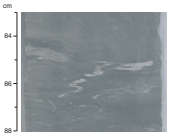

an indistinct vertical dewatering structure in interval 210-1276A-28R-1, 132–140 cm).

The burrowed muddy sandstones and sandstones have dispersed sand- to granule-sized clasts that include a variety of granitic, plutonic, metavolcanic, metasedimentary, and sedimentary lithic fragments. Monomineralic components are quartz, feldspar, muscovite, biotite, and heavy minerals including zircon and tourmaline (Figs. F58, F59). Some radiolarians are present in conjunction with opaline cement. There are rare agglutinated foraminifers (Fig. F60). The matrix mud is similar in composition to the mudstone described below.

Graded Sandstone and Siltstone

There are occasional beds of well-sorted, fine-grained sandstone and siltstone that grade upward to unburrowed mudstone; at the top of these beds is an upward transition to strongly burrowed mudstones. Two of the graded units exhibit a lenticular cross-laminated, medium- to fine-grained sandstone at the base, succeeded by siltstone above a sharp break in grain size (Fig. F61). Such ripple sets are interpreted to represent reworking of the underlying burrowed muddy sand by a turbidity current that then deposited the overlying graded unit. Burrow types are mainly restricted to *Chondrites* in the siltstone and mudstone tops of the graded turbidites.

Detritus in the graded sandstones and siltstones is similar to that in the burrowed sandstones and muddy sandstones, except that there are fewer rock fragments. Petrographic study revealed abundant quartz, glauconite, and other constituents shown in Figure F59. These sandstones are locally cemented by calcite spar. Although the vast majority of coarse sediments in Unit 4 are siliciclastic, there are a small number of medium-grained, glauconite-rich grainstone beds (e.g., in Section 210-1276A-28R-5). These are so minor that they do not warrant a separate heading in this report. The grainstones are white (N9) to moderate brown (5YR 3/4), graded, and contain both planar and cross lamination. In terms of facies, these strongly resemble the graded sandstones described above.

Mudstone

Grayish brown (5YR 3/2) mudstone is present as a minor component throughout Unit 4. Many mudstones form the tops of graded gravity-flow deposits above a basal division of either sandstone or siltstone. Such mudstones are finely laminated to massive. There are also several thin (<5 cm), homogeneous, sharp-based mudstone beds that are only slightly burrowed at their tops by *Chondrites*. Very rarely, muddy sediments are sufficiently calcareous to be termed marlstones (<1% of the recovery), as seen in Section 210-1276A-28R-4. These marlstones replace mudstones in the tops of a few of the graded beds described above. Their carbonate content is mainly nannofossils and minor foraminifers.

The main silt-sized components of the mudstones are quartz, feldspar, muscovite, mica, heavy minerals, glauconite, and organic matter including plant debris. Reddish color in the sediments is caused by the presence of fine-grained iron oxides. Carbonate is dominantly micrite.

XRD analysis shows a predominance of quartz. Calcite is abundant only in the isolated intervals containing grainstones and marlstones. Both plagioclase and alkali feldspar are present in significant amounts. Of the clay minerals, smectite is abundant in the upper part of the unit, above Section 210-1276A-27R-5, but illite (including possible musco-

F57. Typical muddy sandstone, Unit 4, p. 180.

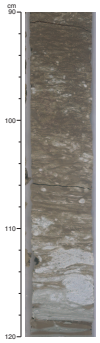

F58. Hematitic sandy mudstone, Unit 4, p. 181.

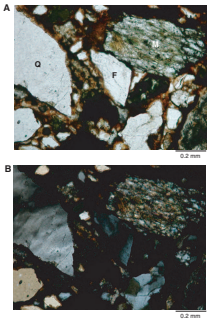

F59. Two siliciclastic intervals, Unit 4, p. 182.

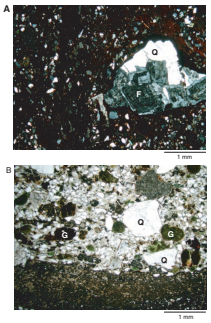

F60. Agglutinated foraminifers, Unit 4, p. 183.

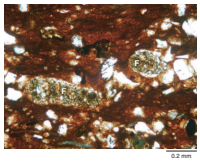

vite) increases in relative abundance beneath this. Kaolinite and chlorite are rare.

Diagenesis

There are a few ~1-cm-thick greenish gray (5GY 6/1) bands where the sediment has been chemically reduced (e.g., Core 210-1276A-28R). In addition, diagenetically controlled mottling and irregular color banding are widespread in both the muddy sandstones and mudstones (e.g., interval 210-1276A-27R-4, 110–133 cm) (Fig. F62). Goethite is more abundant in Unit 4 than in the units above or below, in keeping with the red-brown colors. In addition, manganese minerals are found both as manganite in one concretion and as minor manganese hydroxide layers, based on XRD results.

Depositional Processes, Paleoceanography, and Sediment Provenance

The reddish sediments of Unit 4 correspond to a period of exceedingly slow sedimentation of ~2 m/m.y. or less, depending on how a sedimentation-rate curve is fitted to the biostratigraphic data (see "Biostratigraphy," p. 73). We infer that the deposition of reddish, fine-grained sediments, which are relatively enriched in fine-grained iron oxides (i.e., goethite) and rarely enriched in manganese minerals (i.e., manganese hydroxides), was favored by slow net rates of sediment accumulation and by oxidizing conditions. Slow deposition permitted intense burrowing, destroying almost all primary lamination. The uphole increase in smectite compared to illite and mica is consistent with a change to a warmer, more humid climate in the source landmass (Chamley, 1989).

The style of deposition in Unit 4 is entirely unlike that in Unit 3 (except perhaps Core 210-1276A-22R) and that in the underlying Unit 5 because the bioturbated deposits in Unit 4 are sandy mudstones, muddy sandstones, and, locally, even coarser sandstones. Section 210-1276A-25R-6 even includes dispersed granules of metamorphic and other rock types. In contrast, the finer sediments (siltstones and mudstones) generally represent graded event deposits that are free of burrows, except at their top. We envisage that most of the sand in Unit 4 was initially delivered to the seafloor in small aliquots followed by periods of nondeposition. This provided an opportunity for burrowers largely to rework and mix these sediments with muddy interlayers, so the initial depositional units rarely survived. Gravity flows occasionally deposited thicker beds (as much as tens of centimeters thick) with a sand-silt base and a laminated muddy top. These tops remained unburrowed, perhaps because they were not attractive to burrowing infauna or were only attractive to organisms that fed at shallow levels in the sediment. Locally, incoming muddy gravity flows reworked the tops of muddy sands into a single train of coarse-grained ripples before burying the seafloor with a graded silt to mud layer.

One defining characteristic of the sandy mudstones, muddy sandstones, and bioturbated sandstones in Unit 4 is the presence of gradational coarsening–fining cycles tens of centimeters thick. These strongly resemble the coarsening–fining cycles found in many modern sediment drifts that accumulate under thermohaline currents. These cycles have been explained by bottom-current velocity changes related to long-term variations in the rate of bottom water production or to

F61. Thin, cross-laminated sandstone reworked by turbidity current, Unit 4, p. 184.

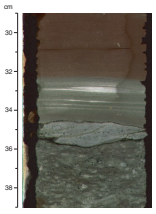

F62. Color banding, Unit 4, p. 185.

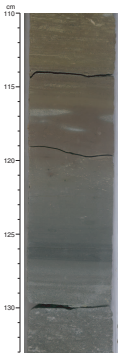

changes in the paths of the currents (Gonthier et al., 1984). The deposits in Unit 4 are much coarser than most modern sediment drifts that have been studied, but there are sandy and even gravelly contourites in Rockall Trough that might be suitable analogs (Masson et al., 2002). Bottom-current redistribution of mixed sandy and silty muds might account for the cycles, and slow accumulation rates can account for the bioturbation.

Unit 4 was deposited near the time of continental breakup and the initiation of seafloor spreading in the Labrador Sea (Srivastava and Verhoef, 1992; Saunders et al., 1997). Perhaps this narrow ocean basin allowed high-latitude waters to spill into the Grand Banks–Iberia corridor, reworking the slowly accumulating sandy sediments of Unit 4. Another possibility is that the inferred bottom currents affecting Unit 4 relate to oceanographic changes as deepwater connections between the North and South Atlantic were established for the first time near the Cenomanian/Turonian boundary (see Sibuet, Ryan, et al., 1979; Tucholke and Vogt, 1979). As a result, there might have been a switch from black shale accumulation (i.e., the underlying Unit 5) in a relatively restricted ocean basin to strongly oxidizing deepwater circulation in a fully interconnected ocean.

The contact between Units 4 and 5 is an erosional unconformity (see **"Seismic-Borehole Correlation,"** p. 107) that could have been created by scouring beneath vigorous bottom currents. Perhaps strong bottom currents first scoured the seafloor and created the unconformity, and then weaker currents permitted accumulation of sandy contourites under oxygenated bottom waters. Currents appear to have waned further toward the top of Unit 4, possibly as a result of changes in paleogeography and flow pathways in the widening ocean basin.

Unit 5

Interval: top: 210-1276A-29R-6, 62 cm; base: 102R-1, 2 cm, through Core 104R (no recovery)
Depth: top: 1067.24 mbsf; base: 1732.12–1736.90 mbsf
Age: latest Aptian–Turonian(?)
Lithology: gray to olive-black sandy to muddy turbidites with lesser burrowed mudrocks, minor debris flows and finely laminated calcareous claystones, and black shales

Unit 5 is the thickest lithologic unit drilled during Leg 210. Its main characteristic is a high proportion of mudrock (mudstone and claystone) and marlstone, which together form 60%–70% of the unit above ~1130 mbsf and 80%–90% or more in deeper cores. There is a variable abundance of coarser-grained redeposited facies that allows a meaningful subdivision of Unit 5. Colors are mainly subdued shades of green, gray, and black. The top of Unit 5 is defined as the base of the lowest occurrence of burrowed sandy mudstone in Unit 4. It extends downhole for 664.88 m to at least the deepest recovery of a diabase sill (Subunit 5C2) at 1732.12 mbsf. The hole is deeper than this—Hole 1276A bottomed at 1736.90 mbsf—but there was no recovery below 1732.12 mbsf.

Subunit 5A is distinguished by an abundance of dark greenish gray gravity-flow deposits plus subordinate, very burrowed olive-gray hemipelagic sediment. In contrast, Subunit 5B is composed of mainly burrowed background hemipelagic sediments that are greenish gray to black plus minor olive-gray to medium gray, slightly coarser deposits from low-density turbidity currents. Subunit 5B includes very finely

laminated, calcareous, carbon-rich sediments (black shales) with TOC abundances of 1.5–4.0 wt%. Subunit 5C, like Subunit 5A, is dominated by thick to very thick, commonly poorly organized olive-gray to medium gray to greenish black gravity-flow deposits, including sandy debris flow deposits and graded beds with abundant syndepositional deformation. It has little true hemipelagic sediment.

Each of Subunits 5A through 5C is summarized below and detailed in subsequent sections. An interpretation of depositional processes and sediment provenance is given after the description of each of the subunits. The clay mineralogy, sediment chemistry, diagenetic processes, and genesis of the black shales are then discussed for Unit 5 as a whole.

Some similarities exist between Subunits 5C and 5A in that most of the sandstones, silty sandstones, grainstones, and mudrocks are present in thick to very thick, graded gravity-flow deposits with planar-laminated bases, syndepositionally deformed transitions from sandstone to mudstone (including load balls, flattened recumbent folds, and sheared-out laminae), and structureless calcareous mudstone tops. Burrows are rarely present in these units and are probably restricted to the escape burrows of buried and trapped organisms. In addition to the graded units with mudstone tops, there are a number of disorganized beds of silty sandstone in Subunit 5C with scattered large sedimentary clasts and sharp bed tops. These are interpreted as sandy debris flow deposits. It is estimated that 80%–90% of Subunit 5C was emplaced by mud-laden turbidity currents or by debris flows; only ~10% is background hemipelagic sediment. One difference between Subunits 5A and 5C is that black shales are more numerous in Subunit 5A, with only rare occurrences in Subunit 5C.

Despite the similarities noted above, the three subunits are somewhat compositionally distinct. Grainstones are present only in Subunits 5A and 5B. The nannofossil content of mudrocks and the foraminifer content of marlstones generally decrease downhole. In the grainstone, sandstone, and siltstone beds of Unit 5, glauconite is much more common in Subunits 5A and 5B, whereas red algal and bryozoan fragments were observed only in Subunit 5C. Lastly, diagenetic carbonate concretions and irregular concretionary layers are present only in Subunit 5B.

Unit 5 accumulated at a relatively rapid rate of 15–100 m/m.y., increasing downhole (see **"Biostratigraphy,"** p. 73). In the intervals dominated by gravity-flow deposits, most of the elapsed time is represented by burrowed hemipelagic mudrocks, even though they account for only a small percentage of the thickness of the succession.

$CaCO_3$ values determined for Unit 5 span a wide range (see **"Carbonate and Organic Carbon,"** p. 96, in "Geochemistry"), consistent with lithologies ranging from noncalcareous claystones to marls, carbonate grainstones, calcite-cemented sandstones, and calcareous black shales, plus several calcareous nodules. Burrowed mudrocks tend to have low $CaCO_3$ concentrations, often <1 wt%, whereas redeposited mudrocks, sandstones, and siltstones have $CaCO_3$ contents occasionally exceeding 50 wt%. Diagenetic nodules have ~80 wt% calculated $CaCO_3$ but are shown by XRD analysis to be siderite and dolomite.

TOC is highest in the calcareous black shales of Subunit 5A, in which many values exceed 6 wt%. The highest TOC value (9.83 wt%) comes from black, very finely laminated marlstone with 49 wt% $CaCO_3$ in Sample 210-1276A-33R-3, 91–95 cm. In Subunit 5B, TOC occasionally reaches 8 wt% in the laminated marlstones of the upper part of the succession and 6 wt% in those of the lower part.

Subunit 5A

Interval 210-1276A-29R-6, 62 cm, through 36R-2, 129 cm
Depth: 1067.24–1129.80 mbsf
Age: Cenomanian–Turonian
Lithology: medium to dark gray calcareous sandstone to mudstone turbidites with lesser burrowed mudrocks and minor black shales, including OAE 2

Subunit 5A occurs between Section 210-1276A-29R-6, 62 cm, and 36R-2, 129 cm (1067.24–1129.80 mbsf). There is a downhole change over a short interval from mainly reddish brown muddy sandstone in Unit 4 to more subdued greens and grays in Subunit 5A. The lower boundary of Subunit 5A is placed where thick, graded gravity-flow deposits pass downhole into extensively burrowed mudrocks with only thin, graded interbeds of grainstone and calcareous siltstone. This boundary is located at Section 210-1276A-36R-2, 129 cm, at the base of a prominent graded grainstone, beneath which mudrocks predominate.

The lithologic proportions in Subunit 5A are ~65% mudrock (both calcareous and essentially noncalcareous), ~20% calcareous sandstone plus minor grainstone, ~10% unlaminated marlstone, and ~5% very finely laminated ("pin-stripe laminated") calcareous claystone and marlstone (i.e., black shales). These lithologies are components of the facies discussed below. The calcareous sandstone, minor grainstone, unlaminated marlstone, and calcareous mudrock form numerous thick depositional units emplaced by mud-dominated gravity flows, and they account for ~80% of the total thickness of Subunit 5A. Individual graded gravity-flow deposits are as thick as 165 cm; many have a marlstone middle division with $CaCO_3$ concentrations of 30–40 wt%. These are interpreted to be the deposits of mud-laden turbidity currents. In addition, minor marlstones that have $CaCO_3$ concentrations of 50–60 wt% and TOC values of as high as 3–4 wt% are recognized as calcareous black shales.

Lithologies

The lithologies discussed below are listed in decreasing order of abundance.

Calcareous Mudstone and Calcareous Siltstone. There are numerous intervals of mainly calcareous mudstone that vary from grayish green (5G 4/1), moderate yellowish green (10GY 7/2), yellowish brown (10YR 5/4), greenish gray (5GY 6/1), to grayish black (N2). The mudstones form intervals as thick as several tens of centimeters that are commonly burrowed. Individual mudstone intervals are sharp-based and marked by a thin interval (several millimeters thick) of laminated siltstone and mudstone at the base, followed above by burrowed or massive mudstone. Individual laminae, where present in the siltstones/mudstones, tend to be spaced several millimeters apart, and on this basis they can be distinguished from more finely laminated black shales (see below).

In addition to dominant clay minerals, the mudstones of Subunit 5A commonly contain quartz, mica, carbonate, heavy and opaque minerals, feldspar, organic debris, rock fragments, and some pyrite. Quartz and mica are more abundant in the siltstones. Calcareous components include micrite and nannofossils.

Graded Sandstone → Siltstone → Mudstone (and Marlstone). Subunit 5A includes numerous continuously graded intervals of calcareous sandstone, siltstone, and calcareous mudstone that mainly range from

light olive gray (5Y 6/1) to greenish gray (5G 6/1). Some of the coarse basal parts of these cycles are rich in carbonate clasts and are termed grainstones (e.g., Cores 210-1276A-32R and 33R). Also, some of the muddy tops of these graded intervals are sufficiently calcareous to be classified as marlstones (e.g., Cores 210-1276A-32R through 34R). Sandstone, siltstone, and grainstone make up ~20% of the recovery of Subunit 5A. An additional indeterminate percentage of the section forms the calcareous mudstone tops of the graded sandstone → siltstone → mudstone (and marlstone) depositional units. These calcareous mudstones (and marlstones) can be distinguished from the background noncalcareous mudrocks only by testing with 10% HCl.

The graded calcareous sandstone to grainstone intervals of the thick gravity-flow deposits are typically several tens of centimeters thick, reaching a maximum of ~1.35 m (Sections 210-1276A-35R-4, 127 cm, through 35R-5, 113 cm). Individual graded sandstones exhibit scoured bases and planar lamination and grade progressively upward to mudstone (Fig. **F63**). Wavy and convolute laminae are locally developed, especially in the medium-grained sand intervals (Fig. **F64**).

The graded units of calcareous sandstone → siltstone → mudstone (or marlstone) are generally devoid of burrows except in the upper few centimeters where burrows are filled with mudstone or claystone from units above. Many of the graded sandstone parts of these units are characterized by alternations of paler and darker laminae. The paler laminae are mainly composed of calcite-cemented siliciclastic material, whereas the dark laminae are rich in clay intraclasts that are typically flattened (Fig. **F65**).

The carbonate fraction of Subunit 5A marlstones is composed of nannofossils with lesser foraminifers and other microcrystalline carbonate. Locally, there are traces of organic matter and authigenic pyrite. The siliciclastic fraction consists of quartz, mica, carbonate, heavy and opaque minerals, feldspar, organic debris, rock fragments, and some pyrite.

Thin section analysis of siltstone and sandstone from Subunit 5A indicates that these samples contain abundant quartz with rare to trace amounts of feldspar, mica, and heavy minerals. Locally, the siltstones are very micaceous. Biogenic components are dominantly foraminifers but include rare fish and organic debris as well as mollusk fragments and other bioclasts. These sediments are pervasively cemented by carbonate microspar. The more calcareous sandstones grade into grainstones that have components similar to those in the sandstones and siltstones, except that they are more enriched in calcareous intraclasts and grains.

Noncalcareous Claystone. Minor amounts of mudrock (~15%) in Subunit 5A are not parts of thick gravity-flow deposits. These mudrocks consist of dark gray (N3) to medium dark gray (N4) to grayish green (5G 3/2) burrowed claystone with variable $CaCO_3$ content that is mostly <2 wt%. These sediments are sporadic throughout the subunit and are interbedded with gravity-flow deposits and black shales. This type of claystone is volumetrically very subordinate to the gravity-flow units, but it is more abundant than black shales.

Laminated Calcareous Claystones to Marlstones, Including Black Shales. There are numerous but volumetrically minor (~5%) very finely laminated claystones in Subunit 5A that are sufficiently enriched in total organic matter (>1 wt%) to be termed black shales (see **"Carbonate and Organic Carbon,"** p. 96, and **"Oceanic and Anoxic Events,"** p. 97, in "Geochemistry"). One of these appears to be OAE 2. Some of the lami-

F63. Graded and laminated sandstone turbidite, Subunit 5A, p. 186.

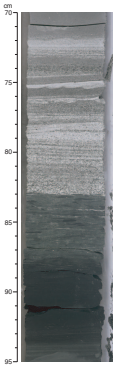

F64. Graded laminated sandstone turbidite with slightly scoured base, Subunit 5A, p. 187.

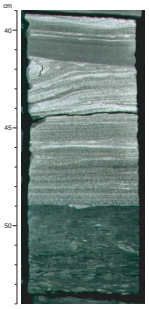

F65. Siltstone turbidite with sharp scoured base and variable lamination, Subunit 5A, p. 188.

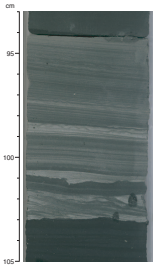

nated intervals contain ~30 wt% carbonate and are therefore marlstones. These distinctive intervals range from several centimeters to tens of centimeters thick. Lighter and darker laminae, each submillimeter to a few millimeters thick, follow each other with extreme regularity. Individual pale laminations are rich in nannofossils, whereas darker laminae are less calcareous and are enriched in organic matter (Figs. F66, F67). Smear slides indicate the presence of terrestrial plant debris, consistent with the results from organic geochemistry (see "Carbonate and Organic Carbon," p. 96, in "Geochemistry"). The siliciclastic fraction of these sediments is similar to the mudrocks described above. Some of the darker laminae include silt. The very finely laminated claystones are completely devoid of bioturbation, except where burrows extend downhole from overlying, paler mudrocks.

Oceanic Anoxic Event 2

OAE 2 was recognized in Sections 210-1276A-31R-3 and 31R-4. Section 210-1276A-31R-3 consists of interbedded dark gray laminated and greenish gray bioturbated mudrocks and minor calcareous sandstones and siltstones (Fig. F68). In this section, black shales are present in intervals 1–17 cm, 19–60 cm, and 74–104 cm. A TOC value of 7.2 wt% was recorded at 52 cm. Preliminary Rock-Eval data suggest these carbon-rich sediments may be rich in algally derived material (see "Oceanic Anoxic Events," p. 97, in "Geochemistry"). These black shales are completely devoid of burrowing. One interval contains a siltstone lamina. Section 210-1276A-31R-4 is similar, with black shales occurring at 44–45 cm, 48–53 cm, 62–70 cm, and 103–108 cm. It should be noted that similar laminated, carbon-rich calcareous sediments are present in adjacent intervals of Subunit 5A, where they are interbedded with mudrocks, sandstones, and siltstones.

Depositional Processes, Paleoceanography, and Sediment Provenance

Subunit 5A is dominated by graded sandstone → siltstone → mudstone intervals that were rapidly emplaced from gravity flows, as suggested by the range of sedimentary structures that include normal grading, scoured bases, planar lamination, convolute lamination, and occasional soft-sediment deformation. Most of these beds grade upward into mudstone that is interpreted to be deposited from the tails of turbidity currents. Similar turbidites are present in both the western Atlantic at DSDP Sites 387 (McCave, 1979) and 534 (Robertson, 1984) and in the eastern Atlantic at DSDP Site 398 (de Graciansky and Chenet, 1979) (see "Comparisons with the Conjugate Iberia Margin and the Western Central North Atlantic," p. 57).

The sandstones and siltstones were derived from a continental area that included metamorphic rocks (e.g., mica schists and quartzite), such as those exposed in Newfoundland and adjacent areas of the Atlantic continental margin (Bell and Howie, 1990). The sandstone and siltstone composition is little different from that of Units 1–4, suggesting that terrestrial provenance did not change significantly with time at Site 1276.

Sharp-based, massive, graded calcareous mudstones are also interpreted to be the deposits of mud-laden turbidity currents. A lack of structures and grading, other than occasional thin basal siltstones, makes it impossible to establish the likely density of these currents. Their calcareous nature, relative to most of the hemipelagic claystones, is attributed to initial accumulation above the CCD as hemipelagic sediments, followed by downslope redeposition to beneath the CCD. Simi-

F66. Very finely laminated carbon-rich claystone (black shale), Subunit 5A, p. 189.

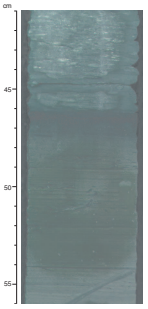

F67. Very thinly laminated claystone and graded facies, Subunit 5A, p. 190.

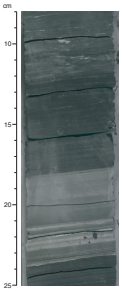

F68. Very finely laminated marlstones (black shales) correlated with OAE 2, Subunit 5A, p. 191.

lar mud turbidites have been described from a range of deep-sea settings (e.g., Pickering et al., 1989; Stow et al., 2001). They are also comparable to unifites, originally described by Stanley (1981) from the Mediterranean Sea and interpreted by him as the record of relatively dense turbidity currents devoid of sand and coarse silt load.

There are also relatively minor bioturbated noncalcareous to weakly calcareous mudrocks (mostly claystone) in Subunit 5A. These are interpreted as background hemipelagic sediments deposited below the CCD.

Subunit 5B

Interval: 210-1276A-36R-2, 129 cm, through 75R-3, 142 cm
Depth: 1129.80–1502.12 mbsf
Age: Albian–Cenomanian
Lithology: medium to dark gray burrowed mudrocks with minor sand- to silt-based turbidites and black shales

Subunit 5B extends from Section 210-1276A-36R-2, 129 cm, to 75R-3, 142 cm (1129.80–1502.12 mbsf). Subunit 5B is 85%–90% mudrock, which is predominantly dark-colored calcareous mudstone to mudstone in the upper part and claystone in the lower part. In addition, there are graded beds of calcareous sandstone and siltstone (~5%) that increase toward the base of the subunit, as well as 5%–10% very finely laminated to subtly planar laminated calcareous, gray-black claystone and marlstone. The base of Subunit 5B is placed at the highest occurrence of underlying (Subunit 5C) disorganized beds that are composed of poorly sorted silty sandstone rich in sedimentary clasts and interpreted as sandy debris flow deposits. Unlike Subunit 5A, the mudrocks in this subunit are almost entirely burrowed or are characterized by subtle planar lamination overprinted by a minor but persistent amount of burrowing. There are occasional diagenetic nodules and concretionary bands of siderite, dolomite, barite, and pyrite. These sediments are interpreted as hemipelagic sediments and mud turbidites rarely interrupted by thin calcareous sandy turbidites. Calcareous, carbon-rich claystones (black shales) in this interval are believed to reflect times of enhanced productivity in surface waters and deposition under anoxic seafloor conditions.

Lithologies

Mudstone and Claystone. Subunit 5B contains a high proportion (85%–90%) of mudrock of subdued colors, ranging from calcareous mudstones to generally less calcareous claystones, with colors from grayish green (5G 4/1), moderate yellowish green (10GY 7/2), and greenish gray (5GY 6/1) to grayish black (N2). Most of the mudstones are essentially homogeneous and well burrowed without much evidence of primary sedimentary structures. However, we stress that a significant proportion of these mudrocks probably is redeposited sediments. Some of the mudstone intervals are sharp-based, marked by an interval of laminated siltstone and mudstone several millimeters thick, and grade upward into mainly burrowed mudstone (Fig. F69).

There are numerous intervals, typically several centimeters to several tens of centimeters thick, composed of greenish (5G5/2) to dark gray (N3) to black (N2) claystones that are commonly carbonate poor (<2 wt%). The greenish claystones are clearly burrowed. In contrast, the dark gray to black beds either lack burrows or show only vague burrow mottling on wet split-core surfaces. These beds are very finely laminated claystones to marlstones that contain 1–10 wt% TOC, and thus they are black shales (Fig. F70) (see

F69. Massive mudstone with siltstone base and overlying claystone, Subunit 5B, p. 192.

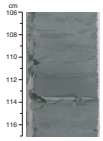

F70. Very finely laminated black shale with planar siltstone laminae and a small siltstone lens, Subunit 5B, p. 193.

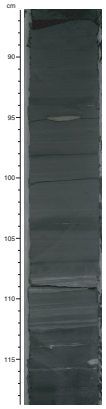

"Carbonate and Organic Carbon," p. 96, and "Oceanic Anoxic Events," p. 97, in "Geochemistry"). The beds are very similar to those described in Subunit 5A (see "Subunit 5A," p. 41) and are relatively few in number. In one case, a black shale is overlain by a brightly colored oxidized interval (Fig. F71) that is comparable to the oxidized tops of Pleistocene sapropels in the Mediterranean Sea (Emeis, Robertson, Richter, et al., 1996).

The claystones and mudstones in Subunit 5B are similar in composition to those in Subunit 5A except that those in Subunit 5B contain foraminifers and slightly more mica. The calcareous mudstones are also similar to those in Subunit 5A and contain carbonate in the form of nannofossils, lithoclasts, bioclasts, micritic matrix, and authigenic cement.

Sandstone → Siltstone → Mudstone and Microconglomerate. There are occasional thin intervals in Subunit 5B of graded sandstone, siltstone, and mudstones as much as tens of centimeters thick (representing <5% of the recovery). Sedimentary structures include planar lamination, cross lamination (Fig. F72), and unusually common convolute lamination (Fig. F73). These intervals are very similar to beds that form a dominant component of Subunit 5A. In addition, there are rare thin (<4 cm thick) beds of sandstone with sharp bases and graded tops, overlain by parallel-laminated sandstone/siltstone. Some of these sandstones show well-developed cross lamination that can be recognized on CT scans (Fig. F74). Descending current-ripple cross lamination was observed in one bed (Fig. F75). Small-scale flame structures are rarely present (Fig. F76). There are some calcareous sandstones with a granule-grade basal division (Fig. F77), and mudstone rip-up clasts are also locally present (Figs. F78, F79). Some very thin sandstones contain subrounded matrix-supported siltstone intraclasts as wide as 0.5 cm (Fig. F80). There are a small number of thin to very thin interbeds of fine calcareous sandstone that grade through calcareous siltstone to calcareous mudstone (or marlstone); these are distributed in predominantly mudstone or claystone intervals (Fig. F81). In addition, there are examples of complex alternations of different facies, as shown in Figure F82.

Thin section studies show that the coarser siltstones and sandstones of Subunit 5B contain abundant quartz and rare to trace amounts of feldspar, mica, glauconite, and heavy minerals (Fig. F83). Locally, the siltstones are very micaceous and contain intraclasts and minor clay matrix (Figs. F84, F85). The rock fragments are dominantly metamorphic, with some sedimentary micritic carbonate grains. The latter might be intraclasts or reworked carbonate lithic fragments. Biogenic components are dominantly foraminifers, with rare fish and organic (plant) debris. Bioclast diversity increases lower in the subunit where echinoderm, ostracode, and mollusk fragments are present. The sandstones and siltstones are pervasively cemented by carbonate microspar and spar. Grainstones in Subunit 5B contain components similar to the sandstones and siltstones, but they are more enriched in calcareous intraclasts and grains and, locally, in radiolarians (Fig. F86).

Structural Features. A synsedimentary fold with an entirely unexpected axial-planar cleavage was observed in interval 210-1276A-69R-4, 70–86 cm. Such axial-planar cleavage is normally assumed to form only as a result of the folding of lithified sedimentary rocks. However, its presence as a synsedimentary fold shows that such deformation may also occur in sediments that are not fully lithified.

F71. Burrowed mudstone with oxidized top, Subunit 5B, p. 194.

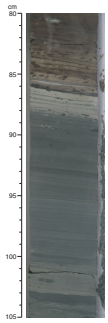

F72. Graded sandstone → siltstone → mudstone turbidite, Subunit 5B, p. 195.

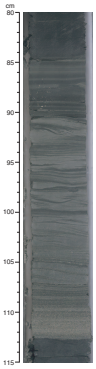

F73. Convolute lamination in sandstone turbidite, Subunit 5A, p. 196.

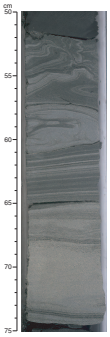

F74. Comparison of sedimentary structures in core and CT scan, Subunit 5B, p. 197.

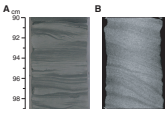

Depositional Setting, Paleoceanography, and Sediment Provenance

Subunit 5B is dominated by the deposition of relatively homogeneous burrow-mottled mudrocks (mudstone and claystone) in an aerobic to dysaerobic setting. Compared with Subunit 5A, background hemipelagic sediments are relatively more abundant, whereas graded calcareous sandstone turbidites are very subordinate. Very finely laminated black shales (calcareous claystones and marlstones) accumulated under anaerobic conditions by the same processes as those in Subunit 5A. Many of the calcareous mudstones that form an important part of this subunit were apparently transported by turbidity currents from farther upslope, above the CCD, to a position beneath the CCD, much as was inferred for Subunit 5A.

Subunit 5C

Interval: top: 210-1276A-75R-3, 142 cm; base: 102R-1, 2 cm, through Core 104R (no recovery)
Depth: top: 1502.12 mbsf; base: 1732.12–1736.90 mbsf
Age: latest Aptian(?)–Albian
Lithology: dark gray to olive-black, disorganized sandy turbidites with thick tops of calcareous mudstone, green to dark gray claystone, minor conglomerate, and hydrothermally altered sediments

The upper contact of Subunit 5C is placed at the first downhole appearance of disorganized beds of silty and muddy sandstone. The base is at or below Section 210-1276A-102R-1, 2 cm. Below this, there was no core recovery down to the bottom of Hole 1276A at the base of Core 210-1276A-104R. The subunit consists of ~75% dark-colored calcareous unburrowed mudrock (mostly mudstone); ~10% burrowed mudrock; ~10% calcareous sandstone, grainstone, and silty sandstone; and ~5% siltstone. The burrowed mudrocks are a combination of calcareous mudstones and claystones that are essentially carbonate free, although a small amount of the claystone is calcareous, as determined by frequent testing with 10% HCl and smear slide analysis.

Although Subunit 5C is dominated by mudrocks, the most spectacular features of the subunit are disorganized sandy turbidites with thick tops of calcareous mudstone; these compose ~10% of the subunit. There are also very rare black shales (<1% of the recovery) and very rare mud-clast conglomerates. Hydrothermally altered sediments (mudrocks and calcareous sandstone) are localized at the contacts of two diabase sills (Subunits 5C1 and 5C2) that cut the lower part of Subunit 5C. The noncalcareous and calcareous mudrocks of Subunit 5C are similar in composition to those of Subunit 5B, except that those in Subunit 5C are relatively enriched in terrestrially derived constituents including mica and carbonized plant material. Marlstones in Subunit 5C are also similar to those in Subunits 5A and 5B, but Subunit 5C marlstones do not contain foraminifers.

Lithologies

Mudrock (Mudstone and Claystone) and Minor Marlstone. Dark greenish to grayish mudrocks compose ~85% of Subunit 5C, but a number of specific depositional facies can be recognized. Predominantly gray (N3 and N4) claystones are mainly noncalcareous and devoid of burrows. These claystones range from moderately massive (Fig. F87) to weakly laminated (Fig. F88) to finely laminated (Fig. F89). In addition, there

F75. Descending cross lamination in sandstone turbidite, Subunit 5B, p. 198.

F76. Microflame structures in fine sandstone, Subunit 5B, p. 199.

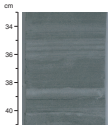

F77. Granule-grade base of a turbidite, Subunit 5B, p. 200.

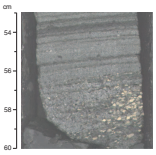

F78. Entrained mudstone rip-up clasts in planar-laminated sandstone, Subunit 5B, p. 201.

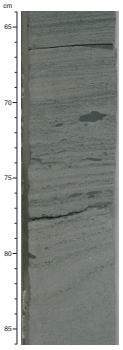

F79. Graded sandstone turbidite with mudstone rip-up clasts, Subunit 5B, p. 202.

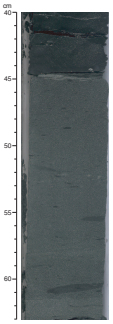

are subordinate intervals of greenish (5G 2/1), more calcareous burrowed claystones and mudstones. Very rarely, a bluish gray (5B 5/1) variety is present; smear slide analysis indicates that this is marlstone.

There are also a number of beds of calcareous siltstone that fine upward into structureless calcareous claystone or mudstone (e.g., Sections 210-1276A-77R-4, 57 cm, through 77R-3, 62 cm; thickness = 145 cm). All of Core 210-1276A-95R is dominated by several intervals of calcareous mudstone, each as thick as ~1.5 m, that are structureless apart from occasional silt laminae. Other beds of calcareous mudrock, as thick as 50 cm, have only a few millimeters of pale laminated siltstone at the base, so >95% of the deposit is mudrock. The individual silt-rich laminae in these units contain quartz, planktonic foraminifers, and inferred fecal pellets. This variety of mudstone is interpreted as a type of gravity-flow deposit, as discussed further below.

Several thick (as much as several meters) intervals of calcareous mudstone pass uphole into claystone or marlstone, each forming an individual depositional unit. These deposits include sedimentary features indicative of deposition from gravity flows. For example, Sections 210-1276A-77R-1, 46 cm, through 77R-2, 10 cm, consist of an interval in which the lower 30 cm of contorted and folded mudstone is overlain by homogeneous claystone. These mudstones are calcareous and contain scattered flattened and elliptical sand–silt intraclasts as large as several millimeters in size. There does not appear to be a coarser-grained base to these depositional units.

In addition, distinctive mudrocks are locally present. Rare intervals of very finely laminated claystone (black shale) are observed in intervals 210-1276A-94R-5, 70–85 cm, 94R-4, 43–46 cm, and 98R-1, 87–110 cm (Fig. **F90**). The last example contains scattered silt grains and fine silty laminae. Several other dark-colored, nonburrowed intervals in this core show weakly developed, thin planar lamination, suggestive of incipient black shale formation.

Given the characteristic dark greenish gray colors of Subunit 5C, an isolated presence of pale reddish brown (10R 5/4) noncalcareous claystone in Section 210-1276A-89R-2 is anomalous. In this section, reddish and greenish to dark gray burrowed claystones alternate with unburrowed dark greenish marlstone on scales of a few centimeters to several tens of centimeters.

An additional feature of interest is anomalously poor consolidation of pale gray to greenish gray burrowed claystones in Core 210-1276A-96R, located between two diabase sills that intrude the lower part of Subunit 5C (see below). It is possible that the sills acted as seals that prevented pore fluid escape and thus inhibited compaction and cementation of these sediments (see **"Physical Properties,"** p. 99).

Muddy Calcareous Sandstones → Mudstones → Claystones. Medium to thick beds of dark olive-green (5GY 3/2) massive calcareous sandstone, grading upward into massive calcareous mudstone or claystone, form a significant part (~10%) of Subunit 5C. For example, in Core 210-1276A-81R a single depositional unit, ~195 cm thick, begins with silty sandstone (Section 210-1276A-81R-3, 135 cm) and grades upward into silty calcareous mudstone/claystone (Section 81R-2, 90 cm) and then into mudstone (Section 81R-1, 90 cm). Internally, this bed is intensely deformed, containing contorted and swirled laminae and streaked-out sandstone and mudstone intraclasts as large as several centimeters. Other calcareous silty sandstone beds reach several meters in thickness. In contrast to the graded calcareous sandstones of Subunits 5A and 5B, these sandstones have a muddy matrix. The sandstones commonly con-

F80. Sandstone lamina with siltstone clasts interpreted as debris flow, Subunit 5B, p. 203.

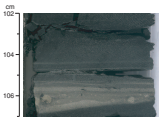

F81. Laminae and fine-grained sandstone and siltstone in dark claystones, Subunit 5B, p. 204.

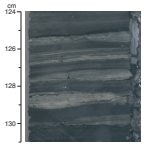

F82. Turbidite structure suggesting irregular seafloor topography, Subunit 5B, p. 205.

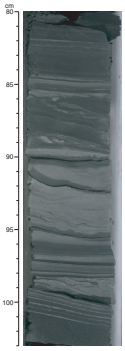

F83. Terrigenous silty sandstone, Subunit 5B, p. 206.

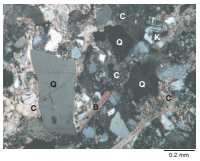

F84. Sandy siltstone with darker mudstone intraclasts, Subunit 5B, p. 207.

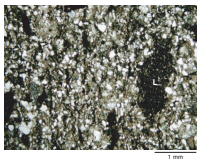

tain fine- to medium-grained sand-sized clasts mainly composed of dark mudstone but also including irregular streaked-out clasts of sandstone (Fig. F91). There are also numerous clasts of black and green claystone/mudstone that range in size from <1 mm to several centimeters (Fig. F92). The calcareous silty and muddy sandstones and the muddy siltstones locally contain scattered elongate fragments of carbonized wood, as long as several centimeters (e.g., interval 210-1276A-94R-2, 40–41 cm). In addition, there are a number of intervals of severely disrupted muddy sandstone and sandy mudstone (Fig. F93).

In Section 210-1276A-85R-4, a calcareous silty sandstone, where it passes uphole into mudstone, displays centimeter-scale recumbent folds with disconnected hinges and intricately deformed laminae (i.e., "similar folds" in structural geology nomenclature). The noses of the folds have been thickened by migration of mud into the hinge area. Sigmoidal siltstone patches in the sediment probably are the remnants of sheared-out fold limbs. Syndepositional deformation structures of this type, particularly reclined to recumbent and seemingly flattened and sheared folds, are widespread in Subunit 5C (Figs. F94, F95, F96). In interval 210-1276A-87R-3, 55–150 cm, dish structures resulting from syndepositional pore-fluid escape are associated with deformed laminae. Well-developed swirled zones in the lower part of Subunit 5C include rip-up clasts of muddy and silty sandstone, smeared-out clasts, mica grains, plant material, and flattened intraclasts (e.g., intervals 210-1276A-94R-1, 90–150 cm, and 94R-2, 0–13 cm).

In the lower part of Subunit 5C, there are several spectacular mudclast conglomerates (almost breccias) associated with intervals of structureless sandy mudstone (Figs. F97, F98). The individual mud clasts are mottled, ranging from green to black and gray. Most of the mud clasts are subangular with irregular margins, suggesting that they were reworked while they were in a plastic state. In places, the internal deformation is so intense that the original clasts and matrix cannot be distinguished in the core (Fig. F99). There are also occasional relatively thick intervals of calcareous sandy siltstone grading uphole into calcareous mudstone; this includes an entire section containing subrounded sandstone intraclasts, as large as 6 cm, and extensive soft-sediment deformation.

Petrographic study of sandstones and siltstones reveals dominantly angular quartz grains, biotite, muscovite, glauconite, rock fragments (e.g., phyllite), bioclastic grains including echinoid spines (Fig. F100), and common terrestrially derived plant material (Fig. F101). In general, the quartzose sandstones and siltstones of Subunit 5C are more feldspathic than those of Subunits 5A and 5B, but they otherwise contain similar types of mica and lithic fragments. They are not as glauconitic as those in the overlying units. Furthermore, the sandstones of Subunit 5C show enhanced diagenesis as reflected in widespread dissolution of feldspar, minor quartz overgrowths, and cementation.

Sandstone/Grainstone. There are a small number of well-sorted, thin- to medium-bedded, graded calcareous sandstones and grainstones (<5% of core recovered) in Subunit 5C. The sandstones are dominantly siliciclastic and contain a carbonate spar cement. The grainstones are also calcite cemented. The carbonate in grainstones includes numerous bioclasts. The calcareous sandstones/grainstones exhibit sharp bases, similar to the typical graded intervals of the younger Subunit 5A.

A small number of the graded sandstone intervals exhibit both planar and cross lamination (Fig. F102) and then fine upward through siltstone into nearly massive mudstone with occasional very small mud-

F85. Laminated terrigenous siltstone, Subunit 5B, p. 208.

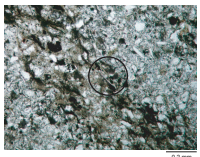

F86. Grainstone containing reworked planktonic foraminifers and radiolarians, Subunit 5B, p. 209.

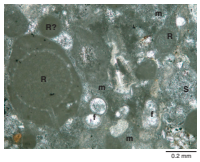

F87. Massive mudstone with a fine sandstone/siltstone parting, Subunit 5C, p. 210.

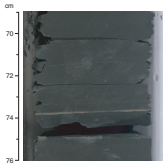

F88. Repeated calcareous mudstones grading into paler siltstones, Subunit 5C, p. 211.

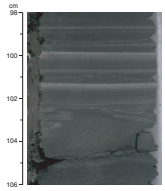

F89. Siltstone laminae deposited by low-density turbidity currents, Subunit 5C, p. 212.

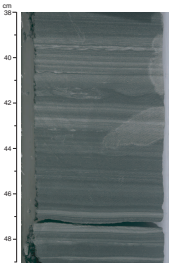

stone clasts (<5 mm). These mudstones are calcareous and completely devoid of burrows. In some depositional units that are tens of centimeters or more thick, the bases are reduced to only a few millimeters of fine-grained sandstone.

Medium gray (N4) to medium light gray (N5) and yellowish gray (5Y 8/1) grainstones form as much as ~25% of several of the cores in Subunit 5C. In Core 210-1276A-80R, there are seven sharp-based graded units in which grainstone, sandstone, or siltstone pass uphole into calcareous claystone. The silty tops of individual grainstones consist of color-banded, planar-, cross-, and occasionally convolute-laminated divisions. Six of the graded intervals in Core 210-1276A-80R are succeeded by greenish gray burrowed mudstone.

Volcanogenic Sediments. Very rare thin (<5 cm thick) intervals of volcanic ash were noted. One of these, just beneath the Subunit 5B/5C boundary, appears to be a tuff in which original volcanic glass was altered to clay minerals (Fig. **F103**). In addition, a thin, probably volcaniclastic interval was identified in marlstone in the lower part in Subunit 5C (interval 210-1276A-89R-1, 18–20 cm). The volcanogenic sediments of both of these intervals are strongly altered.

Depositional Setting, Paleoceanography, and Sediment Provenance

Subunit 5C contains an unusually wide variety of redeposited facies, namely silty and sandy debris flow deposits, siliciclastic turbidites, carbonate-rich turbidites, and silt-mud turbidites, alternating with small amounts of background hemipelagic sediments that are mainly claystones. The greenish gray claystones are burrowed, whereas the dark gray to black mudrocks lack burrowing. The grainstones are assumed to have been derived from contemporary continental shelf or upper slope settings, whereas the more abundant siliciclastic turbidites, like those of Subunits 5A and 5B, were derived from continental source rocks. Similar intercalations of hemipelagic and redeposited sediments of carbonate to siliciclastic composition characterize the margins of other areas of the North Atlantic after continental breakup (Ogg et al., 1983).

The redeposited siliciclastic sediments are interpreted as follows:

1. The predominant silty sandstone and silty mudstone beds with (a) swirled lamination; (b) "floating" clasts of sandstone, siltstone, and mudstone; and (c) sharp tops are interpreted as debris flow deposits. These represent a variety of "slurry bed," as defined by Wood and Smith (1959) and described recently by Lowe et al. (2003). The floating sandstone lithoclasts originated by remobilization of poorly consolidated sand into viscous flows rich in silt and mud. During subsequent downslope transport the sand clasts did not fully disaggregate, and therefore the sand was not thoroughly mixed with the mud and silt fractions.
2. The subordinate graded sandstones → siltstones → mudstones seen throughout Subunit 5C are classic sandstone turbidites.
3. The normally graded beds of grainstone are interpreted as calcareous turbidites derived from a continental shelf or upper slope setting above the CCD.
4. The siltstone → mudstone and mudstone → claystone beds, reaching several meters in thickness, are interpreted as deposits from exceptionally large mud-dominated turbidity currents. These are equivalent to the "megaturbidites" described from outcrop successions (Ricci Lucchi and Valmori, 1980; Hiscott et al., 1986) and from modern abyssal plains (Weaver and Rothwell,

F90. Thermally altered black shale, Subunit 5C, p. 213.

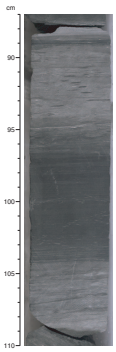

F91. Massive silty sandstone with dispersed sandstone clasts, Subunit 5C, p. 214.

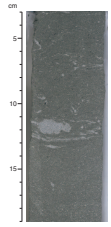

F92. Silty sandstone with "floating" large calcareous mudclast, Subunit 5C, p. 215.

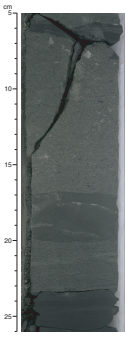

F93. Claystones and thin-bedded lenticular siltstones affected by soft-sediment deformation, Subunit 5C, p. 216.

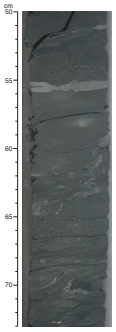

1987). It is envisioned that large volumes of calcareous mud were mobilized from higher on the continental slope (above the CCD) and then redeposited in the vicinity of Site 1276. These fine-grained sediments could easily be mistaken for background hemipelagic sediments. However, they can be distinguished by a slightly paler color, lack of sedimentary structures and burrowing, and a higher carbonate content compared to the dark gray and greenish hemipelagic claystones.

The predominant redeposited facies discussed above are interbedded with minor amounts of greenish to dark gray and black mudrock. Much of the mudrock is interpreted as the tops of mud turbidites, whereas the background hemipelagic sediments are mainly claystones. The greenish burrowed claystones accumulated under conditions that were at least weakly oxidizing, whereas the dark gray and black claystones, devoid of burrows, apparently accumulated under anoxic conditions (see discussion of black shales in **"Implications of Sediment Chemistry,"** p. 53). Where background hemipelagic sediments form a significant part of the succession (e.g., Core 210-1276A-93R), sediments that accumulated under inferred oxic and anoxic conditions are intercalated, typically on a scale of tens of centimeters to meters. In addition, the few reddish (noncalcareous) claystones in the lower part of Subunit 5C are interpreted as pelagic sediments that accumulated under rare, well-oxygenated bottom waters.

Both the greenish claystones and dark gray and black claystones are effectively noncalcareous, indicating deposition beneath the CCD, as was inferred for the overlying Subunits 5A and 5B. However, relatively small amounts of both greenish and dark gray and black claystones are calcareous, as indicated by frequent testing of the cores with 10% HCl, smear slide analyses, and carbonate determinations. One explanation is that these claystones represent the low-density, clay-rich tops of the thick mud turbidites discussed above. However, some of these calcareous intervals in the upper part of Subunit 5C appear to occur independently of identified mud turbidites (e.g., Core 210-1276A-76R). In these cases, an alternative explanation is that these sediments were deposited as calcareous hemipelagic sediments above the CCD, with the implication that Hole 1276A might have been located close to the CCD during Albian time.

The very rare and very finely laminated black claystones (black shales) in the lower part of Subunit 5C are interpreted to have been deposited in a manner similar to that described for Subunits 5A and 5B.

Diagenetic Processes in Unit 5

Unit 5 as a whole is characterized by a range of compaction-related and chemical diagenetic effects. Differential compaction occurred around burrows that are composed of cemented sandstone or siltstone. The clastic sediments filling these burrows were cemented by calcite spar relatively soon after burial and later underwent little deformation, whereas the surrounding mud or clay remained soft and was molded around the lithified burrows (Fig. **F104**).

The rare calcareous sandstones and grainstones are well cemented by carbonate microspar. The more porous sandstone turbidites are similarly well cemented, which imparts a pale color, whereas silty sandstones are less porous and lack carbonate cement. Cementation is locally patchy, with the result that depositional structures (e.g., cross

F94. Gravity-flow deposit showing parallel and convolute lamination, Subunit 5C, p. 217.

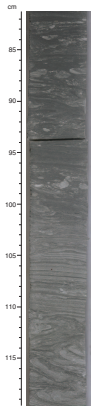

F95. Calcareous sandstone turbidite with swirled and convolute lamination, Subunit 5C, p. 218.

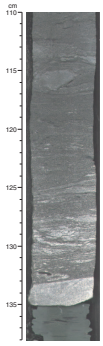

F96. Swirled interval of a sandstone gravity-flow deposit, Subunit 5C, p. 219.

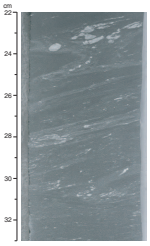

lamination) may be differentially compacted (Fig. F105). Bright spots are observed in CT scans but do not have a visual expression in corresponding core photographs of the same interval; these spots could represent areas of patchy sparry calcite cementation as much as several centimeters across (Fig. F106) or pyrite (Fig. F107).

Layers (<20 cm thick) and isolated nodules of diagenetic limestone are occasionally present in Subunit 5B. These limestones are locally rich in nannofossils but only very rarely contain foraminifers or radiolarians. In thin section, the limestones are composed mainly of microspar to micritic carbonate and they contain a mud fraction that consists of clay minerals, iron oxides, heavy minerals, quartz, and organic matter.

In some cases, the carbonate concretions and nodules do not react with 10% HCl. XRD studies showed that several samples contain dolomite and siderite (Samples 210-1276A-37R-5, 26–27 cm, and 38R-5, 96–98 cm); a few others have abundant siderite and dolomite and minor calcite (Samples 41R-4, 23–24 cm; 42R-4, 23–24 cm; 42R-4, 115–116 cm; 46R-2, 52–53 cm; and 55R-2, 21–22 cm). One nodule contains siderite plus dolomite (Sample 210-1276A-77R-2, 21–23 cm), and another is composed of mainly apatite with subsidiary dolomite and siderite.

Cryptocrystalline siderite forms occasional irregular light yellowish brown layers (<30 cm thick), especially in the less calcareous mudrocks (Fig. F108). These layers are interpreted to be concretions formed by cementation and replacement of mud or mudrocks by siderite. The laminae outside the siderite concretions are considerably more compacted than those within, suggesting that the concretions formed relatively early in diagenesis.

An unusual feature of Subunit 5B is the presence of small nodules (<5 cm in diameter) that are mainly composed of granular carbonate (e.g., interval 210-1276A-47R-7, 42–43 cm). Several nodules exhibit transitional contacts with the surrounding sediment (Fig. F109), whereas others have sharply defined margins. Thin section study of one nodule (Fig. F110) revealed a pelletal texture of circular pellets as large as 1 mm. Internally, the pellets contain clay and nannofossils. Locally, inferred primary porosity is preserved between pellets. Some pellets are partly fused, whereas others are partly or completely fused to form nearly homogeneous claystone. Elsewhere in the nodule, pellets are separated by interstitial claystone. These unusual carbonate nodules are interpreted to be remnants of an original depositional texture of fecal pellets in the mudstones of Subunit 5B and, by implication, the mudstones throughout the Albian interval. This observation is significant because it may help to explain the common occurrence of silt- to granule-sized claystone or mudstone clasts in many of the siliclastic sandstone-siltstone and grainstone turbidites. These might have been pellets rather than mud intraclasts. At the time of its redeposition, pelleted fine-grained sediment may have been sufficiently cohesive to survive transport in gravity flows.

In several adjacent intervals within the lower part of Subunit 5B, small centimeter-scale nodules or lenses with granular texture appear to have been cemented early in diagenesis and then compacted so that lamination is deflected around them (Figs. F111, F112). There are also occasional small (<2 cm) light olive-gray (5Y 6/1) dolomitic concretions, either oval or tabular in shape, in some intervals of dark gray calcareous mudstone. Nodular barite layers are present in Cores 210-1276A-43R, 44R, and 47R. A single septarian concretion was recovered (Fig. F113). This apparently formed relatively late in diagenesis because

F97. Chaotic mudclast conglomerate, Subunit 5C, p. 220.

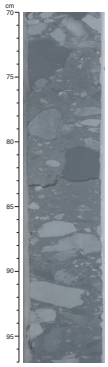

F98. Sharp upper contact of the mudclast conglomerate, Subunit 5C, p. 221.

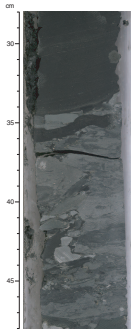

F99. Severely contorted interval of sandstone and mudstone, Subunit 5C, p. 222.

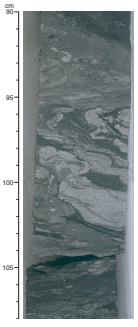

F100. Sandy siltstone, Subunit 5C, p. 223.

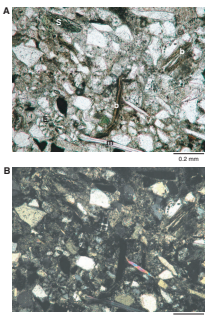

the primary lamination is only slightly deflected around the concretion.

Minor amounts of framboidal pyrite are ubiquitous throughout Unit 5. Pyrite is also present as occasional small nodules and lenses (<3 cm thick) throughout Subunit 5C, especially in the darker, more carbon rich claystones (e.g., Cores 210-1276A-89R, 92R, 95R, and 97R). These claystones occasionally contain pyritized radiolarians with well-preserved tests including spines, whereas most other radiolarians are replaced by carbonate minerals. For this reason, it is likely that the pyrite formed relatively early in diagenesis, preserving the radiolarians from later replacement by carbonate.

A few thin (several centimeters thick) phosphatic layers were observed (e.g., interval 210-1276A-92R-5, 68–72 cm). XRD analysis indicates the presence of a Ca-F apatite, quartz, and kaolinite plus chlorite.

Fine-Grained Sediment Composition of Unit 5 Based on XRD Analysis

The main detrital constituents of the mudrocks and marlstones of Unit 5, in decreasing order of abundance, are quartz, clay minerals, and feldspars. Quartz is generally the most abundant mineral even in the claystones. Plagioclase and alkali feldspar are mainly present in the coarser-grained lithologies (i.e., mudstone, sandy mudstone, and siltstone) but are rare otherwise. The main clay minerals are illite-smectite mixed-layer minerals, illite and muscovite (indistinguishable), chlorite, and kaolin-group minerals (kaolinite and possibly dickite). No attempt was made to determine the relative or absolute abundance of these minerals.

The peak spacing and amplitude of XRD diffractograms of sampled clay minerals were compared throughout Unit 5. To obtain a data set of comparable lithologies, only dark green mudrocks with variable but usually minor or trace amounts of carbonate were selected. These samples are thought to represent background hemipelagic sedimentation, which is characterized by a smaller detrital and organic matter input compared with the interbedded lithologies that are mainly turbidites.

The peak spacing and amplitude of XRD diffractograms of clay minerals were compared, and the results are summarized in Figure **F114.** A minor diffraction bulge at ~14 Å appears irregularly in samples down to the middle of Subunit 5B (Sample 210-1276A-47R-7, 28–29 cm; 1241.26 mbsf). This bulge is attributed to the presence of irregular illite-smectite mixed-layer minerals (IS mixed layers). These irregular minerals are characterized by random intercalation of illite and smectite layers (R = 0) (Moore and Reynolds, 1989; Reynolds, 1980). Below 1240 mbsf, the IS mixed layers are of the regular, higher-order type (R = 1 and R = 3) in all but one sample that came from a layer of altered ash (interval 210-1276A-89R-1, 20–21 cm; 1623.80 mbsf). A pronounced downhole increase in chlorite and kaolinite is detected over roughly the same interval, from 1376.68 mbsf to the bottom of the hole.

The downhole changes in IS mixed layers, together with an increasing abundance of chlorite and kaolinite, are commonly observed in deeply buried successions in other sedimentary basins, and they are common features of mid-Cretaceous sedimentary basins in the Atlantic and the western Tethyan regions (Chamley, 1979; Chamley and Debrabant, 1984; Robert, 1987; Pletsch, 1997). The conventional explanation for these trends is that they relate to burial diagenesis (Dunoyer de Segonzac, 1969). In particular, a downhole change to regular IS mixed lay-

F101. Sandy siltstone at high magnification, Subunit 5C, p. 224.

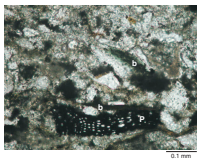

F102. Sandstone turbidite with planar and convolute lamination, Subunit 5C, p. 225.

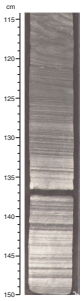

F103. Altered tuff, just beneath the Subunit 5B/5C boundary, p. 226.

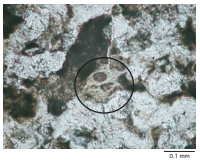

F104. Sandstone fill of burrows cemented by calcite spar, Subunit 5B, p. 227.

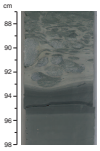

F105. Lenticular sandstone showing irregular calcite cementation, Subunit 5C, p. 228.

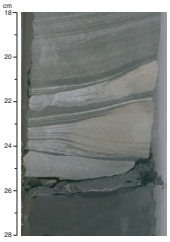

ers can be interpreted as temperature-related diagenesis because irregular IS mixed layers become unstable at temperatures of ~100°C (Pollastro, 1993). However, this explanation is incompatible with observations at Site 1276. At this site, the transition to regular IS mixed layers is ~1240 mbsf, but two lines of evidence indicate that temperatures at this level never reached close to 100°C. First, irregular IS mixed layers are present some 384 m deeper in interval 210-1276A-89R-1, 20–21 cm, at 1624 mbsf. Second, T_{max} values from Rock-Eval pyrolysis of two still-deeper carbon-rich samples in Core 210-1276A-94R are as low as 440°C (see **"Geochemistry,"** p. 95). These values correspond to maximum burial temperatures that are well below the range that should be required if the regular IS mixed layers originated diagenetically. Thus, the clay mineral assemblages at Site 1276 are interpreted to be the result of long-term variation in the input of terrigenous constituents rather than burial diagenesis.

If we consider environmental rather than burial-diagenesis effects, downhole clay mineral changes, such as we observe, could be related to waning effects of extensional tectonics during Aptian to early Albian time, combined with the influence of the first-order sea level maximum during Albian–Turonian time (Haq et al., 1987). According to this hypothesis, the abundance of kaolinite and chlorite in mudrocks in the lower part of Unit 5 could be attributed to the denudation of metamorphic rocks and deeply buried sedimentary rocks, whereas the observed uphole decrease in abundance of the minerals would be related to waning extensional tectonics in source areas of the Site 1276 sediments. However, continental breakup is assumed to have been completed on the Newfoundland margin prior to Aptian time (see **"Comparisons with the Conjugate Iberia Margin and the Western Central North Atlantic,"** p. 57). If the tectonic hypothesis is correct, either tectonism continued beyond breakup or clastic sediments were supplied from other areas, such as the still actively rifting Labrador Sea north of Site 1276.

Another possible controlling factor is the inferred long-term sea level rise during the Albian–Turonian (Haq et al., 1987) that could have limited the input of kaolinite and chlorite. Both of these minerals usually reach the deep ocean as relatively coarse grained particles, as opposed to mostly colloidal IS mixed layers. This can lead to a preferential settling of chlorite and kaolinite in proximal shelf settings, whereas the finer-grained IS mixed layers may largely bypass the shelf and settle in the open ocean (Gibbs, 1977; Chamley, 1989). At Site 1276, chlorite and kaolinite could initially have bypassed a narrow shelf while sea level was relatively low. As sea level rose, the area of shelf deposition would have expanded, trapping chlorite and kaolinite while the IS mixed layers bypassed the shelf to reach the deep ocean.

Implications of Sediment Chemistry

Most of the mudrocks from Unit 5 fall within the range of chemical compositions typical of hemipelagic sediments with variable carbonate contents (ICP-AES geochemistry) (Table **T4**). Calculated carbonate and analyzed Ca values in the mudrocks drop to generally low levels below Core 210-1276A-41R, and absolute values of Al_2O_3, SiO_2, TiO_2, and other terrigenous constituents correspondingly increase. The composition of occasional sandstone turbidites lies within the range of continentally derived sandstones, but one sample (210-1276A-38R-6, 96–98 cm) contains 3.63 wt% MnO, which may relate to diagenetic cementation.

F106. CT scan of calcareous sandstone showing bright spots, Subunit 5C, p. 229.

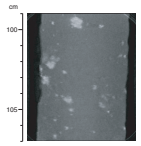

F107. CT scan and core photograph from deformed top of gravity-flow deposit, Subunit 5C, p. 230.

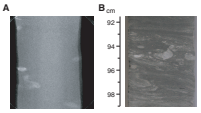

F108. Irregular carbonate concretionary layers, Subunit 5B, p. 231.

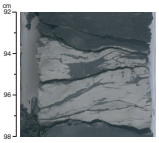

F109. Carbonate-cemented nodule of pelleted clay, Subunit 5B, p. 232.

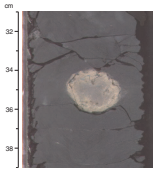

F110. Pelleted mudstone, Subunit 5B, p. 233.

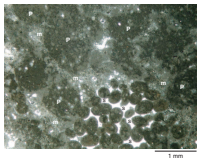

F111. Claystone with diagenetically formed carbonate lenses and granular bodies, Subunit 5B, p. 234.

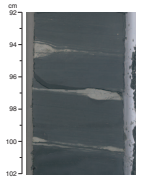

A small number of dark, laminated black shale samples were also chemically analyzed from the interval of Subunit 5A (Cores 210-1276A-32R and 33R) that was stratigraphically correlated with OAE 2 (see "Biostratigraphy," p. 73). These black shales are relatively enriched in TOC, calculated carbonate, Ca, MnO, P_2O_5, Cr, Mn, Ni, Fe, and V, whereas Al_2O_3 and TiO_2 are depleted relative to the preceding list of elements and oxides (see "Oceanic Anoxic Events," p. 97, and "Trace Elements and Redox-Sensitive Metals," p. 98, both in "Geochemistry"). The enrichment in carbonate and Ca in these black shales, in contrast to the adjacent background sediments (claystones and mudstones) that accumulated below the CCD, records a high preservation of biogenic carbonate. This carbonate was derived from either primary pelagic settling (calcareous nannofossils) or calcareous gravity flows (see "Origin of Finely Laminated Black Shales," p. 55). The relative enrichment of Mn in the black shales that correlate with OAE 2 could record the formation of a reduced manganese mineral that was not detected during routine XRD analysis. This further suggests that diagenetic processes played an important role in determining the present composition of the black shales.

The relative enrichment in Cr and Ni in the black shales analyzed from the Cenomanian OAE 2 interval could reflect incorporation of these elements into marine organic matter. However, Ba, commonly used as a productivity index (von Breymann et al., 1992), is not significantly enriched in the carbon-rich horizons, although low Ba levels could result from diagenetic loss of Ba and other constituents. Relative depletion of Al is observed in the Cenomanian OAE 2 interval that is most strongly enriched in TOC; this appears to contrast with some other black shales of Albian age from the North Atlantic that show a marked relative increase in terrigenous constituents (e.g., Al, Ti, K, Mg, and Fe) (Hofmann et al., 2001). Possible explanations of this discrepancy may relate to differences in the nature of the organic matter (i.e., its composition and maturity), sedimentation rate, or diagenesis. Biomarker data are needed from postcruise studies to determine the nature and maturity of the organic matter. However, it should be noted that none of the black shales analyzed appear to show anything like the strong enrichment in trace metals or the very high hydrogen indexes (HIs) (>600 mg HC/g TOC) that are typical of marine organic matter in OAE 2 elsewhere (e.g., in the Hatteras Formation of the central North Atlantic [Jansa et al., 1979; Summerhayes, 1987]). One explanation for the lack of strong trace-metal enrichment in the OAE 2 black shale interval at Site 1276 is that these carbon-rich sediments accumulated relatively rapidly and are dominated by unreactive organic matter. Under these conditions, they did not initially absorb high concentrations of trace metals (e.g., Ni and Cr) from seawater and their chemical composition was later modified during diagenesis.

There was insufficient time during Leg 210 to complete the chemical analysis of mudrocks from near the base of Subunit 5C, including several dark claystone layers (black shales) in Cores 210-1276A-94R and 98R. However, several of the black shale samples were analyzed for carbonate and were found to be strongly calcareous. Also, the Rock-Eval HIs are slightly elevated (<100 mg HC/g TOC) relative to background values (<50 mg HC/g TOC). The rare black shales in Core 210-1276A-94R near the base of Subunit 5C are inferred to be of marine origin based on the HIs (see "Oceanic Anoxic Events," p. 97, in "Geochemistry," and "Biostratigraphy," p. 73), and they may correlate with OAE 1b. There are also two other thin black shale intervals in Subunit 5B

F112. Mudstone with carbonate-rich micro-concretions, Subunit 5B, p. 235.

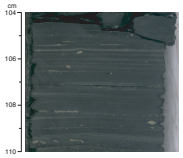

F113. Septarian concretion in laminated claystone, Subunit 5C, p. 236.

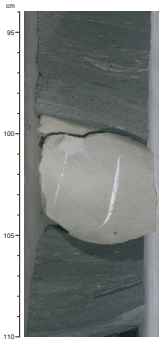

F114. XRD from dark green, bioturbated background lithologies, p. 237.

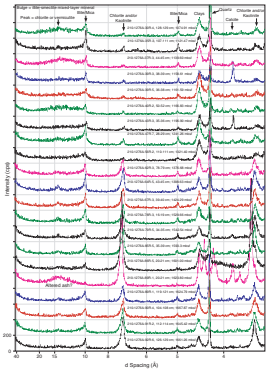

that show slight elevations in HIs compared to background values, and these might conceivably correlate with OAEs (e.g., OAE 1c and OAE 1d). It should also be noted that only a few of the total number of laminated black shale intervals in Subunits 5A and 5B were chemically analyzed on the ship.

In summary, the bulk sedimentary geochemistry is consistent with a dominantly terrigenous origin of the black shales. The main exception may be the upper Cenomanian–lowermost Turonian OAE 2 interval, which was determined to have a significant amount of marine (algal) organic matter. Another exception may be OAE 1b, of early Albian age, assuming this event is confirmed by postcruise studies (see **"Oceanic Anoxic Events,"** p. 97, in "Geochemistry").

Origin of Finely Laminated Black Shales

Based on shipboard data, including the geochemical data summarized above, the occurrence of very finely laminated black shales in Subunits 5A and 5B (and very rarely in Subunit 5C) can be explained by an increase in plankton productivity or an increase in the input of terrestrial organic matter (i.e., plant debris). Six horizons marked by higher TOC contents and S_2 values were recorded. These include upper Cenomanian–lowermost Turonian OAE 2 and possibly also OAEs 1b, 1c, and 1d (see **"Oceanic Anoxic Events,"** p. 97, in "Geochemistry").

Productivity Hypothesis

One hypothesis is that black shales represent periods of enhanced primary productivity followed by pelagic settling, coupled with preferential preservation in an anoxic setting (Tucholke and Vogt 1979; Wignall, 1994; Calvert et al., 1992; Tyson, 1995). The calcareous laminae, rich in nannofossils, reflect short-term variations (i.e., blooms) in plankton productivity (Arthur et al., 1987; Hofmann et al., 2001; Tyson, 1995). For example, very finely laminated claystones and black shales in the Lower to mid-Cretaceous Hatteras Formation in the western North Atlantic, similar to those in Unit 5, were attributed to periodic surface water blooms of calcareous nannoplankton (Robertson and Bliefnick, 1983). Increased calcareous nannofossil productivity could have depressed the CCD, allowing preferential carbonate preservation. The seafloor was possibly anoxic owing to an absence of deep circulation of oxygenated bottom waters. A similar explanation might apply to the Cenomanian black shales of OAE 2.

Terrestrial-Input Hypothesis

A second hypothesis is that the very finely laminated black shales (i.e., marlstones and calcareous claystones) represent accumulations from low-density turbidity currents derived from the continental rise above the CCD (Arthur et al., 1984; Stow, 2001). Most of this organic matter would be of terrestrial origin. High accumulation rates at the final site of deposition would allow the preservation of organic carbon and transported carbonate below the CCD, as in the first hypothesis. The bottom water just above the seafloor remained oxygenated, but the pore water in the redeposited carbon-rich sediments was anoxic and inhibited burrowing. Bioturbation resumed as oxygenated water diffused into the slowly oxidizing surface sediments, prior to the arrival of the next turbidity current. This explanation may apply to the majority of the black shales cored at Site 1276 because the background green clay-

stones are burrowed, indicating that the seafloor remained at least weakly oxidizing except during periods of carbon-rich clay deposition.

Discussion

A problematic aspect of the "productivity" hypothesis is that most of the black shales contain abundant terrigenous silt and terrestrial organic matter, suggesting that marine organic productivity was not the dominant control except possibly during formation of OAE 2 and OAE 1b. In the "terrestrial-input" hypothesis, the silt in the finely laminated black shales could have been introduced by the same low-density turbidity currents that transported the organic detritus. A problematic aspect of the terrestrial-input hypothesis is that many of the laminated black shales do not appear to be graded or have sharp bases, unlike the numerous mud turbidites in adjacent intervals. Also, in some cases the black shales form relatively thick intervals (as thick as tens of centimeters) that appear to be independent of the presence of mud turbidites.

Binocular-microscope examination reveals alternations of clay- and silt-sized particles that are not seen in the much more numerous mud turbidites. These laminae imply the occurrence of repeated pulses of sediment, with each lamina potentially deposited by a separate turbidity current. Terrestrial input therefore might have been fine-grained clay, silt, and terrestrial organic matter, which was resedimented from the continental slope above the CCD by low-density turbidity currents. These may have been very dilute "lutite flows" (McCave, 1972; Gorsline et al., 1984), perhaps originating from storm-induced resuspension or internal waves (Cacchione and Drake, 1986) that were active along the upper continental slope. In this scenario, bottom water remained relatively oxygenated most of the time, giving rise to green burrowed claystones. During intermittent times of high organic matter input, the sediments became anoxic beneath the sediment/water interface, thus inhibiting bioturbation. In addition, occasionally enhanced productivity of marine organic matter may have promoted the formation and preservation of black shales (e.g., during OAE 2 and OAE 1b).

Hydrothermally Altered Sediments

Two thick diabase sills (Subunits 5C1 and 5C2) cut the lower part of Subunit 5C. The lower sill (Subunit 5C2) is a complex that includes two smaller sills (see Fig. **F130** and **"Igneous and Metamorphic Petrology,"** p. 64, for details of intervals). The upper sill is ~10 m thick, and the main lower sill is >17.50 m thick. The uncertainty of the exact thickness of the lower sill is due to the incomplete recovery of the sill. Sediments typical of Subunit 5C were affected by a range of thermal and hydrothermal alteration effects in the vicinity of these sills.

Calcareous mudstone intervals in Core 210-1276A-87R, above the upper sill, include elongate, light-colored porphyroblasts (Fig. **F115**) and local recrystallization of carbonate to marble (interval 210-1276A-87R-6, 5–72 cm). Spectacular alteration effects are also seen in Core 210-1276A-98R just above the lower sill that entirely occupies Core 99R. This is highly altered claystone that is interpreted to have been leached and chemically reduced. Porphyroblasts are also present at this level. The porphyroblasts in both Cores 210-1276A-87R and 98R are composed of albite, quartz, alkali feldspar, and magnesian chlorite, based on XRD analysis. As they were precipitated they produced a "spotted hornfels" texture in the two intervals (Figs. **F115, F116**). In interval 210-1276A-98R-3, 40–50 cm, above the lower sill (Fig. **F117**), the

F115. Core photograph and CT images of a porphyroblastic mudrock, Subunit 5C, p. 238.

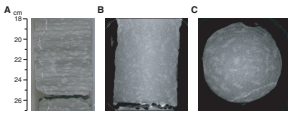

F116. Porphyroblastic mudrock from an interval affected by sill intrusion, Subunit 5C, p. 239.

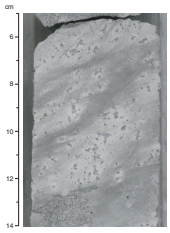

F117. Hydrothermally altered sediment adjacent to a diabase sill, Subunit 5C, p. 240.

rock is composed almost entirely of crystalline albite, sudoite (magnesium chlorite), nonstoichiometric calcite (possibly Mg rich), pyrite, and zeolite, based on XRD analysis. This rock probably originated as a bed of calcareous sand (i.e., base of a turbidite). There is some evidence that these sediments were only partially consolidated at the time of intrusion of the sills (see "Physical Properties," p. 99). Before lithification, this calcareous sand would have been a porous and permeable interval compared to the interbedded muds and it is likely to have channeled fluid flow that resulted in metasomatism. Adjacent graded calcareous sands and muds were also hydrothermally altered, although primary sedimentary textures, including burrowing, can still be recognized.

Approximately 10 cm above a small sill at 1711 mbsf, Subunit 5C2 (Fig. F130), a rare interval of black shale (interval 210-1276A-98R-1, 95–104 cm) was baked by heat from the sill, as indicated by smear slide study of the organic matter in the black shale.

Finally, a small (9 cm thick) "breccia pipe" (interval 210-1276A-97R-3, 140–149 cm) was identified above the lower Subunit 5C2 diabase sill (Figs. F130, F131). This is a small diabase intrusion that shows chilled margins against mudrock and has internal diabase breccia with coarse calcite-spar cement. The diabase breccia clasts also have chilled margins. A possible explanation is that intrusion of the diabase sill (defined as Subunit 5C2) locally created gas from carbon-rich sediments and caused an initial upward, gas-driven expulsion from a gas-magma mixture that cracked and brecciated the diabase (interval 210-1276A-97R-3, 144–147 cm) (Fig. F131). As the cracks widened, more magma was intruded and chilled against the mudrock (Sections 210-1276A-97R-3, 141 cm, and 97R-3, 148 cm). After intrusion, the by-then brecciated interior was filled by calcite of possible hydrothermal origin, followed by minor deformation.

Comparisons with the Conjugate Iberia Margin and the Western Central North Atlantic

The first part of this section provides a brief comparison of the Site 1276 lithostratigraphic successions and depositional settings with sediments of the same age cored on the conjugate Iberia margin. The second part extends the comparisons to the lithostratigraphy of the central North Atlantic. The information summarized in Figure F118 and the discussion in the first part is based on information published in the "Site 398" chapter in the DSDP Leg 47B *Initial Reports* volume (Shipboard Scientific Party, 1979; Sibuet, Ryan, et al., 1979) and *Initial Reports* volumes for ODP Legs 149 (Sawyer, Whitmarsh, Klaus, et al., 1994) and 173 (Whitmarsh, Beslier, Wallace, et al., 1998). Discussion in the second part compares core recovery at Site 1276 with lithostratigraphy of the North American Basin (i.e., the western central North Atlantic) as described by Jansa et al. (1979). These publications are not cited again in the text below. Table T5 summarizes the sedimentation rates determined for the Newfoundland and Iberia conjugate margins.

F118. Simplified time stratigraphic chart of lithofacies, p. 241.

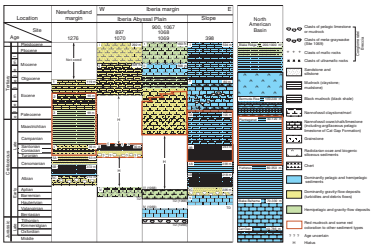

T5. Comparison of approximate sedimentation rates, p. 329.

The Newfoundland–Iberia Conjugate Margins

Despite the fact that 11 DSDP and ODP sites have been occupied across the Iberia margin, only at Site 398 was an almost continuous succession from the Pleistocene down to the Hauterivian penetrated and recovered. The other sites are situated over basement highs (Fig. F4, p. 43, in the "Leg 210 Summary" chapter) that were progressively bur-

ied during the Cretaceous and early Paleogene, resulting in an incomplete Cretaceous to Eocene section.

In making lithostratigraphic comparisons across the Newfoundland and Iberia margins, it is important to keep in mind that interregional oceanographic controls on deposition, such as changing plankton productivity and depths of the CCD, may be modified by more local topographic and tectonic influences that change over time. The present-day setting of the sites described below is the result of tectonic and depositional history from the time of continental rifting. The locations of the drill sites on present-day abyssal plains, continental rises, and slopes are not necessarily indications of their settings during the Cretaceous and Paleogene. In particular, fault-related basement highs were draped by early postrift sediments and subsequently covered by prograding sediments across the ocean–continent transition.

All the sites except Site 398 (which is on the "continental slope" on the southern flank of Galicia Bank) are situated on present-day abyssal plains (the Newfoundland Basin and the Iberia Abyssal Plain). The westernmost Iberia sites are several tens of kilometers from the continental rise. Hence, there are three settings: abyssal plain (Sites 1070, 897–899, and 1069), margin of the abyssal plain (Sites 900, 901, 1065, 1067, 1068, and 1276), and continental slope (Site 398). Each is likely to have received different proportions of pelagic, hemipelagic, and turbiditic sediments and to have been subjected to differing amounts of mass wasting during its development.

In general, turbidity currents bypass the continental slope to be deposited on the abyssal plain, resulting in slope settings that are dominated by pelagic and/or hemipelagic sediments, with possible reworking by bottom currents. Such slope bypassing is likely to have been significant during the history of the Newfoundland and Iberia conjugate margins. The contrast between slope and abyssal plain sediments is well developed in the Pliocene–Pleistocene sediments drilled during Leg 149. Sediments of this age in the Iberia Abyssal Plain range in thickness from 50 m (Site 899) to 292 m (Site 897). These sediments contain many siliciclastic sand- to mud-grade turbidites that are covered by nannofossil ooze and/or nannofossil clay. The sedimentation rate at Site 897 is 92 m/m.y. In contrast, the 96-m-thick Pliocene–Pleistocene sequence at Site 900, which is situated on the edge of the abyssal plain at the foot of the continental rise, consists almost entirely of nannofossil ooze, nannofossil clay, and clay deposited at a rate of 22.5 m/m.y. The dominance of pelagic and hemipelagic deposits and the low sedimentation rate at Site 900 reflect bypassing by turbidity currents that so strongly controlled sedimentation at Site 897.

Below, each comparison of lithostratigraphy between the Newfoundland and Iberia margins begins with a brief summary of features of Site 1276 lithologic units and then relates them to intervals of the same age on the Iberia margin.

Unit 1 (Middle Eocene to Lower Oligocene)

Unit 1 at Site 1276 is the basal 118 m of an apparent abyssal fan interpreted from the seismic reflection records that cross the site. On the depth-converted seismic section, this wedge of sediment is ~800 m thick at Site 1276. Recovered sediments record dominant hemipelagic deposition that was interrupted by turbidity currents and debris flows. Clasts of Cretaceous hemipelagic and pelagic sediment in the debris flows (including a clast of Valanginian age) indicate that at times there was significant erosion of material from the adjacent continental slope.

At the Iberia Abyssal Plain sites, sedimentary rocks equivalent in age constitute lithologic Unit II. They consist of upward-fining and -darkening intervals (10–50 cm thick) of carbonate mud–dominated turbidites with thin siliciclastic sandstone bases interbedded with hemipelagic/pelagic deposits. The sediments do not show evidence of slumping, debris flows, or grainstones like those at Site 1276, and thus they do not show extensive reworking of carbonate detritus from the continental slope or shelf.

Age-equivalent lower Oligocene to middle Eocene sedimentary rocks at Site 398 on the Galicia continental slope consist of biogenic siliceous marly chalks interrupted by 1- to 5-cm-thick layers of siliciclastic and calcareous siltstone/sandstone. The calcareous sand fraction is composed dominantly of foraminifers, carbonate fragments, and a matrix that is largely nannofossils. The siltstone and sandstone layers show parallel and cross lamination, which, it is suggested in the site report for Site 398, records "geostrophic flow." In contrast, Maldonado (1979) estimates that 30%–40% of the interval is turbidites, the bulk of which are nannofossil-rich mudrocks. This interpretation, and later drilling results from Legs 149 and 173, suggests an alternate explanation that the sandstone layers were deposited by turbidity currents, although most of the entrained sediment was carried downslope to the abyssal plain below. Because the succession at Site 398 is largely composed of bioturbated nannofossil chalks, the chalks that accumulated from turbidity currents must have been deposited in relatively thin units—a conclusion that is consistent with the low sedimentation rate for this interval at Site 398 (Table T5).

From the foregoing summary it is evident that middle Eocene to Oligocene sediments both at Site 1276 and beneath the Iberia Abyssal Plain are dominated by redeposited sediments. Turbidity currents transported carbonate sediments (including nannofossil-rich sediments) from locations on and above the continental slope, as well as minor amounts of siliciclastic and carbonate material that originated from the upper slope or outer shelf. These density flows largely bypassed Site 398. There is a higher proportion of shallow-water material present in the grainstone turbidites at Site 1276 off Newfoundland. On both margins, noncarbonate bioturbated hemipelagic mudrock between the turbidites indicates deposition below the CCD of at least ~4.5 km below sea level at the time (Tucholke and Vogt, 1979). Pelagic nannofossil-rich sediments at the shallower Site 398 indicate that the seafloor there was above the CCD. Significant amounts of biogenic silica are present only at Site 398, suggesting either upwelling of nutrients along the Iberia margin or dissolution of biogenic silica at other sites.

Unit 2 (Upper Paleocene to Middle Eocene)

Lithologic Unit 2 at Site 1276 consists of ~65 m of predominantly light colored calcareous sandstones, grainstones, and marlstones, together with darker-colored mudrocks. These lithologies are arranged in upward-fining and -darkening intervals that are 20 to 140 cm thick. Unit 2 is interpreted as carbonate-rich turbidites interbedded with bioturbated hemipelagic mudrocks. The carbonates were derived from locations on the continental slope and possibly the outer shelf, and they consist of both contemporaneous sediments and material recycled from Cretaceous deposits.

At Sites 900, 1067, and 1068, carbonate turbidites (10–50 cm thick) dominate the age-equivalent upper Paleocene to middle Eocene section beneath the Iberia Abyssal Plain. The turbidites have thin, basal, mixed

siliciclastic and calcareous sandstones that pass upward into nannofossil chalks and claystones capped by bioturbated dark-colored hemipelagic claystones. The hemipelagic sediments are reddish brown in the lower parts of the intervals cored at these sites. At Site 1068, reddish colors appear from basement up to the base of the Lutetian (middle Eocene), whereas at Site 900 (situated only 800 m to the east), they extend up into the upper Lutetian. This suggests that the distribution of the colors is more likely to be diagenetic than primary.

All or part of the Paleocene–Eocene succession is missing at Sites 1070, 897, and 899 because the crests of the basement ridges on which the sites were drilled still projected above parts of the abyssal plain at this time. Sediments deposited on the ridge flanks (as seen on seismic reflection profiles) were transported from the margin of Galicia Bank to the north.

At Site 398 on the Galicia slope, biogenic siliceous marly chalks with thin siliciclastic sandstones are similar to those described above from Unit 2 at Site 1276 (Fig. **F118**). However, silica is more common, rising to 20%–30%, and the sediments are 50%–60% pelagic carbonates. Reddish colors begin to appear about two-thirds of the way down the age-equivalent section at Site 398. The chalks are laminated in places, and some exhibit soft-sediment folds, claystone clasts, and stretched burrows accompanied by pebbly mudstones containing fine-grained carbonate clasts. These features indicate episodes of downslope movement of slumps and gravity flows (Maldonado, 1979).

Turbidity currents delivered carbonate sediments to the abyssal plains on both sides of the Atlantic during the late Paleocene to middle Eocene, but they largely bypassed Site 398. The carbonate turbidites at Site 1276 are thicker than those off Iberia and contain a greater proportion of carbonate allochems than the fine-grained nannofossil-rich sediments redeposited on the Iberia Abyssal Plain.

Sedimentation rates at Sites 1276 and 398 were similar (5–7 m/m.y.), but they were greater beneath the Iberia Abyssal Plain at Sites 900 and 1068 (~18 m/m.y.) because a greater volume of sediment was carried there by gravity flows.

Significant amounts of biogenic silica are present only at Site 398, suggesting either upwelling of nutrients above the Galicia slope or dissolution of the silica during diagenesis at the other sites.

Unit 3 (Lowermost Campanian to Upper Paleocene)

Lithologic Unit 3 at Site 1276 contains much less grainstone (carbonate sand) than Unit 2, and it is composed largely (80%–90%) of mudrocks deposited either from density flows or as background settling of hemipelagic material.

At Site 1068 on the margin of the Iberia Abyssal Plain, age-equivalent sediments have thicker turbidite intervals (as thick as a meter) and sand-sized sediment at the bases of individual turbidites is more carbonate rich. These sediments include foraminiferal sands plus peloidal and intraclastic packstones and grainstones. Siliciclastic sands are predominantly quartz, but those of granule size also contain shallow-water carbonate particles and rock fragments of green phyllite. Similar sediments appear in the Paleocene section at Site 1069 in the Iberia Abyssal Plain.

At Site 398 on the Galicia slope, red to brown marly chalks, marlstones, and claystones, with thin intervals of siliciclastic sandstone and siltstones sporadically spaced every 50 cm to 1 m, were deposited during the early Campanian to Paleocene. Reddish brown mudstones form

30%–50% of the sediments (Maldonado, 1979), similar to the lower part of Unit 3 at Site 1276. These sediments contain only small amounts of biogenic silica, suggesting that there was little upwelling compared to the overlying section. Otherwise, overall depositional processes and sedimentary settings were the same as those for the overlying upper Paleocene to middle Eocene section.

Compared to the Iberia Abyssal Plain area (Sites 900, 1067, and 1068), the influx of redeposited carbonate sediment to Site 1276 was much smaller. However, sedimentation rates were low on both margins where this interval was drilled.

Unit 4 (Turonian to Uppermost Santonian)

Lithologic Unit 4 at Site 1276 consists of reddish brown, thoroughly bioturbated sandstone, muddy sandstone, sandy mudstone, and mudstone. Pervasive bioturbation is attributed to a favorable environment for burrowing organisms (e.g., oxygenation and food supply) and a very slow sedimentation rate (~2 m/m.y. or less). Gradational coarsening–fining cycles tens of centimeters thick suggest reworking by bottom currents.

At Site 398 on the Galicia slope, an interval of reddish brown unfossiliferous claystone, contemporaneous with Unit 4 at Site 1276, is sandwiched between nannofossil-bearing rocks that provide the age control. Similar unfossiliferous sediments are present at Sites 897, 898, and 1070 in the Iberia Abyssal Plain, but their age is not well constrained by sediments above and below: the oldest sediment above is middle Eocene (Site 897), and the youngest sediment below is Aptian at all three sites. However, because the sediments are so similar to those at Sites 1276 and 398, it is tempting to infer that they are the same age. At Sites 897 and 1070, volcaniclastic material is present in sandy layers in the unfossiliferous claystones. At Sites 897 and 899, a basal interval of upward-fining, poorly sorted sandstones and conglomerates is present. The clasts are composed mainly of fine-grained limestone, chalk, and nannofossil claystone. Some of these clasts yield nannofossils of late Hauterivian, Barremian, or Aptian age.

Reddish sediment colors and low sedimentation rates on both margins suggest very limited sediment input into well-oxygenated basins. At Site 1276, the muddy sandstones deposited by gravity flows probably were reworked by bottom currents.

Unit 5 (Uppermost Aptian(?) to Turonian)

A thick (~700 m) sedimentary succession of late Aptian(?) to Turonian age, dominated by dark gray to black mudrocks, is present at Sites 1276 and 398. This interval was not drilled beneath the Iberia Abyssal Plain because the basement highs that were drilled were not covered by sediment until Late Cretaceous to Paleogene time. However, older sediments are clearly present between the basement highs as seen in seismic reflection profiles; the sediments form a semitransparent interval termed seismic Unit 3 by Groupe Galice (1979) and seismic Unit 5 by Wilson et al. (1996, 2001). At Site 1276, an almost identical semitransparent interval is present above the U reflection (see **"Leg 210 Summary"** chapter, including Fig. **F12,** p. 54). Synthetic seismograms facilitate ties between the lithostratigraphy and the seismic units at both Sites 398 and 1276 (Bouquigny and Willm, 1979) (see **"Seismic-Borehole Correlation,"** p. 107).

Three lithologic subunits are identified at Site 1276. Subunit 5A contains abundant gravity-flow deposits consisting dominantly of mud-

rock and occasional marlstone above calcareous sandstone and siltstone and/or grainstone. Gravity flows were responsible for depositing ~80% of the succession, the remainder of which is either bioturbated hemipelagic mudrock or black shale. The latter may be hemipelagic and deposited when sea-bottom conditions were anoxic, or material redeposited from an oxygen-minimum zone upslope, or both. In contrast, Subunit 5B is dominated by bioturbated hemipelagic mudrocks with some carbon-rich black shale intervals and minor amounts of coarser sediment like that in Subunit 5A. The presence of siderite, dolomite, and calcite nodules is also a characteristic feature. In Subunit 5C, massive calcareous mudrocks constitute ~75% of the interval, predominantly in thick tops of turbidites. The turbidites contain basal parallel-laminated sandstone or siltstone, grading upward into disorganized fine-grained muddy siltstone with contorted and "swirled" laminae and then into mudrock tops.

At Site 398, the time-equivalent mudrock interval is also divided into three subunits (4A–4C). The oldest of these extends down into the Aptian and Barremian, in contrast to Subunit 5C at Site 1276, which is uppermost Aptian(?) to lowermost Albian. Arthur (1979) provided a succinct summary of features and environmental interpretation of subunits at Site 398, which is summarized below from the top down.

Subunit 4A at Site 398 (middle Albian to mid-Cenomanian) consists of nannofossil chalk and claystone interbedded with dark-colored claystone, with some graded silt- and sand-sized grainstone (referred to as "mudchip siltstone and sandstone") and some radiolarian sands in the upper part. Unlike sedimentary rocks of similar age at Site 1276, nannofossil-rich pelagic deposits indicate that Site 398 was just above the CCD. Otherwise, depositional processes were similar; turbidity currents transported terrigenous sand, silt and mud, contemporaneous pelagic carbonate, and older carbonates reworked from outcrops. Seafloor conditions fluctuated between slightly oxygenated and anoxic. Arthur (1979) reported an interval of dark carbon-rich mudrocks of Cenomanian age, which presumably corresponds to OAE 2, in Cores 210-1276A-32R and 33R.

Subunit 4B at Site 398 (lower to middle Albian) consists of very dark gray to black, laminated to homogeneous claystone interbedded with mudstone (including black shales) and calcareous mudstone, of which the lighter-colored varieties are bioturbated. Carbonate contents are low, organic carbon values are high because of the presence of terrigenous plant debris, and siderite nodules are common. Arthur (1979, p. 721) suggested that deposition occurred in an "outer deep sea fan" setting. Deposition is inferred to have been below the CCD, yet ammonites are relatively common. This paradox was seemingly resolved by de Graciansky and Chenet (1979), who suggested that the ammonites were transported from shallower areas by debris flows and were buried so quickly that they were not dissolved. Turbidity flows also could have been the transportation mechanism. The sedimentation rate for this subunit is ~50 m/m.y., essentially the same as the rate for the age-equivalent Subunit 5B at Site 1276 (~20–100 m/m.y.) (Table T5).

Subunit 4C at Site 398 (upper Barremian to upper Aptian) consists of dark-colored mudrock and calcareous claystone interbedded with conglomeratic debris flow deposits containing pebbles of mudrock (which were soft the time of transport) and light-colored, fine-grained limestones (including some of Tithonian age). The conglomerates are very similar to those at Site 1276 (Section 210-1276A-93R-3) (Fig. F97). Siderite concretions are less common in Subunit 4C at Site 398 than in over-

lying subunits, but the amount of terrestrial plant debris is considerably higher. In the lower part of the subunit, siliciclastic sandstones and siltstones occur at the bases of turbidites, as do a few graded mudchip sandstones (equivalent to sediments described as grainstones at Site 1276). Arthur (1979, p. 721) suggested that Subunit 4C accumulated probably below the CCD by "prodelta or submarine fan deposition with various sediment sources including nearby slopes and scarps from which calcareous mudchip sands and silts, carbonate-pebble conglomerates and debris flows and slump units were derived." Subunit 4C at Site 398 is lithologically very similar to Subunit 5C at Site 1276, but it is older.

Comparisons with Central North Atlantic Stratigraphy

Based on DSDP results, Jansa et al. (1979) defined six sedimentary formations that extend over much of the North American Basin (i.e., the western part of the central North Atlantic). A schematic summary of the lithology and age of these formations is shown in Figure **F118.** The brief discussion below highlights similarities and differences between the central North Atlantic formations and the successions drilled on the Newfoundland and Iberia conjugate margins. It also refers to the changes in the depths of the CCD charted by Tucholke and Vogt (1979) for the North American Basin.

Blake Ridge Formation (Middle Eocene to Pliocene; 200–1000 m Thick)

The Blake Ridge Formation is dominated by greenish gray and brown hemipelagic mud, a lithology that forms the background sedimentation between the turbidites of similar age at Site 1276 and beneath the Iberia Abyssal Plain. At Site 398, nannofossil-rich sediments predominate because the seafloor was above the CCD at the time of deposition. The Iberia Abyssal Plain sites were below the CCD until the middle Miocene, when nannofossil-rich sediments appeared. The sediments at Site 1276 show that it was below the CCD at least until the early Oligocene; no sediments younger than this age were cored at the site.

Bermuda Rise Formation (Lower to Middle Eocene; 130–220 m Thick)

The presence of significant amounts of biogenic silica is the defining feature of the Bermuda Rise Formation, which contains siliceous claystone and chert plus radiolarian and calcareous mudstone. The siliceous marly chalks of Unit 2 at Site 398 equate with the Bermuda Rise Formation, but no siliceous sediments of similar age were cored beneath the Iberia Abyssal Plain or at Site 1276. This difference could be caused by lack of nutrient upwelling off the Newfoundland margin and/or dissolution of biogenic silica on both margins.

All the sites on the Newfoundland and Iberia conjugate margins were below the CCD during this time interval, excepting Site 398 where pelagic carbonate sediments were deposited.

Plantagenet Formation (Upper Cenomanian to Paleocene; 30–120 m Thick)

Reddish brown noncalcareous claystone characteristic of the Plantagenet Formation is present in Unit 3 at Site 1276 and extends uphole into the background mudrocks of uppermost Paleocene to middle Eocene Unit 2. In Unit 4 at Site 1276, mudrocks are subsidiary to intensely bioturbated reddish muddy sandstones interpreted to be turbiditic sands reworked by bottom currents. Reddish brown claystones are also present at Iberia Sites 897, 899, and 1070 and in Unit 3 at Site 398. They contain volcaniclastic material at Site 1070 and lie above upward-

fining conglomerates and sandstones at the other two sites. These coarser sediments were deposited by debris flows and contain pebbles of Lower Cretaceous limestone and claystone. The red claystones are Cenomanian to upper Santonian off Iberia, but red colors continue uphole into the Paleocene at Site 398. Likewise, at Sites 900 and 1068, hemipelagic mudrocks (capping carbonate turbidites) are brownish red up to the middle Eocene, but as discussed earlier, the red color disappears at different times at the two sites, suggesting that the color might be affected by diagenesis.

The change from deposition of dark-colored mudrocks and black shale facies characteristic of the underlying Hatteras Formation to the reddish sediments of the Plantagenet Formation might have been caused by enhanced bottom water circulation that led to oxygenated conditions on the seafloor. This change could relate to the separation of the Rockall Plateau from northwest Europe if it enabled cooler waters from the north to flow southward (Shipboard Scientific Party, 1979). Given that temperatures at high latitudes were still warm at this time, however, this explanation seems unlikely. It is possible that the opening of a deepwater connection between the North and South Atlantic could have led to the oxygenation of the deep North Atlantic basins near the Cenomanian/Turonian boundary (Tucholke and Vogt, 1979).

Hatteras Formation (Barremian to Cenomanian; 80–350 m Thick)

The Hatteras Formation consists of black to dark greenish gray carbonaceous clay and laminated marl, including the black shale facies characteristic of OAEs. The formation is very similar to Unit 5 at Site 1276 and Unit 4 at Site 398, except that at these sites the equivalent section is considerably thicker (~700 m).

A combination of environmental factors probably contributed to the accumulation of these dark-colored sediments under intermittently dysoxic to anoxic conditions in the North Atlantic. During the latter part of the Early Cretaceous, global sea level began to rise toward its Late Cretaceous peak (Haq et al., 1987). The climate became warm and humid, increasing weathering rates, and there was a dramatic increase in carbonate productivity (Skelton et al., 2003). Most of the coarser sediment and carbonate was sequestered on the shallow continental margins. The deep basin was below the CCD and received only fine sediment carried in suspension from the shallow margins and pelagic biogenic sediment deposited during episodes of enhanced surface water productivity. This background hemipelagic sedimentation on a poorly oxygenated seafloor is typical of the Hatteras Formation.

Off Newfoundland and Iberia, the background hemipelagic sedimentation was interrupted by numerous gravity-flow deposits derived from material that accumulated on the adjacent, shallow margins. Because the ocean basin was also relatively narrow at the time (600–1000 km) and had only restricted connections with small shallow seas to the north (Tucholke and McCoy, 1986), it probably accumulated larger-than-normal volumes of hemipelagic sediments from the margins. As a result, unusually thick sequences of Hatteras-equivalent sediments were deposited off Newfoundland and Iberia.

IGNEOUS AND METAMORPHIC PETROLOGY

At Site 1276, igneous rocks were recovered from diabase sills that intrude lithologic Subunit 5C (see **"Site 1276 Thin Sections"** and piece

logs in "Site 1276 Core Descriptions"). An upper sill (Subunit 5C1) was recovered in Sections 210-1276A-87R-6, 72 cm, through 88R-7, 122 cm. A second interval comprising several sills, here termed a "sill complex," was drilled deeper in the hole from the top of Core 210-1276A-97R through Core 102R (Subunit 5C2). The individual sills in the lower complex range from a few centimeters to >4 m in thickness. The cored igneous rocks are all aphyric diabase composed of primary plagioclase, pyroxene, magnetite, olivine, apatite, biotite, and glass. Near the contacts of the sills, hydrothermal alteration of the diabase ranges from strong to total; it becomes less intense toward the center of the sills. Secondary mineral phases include various clay minerals (mainly smectite, kaolinite, and chlorite), calcite, quartz, analcime, and, in rare cases, serpentine (Table T3).

Most of the sills preserve chilled margins. The average crystal size increases from the margins toward the centers of the sills, with a crystal size as large as 1 mm in the centers of the larger sills. Crystal size variations are accompanied by changes from a predominantly intersertal texture near the sill contacts to an intergranular to subophitic texture toward the centers of the sills. Where primary contacts with the sediments are preserved, the sediments are baked over a distance of as much as 1 m and are associated with marked color changes. Recrystallization and the formation of new minerals and very high reflectance of the organic matter observed in the sediments only occur near the intrusive contacts.

Upper Sill (Subunit 5C1)

The upper sill, forming Subunit 5C1, extends from Section 210-1276A-87R-6, 72 cm (top of sill at 1612.72 mbsf), to Section 88R-7, 117 cm (base of the sill at 1623.00 mbsf). The rocks are aphanitic to fine-grained aphyric diabase. Hydrothermal alteration is high to total at the margins and moderate toward the center of the sill.

The high recovery (Core 210-1276A-87R = 93.6% and Core 88R = 97.1%) and lack of drilling disturbance make it possible to document the sill/sediment relationships, as well as the lithologic and textural variations across the sill. The sediments show a baked contact at the top of the sill, which is well preserved in Section 210-1276A-87R-6 (Fig. F119). The sill is ~10 m thick and preserves chilled margins at its upper and lower contacts. Although hydrothermal alteration is high to complete at the margins and moderate in the center of the sill, the primary magmatic textures can still be recognized, allowing three zones of magmatic origin to be defined based on grain size and textural variations (Fig. F120). From the margin to the center sill, zone 1 is marked by crystal sizes <0.3 mm in diameter and a predominant intersertal texture; zone 2 is defined by crystal sizes ranging between 0.5 and 0.8 mm in diameter and shows intersertal, intergranular, and subophitic textures; in zone 3, the average grain size is 0.8 mm in diameter and the texture is predominantly subophitic. The contacts between these zones are gradual and were determined based on observations made on the core and from thin section analysis.

Contacts and Relationships to Sediments

The upper contact of the sill is sharp and parallel to bedding of the overlying sediments. The contact is preserved in Section 210-1276A-87R-6 (Piece 3A) (Fig. F119). Sediments overlying the contact are recrys-

F119. Upper contact of Subunit 5C1 igneous sill, p. 242.

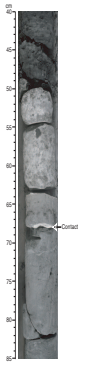

F120. Upper sill observations, p. 243.

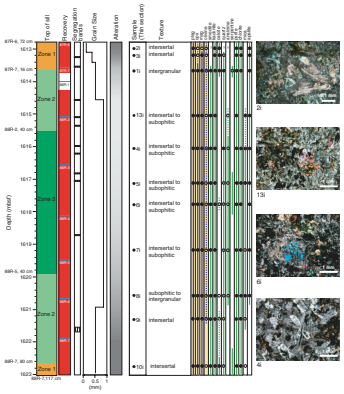

tallized grainstones (i.e., marbles) and calcareous siltstones that preserve a primary sedimentary lamination (Fig. F121). In the calcareous siltstones, calcite porphyroblasts are observed (for details see Fig. F115). They decrease in size away from the contact and become gradually less prominent until they can no longer be seen >66 cm from the contact (Section 210-1276A-87R-6, 6 cm) (Fig. F121); their maximum size near the contact is ~1 cm. These porphyroblasts, together with the recrystallized metagrainstones, are interpreted to record a thermal overprint related to emplacement of the sill. The results of this thermal overprint can be observed in interval 210-1276A-87R-6, 6–72 cm (Fig. F121). In smear slides, evidence for a thermal overprint is seen in Sample 210-1276A-87R-6, 41–42 cm, where a high reflectance of organic matter is observed. In Sample 210-1276A-87R-6, 67 cm, euhedral biotite is present and it could be an alteration product (see "Site 1276 Smear Slides"), although a detrital origin cannot be excluded.

In the calcareous siltstones overlying the sill, a subvertical crenulated vein occurs in interval 210-1276A-87R-6, 5–41 cm (Fig. F121). This vein is filled with calcite and pyrite. Folding of the vein is most likely related to compaction, indicating that the vein formed before there was significant compaction of the sediment into which the sill intruded (see "Physical Properties," p. 99). In interval 210-1276A-87R-6, 46–55 cm, sediment laminae warp around the calcite porphyroblasts, suggesting that they also predate compaction. Assuming that both the porphyroblasts and the vein formed as a consequence of sill intrusion, it is likely that the sill was emplaced at a very shallow level in weakly consolidated sediments. Thus, the age of emplacement may be close to that of the surrounding sediments (i.e., uppermost Aptian[?]–lower Albian; see "Biostratigraphy," p. 73).

The lower contact of the sill was not recovered in one piece (Fig. F122). A chilled margin marks the base of the sill, but no baked contact is preserved in the underlying sediments. It is therefore difficult to estimate the extent of thermal overprint of these sediments. The sediments are calcareous claystones that preserve sediment laminations, and no direct evidence for a thermal overprint was found in a smear slide of the sediments (Sample 210-1276A-88R-7, 119–120 cm) (see "Site 1276 Smear Slides").

F121. Calcareous siltstones overlying the upper sill, p. 244.

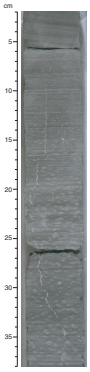

F122. Lower contact of the upper sill, p. 245.

Lithologic and Textural Variations across the Sill

The primary mineralogy and composition of the rocks forming the sill are very similar throughout Sections 210-1276A-87R-6 through 88R-7. The igneous intrusion is diabase with a groundmass consisting of plagioclase (40%–60%), clinopyroxene (10%–30%), magnetite (<5%), subordinate olivine (<5%), and glass (<20%) (see "Site 1276 Thin Sections").

Zone 1

Zone 1 forms the outer parts of the sill; it includes the interval from Sections 210-1276A-87R-6, 72 cm, to 87R-7, 16 cm, and the interval from Sections 88R-7, 80 cm, to 88R-7, 117 cm. The outer margins of the zone are marked by sharp chilled margins. The inner margins are gradational to zone 2. Structures and veins are rare; vesicles are observed only in interval 210-1276A-87R-6, 78–85 cm. The rocks in this zone are massive greenish gray aphyric diabase with crystal sizes <0.5 mm. Thin sections used to classify the mineralogy and textures of zone 1 were taken from intervals 210-1276A-87R-6, 86–89 cm (2i in Fig. F120), 87R-6,

108–113 cm (3i in Fig. F120), and 88R-7, 93–96 cm (10i in Fig. F120) (see "Site 1276 Thin Sections"). XRD samples were taken adjacent to the thin section locations and were used to identify the groundmass mineral composition (Table T3). Primary minerals are rarely preserved in zone 1, and they are replaced by clay minerals (mainly kaolinite and chlorite), calcite, quartz, pyrite, and, in one sample, rare serpentine. The primary mineral composition was estimated to be plagioclase (60%), clinopyroxene (10%), magnetite (<5%), subordinate olivine (<5%), and glass (<20%). The dominant magmatic textures are intersertal (Fig. F123).

Zone 2

Zone 2 includes the interval from Sections 210-1276A-87R-7, 16 cm, to 88R-2, 40 cm, and the interval from Sections 88R-5, 40 cm, to 88R-7, 80 cm. Contacts with zones 1 and 3 are gradational. The rock in this zone is greenish gray massive diabase with crystal sizes ranging between 0.5 and 0.8 mm. Thin sections used to classify the mineralogy and textures of zone 2 include Samples 210-1276A-87R-7, 16–19 cm (1i in Fig. F120), 88R-1, 93–95 cm (13i in Fig. F120), 88R-5, 104–109 cm (8i in Fig. F120), and 88R-6, 69–72 cm (9i in Fig. F120) (see "Site 1276 Thin Sections").

Primary minerals are locally well preserved, and their composition is estimated to be plagioclase (60%), clinopyroxene (20%), magnetite (<5%), subordinate olivine (<5%), and glass (<10%). Magmatic textures in zone 2 are more variable than in the remainder of the sill. The dominant magmatic textures are intergranular. Intersertal and subophitic textures are also observed in contiguous domains within the same thin sections (Fig. F124). Secondary minerals are smectite- and kaolinite-group clay minerals, quartz, and pyrite (see XRD results in Table T3). Apatite, analcime, and serpentine are found only in single samples and do not occur throughout zone 2.

Zone 3

Zone 3 forms the center of the sill and includes the interval from Sections 210-1276A-88R-2, 40 cm, to 88R-5, 40 cm. The rocks in this zone are greenish gray diabase that exhibits a characteristic "patchy" pattern. Average crystal size is homogeneous and is on the order of 0.8 mm throughout the zone (Figs. F125, F126). Thin sections used to characterize the mineralogy and textures of zone 3 include Samples 210-1276A-88R-2, 93–96 cm (4i in Fig. F120), 88R-3, 56–59 cm (5i in Fig. F120), 88R-3, 121–125 cm (6i in Fig. F120), and 88R-4, 111–115 cm (7i in Fig. F120) (see "Site 1276 Thin Sections" and Table T3). The primary mineral assemblage is locally well preserved; its composition is estimated to be plagioclase (60%), clinopyroxene (30%), magnetite (<5%), subordinate olivine (<5%), and glass (<5%). The magmatic texture in zone 3 is predominantly subophitic. Intergranular and intersertal textures occur in the same thin sections but are less abundant (Fig. F127). In all the samples analyzed by XRD from zone 3, smectite- and kaolinite-group clay minerals, quartz, pyrite, and analcime are present as secondary minerals. Apatite, analcime, and serpentine are found only in occasional samples.

Segregation Bands

Segregation bands occur throughout the sill (Fig. F120) but form <5% of the total recovered interval. The bands are typically as thick as 5 cm,

F123. Textural characteristics of zone 1 in the upper sill, p. 246.

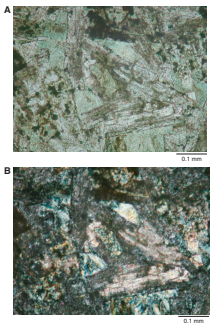

F124. Intersertal and intergranular textures, zone 2, upper sill, p. 247.

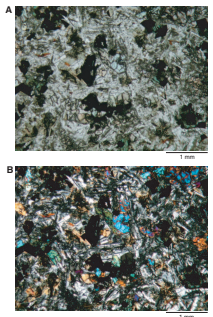

F125. Textural characteristics of zone 3 in the upper sill, p. 248.

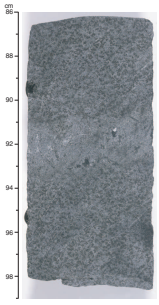

F126. Texture characteristic of zone 3 in the upper sill, p. 249.

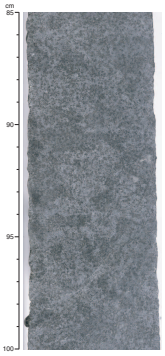

light colored, and subhorizontal with distinct (but not sharp) contacts with the host rock. An example of a segregation band is observed in interval 210-1276A-88R-2, 91–94 cm (Fig. F125). In thin section, this lithology shows texture, composition, and crystal shape that are different from the host rock. The major mineral phase observed in these bands is zoned plagioclase crystals as much as 1 mm in diameter. Clinopyroxene is rare or absent. Some of the bands are strongly altered. Large calcite crystals (as large as 4 mm in diameter) are observed in the bands. Pyrite shows characteristic acicular crystals that are as large as 5 mm.

F127. Thin section, zone 3 of upper sill, p. 250.

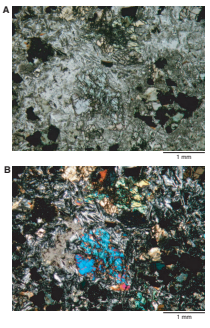

Hydrothermal Alteration

The intensity of alteration is high to complete at the margins of the sill, but alteration decreases to moderate levels toward the center of the sill. It is not clear to what extent alteration is controlled by magmatic textures and crystal size, both of which define the different zones in the sill. It appears that the alteration was not sufficiently strong to mask the internal magmatic zonation of the sill. The observation that calcite and chlorite occur only at the contacts of the sill, whereas analcime is found only in the center, suggests that the sills experienced a polyphase alteration history, which merits postcruise investigation.

ICP-AES Data

Twelve samples from Hole 1276A were analyzed by ICP-AES for major and trace element abundance. The results are given in Table T6. Sample preparation and analytical methods are given in "Geochemistry," p. 25, in the "Explanatory Notes" chapter. At least two representative samples were taken from each of the zones discussed above. The ICP-AES samples were taken close to the thin section and XRD samples, which enables us to link compositional variations with mineralogical and textural observations.

T6. ICP-AES major and trace element analysis of upper and lower sill sediments, p. 330.

Major and trace element variation diagrams are shown in Figure F128. Apart from two samples from the altered margins of zone 1 (Samples 210-1276A-87R-6, 86–89 cm, and 87R-6, 107–108 cm), the major and trace element concentration plots might conceivably be interpreted as primary magmatic trends (e.g., K_2O, Na_2O, and CaO vs. SiO_2) (Fig. F128). However, the presence of analcime and quartz (both determined by XRD) indicates that some mobilization of major element oxides has taken place. One sample from zone 3 (center of the sill) shows higher values of SiO_2 and Zr and is interpreted as possibly a more differentiated magma (Sample 210-1276A-88R-4, 110–111 cm). The high Zr values in this one sample deviate from any inferred magmatic trend, possibly because of the presence of the mineral zircon in this sample. In thin section, this sample contains zoned feldspar phenocrysts typical of a segregation band, suggesting that it is not representative of the whole-rock composition and, again, alteration effects are likely.

F128. Major and trace element variation diagrams, upper sill, p. 251.

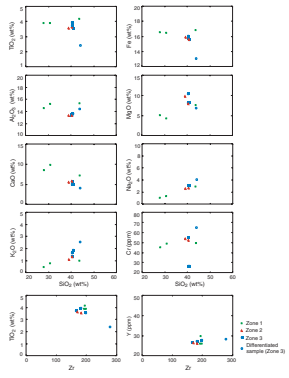

Plots of TiO_2 vs. Zr and Y vs. Zr (bottom of Fig. F128), elements that are considered to be immobile under low-temperature alteration processes (subgreenschist facies in this case), may distinguish magmatic trends from alteration effects. In these plots, all of the strongly altered samples of zone 1 plot into a very narrow field that generally is indistinguishable from data points for the less altered samples of zones 2 and 3 (except for the more differentiated Sample 210-1276A-88R-4, 110–111 cm). The absence of any clear chemical distinction between samples

from these three zones of the sill on these plots suggests that all three zones are magmatically related.

When the compositions of the diabase samples of zones 2 and 3 are plotted on the $Na_2O + K_2O$ vs. SiO_2 classification diagram of Le Bas et al. (1986), most plot outside the diagram because of anomalously low SiO_2 contents (Fig. F129). At face value, the plots are suggestive of fractionation of an undersaturated magma giving rise to highly alkaline rocks such as basanite. However, the apparent absence of nepheline, a major phase in basanites, causes us to question whether the magma was really so alkaline. Silica mobility (see above) could have displaced compositions from an originally more basaltic character. For comparison, data from volcanic rocks recovered from the New England seamounts located off the eastern United States (Pe-Piper et al., 1990) plot on the $Na_2O + K_2O$ vs. SiO_2 classification diagram in the same field as the Site 1276 samples (i.e., alkaline). Volcanic rocks from the Newfoundland seamounts 180 km to the south are considerably more differentiated, and they also show an alkaline trend. Our provisional interpretation, based largely on the immobile major and trace elements chemistry, is that the diabase sills are likely to be of alkaline composition, but the extent of magmatic fractionation and chemical alteration require post-cruise chemical data to elucidate.

F129. $Na_2O + K_2O$ vs. SiO_2 classification diagram with Site 1276 diabase sill samples, p. 252.

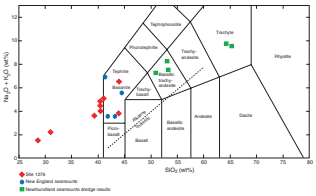

Lower Sill Complex (Subunit 5C2)

The lower sill complex (Subunit 5C2) extends from Sections 210-1276A-97R-3 to 102R-1 at the base of the hole. Igneous rocks are observed in five intervals (210-1276A-97R-3, 141–150 cm; 97R-4, 0–3 cm; 98R-1, 112–137 cm; 98R-2, 1–31 cm; and from 98R-CC, 10 cm, to the last recovery in 102R-1, 0–2 cm) (Fig. F130). In the first four intervals, the sills range in thickness from decimeters to a few centimeters; the thinner sills may represent small apophysies (magmatic fingers) related to the larger sills. From Core 210-1276A-98R to the base of the hole, low recovery and strong drilling disturbance make it difficult to determine if this complex is a single thick sill or several thinner sills.

The rocks forming the sill complex are aphanitic to medium-grained aphyric to seriate diabase. The primary phases in most of the rocks are plagioclase, pyroxene, olivine, magnetite, and glass. In contrast to the upper sill, the lithologies forming the lower sill complex are more heterogeneous. Hydrothermal alteration of minerals is strong to complete in the smaller sills and moderate in the diabase cored in Core 210-1276A-99R. Secondary minerals are clay minerals (mainly smectite, kaolinite, and chlorite), quartz, pyrite, and calcite.

F130. Stratigraphic relations between lower sill units and sediments, p. 253.

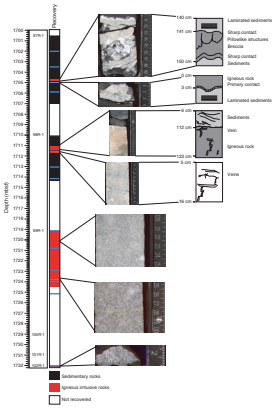

Contact and Relationships to Sediments

In the lower sill complex, most of the sediment/sill contacts are strongly affected by drilling disturbance and only one was recovered (interval 210-1276A-97R-3, 139–150 cm) (Fig. F131A). In this interval, the sill margin is chilled; the adjacent sediments are only slightly altered and still preserve sedimentary structures. A thin section from the upper margin (Fig. F131B), a few millimeters thick, consists of a glassy matrix separating sediments from aphanitic diabase. Evidence for recrystallization is not observed in the sediments. In the diabase, vesicles of irregular to elongate shape are seen and are filled with aggregates of small calcite crystals. Curved chilled contacts, some of which overlie a complex zone composed of sparry calcite, contain clasts of diabase and

F131. "Breccia pipe" and sill/sediment contact in the lower sill complex, p. 254.

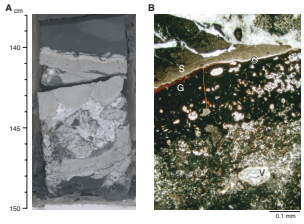

show a geopetal fabric (Fig. F131A). These structures, together with the vesicles, suggest that the emplacement of the sills occurred at very shallow levels in the sediments.

Thermal overprint in the sediments is manifested by color changes in Core 210-1276A-98R (see "Images" in "Site 1276 Core Descriptions"). In this core, color changes occur over a 188-cm interval from Sections 210-1276B-98R-2, 89 cm, to 98R-CC, 10 cm. In this interval, the sediments preserve their primary characteristics (see "Hydrothermally Altered Sediments," p. 56, in "Unit 5" in "Lithostratigraphy") and, aside from the color change, no further macroscopic evidence for a thermal overprint is observed. However, smear slides from this interval (see "Site 1276 Smear Slides") show very high reflectance of organic matter as well as recrystallization of calcite and clay minerals that record a thermal overprint. In this context, it is also important to mention that smectites appear in the sedimentary rocks separating the upper and lower sills. This indicates that the thermal overprint of the sills was strongly localized to the immediate vicinity of the contact zones; otherwise, smectites probably would not have been preserved.

Lithologic and Textural Variations Observed in the Lower Sill Complex

In the lower sill complex individual sills vary substantially in thickness, and they consequently preserve different textures and crystal sizes (Figs. F130, F131). The very thin sills in Cores 210-1276A-97R and 98R are aphanitic diabase that is dominated by intersertal textures. Crystal size and textural variations that are similar to those observed in the upper sill can be observed in the deeper sill cored in Core 210-1276A-99R. However, there are some differences. For example, ophitic and seriate textures appear in Core 210-1276A-99R; this mainly reflects the larger crystal sizes of augites that are as large as 3 mm in diameter (Fig. F132).

No complete geochemical data set is available for the lower sill complex because there was insufficient time to analyze samples on the ship. A few analyses that were entered in the Janus database should be treated with caution. Some of the silica and loss on ignition values appear to be unrealistic. Postcruise chemical data are needed to resolve this issue.

F132. Intrusive rocks in the lower section, lower sill complex, p. 255.

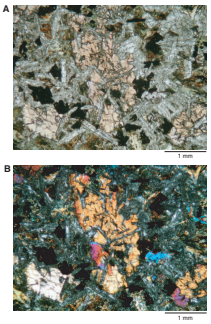

STRUCTURAL GEOLOGY

A variety of deformation structures, including folds, faults, and shear zones in sediments, were observed at Site 1276. Apart from compaction-related deformation, which can be observed throughout the cored sequence, deformation structures are rare but nonetheless occur in all sedimentary units. The measured apparent dip (i.e., on the face of the split core) of sedimentary bedding shows gentle dips of as much as 25° from 800 to 853 mbsf (Section 210-1276A-7R-4). Lower dips (<10°) are observed downhole to 1060 mbsf (Section 210-1276A-29R-1), and dips of as much as 15° occur from 1060 mbsf to the bottom of the hole (Fig. F133). Changes in measured apparent dip of bedding generally match the lithostratigraphic unit boundaries (see "Lithostratigraphy," p. 20).

We here describe some of the deformation structures observed in the different lithologic units (see "Lithostratigraphy," p. 20). Describing deformation, particularly where strain is low, depends on the presence of strain markers such as laminations, lithologic boundaries, or biotur-

F133. Apparent dip of sedimentary beds and distribution of deformation structures, p. 256.

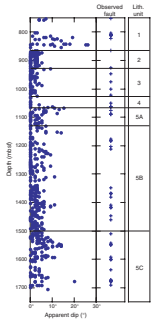

bation. The common occurrence of massive, homogeneous claystone and mudstone makes it difficult to determine the strain distribution in the sediments at Site 1276. Discrepancies between the observed distribution of deformation structures and the measured apparent dip of sedimentary bedding (Fig. F133) suggest that some of the deformation may have been distributed in the more ductile claystones and mudstones. The low finite strains encountered at Site 1276 also make it difficult to distinguish between compaction-related deformation (mainly pure shear dominated) and deformation related to gravitational instabilities or tectonic processes (mainly simple shear dominated).

Compaction-related structures are observed throughout Site 1276. They are responsible for a flattening of burrow structures (i.e., a shortening parallel to their subvertical axis). Other compaction-related structures, such as cleavage or foliation, are not observed, except for zones of high shear deformation, which were observed mainly in Unit 1. Stylolites indicating the presence of pressure solution are observed, but they occur only in carbonate-rich lithologies (e.g., interval 210-1276A-25R-4, 47–62 cm). Veins were observed only in intervals 210-1276A-19R-2, 102–105 cm, and 87R-6, 6–55 cm (see "Igneous and Metamorphic Petrology," p. 64, and Fig. F121).

Another commonly observed structure that may be misinterpreted as deformation structure is convolute lamination, which occurs mainly in the silt fraction of graded turbidites in Unit 5 as discussed in "Lithostratigraphy," p. 20. Despite these limitations, the observed structures allow us to draw some conclusions on the postdepositional history of the sediments drilled at Site 1276.

For further description of core deformation, see also "Lithostratigraphy," p. 20.

Deformation Structures in Lithologic Unit 1

Deformation structures in Unit 1 are represented by rare faults, folds, and zones of increased shear strain marked by incipient formation of a foliation. These structures are observed in Cores 210-1276A-1R to 3R and Section 3R-4 but are rare or absent in the remainder of Unit 1. Faults are mainly normal faults, but conjugate systems and reverse faults also occur locally. The displacement along these faults is small, commonly <1 cm.

Folds observed in Unit 1 are on a centimeter scale, commonly observed in sediments that are highly strained. The axial planes of the folds are subhorizontal. All the observed deformation structures affect sediments that are already bioturbated. In interval 210-1276A-2R-3, 34–36 cm, a localized deformation zone is observed in which sedimentary structures are rotated into the inferred direction of the shear transport. Evidence for ductile plastic deformation is observed in claystones in Core 210-1276A-7R.

The observations made in Unit 1 show that deformation may have occurred after consolidation of the sediments but probably not at a very deep level. Although deformation structures are observed only down to Section 210-1276A-3R-4 in Unit 1, sedimentary bedding shows high apparent dips down to Core 210-1276A-8R at the base of Unit 1 (Fig. F133). Thus, tilting of sedimentary bedding may also be a consequence of distributed ductile deformation accommodated in mudstones and claystones, which is not documented by small-scale deformation structures. The scarcity of both contractional structures (e.g., reverse faults and folds with inclined fold axial planes) and conjugate normal faults

suggests that the rocks cored in Unit 1 were deformed on a slope. In contrast, contractional structures might be expected in a base-of-slope setting oceanward of Site 1276.

Deformation Structures in Lithologic Unit 2

Deformation structures are rare in Unit 2 and are observed mainly in Cores 210-1276A-14R and 15R. The measured apparent dip of the sedimentary bedding varies between 0° and 5° (Fig. F133). Deformation structures include faults and folds. The folds are commonly on a centimeter scale, and fold axial planes are commonly subhorizontal and parallel to bedding. In interval 210-1276A-14R-2, 8–32 cm, a well-developed chevron fold is observed (Fig. F134). The presence of such ductile folds indicates that deformation occurred after deposition and compaction but before lithification of the sediments.

In Unit 2, faults are observed only in Core 210-1276A-15R; all are normal faults. These faults show apparent displacements of as much as 1 cm. A well-developed conjugate normal fault system is also observed in interval 210-1276A-15R-2, 71–74 cm, at the base of Unit 2 (Fig. F135). The conjugate fault system shows a classic graben structure bounded by symmetric faults, indicating that the orientation of the maximum principal stress ($\sigma 1$) that formed the normal fault system was subvertical. This suggests either extension or compaction-related vertical shortening. This observation is also valid for other observed conjugate fault systems in Units 2 through 4.

The scarcity of deformation structures as well as the general subhorizontal dip of sediment bedding in Unit 2 suggests that the unit was only very weakly affected by postdepositional deformation. Thus, Units 1 and 2 experienced different postdepositional deformation histories, with Unit 1 showing much more evidence of disturbance after deposition.

Deformation Structures in Lithologic Unit 3

In Unit 3, deformation structures are very similar to those in Unit 2 but are more abundant. The most common structures are normal faults, which are observed in 4 out of 10 cores. Folds are rare in Unit 3. In interval 210-1276A-17R-5, 83–88 cm, a folded burrow is observed (Fig. F136). The folds have subhorizontal fold axial planes, and the fold limbs are commonly extended, indicating subvertical compaction of the sediments. Further evidence for compaction is indicated by the occurrence of stylolites in interval 210-1276A-21R-4, 125–132 cm (Fig. F137). These structures are observed only in the sandy fraction of calcareous turbidite units.

Relatively scarce deformation structures and the low apparent dip values of the sedimentary bedding (<5°) (Fig. F133) indicate that Unit 3 is only weakly deformed, similar to Unit 2. This suggests a similar postdepositional history for the two units.

Deformation Structures in Lithologic Unit 4

Deformation structures are observed in the majority of cores in Unit 4. The most common structures are normal faults and ductile shear zones in mudstones. A good example of a ductile shear zone is observed in interval 210-1276A-27R-3, 34–40 cm (Fig. F138). The shear component is indicated by the presence of asymmetric folds and elongated

F134. Chevron-type folds with subhorizontal axial planes, p. 257.

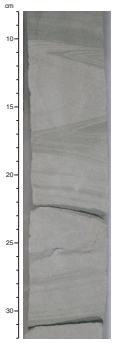

F135. Conjugate normal fault system forming a symmetric graben, p. 258.

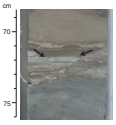

F136. Folded burrow, explained as a compaction effect, p. 259.

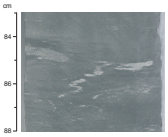

F137. Stylolites in the sandy fraction of a calcareous turbidite, p. 260.

F138. Ductile shear zone in bioturbated mudstone, p. 261.

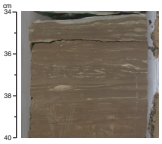

burrows that are aligned at a slightly oblique angle to the shear zone boundaries.

Unit 4 is more deformed than the overlying Units 2 and 3, and the apparent dip of the sedimentary bedding increases at the base of the unit (Fig. F133). Unlike Unit 1, Unit 4 shows a direct relationship between the dip of sedimentary bedding and an increased occurrence of deformation structures in the cores (Fig. F133). Thus, the dip and the deformation structure probably developed at the same time, most likely in poorly consolidated sediments.

Deformation Structures in Lithologic Unit 5

In Unit 5, deformation structures are observed in Cores 210-1276A-30R through 32R, 41R through 45R, 61R, 65R, 66R, 69R, 71R, 76R, 79R, 80R, 85R, 86R, 90R, and 94R (Fig. F133). The majority of these deformation structures are normal faults. The faults range from microscale normal faults with displacements of a few millimeters to larger faults with displacements >5 cm. Displacements >1 cm are restricted to the lowermost part of Unit 5 in Sections 210-1276A-80R-4, 69 cm, 90R-3, 37 cm, 94R-5, 22 cm, 94R-6, 39 cm, and 94R-6, 56 cm. Normal faults with slickensides are recorded in mudstones and claystones in Cores 210-1276A-80R, 86R, and 90R. Some faults also show a strike-slip component.

Reverse faults are observed in Sections 210-1276A-32R-1, 32R-3, 94R-4, and 94R-5. Figure F139 illustrates a reverse fault in interval 210-1276A-94R-5, 20–27 cm. Other structures occurring in Unit 5 include subvertical faults and microduplex structures in Section 210-1276A-79R-4, ductile shear zones in Section 76R-1, and styolites in Section 92R-3.

F139. Example of a reverse fault, p. 262.

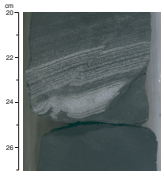

Postdepositional folds are observed only in Cores 210-1276A-76R, 79R, and 94R. Folds are distinguished from convolute-bedding folding by the deformation of sedimentary structures such as bioturbated layers, showing that the folding took place some time after deposition. Most of the structural folds recorded in Unit 5 are shear folds (e.g., Sections 210-1276A-76R-1 and 76R-2).

Dips of apparent bedding increase slightly toward the bottom of Unit 5 (Fig. F133). This may represent deviation of the hole. Hole deviation was measured with the Tensor tool during retrieval of Core 210-1276A-92R (1662.1 mbsf), and the tool indicated that the hole deviated 7.4° from vertical. On the other hand, intervals of high apparent dip (as much as 10°) correspond to sections with increased frequency of normal faults as well as the presence of a few reverse faults. Other deformation structures are more common, and displacement (accommodated strain) is more important in the lowermost part of the hole at Site 1276. Thus, the increase in apparent dip may be a real feature.

In summary, the various (nondepositional) structures recovered at Site 1276 can be attributed to postdepositional gravity instability and sedimentary compaction on the Newfoundland rifted margin. In some cases the instability occurred very soon after sediment deposition and apparently continued until the sediments became relatively well lithified.

BIOSTRATIGRAPHY

Abyssal depths below the CCD characterize the environment of the Paleogene and Cretaceous section cored at Site 1276. Consequently, car-

bonate microfossil assemblages, particularly the foraminifers, were significantly impacted by dissolution. Calcareous nannofossils, owing to their transport to the seafloor in zooplankton fecal pellets (Honjo, 1975, 1976; Pilskaln and Honjo, 1987; Steinmetz, 1994), fared much better against the ravages of dissolution than the calcareous foraminifers. The nannofossils show variable abundance and preservation through the section but provide excellent biostratigraphic control in most sampled intervals. Palynomorphs (predominantly dinocysts and sporomorphs) are very well preserved in carbon-rich, dark-colored sediments, and they provide a critical component of the biostratigraphic age control for the site.

Planktonic foraminifers are generally rare or absent in shale and mudrock facies at this site, but they are typically present in turbiditic units and provide complementary biostratigraphic control through much of the Paleogene and Cretaceous. Most foraminiferal samples (>63-µm residues) contain fairly diverse and generally well preserved assemblages of in situ abyssal (>2000 m) agglutinated benthic foraminifers. A summary of the microfossil biostratigraphy is compared to the lithology and core recovery in Figure **F140,** and major micropaleontological features of the shipboard core catcher samples and thin sections are summarized in Table **T7.**

Where present, planktonic and calcareous benthic foraminifers are often very small (<125 µm). They likely are size sorted by processes associated with downslope transport in turbidity currents, a supposition that is based on the similar size of co-occurring quartz grains. Calcareous benthic foraminifers indicate that the source areas for the turbidites cored at Site 1276 have varied through the section from neritic (<200 m) to bathyal (200–2000 m) depths along the adjacent continental margin. Reworking of Upper Cretaceous material is prevalent in the Paleogene, but redeposition processes were largely penecontemporaneous during the Cretaceous, based on a uniform age progression of the samples and minimal reworking of older material in calcareous nannofossil, palynomorph, and foraminifer samples.

An unconformity separates lithologic Units 1 and 2 in Core 210-1276A-8R, based on palynomorph and calcareous nannoplankton evidence, and two condensed intervals are identified in the Upper Cretaceous (lower to middle Maastrichtian in Core 22R, and uppermost Turonian–Coniacian to upper Campanian in Cores 25R through 28R). Core 210-1276A-14R crosses the PETM but did not recover the dissolution interval that characterizes this event. The K/T boundary interval may be biostratigraphically complete in Section 210-1276A-21R-4 based on calcareous nannofossil and planktonic foraminiferal evidence. It is likely that Cenomanian–Turonian OAE 2 ("Bonarelli" event) is represented by the laminated black shales in Sections 210-1276A-31R-2 and 31R-3, as constrained by the shipboard biostratigraphy. Basal Albian OAE 1b ("Paquier" event) was not conclusively defined by routine shipboard biostratigraphy, but it likely occurs above the lower sill in Core 210-1276A-94R, based on supporting geochemical data. Other apparent OAEs are also outlined in **"Oceanic Anoxic Events,"** p. 97, in "Geochemistry."

Calcareous nannofossils, dinocysts, and planktonic foraminiferal assemblages indicate that Site 1276 was influenced by transitional surface water masses for much of its Paleogene and Cretaceous history. This is indicated by the presence of select high-latitude taxa and by the absence or paucity of some key low-latitude Tethyan taxa.

F140. Microfossil zones, Site 1276, p. 263.

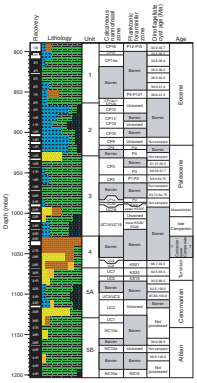

T7. Paleontological observations of shipboard samples, Site 1276, p. 331.

Calcareous Nannofossils

Calcareous nannofossils recovered at Site 1276 exhibit a wide range of preservation and abundance. Abundance and preservation are usually best in the tops of the sandy turbidites found throughout the drilled section. The hemipelagic sediments generally either contain very poorly preserved and impoverished assemblages or they are completely barren, indicating deposition well below the CCD.

Nannofossil distribution in Hole 1276A was found to be discontinuous because of the dissolution of carbonates. Nonetheless, the distribution allowed a fairly complete biostratigraphic analysis. However, the dominance of redeposited sediments and the common presence of reworked taxa make the use of last occurrence (LO) datums problematic.

Paleogene

Lithologic Units 1–3 consist of hemipelagic mudrocks interrupted by turbidites and debris flows. The redeposited sediments are the only lithologies suitable for calcareous nannofossil analysis because the mudstones are completely devoid of calcium carbonate.

The interval between Samples 210-1276A-1W-CC and 2R-CC contains rare to abundant, moderately well preserved nannofossils with common reworked taxa from older Paleogene and Cretaceous strata. Samples 210-1276A-1W-4, 37 cm, and 1W-CC belong to uppermost Eocene–lower Oligocene Zone CP16, based on the presence of *Reticulofenestra umbilicus, R. bisecta, R. oamaroensis, Isthmolithus recurvus,* and *Chiasmolithus altus* and the absence of "rosette" discoasters (*D. barbadiensis* and *D. saipanensis*) (Table T8). Also present in these samples are moderately well preserved specimens of *Chiasmolithus expansus, Pemma basquensis, P. papillatum, Coccolithus formosus,* and *Blackites spinosus*. Specimens of *Cribrocentrum reticulatum* and very rare *Discoaster saipanensis* are considered to be reworked.

T8. Cenozoic calcareous nannofossils, Site 1276, p. 332

Sample 210-1276A-2R-1, 144 cm, is assigned to upper Eocene Zone CP15 based on the presence of *Reticulofenestra oamaroensis*. Sample 210-1276A-2R-CC is assigned to undifferentiated Subzone CP14b–Zone CP15 based on the presence of *Reticulofenestra bisecta, R. umbilicus,* and *C. grandis*. Many of the larger clasts in the debris flows in this core (Samples 210-1276A-2R-2, 83 cm, and 2R-3, 36 cm) contain well-preserved and diverse assemblages of older middle Eocene taxa (Zone CP13). Samples 210-1276A-3R-2, 51 cm, and 3R-CC are assigned to middle Eocene Subzone CP14a based on the presence of *Chiasmolithus solitus* occurring with *R. umbilicus*. Samples 210-1276A-4R-CC through 7R-CC are barren of nannofossils.

Samples 210-1276A-8R-CC through 11R-CC yield fairly abundant and moderately to poorly preserved assemblages. There is a marked difference in the preservation of nannofossils between lithologic Units 1 and 2, with preservation being much better in the former. The presence of *Rhabdosphaera inflata* together with questionable *Nannotetrina fulgens* in Sample 210-1276A-8R-CC indicates lower middle Eocene Subzone CP12b or, perhaps, Subzone CP13a. Also present in this sample are *Discoaster lodoensis, D. sublodoensis, Ellipsolithus macellus,* and *E. lajollaensis*. The absence of *R. inflata* in Sample 210-1276A-9R-CC indicates Subzone CP12a.

Samples 210-1276A-10R-CC and 11R-CC are assigned to the undifferentiated lower Eocene Zones CP10–CP11 based on the presence of *D. lodoensis* in the absence of *D. sublodoensis*. Zones CP10 and CP11 could

not be differentiated because *Toweius crassus* was not observed in these sediments. However, Sample 210-1276A-12R-4, 55 cm, may be constrained to lower Eocene Zone CP10 based on a few occurrences of *Tribrachiatus orthostylus*. Sample 210-1276A-12R-CC is barren of nannofossils, and Sample 13R-CC contains only rare specimens of *Discoaster multiradiatus*.

The Paleocene/Eocene Boundary

The Paleocene/Eocene (P/E) boundary is characterized by an abrupt worldwide warming event referred to as the PETM. In the oceanic sedimentary record, the PETM interval typically corresponds to a sharp lithologic change uphole from light calcareous marl to a dark, clayey, calcite-free dissolution interval a few centimeters to decimeters thick. This interval is also distinguished by a sharp negative $\delta^{13}C$ excursion and a benthic foraminiferal extinction event (Zachos et al., 1993; Thomas and Shackleton, 1996). Biostratigraphically, the PETM lies at the top of calcareous nannofossil Zone CP8. At the Paleocene–Eocene transition, the calcareous nannoplankton community shows a great turnover characterized by peculiar biotic changes: the first members of the *Rhomboaster-Tribrachiatus* lineage (*Rhomboaster* spp. and *R. cuspis*) are present just above the dissolution interval and are followed by a sharp decrease in fasciculithid abundance and an increase in *Zygrhablithus bijugatus* abundance (Bralower et al., 1995). During this time interval until the recovery, the calcareous nannofossil assemblages are dominated by the genus *Discoaster*.

The search for the P/E boundary at Site 1276 was difficult for two important reasons: (1) the presence of numerous clayey, calcite-free intervals deposited below the CCD and (2) the occurrence of turbidites and debris flows, which blur the typically distinct lithologic and paleontological record, specifically, the absence of a single dissolution interval and the reworking of key taxa. To better constrain the placement of the PETM and the P/E boundary at Site 1276, a preliminary analysis was conducted on samples spanning the interval from Sections 210-1276A-13R-1 through 15R-3. The samples from Core 210-1276A-13R contain low-abundance and low-diversity assemblages dominated by *Discoaster* spp. and *Rhomboaster* spp., and they lack fasciculithids. These assemblages are affected by dissolution, which hinders the recognition of key species. The highest *Tribrachiatus orthostylus* specimen occurs in Sample 210-1276A-13R-1, 35 cm, indicating lower Eocene Subzone CP9b. The first occurrence (FO) of *T. contortus* occurs in Sample 210-1276A-13R-1, 96 cm; this event lies near the base of Subzone CP9a, which is defined by the FOs of *Discoaster diastypus* and *Tribrachiatus bramlettei* in Sample 14R-1, 24–25 cm. The LO of *Fasciculithus tympaniformis* occurs in Sample 210-1276A-14R-1, 104–105 cm; few to rare fasciculiths are recorded from this sample downhole to Sample 14R-CC, which contains a diverse assemblage of nannofossils, including common fasciculithids. Almost all samples from Core 210-1276A-14R are characterized by very poorly preserved, low-diversity, and low-abundance assemblages. The most common taxa in these poor assemblages are *Discoaster* spp. and *Rhomboaster* spp. These preliminary results suggest that the recovered sediments of Sections 210-1276A-14R-1 to 14R-4 contain only the characteristic post-PETM-excursion calcareous nannofossil assemblages and succession of biotic events. Therefore, the PETM dissolution interval likely occurred in the unrecovered interval between Samples 210-1276A-14R-4, 105–106 cm, and 14R-CC.

Sample 210-1276A-15R-2, 25–27 cm, is assigned to upper Paleocene Zone CP8 based on the presence of *Discoaster multiradiatus* and *Chiasmolithus bidens* and the absence of typical Eocene taxa. Sample 210-1276A-15R-CC is barren of nannofossils, but Samples 16R-CC and 17R-CC contain low-diversity and poorly preserved calcareous nannofossil assemblages with common reworked Cretaceous species. The marker for mid-Paleocene Zone CP3, *Ellipsolithus macellus,* was not found but is known to be dissolution prone. These samples are nonetheless assigned to Zone CP3 because of the presence of *Fasciculithus ulii* in Sample 210-1276A-16R-CC and *F. magnus* in Sample 17R-CC. *Chiasmolithus danicus,* which fixes the base of lower Paleocene Zone CP2, is common in both of these samples. Sample 210-1276A-18R-CC is assigned to an undifferentiated Zone CP2–CP3 based on the absence of any *Fasciculithus* species and the presence of *C. danicus*. The missing Zones CP4–CP7 may be differentiated with more detailed sampling of Cores 210-1276A-15R and 16R.

Samples 210-1276A-19R-CC and 20R-CC are barren; however Sample 20R-5, 104–105 cm, contains *Cruciplacolithus primus, Biantholithus sparsus,* common *Markalius inversus,* and *Neocrepidolithus neocrassus,* together with numerous fragments of *Thoracosphaera* spp. This assemblage is typical of basal Paleocene Subzone CP1a.

The Cretaceous/Tertiary Boundary

Determining the position of the K/T boundary transition in Site 1276 was difficult because of extensive reworking and the presence of several intervals of carbonate-free sediments. In several low-latitude localities that contain a biostratigraphically continuous transition between the uppermost Maastrichtian and the lowermost Danian, the K/T boundary is marked by peculiar biotic changes in the calcareous nannoplankton community (Gardin and Monechi, 1998, and references therein). These changes include the following: the lowest Danian sediments are characterized by a dramatic increase in the abundance of the calcareous dinocyst *Thoracosphaera* spp. ("*Thoracosphaera* bloom"), occurring together with abundant Cretaceous species that are considered to be reworked. This first bloom of *Thoracosphaera* spp. is followed by an increase in abundance of survivor species such as *Markalius inversus, Cyclagelosphaera reinhardtii,* and *Braarudosphaera bigelowii* and by blooms of dwarf incoming Danian species such as *Neobiscutum romeinii* and *N. parvulum* ("dwarf *Biscutum* bloom;" Gardin and Monechi, 1998). The first more complex Danian species, *Cruciplacolithus primus,* appears during this time and rapidly increases in size and abundance.

All these biotic signals help to constrain the K/T boundary transition at Site 1276 to Section 210-1276A-21R-4. Samples 210-1276A-21R-4, 53–54 cm, and 21R-4, 77 cm, contain abundant and diverse uppermost Maastrichtian assemblages belonging to the *Micula prinsii* Subzone UC20d. No thoracosphaerid fragments or unusually high abundances of survivor species are found in these samples, and as such, they are considered to be in situ. Sample 210-1276A-21R-4, 56–57 cm, is from a dark brownish green clay layer and yields only very rare, dissolution-resistant Cretaceous species such as *Micula decussata* and *Watznaueria barnesae*. Sample 210-1276A-21R-4, 49 cm, from the carbonate turbidite overlying this clay layer, also contains abundant and diverse Maastrichtian assemblages with no apparent Danian biotic components. Sample 210-1276A-21R-4, 41 cm, still contains abundant Maastrichtian species but has Danian thoracosphaerid fragments and is interpreted to be in

situ. Samples 210-1276A-21R-2, 26 cm, and 21R-3, 52 cm, are also characterized by abundant Cretaceous species, with frequent *Thoracosphaera* spp. and very abundant *Neobiscutum parvulum* and *N. romeinii*. This succession of assemblages is comparable to that observed elsewhere at the K/T transition, even though the abundance of Cretaceous species above the transition at Site 1276 is remarkably high due to redeposition. Based on the calcareous nannofossil assemblages, the K/T boundary can be biostratigraphically placed in Section 210-1276A-21R-4 between 41 and 49 cm. However, it is possible that the Maastrichtian assemblage found in Sample 210-1276A-21R-4, 49 cm, consists of entirely reworked fossils in a barren lower Danian clay layer.

Upper Cretaceous

Sample 210-1276A-21R-CC yields a poorly preserved assemblage that is characterized here as upper Maastrichtian Zone UC20 based on the presence of *M. prinsii* (Table T9). Sample 210-1276A-22R-1, 2 cm, is better preserved and indicates the presence of upper Maastrichtian Subzones UC20a–UC20c based on the lack of *M. prinsii* and the presence of common *Lithraphidites quadratus, Cribrocorona gallica, Arkhangelskiella maastrichtiana,* and *Nephrolithus frequens*. The assemblage in Sample 210-1276A-22R-2, 50 cm, is characterized by the absence of *L. quadratus* and *Tranolithus orionatus,* which could indicate undifferentiated mid-Maastrichtian Zones UC19–UC18. Sporadic occurrences of *Reinhardtites levis* and *Uniplanarius trifidus* in this sample are considered to be reworked. Samples 210-1276A-22R-CC through 25R-5, 48–49 cm, contain common *R. levis, U. trifidus,* and *Broinsonia parca constricta,* which indicate mid- to upper Campanian Zones UC15–UC16. These results imply that lower Maastrichtian Zone UC17 is missing or difficult to distinguish because of reworking. It is likely that much of the Maastrichtian at this site is condensed in Core 210-1276A-22R.

T9. Mesozoic calcareous nannofossils, Site 1276, p. 335.

The upper Campanian and upper Maastrichtian assemblages are characterized by typical low-latitude Tethyan taxa such as *U. trifidus* and *L. quadratus,* mixed with cooler-water high-latitude species such as *Cribrosphaerella daniae* and *Psyktosphaera firthii*. *Nephrolithus frequens,* the marker taxon of upper Maastrichtian Zone CC26 (Sissingh, 1977), is common, whereas the tropical species *Micula murus* (a marker for this zone at low latitudes) is very rare at Site 1276. These data suggest that Site 1276 occupied an intermediate region between the Boreal and Tethyan provinces and that mixed assemblages were common during this time period.

Sections between 210-1276A-25R-6 and 28R-5 are barren of calcareous microfossils. Many samples were taken from different lithologies in this thick interval in an attempt to constrain the age, but none yielded nannofossils. It is assumed that the interval contains all of the zones between mid-Campanian Zone UC15 and upper Coniacian Zone UC10. Samples 210-1276A-28R-5, 76–77 cm, and 28R-CC contain a rather depauperate assemblage assigned to uppermost Turonian to lower Coniacian Zone UC9, based on the absence of *Broinsonia* spp., *Arkhangelskiella cymbiformis,* and *Micula decussata* and on the presence of *Eiffellithus eximius, Quadrum gartneri, Lithastrinus septenarius, Kamptnerius magnificus,* and *Marthasterites furcatus*. This age assignment indicates that most of the Coniacian through the lower Campanian is either missing or is condensed in the barren red sandstones to mudstones of Cores 210-1276A-25R through 28R.

Sample 210-1276A-29R-CC is middle to upper Turonian Zone UC8 based on the presence of *Eiffellithus eximius,* and Sample 30R-CC is lower Turonian Zone UC7 based on the presence of *Eprolithus moratus, E. octopetalus,* and *Quadrum gartneri*. Samples 210-1276A-31R-CC and 32R-CC are barren, but Samples 31R-1, 25–26 cm, and 31R-4, 120–121 cm, yield moderately well preserved and abundant assemblages that help constrain the placement of the Cenomanian/Turonian boundary. The FO of *E. octopetalus* is recorded in Sample 210-1276A-31R-1, 25–26 cm, indicating an early Turonian age, whereas Samples 31R-4, 120–121 cm, and 33R-CC are assigned to undifferentiated Cenomanian Zone UC3–UC5 based on the presence of *Quadrum intermedium* and the absence of *E. octopetalus*. Unfortunately, the common presence of reworked taxa prevents the reliable recognition of important last occurrences that characterize the upper Cenomanian to lower Turonian transition, including *Lithraphidites acutus, Corollithion kennedyi,* and *Helenea chiastia*. Samples 210-1276A-30R-CC through 34R-CC are also characterized by fairly high values of TOC. These results, in conjunction with the planktonic foraminiferal biostratigraphic data, indicate the likely presence of the OAE 2 "Bonarelli event" in Sections 210-1276A-31R-2 and 31R-3.

Samples 210-1276A-34R-CC and 35R-CC are placed into upper Cenomanian Zone UC3 based on the presence of frequent *Lithraphidites acutus* and the absence of *Cylindralithus biarcus*. This assemblage is also characterized by common *Axopodorhabdus albianus, Eiffellithus turriseiffelii, Helicolithus compactus, Rhagodiscus achlyostaurion, R. asper,* and *Corollithion kennedyi*.

Sample 210-1276A-36R-CC is assigned to lower Cenomanian Zone UC1 based on the presence of *C. kennedyi* in the absence of *L. acutus* and *Gartnerago segmentatum*. Samples 210-1276A-37R-CC through 44R-CC are placed into upper Albian–basal Cenomanian Subzone NC10a based on the absence of *C. kennedyi* and the continued presence of *E. turriseiffelii*. Samples 210-1276A-39R-CC, 41R-CC, and 42R-CC are barren of nannofossils.

Lower Cretaceous

The Albian/Cenomanian boundary is straddled by Subzone NC10a, which is discussed in the section above. Upper Albian Subzone NC9b persists from Samples 210-1276A-45R-CC through 51R-CC based on the presence of *Eiffellithus monechiae* and the absence of *E. turriseiffelii*. In this interval, Sample 210-1276A-50R-CC (black mudstone) is barren of nannofossils. Sample 210-1276A-52R-CC is also nearly barren but may belong to this zone because of the rare occurrence of *Eiffellithus* cf. *E. monechiae* in Sample 54R-CC. However, these specimens may be ancestral forms.

Beginning with Sample 210-1276A-53R-CC and persisting through 75R-CC, the very rare occurrence of *Axopodorhabdus albianus* in the absence of *E. monechiae* indicates that this interval belongs to middle Albian Subzone NC9a. Samples 210-1276A-56R-CC through 58R-CC and 61R-CC, 66R-CC, 68R-CC, and 70R-CC through 72R-CC are barren of calcareous nannofossils. Throughout this part of the section there are occasional occurrences of *Hayesites albiensis, Eprolithus floralis, Cylindralithus nudus, Braarudosphaera stenoretha, Lithraphidites carniolensis,* and nannoconid species such as *Nannoconus truitti, N. wassallii,* and *N. steinmannii.*

Sample 210-1276A-76R-CC is assigned to middle Albian Subzone NC8c based on the presence of *Tranolithus orionatus* and *H. albiensis,* together with *Prediscosphaera columnata*. In the interval from Sample 210-1276A-77R-CC to 90R-CC, a number of core catcher samples are either barren of calcareous nannofossils (Table T9) or the absence of secondary marker taxa prohibits consistent subdivision of Zone NC8. Uppermost Aptian–lower Albian Subzone NC8a is assigned to Samples 210-1276A-91R-CC and 93R-CC through 96R-CC based on the occurrence of *P. columnata* in the absence of *H. albiensis*. Sample 210-1276A-97R-CC is barren.

Planktonic Foraminifers

Paleogene

Most of the 20 Paleogene core catcher samples investigated shipboard are barren of planktonic foraminifers or contain rare to few specimens (<50 tests), and only 2 of these core catcher samples contain age-diagnostic planktonic foraminiferal assemblages (Table T7). A number of thin sections of Paleogene sandstones provide additional age information based on planktonic foraminifers. A thin section from Sample 210-1276A-1W, 47–49 cm, indicates undifferentiated upper middle Eocene to lower upper Eocene Zones P12–P15 based on the presence of *Turborotalia pomeroli*. However, the presence of latest Eocene–early Oligocene age calcareous nannofossils and dinocysts in Core 210-1276A-1W suggests that the *T. pomeroli* and other planktonic foraminifers are reworked from older deposits. Undifferentiated uppermost lower Eocene to middle Eocene Zones P9–P12 are suggested by the presence of *Acarinina bullbrooki, A. primitiva, Globigerinatheka* cf. *G. index, Truncorotaloides rohri,* and *Morozovella* cf. *M. spinulosa* in thin sections from Samples 210-1276A-7R-2, 35–39 cm, and 7R-4, 94–98 cm.

Sample 210-1276A-8R-CC, located below the unconformity separating lithologic Units 1 and 2, contains rare and tiny planktonic foraminifers and is also assigned to undifferentiated uppermost lower Eocene to middle Eocene Zones P9–P12 based on the presence of *A. bullbrooki*. Sample 210-1276A-14R-CC is assigned to upper Paleocene Subzone P4c based on the co-occurrence of *Globanomalina pseudomenardii, Morozovella aequa,* and *Igorina albeari*. The barren Eocene and Paleocene samples reflect either dissolution of foraminiferal tests during settling through the lysocline and CCD or postdepositional loss due to acidic conditions in sediments rich in organic matter. The greatest concentrations of planktonic foraminifer tests occur in mudstone with coarse siltstone or very fine sandstone laminae, or they are in very fine to fine grainstone turbidites. Preservation is generally moderate, and whole specimens are filled with calcite. Reworked Late Cretaceous (Campanian–Maastrichtian) planktonic foraminifers are noted in Samples 210-1276A-9R-CC and 14R-CC.

Most of the grainstone thin sections from Core 210-1276A-15R to Section 21R-4 contain rare to abundant reworked Late Cretaceous planktonic foraminifers. A mid- to late Maastrichtian age for the reworked material is indicated by the presence of diverse species, including *Abathomphalus mayaroensis, Racemiguembelina fructicosa, Contusotruncana contusa, Globotruncana stuarti,* and *G. conica*. Sample 210-1276A-15R-1, 124–126 cm, is assigned to upper Paleocene Zone P4 based on the presence of the nominate taxon *Globanomalina pseudomenardii*. The presence of *Morozovella conicotruncana* in the thin section

from Sample 210-1276A-17R-4, 98–99 cm, indicates lower upper Paleocene Zone P3. Samples 210-1276A-18R-6, 52–55 cm, and 18R-6, 88–90 cm, contain *Parasubbotina pseudobulloides,* which suggests undifferentiated lower Paleocene Zones P1–P2.

Sample 210-1276A-21R-4, 19–21 cm, lies 20–30 cm above the K/T boundary. This thin section contains common small planktonic foraminifers indicative of basal Paleocene Zone Pα as well as the calcareous dinoflagellate *Thoracosphaera* spp. against a backdrop of abundant reworked upper Maastrichtian planktonic foraminifers of the *Abathomphalus mayaroensis* Zone (Zone KS31). Age-diagnostic taxa from this interval include *Guembelitria cretacea, Parvularugoglobigerina eugubina,* and *Woodringina* sp.

Upper Cretaceous

The richest assemblages of planktonic foraminifers are present in coarser-grained mudstones and very fine to fine sandstones that reflect downslope transport and size sorting. Sample 210-1276A-21R-CC is assigned to upper Maastrichtian *Abathomphalus mayaroensis* Zone (Zone KS31) based on the presence of the nominate taxon and a moderately diverse assemblage of globotruncanids and rugoglobigerinids (Table T7). A thin section from Sample 210-1276A-21R-4, 127–129 cm, contains a similarly diverse assemblage of planktonic foraminifers indicative of Zone KS31 including the taxa *A. mayaroensis, Racemiguembelina fructicosa,* and *Contusotruncana contusa*. Sample 210-1276A-22R-CC is missing species of the genus *Gansserina* but contains *Globotruncana falsostuarti,* which suggests the lower Maastrichtian part of Zone KS30. Mid-Maastrichtian marker taxa *R. fructicosa* and *C. contusa* are also absent from this core catcher sample. The absence or paucity of large biserial planktonic foraminifers (e.g., species of *Racemiguembelina, Planoglobulina,* and *Gublerina*), typical of Maastrichtian-age low-latitude (Tethyan) assemblages, suggests that Site 1276 may have been influenced by transitional or Boreal water masses at times during the latest Cretaceous. Alternatively, dissolution during settling may have selectively removed some of these larger taxa in all but the turbiditic sandstones. Sample 210-1276A-24R-CC is late Campanian in age (Zone KS28 or KS29) based on the presence of *Globotruncana ventricosa* and *G. aegyptiaca* and the absence of *G. falsostuarti* and *Globotruncanita calcarata*.

An elevated CCD (~2500–3000 m) in the North Atlantic Basin during the Aptian–Campanian (Thierstein, 1979; Tucholke and Vogt, 1979) exacerbated the problem of planktonic foraminiferal dissolution at the abyssal paleodepths of Site 1276. Samples 210-1276A-25R-CC through 28R-CC are barren of calcareous microfossils, a likely consequence of the high eustatic sea level, elevated CCD, and reduction of gravity flows to the deep sea during this part of the Cretaceous. Below this barren interval, a late early Turonian to early late Turonian age (Zone KS21) is indicated for Sample 210-1276A-29R-CC based on the co-occurrence of *Marginotruncana renzi, M. sigali, Dicarinella imbricata, Praeglobotruncana praehelvetica,* and *Whiteinella aprica*. However, planktonic foraminifers are very rare and poorly preserved in this sample.

Sample 210-1276A-30R-CC is barren of planktonic foraminifers, but thin sections from Samples 30R-5, 92–96 cm, and 31R-1, 81–84 cm, are assigned to uppermost Cenomanian–lowermost Turonian *Whiteinella archaeocretacea* Zone (Zone KS20) based on the presence of the nominate taxon together with *Dicarinella* cf. *D. caniculata* and *Praeglobotruncana* cf. *P. praehelvetica*. The upper Cenomanian *Rotalipora cushmani*

Zone (Zone KS19) is recognized in the thin section from Sample 210-1276A-31R-5, 18–20 cm, based on the presence of *R. cushmani* and *W. archaeocretacea*.

Samples 210-1276A-31R-CC through 42R-CC are barren of planktonic foraminifers or contain only very tiny (<125 µm) specimens. The latter type of sample contains very fine to fine grains of quartz sand that are of similar size to the foraminifers, suggesting that the microfossils were size sorted during transport in distal turbidity currents. Despite the evidence for vigorous transport energy, these foraminiferal assemblages are typically moderately to moderately well preserved and contain species of the genera *Heterohelix, Hedbergella, Globigerinelloides, Guembelitria,* and *Schackoina*. Sample 210-1276A-35R-CC contains a moderately diverse assemblage that includes the species *Hedbergella delrioensis, H. planispira, Globigerinelloides bentonensis, G. ultramicrus, Clavihedbergella simplex,* and *Praeglobotruncana delrioensis*. However, the lack of any species of the genus *Rotalipora* (including juvenile specimens) in this sample may be another indication that cooler transitional or Boreal surface waters influenced the area of Site 1276 during the Cenomanian. A thin section from Sample 210-1276A-36R-2, 123–127 cm, is assigned to lower Cenomanian *Rotalipora globotruncanoides* Zone (Zone KS17) based on the presence of the nominate taxon together with *Rotalipora appenninica, P. delrioensis, P. stephani,* and *Hedbergella libyca*. The presence of the last taxon suggests that this sample lies in the basal Cenomanian because *H. libyca* is known to occur in a narrow zone straddling the Albian/Cenomanian boundary interval (Leckie, 1984).

Lower Cretaceous

The upper Albian at Site 1276 is characterized by moderately preserved and rare to abundant assemblages of planktonic foraminifers. These assemblages do not show the pronounced size sorting observed in the Cenomanian–Turonian interval. A thin section from Sample 210-1276A-41R-2, 88–91 cm, indicates upper Albian *Rotalipora appenninica* Zone (Zone KS16) based on the presence of *R. appenninica* in the absence of *R. globotruncanoides*. Samples 210-1276A-43R-CC and 44R-CC are likewise assigned to uppermost Albian Zone KS16 based on the presence of *R. appenninica, R. ticinensis, Planomalina buxtorfi, Praehedbergella delrioensis,* and *Hedbergella libyca*. Sample 210-1276A-45R-2, 112–114 cm, likely belongs to the same zone based on the co-occurrence of *R. appenninica* and *P. buxtorfi*. Upper Albian Zone KS15 occurs in Samples 210-1276A-45R-CC through 48R-CC. This zone is characterized by the presence of *Rotalipora ticinensis, R. subticinensis, Ticinella roberti, T. primula, Biticinella breggiensis,* and *Globigerinelloides bentonensis*. The greater abundance of planktonic foraminifers parallels generally higher concentrations of carbonate along continental margins during the late Albian, as well as larger sizes and more calcified species of planktonic foraminifers at this time (Leckie et al., 2002).

The interval from Samples 210-1276A-49R-CC to 80R-CC again contains sporadic occurrences of planktonic foraminifers, with a mix of either barren or size-sorted assemblages of juvenile specimens similar to those of the Cenomanian–Turonian interval. Samples 210-1276A-52R-CC and 54R-CC contain assemblages indicative of the lower part of upper Albian Zone KS14 based on the presence of *Biticinella breggiensis, Ticinella praeticinensis, T. primula,* and *T. raynaudi*. Sample 210-1276A-54R-CC, like Sample 48R-CC, is also an exception to typical mid-Cretaceous (Albian–Turonian) samples in that both samples contain abundant

planktonic foraminifers in addition to few to abundant calcareous and agglutinated foraminifers and radiolarians. Sample 210-1276A-59R-CC contains *T. primula* and *Hedbergella planispira* in the absence of *Biticinella* and other species of *Ticinella* and indicates middle Albian Zone KS13. Samples 210-1276A-63R-CC and 73R-CC may also be assigned to Zone KS13, but the specimens are very small and too few in number to make a firm age determination. Most of the core catcher samples from Sections 210-1276A-74R-CC through 97R-CC are barren of planktonic foraminifers.

Benthic Foraminifers

The utility of benthic foraminifers as stratigraphic index markers is limited by the long ranges and/or the geographic occurrence patterns of the majority of taxa. The group is most useful when considered in succession as characteristic assemblages, particularly in areas where regional stratigraphic zones have been proposed and tested (e.g., Kuhnt and Kaminski, 1997). Benthic foraminifers also are particularly useful as indicators of depositional environments.

Benthic foraminiferal assemblages recovered from Site 1276 fall into two associations that correspond to different stratigraphic intervals. Calcareous assemblages characterize the upper Eocene, lower Eocene to upper Paleocene, and Maastrichtian to upper Campanian. Agglutinated species dominate the assemblages in the remainder of the Eocene to Paleocene and in the upper Campanian to Albian sediments. The preservation of Paleogene and Maastrichtian calcareous benthic foraminifers is poor to moderate. Albian calcareous benthic foraminifers are well to moderately preserved in black shale and mudstone, and they are generally poorly preserved in sandstone lithofacies. Preservation of agglutinated foraminifers is variable among samples, and many taxa are commonly deformed. All tube-shaped forms such as *Rhizammina, Bathysiphon,* and *Hyperammina* are fragmented. Samples 210-1276A-3R-CC, 5R-CC, 20R-CC, 37R-CC, 51R-CC, 78R-CC through 80R-CC, 83R-CC, 85R-CC, 86R-CC, 89R-CC, 90R-CC, and 94R-CC through 96R-CC are barren. The distribution of benthic foraminifers is reported in Table **T10.**

T10. Benthic foraminifers, Site 1276, p. 336.

Rare calcareous benthic foraminifers, including *Bulimina tuxpamensis* and *Cibicidoides praemundulus,* are present in the upper Eocene Sample 210-1276A-2R-CC. Agglutinated species are not observed in this sample. Eocene to Paleocene benthic foraminiferal assemblages fall into two categories that correspond to different lithologies. Assemblages in mudstone are typically characterized by various agglutinated species of the genera *Ammodiscus, Spiroplectammina, Trochammina,* and fragments of tube-shaped species of the genera *Rhizammina* and *Bathysiphon* (Samples 210-1276A-6R-CC, 7R-CC, and 15R-CC). *Reticulophragmium* sp. and *Cyclammina cancellata* are present in Samples 210-1276A-6R-CC and 7R-CC. The presence of these agglutinated taxa in the absence of *Nuttallides truempyi* indicate an abyssal paleodepth below the CCD (e.g., Kuhnt and Collins, 1996). The same constituents are observed in Samples 210-1276A-4R-CC, 10R-CC, 11R-CC, and 16R-CC through 19R-CC, although their abundances are very low. In contrast, sandy Samples 210-1276A-8R-CC, 9R-CC, 12R-CC, 13R-CC, and 14R-CC in lithologic Unit 2 are characterized by calcareous species including *Cibicidoides* spp., *Astrononion novozealandicum, Nonionella* sp., and species of *Gyroidinoides*. These species are poorly preserved. The genus *Cibicidoides* lives attached to seaweed or coarse-grained materials (Kitazato, 1994), and it

is a common constituent in the neritic zone (Murray, 1991). The genera *Astrononion* and *Nonionella* are likewise characteristic of shelfal depths (Murray, 1991; Leckie and Olson, 2003). Hence, it is judged that these calcareous species are derived from a neritic environment (<200 m) and are displaced downslope by turbidity currents.

Maastrichtian to Campanian benthic foraminiferal assemblages are recognized in Samples 210-1276A-21R-CC, 22R-CC (claystone), 22R-CC (sandstone), and 24R-CC. These assemblages are characterized by moderately diverse calcareous species, including polymorphinids, *Bolivina* spp., buliminids, *Gavelinella* spp., and *Gyroidina* spp., whereas agglutinated forms are rarely present. These calcareous taxa are believed to be common constituents in bathyal (200–2000 m) to abyssal (>2000 m) depths (Sliter and Baker, 1972; Tjalsma and Lohmann, 1983). *Aragonia velascoensis* is an abyssal calcareous benthic foraminifer (Tjalsma and Lohmann, 1983) that also occurs in a sandstone in Sample 210-1276A-22R-CC. As such, these calcareous assemblages are interpreted to be a mixed fauna of in situ abyssal and transported bathyal taxa.

A sample examined from Section 210-1276A-23R-4 yields an assemblage of planktonic foraminifers together with common specimens of the agglutinated foraminiferal taxon *Caudammina gigantea,* a characteristic element of deepwater Upper Cretaceous sediments. The foraminiferal assemblage is moderately well preserved and not size sorted, which indicates that this sample contains in situ benthic foraminifers. This evidence suggests that the depositional environment was above the CCD (e.g., Kuhnt and Urquhart, 2001).

Campanian to Albian foraminiferal assemblages from mudstone are characterized by moderately diverse agglutinated forms, including *Lagenammina* spp., *Glomospira* spp., *Ammobaculites* spp., *Ammodiscus* spp., *Spiroplectammina spectabilis, Trochammina* spp., and fragments of tube-shaped species (Samples 210-1276A-24R-CC to 97R-CC). Similar taxa have been reported from the mid-Cretaceous at other abyssal sites in the North Atlantic (Gradstein, 1978; Sigal, 1979). *Gyroidinoides* cf. *G. nitidus* and *Gavelinella* cf. *G. intermedia* occur rarely but almost continuously between Samples 210-1276A-43R-CC and 74R-CC (upper to middle Albian). Because preservation of these calcareous species is moderate to good, it is possible that they lived together with agglutinated taxa in the abyssal zone above the depth of the paleo-CCD. However, the abundance of agglutinated species and the absence or paucity of calcareous bathyal forms suggests an abyssal paleodepth below the CCD. The presence of the genus *Spiroplectammina* is interesting, as this taxon incorporates calcium carbonate cement into the test wall. Thus, it is expected that these forms would not inhabit environments below the CCD. However, the possibility that these specimens of *Spiroplectammina,* like the calcareous benthic genera *Gyroidinoides* and *Gavelinella,* have been redeposited from upslope sites above the CCD and then subjected to rapid burial cannot be entirely discounted.

In contrast, benthic foraminifers are rarely observed in sandstone samples. However, small *Praebulimina* spp., *Bolivina* spp., and *Gyroidina* spp. occur sporadically (e.g., Samples 210-1276A-75R-CC and 76R-CC). *Praebulimina* spp. and *Bolivina* spp. are thought to be characteristic taxa of the oxygen minimum zone in upper bathyal depths (200–600 m) (Nyong and Olsson, 1984; Holbourn et al., 1999; Leckie and Olson, 2003). These calcareous forms are likely to have been transported from upper bathyal depths by turbidity currents.

Palynology

Paleogene

Eleven of the twenty core catcher samples from the Paleogene that were investigated aboard the ship contain palynomorph assemblages with very good preservation. Lithologic Units 1 and 3 are represented in seven and four palynomorph-bearing samples, respectively. Core catcher samples from lithologic Unit 2 are barren of palynomorphs (Table T11). All Paleogene assemblages investigated are strongly dominated by dinoflagellate cysts (dinocysts). Other marine palynomorphs (acritarchs, prasinophytes, and foraminifer test linings) are generally present as single specimens only. Terrestrial palynomorphs, which are present in low abundances throughout the Paleogene intervals investigated, mainly comprise bisaccate pollen.

T11. Palynomorphs, Site 1276, p. 337.

Sample 210-1276A-1W-CC is assigned an early Rupelian age (33.7–32 Ma; early Oligocene) based on the presence of *Areoligera semicirculata* and *Glaphyrocysta semitecta*. The maximum age of this sample has been determined based on the mid-Northern Hemisphere FO of 33.7 Ma for *A. semicirculata* (Williams et al., unpubl. data [N1]). Thus, this age assignment is more reliable than if it were based on LOs alone. This early Oligocene age assignment is supported by the absence of *Lentinia serrata,* which has a mid-Northern Hemisphere LO of 33.5 Ma (Williams et al., unpubl. data [N1]).

The dating of Sample 210-1276A-2R-CC as ~37.0 Ma (Priabonian to earliest Rupelian; late Eocene to earliest Oligocene) is based on the presence of *Enneadocysta pectiniformis* and *Lentinia serrata*. However, *Areosphaeridium dictyoplokum,* whose LO has been shown to be a reliable marker for the Eocene/Oligocene boundary in many Tethyan and northern European sections (e.g., Brinkhuis and Visscher, 1995), is only found lower in the section. Sample 210-1276A-3R-CC is dated as Priabonian (~37.0–33.6 Ma; late Eocene) based on the presence of *Hemiplacophora semilunifera, E. pectiniformis,* and *L. serrata. Cerebrocysta bartonensis* is present in this sample, in disagreement with the previously described range of this species in the northern mid-latitudes (41–38 Ma) (Williams et al., unpubl. data [N1]). It has yet to be resolved if this inconsistency is due to biogeographic differences or to reworking. The presence of *Charlesdowniea coleothrypta* and *Dracodinium condylos* is ascribed to reworking of Ypresian (lower Eocene) and Lutetian (lower middle Eocene) strata. Sample 210-1276A-4R-CC has been tentatively assigned an early Priabonian to late Bartonian age (latest middle Eocene; 38?–36.5 Ma) based on the presence of *Adnatosphaeridium multispinosum, E. pectiniformis,* and *Phthanoperidinium echinatum*. Other taxa typical for this interval are *Charlesdowniea clathrata, Heteraulacacysta leptalea, Rhombodinium draco,* and *Wetzeliella spinula*. Reworking is indicated by findings of *Areoligera senonensis* and *Cerodinium wardense,* both of which have Lutetian LOs.

Samples 210-1276A-5R-CC, 6R-CC, and 7R-CC contain Bartonian (upper middle Eocene) assemblages (40–38.5, 41–39, and 41–38 Ma, respectively). Age control is primarily based on the presence/absence of *A. multispinosum, Cerebrocysta bartonensis, Diphyes colligerum, Lentinia serrata, Phthanoperidinium echinatum,* and *Rhombodinium draco*. The presence of the Oligocene marker taxon *Phthanoperidinium amoenum* in Sample 210-1276A-5R-CC is attributed to downcore contamination resulting from drilling. For Sample 210-1276A-7R-CC, the presence of *A.*

senonensis again indicates reworking of Lutetian (lower middle Eocene) or older strata.

Other than single reworked specimens identified in the Priabonian to Bartonian samples (see above), Selandian to Lutetian (lower upper Paleocene–lower middle Eocene) palynomorph assemblages were not observed at Site 1276. Samples 210-1276A-8R-CC through 15R-CC proved to be barren of palynomorphs. This is attributed to the strongly oxidized or the partly secondary, reduced nature of the respective sediments.

Assemblages suggesting Danian (early Paleocene) ages were identified in Samples 210-1276A-16R-CC to 18R-CC and 20R-CC. In this interval, palynological age control is predominantly based on the presence of *Alisocysta circumtabulata, A. margarita, A. reticulata, Carpatella cornuta, Cerodinium diebelii, Damassadinium californicum, Oligosphaeridium pulcherrimum, Palaeocystodinium australinum, Palaeoperidinium pyrophorum, Senoniasphaera inornata,* and *Spongodinium delitiense*. Species of the genus *Alisocysta,* which are among the most age-diagnostic taxa for the early Paleogene, are rare at Site 1276. The presence of *Achomosphaera alcicornu* in Sample 210-1276A-16R-CC, which predates the commonly used mid-northern latitude FO of this species by at least 4.2 m.y., may be due to either downcore contamination or an earlier appearance of *A. alcicornu* at Site 1276 than at more southerly locations.

Cretaceous

Nine of the twenty-one core catcher samples from the Cretaceous that were investigated aboard ship yield palynomorph assemblages with very good to excellent preservation. All productive samples are from lithologic Unit 5 (uppermost Aptian[?]–lower Albian to lowermost Turonian). Samples from the Cretaceous part of lithologic Unit 3 as well as from lithologic Unit 4 are barren of palynomorphs (Table **T12**). There is a downhole trend toward increasing terrestrial influence (documented in increasing amounts of terrigenous palynoclasts and sporomorphs) in lithologic Unit 5. Dinocysts are, however, also abundant in these samples.

T12. Calcareous nannofossil and dinoflagellate cyst datums, Site 1276, p. 338.

Samples 210-1276A-29R-CC and 30R-CC are the youngest productive samples from the Cretaceous at Site 1276. They were assigned late Turonian (92.5–88.7 Ma) and early Turonian (93.5–92.5 Ma) ages, respectively, based on the presence of *Chatangiella verrucosa, Epelidosphaeridia spinosa, Litosphaeridium siphoniphorum, Senoniasphaera rotundata alveoata,* and *Trithyrodinium suspectum*. Extremely abundant terrestrial phytoclasts (mainly black wood) in Sample 210-1276A-29R-CC indicate a strong allochthonous signal that is fully compatible with the sedimentologically inferred turbiditic origin. Sample 210-1276A-31R-CC is dated as mid-Cenomanian to early Turonian (96–92.5 Ma) based on the LO of *E. spinosa* and the FO of *Florentinia deanei*. Other characteristic dinocyst taxa of this interval include *Oligosphaeridium asterigum, Pervosphaeridium truncatum,* and *Tehamadinium mazaganensis*.

Cenomanian ages were assigned to Samples 210-1276A-32R-CC, 33R-CC, and 39R-CC (100.5–92.5, 100–95.8, and 98.9–96 Ma, respectively). Palynological age control in the Cenomanian of Site 1276 is mainly based on the presence of *Cyclonephelium membraniphorum, Epelidosphaeridia spinosa, Hapsocysta peridictya, Litosphaeridium siphoniphorum, Ovoidinium verrucosum,* and *Xiphophorum alatum*. All three samples exhibit high abundances of *Palaeohystrichophora infusorioides*.

Dinocyst assemblages from Samples 210-1276A-41R-CC and 45R-CC yield late Albian ages (100–98.9 and 103.2–101.06 Ma, respectively). Diagnostic taxa are, among others, *Carpodinium obliquicostatum, Chichaodinium vestitum, Litosphaeridium siphoniphorum, L. conispinum,* and *Ovoidinium verrucosum*. Sample 210-1276A-56R-CC is assigned a middle Albian age (107–103 Ma) based on the presence of *Callaiosphaeridium* cf. *C. trycherium, Carpodinium granulatum, Dinopterygium cladoides,* and *Stephodinium coronatum*.

The evidence presented above indicates very good preservation of palynomorphs in combination with high sedimentation rates. Thus, there is excellent potential for in-depth palynological studies covering the interval from the Turonian through the Albian in Site 1276 sediments.

Radiolarians

Radiolarians have previously been recorded in abundance from sediments deposited in the North Atlantic during Paleogene to Cretaceous time. The most notable radiolarian blooms previously documented in the literature are recorded in sediments deposited during early Eocene and Campanian times and in the Albian/Cenomanian boundary interval (Thurow, 1988). Radiolarian faunas are also a common component of Mesozoic Tethyan sediments. As such, it was anticipated that these chronological intervals would prove to be the most productive for radiolarian recovery during Leg 210. Mesozoic radiolarians are usually preserved as opal-CT, quartz, or pyrite, depending on diagenetic history. Mineral replacement of the test does not commonly obscure identifying features of the taxa, and in some instances the diagenetic replacement can be advantageous to fossil preservation. Palynological preparations processed from Site 1276 yielded pyritized fragments of both radiolarians and diatoms, giving a good indication that the depositional environments were normal open-marine conditions. The presence of these fragments helps us to focus on the potentially most productive samples for further, more rigorous processing methods.

At Site 1276, Paleogene radiolarian faunas were recovered from the >63-µm fraction of the washed residues of Samples 210-1276A-5R-CC, 9R-CC, 10R-CC, 11R-CC, and 13R-CC. The assigned calcareous nannofossil age for these samples is early to middle Eocene, consistent with widespread siliceous deposits of Eocene age in the Atlantic Ocean. Radiolarians were also recovered from Samples 210-1276A-14R-CC and 18R-CC, which are Paleocene in age based on calcareous nannofossils. Although all these Paleogene occurrences are sometimes abundant, the preservation of the specimens is too poor for positive identification. The assemblages consist mostly of small and seemingly spherical forms.

Published occurrences of Mesozoic radiolarians from North Atlantic sediments recorded to date are few, and the most notable descriptions include those by Foreman (1977), Empson-Morin (1984), and Thurow (1988). In the Mesozoic section cored at Site 1276, rich and diverse radiolarian assemblages were recovered from only three core catcher samples: 210-1276A-48R-CC, 54R-CC, and 96R-CC. Samples 210-1276A-48R-CC and 54R-CC are upper Albian sediments of lithologic Subunit 5B, a lithologic unit characterized by dark greenish gray, medium brown, and greenish black mudstones and claystones. In both of these samples, the radiolarian assemblages are associated with abundant planktonic foraminifers. The radiolarian tests occur as opal-CT and are moderately well preserved. The diverse assemblages are dominated by nassellarians including abundant cryptocephalic taxa together with

species of *Xitus, Archaeodictyomitra, Dictyomitra,* and *Amphipyndax*. The assemblages differ slightly from typical Albian-age Tethyan faunas in that there are very few spumellarians. In particular, the characteristic Mesozoic pseudoaulophacid and hagiastrid taxa are absent. The assemblages show components and preservational characteristics similar to radiolarian faunas recovered from the Albian Gault Clay of southern Britain (Urquhart and Wilkinson, 1997). The radiolarian assemblage recovered from Sample 210-1276A-96R-CC is quite different in terms of preservation in that the majority of specimens are replaced by pyrite. This replacement mineralization has not, however, obscured the external morphologies used for identification of Mesozoic radiolarians. The specimens are moderately well preserved, and the assemblage has a typically Aptian–Albian faunal aspect. Despite this, the sample has not yet yielded age-diagnostic marker species, the presence of which would allow a more refined zonal assignment to be placed on this sample.

Diatoms

Small (<125 µm) pyritized and indeterminate centric diatoms are common in the >63-µm size fraction of the washed residue of the lower Paleocene dark gray mudstone in Sample 210-1276A-20R-CC. As mentioned above, pyritized diatoms and diatom fragments are also present in many of the palynological preparations.

Other Fossils

Ichthyoliths (fish teeth) and fish bones are present in most samples throughout the hole but are rare; this suggests normal marine conditions but poor preservational environments. Ostracodes are recovered sporadically in the mid-Albian section in low abundances, usually as single specimens. Calcite prisms of inoceramid bivalve shells are present in a number of Albian-age samples. These prisms are a common and characteristic component of Cretaceous sediments, especially those deposited during the Campanian and early Maastrichtian. Their relative scarcity in sediments recovered at Site 1276 suggests depositional environments below the CCD.

Sedimentation Rates

Sedimentation rates were determined by connecting straight-line segments through median depths in an age-depth plot depicting key calcareous nannofossil FOs or LOs (Fig. **F141**). Select palynomorph FOs and LOs are also shown. In Figure **F142,** the minimum and maximum ages of calcareous nannofossil, planktonic foraminifer, and palynomorph zones (or ages) for each sample are shown by conjugate triangles that are color-coded by microfossil group. See Table **T12** for the datums used to construct the age-depth curve for Site 1276 and Table **T13** for the datums used to construct the age-depth curve for DSDP Site 398.

The first core taken at Hole 1276A is a wash core (210-1276A-1W), and its placement in the interval from ~753 to ~800 mbsf is uncertain; therefore, biostratigraphic datums from Core 1W are not used in the sedimentation rate calculations. The age-depth plot reveals a number of marked changes in sedimentation rate; at least one, and possibly two, unconformities; and two condensed intervals. The changes in slope correspond closely to lithologic unit boundaries (see **"Lithostratigraphy,"** p. 20). Samples 210-1276A-2R-CC through 7R-CC (basal Oligocene to

F141. Age-depth plots, Sites 1276 and 398, p. 266.

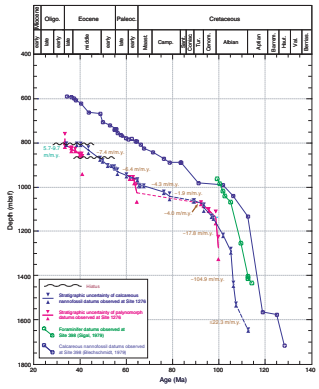

F142. Age-depth plots and zonal boundary ages, p. 267

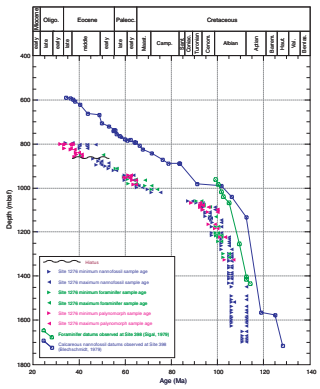

T13. Calcareous nannofossil and foraminifer datums, Site 398, p. 339.

middle Eocene) correspond to lithologic Unit 1 and show an average sedimentation rate of ~7.4 m/m.y. based on calcareous nannofossil datums and a range of 5.7–9.7 m/m.y. based on palynomorphs.

The apparent discrepancy between the (younger) palynomorph and (older) calcareous nannofossil–based ages in Sections 210-1276A-2R-CC through 7R-CC can be explained in several ways, the foremost being dissolution of calcareous microfossils in combination with extensive reworking. Deposition of sediments below the CCD probably reduced the numbers of in situ calcareous nannofossils that were then diluted by allochthonous (reworked) specimens. The dissolution effect can be excluded for the (organic walled) palynomorphs. Moreover, the palynomorph data for this time interval rely more on FOs in comparison to the nannoplankton data, which makes them less prone to problems associated with reworking. Another factor contributing to the age discrepancies between the calcareous nannofossil and dinoflagellates in the middle Eocene–lower Oligocene of Hole 1276A was the use of a low-latitude tropical calcareous nannofossil zonation for a site that was, at times, influenced by cooler-water masses (the paucity of Discoasters at this site could be evidence of this influence); therefore, biostratigraphic data based on Discoasters may be less reliable. In addition, direct calibration of dinoflagellate events with magnetic polarity stratigraphy in deep-ocean cores is in its infancy.

Calcareous nannofossil datums in the upper part of Core 210-1276A-2R suggest the presence of an unconformity or condensed interval spanning the upper middle and upper Eocene, although additional shore-based research is required to constrain the duration. A second, deeper unconformity spanning as much as 8.5 m.y. may be present at the boundary between lithologic Units 1 and 2 in Section 210-1276A-8R-5. This estimate is based on the combination of young FOs of the dinocysts *Lentinia serrata* and *Rhombodinium draco* in Sample 210-1276A-6R-CC and the much older FO of the calcareous nannoplankton taxa *Rhabdosphaera inflata* in Sample 8R-CC. An erosional event of much shorter duration would be indicated by the calcareous nannoplankton datums alone, but barren samples in Cores 210-1276A-4R through 7R hampered shipboard resolution of the unconformity.

An average sedimentation rate of 7.4 m/m.y. persists through the middle and lower Eocene (Samples 210-1276A-8R-CC to 14R-1, 104 cm) of Site 1276 based on the calcareous nannofossil data. This interval corresponds to much of lithologic Unit 2. The Paleocene–upper Maastrichtian interval corresponds to the basal part of lithologic Unit 2 and much of lithologic Unit 3, and it accumulated at an average rate of ~6.4 m/m.y. The lower Maastrichtian is condensed or missing at this site and is represented by the red sediments of Core 210-1276A-22R. The calcareous nannofossil datums found in the lower part of lithologic Unit 3 suggest that the upper Campanian sediments accumulated at an average rate of ~4.3 m/m.y.

An interval of paleontologically barren samples occurs in Cores 210-1276A-25R through 28R. This interval represents the bulk of lithologic Unit 4, which accumulated at an average rate of ~1.9 m/m.y. based on the bracketing calcareous nannofossil datums above and below. Because of the lack of age control, this interval could include an undetected hiatus. The Turonian (basal part of lithologic Unit 4 and uppermost part of Unit 5) accumulated at an average rate of 4.0 m/m.y. The middle Albian–Cenomanian part of lithologic Unit 5 (Cores 210-1276A-31R through 51R) accumulated at an average sedimentation rate of 17.8 m/m.y., whereas the middle Albian (Cores 52R–77R) accumulated at a

greatly increased average rate of ~104.9 m/m.y. The uppermost Aptian(?)–lower Albian interval (Cores 210-1276A-78R through 97R) records an average sedimentation rate of 22.3 m/m.y. The overall pattern of changing sedimentation rates at Site 1276 is strikingly similar to that of DSDP Site 398 on the conjugate margin of the Iberia Peninsula (Figs. F141, F142).

PALEOMAGNETISM

We made pass-through magnetometer measurements and magnetic susceptibility measurements on all split-core archive sections at 2-cm intervals. In order to isolate the characteristic remanent magnetization (ChRM), we subjected the cores to alternating-field (AF) demagnetization. The number of AF demagnetization steps and the peak-field intensity varied depending on lithology, the natural remanent magnetization (NRM) intensity, and the amount of time available for analysis. On average, sediment half cores were demagnetized using three AF steps in addition to the measurement of NRM. Some half cores were demagnetized using as many as six AF steps. The maximum applied field ranged from 20 to 60 mT. In order to assess the half-core data and to identify magnetic carriers, we demagnetized several discrete samples using both AF and thermal techniques. We analyzed the results in Zijderveld and stereoplot diagrams, and, where possible, we calculated the ChRM direction using principal component analysis (Kirschvink, 1980). In addition, we determined magnetic susceptibility on all whole cores from Site 1276 at 2.5-cm intervals as part of the multisensor track (MST) analysis and we measured split-core sections at 2-cm intervals with the point-susceptibility meter on the archive multisensor track (AMST). The two magnetic susceptibility data sets compare well with one another.

Natural Remanent Magnetization Intensity and Magnetic Susceptibility

Paleomagnetic data obtained at Site 1276 exhibit considerable variations in demagnetization behavior among various lithologies, with the most common features summarized as follows. Variations in magnetic susceptibility broadly correlate with the variations in NRM intensity (Fig. F143). A pervasive remagnetization imparted by the coring process is commonly encountered, as was noted during previous legs (e.g., Gee et al., 1989; Zhao et al., 1994). This remagnetization is characterized by NRM inclinations that are strongly biased toward steep downward inclination, and it can be removed at initial stages of demagnetization. An example is shown in Figure F144, where the NRM inclinations observed in Section 210-1276A-35R-5 are biased toward steep positive values (Fig. F144A). With 30-mT demagnetization, we observed a shift toward shallower inclinations (Fig. F144A) and a significant decrease in intensity (Fig. F144B). Although the maximum level of AF demagnetization on the ship's cryogenic magnetometer was not always able to remove these overprints, ChRM directions can generally be determined from the pass-through measurements. Examples of good-quality AF demagnetization results are shown in Figure F145.

In general, we find that the magnetic properties of sediments recovered from Hole 1276A correlate with the lithology (see Fig. F143). Below we describe the magnetic characteristics of the main lithologic units.

F143. Magnetic susceptibility and NRM intensity, p. 268.

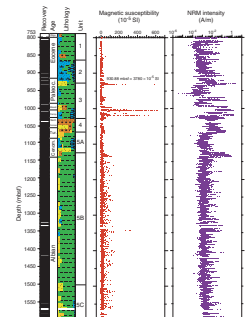

F144. Inclination and intensity, p. 269.

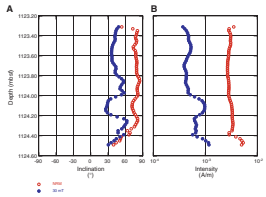

F145. Zijderveld diagrams, p. 270.

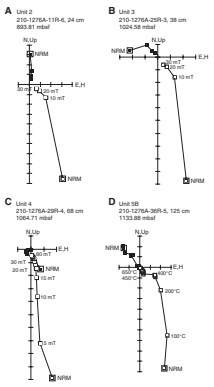

Unit 1

In the middle to upper Eocene Cores 210-1276A-2R through 8R, variably burrowed, varicolored mudstones and claystones have low NRM intensity and low magnetic susceptibility. NRM intensities generally range between 3.7×10^{-5} and 3×10^{-1} A/m (mean = 3.5×10^{-3} A/m). Magnetic susceptibility averages 4.3×10^{-5} SI units. A few discrete peaks of higher NRM and susceptibility values could in some cases be tied directly to the visible presence of pyrite. By analogy to previous studies of lower Oligocene to middle Eocene sediments on the Iberia margin, we speculate that primary magnetite in these claystones and mudstones has suffered diagenetic reduction to pyrite, thereby destroying the primary remanent magnetization. For these cores, reliably defining the primary remanent magnetization was impossible.

Unit 2

Sediment recovery in the upper Paleocene to middle Eocene section was somewhat lower than in Unit 1. Although the NRM intensity of the unit is still low (ranging from 1.4×10^{-4} A/m to 2×10^{-1} A/m; mean = 4.5×10^{-3} A/m), we were able to define the ChRM direction from a few intact cores (see Fig. **F145**). Magnetic susceptibility in this interval ranges from 6.9×10^{-4} to 6×10^{-5} SI units (mean = 3.1×10^{-5} SI units).

Unit 3

The lower Campanian to lower Paleocene Unit 3 consists of mainly claystone and mudstone with the exception of Cores 210-1276A-24R and 25R, where marlstone and grainstone are present (see **"Lithostratigraphy,"** p. 20). The claystones and mudstones have relatively high NRM intensity and magnetic susceptibility, caused by the presence of numerous dark burrowed beds that have relatively high concentrations of magnetic minerals. The mean values for NRM intensity and magnetic susceptibility are 6×10^{-2} A/m and 2.4×10^{-4} SI units, respectively. One interesting observation is that the AMST and MST magnetic susceptibility data and pass-through cryogenic magnetometer NRM intensity records show an anomalous peak for sandstones in interval 210-1276A-15R-4, 132–142 cm (930.82–930.92 mbsf) (see Fig. **F143**). This sharp increase in magnetic susceptibility is present at approximately the lower/upper Paleocene boundary. The cause of this susceptibility high is not clear and awaits determination by shore-based studies. In addition to this susceptibility high, the interval between 1013.40 and 1018.72 mbsf (Sections 210-1276A-24R-2, 30 cm, and 24R-5, 112 cm) in Unit 3 displays high NRM intensity and magnetic susceptibility values (Fig. **F143**), corresponding to marlstones and grainstones.

Unit 4

These sediments are mainly sandy mudstones and muddy sandstones that slowly accumulated during Turonian to latest Santonian time (see **"Biostratigraphy,"** p. 73). The characteristic color of Unit 4 is moderate brown, which is perhaps related to the presence of fine-grained iron oxides (see **"Lithostratigraphy,"** p. 20). Accordingly, the mean NRM intensity (3×10^{-2} A/m) and magnetic susceptibility (1×10^{-4} SI units) are relatively high. A strong drilling-induced overprint is present throughout Unit 4, which severely limits paleomagnetic work.

Unit 5

Sediments in lithologic Unit 5 are uppermost Aptian(?) to lower Turonian claystones and mudstones that have low NRM intensities (mean = ~2.5 × 10^{-3} A/m) and magnetic susceptibilities (mean = ~8 × 10^{-5} SI units). There are more significant variations in susceptibility in Unit 5 than in Unit 4. Characteristic susceptibility peaks reflect carbonate and sandstone layers, and troughs correspond to green and gray claystone and mudstone. The susceptibility peaks of carbonates may reflect an iron component in these rocks, most likely in siderite. Finely laminated claystones (black shales) are well developed and numerous throughout Unit 5. The magnetization of these dark claystones is typically an order of magnitude (in some cases even two orders) weaker than that of light-colored sediments. Although the ChRM directions can still be defined from these black shales using stepwise demagnetization (Fig. F145), we suspect that the magnetic remanence is secondary. Interestingly, some muddy sandstones below 1125 mbsf in Sections 210-1276A-35R-7 through 36R-6 (~1135 mbsf) show high peaks in both NRM intensity and magnetic susceptibility (Fig. F146). The high-intensity peaks were maintained even after 30-mT AF demagnetization, suggesting that it is unlikely that they are caused by drilling-induced remagnetization.

Remanent magnetization of discrete samples from these five lithologic units was investigated using stepwise AF or thermal demagnetization. In most cases, the steep downward component of magnetization imparted by the coring process is easily removed by AF demagnetization. Thermal demagnetization also successfully removed this drilling-induced component. Most samples show unblocking temperatures between 350° and 550°C, indicating that titanomagnetites are likely the main magnetic carriers in the samples.

Results from Diabase Sills

Drilling in Subunit 5C yielded diabase in one sill and one deeper sill complex. We performed detailed AF demagnetization on all coherent diabase pieces that could be oriented unambiguously with respect to the top of the core (Figs. F147, F148). All pieces contained a vertical secondary component, most likely induced during drilling. In almost all cases, we were able to remove this secondary magnetization by 10- to 20-mT AF demagnetization and by isolating the ChRM direction at higher fields (e.g., Fig. F149). The inclinations of the ChRM direction for the two diabase sills are all positive. The simplest explanation of the positive inclinations is that they represent normal-polarity magnetization, probably acquired within the Cretaceous Normal Superchron (CNS). This interpretation is compatible with time of emplacement inferred from other shipboard studies (see "Igneous and Metamorphic Petrology," p. 64 and "Physical Properties," p. 99). In order to test inclinations determined from the half-core data, several discrete samples from the two sills were thermally treated and measured. The results (squares in Figs. F147, F148) are in good agreement with the half-core measurements. However, more complete shore-based demagnetization and statistical analysis of the data are needed.

A problem was encountered during half-core measurements on diabase pieces because the diabase cores are broken into segments. Because the short pieces have no azimuthal orientation relative to one another and the measurement region of the pass-through magnetometer (~15 cm) is comparable to piece size, we observed significant magnetic inter-

F146. Magnetic susceptibility and intensity before and after 30-mT AF demagnetization, p. 271.

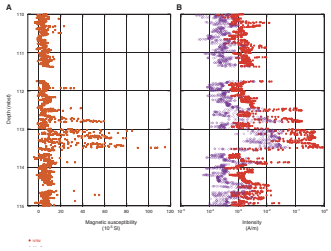

F147. Magnetic susceptibility, intensity, and inclination in the upper diabase sill, p. 272.

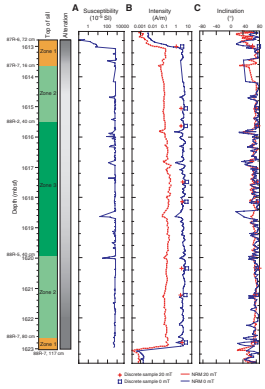

F148. Magnetic susceptibility, intensity, and inclination in the lower diabase sill, p. 273.

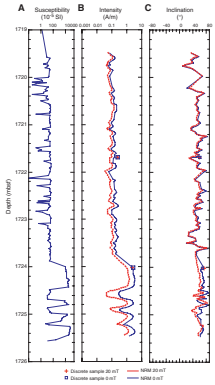

F149. Zijderveld diagrams for diabase sills, p. 274.

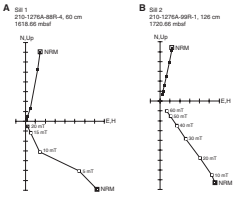

ference between the pieces; this leads to artificially low NRM intensities and varying inclinations from piece to piece. For this reason, we omitted data points for short pieces in Figures F147 and F148. We used the following criteria to select only reliable inclination values. The pieces had to be at least 7 cm long, the maximum angular deviation of the principal component analysis had to be <3°, and the pieces had to be homogeneously magnetized. Analyzed pieces that fulfill these criteria are summarized in Table T14. Significant changes in inclination and intensity values in the upper sill (Table T14) suggest that this sill may contain two subunits.

T14. Paleomagnetic results, p. 340.

Although the NRM intensities and inclinations are quite variable, we identified distinct differences between the upper and lower diabase sills. The lower sill (Sections 210-1276A-99R-1 through 99R-6; ~1719–1725 mbsf) is generally more weakly magnetized: the average intensity and magnetic susceptibility are 0.8 A/m and 3.2×10^{-3} SI units, respectively (Fig. F148). The upper sill (Sections 210-1276A-87R-6 through 88R-7; ~1613–1623 mbsf) is more magnetic and has average intensity (>3.8 A/m) and magnetic susceptibility (5.6×10^{-2} SI units) values that are consistently higher than the lower sill. The result is that the average Königsberger ratio, *Q* (defined as the ratio of the NRM intensity to the induced magnetization in the local Earth's field) (see "Paleomagnetism," p. 22, in the "Explanatory Notes" chapter), for the upper sill is ~1.9, whereas *Q* values in the lower sill have a mean of 9.5 (Table T14).

Magnetostratigraphy

As mentioned, shipboard pass-through measurements did not yield reliable primary remanent magnetization from sediments in Unit 1, so the magnetic polarity stratigraphy of the lower to upper Eocene cores cannot be established at present. Based on biostratigraphic data in Unit 2, however, we were able to tentatively correlate certain elements of the observed magnetic polarity interval in upper Paleocene to middle Eocene sediments with the geomagnetic polarity timescale. In particular, the reversed polarity interval in Section 210-1276A-9R-5 may represent Chron C21r of the early middle Eocene. However, because only this section displays an indisputable reversed polarity, the magnetostratigraphic potential for Unit 2 is obviously limited.

Shipboard micropaleontological study suggests that the K/T boundary is in Section 210-1276A-21R-4 of Unit 3 (see "Biostratigraphy," p. 73). From the magnetostratigraphic point of view, however, no well-defined reversed zone can be identified at the inferred boundary, even though we expect to find one (i.e., Chron C29r). Failure to detect a reversal could be due to severe drilling-induced overprint. Detailed demagnetization work on discrete samples from this unit is needed.

The biostratigraphic ages for Unit 4 suggest that there should be at least one reversed polarity magnetozone (Chron C33r; 83–79 Ma) in this cored interval (Turonian–uppermost Santonian). However, the recovered sediments are all normally magnetized. It is possible that our sampling interval (2 cm) and the size of the region sensed by the magnetometer are too large to detect fine-scale magnetization changes. Shore-based studies of discrete samples may help to identify small-scale features not discernible in our pass-through measurements. The sedimentation rate is ~2 m/m.y. in this interval; thus, Chron C33r should occur over ~8 m of core. However, Cores 210-1276A-25R through 28R are barren of fossils and it is possible that a hiatus is present and Chron C33r sediments are missing.

The age of the succession in Unit 5 is latest Aptian(?) to early Turonian, which is within the CNS, and, accordingly, cores in Unit 5 are all normally magnetized. However, we cannot exclude the possibility that the normal polarity also could represent late-stage remagnetization in a normal field.

Comparison of Magnetic vs. Nonmagnetic Core Barrel

Since the beginning of DSDP in 1968, paleomagnetists have been complaining about the presence of a magnetic remanence that is thought to be acquired during drilling and/or recovery of the core (e.g., see Stokking et al., 1993). Numerous investigations of the magnetic fields of the various tool components used in coring have been conducted previously on the advanced piston corer and extended core barrel (e.g., Fuller and Garrett, 1998; Fuller et al., 1998). Results, suggest that there can be very strong local fields in the bits and in the pipe (e.g., Stokking et al., 1993; Herr et al., 1998; Fuller et al., 2000). During Leg 210, we used an RCB that was half nonmagnetic (lower) and half normal (upper) steel for Cores 210-1276A-1W through 57R (this type of core barrel was tried during Leg 209, but there was no documentation of its effect on the magnetization of cores). Starting with Core 210-1276A-59R, we used a full nonmagnetic RCB for the first time. The nonmagnetic barrels were made with 15-15-LC steel, which is a nonmagnetic material commonly used in the petroleum industry. All the odd-numbered cores from 210-1276A-59R through total depth were retrieved with this nonmagnetic core barrel, whereas even-numbered cores were recovered with a regular RCB (magnetic). This allowed us to test the effects of the magnetic vs. nonmagnetic RCBs on remanence intensities and directions. In this experiment, we were fortunate that sedimentary rocks from Cores 210-1276A-58R through 68R in Unit 5 have quite uniform lithology and composition and the sediments all have normal polarity (i.e., there is no complication due to a reversal sequence). As shown in Figure **F150A** there is a clear indication that cores obtained with a regular core barrel are more strongly magnetized than those with the nonmagnetic core barrel. After 20-mT demagnetization, the difference in remanence intensity clearly remains but it is generally reduced compared with the NRM (Fig. **F150B**).

Although we focused our comparison on the overall remanence intensity, we also compared inclinations (Fig. **F151**). Curiously, there appears to be a tendency toward anomalously steep negative inclinations (both before and after 20-mT demagnetization) at the top of every core, regardless of which core barrel was used. A closer examination of the remanence-intensity record reveals that there are intensity spikes exactly at the same positions as the steep inclinations (Fig. **F151A**). This suggests that some coring component (or perhaps rust from inside the drill pipe) that is strongly magnetized with upward inclination can remagnetize the top portion of the core material. At this time we can only speculate, but it is also possible that the remagnetization occurs upon core retrieval (e.g., it may be affected by the "stabber bar" and/or its swivel connecting to the core cable).

Understanding the magnetic effects of core barrels is very important for the new Integrated Ocean Drilling Program. Our results demonstrate that strong magnetization of conventional core barrels provides a potential "source field" in which the sediments could acquire barrel-induced magnetization. There is no longer any doubt that standard core barrels should be replaced with the nonmagnetic core barrels dur-

F150. Core magnetization intensity for magnetic vs. nonmagnetic core barrels, p. 275.

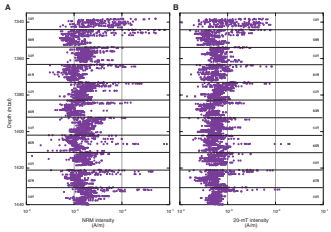

F151. Core magnetic inclination for magnetic vs. nonmagnetic core barrels, p. 276.

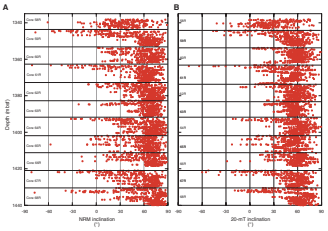

ing future drilling legs, especially those targeted for paleoceanographic investigation at low latitudes.

GEOCHEMISTRY

Volatile Hydrocarbons

Headspace gas analysis was conducted as part of the standard protocol required for shipboard safety and pollution prevention monitoring. On average, two samples per core were analyzed (Table T15). Methane (C_1) concentrations remain at low background levels (≤7 ppmv; average = 3 ppmv) to a depth of 1140 mbsf in lithologic Subunit 5B (Fig. F152). From 1140 to 1610.58 mbsf, just above the upper diabase sill (Subunit 5C1), C_1 concentrations generally increase downhole with a range of values between 1 and 1353 ppmv. Small amounts (≤1 ppmv) of ethane (C_2) were detected in only five samples above 1176 mbsf (Table T15; Fig. F152). Below this level, down to 1610.58 mbsf, ethane was detected in almost every sample, and its concentrations increase downhole (up to 74 ppmv).

The C_1 concentrations increase dramatically to 5854 ppmv in the sediments just below Subunit 5C1 (diabase sill) in Core 210-1276A-88R (1624.01 mbsf), and high concentrations persist in deeper cores (Table T15; Fig. F152). Layers of anomalously unconsolidated high-porosity clay-rich sediments are present in Cores 210-1276A-96R and 97R (1692.33–1703.5 mbsf) (see **"Undercompacted Systems: High-Porosity and Low-Velocity Mudstones,"** p. 101, in "Density and Porosity," in "Physical Properties"). In these layers, C_1 levels rise to 18,669 ppmv. At 1713.01 mbsf (Core 210-1276A-98R), C_1 concentrations drop to 556 ppmv in strongly hydrothermally altered sediments. Between 1624.01 and 1703.5 mbsf, the high methane concentrations may be caused by the sill acting as a seal, preventing gas and interstitial water from escaping. In this same interval, C_2 concentrations (95–7501 ppmv) increase with depth, following the C_1 profile (Fig. F152).

Propane (C_3) (up to 1417 ppmv) and traces of branched and straight-chain C_4 (up to 102 ppmv) and C_5 (up to 6 ppmv) components were commonly detected below 1470 mbsf and always detected below the upper sill (>1624.01 mbsf). C_6 was detected in only two samples (210-1276A-94R-4, 0–1 cm, and 97R-3, 0–1 cm), both below the upper sill (Table T15).

C_1/C_2 ratios are useful to distinguish between biogenic and thermogenic gaseous hydrocarbons. Biogenic gases generally have ratios >1000, whereas ratios <200 may indicate gas generation related to increasing depth and temperature (Claypool and Kvenvolden, 1983; Stein et al., 1995; Whiticar, 1999). C_1/C_2 ratios in lithologic Subunits 5B and below show a trend of decreasing values with depth (Fig. F152), from values of ~100 at 1200 mbsf to ~10 at 1610.58 mbsf (Table T15). Below the upper sill (1624.01 mbsf), C_1/C_2 ratios stabilize at low values, ranging between 2 and 6. Overall, low C_1/C_2 ratios and the presence of longer-chain volatile hydrocarbons indicate that along the cored sequence, thermogenically derived gas is present, either generated in situ or migrating from a source. A weak correspondence exists between higher organic carbon percentages and higher methane concentrations between 1140 and 1684 mbsf (Fig. F153). This suggests that the amount of organic matter present may play a role in the generation of methane.

T15. C_1–C_5 hydrocarbons in headspace gas, p. 342.

F152. C_1 and C_2 concentrations and C_1/C_2 ratios, p. 277.

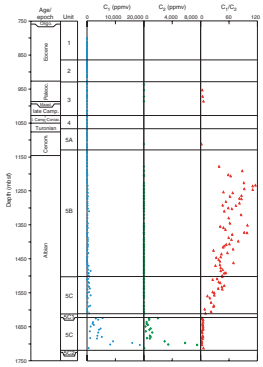

F153. C_1 and TOC, p. 278

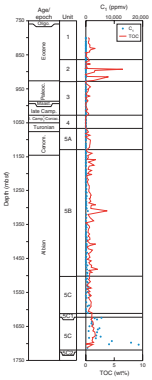

Carbonate and Organic Carbon

Carbonate determinations were made for a total of 758 samples from Hole 1276A (Table T16). Samples were selected to provide a measure of the carbonate content in different lithologic units and to assess the influence of carbonate content on seismic velocity (see "Velocity Structure of Turbidite Sequences," p. 103, in "Factors Affecting Sediment Velocity" in "Physical Properties"). Carbonate contents range between 0.1 and 92.9 wt% (Fig. F154). Although the carbonate content profile shows widely varying values downhole, there is a general correlation with the lithologic units. Units 1 (mudstone) and 4 (burrowed mudstones and sandstones) show lower carbonate values (averages = 6.7 and 8 wt%, respectively), whereas Unit 2 (grainstones and marlstones) shows the highest carbonate contents (average = 30.6 wt%). In Unit 5, average carbonate content tends to decrease downhole (average = 22 wt% in Subunit 5A, 14.1 wt% in Subunit 5B, and 9.5 wt% in Subunit 5C) in association with an increase of the mud/clay fraction and a general downhole increase in Al (Fig. F155).

Elemental concentrations of C, N, and H were measured for a total of 443 samples (Table T17; Fig. F154). TOC contents vary between 0 and 9.4 wt%. Unit 4 has uniformly low TOC percentages (average = 0.1 wt%), whereas Unit 5 (mainly dark claystones) shows intermittently higher values but a somewhat low average of 1 wt% (Fig. F154).

C/N ratios range between 0 and 136.8 (Table T17; Fig. F154). C/N ratios are often used as indicators of the origin of organic matter, with lower values (4–10) typical of marine algae and higher values (>20) considered to be typical of land-derived material (Meyers, 1994). In Unit 4, C/N ratios (<9.6) are characteristic of algal material, which could indicate a pelagic origin for the organic fraction. C/N ratios show scattered high and low values in the other lithologic units, although averages of Units 1 and 3 are still typical of marine-derived organic matter (12.2 and 12.7, respectively). These units also show scattered higher values (>25–30), more typical of land-plant material, that could be explained by strong terrigenous turbidite influence. Subunits 5A, 5B, and 5C show somewhat higher C/N values (averages = 21, 16.6, and 18.6, respectively) together with higher organic carbon contents.

A general correlation exists between higher C/N ratios and higher TOC contents in Hole 1276A (Fig. F154), suggesting the possible importance of a terrigenous contribution to the sedimentary organic matter. Smear slide observations (see "Unit 5," p. 39, in "Lithostratigraphy" and "Site 1276 Smear Slides") confirm an abundance of terrestrial organic matter over the whole cored sequence, with algal material mainly localized in higher-TOC intervals. However, many Cretaceous black shales (Meyers et al., 1984; Meyers, 1987) and Mediterranean sapropels (Bouloubassi et al., 1999; Meyers and Doose, 1999; Nijenhuis and de Lange, 2000) have high C/N ratios even though the organic matter appears to be marine derived. Correspondence of high C/N ratios with high TOC percentages has been postulated to result from a coupling between higher fluxes of organic matter and improved preservation of carbon content (Twichell et al., 2002). This process is promoted by suboxic conditions and appears to be driven by denitrification (Van Mooy et al., 2002).

From the above considerations, C/N values in Unit 5 may indicate partial input of terrestrial material and/or differential nitrogen cycling in this black shale–dominated sequence.

T16. Carbonate content, p. 345.

F154. $CaCO_3$, TOC contents, and C/N ratios, p. 279.

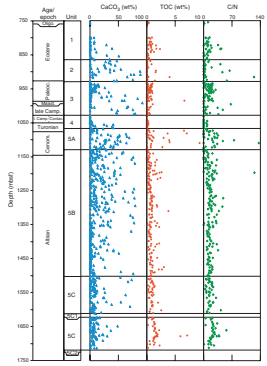

F155. TOC, Al, and Ba/Al, Ni/Al, Cr/Al, and V/Al, p. 280.

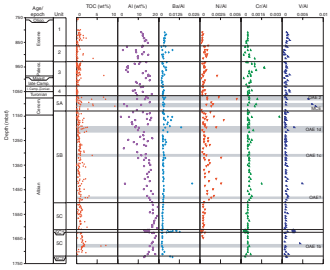

T17. Results from CNH analysis, p. 349.

Rock-Eval Pyrolysis

Rock-Eval investigations were conducted for purposes of safety and pollution prevention, with a resolution of two samples per core. To minimize mineral matrix effects, only results from samples with TOC ≥0.5 wt% (Peters, 1986; Bordenave et al., 1993) and $CaCO_3$ ≤50 wt% (G.E. Claypool, pers. comm., 2003) were considered. Samples with <0.5 wt% TOC and >50 wt% $CaCO_3$ are included in the data table (Table T18) but are not included in the interpretative plots (Fig. F156). During Leg 210, because of technical problems with the Delsi Nermag Rock-Eval II, S_3 and TOC data were not acquired. In order to calculate the HI, TOC results from the CHNS analyzer were employed. Rock-Eval parameters are useful in constraining the origin of organic matter and its thermal maturity.

Most samples exhibit T_{max} between 435° and 470°C (Table T18; Fig. F156), typical of thermally mature organic matter. Nonetheless, S_2 is generally low (<1 mg HC/g sediment), indicating poor hydrocarbon-generating potential. Moreover, low hydrogen indexes along the cored sequence (HI < 100 mg HC/g TOC) indicate that kerogen is predominantly of hydrogen-depleted type III/IV (Fig. F157). This suggests that in Hole 1276A, kerogen might be mainly derived from reworked, preheated terrestrial components (Wagner and Pletsch, 2001).

High T_{max} values at 1624 mbsf (528°C) and at ~1692.33 mbsf (up to 575°C) (Fig. F156) might be due to thermal alteration of the organic matter as a result of sill emplacement. However, because of the low S_2 values for these samples, we cannot be certain of the accuracy of these T_{max} results.

Oceanic Anoxic Events

Shipboard analyses revealed promising indications of black shales that may be related to OAEs in Hole 1276A (see "Origin of Finely Laminated Black Shales," p. 55, in "Unit 5" in "Lithostratigraphy"). In Unit 5, it is possible to identify six horizons characterized by higher TOC contents and S_2 values (Table T18; Fig. F156).

The top of Subunit 5A (Cores 210-1276A-30R through 31R) has TOC up to 7 wt% and HI up to 452 mg HC/g TOC, indicative of type II marine-derived kerogen. This interval is upper Cenomanian to lowermost Turonian, and it likely corresponds to the "Bonarelli" event, OAE 2.

Core 210-1276A-33R (middle of Subunit 5A) (TOC = 4 wt%; HI = 187 mg HC/g TOC), probably represents the MCE (Leckie et al., 2002), with kerogen indicative of a weak marine origin.

The upper part of Subunit 5B (Cores 210-1276A-42R through 44R) has TOC contents of up to 2.6 wt% and HI typical of terrestrial kerogen. Biostratigraphically, this layer may correspond to OAE 1d (latest Albian), dominated by terrigenous organic matter (Leckie et al., 2002).

Core 210-1276A-55R in Subunit 5B (TOC = 3.8 wt%; S_2 values = 2.8 mg HC/g sediment; HI = 73 mg HC/g TOC) is characterized by terrestrially derived type III kerogen. From biostratigraphic constraints, this layer seems to correspond to OAE 1c, which is dominated by terrigenous organic matter (Erbacher and Thurow, 1997).

The bottom of Subunit 5B (Core 210-1276A-73R) is characterized by TOC contents of up to 2.7 wt% and HI of 158 mg HC/g TOC, characteristic of a weak marine origin of the kerogen. Even though this horizon

T18. Organic carbon and Rock-Eval pyrolysis results, p. 353.

F156. TOC contents and Rock-Eval pyrolysis results, p. 281.

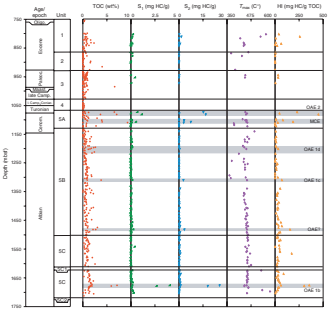

F157. Comparison of HI and T_{max}, p. 282.

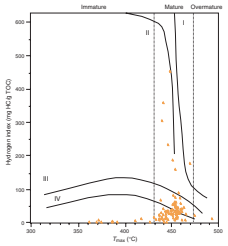

does not correspond to any known OAEs, it has the potential to represent an OAE-type layer.

Core 210-1276A-94R, in the middle of Subunit 5C between the diabase sills, has TOC up to 7.1 wt% and HI up to 357 mg HC/g TOC, indicative of type II marine-derived kerogen. This interval is lower Albian, and it might represent the "Paquier" event, OAE 1b.

The investigation and characterization of these layers will be the subject of detailed shore-based geochemical and biostratigraphic studies.

Interstitial Water Chemistry

Two interstitial water samples were collected from the top of the cored sequence in Cores 210-1276A-2R and 3R (Table T19). Our goal was to measure the concentration of pore water sulfate to evaluate the possible presence of biogenous methane. The samples had low sulfate and methane concentrations, and, because of the dense lithification of the formation (very little pore fluid), we decided to stop interstitial water sampling below Core 210-1276A-3R.

T19. Sulfate concentrations, p. 356.

Trace Elements and Redox-Sensitive Metals

Aluminum concentrations vary between 3.3 and 20.1 wt% (Table T4; Fig. F155). Whereas in the upper part of the sequence aluminum contents show high variability, in Unit 5 there is a trend of moderately increasing values downhole (see "Implications of Sediment Chemistry," p. 53, in "Subunit 5C" in "Unit 5" in "Lithostratigraphy").

Trace and redox-sensitive elements are plotted relative to Al to account for possible varying dilution by detrital minerals. Barium is generally a good proxy for paleoproductivity, especially in the deep ocean (Dymond et al., 1992). In particular, there seems to be an important correlation between fluxes of organic carbon to the seafloor and sedimentary accumulations of barite, which is formed in the water column by the simultaneous decomposition of organic matter and uptake of Ba in settling particles (Dymond et al., 1992). Ba/Al ratios, contrary to expectation, do not show enrichments in relation to OAE 2, the MCE, or OAE 1b (lower Albian) (Fig. F155), which are associated with increased marine productivity. This might be related to a sampling bias because ICP-AES samples and TOC/Rock-Eval samples did not coincide. Alternatively, the absence of enrichments might be due to the presence of extremely anoxic conditions during deposition. Mobilization of barite (Ba sulfate) can occur under sulfate-reducing conditions (Dymond et al., 1992).

Redox-sensitive elements (like Cr and V) are sensitive to changes in their oxidation states and to concomitant changes in chemical behaviors, whereas chalcophile elements (like Ni) are associated with sulfide mineralization (Van der Weijden, 1993). Both redox-sensitive and chalcophile elements are precipitated from seawater, and their accumulation and immobilization in sediment is associated with dysoxic/anoxic conditions either in the water column or in the sediment. Downhole variations of Ni/Al, Cr/Al, and V/Al (Fig. F155) suggest the presence of dysoxic/anoxic conditions in lithologic Unit 5 in correspondence to the possible OAE black shales, particularly Cenomanian–Turonian OAE 2, the MCE, and latest Albian OAE 1d.

PHYSICAL PROPERTIES

Evaluation of physical properties at Site 1276 included nondestructive measurements of bulk density by gamma ray attenuation (GRA) bulk density, bulk magnetic susceptibility, and natural gamma radiation (NGR) on whole cores using the MST. Horizontal (x- and y-direction) and vertical (z-direction) compressional wave (*P*-wave) velocities were measured on cubes cut from half-core samples. Porosity and density were determined from cylinders shaped from the velocity-determination cubes. Thermal conductivity was measured on lithified half-core samples. High core recovery facilitated acquisition of an excellent physical property data set. Apart from an initial wash core (Core 210-1276A-1W), core recovery commenced at 800 mbsf and continued to 1729 mbsf (Cores 2R through 99R).

Density and Porosity

Bulk density at Site 1276 was computed from GRA bulk density measurement of unsplit cores. Bulk density, grain density, and porosity were calculated from the wet mass, dry mass, and dry volume of discrete samples using the moisture and density (MAD) method C (Blum, 1997) for lithified sedimentary and igneous rocks in Cores 210-1276A-2R through 99R (800–1729 mbsf).

The absolute values of the GRA density data (Fig. **F158**) should be ignored; they are consistently too low because the RCB core did not fill the core liner. The MAD bulk density values are consistently higher by 0.25–0.5 g/cm³ (Fig. **F158**). The many very low GRA density values reflect core gaps and biscuiting. However, the downhole trends of the clustered high values may be trusted to generally reflect the downhole variation of bulk density. The MAD bulk density data are substantially more accurate, and we will use these data to describe the downhole density variation.

MAD bulk density generally increases downhole (Fig. **F158**). Because we began coring at 800 mbsf, we bypassed the part of the sediment column where most sediment compaction occurs. The background density variation in the hole, from ~1.9 g/cm³ at 800 mbsf to 2.3 g/cm³ in claystones near the bottom of the hole, is explained by more gradual compaction of mudstones and claystones. Variations of density from this background trend are largely the result of lithologic differences. At most levels in the hole, there are sporadic samples with higher density than those of the background sediment. These are generally associated with carbonate/siderite concretions and very well cemented grainstones and sandstones. Sediments of somewhat low density are noted in the upper part of lithologic Unit 1. Lithologic Unit 2 and the lower part of Unit 3 are characterized by scattered density, generally higher than the background trend. Significant density changes, either offsets or changes in the scatter of values, are associated with each of the lithologic unit boundaries. High density of two diabase sills (in Cores 210-1276A-88R and 99R) is noted near 1620 mbsf (upper sill) and 1720 mbsf (lower sill). The upper sill has slightly lower density (2.73 g/cm³) than the lower sill (2.85 g/cm³). The sediments in the few meters above and below the upper sill were recovered and have higher density than normal because of hydrothermal alteration, although this is not well illustrated in the small-scale figures presented. Perhaps the most interesting density anomalies in the hole are located in and around the lower diabase

F158. GRA and MAD bulk density, p. 283.

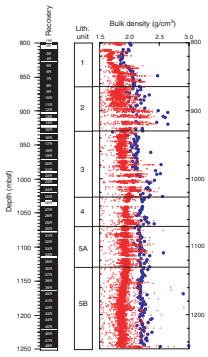

sill. In the 10 m above the lower sill, density is dramatically less than normal in an undercompacted section of mudstones. We discuss the observations in and around the sills later in this section (see **"Undercompacted Systems: High-Porosity and Low-Velocity Mudstones,"** p. 101).

MAD grain density and porosity, together with bulk density, are plotted in Figure **F159.** Note that the lithologic identification of each sample was obtained by automated interrogation of the AppleCORE visual core description database for Hole 1276A. Symbols used for plotting physical property data according to major lithology are found in Figure **F160**.

MAD grain density is very consistent at 2.65 ± 0.15 g/cm³ throughout the hole. Typical values of common minerals are 2.6 g/cm³ for quartz grains and 2.8 g/cm³ for carbonate grains. There is some scatter in grain density in lithologic Units 1–3. There is also a slight cyclicity of grain density with depth, with an observed wavelength of ~75 m, which is particularly noticeable in lithologic Subunits 5A and 5B. The outlying, higher grain density values are accurate measurements and correspond to carbonate/siderite concretions and very well lithified carbonate-cemented sandstones. The density of pure siderite is 3.96 g/cm³. The expected density is lower if Mn, Mg, or Ca substitute for Fe in siderite. It is less clear why the grain density is so high for the carbonate-cemented sandstones. Perhaps there is an appreciable Fe/siderite component in the cement.

Porosity generally reflects a combination of stress history and sedimentologic and diagenetic effects (e.g., compressibility, permeability, sorting, grain fabric, and cementation). Porosity is calculated from the volume of pore water, assuming complete saturation of the wet sediment sample (Blum, 1997) (see **"Physical Properties,"** p. 28, in the "Explanatory Notes" chapter). The porosity curve is a mirror image of the bulk density curve except for minor variations caused by changes in grain density (Fig. **F159**). MAD porosities generally decrease with depth in Hole 1276A. The general trend of porosity in lithologic Units 1 and 2, between 800 and 929 mbsf, decreases steeply from ~47% ± 10% at the top to 30% ± 10% at the base of Unit 2. Porosity in lithologic Units 3 and 4 and Subunits 5A and 5B, between 929 and 1502 mbsf, decreases less steeply, from ~35% ± 10% at the top to 23% ± 10% at the base. The general trend of porosity in lithologic Subunit 5C, between 1502 and ~1719 mbsf, is roughly uniform at 20% ± 10%. In lithologic Unit 2 through Subunit 5C, ~10% of the samples, which are randomly distributed through the interval, have porosities as much as 20% lower than the general trend. These are generally samples taken from carbonate/siderite concretions or from very well lithified carbonate-cemented sandstones. In the lower portion of lithologic Subunit 5C between the two diabase sills (Subunits 5C1 and 5C2), porosity is 40% ± 10%, which is unusually high for rocks at this depth (Fig. **F159B**). These sediments are clearly undercompacted. This topic is discussed further below.

We place the observed porosities in perspective by removing the anomalous porosities associated with carbonate/siderite concretions, well-lithified carbonate-cemented sandstones, and those sediments that are hornfels and then plotting them together with a best-fit compaction curve (Fig. **F161**). We assume that porosity can be approximated by an exponential function of depth (e.g., Athy, 1930):

$$\phi(z) = \phi_0 e^{-kz},$$

F159. Bulk density, grain density, and porosity, p. 285.

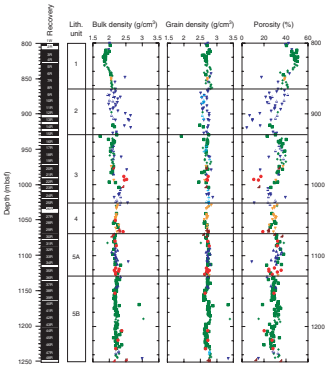

F160. Lithologic symbols, p. 287.

F161. MAD porosity vs. depth, p. 288.

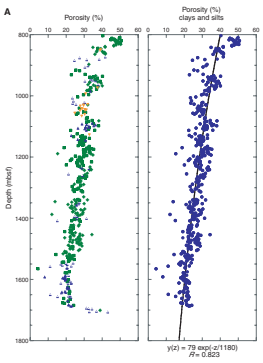

where

$\phi(z)$ = the porosity as a function of depth,
z = the depth,
ϕ_0 = the surface porosity, and
k controls the rate of porosity reduction with depth.

The parameter k is often expressed as its reciprocal, thus having units of length. By fitting the measured porosity-depth data for claystones, mudstones, and siltstones, we estimated $\phi_0 = 79\%$ and $k^{-1} = 1.18$ km. The parameters we obtained are similar to values obtained for mudrock (shale) compaction in the literature. Many of the porosity values that lie to the low side of this curve were measured on grainstones, sandstones, and chemically cemented rocks. In each case, these rocks are expected to be less porous than burial-compacted mudrocks.

Undercompacted Systems: High-Porosity and Low-Velocity Mudstones

In lithologic Subunit 5C in Cores 210-1276A-96R through Section 98R-1 (1693–1710 mbsf), mudstones and calcareous mudstones have unusually high porosities (27%–39%) and low horizontal velocity (1689–1958 m/s), considering the depth of their recovery (Figs. **F159, F161B**). Furthermore, these intervals are found to be very soft, with consistencies comparable to modeling clay. The porosity, velocity, and consistency properties of these mudstones are more comparable to those of normally compacted sediments recovered in the upper part of the hole (~840–1020 mbsf) (Fig. **F159**), and they clearly demonstrate that the mudstones are undercompacted with respect to their depth.

The mechanical compaction process in these mudstones was halted at a relatively shallow burial depth. This was likely facilitated by emplacement of two diabase sills, one above this undercompacted interval (1620 mbsf) and one below (1719 mbsf). It is possible, but not necessary, that this interval was overpressured prior to Leg 210 drilling. Evidence of past fluid flow exists in the hydrothermally altered sedimentary rocks immediately above the lower sill and underlying the undercompacted mudstones (Fig. **F161B**). The highest measured concentration of hydrocarbons exists in this 20-m interval. Geochemical analysis measured concentrations of C_1 (methane) levels of nearly 19,000 ppmv (Fig. **F161B**) (See **"Volatile Hydrocarbons,"** p. 95, in "Geochemistry"), implying that fluids in this interval were trapped. This interval was clearly incapable of normally compacting and expelling pore fluids and perhaps was sealed off by the bounding igneous intrusions.

Compressional Wave Velocity

Downhole Trends

Compressional wave velocity was measured with the *P*-wave sensor 3 contact probe system on ~8-cm³ cube samples of lithified sediments. The cubes were used to measure velocity in the horizontal (x and y) and vertical (z) directions. Seismic anisotropy was calculated from the measured velocity.

Vertical velocity of the sedimentary rocks in Hole 1276A can best be described in terms of a general trend of the bulk of the measurements and then of the deviations of the remaining measurements from the trend. The bulk of the measurements were obtained from claystones, mudstones, and siltstones. The general trend in lithologic Unit 1 is uniform velocity of 1900 ± 100 m/s (Fig. **F162**). Lithologic Unit 2 consists largely of grainstones and marlstones with velocity that is variable between 2000 and 4900 m/s. The general trend in lithologic Unit 3 is velocity varying between 1950 and 2600 m/s. There are also scattered higher velocities, up to 4200 m/s in grainstones and sandstones. Lithologic Unit 4 is characterized by velocity between 2000 and 2300 m/s, with two slightly higher values in a sandstone and silty sandstone. The general trend of vertical velocity in lithologic Unit 5 is a gradual increase from 2100 ± 100 m/s at 1069 mbsf to 2300 ± 200 m/s at 1680 mbsf. Throughout Unit 5, there are 1- to 100-cm-thick layers with velocities scattered between the general-trend velocity and 5000 m/s. These higher velocities were usually measured in grainstones, marlstones, carbonate concretions, sandstones, and silty sandstones.

The vertical velocity in the upper diabase sill, lithologic Subunit 5C1, varies from 4738 to 5030 m/s. The vertical velocity in the lower diabase sill, lithologic Subunit 5C2, is 5527–6193 m/s. The velocity of the sediments of lithologic Subunit 5C that lie between the sills is scattered from 1650 to 3200 m/s. The extraordinarily low velocity sediments in this interval are undercompacted, and possibly overpressured, mudstones (Fig. **161B**).

Velocity data in the x-, y-, and z-directions were used to define velocity anisotropy. Velocity anisotropy was calculated as follows:

$$\text{Anisotropy (\%)} = (V_h - V_v)/[(V_h + V_v)/2] \times 100,$$

where V_h is the mean horizontal (x and y) *P*-wave velocity and V_v is the vertical (z) velocity.

Velocity anisotropy in sediments is mostly positive (Fig. **F163**), indicating that the vertical velocity is slower than the horizontal velocity, and it generally increases downhole. Positive anisotropy in sediments is generally caused by grain orientation along near-horizontal bedding planes. Sound waves traveling vertically must traverse both slower and faster lithologies, whereas horizontal sound waves can travel preferentially in the faster lithologies. Anisotropy often increases downhole because deeper rocks have experienced more compaction in place and greater decompression prior to measurement in the laboratory. This decompression is thought to induce microcracking along bedding planes. The anisotropy in Hole 1276A increases from ~4%–5% at 800 mbsf to ~10% in the deepest sediments recovered. In contrast to the sedimentary rocks, the upper diabase sill shows negative seismic anisotropy of approximately –2%–3%. Surprisingly, the lower diabase is nearly isotropic.

F162. *P*-wave sensor 3 velocity, p. 290.

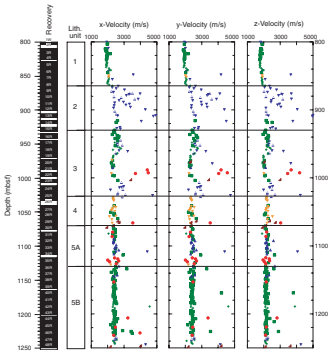

F163. Velocity anisotropy, p. 295.

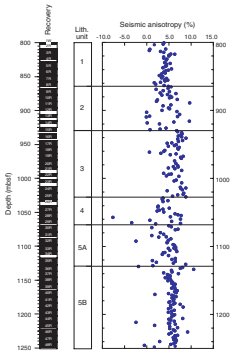

Factors Affecting Sediment Velocity

During the course of physical property sampling and velocity measurement, several targets for more detailed velocity analysis were identified. The first category of targets included several turbidites whose velocity characteristics appeared to vary systematically depending on where in the turbidite the routine physical property sample was taken. The second target was the sediment/sill contact preserved at the top of

the upper sill. In both cases, detailed velocity measurements allowed us to define systematic changes in velocity that correlate with changing lithology. In the chosen sections, x-direction velocity was measured every 2–10 cm over the relevant interval. X-direction velocity can be obtained at regular intervals on pieces of the working half of the core without cutting cubes, so this velocity analysis is not destructive and provides an excellent means of understanding velocity changes along the core. Below, the results of detailed velocity analysis over several turbidites in lithologic Unit 5 (Cores 68R, 79R, and 80R) and over the sill/sediment contact in Section 210-1276A-87R-6 are presented.

Velocity Structure of Turbidite Sequences

Turbidites are found in nearly every lithologic unit encountered at Site 1276, and they range in thickness from 10 cm to >2 m. During standard physical property sampling, different parts of these turbidites were selected for measurements of velocity and bulk density. Samples from different parts of the turbidites displayed different velocity and density characteristics depending on where in the turbidite the sample was taken. To investigate the velocity structure of turbidites, detailed measurements of x-direction velocity was taken on three turbidites, including Sections 210-1276A-68R-3 and 68R-4, 79R-2, and 80R-3 (Fig. **F162C**). This velocity study reveals systematic trends in turbidite velocity that can be used as a general framework in which individual physical property samples of turbidites can be placed. In all measured turbidites, velocity increases from the muddy turbidite top (~2200 m/s) downhole until the highest velocity (~4500 m/s) is encountered in the well-cemented, fine-grained sandstone near but somewhat above the bed base. As grain size increases from this fine-grained sandstone to the underlying coarse sandstone turbidite base, velocity decreases by ~1000 m/s. Figure **F162C** shows core photographs and velocity variations for the three turbidites we measured. Velocity varies consistently between minimum values near 2200 m/s and maximum values of ~4500 m/s.

Investigation of trends in individual turbidites also reveals a correlation between velocity and weight percentage of $CaCO_3$ (Fig. **F162C**). High $CaCO_3$ content consistently corresponds to the sandstones that have higher velocity, suggesting that carbonate cementation may play a primary role in controlling velocity within these turbidites. For example, Section 210-1276A-68R-3 contains 51 wt% $CaCO_3$ at 1434.58 mbsf, where the velocities in the x-, y-, and z-directions reach their maximum. Combined, these results allow the extrapolation of velocity and carbonate cementation away from routine physical property samples to help characterize turbidite sequences in general. These observations can be used to help constrain a velocity function from physical property data to be used to link core data with seismic reflection data.

For a number of intervals in Hole 1276A, there is strong positive correlation between $CaCO_3$ content and seismic velocity (Fig. **F162D**). Because of the centimeter- to meter-scale variations in lithology in the hole, displaying the data at full detail was not enlightening for exploring correlations. Therefore, we normalized the x-velocity by subtracting 1792 m/s and dividing by 64 (maximum velocity/100, giving a resulting range of 0–100 m/s). We also applied a filter to both data sets that removes short-wavelength variations. We have not determined quantitative correlation values, but we note convincing visual correlation. Correlation appears to be best for velocity and $CaCO_3$ variations at 25- to 75-m periods. Correlation is not present in some intervals. For example, notable exceptions include uncemented grainstones that show a

high carbonate content but relatively low velocity and fine sandstones with low carbonate content and high velocity.

Velocity Structure of Sediment/Sill Contact

The presence of intercalated sills and sedimentary rocks creates a highly variable velocity structure in the lower part of Hole 1276A (1600–1737 mbsf). Igneous sills with velocity as high as ~6300 m/s alternate with sedimentary rocks that have velocity as low as ~1600 m/s. Abrupt increases and decreases in velocity over short intervals (~10 m) would be expected to generate a complicated pattern of reflections in seismic reflection profiles. The nature of observed reflection patterns is controlled not only by the magnitude and spacing of velocity variations but also the extent to which these velocity boundaries are gradational or sharp.

To help define the velocity structure of the contact between sills and the surrounding sedimentary rocks for use with seismic stratigraphy studies, the x-direction velocity was measured every 2 cm across relatively unmetamorphosed sediments, across the zone of contact metamorphism at the margin of the upper sill, and in the sill itself (Fig. F162E). Section 210-1276A-87R-6 is the only place where the entire contact between sediments and sill is preserved; all of the other sill/sediment contacts fall between cores. These measurements reveal a sharp contact between the overlying sedimentary rocks (~2500 m/s) and the upper diabase sill (3500–4500 m/s). Contact-metamorphosed sediments (porphyroblastic mudstones; 1612.1–1612.65 mbsf) are separated from the upper sill (>1612.85 mbsf) by a thin zone of contact metamorphism where the sedimentary rocks display very high velocity (~4900 m/s). These latter metamorphosed sediments show velocities comparable to maximum sill velocities, which are not achieved until the center of the sill itself. This information on the velocity structure of the sill/sediment contact can be used as input into synthetic-seismogram creation. Introduction of a sharp velocity contact at the top of the sills will likely have a profound effect on the predicted reflection signature of these sills in seismic profiles.

Thermal Conductivity

Thermal conductivity was measured on intact pieces of half-round core of at least 10 cm length. Mudrocks, such as those that dominate the recovered Albian section (1100–1338 mbsf), tended to break up into ~1-cm-long pieces and therefore were seldom measured. As a result, we found that they were severely underrepresented in our sampling of thermal conductivity in the upper part of the hole. After recognizing this problem, we developed two new methods, a shrink-wrap method and a clamp method, to measure thermal conductivity on these fragile but abundant materials. Acceptable measurements were obtained using both methods, although the clamp method yielded more repeatable and, therefore, probably superior, measurements. Claystones and mudstones are more appropriately represented in our sampling below 1340 mbsf in Hole 1276A.

Measured thermal conductivity in sediments shows an overall increase with depth (Fig. F164). Values in sediments (with the exception of a few outliers) range from 1.4 to 2.8 W/(m·K) (mean = 2.1 W/[m·K]). Thermal conductivity near the top of the cored interval (800–900 mbsf) averages 1.7 W/(m·K). Thermal conductivity in the deepest interval cored (1500–1700 mbsf) averages 2.4 W/(m·K). A linear relation be-

F164. Thermal conductivity, p. 297.

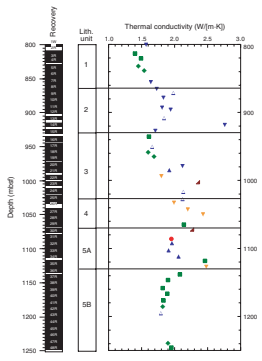

tween these average values would reasonably approximate the thermal conductivity for this sedimentary column for most thermal studies. Deviation from this trend by more than ±0.3 W/(m·K) occurs mainly in the interval 980–1140 mbsf, where values are scattered and high (~1.8–2.5 W/[m·K]). No obvious relationship is seen in values of thermal conductivity as a function of lithology (Fig. F164). However, in general, thermal conductivity values for mudstones (1.3–2.7 W/[m·K]) are lower than those for sandstones (1.9–3.0 W/[m·K]).

Measurements of thermal conductivity in the upper and lower diabase sills (1620 mbsf and 1720 mbsf) show values of 1.7 and 2.0 W/(m·K), respectively.

Natural Gamma Radiation

The NGR count was recorded on the MST. Clay minerals, being charged particles, tend to attract and bond with K, U, and Th atoms so that an increasing NGR count typically correlates with increasing clay content. In contrast, sand-prone and carbonate units usually are characterized by low NGR count. These relationships can help to define the location of mud- and sand-prone formations downhole. However, the relationships will begin to break down in poorly sorted successions or in those with peculiarities in mineralogy.

The NGR profile is most easily characterized in terms of the described lithologic units (Figs. F165, F166; see "Lithostratigraphy," p. 20). For convenience, we will refer to intervals with upward-increasing NGR count as "upward fining" and those with upward-decreasing NGR count as "upward coarsening." The explanation for these trends may be other than actual grain size distributions. However, excellent agreement is observed between increasing and decreasing sandstone/mudrock (sand/shale) ratios and low/high NGR counts, respectively (e.g., Fig. F167).

Lithologic Unit 1 consists of an upward-fining sequence stratigraphically above an upward-coarsening sequence (Figs. F165, F166). Lithologic Unit 2 has generally lower ("coarser") but more scattered NGR count than Unit 1. The boundaries between lithologic Units 1 and 2 and Units 2 and 3 are very sharp in the NGR data. Lithologic Unit 3, from top to bottom, contains an upward-fining sequence, a sequence of generally high but scattered values, and a sequence of generally low but scattered values. There is a sharp change in NGR count just below the lithologic Unit 3/4 boundary. Lithologic Unit 4 shows an upward-fining sequence above a sequence of intermediate and scattered values. Lithologic Subunit 5A, like lithologic Unit 4, fines upward at the top and is intermediate and scattered below. The upper part of lithologic Subunit 5B is a thick (>200 m) sequence of very uniform, high-value, and scattered NGR count. NGR changes at the boundaries between lithologic Unit 4 and Subunits 5A and 5B are not as dramatic as those between lithologic Units 1, 2, 3, and 4. Below ~1320 mbsf, the count drops. We suspect that this is due to a dramatic reduction of core diameter preceding bit failure at 1340 mbsf, rather than due to an actual change in the NGR signature of the cores. From 1340 to 1502 mbsf, the lower part of lithologic Subunit 5B, NGR count gradually increases with depth. In lithologic Subunit 5C, below 1502 mbsf, the count continues a gradual rise and becomes more scattered as lithologic variation increases. The NGR count drops dramatically in the upper and lower sills (lithologic Subunits 5C1 and 5C2) but follows the general trend between the sills. The count decreases toward the top of the lower sill. We point out that

F165. NGR and magnetic susceptibility, p. 299.

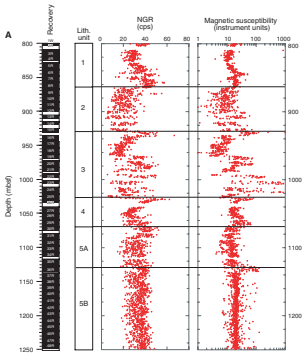

F166. Smoothed NGR and magnetic susceptibility, p. 301.

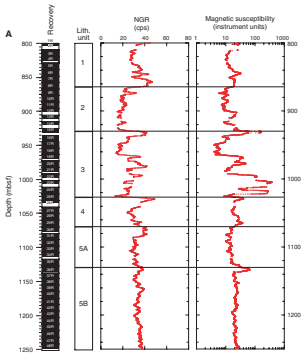

F167. Digital core images, NGR, and x-direction velocity, p. 303.

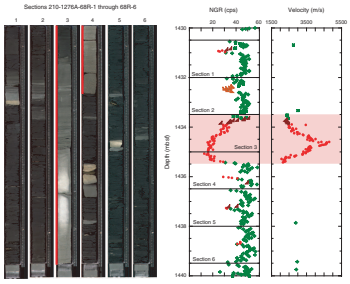

this is only a general description of the NGR data set on the lithologic unit scale; these data are incredibly detailed and also capture significant information at the core and section scale.

Figure F167 shows an example of the correlation between NGR, lithologic facies, and x-direction velocity. The core photograph identifies the position of a thick turbidite in Sections 210-1276A-68R-3 and 68R-4. This unit grades from a coarse sand at its base up through silty sands and finally terminates in mudstones and claystones. Concomitant with this is a major decrease and then increase in NGR count. The shape of the NGR response does not strictly correlate with megascopic grain size distribution at the base of the turbidite, but it shows good correlation above the base. Interestingly, the velocity shows a different response; it is sensitive to grain size and also to the degree of carbonate cementation. Minor turbidites are recognized in all of the sections in Core 210-1276A-68R, also corresponding to minor excursions in NGR (Fig. F167).

Magnetic Susceptibility

Magnetic susceptibility was recorded on the MST. The quality of these data is degraded in RCB sections because the core is usually undersized with respect to liner diameter and is often disturbed by drilling. Nevertheless, the general downhole trends can be useful for stratigraphic interpretations.

The major contribution to the magnetic susceptibility comes from ferro- and ferrimagnetic minerals such as magnetite, hematite, goethite, and titanomagnetite. Paramagnetic minerals such as clays, glauconite, and siderite contribute significantly less to the magnetic susceptibility amplitude. Strongly magnetic minerals such as magnetite and hematite are mainly associated with terrigenous material. Autochthonous diagenetic processes, such as the precipitation of siderite, also help to concentrate magnetic material.

Raw (i.e., unfiltered) magnetic susceptibility amplitudes range from 8 to 22,000 $\times 10^{-6}$ SI (12 to 9990 instrument units) downhole (Figs. F165, F166). Amplitudes are relatively constant below 1026 mbsf (i.e., in lithologic Units 4 and 5), ranging between ~10 and 40 instrument units, except for two extreme peaks from the two diabase sills (~1620 and 1720 mbsf). Filtered magnetic susceptibility data (filtered using a 50-point averaging technique) show amplitudes ranging between 100 and 1650 $\times 10^{-6}$ SI (15 to 250 instrument units) and more clearly show the trends in the magnetic susceptibility data (Fig. F166). There is an important change in magnetic susceptibility character at 1026 mbsf, with relatively large amplitude variations above (65 to 650 $\times 10^{-6}$ SI [10 to 100 instrument units]) and relatively constant amplitudes below (65 to 200 $\times 10^{-6}$ SI [10 to 20 instrument units]), with the exception of the sill peaks. There is a fair correlation between the magnetic susceptibility and NGR profiles (Fig. F166), such as across lithologic boundaries at the bases of Units 1, 2, and 3 and across the Subunit 5A/5B boundary. Elsewhere, correlations are cruder or they are not observed (e.g., the lower part of lithologic Unit 3).

There is a correlation between magnetic susceptibility and remanent magnetization intensity (see "Paleomagnetism," p. 90). This indicates that the minerals carrying the magnetic remanence are also responsible for the susceptibility. A particularly high magnitude magnetic susceptibility peak occurs near the base of Section 210-1276A-15R-4 (Fig. F166A), and this is confirmed by AMST susceptibility data (see "Paleo-

magnetism," p. 90). The origin of this spike is as yet unexplained, despite careful examination of the core for metal fragments detached from coring tools and other features. One possible explanation is that the susceptibility spike relates to ash layers tentatively recognized in Core 210-1276A-15R (see "Lithostratigraphy," p. 20).

Whereas there is only a general correlation between magnetic susceptibility and lithologic units as described above, this is not the case for specific diagenetic minerals precipitated throughout the cores or for the igneous intrusions. The former can show excellent correlations with the magnetic susceptibility data. For example, Figure F168 shows the magnetic susceptibility for Sections 210-1276A-50R-1 and 52R-6 compared with images of the sections. The white "layers" in the core are concretions or strongly cemented grainstones that contain quartz, calcite, and siderite based on XRD analysis (see "Lithostratigraphy," p. 20). It appears that the siderite-enriched carbonate cement is capable of generating large magnetic susceptibility peaks. In some cases, amplitudes reach 2650×10^{-6} SI (400 instrument units).

The value of magnetic susceptibility in characterizing aspects of the lithology of igneous rocks is illustrated in Figure F169. Section 210-1276A-87R-6 contains the baked mudstones above the upper diabase sill, the chilled margin within the sill, and the upper unchilled part of the sill. Magnetic susceptibility increases downhole with a step at each of these boundaries. Magnetic susceptibility of the hydrothermally altered mudstone is very low, <20 instrument units. Magnetic susceptibility of the chilled margin of the sill rises to values of 100–300 instrument units. Based on XRD analyses (see "Igneous and Metamorphic Petrology," p. 64) the whole sill, including the chilled upper margin, contains pyrite. This is consistent with the observed level of magnetic susceptibility in the upper chilled margin. Magnetic susceptibility of the interior of the sill is ~10,000 instrument units. This is consistent with the presence of magnetite in addition to pyrite in the interior of the sill. It is likely that both magmatic and alteration processes have affected the distribution of pyrite and magnetite in the sill. We note that there is a slight drop in magnetic susceptibility near the segregation band at 1613.24 mbsf and a large drop in magnetic susceptibility near the bottom of Section 210-1276A-87R-6; these may provide clues to subtle chemical variations through the sill (Fig. F169).

F168. Digital core images and magnetic susceptibilities, p. 304.

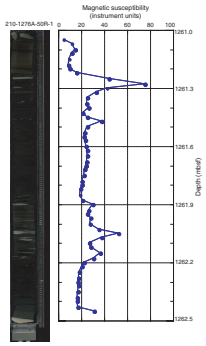

F169. Digital core image and MST magnetic susceptibility, p. 306.

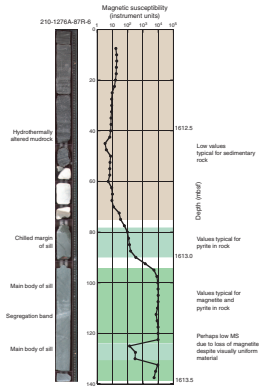

SEISMIC-BOREHOLE CORRELATION

In ideal circumstances, logging data provide the critical link between cores and seismic reflection profiles by measuring the in situ geophysical properties of borehole lithologies at a scale intermediate between the seismic and the core data. This linkage is essential because it allows detailed information obtained by core analysis to be extended to the entire seismic reflection data set. The seismic data can then provide constraints on the regional extent and nature of lithologic and age boundaries observed at the drill site.

Logging data could not be collected at Site 1276 because of poor hole conditions. In lieu of sonic and density downhole logs, laboratory measurements of velocity and density taken on discrete, representative samples from each core section were used to generate a time-depth relationship and to create synthetic seismograms to link the seismic reflection and core data. Excellent core recovery throughout Site 1276 allowed us to construct a robust time-depth relationship from 800 to 1730 mbsf.

This made it possible to track our progress toward drilling targets identified on time-migrated seismic reflection sections and to correlate major lithologic units with the seismic data. However, to understand how geologic features that are encountered during drilling are manifested in seismic data as reflections, we took one additional step and generated synthetic seismograms.

Measured density and velocity vary systematically between primary lithologic units, particularly between Units 1 and 2 (Figs. F159, F162A, F162B). Because velocity and density contrasts exert primary control on the amplitudes of seismic reflections, we anticipated that the creation of synthetic seismograms from the laboratory data would facilitate correlation of lithologic units with reflections in the seismic data. In the upper 1000 m of Site 1276, reflections predicted in synthetic seismograms can be readily correlated with observed reflections in Study of Continental Rifting and Extension on the Eastern Canadian Shelf (SCREECH) line 2MCS and line 303, which cross Site 1276 (Fig. F170). However, predicted reflection patterns near the U reflection do not match observed patterns, suggesting that the velocity structure created by the alternating high and low velocities of interlayered igneous sills and sediments, respectively, might result in complex tuning effects in seismic reflection data. Further postcruise modeling will be required to understand the manner in which sills and sediments are manifested in the site survey seismic reflection dataset.

F170. Seismic reflection profiles of SCREECH lines 2MCS and 303, p. 307.

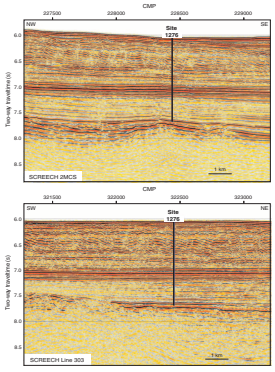

Laboratory Measurements Used for Time-Depth Conversion and Synthetic-Seismogram Creation

Shipboard physical property measurements were used as input into this procedure. As described in "Physical Properties," p. 99, horizontal and vertical velocities were measured on representative sediment and rock samples (~8 cm^3) from each section of core. We chose to use the vertical (z) component of velocity measurements to build a time-depth relationship because they most closely approximate the path of seismic waves recorded in multichannel seismic (MCS) reflection data sets.

Two types of density measurements were used to calculate synthetic seismograms; each of these has limitations for this application. These measurements are described below.

GRA Bulk Density

GRA bulk density data represent evenly spaced measurements of density obtained over the entirety of each core prior to the core being split. Although this procedure provides continuous density measurements, the lithified rocks recovered using RCB drilling typically fracture when they are recovered, leading to breaks in the core and thus to significant artificial variations in the density data. Additionally, GRA bulk density measurements are systematically low because recovered cores do not completely fill the core liner.

MAD Bulk Density

Bulk density (MAD) was also measured on discrete samples taken from every section of each core. Because the samples analyzed were small and hand selected, they are not influenced by the fractures that degrade the GRA density. However, these samples do not contain regularly sampled and relatively unbiased information on the distribution

of lithologies (and corresponding changes in density and velocity) that would be encompassed in logging data sets. Furthermore, MAD density is obtained from the same samples used for velocity measurements, so any sampling biases that exist in the velocity data are also present in the density measurements.

The use of physical property data instead of traditional sonic and density logs requires several additional considerations to ensure that velocity and density measurements are representative of overall core properties. Some of these steps were conducted in the following analysis, and others will be addressed in postcruise work. First, velocity measured on samples from intervals described as "concretions" by sedimentologists was removed from the data set. This included eight measurements with vertical component velocity ranging from 2126 to 4625 m/s. The exclusion of these data points does not affect the time-depth relationship, which comprises 553 other data points (Fig. F171). However, their presence could affect synthetic seismograms, which are sensitive to small velocity perturbations.

F171. Horizontal and vertical compressional wave velocities, p. 308.

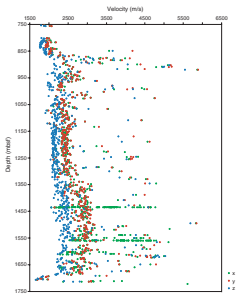

Second, additional data were collected by the physical property group to characterize velocity variations over specific lithologic intervals likely to display important velocity characteristics (e.g., turbidites throughout the sedimentary section and the sediment/sill contact preserved in Section 210-1276A-87R-6). As described fully in "Physical Properties," p. 99, measurements of x-direction (horizontal) velocity taken every 2–10 cm over several turbidites revealed that turbidites commonly display consistent velocity trends. Velocity tends to increase from the muddy turbidite tops downward, with maximum velocity occurring in well-cemented, fine-grained sandstones. Below, velocity decreases in the coarse turbidite base. This velocity distribution can be used to predict velocity surrounding routine measurements taken within turbidites.

Detailed velocity measurements made across the contact between the upper sill and the overlying sediments show that the change from sedimentary velocity (2300 m/s) to diabase velocity (~5500 m/s) occurs over a very short interval despite a broad zone of contact metamorphism, thus creating a sharp velocity contrast rather than a gradational boundary. Including a boundary where velocity increases from 2300 to 5500 m/s over tens of centimeters rather than over 3 m (spacing between routine physical property samples) yields a substantially higher reflection coefficient.

A third means of conditioning the velocity function was attempted to better represent velocity changes in cores. A velocity function was constructed using the average velocity of all samples measured for every combination of lithology and grain size in each major lithologic unit. Information on the lithology and grain size for each physical property sample taken was obtained by linking visual core descriptions to samples (see "Physical Properties," p. 99). These average velocities were inserted where each combination of lithology and grain size was documented in the visual core descriptions. The problem with this approach, which is well illustrated in Figure F162A and F162B, is that velocity measured on samples with the same lithologic and grain size classification often varies substantially, and averaging masks actual velocity changes.

Another important consideration in using laboratory velocity rather than logging velocity is the difference in velocity expected at depth vs. that at atmospheric pressures. Throughout the sedimentary section of Site 1276, a notable anisotropy in horizontal vs. vertical velocities was

measured, where z-direction velocity (vertical) is typically 200–300 m/s slower than the corresponding x- and y-direction velocities (horizontal). However, a sharp increase in observed seismic anisotropy occurs at ~1350 mbsf, with z-direction velocity often being >500 m/s slower than the equivalent horizontal components (Fig. F171). This might be explained by preferential fracturing of cores along horizontal bedding planes as they are unloaded or disrupted by drilling. Decompaction or a change in rock properties could also explain the change.

A critical piece of information missing from our analysis is a "checkshot" that normally would be provided by logging. By firing an air gun at the surface and measuring the traveltime to a geophone positioned in the hole, direct links between depth and two-way traveltime in seismic reflection data can be obtained. We lack this direct link, so we have to assume a tie between depth and the traveltime of some reflection. The reflection at ~6.98 s is the best candidate to make this link (Fig. F170). Seismic reflection character changes dramatically at this depth. Discontinuous low-amplitude reflections lie above this horizon, and continuous high-amplitude reflections are found below. The depth to this horizon, estimated from velocity obtained from semblance plots of MCS data, is ~900 mbsf. This is close (<4% error) to the depth at which fundamental changes in lithology are observed in the borehole between lithologic Units 1 and 2 (864 mbsf). Sediments change downhole from mudstones and claystones (lithologic Unit 1) to alternating layers of grainstones and claystones (lithologic Unit 2). The grainstones have exceptionally high velocity (up to 5.8 km/s) compared to the overlying mudrocks (~2–2.5 km/s) and thus would be expected to produce high-amplitude reflections. Because of these correlations, we chose this horizon as our checkshot. Below this level, the time-depth relationship was determined from the measured vertical compressional wave velocity.

Creation of Time-Depth Curve

Two-way traveltime and depth are related by velocity. To obtain a time-depth curve, z-component slownesses (inverse of velocity) for velocity samples were integrated over depth. The resulting time-depth curve is shown in Figure F172. Note the subtle steepening of this curve between ~850 and 920 mbsf, where high-velocity (~3500–5000 m/s), carbonate-cemented grainstones form a significant portion of the sediments. This curve is considered to be robust because of excellent core recovery and close spacing of velocity measurements. Figure F173 shows a histogram of z-direction velocity measured throughout Site 1276. This velocity distribution is clearly dominated by samples with velocities of 2100–2500 m/s. Although there are some outliers in the z-direction velocity data, the contribution of individual outliers has a minimal effect on the area obtained by integrating the time-depth curve.

F172. Time-depth relationship, p. 309.

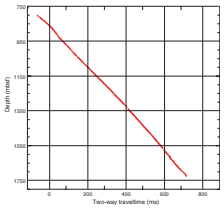

F173. Distribution of z-component velocity, p. 310.

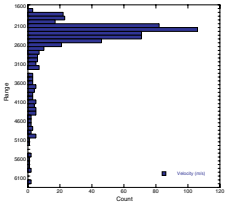

Construction of Synthetic Seismograms

To create a synthetic seismogram, the source wavelet of the real seismic data must be estimated and the reflection coefficient series of the formation must be determined. Density and velocity are the key variables in calculating the reflection coefficients, which in turn control the amplitudes of seismic reflections. For the interface between two layers (1 and 2), reflection coefficient (R_c), density (ρ), and vertical compressional wave velocity (V) are related by the following expression:

$$R_c = (\rho_2 V_2 - \rho_1 V_1)/(\rho_2 V_2 + \rho_1 V_1).$$

A series of reflection coefficients can be calculated for the depths of interest in this manner. This expression is valid only for a vertically incident seismic wave.

The source wavelet was extracted from the site survey reflection data by calculating the power spectrum (squared amplitude) of each trace in a user-defined window and averaging these power spectra. This assumes that over a sufficiently large window, the reflection-coefficient series is random and the signal-to-noise ratio is large enough so that

$$S^2(f) = W^2(f) \cdot R^2(f) + N^2(f)$$

can be approximated by

$$S^2(f) = W^2(f),$$

where $S^2(f)$, $W^2(f)$, $R^2(f)$, and $N^2(f)$ are the power spectra of the seismogram, the source wavelet, the reflection coefficient series, and the noise, respectively, and f denotes that these variables are related as indicated in the frequency domain. After averaging the power spectra of the traces in the frequency domain, conversion back to an amplitude time series yields a source wavelet in the time domain. Once the reflection coefficient series and the source wavelet are determined, the two are convolved to create a synthetic seismogram. All of these steps are carried out in GeoFrame's IESX computer package, which we used in the shipboard downhole measurements laboratory.

Correlation

The methods described above result in two sets of synthetic seismograms, with one created from each of the two types of density data (Fig. F174). From 800 to 1100 mbsf, the synthetic seismograms display distinct features that are very similar to those observed in the seismic reflection sections at Site 1276. This is true of synthetics produced from both GRA density and MAD bulk density. Below 1600 mbsf, however, correlations between the synthetic and the actual seismic data are less apparent, and they will require postcruise modeling to understand.

Using the time-depth relationship given in Figure F172 (interpreted checkshot correlation of the lithologic Unit 1/2 boundary with the strong reflection at 6.98 s in SCREECH line 2MCS data) and the synthetic seismograms shown in Figure F174, we made initial correlations between major lithologic units and seismic reflection profiles. Table T20 gives the depths in the borehole and predicted two-way traveltimes derived for the boundaries between primary lithologic units. We summarize below the characteristics of the seismic reflection data (Figs. F170, F175, F176) and the synthetic seismograms for each lithologic unit. For a complete description of seismic facies, see "Geological Setting," p. 4, in the "Leg 210 Summary" chapter.

Lithologic Unit 1

Discontinuous, relatively weak reflections appear in the time interval corresponding to lithologic Unit 1 in both the seismic reflection data (Figs. F175, F176) and the synthetic seismogram (Fig. F174). The same

F174. Synthetic seismograms, p. 311.

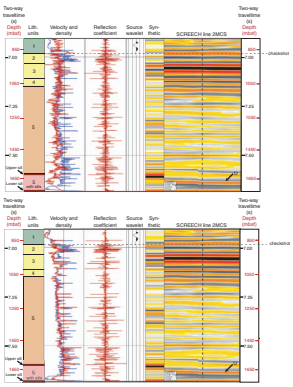

T20. Predicted two-way traveltimes of contacts between lithologic units, p. 357.

F175. Correlation of lithologic units with seismic reflection patterns, p. 312.

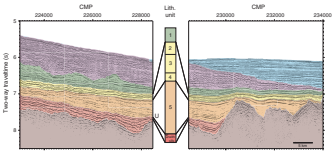

F176. SCREECH line 2MCS, p. 313.

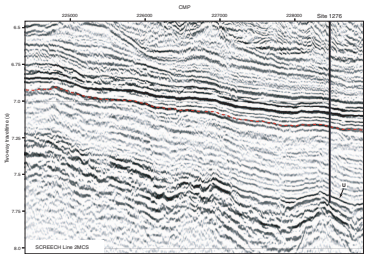

seismic character continues above the first core (753 mbsf) for ~40 ms (50 m).

Lithologic Units 2–4

The boundary between Units 1 and 2 is marked by a sharp change in character in both the seismic reflection profile and the synthetic seismogram. Units 2–4 are represented by high-amplitude, laterally continuous reflections (Figs. **F175, F176**). In the synthetic seismogram, these bright reflections are generated by interlayered high-velocity carbonate-cemented grainstones and low-velocity claystones and mudstones in Unit 2 and, to a lesser extent, in Units 3 and 4.

The most obvious correlation between synthetic and actual seismic data from SCREECH line 2MCS occurs at a depth of 7.04 s, or ~60 ms beneath the checkshot tie point between seismic and core data described above, where a high-amplitude reflection is found in both the synthetic and actual seismic traces. Without applying any corrections to the time-depth relationship, this reflection is predicted at almost exactly the same time (within ~5 ms) as the actual reflection data.

The base of Unit 4 is predicted to be at 7.147 s. It most likely corresponds to a slightly deeper reflection with an onset at ~7.16 s in the MCS data. This reflection truncates underlying reflections and seismically represents an unconformity (Fig. **F176**). Lithostratigraphic and biostratigraphic data are consistent with a period of either very slow sedimentation or a hiatus near this boundary, although this is not well constrained because the cores are barren of microfossils (Fig. **F141**).

Lithologic Unit 5

Lithologic Unit 5 is characterized by low reflection amplitudes in both the synthetic seismogram and actual seismic data. The lowest-amplitude reflections occur in the upper portion of Subunit 5B, where the sediments are comparatively homogeneous and where density and velocity patterns are relatively featureless (Figs. **F159, F162A, 162B**). At the base of Subunit 5B and the top of Subunit 5C, reflection amplitudes increase.

A significant discrepancy between the synthetic seismograms and actual seismic data occurs at depths of 7.335 and 7.375 s (Fig. **F174**), where notably strong reflections occur in the synthetic seismogram but not in the seismic data. At present, these mismatches are unexplained.

Sills

Correlation of the two sills cored at the base of Site 1276 with seismic reflection data is the most perplexing aspect of our seismic-core correlation. The upper sill is predicted at a two-way traveltime of 7.598 s, and the lower sill is predicted at a two-way traveltime of 7.681 s. These two predictions fall on either side of the U reflection, which has an onset at ~7.63 s. The proximity of both of the synthetic reflections to U and underlying high-amplitude reflections strongly suggests that the sills are at the level of U. However, our initial synthetic seismograms produce a high-amplitude, positive–negative couplet for the shallower reflection (Fig. **F174**) and it seems likely that this correlates with the similar U reflection in the SCREECH 2MCS record. The reflection created by the top of the lower sill in the synthetic seismogram also displays high amplitude and positive polarity; a large, positive impedance contrast here re-

sults from velocity and density differences between the diabase sill and overlying undercompacted sediments (see "Physical Properties," p. 99). This reflection is substantially deeper than the depth estimated for U and is probably within the U-basement sequence.

Velocity and density structure at the base of Site 1276 is considerably more complicated than in the remainder of the hole, with variations of >4500 m/s in velocity and 0.8 g/cm^3 in density over tens of meters in depth. These extreme variations may cause seismic tuning effects, where the interference of reflections generated from closely spaced velocity interfaces combine to create a reflectivity pattern that cannot be readily correlated to lithology. Constraints provided by detailed analysis of the top of the upper sill have been included in the velocity function used to create synthetic seismograms, but similar constraints on the other boundaries between sills and sediments are absent because of incomplete core recovery at these interfaces. Postcruise analysis will consider different possible velocity models that might reproduce the observed seismic reflections.

Summary

A number of primary lithologic boundaries and characteristics observed in Site 1276 cores appear to correlate with seismic reflections on SCREECH line 2MCS. However, more work is required to understand the complicated velocity structure around the diabase sills at the bottom of the hole and to model this interval with synthetic seismograms. The interbedded high-velocity sills and low-velocity sediments may create tuning effects that complicate seismic interpretation of this interval.

REFERENCES

Arthur, M.A., 1979. North Atlantic Cretaceous black shales: the record at Site 398 and a brief comparison with other occurrences. *In* Sibuet, J.-C., Ryan, W.B.F., et al., *Init. Repts. DSDP,* 47 (Pt. 2): Washington (U.S. Govt. Printing Office), 719–751.

Arthur, M.A., Dean, W.E., and Stow, D.A.V., 1984. Models for the deposition of Mesozoic–Cenozoic fine-grained, organic-carbon–rich sediment in the deep-sea. *In* Stow, D.A.V., and Piper, D.J.W (Eds.), *Fine-Grained Sediments: Deep-Water Processes and Facies*. Geol. Soc. Spec. Publ., 15:527–560.

Arthur, M.A., Schlanger, S.O., and Jenkyns, H.C., 1987. The Cenomanian–Turonian oceanic anoxic event, II. Palaeoceanographic controls on organic-matter production and preservation. *In* Brooks, J., and Fleet, A.J. (Eds.), *Marine Petroleum Source Rocks*. Geol. Soc. Spec. Publ., 26:401–420.

Athy, L.F., 1930. Density, porosity, and compaction of sedimentary rocks. *AAPG Bull.,* 14:1–24.

Barnes, P.M., and Lewis, K.B., 1991. Sheet slides and rotational failures on a convergent margin: the Kidnappers Slide, New Zealand. *Sedimentology,* 38:205–221.

Bell, J.S., and Howie, R.D., 1990. Paleozoic geology. *In* Keen, M.J., and Williams, G.L. (Eds.), *Geology of the Continental Margin of Eastern Canada*. Geol. Soc. Am., 2:141–165.

Blechschmidt, G., 1979. Biostratigraphy of calcareous nannofossils: Leg 47B, Deep Sea Drilling Project. *In* von Rad, U., Ryan, W.B.F., et al., *Init. Repts. DSDP,* 47 (Pt. 1): Washington (U.S. Govt. Printing Office), 327–360.

Blum, P., 1997. Physical properties handbook: a guide to the shipboard measurement of physical properties of deep-sea cores. *ODP Tech. Note,* 26 [Online]. Available from World Wide Web: <http://www-odp.tamu.edu/publications/tnotes/tn26/INDEX.HTM>. [Cited 2003-09-05]

Bordenave, M.L., Espitalie, J., Leplat, P., Oudin, J.L., and Vandenbroucke, M., 1993. Screening techniques for source rock evaluation. *In* Bordenave, M.L. (Ed.), *Applied Petroleum Geochemistry:* Paris (Editions Technip), 217–279.

Bouloubassi, I., Rullkötter, J., and Meyers, P.A., 1999. Origin and transformation of organic matter in Pliocene–Pleistocene Mediterranean sapropels: organic geochemical evidence. *Mar. Geol.,* 153:177–197.

Bouma, A.H., 1962. *Sedimentology of Some Flysch Deposits: A Graphic Approach to Facies Interpretation:* Amsterdam (Elsevier).

Bouquigny, R., and Willm, C., 1979. Tentative calibration of Site 398 and special processing of parts of Lines GP-19 and GP-23. *In* Sibuet, J.-C., Ryan, W.B.F., et al., *Init. Repts. DSDP,* 47 (Pt. 2): Washington (U.S. Govt. Printing Office), 623–629.

Bralower, T.J., Zachos, J.C., Thomas, E., Parrow, M., Paull, C.K., Kelly, D.C., Premoli Silva, I., Sliter, W.V., and Lohmann, K.C., 1995. Late Paleocene to Eocene paleoceanography of the equatorial Pacific Ocean: stable isotopes recorded at Ocean Drilling Program Site 865, Allison Guyot. *Paleoceanography,* 10:841–865.

Brinkhuis, H., and Visscher, H., 1995. The upper boundary of the Eocene Series: a reappraisal based on dinoflagellate cyst biostratigraphy and sequence stratigraphy. *In* Berggren, W.A., Kent, D.V., Aubry, M.-P., and Hardenbol, J. (Eds.), *Geochronology, Time Scales and Global Stratigraphic Correlation*. Spec. Publ.—Soc. Econ. Paleontol. Mineral. (Soc. Sediment. Geol.), 54:295–304.

Cacchione, D.A., and Drake, D.E., 1986. Nepheloid layers and internal waves over continental shelves and slopes. *Geo-Mar. Lett.,* 6:147–52.

Calvert, S.E., Nielsen, B., and Fontugne, M.R., 1992. Evidence from nitrogen isotope ratios for enhanced productivity during formation of eastern Mediterranean sapropels. *Nature,* 359:223–225.

Chamley, H., 1979. North-Atlantic clay sedimentation and palaeoenvironment since the Late Jurassic. *In* Talwani, M., Hay, W., and Ryan, W.B.F. (Eds), *Deep Drilling*

Results in the Atlantic Ocean: Continental Margins and Paleoenvironment. Am. Geophys. Union, Maurice Ewing Ser., 3:342–361.

Chamley, H., 1989. *Clay Sedimentology:* Berlin (Springer-Verlag).

Chamley, H., and Debrabant, P., 1984. Paleoenvironmental history of the North Atlantic region from mineralogical and geochemical data. *Sedimentology,* 40:151–167.

Chamley, H., Debrabant, P., and Flicoteaux, R., 1988. Comparative sedimentology of the Senegal and eastern central Atlantic Basins, from mineralogical and geochemical investigations. *Sedimentology,* 35:85–103.

Claypool, G.E., and Kvenvolden, K.A., 1983. Methane and other hydrocarbon gases in marine sediment. *Annu. Rev. Earth Planet. Sci.,* 11:299–327.

Davies, R., Cartwright, J., Pike, J., and Line, C., 2001. Early Oligocene initiation of North Atlantic Deep Water formation. *Nature,* 410:917–920.

de Graciansky, P.C., and Chenet, P.Y., 1979. Sedimentological study of cores 138 to 56 (upper Hauterivian to middle Cenomanian): an attempt at reconstruction of paleoenvironments. *Init. Repts. DSDP,* 47 (Part 2): Washington (U.S. Govt. Printing Office), 403–418.

Dunoyer de Segonzac, G., 1969. Les minéraux argileux dans la diagenèse passage au métamorphisme. *Mem. Serv. Carte Geol. Alsace Lorraine,* Thèse doctorat, Faculté des Sciences de l'Université de Strasbourg, 29:320.

Dymond, J., Suess, E., and Lyle, M., 1992. Barium in deep-sea sediment: a geochemical proxy for paleoproductivity. *Paleoceanography,* 7:163–181.

Emeis, K.-C., Robertson, A.H.F., Richter, C., et al., 1996. *Proc. ODP, Init. Repts.,* 160: College Station, TX (Ocean Drilling Program).

Empson-Morin, K.M., 1984. Depth and latitude distribution of radiolaria in Campanian (Late Cretaceous) tropical and subtropical oceans. *Micropaleontology,* 30:87–115.

Erbacher, J., and Thurow, J., 1997. Influence of oceanic anoxic events on the evolution of mid-Cretaceous radiolaria in the North Atlantic and western Tethys. *Mar. Micropalaeontol.,* 30:139–158.

Foreman, H.P., 1977. Mesozoic radiolaria from the Atlantic Basin and its borderlands. *In* Swain, F.M. (Ed.), *Stratigraphic Micropaleontology of Atlantic Basin and Borderlands:* Amsterdam (Elsevier), 305–320.

Fuller, M., and Garrett, E., 1998. Site 395 appendix: magnetic experiments. *In* Becker, K., Malone, M.J., et al., *Proc. ODP, Init. Repts.,* 174B, 47–49 [CD-ROM]. Available from: Ocean Drilling Program, Texas A&M University, College Station, TX 77845-9547, U.S.A.

Fuller, M., Hastedt, M., and Herr, B., 1998. Coring-induced magnetization of recovered sediment. *In* Weaver, P.P.E., Schmincke, H.-U., Firth, J.V., and Duffield, W. (Eds.), *Proc. ODP, Sci. Results,* 157: College Station, TX (Ocean Drilling Program), 47–56.

Fuller, M., Molina Garza, R.S., and Shipboard Scientific Party, 2000. Appendix: magnetics experiment. *In* Feary, D.A., Hine, A.C., Malone, M.J., et al., *Proc. ODP, Init. Repts.,* 182 [Online]. Available from World Wide Web: <http://www-odp.tamu.edu/publications/182_IR/appen/appen.htm>. [Cited 2003-8-20]

Gardin, S., and Monechi, S., 1998. Paleoecological change in middle- to low-latitude calcareous nannoplankton at the Cretaceous/Tertiary boundary. *Bull. Soc. Geol. Fr.,* 169:709–723.

Gee, J., Staudigel, H., and Tauxe, L., 1989. Contribution of induced magnetization to magnetization of seamounts. *Nature,* 342:170–173.

Gibbs, R.J., 1977. Clay mineral segregation in the marine environment. *J. Sediment. Petrol.,* 47:237–243.

Gonthier, E.G., Faugeres, J.C., and Stow, D.A.V., 1984. Contourite facies of the Faro Drift, Gulf of Cadiz. *In* Stow, D.A.V., and Piper, D.J.W. (Eds.), *Fine-Grained Sediments: Deep-Water Processes and Facies.* Geol. Soc. Spec. Publ., 15:275–292.

Gorsline, D.S., 1984. A review of fine-grained sediment origins, characteristics, transport, and deposition. *In* Stow, D.A.V., and Piper, D.J.W. (Eds.), *Fine-Grained Sediments: Deep-Water Processes and Facies*. Geol. Soc. Spec. Publ., 15:17–34.

Gradstein, F.M., 1978. Biostratigraphy of Lower Cretaceous Blake Nose and Blake Bahama Basin foraminifera, DSDP Leg 44, western North Atlantic Ocean. *In* Benson, W.E., Sheridan, R.E., et al., *Init. Repts. DSDP,* 44: Washington (U.S. Govt. Printing Office), 663–702.

Grant, A.C., and McAlpine, K.D., 1990. The continental margin around Newfoundland. *In* Keen, M.J., and Williams, G.L. (Eds.), *Geology of the Continental Margin of Eastern Canada*. Geol. Surv. Can., Geol. of Can., 2:239–292.

Groupe Galice, 1979. The continental margin off Galicia and Portugal: acoustical stratigraphy, dredge stratigraphy, and structural evolution. *In* Sibuet, J.-C., Ryan, W.B.F., et al., *Init. Repts. DSDP,* 47 (Pt. 2): Washington (U.S. Govt. Printing Office), 633–662.

Haq, B.U., Hardenbol, J., and Vail, P.R., 1987. Chronology of fluctuating sea levels since the Triassic. *Science,* 235:1156–1167.

Heezen, B.C., and Hollister, C.D., 1971. *The Face of the Deep:* New York (Oxford University Press).

Herr, B., Fuller, M., Haag, M., and Heider, F., 1998. The influence of drilling on two records of the Matuyama–Brunhes polarity transition in marine sediment cores near Gran Canaria. *In* Weaver, P.P.E., Schmincke, H.-U., Firth, J.V., and Duffield, W. (Eds.), *Proc. ODP, Sci. Results,* 157: College Station, TX (Ocean Drilling Program), 57–69.

Hiscott, R.N., Pickering, K.T., and Beeden, D.R., 1986. Progressive filling of a confined Middle Ordovician foreland basin associated with the Taconic Orogeny, Quebec, Canada. *In* Allen, P.A., and Homewood, P. (Eds.), *Foreland Basins*. Spec. Publ., Internat. Assoc. Sedimentol., 8:309–325.

Hofmann, P., Ricken, W., Schwark, L., and, Leythaeuser, D., 2001. Geochemical signature and related climatic-oceanographic process for early Albian black shales: Site 417D, North Atlantic Ocean. *Cretaceous Res.,* 22:243–257.

Holbourn, A., Kuhnt, W., El Albani, A., Ly, A., Gomez, R., and Herbin, J.P., 1999. Palaeoenvironments and palaeobiogeography of the Late Cretaceous Casamance transect (Senegal, NW Africa): distribution patterns of benthic foraminifera, organic carbon and terrigenous flux. *In* Kuhnt, W., Erbacher, J., Graefe, K.U., and Wiedman, J. (Eds.), *Contributions to Cretaceous Stratigraphy and Palaeobiogeography in Honor of Jos Wiedmann*. Neues. Jahrb. Geol. Palaeontol., Abh., 212:335–377.

Honjo, S., 1975. Dissolution of suspended coccoliths in the deep-sea water column and sedimentation of coccolith ooze. *In* Sliter, W.V., Bé, A.W.H., and Berger, W.H. (Eds.), *Dissolution of Deep-Sea Carbonates*. Spec. Publ.—Cushman Found. Foraminiferal Res., 13:115–128.

Honjo, S., 1976. Coccoliths: production, transportation and sedimentation. *Mar. Micropaleontol.,* 1:65–79.

Jansa, L.F., Enos, P., Tucholke, B.E., Gradstein, F.M., and Sheridan, R.E., 1979. Mesozoic–Cenozoic sedimentary formations of the North American Basin, western North Atlantic. *In* Talwani, M., Hay, W., and Ryan, W.B.F. (Eds.), *Deep Drilling Results in the Atlantic Ocean: Continental Margins and Paleoenvironment*. Am. Geophys. Union, Maurice Ewing Ser., 3:1–57.

Jansa, L.F., and Wade, J.A., 1975. Geology of the continental margin off Nova Scotia and Newfoundland. *In* Linden, W.J.M., and Wade, J.A. (Eds.), *Offshore Geology of Eastern Canada: Volume 2, Regional Geology*. Pap.—Geol. Surv. Can., 51–105.

Kirschvink, J.L., 1980. The least-squares line and plane and the analysis of palaeomagnetic data. *Geophys. J. R. Astron. Soc.,* 62:699–718.

Kitazato, H., 1994. Foraminiferal microhabitats in four marine environments around Japan. *Mar. Micropaleontol.,* 24:29–41.

Komar, P.D., 1971. Hydraulic jumps in turbidity currents. *Geol. Soc. Am. Bull.,* 82:1477–1488.

Kuhnt, W., and Collins, E.S., 1996. Cretaceous to Paleogene benthic foraminifers from the Iberia Abyssal Plain. *In* Whitmarsh, R.B., Sawyer, D.S., Klaus, A., and Masson, D.G. (Eds.), *Proc. ODP, Sci. Results,* 149: College Station, TX (Ocean Drilling Program), 203–216.

Kuhnt, W., and Kaminski, M.A., 1997. Cenomanian to lower Eocene deep-water agglutinated foraminifera from the Zumaya section, northern Spain. *Ann. Soc. Geol. Pol.,* 67:257–270.

Kuhnt, W., and Urquhart, E., 2001. Tethyan flysch-type benthic foraminiferal assemblages in the North Atlantic: Cretaceous to Paleogene deep-water agglutinated foraminifers from the Iberia Abyssal Plain (ODP Leg 173). *Rev. Micropaleontol.,* 44:27–59.

Ladner, B.C., and Wise, S.W., Jr., 2001. Calcareous nannofossil biostratigraphy of Upper Cretaceous to Paleocene sediments from Leg 173, Iberia Abyssal Plain, Sites 1067–1069. *In* Beslier, M.-O., Whitmarsh, R.B., Wallace, P.J., and Girardeau, J. (Eds.), *Proc. ODP, Sci. Results,* 173 [Online]. Available from World Wide Web: <http://www-odp.tamu.edu/publications/173_SR/chap_05/chap_05.htm>. [Cited 2003-09-05]

Le Bas, M.J., Le Maitre, R.W., Streckeisen, A., and Zanettin, B., 1986. A chemical classification of volcanic rocks based on the total alkali-silica diagram. *J. Petrol.,* 27:745–750.

Leckie, R.M., 1984. Mid-Cretaceous planktonic foraminiferal biostratigraphy off central Morocco, DSDP Leg 79, Sites 545 and 547. *In* Hinz, K., Winterer, E.L., et al., *Init. Repts. DSDP,* 79: Washington (U.S. Govt. Printing Office), 579–620.

Leckie, R.M., Bralower, T.J., and Cashman, R., 2002. Oceanic anoxic events and plankton evolution: biotic response to tectonic forcing during the Mid-Cretaceous. *Paleoceanography,* 17:10.1029/2001PA000623.

Leckie, R.M., and Olson, H.C., 2003. Foraminifera as proxies of sea-level change on siliciclastic margins. *In* Olson, H.C., and Leckie, R.M. (Eds.), *Micropaleontologic Proxies of Sea-Level Change and Stratigraphic Discontinuities*. Spec. Publ.—SEPM (Soc. Sediment. Geol.), 75:5–19.

Lowe, D.R., Guy, M., and Palfrey, A., 2003. Facies of slurry-flow deposits, Britannia formation (Lower Cretaceous), North Sea: implications for flow evolution and deposit geometry. *Sedimentology,* 50:45–80.

Maldonado, A., 1979. Upper Cretaceous and Cenozoic depositional processes and facies in the distal North Atlantic continental margin off Portugal, DSDP Site 398. *In* Sibuet, J.-C., Ryan, W.B.F., et al., *Init. Repts. DSDP,* 47 (Pt. 2): Washington (U.S. Govt. Printing Office), 373–402.

Masson, D.G., Howe, J.A., and Stoker, M.S., 2002. Bottom-current sediment waves, sediment drifts and contourites in the northern Rockall Trough. *Mar. Geol.,* 192:215–237.

McCave, I.N., 1972. Transport and escape of fine-grained sediment from shelf areas. *In* Swift, D.J.P., Duane, D.B., and Pilkey, O.H. (Eds.), *Shelf Sediment Transport: Process and Pattern:* Stroudsburg, PA (Dowden, Hutchinson and Ross), 225–248.

McCave, I.N., 1979. Depositional features of organic-carbon-rich black and green mudstones at DSDP Sites 386 and 387, western North Atlantic. *In* Tucholke, B.E., Vogt, P.R., et al., *Init. Repts. DSDP,* 43: Washington (U.S. Govt. Printing Office), 411–416.

Meyers, P.A., 1987. Organic-carbon content of sediments and rocks from Deep Sea Drilling Project Sites 603, 604, and 605, western margin of the North Atlantic. *In* van Hinte, J.E., Wise, S.W., Jr., et al., *Init. Repts. DSDP,* 93 (Pt. 2): Washington (U.S. Govt. Printing Office), 1187–1194.

Meyers, P.A., 1994. Preservation of elemental and isotopic source identification of sedimentary organic matter. *Chem. Geol.,* 144:289–302.

Meyers, P.A., Brassell, S.C., and Huc, A.Y., 1984. Geochemistry of organic carbon in South Atlantic sediments from DSDP Leg 75. *In* Hay, W.W., Sibuet, J.-C., et al., *Init. Repts. DSDP,* 75 (Pt. 2): Washington (U.S. Govt. Printing Office), 967–981.

Meyers, P.A., and Doose, H., 1999. Sources, preservation, and thermal maturity of organic matter in Pliocene–Pleistocene organic-carbon-rich sediments of the western Mediterranean Sea. *In* Zahn, R., Comas, M.C., and Klaus, A. (Eds.), *Proc. ODP, Sci. Results,* 161: College Station, TX (Ocean Drilling Program), 383–390.

Middleton, G.V., and Southard, J.B., 1984. Mechanics of sediment transport (2nd ed.). *SEPM Short Course,* No. 3.

Miller, K.G., and Tucholke, B.E., 1983. Development of Cenozoic abyssal circulation south of the Greenland–Scotland Ridge. *In* Bott, M., Saxov, S., Talwani, M., and Thiede, J. (Eds.), *Structure and Development of the Greenland–Scotland Ridge: New Methods and Concepts:* New York (Plenum), 549–590.

Moore, D.M., and Reynolds, R.C., Jr., 1989. *X-Ray Diffraction and the Identification and Analysis of Clay Minerals:* Oxford (Oxford Univ. Press).

Murray, J.W., 1991. *Ecology and Palaeoecology of Benthic Foraminifera:* London (Longman).

Nijenhuis, I.A., and de Lange, G.J., 2000. Geochemical constraints on Pliocene sapropel formation in the eastern Mediterranean. *Mar. Geol.,* 163:41–63.

Nyong, E.E., and Olsson, R.K., 1984. A paleoslope model of Campanian to lower Maestrichtian foraminifera in the North American Basin and adjacent continental margin. *Mar. Micropaleontol.,* 8:437–477.

Ogg, J.G., Robertson, A.H.F., and Jansa, L.F., 1983. Jurassic sedimentation history of Site 534 (western North Atlantic) and the Atlantic-Tethys seaway. *In* Sheridan, R.E., Gradstein, F.M., et al., *Init. Repts. DSDP,* 76: Washington (U.S. Govt. Printing Office), 829–884.

Pe-Piper, G., Piper, D.J.W., Keen, M.J., and McMillan, N.J., 1990. Igneous rocks of the continental margin: tectonic and geophysical overview. *In* Keen, M.J., and Williams, G.L. (Eds.), *Geology of the Continental Margin of Eastern Canada.* Mem.—Geol. Soc. Am., 2:855.

Peters, K.E., 1986. Guidelines for evaluating petroleum source rock using programmed pyrolysis. *AAPG Bull.,* 70:318–329.

Pickering, K.T., and Hiscott, R.N., 1985. Contained (reflected) turbidity currents from the Middle Ordovician Cloridorme Formation, Quebec, Canada: an alternative to the antidune hypothesis. *Sedimentology,* 32:373–394.

Pickering, K.T., Hiscott, R., and Hein, F.J., 1989. *Deep-Marine Environments: Clastic Sedimentation and Tectonics:* London (Unwin Hyman).

Pilskaln, C.H., and Honjo, S., 1987. The fecal pellet fraction of biogeochemical particle fluxes to the deep sea. *Global Biogeochem. Cycles,* 1:31–48.

Pletsch, T., 1997. Clay minerals in Cretaceous deep-water formations of the Rif and the Betic Cordillera (northern Morocco and southern Spain). *Ann., Soc. Geol. Nord,* 26:1–106.

Pollastro, R.M., 1993. Considerations and applications of the illite/smectite geothermometer in hydrocarbon-bearing rocks of Miocene to Mississippian age. *Clays Clay Miner.,* 41:119–133.

Reynolds, R.C., Jr., 1980. Interstratified clay minerals. *In* Brindley, G.W., and Brown, G. (Eds.), *Crystal Structures of Clay Minerals and Their X-Ray Identification.* Mineral. Soc. London Monogr., 5:249–303.

Ricci Lucchi, F., and Valmori, E., 1980. Basin-wide turbidites in a Miocene, oversupplied deep-sea plain: a geometrical analysis. *Sedimentology,* 27:241–270.

Robert, C., 1987. Clay mineral associations and structural evolution of the South Atlantic: Jurassic to Eocene. *Palaeogeogr., Palaeoclimatol., Palaeoecol.,* 58:87–108.

Robertson, A.H.F., 1984. Origin of varve-type lamination, graded claystones and limestone-shale "couplets" in the Lower Cretaceous of the western North Atlantic. *In* Stow, D.A.V., and Piper, D.J.W. (Eds.), *Fine-Grained Sediments: Deep-Water Processes and Facies.* Geol Soc. Spec. Publ., 15:437–452.

Robertson, A.H.F., and Bliefnick, D.M., 1983. Sedimentology and origin of Lower Cretaceous pelagic carbonates and redeposited clastics, Blake-Bahama Formation, Deep Sea Drilling Project Site 534, western equatorial Atlantic. *In* Sheridan, R.E.,

Gradstein, F.M., et al., *Init. Repts. DSDP,* 76: Washington (U.S. Govt. Printing Office), 795–828.

Saunders, A.D., Fitton, J.G., Kerr, A.C., Norry, M.J., and Kent, R.W., 1997. The North Atlantic igneous province. *In* Mahoney, J.J., and Coffin, M.F. (Eds.), *Large Igneous Provinces: Continental, Oceanic, and Planetary Flood Volcanism*. Geophys. Monogr., 100:45–93.

Sawyer, D.S., Whitmarsh, R.B., Klaus, A., et al., 1994. *Proc. ODP, Init. Repts.,* 149: College Station, TX (Ocean Drilling Program).

Shipboard Scientific Party, 1979. Site 398. *In* Sibuet, J.-C., Ryan, W.B.F., et al., *Init. Repts. DSDP,* 47 (Pt. 2): Washington (U.S. Govt. Printing Office), 25–233.

Shipboard Scientific Party, 1994a. Site 897. *In* Sawyer, D.S., Whitmarsh, R.B., Klaus, A., et al., *Proc. ODP, Init. Repts.,* 149: College Station, TX (Ocean Drilling Program), 41–113.

Shipboard Scientific Party, 1994b. Site 900. *In* Sawyer, D.S., Whitmarsh, R.B., Klaus, A., et al., *Proc. ODP, Init. Repts.,* 149: College Station, TX (Ocean Drilling Program), 211–262.

Shipboard Scientific Party, 1998. Site 1068. *In* Whitmarsh, R.B., Beslier, M.-O., Wallace, P.J., et al., *Proc. ODP, Init. Repts.,* 173: College Station, TX (Ocean Drilling Program), 163–218.

Sibuet, J.-C., Ryan, W.B.F., et al., 1979. *Init. Repts. DSDP,* 47 (Pt. 2): Washington (U.S. Govt. Printing Office).

Sigal, J., 1979. Chronostratigraphy and ecostratigraphy of Cretaceous formations recovered on DSDP Leg 47B, Site 398. *In* Sibuet, J.-C., Ryan, W.B.F., et al., *Init. Repts. DSDP,* 47 (Pt. 2): Washington (U.S. Govt. Printing Office), 287–326.

Sissingh, W., 1977. Biostratigraphy of Cretaceous calcareous nannoplankton. *Geol. Mijnbouw,* 56:37–65.

Skelton, P.W., Spicer, R.A., Kelley, S.P., and Gilmour, I., 2003. *The Cretaceous World:* Cambridge (Cambridge Univ. Press).

Skipper, K., and Middleton, G.V., 1975. The sedimentary structures and depositional mechanics of certain Ordovician turbidites, Cloridorme Formation, Gaspé Peninsula, Quebec. *Can. J. Earth Sci.,* 12:1934–1952.

Sliter, W.V., and Baker, R.A., 1972. Cretaceous bathymetric distribution of benthic foraminifera. *J. Foraminiferal Res.,* 2:167–183.

Srivastava, S.P., and Verhoef, J., 1992. Evolution of Mesozoic sedimentary basins around the North Central Atlantic: a preliminary plate kinematic solution. *In* Parnell, J. (Ed.), *Basins of the Atlantic Seaboard: Petroleum Geology, Sedimentology and Basin Evolution*. Spec. Publ.—Geol. Soc. London, 62:397–420.

Stanley, D.J., 1981. Unifites: structureless muds of gravity-flow origin in Mediterranean basins. *Geo-Mar. Lett.,* 1:77–84.

Stein, R., Brass, G., Graham, D., Pimmel, A., and the Shipboard Scientific Party, 1995. Hydrocarbon measurements at Arctic Gateways sites (ODP Leg 151). *In* Myhre, A.M., Thiede, J., Firth, J.V., et al., *Proc. ODP, Init. Repts.,* 151: College Station, TX (Ocean Drilling Program), 385–395.

Steinmetz, J., 1994. Sedimentation of coccolithophores. *In* Winter, A., and Siesser, W.G. (Eds.), *Coccolithophores:* Cambridge (Cambridge Univ. Press), 179–197.

Stokking, L.B., Musgrave, R.J., Bontempo, D., and Autio, W., 1993. Handbook for Shipboard Paleomagnetists. *ODP Tech. Note,* 18: College Station, TX (Ocean Drilling Program).

Stow, D.A.V., Huc, A.-Y., and Bertrand, P., 2001. Depositional processes of black shales in deep water. *Mar. Pet. Geol.,* 18:491–498.

Summerhayes, C., 1987. Organic-rich Cretaceous sediments from the North Atlantic. *In* Brooks, J., and Fleet, A.J. (Eds.), *Marine Petroleum Source Rocks*. Geol. Soc. Spec. Publ., 26:301–316.

Thierstein, H.R., 1979. Paleoceanographic implications of organic carbon and carbonate distribution in Mesozoic deep sea sediments. *In* Talwani, M., Hay, W., and

Ryan, W.B.F. (Eds.), *Deep Drilling Results in the Atlantic Ocean: Continental Margins and Paleoenvironment.* Am. Geophys. Union, Maurice Ewing Ser., 3:249–274.

Thomas, E., and Shackleton, N., 1996. The Palaeocene–Eocene benthic foraminiferal extinction and stable isotope anomalies. *In* Knox, R.W.O'B., Corfield, R.M., and Dunay, R.E. (Eds.), *Correlation of the Early Paleogene in Northwest Europe*. Geol. Soc. Spec. Publ., 101:401–441.

Thurow, J., 1988. Cretaceous radiolarians of the North Atlantic Ocean: ODP Leg 103 (Sites 638, 640, and 641) and DSDP Legs 93 (Site 603) and 47B (Site 398). *In* Boillot, G., Winterer, E.L., et al., *Proc. ODP, Sci. Results,* 103: College Station, TX (Ocean Drilling Program), 379–418.

Tjalsma, R.C., and Lohmann, G.P., 1983. *Paleocene–Eocene Bathyal and Abyssal Benthic Foraminifera from the Atlantic Ocean*. Micropaleontology, Spec. Publ., 4:1–90.

Tucholke, B.E., and Vogt, P.R., 1979. Western North Atlantic: sedimentary evolution and aspects of tectonic history. *In* Tucholke, B.E., Vogt, P.R., et al., *Init. Repts. DSDP,* 43: Washington (U.S. Govt. Printing Office), 791–825.

Twichell, S.C., Meyers, P.A., and Diester-Haass, L., 2002. Significance of high C/N ratios in organic-carbon-rich Neogene sediments under the Benguela Current upwelling system. *Org. Geochem.,* 33:715–722.

Tyson, R.V., 1995. *Sedimentary Organic Matter: Organic Facies and Palynofacies:* London (Chapman and Hall).

Urquhart, E., and Wilkinson, I.P., 1997. Lower Cretaceous radiolaria from southern England [InterRad VIII 1997, 8th Meeting of the International Association of Radiolarian Paleontologists, Paris/Bierville, 8–13 September, 1997]. (Abstract)

Van der Weijden, C.H., 1993. Geochemical signatures preserved in sediments of the Semaforo and Vrica sections (Calabria, Italy) and their relations with variations of the sedimentary regime. *Palaeogeogr., Palaeoclimatol., Palaeoecol.,* 103:203–221.

Van Mooy, B.A.S., Keil, R.G., and Devol, A.H., 2002. Impact of suboxia on sinking particulate organic carbon: enhanced carbon flux and preferential degradation of amino acids via denitrification. *Geochim. Cosmochim. Acta,* 66:457–465.

von Breymann, M.T., Emeis, K.-C., and Suess, E., 1992. Water depth and diagenetic constraints on the use of barium as a palaeoproductivity indicator. *In* Summerhayes, C.P., Prell, W.L., and Emeis, K.-C. (Eds.), *Upwelling Systems: Evolution Since the Early Miocene.* Geol. Soc. Spec. Publ., 64:273–284.

Wagner, T., and Pletsch, T., 2001. No major thermal event on the mid-Cretaceous Côte d'Ivoire-Ghana Transform Margin. *Terra Nova,* 13:165–171.

Weaver, P.P.E., and Rothwell, R.G., 1987. Sedimentation on the Madeira Abyssal Plain over the last 300,000 years. *In* Weaver, P.P.E., and Thomson, J. (Eds.), *Geology and Geochemistry of Abyssal Plains*. Geol. Soc. Spec. Publ., 31:71–86.

Weaver, P.P.E., Searle, R.C., and Kuijpers, A., 1986. Turbidite deposition and the origin of the Madeira Abyssal Plain. *In* Summerhayes, C.P., and Shackleton, N.J. (Eds.), *North Atlantic Palaeoceanography.* Geol. Soc. Spec. Pub., 21:131–143.

Whiticar, M.J., 1999. Carbon and hydrogen isotope systematics of bacterial formation and oxidation of methane. *Chem. Geol.,* 161:291–314.

Whitmarsh, R.B., Beslier, M.-O., Wallace, P.J., et al., 1998. *Proc. ODP, Init. Repts.,* 173: College Station, TX (Ocean Drilling Program).

Wignall, P.B., 1994. *Black Shales:* Oxford (Claredon Press).

Wilson, R.C.L., Manatschal, G., and Wise, S., 2001. Rifting along non-volcanic passive margins: stratigraphic and seismic evidence from the Mesozoic of the Alps and Western Iberia. *In* Wilson, R.C.L., Whitmarsh, R.B., Taylor, B., and Froitzheim, N. (Eds.), *Non-Volcanic Rifting of Continental Margins: A Comparison of Evidence from Land and Sea*. Geol. Soc. Spec. Publ., 187:429–452.

Wilson, R.C.L., Sawyer, D.S., Whitmarsh, R.B., Zerong, J., and Carbonell, J., 1996. Seismic stratigraphy and tectonic history of the Iberia Abyssal Plain. *In* Whitmarsh, R.B., Sawyer, D.S., Klaus, A., and Masson, D.G. (Eds.), *Proc. ODP, Sci. Results,* 149: College Station, TX (Ocean Drilling Program), 617–633.

Wood, A., and Smith, A.J., 1959. The sedimentation and sedimentary history of the Aberystwyth Grits (upper Llandoverian). *J. Geol. Soc. (London, U.K.),* 114:163–195.

Zachos, J.C., Lohmann, K.C., Walker, J.C.G., and Wise, S.W., Jr., 1993. Abrupt climate changes and transient climates during the Paleogene: a marine perspective. *J. Geol.,* 101:191–213.

Zhao, X., Roperch, P., and Stokking, L.B., 1994. Magnetostratigraphy of the North Aoba Basin. *In* Greene, H.G., Collot, J.-Y., Stokking, L.B., et al., *Proc. ODP, Sci. Results,* 134: College Station, TX (Ocean Drilling Program), 457–474.

Zijderveld, J.D.A., 1967. AC demagnetization of rocks: analysis of results. *In* Collinson, D.W., Creer, K.M., and Runcorn, S.K. (Eds.), *Methods in Palaeomagnetism:* New York (Elsevier), 254–286.

Figure F1. Schematic illustration of actual Site 1276 installation and cored intervals. The depth of the seafloor was determined by observing a reduction in drill string weight, so the seafloor depth of 4549.1 m below sea level is likely deeper than the true sediment/water interface. The exact sediment thickness over the reentry cone is unknown. RCB = rotary core barrel.

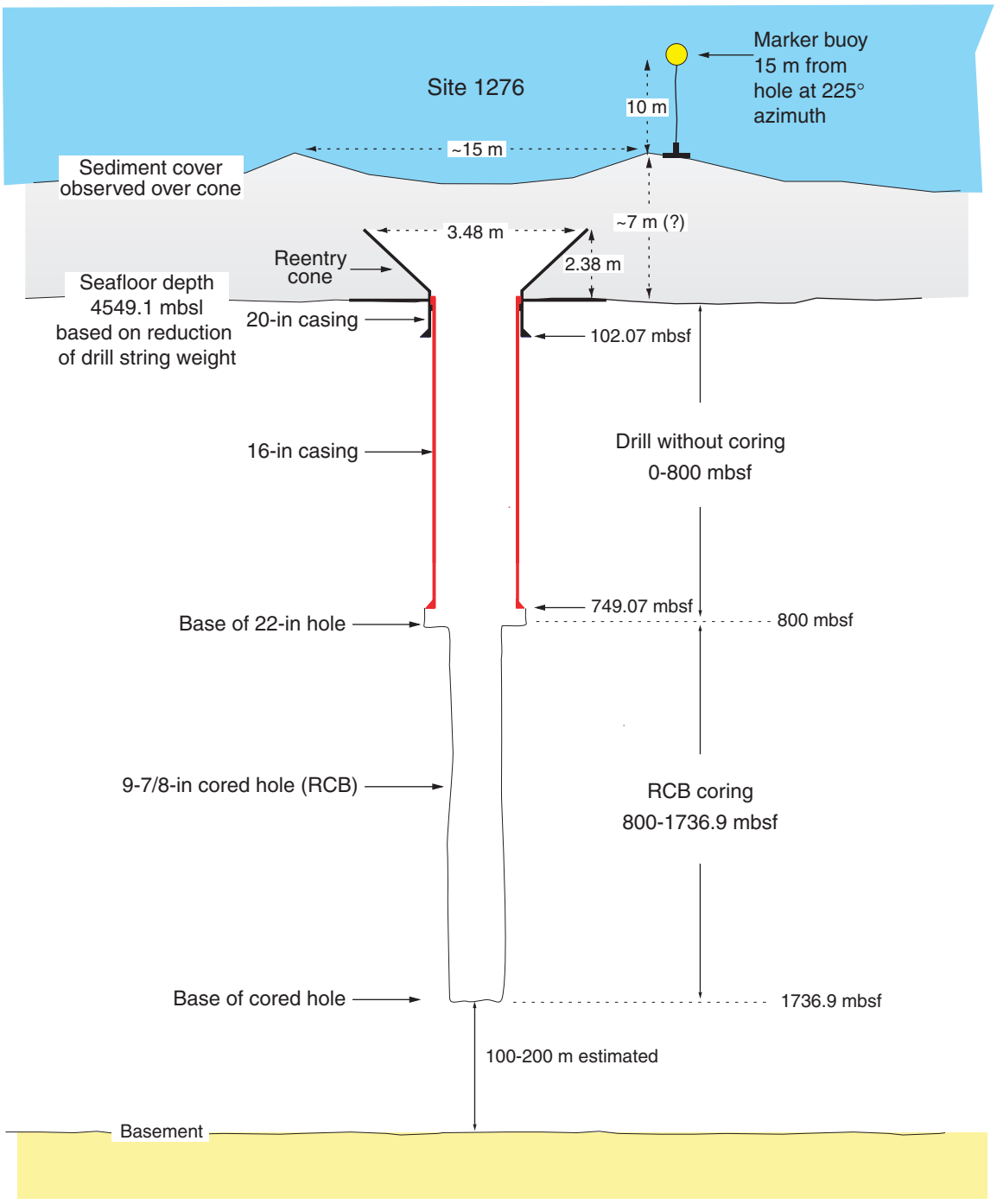

Figure F2. Video sequence of drill pipe in the Hole 1276A shortly after reentry 3 (30 July 2003). The edge of the sedimentary cone or crater above the buried reentry cone is visible at the lower right edge of the frame. Debris, pumped out of the hole during drilling, is streaking along the edge of the crater. (QuickTime software is available for Macintosh and Windows platforms only. Please see **"QuickTime Software"** in README.PDF for further information. Click the image to play the movie.)

Figure F3. Video sequence of the drill pipe at the seafloor during reentry 6 (15 August 2003) at Site 1276. The bit is centered above the sedimentary crater that overlies the buried reentry cone. The circular edge of the crater is visible in the lower half of the frame. (QuickTime software is available for Macintosh and Windows platforms only. Please see **"QuickTime Software"** in README.PDF for further information. Click the image to play the movie.)

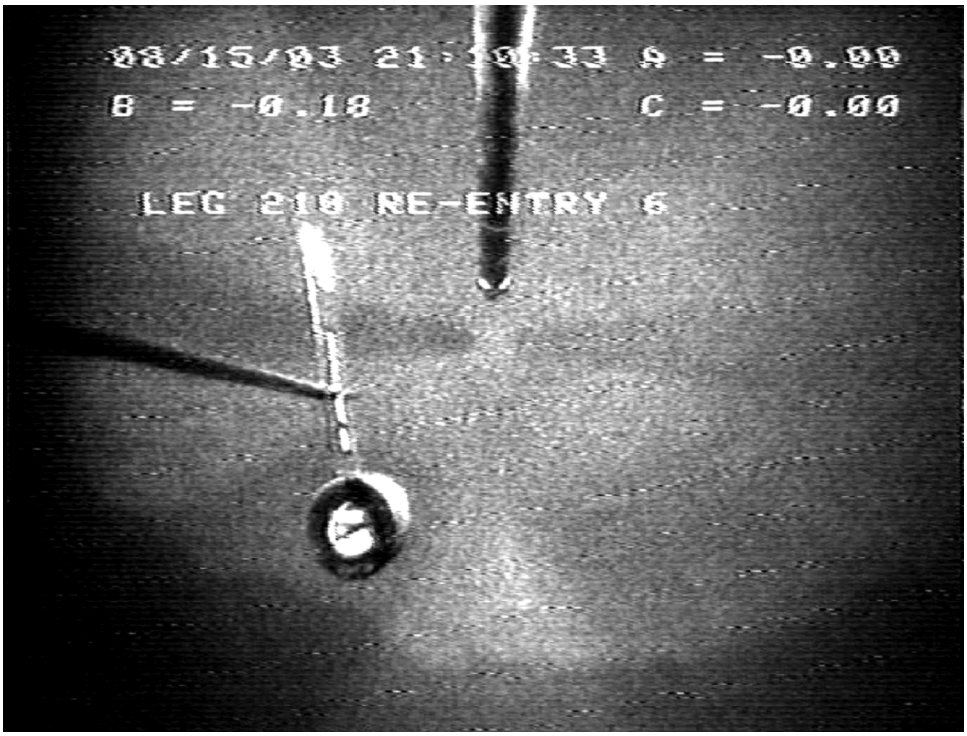

Figure F4. Video sequence of an attempted reentry during reentry 8 (29 August 2003) at Site 1276. The sedimentary crater above the buried reentry cone is obscured by mud falling from the drill string and is carried in westward-flowing bottom currents. Successful reentry was achieved ~16.5 hr after the time of this clip. (QuickTime software is available for Macintosh and Windows platforms only. Please see **"QuickTime Software"** in README.PDF for further information. Click the image to play the movie.)

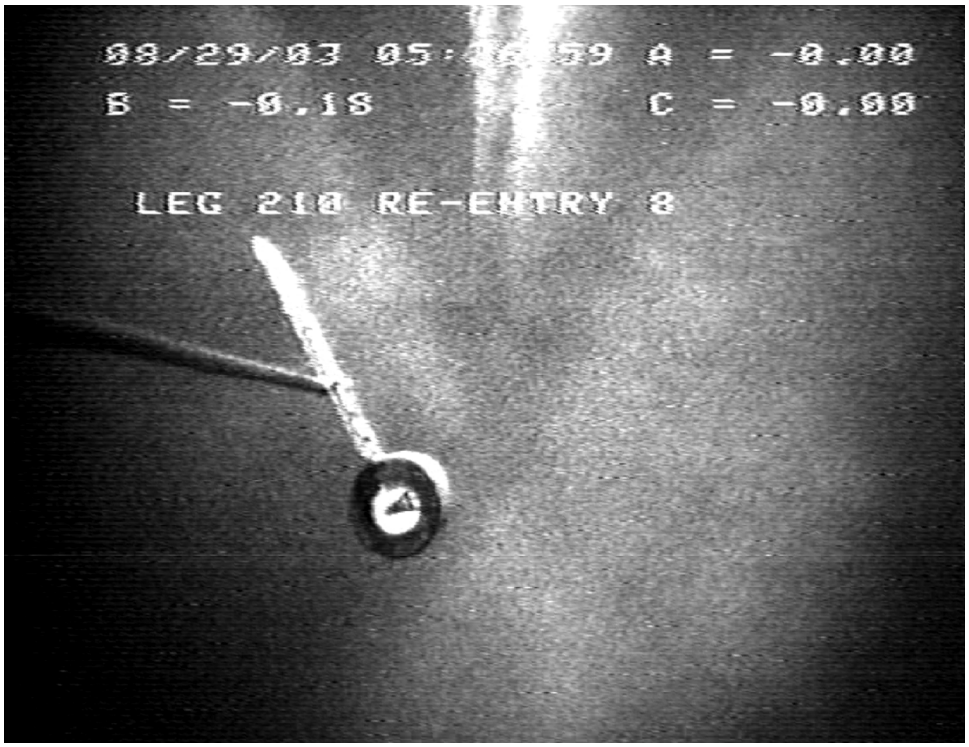

Figure F5. Photograph showing a 600-kHz scanning sonar image displayed on the sonar screen in the dynamic-positioning (DP) room during a reentry at Site 1276. The sonar, mounted on the drill string camera frame, is at the center of the image and scans 360° around the drill pipe. The first sonar return is from the seafloor, and the outer rings are interference patterns. The far lip of the seafloor sedimentary crater above the buried reentry cone is visible at the upper left as a bright, arcuate return. The high-frequency sonar signal did not penetrate the seafloor to image the buried cone, but it was essential for identifying the sedimentary crater above the cone so that the drill pipe and camera system could be guided into visual range for hole reentry. The yellow highlights at the top center of the image are reflections from the sonar screen in the DP room.

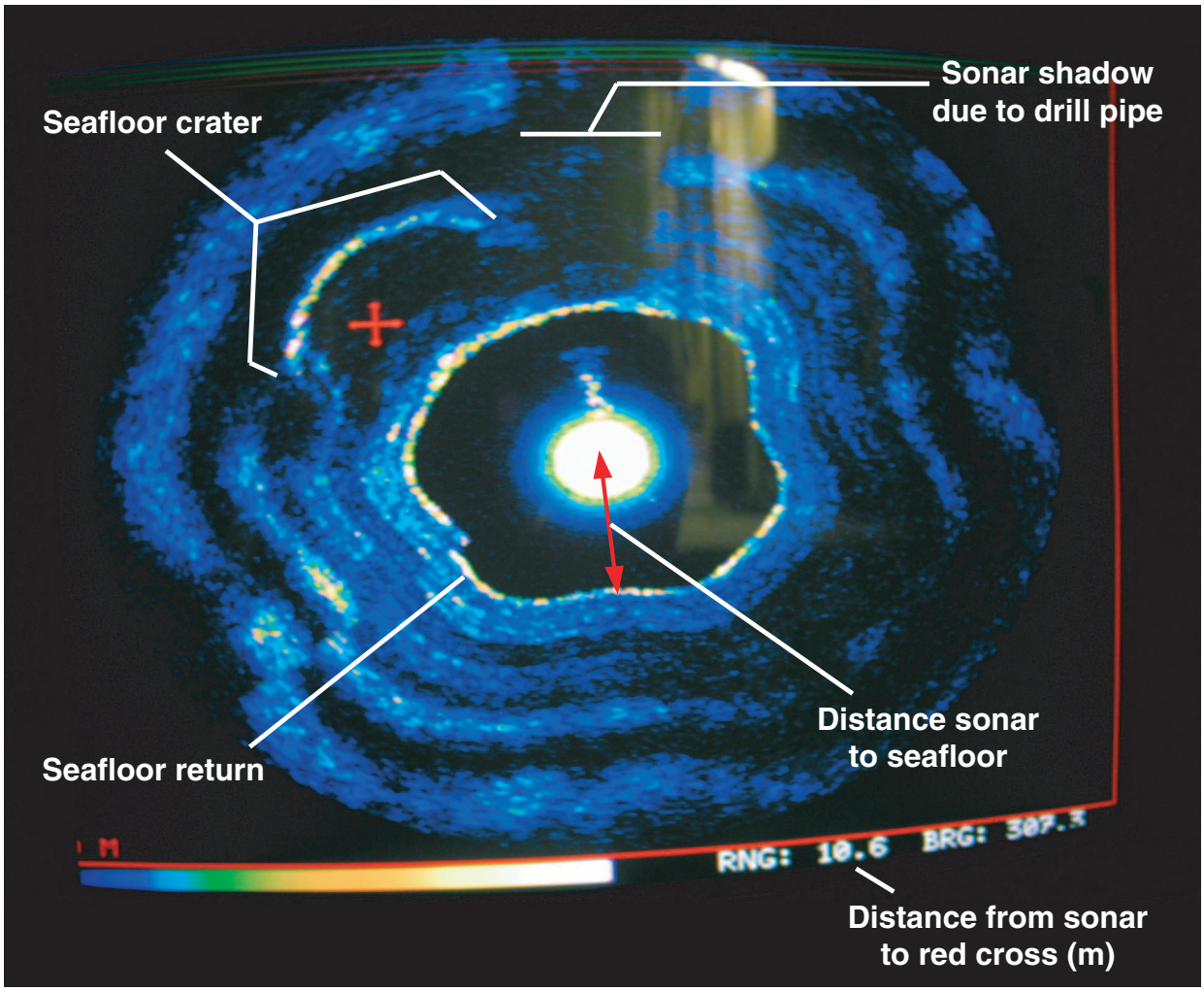

Figure F6. Lithostratigraphic summary for Hole 1276A, including a graphic display of the core recovery, ages, the proportions of lithologies on a core-by-core basis, an indication of grain size variation, the location of unit boundaries, and summaries of the characteristics of each unit and subunit. The patterns for lithology are presented in Fig. F4, p. 45, in the "Explanatory Notes" chapter and are the same as those used on Leg 210 visual core descriptions, except that the "claystone" pattern depicts the siliciclastic fraction of claystones, mudstones, and marlstones, whereas the "calcareous chalk" pattern indicates the carbonate fraction of marlstones. In the graphic section: diamonds = large sedimentary clasts; ∫, ∫∫, and ∫∫∫ = slight, moderate, and pervasive bioturbation; BS = cores where black shales were identified. TOC = total organic carbon. (Continued on next two pages.)

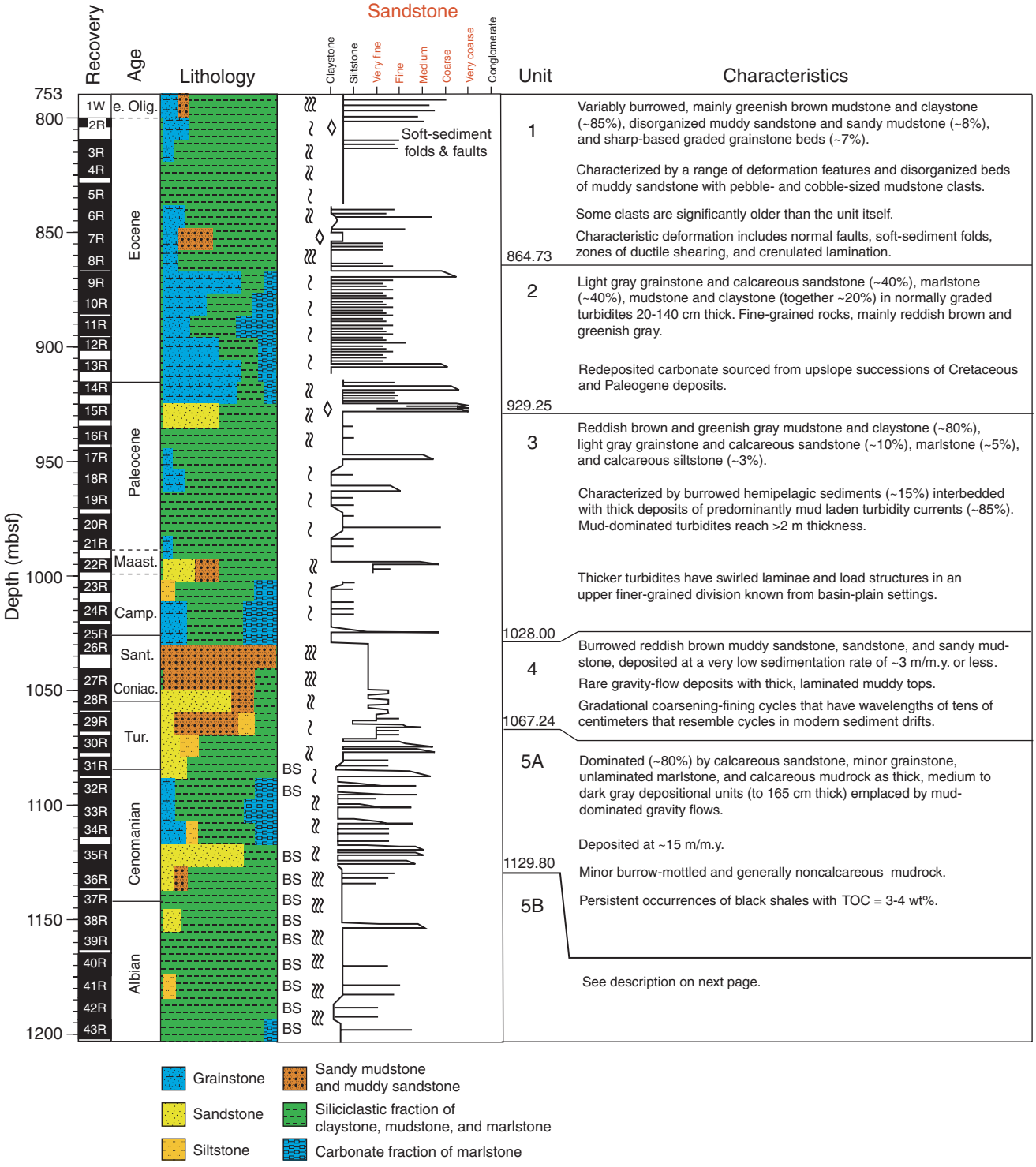

Figure F6 (continued).

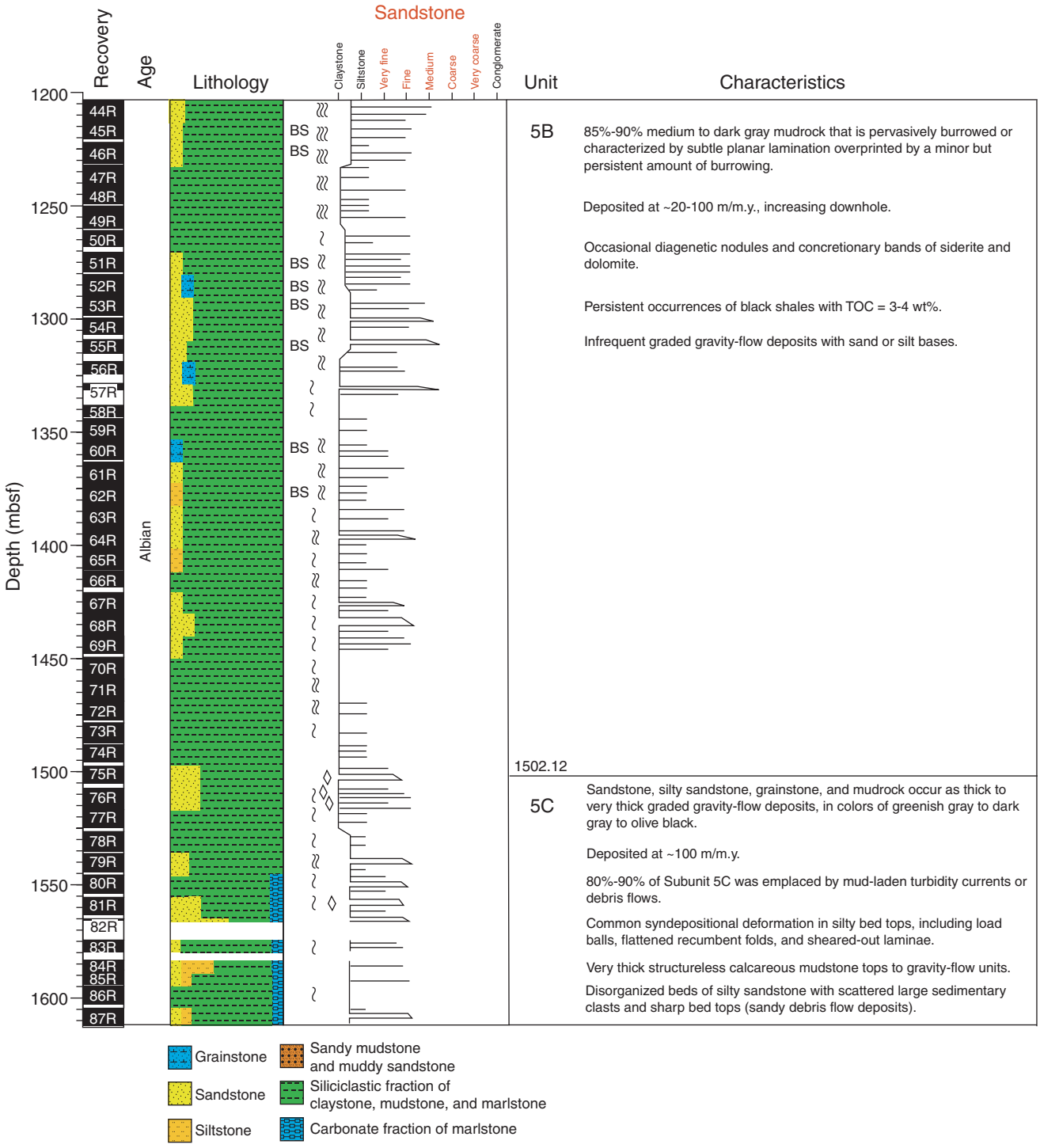

Figure F6 (continued).

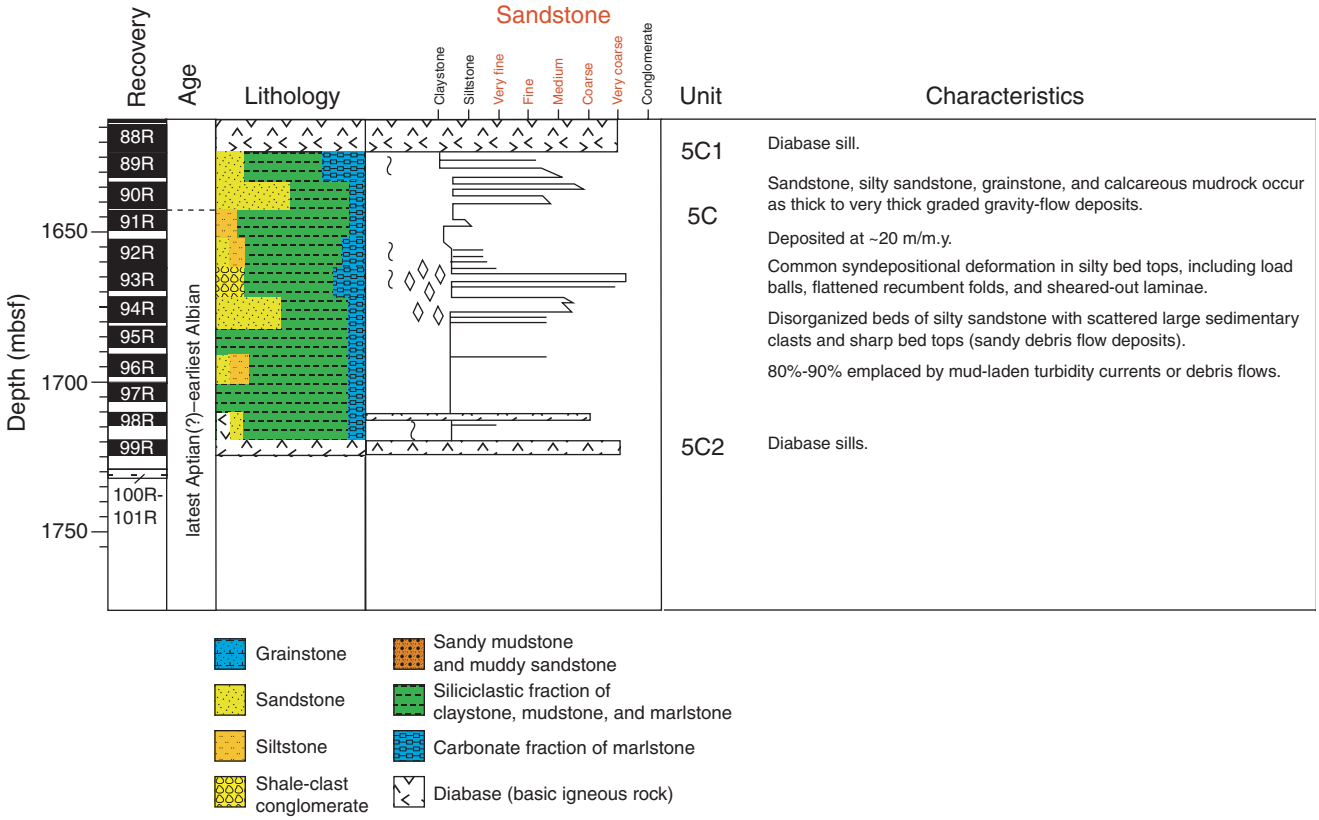

Figure F7. Close-up of laminated sandstone showing mud-filled burrows at 145–150 cm. This sediment was burrowed down from the overlying mudstone bed (Unit 1: interval 210-1276A-6R-2, 135–150 cm).

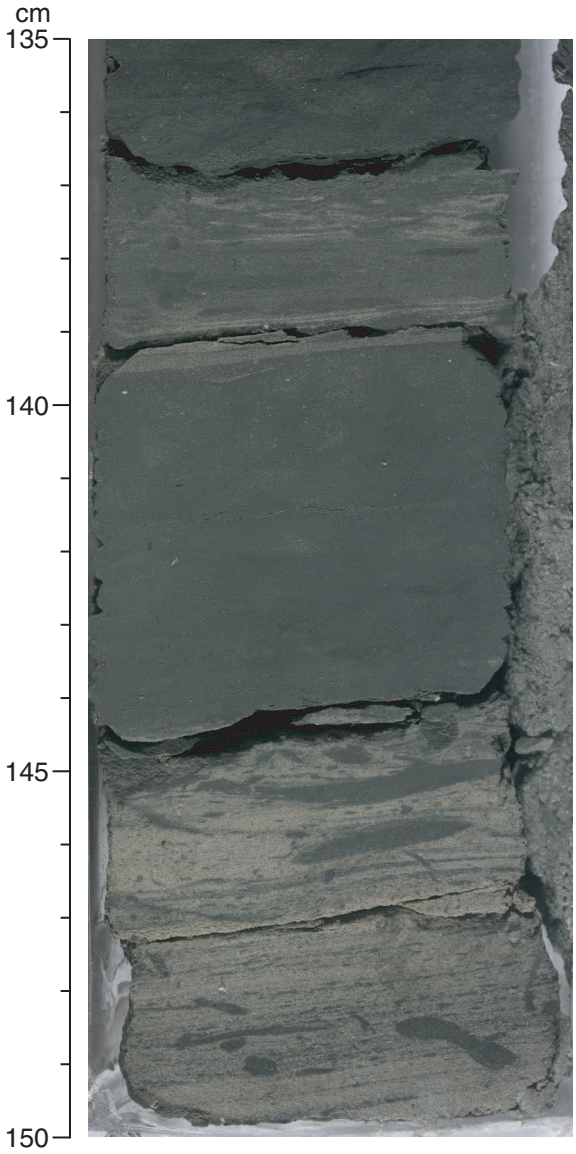

Figure F8. Close-up of grainstone turbidite showing upward gradation from weakly laminated grainstone (74–87 cm) to more distinctly laminated grainstone (52–74 cm). The color variation is mainly related to the relative abundance of carbonate allochems (pale) and glauconite (dark) (Unit 1: interval 210-1276A-1W-1, 52–87 cm).

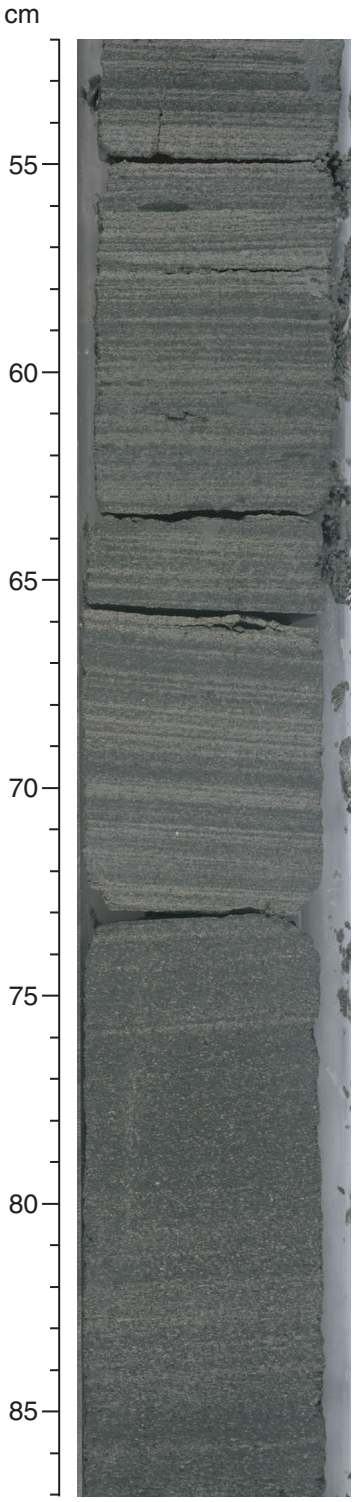

Figure F9. Close-up of redeposited, graded grainstone (50–77 cm) containing small subrounded mudstone rip-up clasts. This grainstone was emplaced by subaqueous mass flow (Unit 1: interval 210-1276A-2R-1, 43–80 cm).

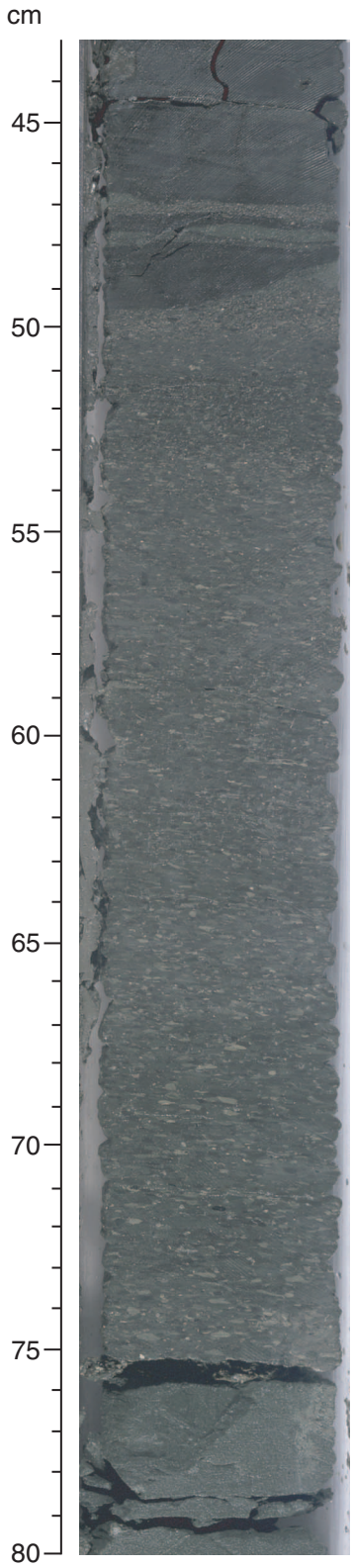

Figure F10. Photomicrographs of grainstone from Unit 1 (Sample 210-1276A-3R-4, 47–49 cm). **A.** View showing fragments of miliolid (M; tan) and other planktonic foraminifers (P) and siliceous sponge spicules (hollow tubes; S). Porous structure at bottom edge is opaline radiolarian test (R). Black spots are pyrite within porous bioclasts. Very low birefringent chalcedonic quartz fills some pores. **B.** Same view as A in cross-polarized light to differentiate calcareous (birefringent; C) from opaline (isotropic; O) components.

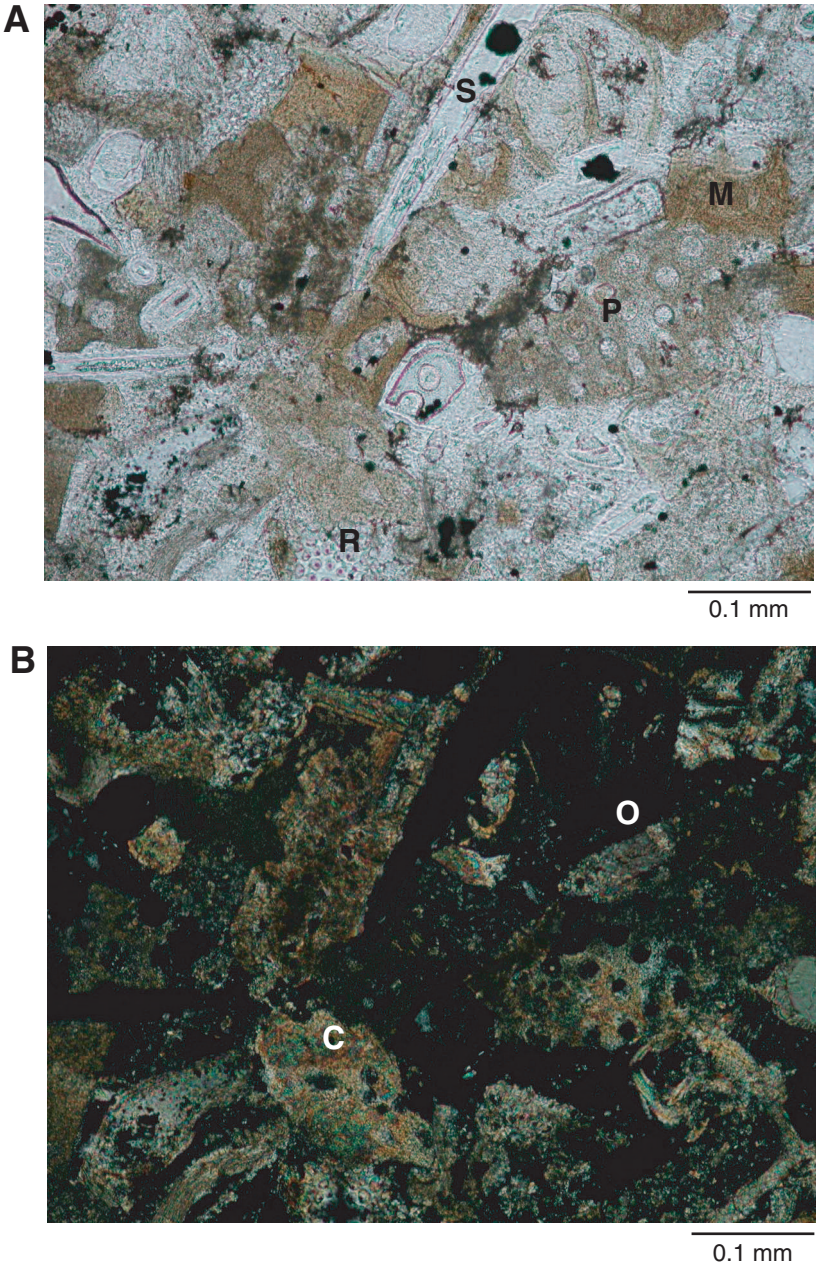

Figure F11. Close-up of massive sandy mudstone with carbonate granules (mainly bioclasts) and calcareous mudstone rip-up clasts. This interval is interpreted as a sandy debris flow (Unit 1: interval 210-1276A-7R-3, 94–126 cm).

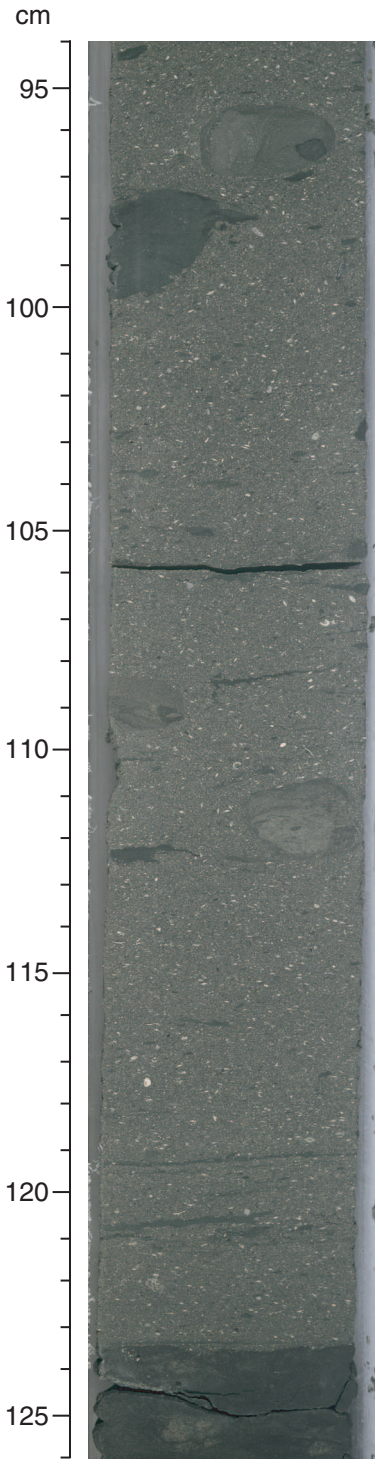

Figure F12. Close-up of massive sandy mudstone with carbonate granules (mainly bioclasts) showing a swirled texture resulting from soft-sediment deformation (Unit 1: interval 210-1276A-7R-2, 16–40 cm).

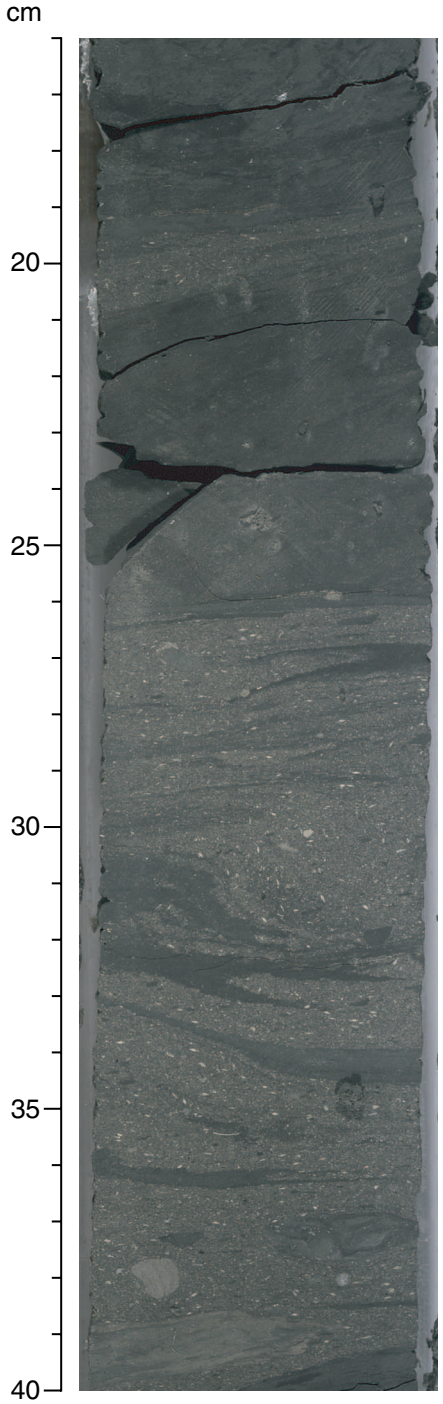

Figure F13. Close-up of inferred shear band (35–48 cm) indicated by extreme elongation of burrows together with crenulation and small-scale folding. This deformation took place while the sediment was still soft. Note the contrast with the adjacent, less deformed sediment (30–34 cm). The deformed sediment might be a clast (Unit 1: interval 210-1276A-2R-3, 30–50 cm).

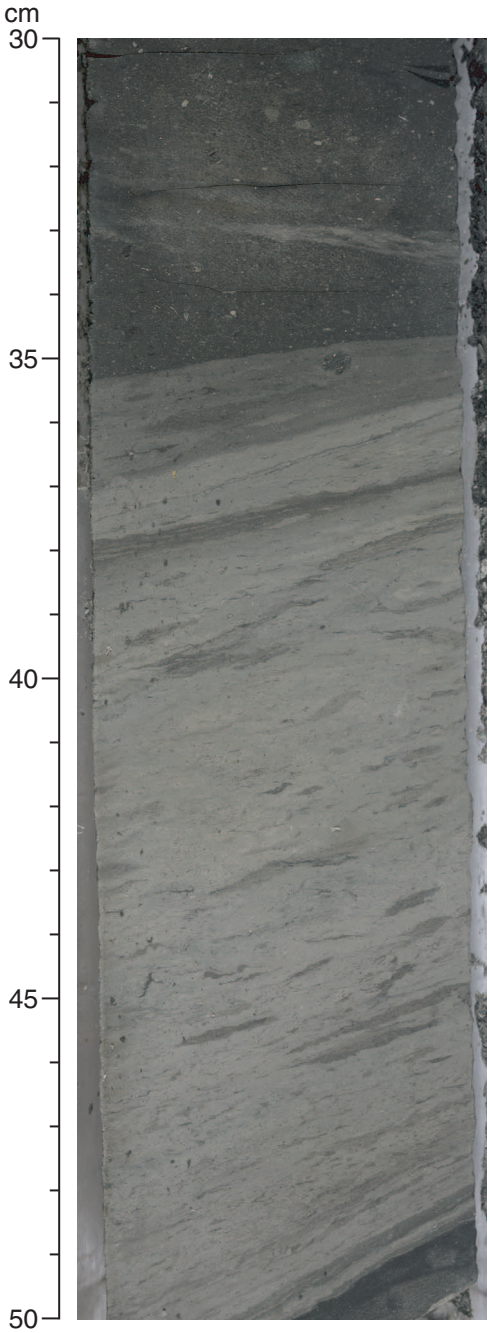

Figure F14. Close-up of soft-sediment deformation in the upper part of Unit 1. Note the crenulated lamination and soft-sediment folding between 2 and 5 cm (interval 210-1276A-2R-CC, 0–18 cm).

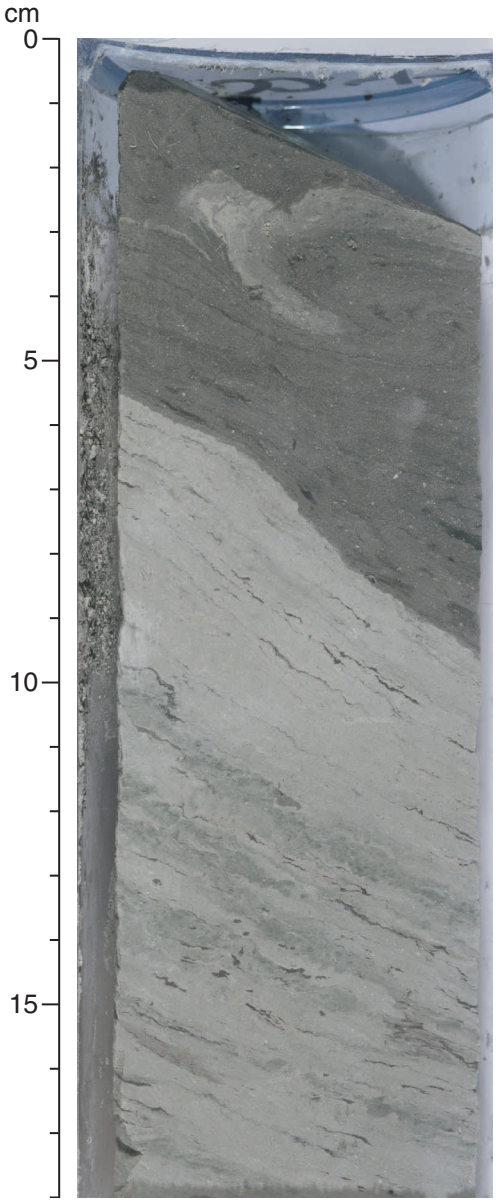

Figure F15. Close-up of small reverse fault in graded grainstone (48–52 cm). Such faults formed before complete lithification of the sediment, as shown by the deformed lamination. They occur in an interval of soft-sediment deformation in the upper part of Unit 1 (interval 210-1276A-3R-4, 46–56 cm).

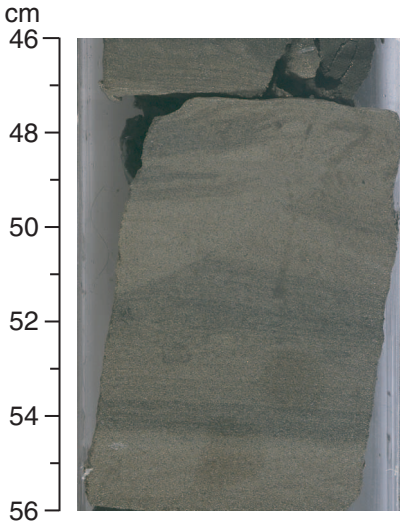

Figure F16. Close-up of repeated graded intervals. Note the sharp bases of the inferred turbidites and fining upward into burrowed and laminated intervals (Unit 2: interval 210-1276A-9R-2, 96–120 cm).

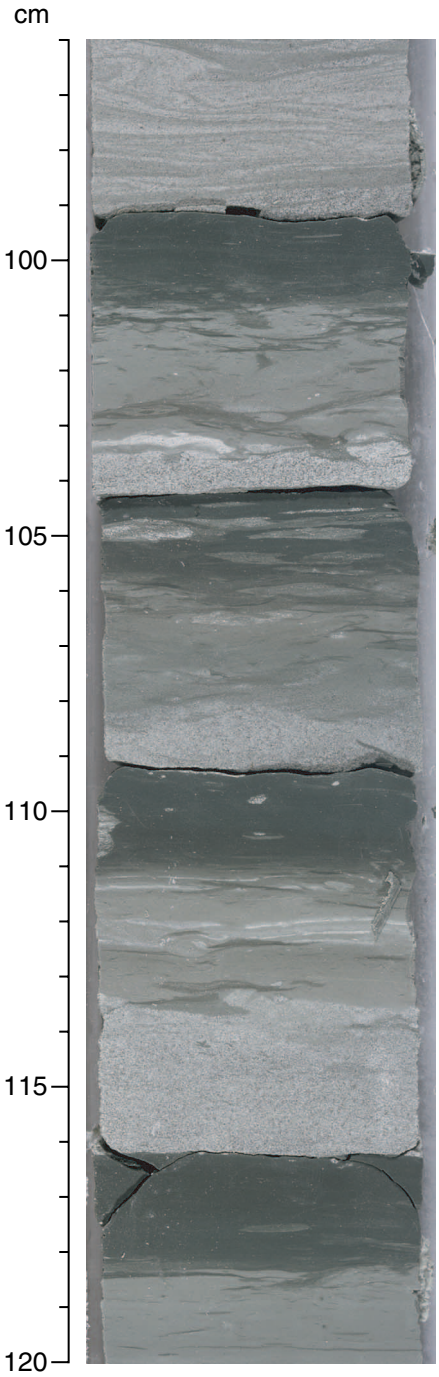

Figure F17. Close-up of typical normally graded intervals. Grainstone (12–14 cm and 23–28 cm) grades up into mudstone (9–11 cm and 14–18 cm). The mudstone is burrowed down into the underlying lithology (11–14 cm and 18–22 cm) (Unit 2: interval 210-1276A-8R-6, 5–28 cm).

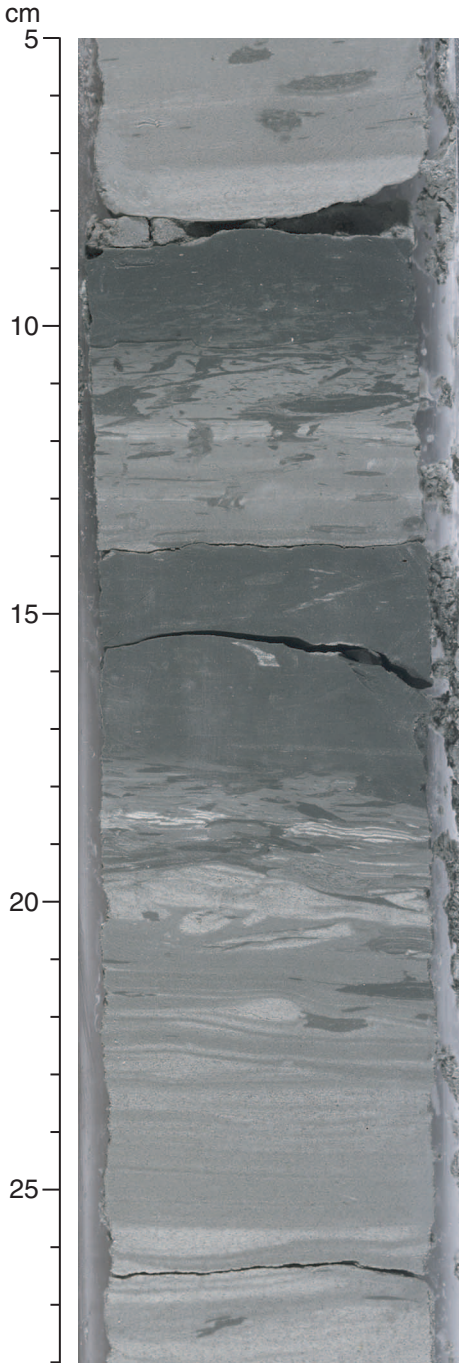

Figure F18. Close-up of typical graded grainstone of Unit 2, showing a nearly homogeneous lower part (44–48 cm) and a laminated upper part (37–44 cm) (interval 210-1276A-9R-6, 37–49 cm).

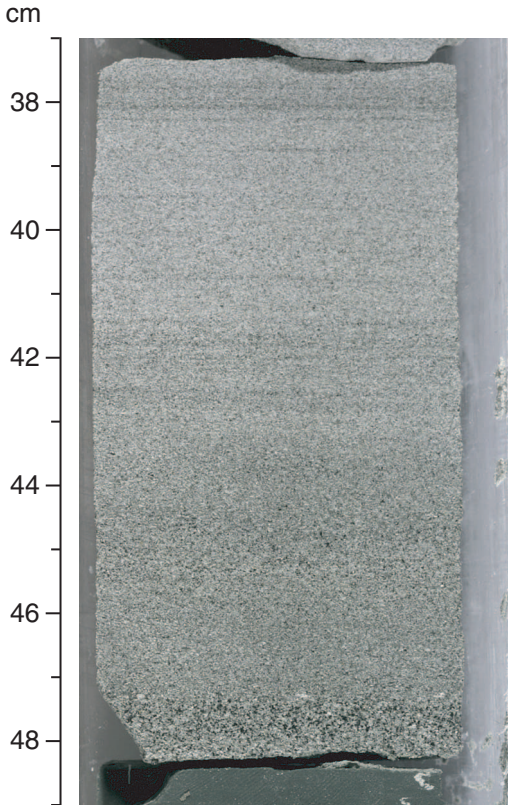

Figure F19. Close-up of medium- to fine-grained, graded carbonate grainstone showing a scoured base above fine-grained laminated sediment (92 cm). The grainstone grades up into a slightly darker interval (85–89 cm) interpreted as the mudstone top of a turbidite and then into much darker claystone interpreted as background hemipelagic sediment (83–85 cm). The latter is burrowed down into the underlying mudstone (Unit 2: interval 210-1276A-9R-6, 82–93 cm).

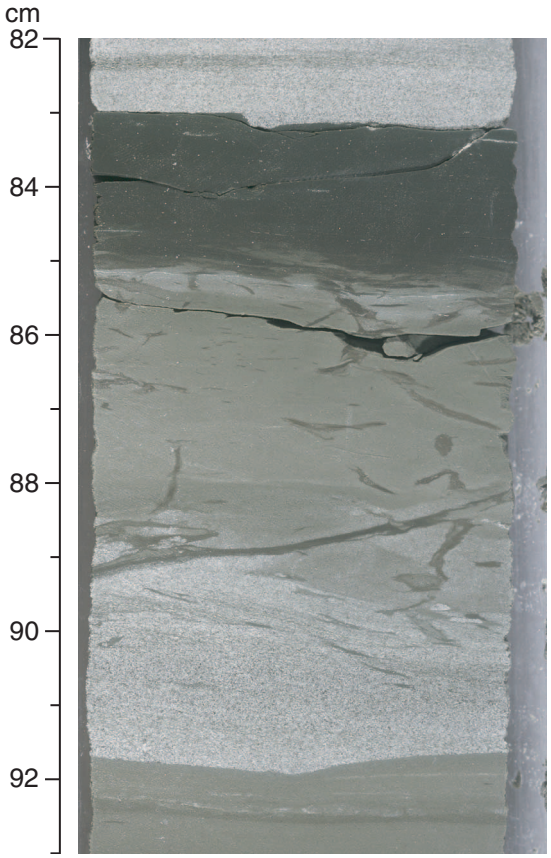

Figure F20. Close-up of cross lamination with anastomosing darker and lighter laminae in carbonate grainstone (Unit 2: interval 210-1276A-12R-3, 58–65 cm).

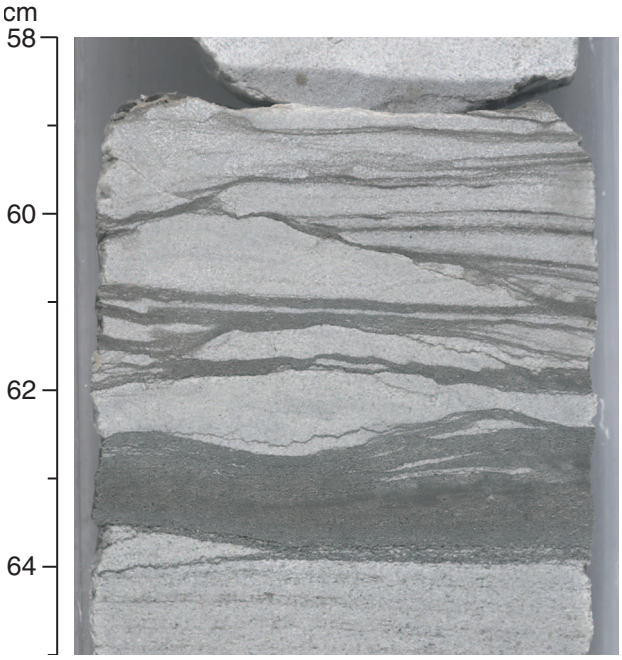

Figure F21. Close-up of middle Eocene unconformity and sedimentary dike. The interval 111–113 cm marks the position of a middle Eocene unconformity defined by biostratigraphic studies. The graded grainstone from 123 to 137 cm overlies a sedimentary dike. Three-dimensional examination of the core shows that this is a folded sheet of sand-grade sediment extending down from the base of the overlying grainstone bed. The grain size of the dike is identical to that in the overlying carbonate grainstone, showing that the sediment protruded downward from the bed base. It differs in shape from, and crosscuts, the adjacent burrows (top of Unit 2: interval 210-1276A-8R-5, 109–142 cm).

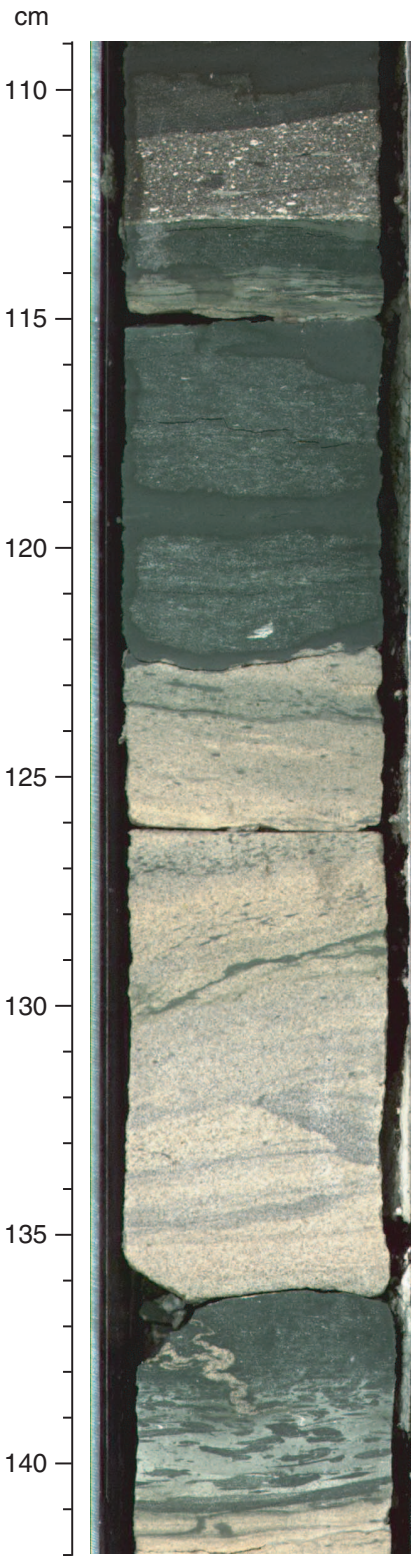

Figure F22. Close-up of scattered granules and rounded to subrounded pebbles in a coarse carbonate grainstone. Note the inverse grading at the base of this bed, which is consistent with a mass-flow mode of emplacement (Unit 2: interval 210-1276A-9R-2, 65–73 cm).

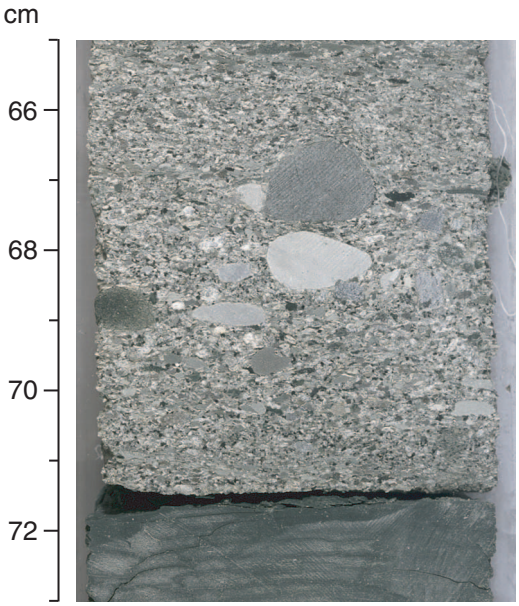

Figure F23. Close-up of graded conglomerate → grainstone → sandstone with mudstone rip-up clasts at the top, characteristic of clastic sediments emplaced by mass flows at the base of Unit 2 (interval 210-1276A-15R-3, 92–126 cm).

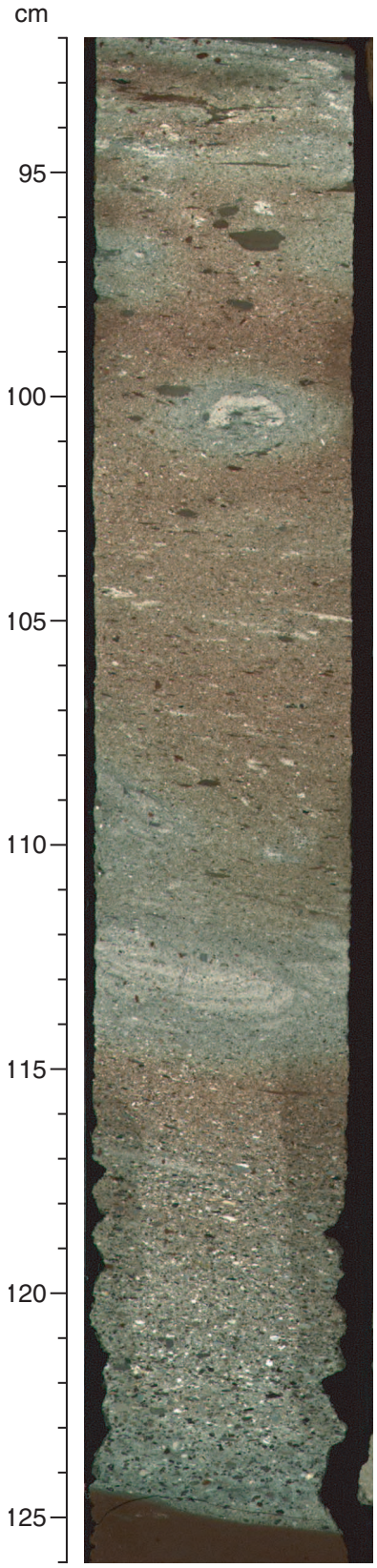

Figure F24. Close-up of syndepositional deformation of coarse clastic sediments near the base of Unit 2. These sediments were emplaced by a poorly organized mass flow (interval 210-1276A-15R-1, 119–136 cm).

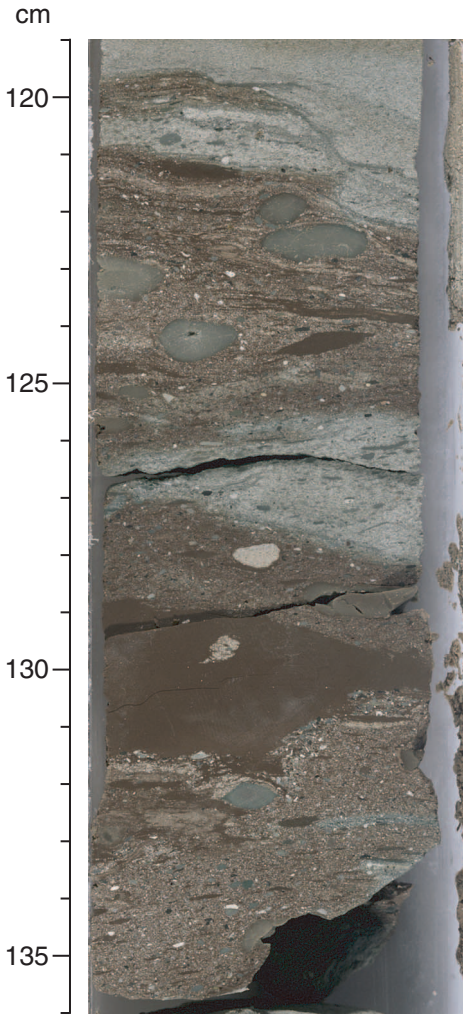

Figure F25. Close-up of coarse-grained sediments showing synsedimentary folding and shearing (28–45 cm). These sediments form part of an inferred mass flow in the lower part of Unit 2 (interval 210-1276A-15R-2, 24–50 cm).

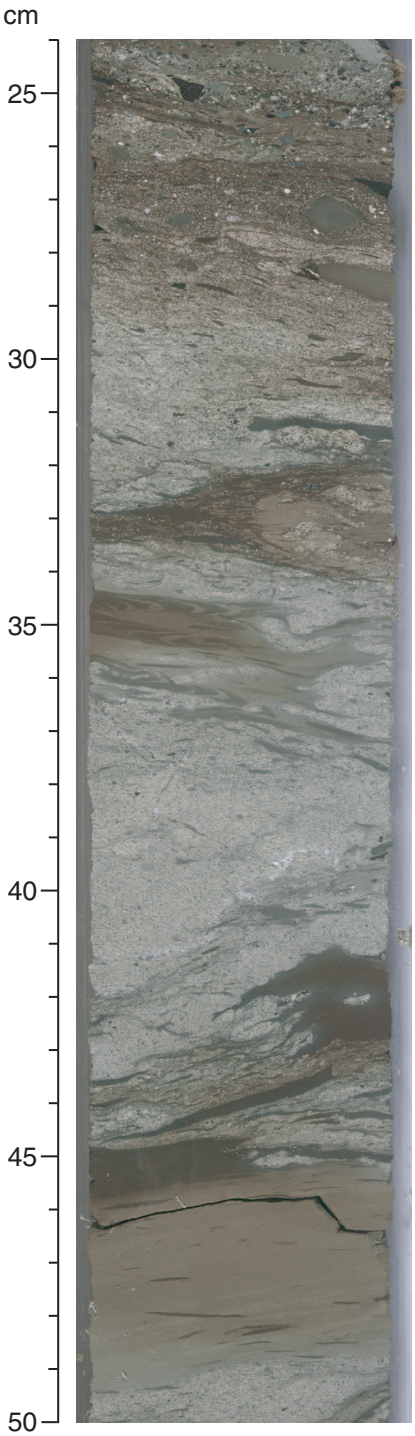

Figure F26. Photomicrographs of grainstones from near the top of Unit 2. Both views are in plane-polarized light. The largest grains are whole to fragmented benthic foraminifers. Dark grains (M) are micritic carbonate lithic clasts or red algae. White grains are mainly quartz (Q). Sparse glauconite pellets are green. Both samples are only moderately sorted and show depositional alignment of elongate foraminifers and clasts. **A.** Grainstone with muddy matrix (Sample 210-1276A-8R-6, 69–71 cm). **B.** Grainstone with carbonate cement (Sample 210-1276A-11R-CC, 14–17 cm).

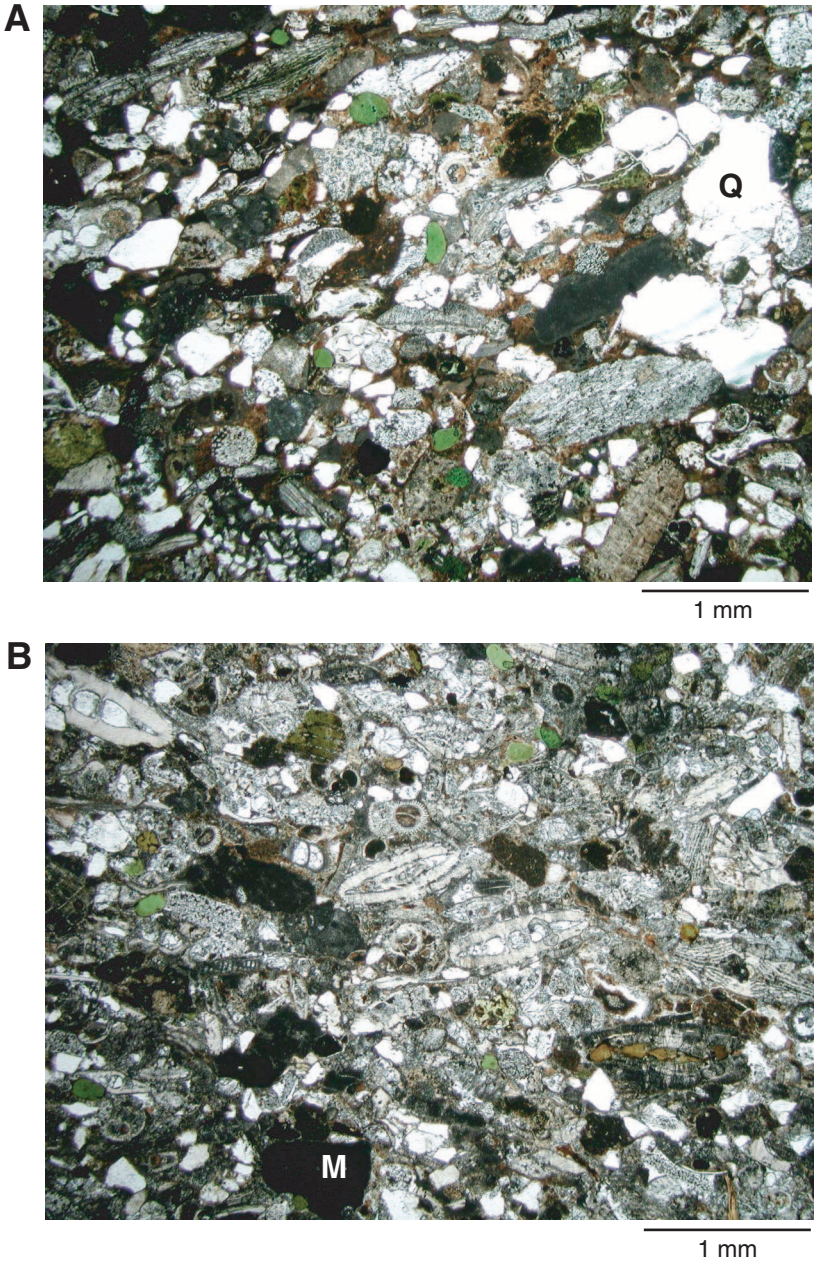

Figure F27. Photomicrographs of grainstones from Unit 2 at high magnification in plane-polarized light. **A.** Field of view contains several whole benthic foraminifers (discoid; F) and one large broken fragment (B). Bioclastic debris above the prominent green glauconite pellet is replaced by epigenetic glauconite (E). There is a quartz-rich siltstone fragment (S) in upper left corner and a fragment of biotite schist (SH) at left, center. Note poor sorting and brownish muddy matrix (M) (Sample 210-1276A-8R-6, 69–71 cm). **B.** This image shows several planktonic (C, MA) and benthic (B) foraminifers. Foraminifers on left are filled with carbonate microspar (C), whereas the planktonic foraminifers to right are partly filled by muddy matrix (MA). Dark rounded clast at lower left (L) is micritic limestone (Sample 210-1276A-11R-CC, 14–17 cm).

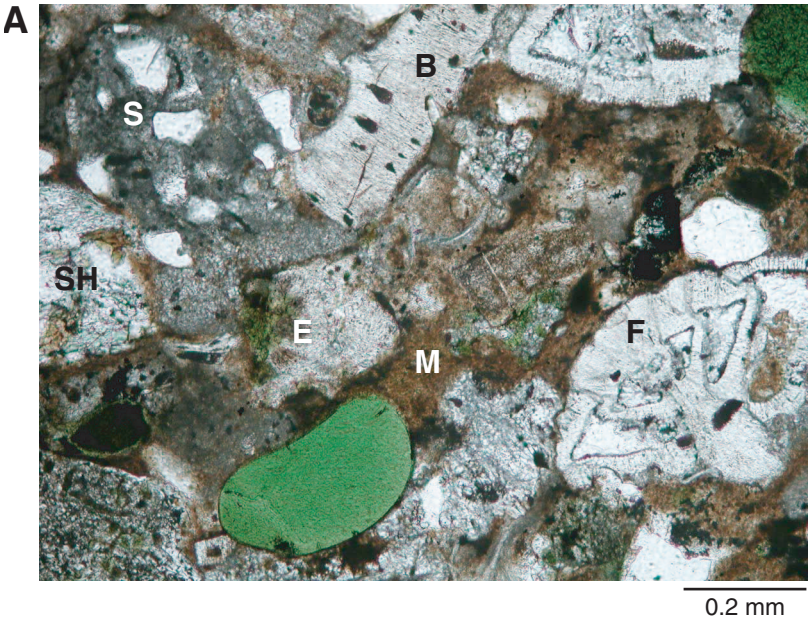

Figure F28. High- and low-magnification photomicrographs of carbonate-cemented grainstone in Unit 2 (Sample 210-1276A-13R-2, 60–63 cm). Both images are in plane-polarized light. **A.** Close-up view showing some of the main components in Unit 2 grainstones: bryozoan (B) on left, broken benthic foraminifer fragment (D; discocyclinid?), and convex fragment of ostracode shell (O) in right center. **B.** General view showing moderate sorting and alignment of large disc-shaped (D; discocyclinid?) and thicker-walled (N; nummulitid?) benthic foraminifers.

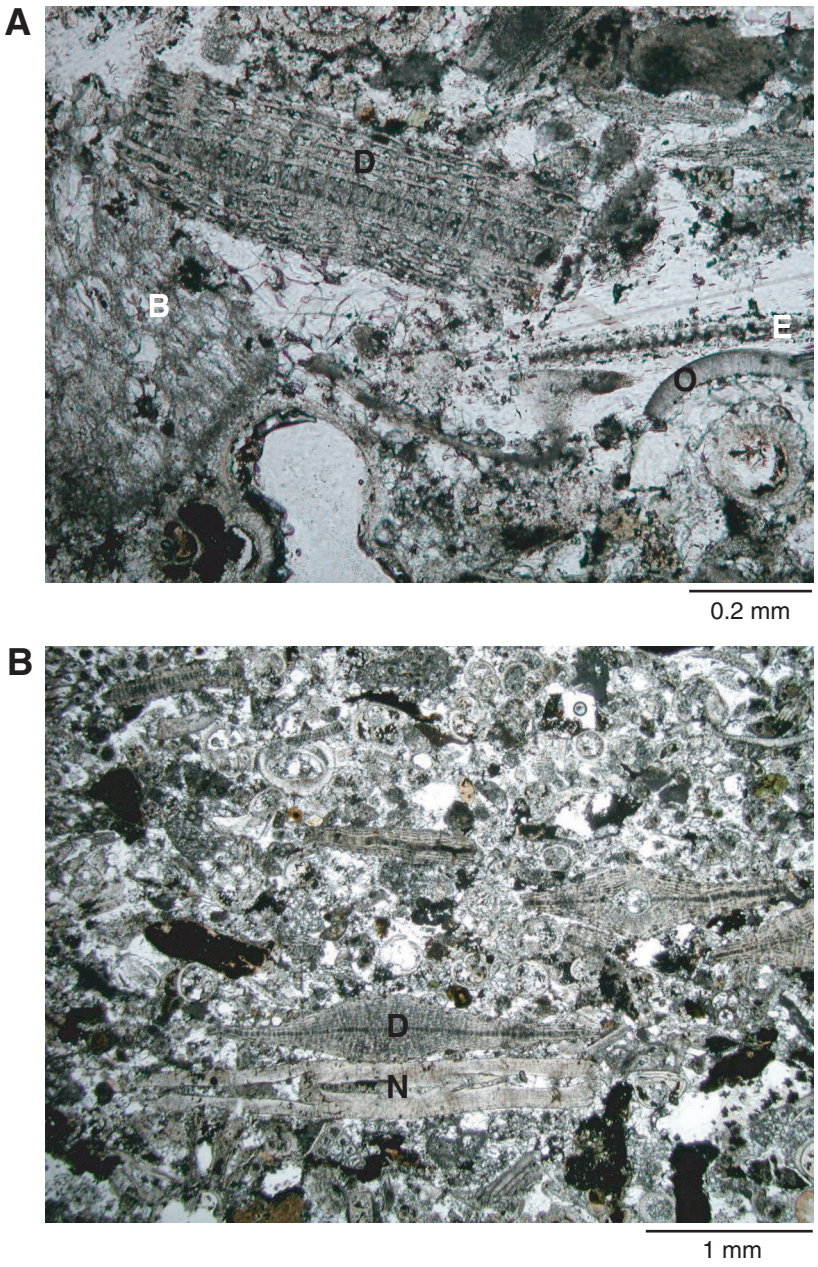

Figure F29. Photomicrographs of volcaniclastic sediment from near the base of Unit 2 (Sample 210-1276A-15R-2, 25–27 cm). Both views are from the same thin section, in which large sand grains are set in an iron-stained marlstone matrix (see Fig. F25, p. 148, for sample location). **A.** Cross-polarized light emphasizes birefringent calcareous components in darker, iron-stained mud matrix. Darker, nearly isotropic grain in upper right corner may be felsic glass (F). Euhedral quartz grain (Q) in center bottom is probably of volcanic origin. Light tan grain with cleavage at center is biotite (B). Other irregular grains (light tan) are calcareous bioclasts and lithic debris. Note that the greenish glauconite grains are not all the same shade of green, perhaps suggesting different chemical compositions and different provenance. **B.** View of a different part of the thin section in plane-polarized light showing prominent rounded, altered microlitic glass (brown, in center). White rectangular plagioclase microlites in this glass are set in a vitric groundmass now devitrified and altered to clay minerals. Dark patches might be a combination of vesicle fills (round) and altered mafic minerals. Texture and alteration style suggest that this grain is of mafic composition. Note severe cracking of surrounding tan matrix, probably caused by shrinkage of matrix clay minerals during thin section preparation. Lighter fragments in the matrix are foraminifers and micritic carbonate.

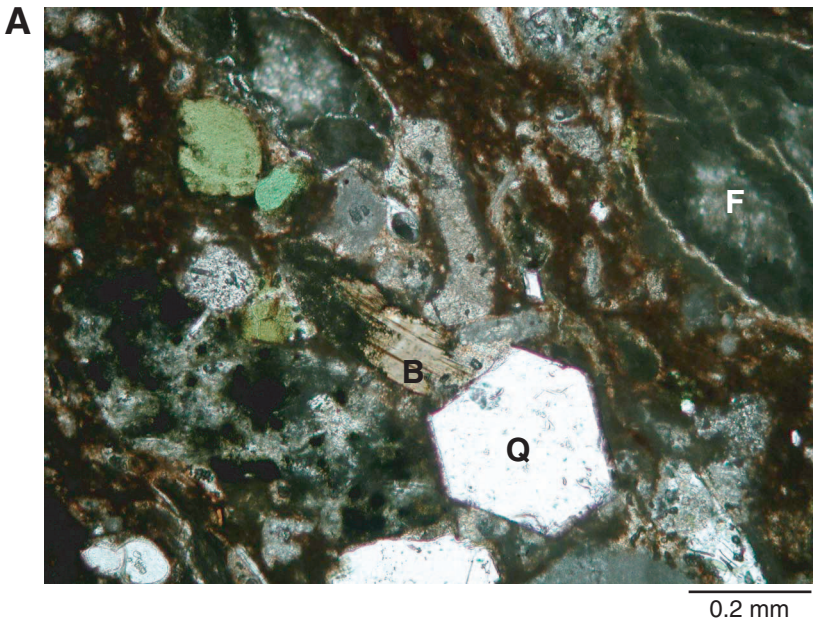

Figure F30. Close-up of lenticular sandstones that were affected by burrowing (54–55 cm and 57–58 cm) and then modified by differential compaction. Note also the *Chrondrites* burrows in the lower part of the image (61–64 cm) (Unit 2: interval 210-1276A-14R-4, 53–63 cm).

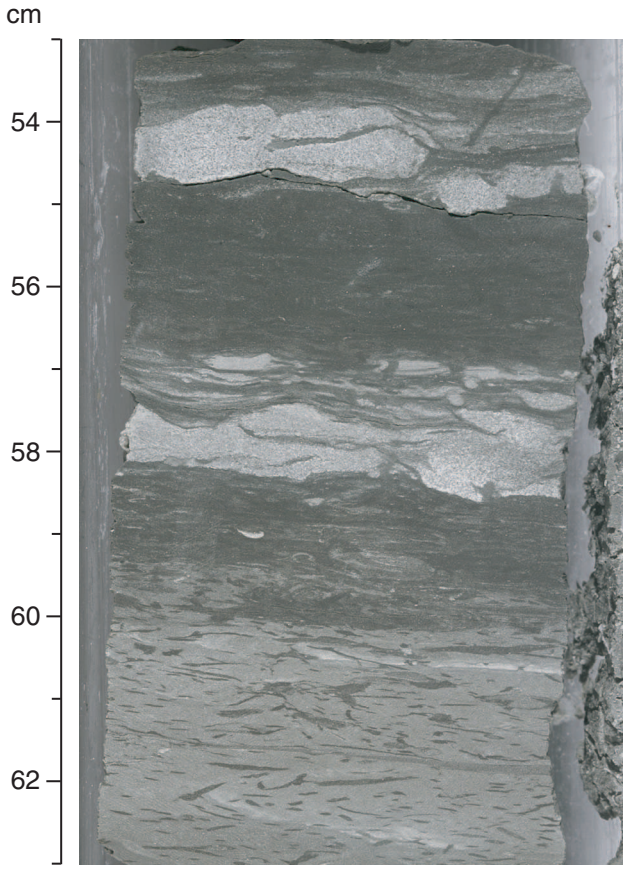

Figure F31. Close-up of the effect of differential compaction of burrows. The top of the grainstone at 87–89 cm is strongly burrowed. This granular carbonate was lithified relatively early in diagenesis, whereas the adjacent mudstone remained soft, allowing this distinctive structure to form during compaction (Unit 2: interval 210-1276A-12R-4, 84–93 cm).

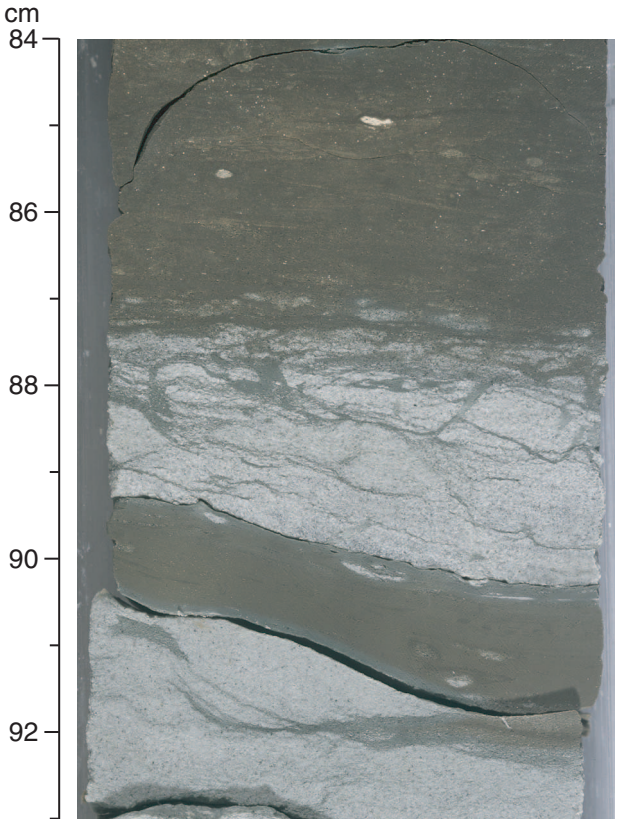

Figure F32. Close-up of alternating darker and lighter seams in a grainstone turbidite. The grain size varies smoothly through this grainstone; the color banding is thought to result from diagenesis, including compaction and incipient pressure solution, rather than being a primary depositional feature. With further compaction, these seams would likely develop into stylolites similar to those found deeper in the succession at Site 1276 (Unit 2: interval 210-1276A-12R-3, 77–90 cm).

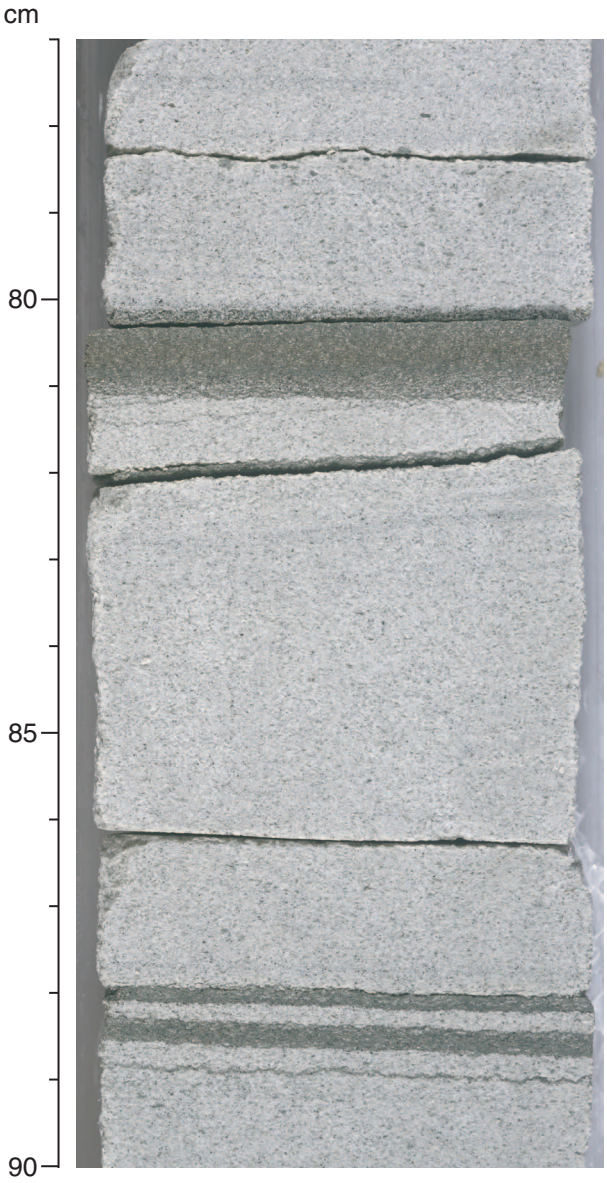

Figure F33. Close-up of a rare example of soft-sediment folding in a grainstone of Unit 2 (interval 210-1276A-14R-2, 8–32 cm).

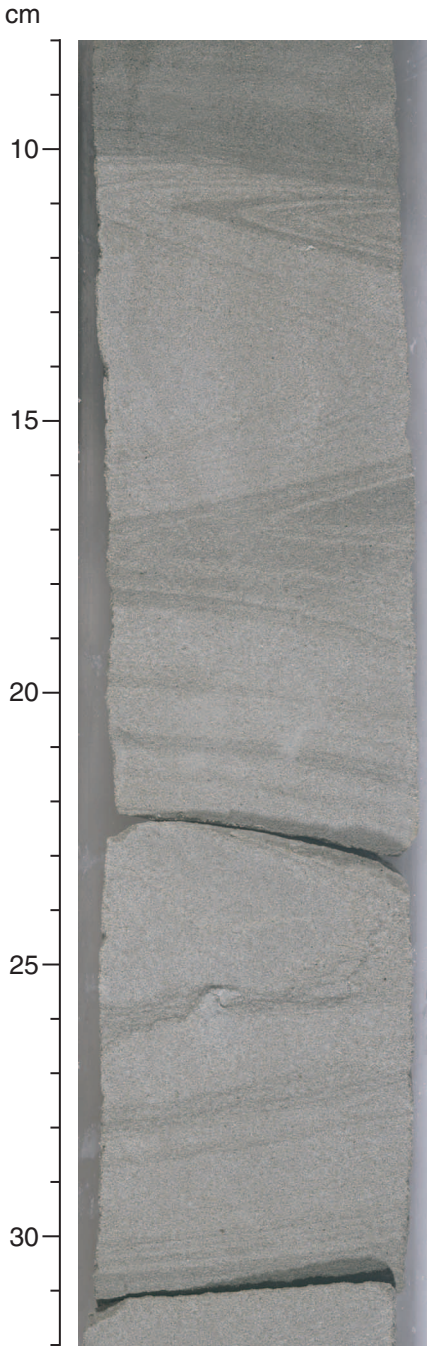

Figure F34. Close-up of a strongly deformed interval interpreted to be the result of mass-flow emplacement near the base of Unit 2. Note the plastic deformation and minor faulting of these coarse-grained sediments (interval 210-1276A-15R-2, 60–83 cm).

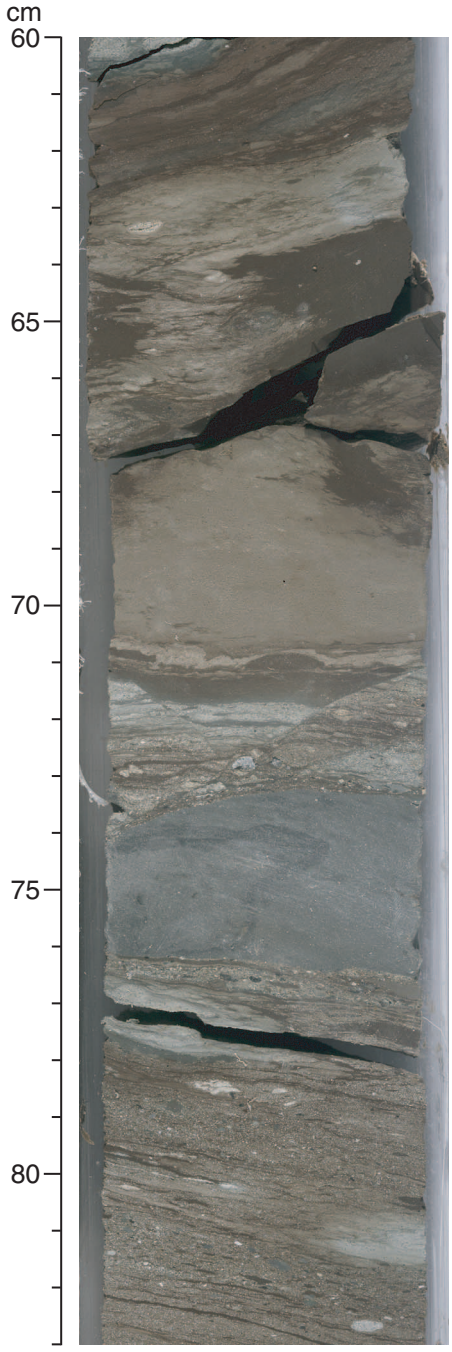

Figure F35. Close-up of dark silty mudstone with *Chondrites* traces (Unit 3: interval 210-1276A-23R-1, 76–82 cm).

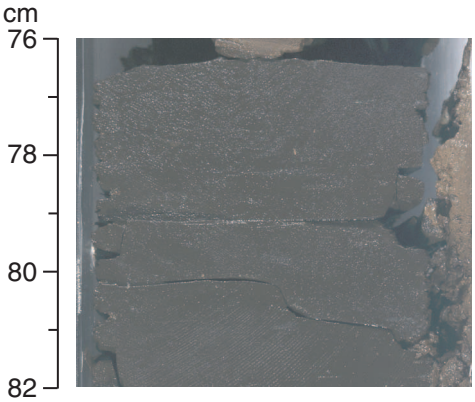

Figure F36. Close-up of *Zoophycos* burrows overprinted by diagenetic color banding (Unit 3: interval 210-1276A-22R-4, 67–78 cm).

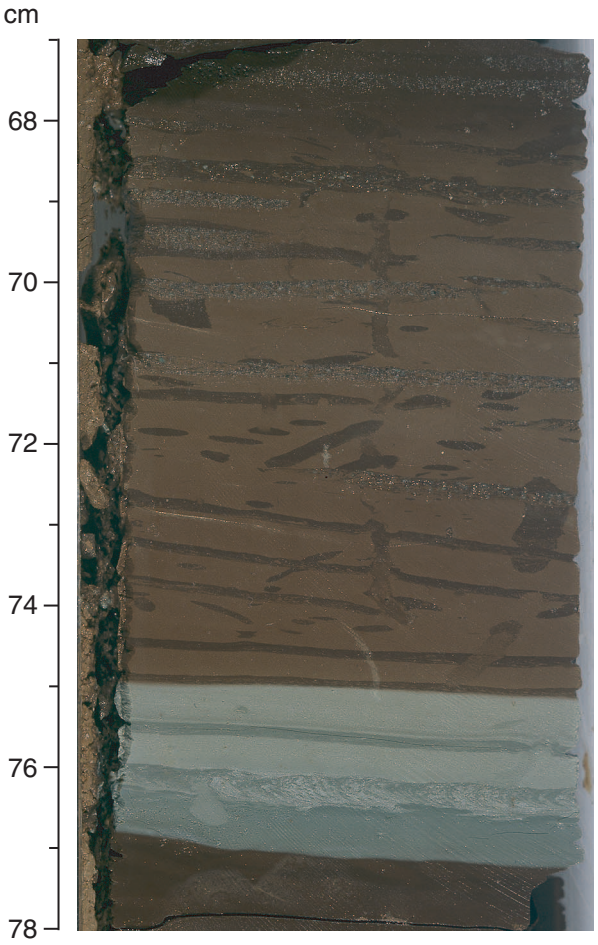

Figure F37. Close-up of *Zoophycos* burrow system in calcareous mudstone (Unit 3: interval 210-1276A-22R-CC, 3–22 cm).

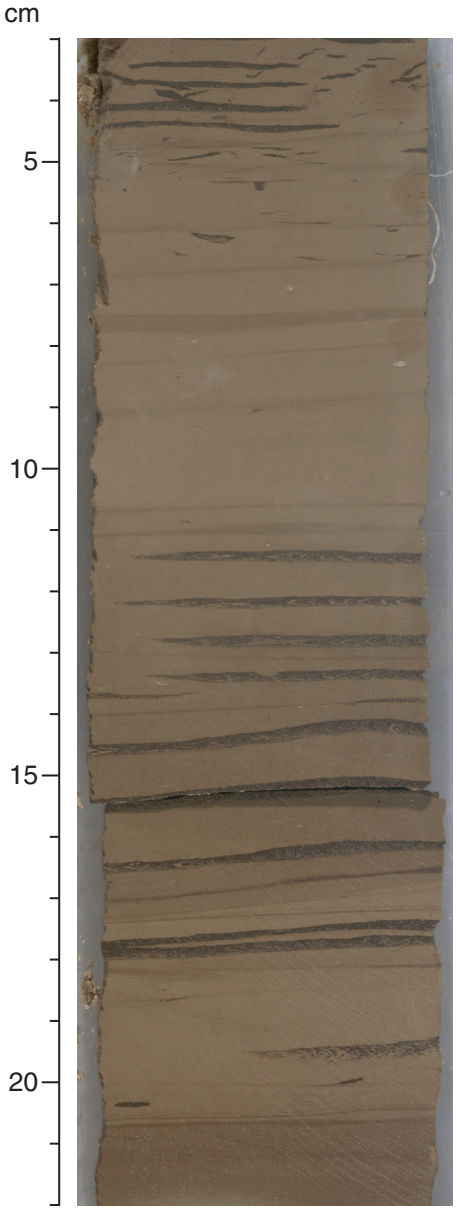

Figure F38. Close-up of *Chondrites* burrows in calcareous claystone that forms a minor part of Unit 3 (interval 210-1276A-17R-1, 10–20 cm).

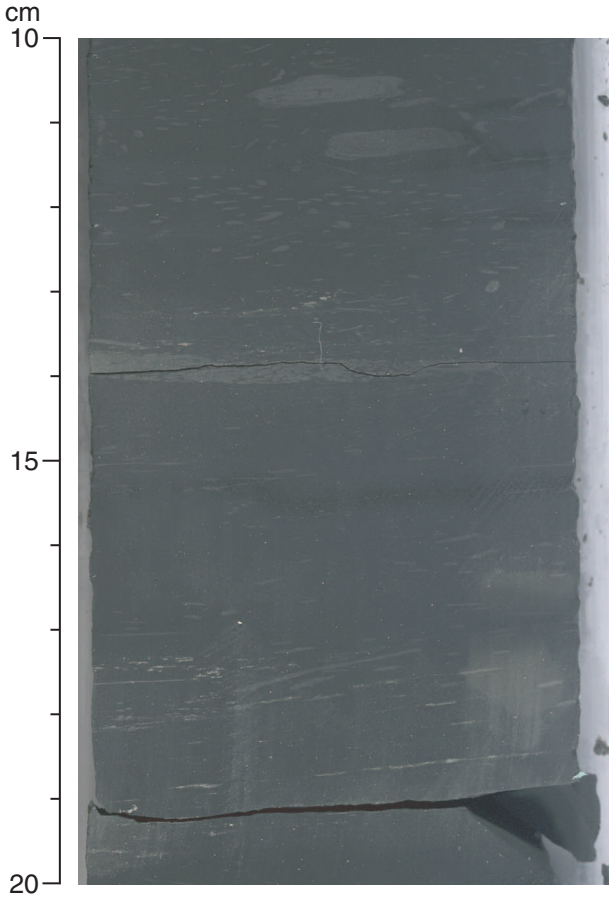

Figure F39. Close-up of color-banded marlstone with *Chondrites* burrows in intervals 76–80 and 86–88 cm. The irregular color banding (81–89 cm) was formed by diagenesis (Unit 3: interval 210-1276A-21R-4, 75–92 cm).

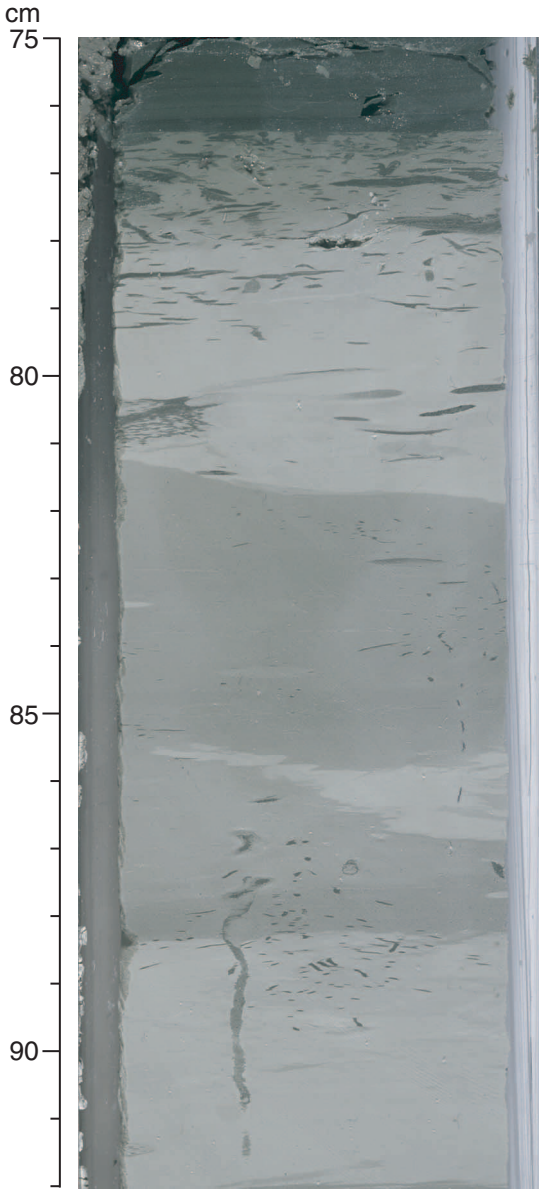

Figure F40. Close-up of carbonate grainstone → marlstone turbidite. Features: 105–110 cm, planar-laminated fine sand- and silt-sized grainstone; 80–105 cm, massive fine sand to silt-sized grainstone with small flattened siltstone clasts grading up into marlstone (Unit 3: interval 210-1276A-19R-5, 80–112 cm).

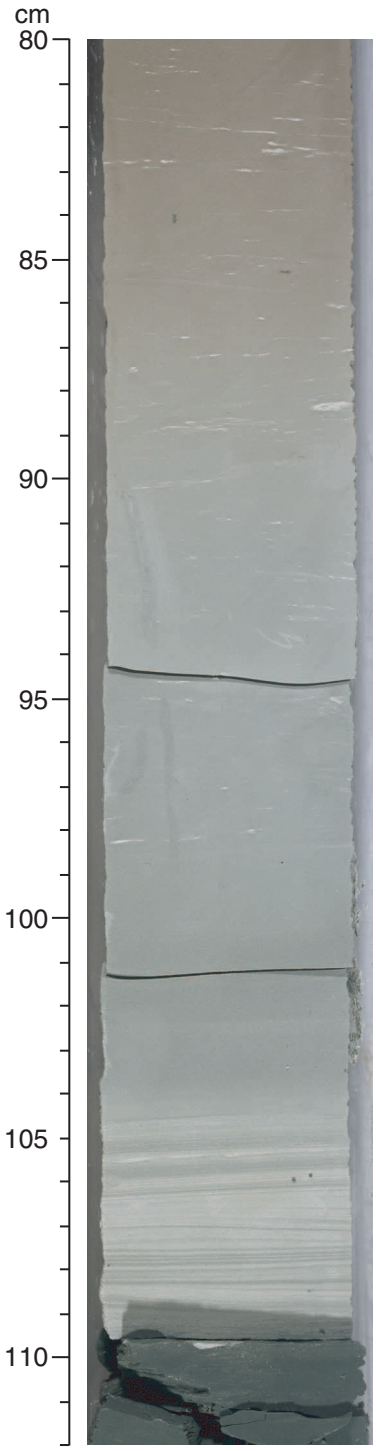

Figure F41. Close-up of base of a granule-grade turbidite showing parallel lamination and altered pyrite concretions at 93 cm (Unit 3: interval 210-1276A-17R-4, 91–101 cm).

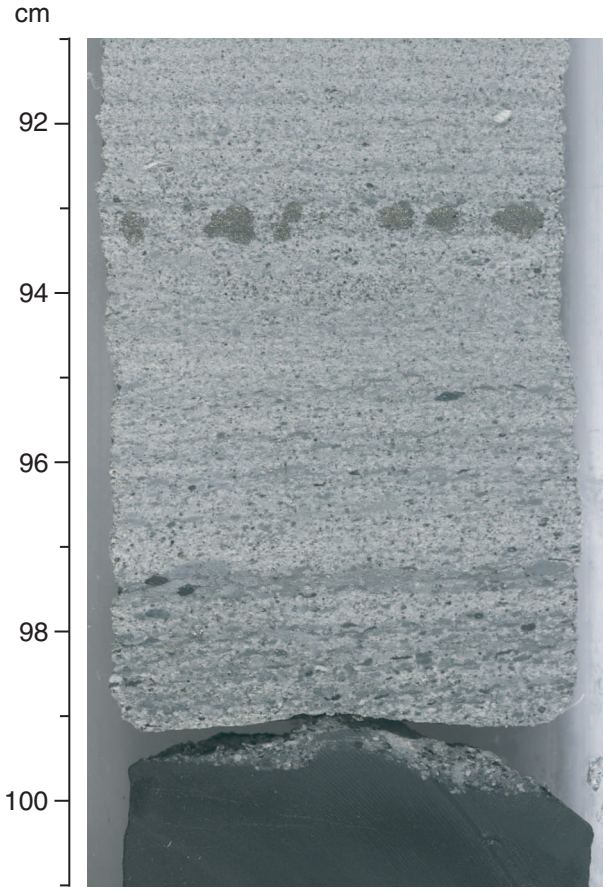

Figure F42. Close-up of grainstone turbidite. Features: 81 cm, scoured base; 47–81 cm, grading through planar-laminated, low-angle cross-laminated, and wavy/planar-laminated intervals into burrowed siltstone/mudstone (47–52 cm). The grain size varies smoothly across 69–70 cm, an interval rich in mud grains. The truncation of cross lamination at 70 cm might have been facilitated by cohesive behavior of the sediment in this part of the turbidity current (Unit 3: interval 210-1276A-20R-5, 47–84 cm).

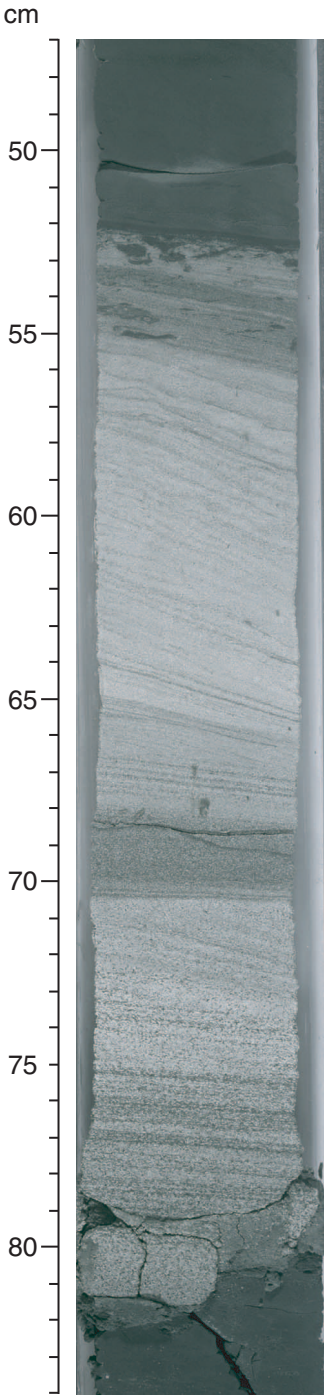

Figure F43. Comparison of core photograph with CT scan. (**A**) Core photograph of planar- to cross-laminated grainstone compared to (**B**) CT scan of part of the same interval acquired before core splitting. A and B have the same scale. The well-cemented carbonate grainstone provides little contrast for X-radiography, so only the most prominent clay-rich bands are imaged. This lack of suitable contrast is typical of Units 1–3 (Unit 3: interval 210-1276A-21R-4, 108–119 cm).

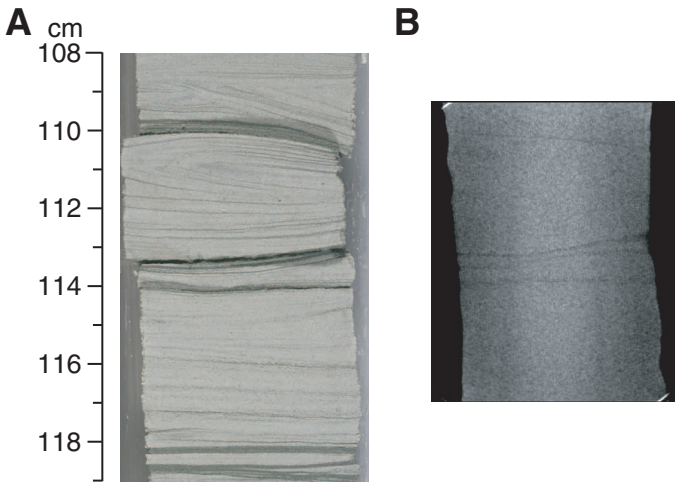

Figure F44. Close-up of grainstone turbidite showing large cylindrical burrows that may record unsuccessful attempts by transported organisms to escape to the surface after burial by the upper part of the turbidite (Unit 3: interval 210-1276A-17R-4, 69–90 cm).

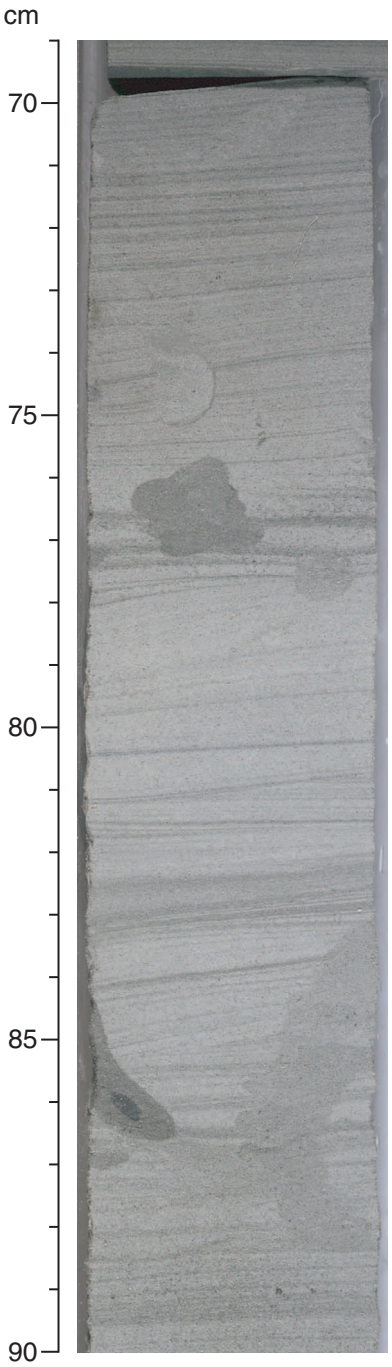

Figure F45. Sketches of four beds thicker than 1 m, showing upper silt- to mud-grade divisions with wet-sediment features, including load casts, contorted laminae, and other structures produced by mass-flow processes. Relevant ODP sections and intervals are labeled at the base of each sketch, whereas the scale to show deposit thickness begins at the base of each bed. Note locations of close-up photographs in other figures (Figs. **F46,** p. 169, **F47,** p. 170).

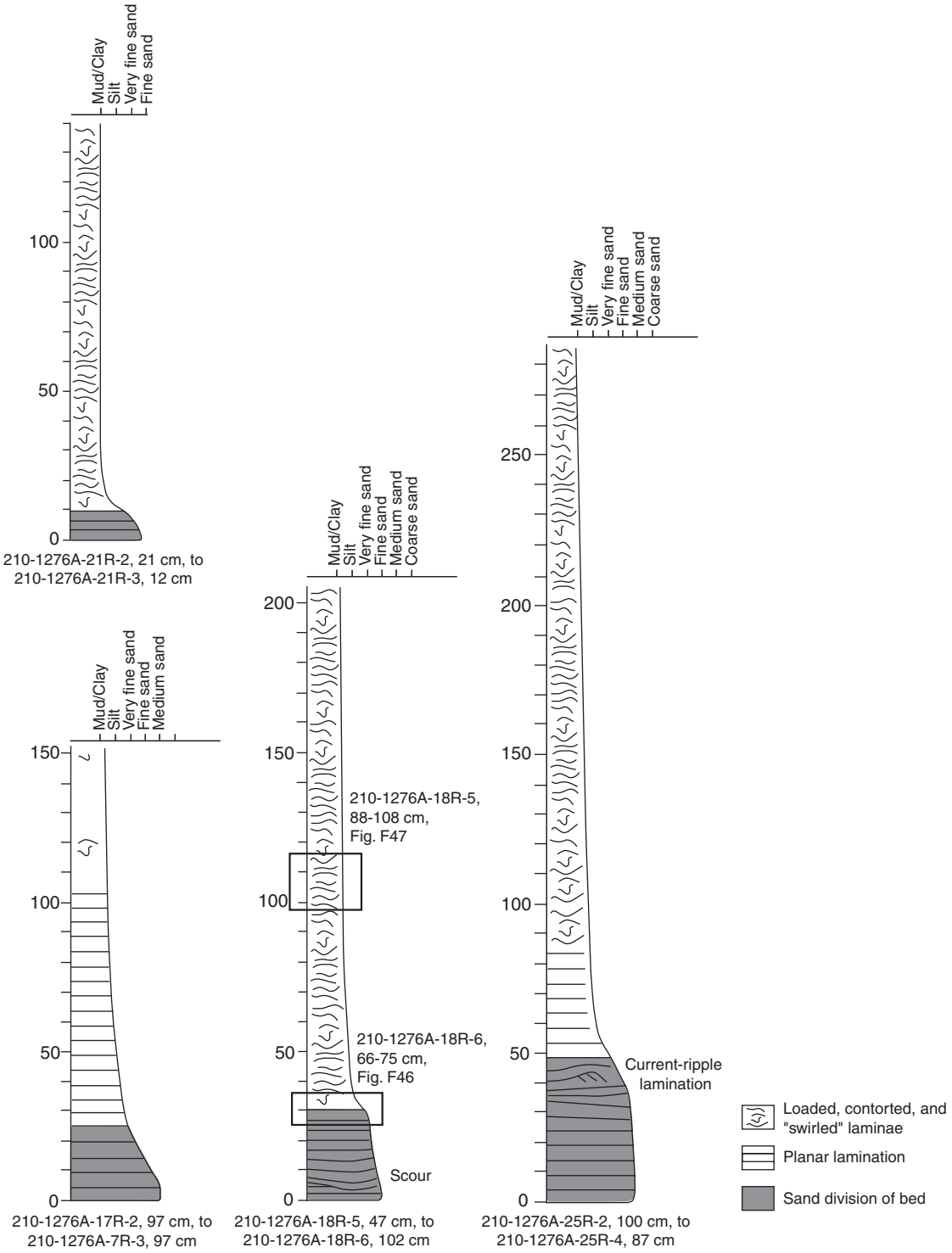

Figure F46. Close-up of planar-laminated lower part of a grainstone → mudstone turbidite. The grain size fines upward irrespective of changes in color (Unit 3: interval 210-1276A-18R-6, 66–75 cm). See Figure **F45,** p. 168, for location within a very thick depositional unit.

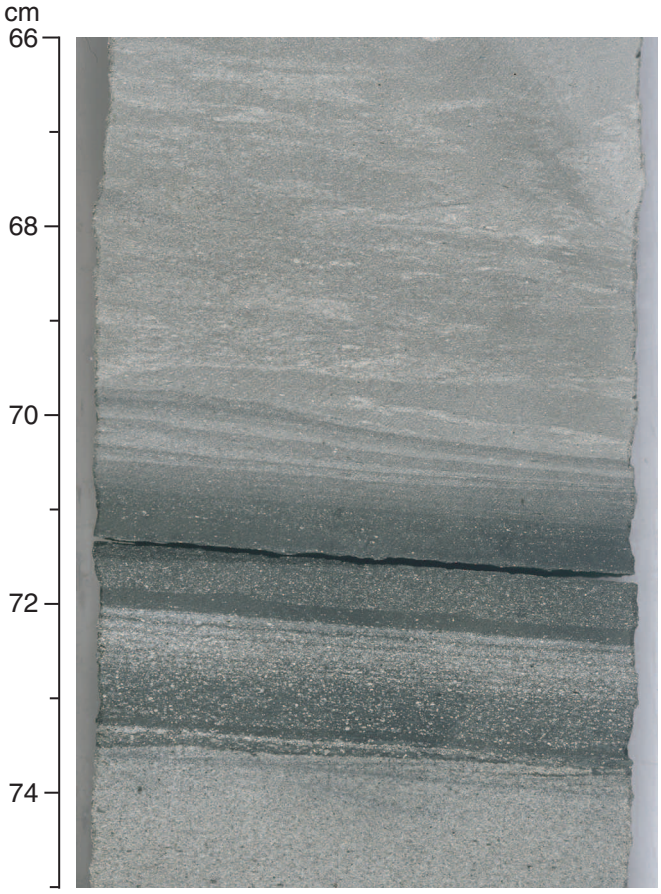

Figure F47. Close-up of soft-sediment deformation in the central part of a very thick turbidite from Unit 3. Over this interval, the sediment has a size of medium to fine silt. Note the evidence of ductile shear and microfolding at 100–108 cm (Unit 3: interval 210-1276A-18R-5, 88–108 cm). See Figure **F45,** p. 168, for location within the very thick depositional unit.

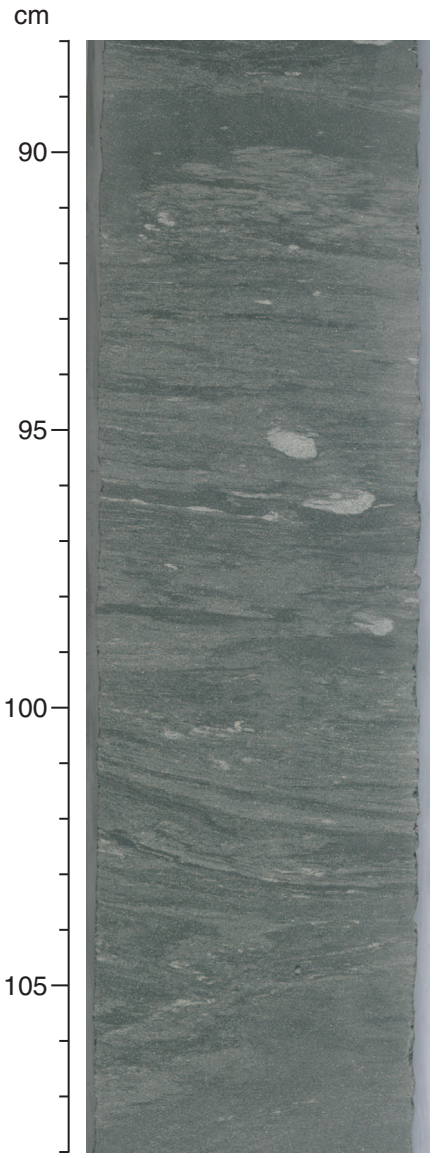

Figure F48. Photomicrographs in plane-polarized light showing examples of foraminifers from Unit 3. **A.** Keeled planktonic foraminifer (*Globotruncana orientalis*) of middle to late Maastrichtian age (center top) in Paleocene grainstone. Darker area is a sedimentary lithic clast (Sample 210-1276A-17R-4, 98–99 cm). **B.** Grainstone with large yellow phosphatic (P) grains (fecal pellets?) surrounded by a wide variety of planktonic foraminifers and other bioclastic debris, set in a darker clay matrix. Some foraminifers are partly filled by carbonate cement and pyrite (Sample 210-1276A-18R-6, 88–99 cm).

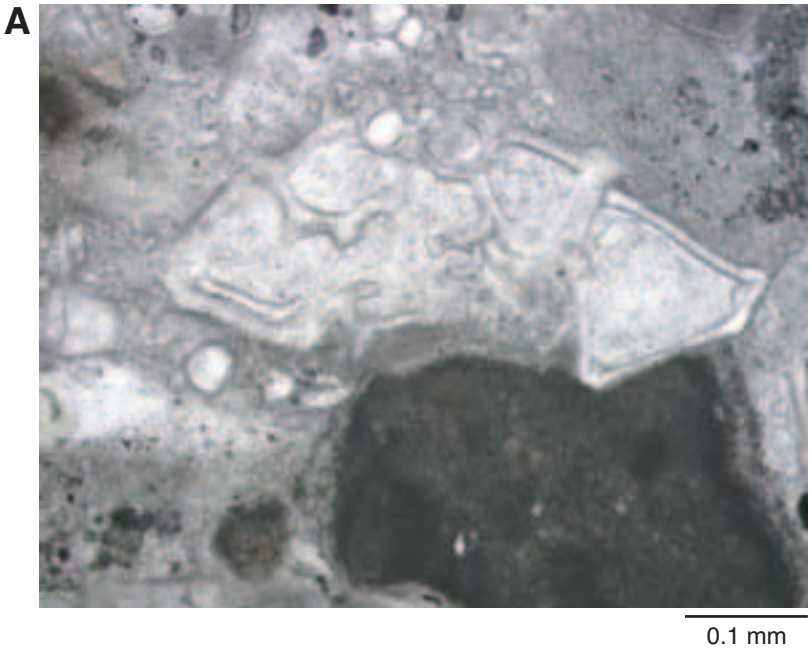

Figure F49. Close-up of calcareous sandstone that extends from a scoured base at 47 cm into a finely laminated, muddy top above 36 cm. Color variation in the turbidite is controlled mainly by relative amounts of calcite spar (pale patches) (Unit 3: interval 210-1276A-23R-1, 34–57 cm).

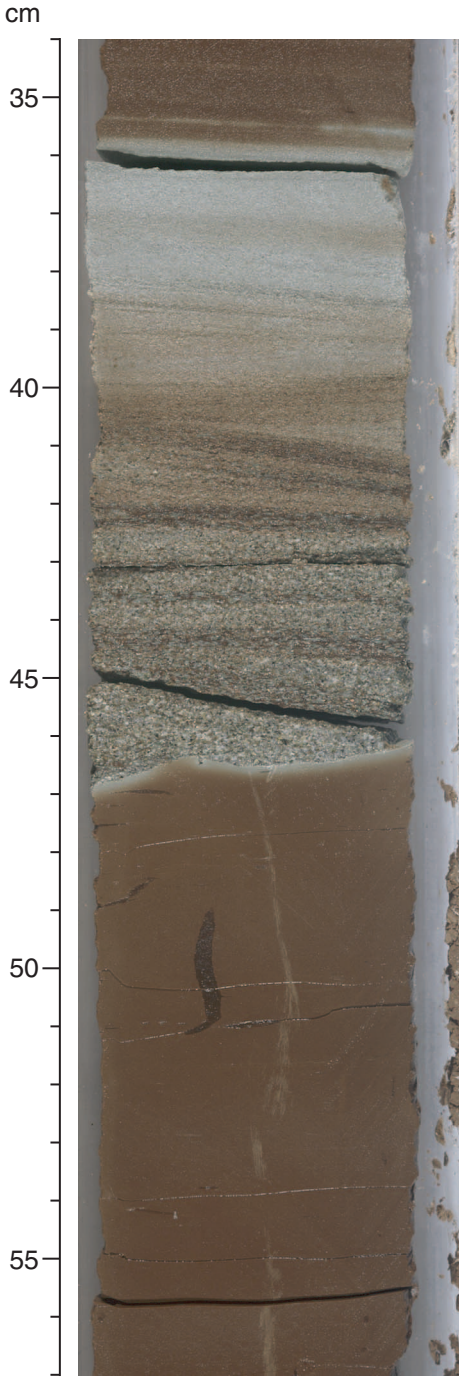

Figure F50. Close-up of sandstone turbidite cut by *Zoophycos* burrows. This interval shows complex variations in primary grain size that are interpreted to result from fluctuations in current strength during emplacement (Unit 3: interval 210-1276A-22R-2, 80–100 cm).

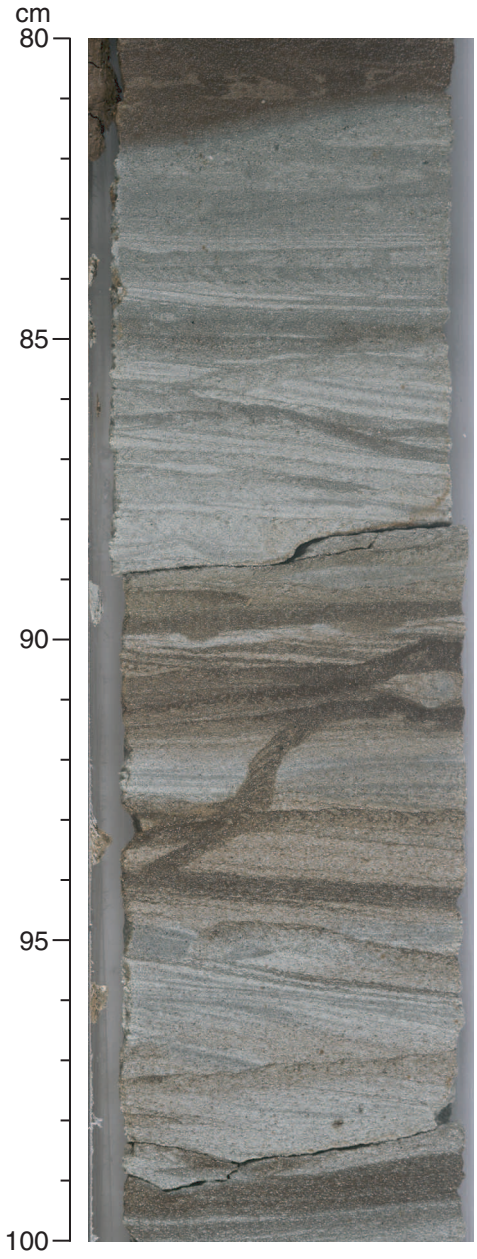

Figure F51. Photomicrographs in plane-polarized light of an interval that is associated with high magnetic susceptibility near the top of Unit 3 (Sample 210-1276A-15R-4, 136–138 cm). **A.** Large, subrounded volcanic clast in upper right corner is composed of colorless glass (C) with plagioclase microlites (P) and an isolated vesicle (V). The surrounding matrix includes biotite (B) and quartz (Q). **B.** Concentration of smaller opaque minerals (O) and large, mostly euhedral quartz crystals (Q) within a lamina. Given the high magnetic susceptibility of this interval, the opaque minerals are probably magnetite.

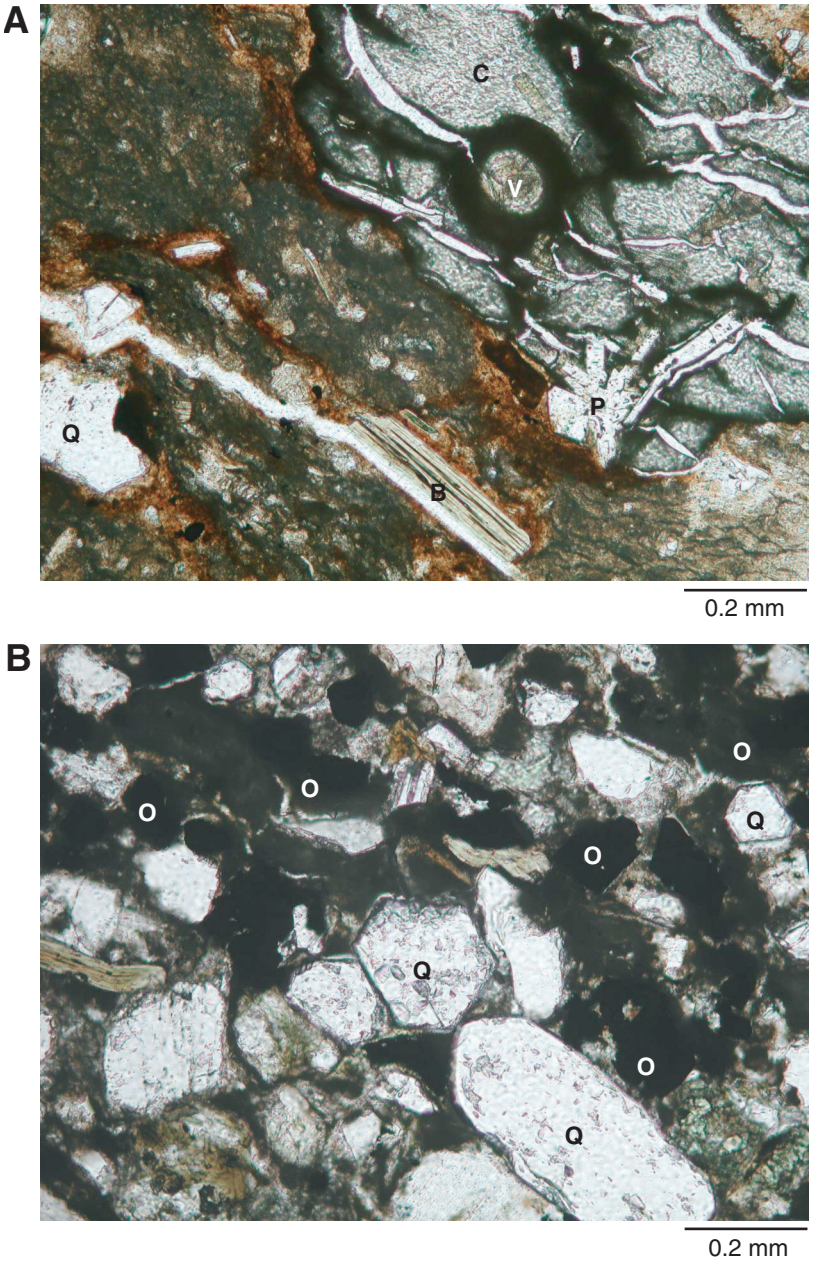

Figure F52. Photomicrograph of a tuffaceous siltstone that has been highly altered and replaced by carbonate (white). Despite alteration, local relict shard and vesicle textures are preserved (e.g., circled area), which indicate the former presence of vitric pyroclasts (Unit 3: Sample 210-1276A-24R-5, 82–84 cm).

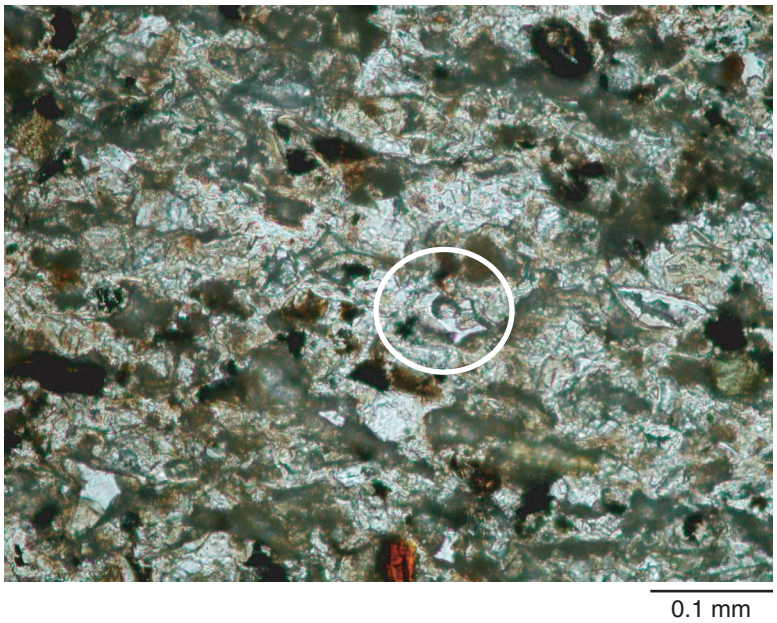

Figure F53. Close-up of the middle part of a well-sorted, graded grainstone → mudstone turbidite showing unusual wavy or wispy lamination. The more porous, paler grainstones appear to have been preferentially cemented during diagenesis, whereas laminae richer in clay particles (darker) were more compacted during diagenesis (Unit 3: interval 210-1276A-18R-7, 85–105 cm).

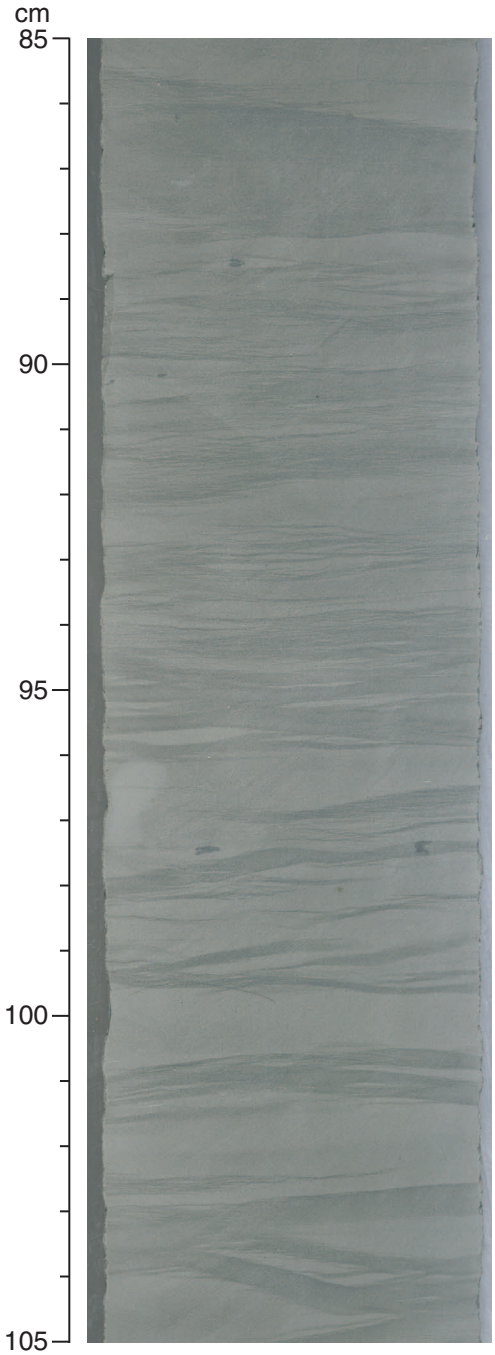

Figure F54. Close-up of the inferred location of the Cretaceous/Tertiary boundary between 41 and 47 cm. Note the scattered coarser grains in two mudstone intervals (54–58 cm and 41–43 cm). The burrowed unit between 47 and 54 cm is marlstone. See text for discussion of possible significance (interval 210-1276A-21R-4, 39–65 cm).

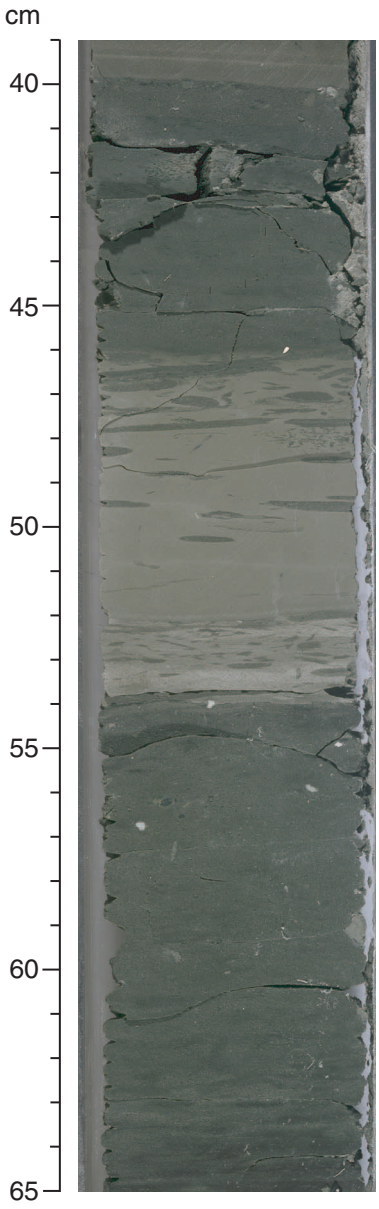

Figure F55. Close-up of stylolites (pressure-solution effects) in graded grainstones. These are anastomosing seams enriched in clays and other insoluble material (Unit 3: interval 210-1276A-21R-4, 117–128 cm).

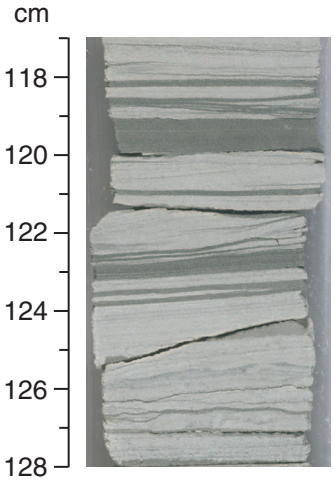

Figure F56. Close-up of deformed siltstone laminae characterized by millimeter-scale recumbent folds and fine-scale ductile-flow features. These features reflect shearing during deposition (Unit 3: interval 210-1276A-17R-5, 83–88 cm).

Figure F57. Close-up of typical muddy sandstone of Unit 4. Note the poorly sorted, muddy nature of the reddish sediment (interval 210-1276A-29R-1, 90–120 cm).

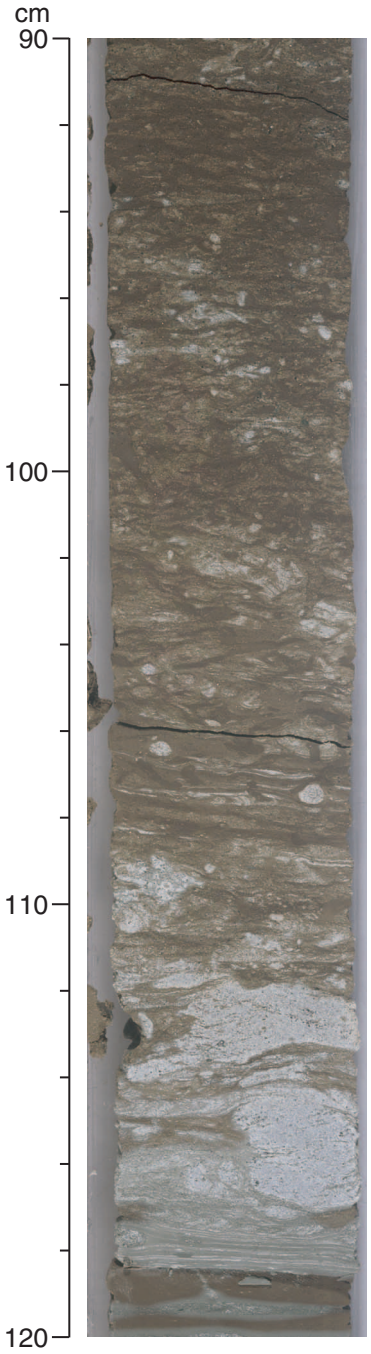

Figure F58. Photomicrographs of hematitic sandy mudstone from Unit 4 (Sample 210-1276A-25R-6, 73–77 cm). The same view is shown in (**A**) plane-polarized light and (**B**) cross-polarized light. Pictured are large angular grains of quartz (Q) and feldspar (F) and a subrounded meta-sedimentary fragment (M). Sorting is poor, and the clay matrix is heavily pigmented by iron oxides. Note that in cross-polarized light both the quartz and the feldspar exhibit wavy or undulose extinction.

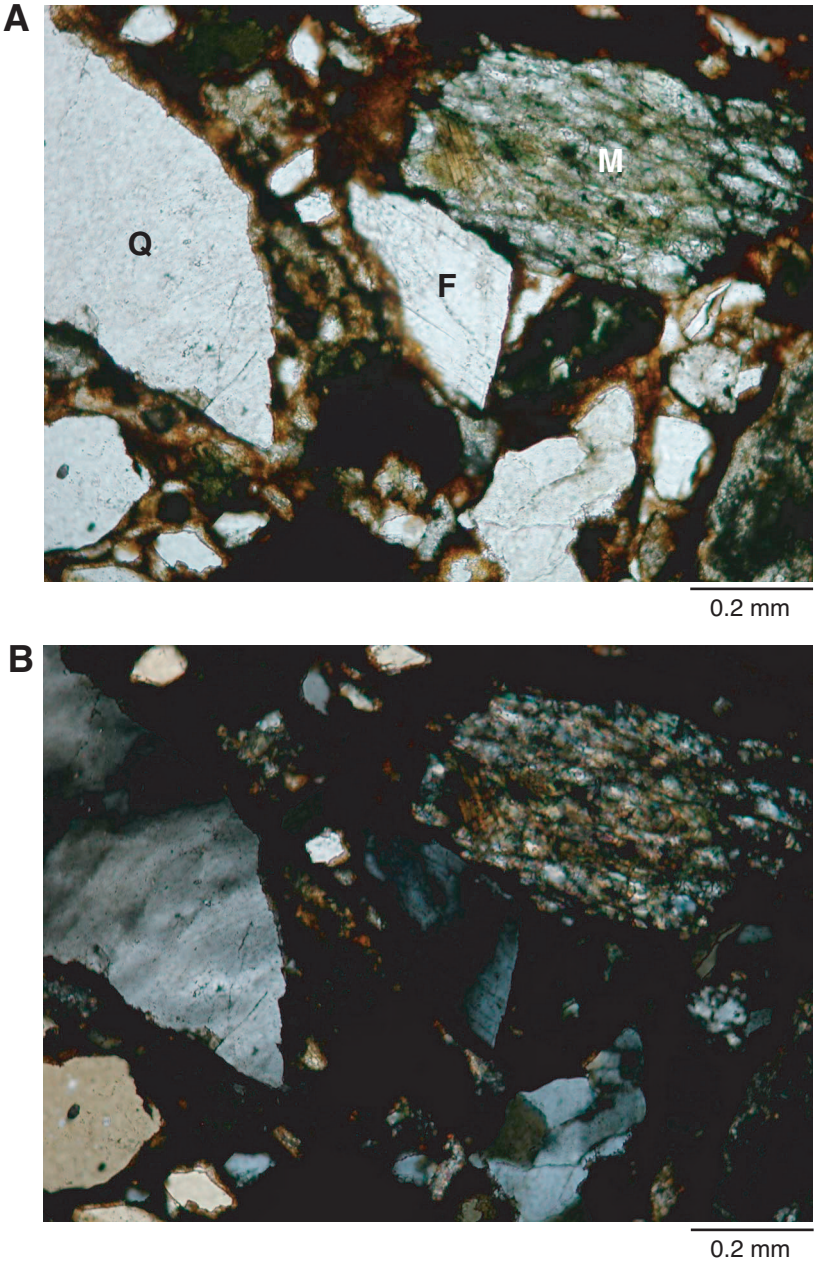

Figure F59. Photomicrographs of two siliciclastic intervals from Unit 4. **A.** From the top of the unit, in cross-polarized light. Large subangular plutonic clast composed of quartz (Q; white) and zoned, slightly sericitized feldspar (F; shades of gray) is set in a hematitic muddy matrix (Sample 210-1276A-25R-6, 73–77 cm). **B.** From the middle of the unit, showing the base of a sandy turbidite bed in abrupt contact with underlying darker mudstone. The turbidite has large grains of quartz (Q; white) and glauconite (G; green) in a finer sandy matrix. The texture is bimodal (Sample 210-1276A-27R-6, 11–14 cm).

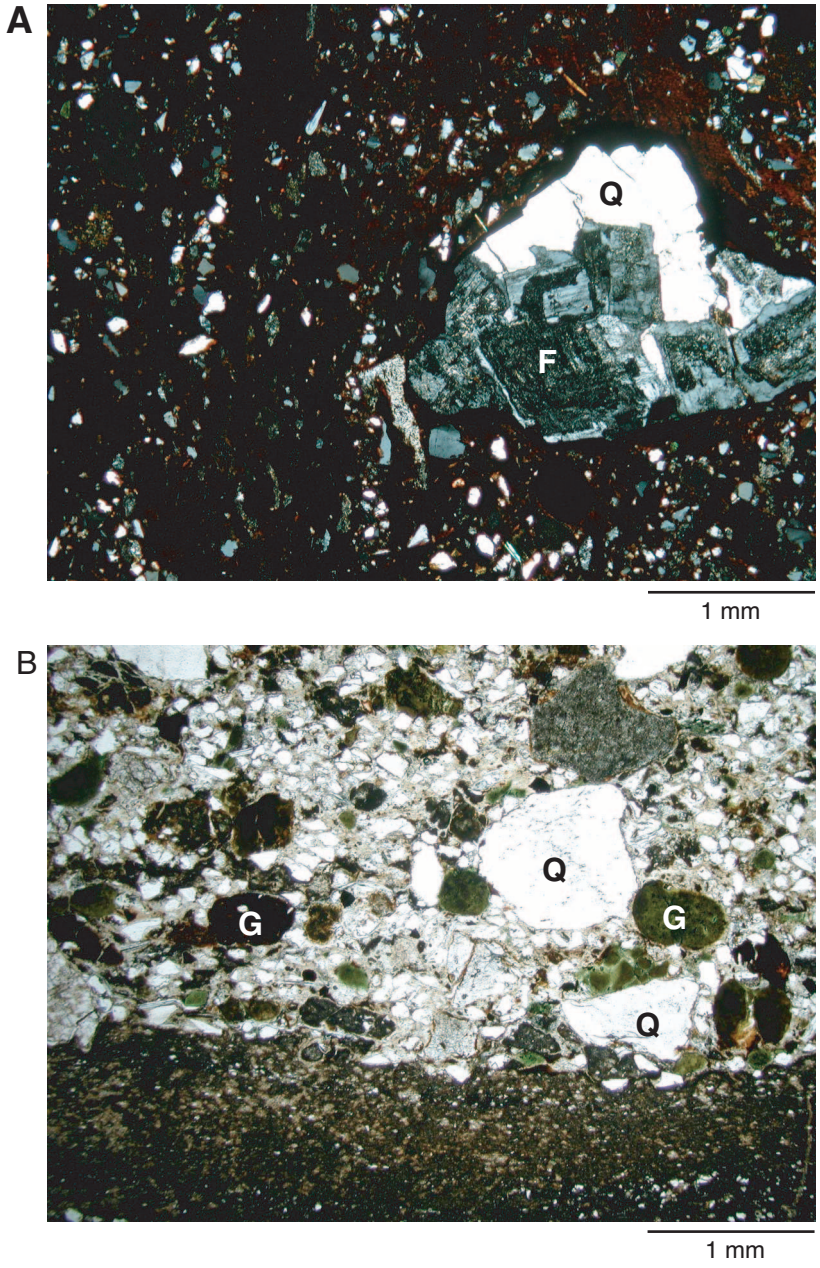

Figure F60. Photomicrograph of agglutinated foraminifers (F; rounded to elongate) in Unit 4 exhibiting crude chamberlike features. The view is in plane-polarized light (Sample 210-1276A-25R-6, 73–77 cm).

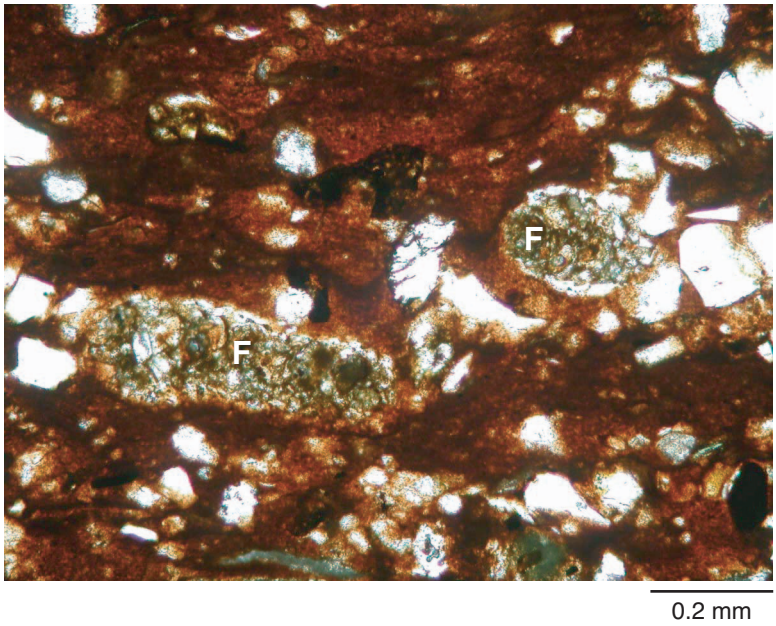

Figure F61. Close-up of thin, well-sorted, cross-laminated sandstone (35–36 cm) between burrowed muddy sandstone below and laminated → massive mudstone above. The thin sandstone is interpreted to be the top of the underlying muddy sandstone that was reworked into a train of current ripples by a muddy turbidity current (Unit 4: interval 210-1276A-29R-1, 29–39 cm).

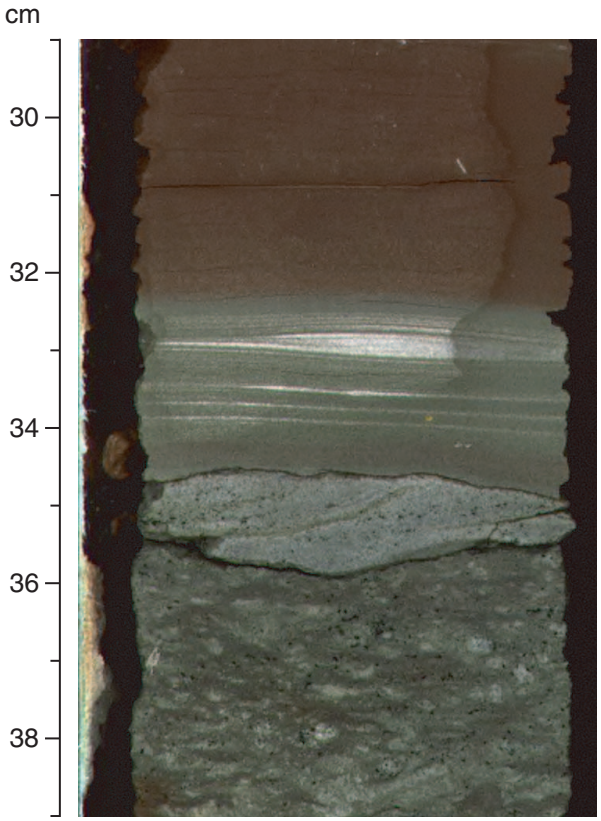

Figure F62. Close-up of color banding resulting from redox-controlled alteration of mudstones and siltstones (Unit 4: interval 210-1276A-27R-4, 110–133 cm).

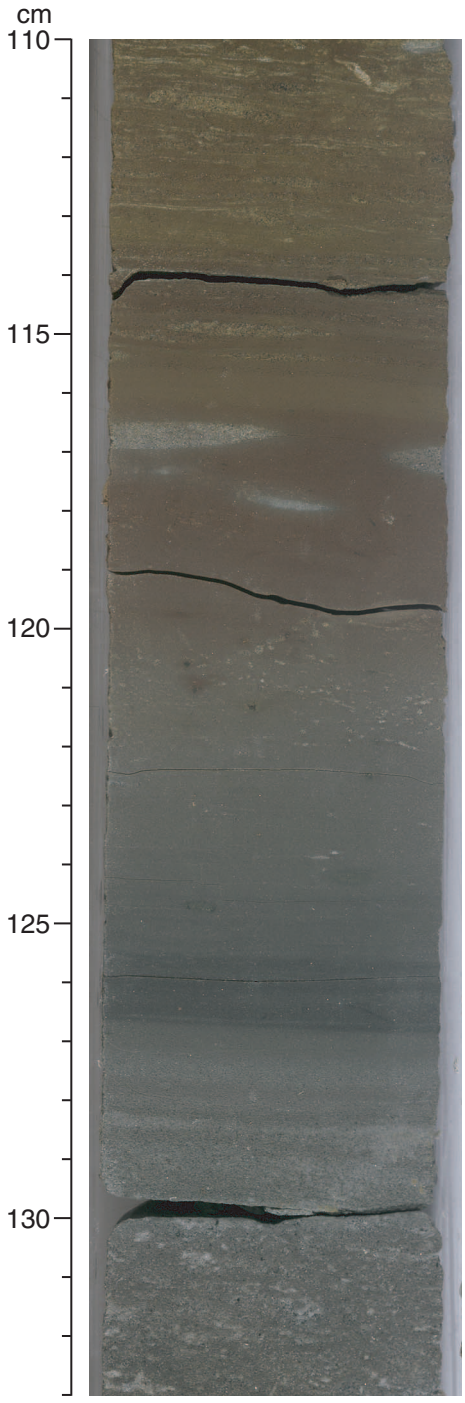

Figure F63. Close-up of graded sandstone turbidite (72–83 cm), passing up through planar- and ripple-laminated divisions into planar-laminated, fine-grained sandstone and then mudstone (70–72 cm). The lower part of the image (88–94 cm) is black shale below burrowed claystone (83–88 cm) (Subunit 5A: interval 210-1276A-32R-3, 70–95 cm).

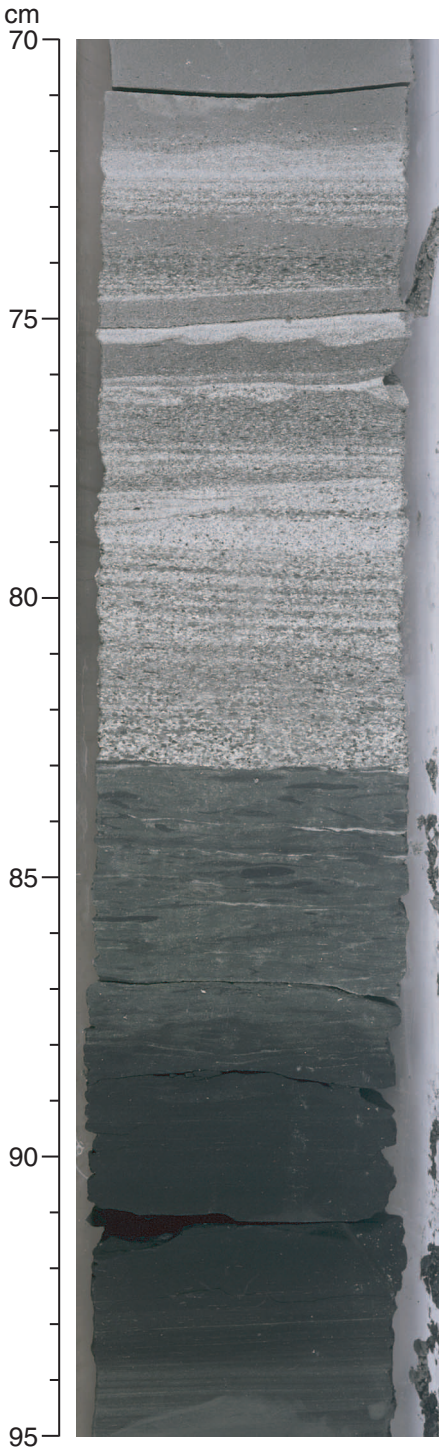

Figure F64. Close-up of a graded sandstone turbidite with a slightly scoured base (49 cm), overlain first by planar lamination and then a convolute division, above which there is a sharp passage into laminated mudrock. The greenish gray bioturbated mudrock beneath the turbidite is a hemipelagic background deposit (interval 210-1276A-32R-1, 39–54 cm).

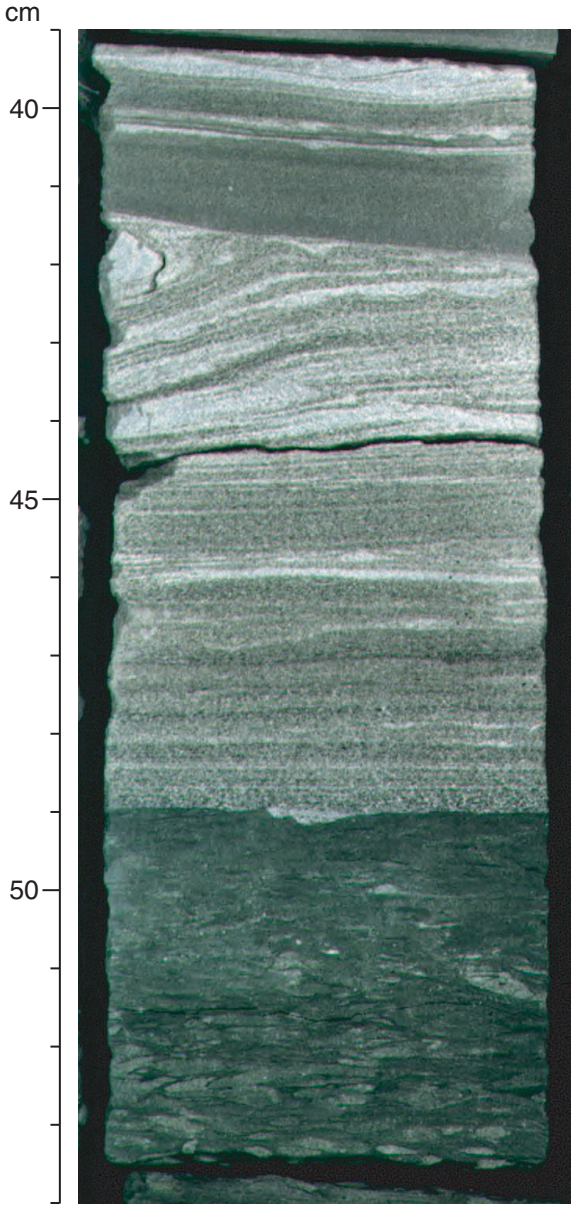

Figure F65. Close-up of siltstone turbidite, showing a sharp scoured base (103 cm), overlain first by current-ripple cross lamination (101–103 cm), then by low-angle cross lamination with some internal loading features (94–101.5 cm), followed by a featureless mudstone top (Subunit 5A: interval 210-1276A-31R-4, 93–105 cm).

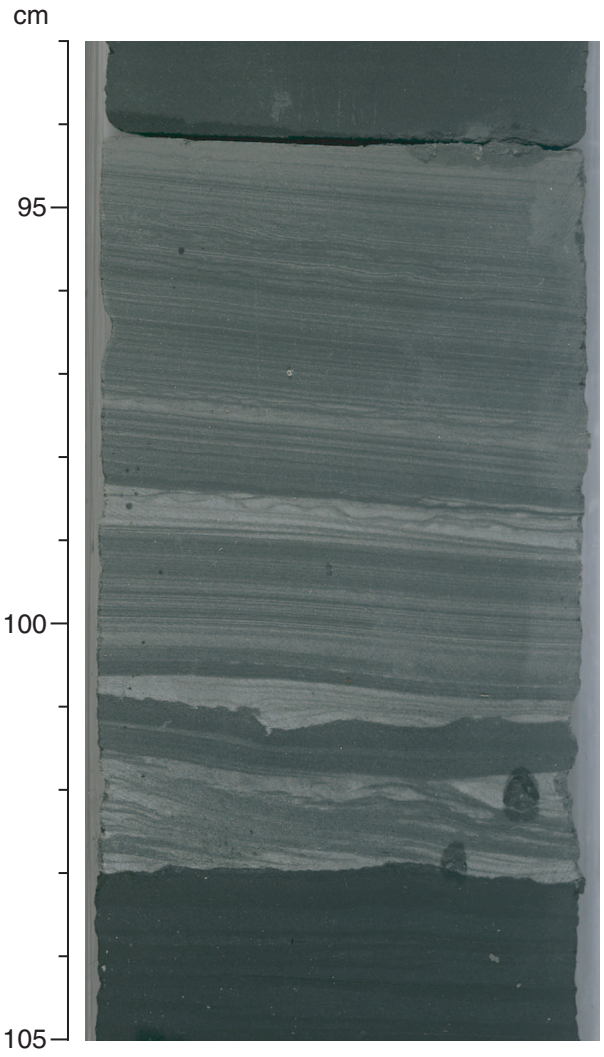

Figure F66. Close-up of very finely laminated carbon-rich claystone (black shale) (46–54 cm), with bioturbated greenish claystone or mudstone above and below (Subunit 5A: interval 210-1276A-32R-2, 41–56 cm).

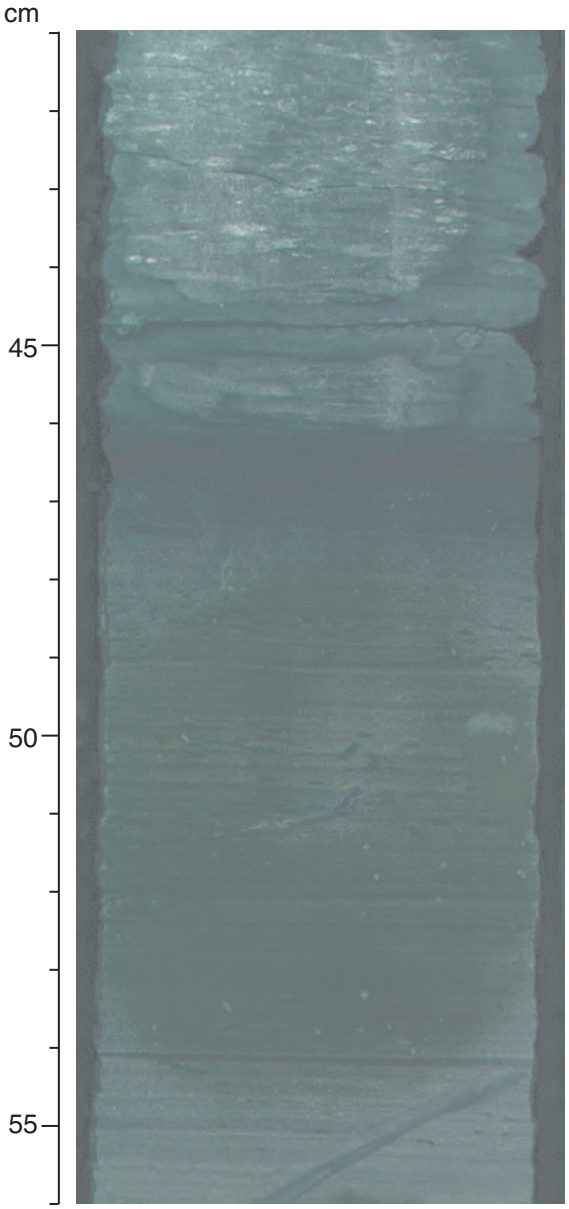

Figure F67. Close-up of very thinly laminated claystone (24–25 cm), overlain by a graded siltstone/mudstone interval (18–23.5 cm), then by very thinly laminated claystone (black shale) (12.5–18 cm), passing upward into weakly laminated, partly burrowed (8–12.5 cm) claystone. The paler claystone is burrowed down into the top of the dark laminated claystone at 12.5 cm (Subunit 5A: interval 210-1276A-33R-3, 8–25 cm).

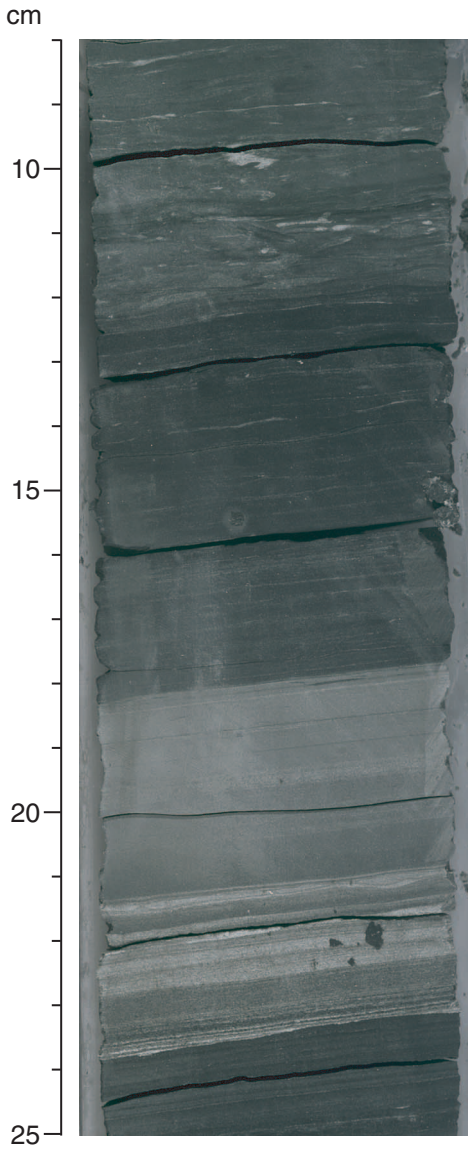

Figure F68. Close-up of a whole-core photograph including very finely laminated marlstones (black shales) correlated with OAE 2. Black shales occur at 19–60 cm (i.e., extending above the interval shown) and at 74–104 cm. The interbedded sediments are greenish and grayish fine-grained calcareous sandstones and calcareous mudstones (Subunit 5A: interval 210-1276A-31R-3, 40–106 cm).

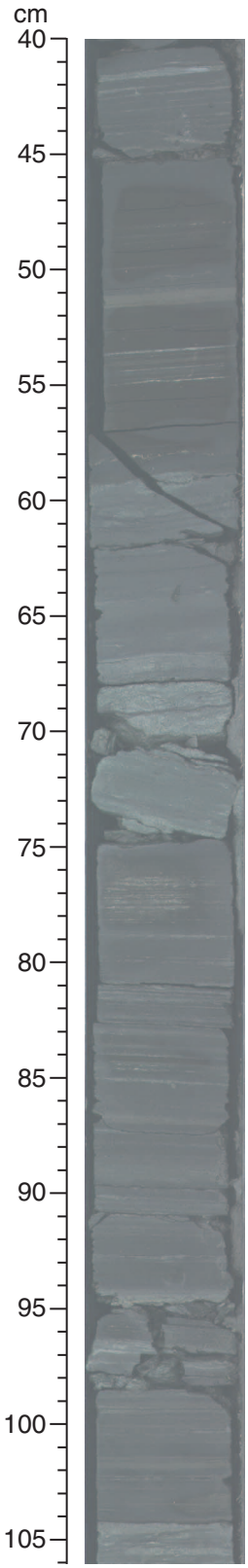

Figure F69. Close-up of massive mudstone containing a siltstone base (112–114 cm) and overlying greenish gray claystone (106–112 cm). This is interpreted to be a silt-mud turbidite redeposited from higher on the continental slope; it is overlain by burrowed hemipelagic claystone (Subunit 5B: interval 210-1276A-39R-5, 106–117 cm).

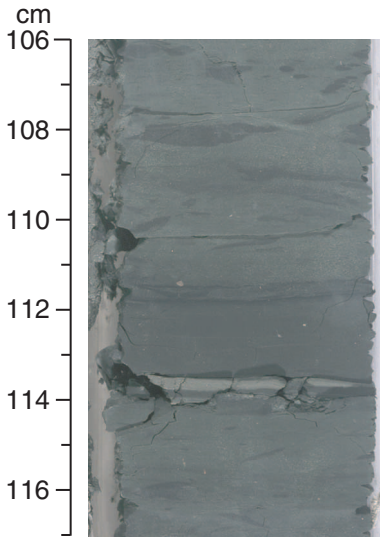

Figure F70. Close-up of very finely laminated black shale with planar siltstone laminae and a small siltstone lens (at 95 cm). See text for alternate hypotheses concerning the origin of these laminated sediments (Subunit 5B: interval 210-1276A-43R-2, 86–119 cm).

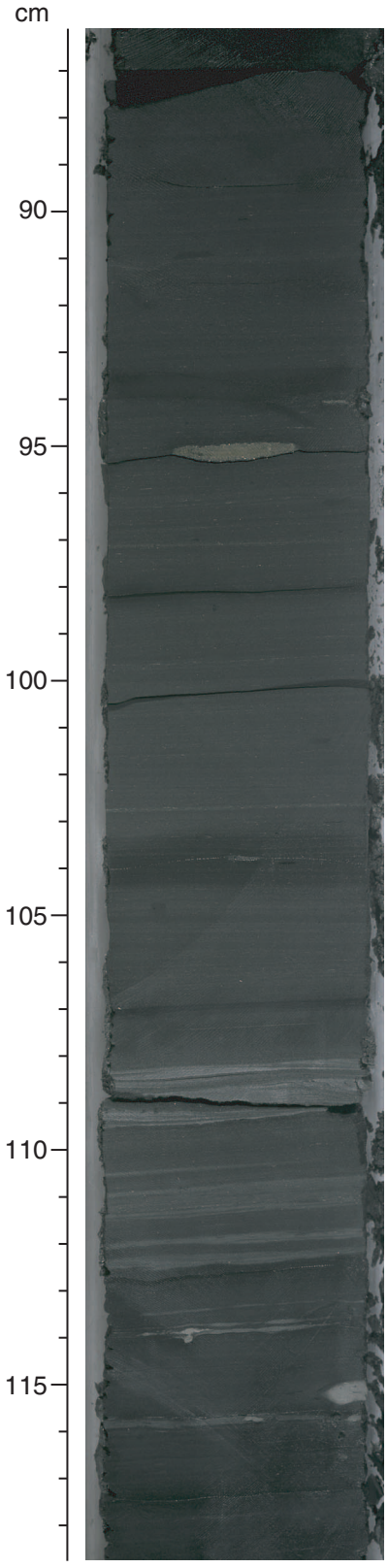

Figure F71. Close-up of burrowed mudstone (101–105 cm), overlain by very finely laminated claystones (88–101 cm), and then passing up into a brilliantly colored interval (80–88 cm) interpreted to be caused by seafloor oxidization of black shale. The spotted appearance is mainly the result of iron oxide segregation, although some burrowing is also present near the top of the image (Subunit 5B: interval 210-1276A-36R-6, 80–105 cm).

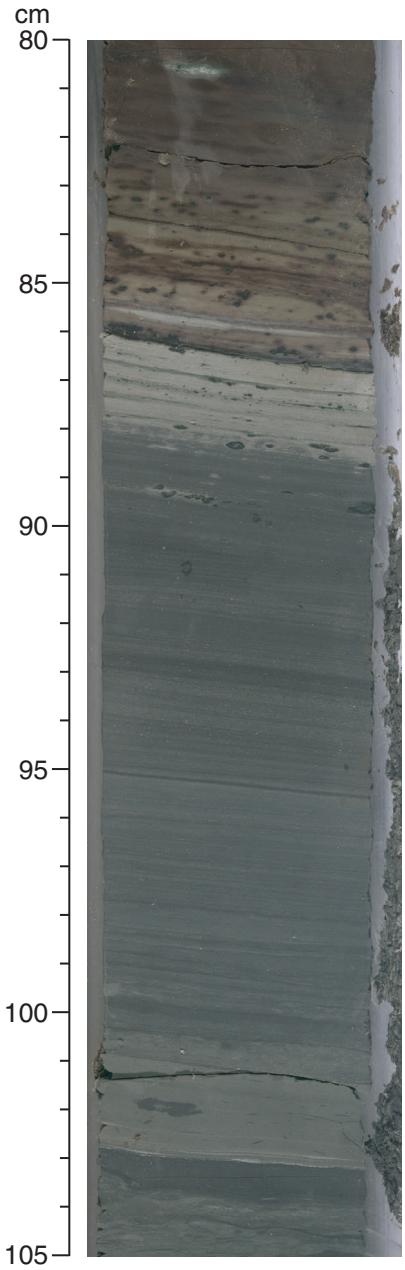

Figure F72. Close-up of a graded sandstone → siltstone → mudstone turbidite showing a graded basal division (110–112 cm), well-developed planar lamination (107–110 cm), overlain in turn by mainly cross lamination (90.5–107 cm), and then by planar lamination (84–90.5 cm), passing into laminated siltstone and mudstone (80–84 cm) (Subunit 5B: interval 210-1276A-45R-2, 80–115 cm).

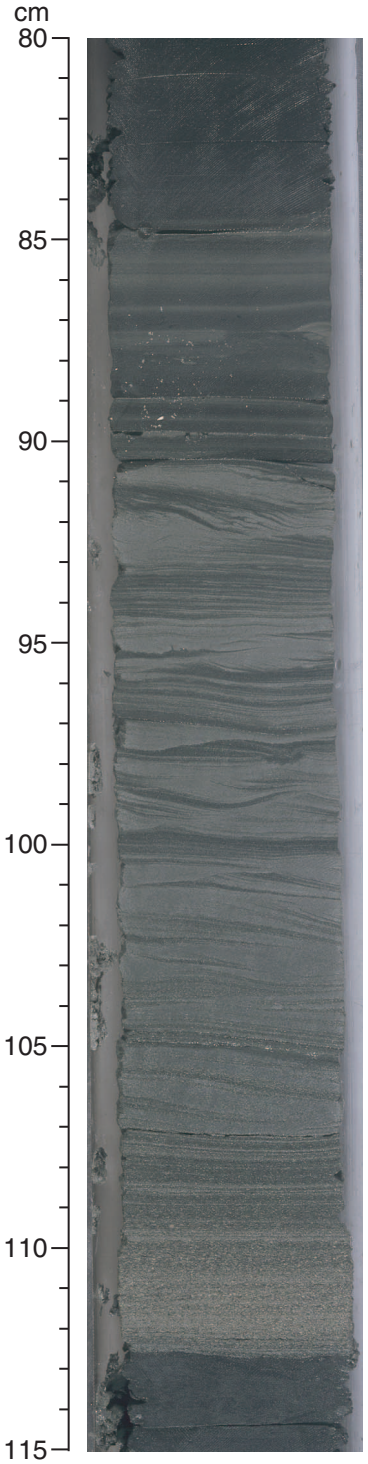

Figure F73. Close-up of spectacular convolute lamination (52–61 cm) in the upper part of graded sandstone turbidite. The convolute lamination tends to form in material of very fine sand size, mostly found toward the top of individual sandstone turbidites. The pale color of the lower part of the image (68–74 cm) is the result of well-developed calcite-spar cement in a well-sorted, porous sandstone (Subunit 5B: interval 210-1276A-61R-4, 50–75 cm).

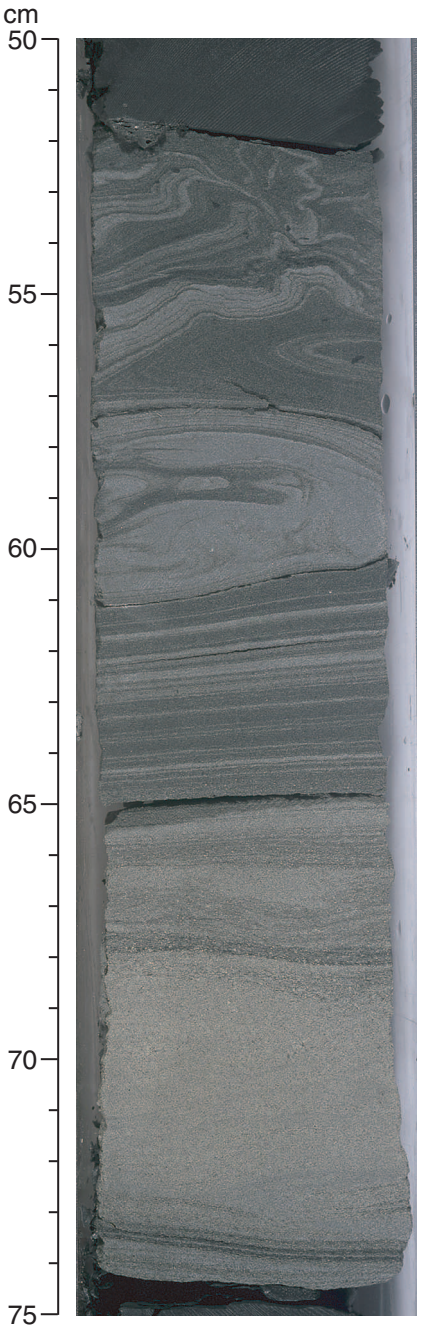

Figure F74. Comparison of sedimentary structures visible on a core photograph compared to a CT scan viewed from a different angle. **A.** Core photograph. Planar, wavy, and cross lamination. **B.** CT scan. Cross lamination is visible in the same interval. The photograph and the CT scan show a strike view and a dip view, respectively. The CT scan has the advantage of showing the maximum angle of dip of the bedding that cannot be readily observed in the split cores. This interval is included in Figure F72, p. 195 (Subunit 5B: interval 210-1276A-45R-2, 90–99 cm).

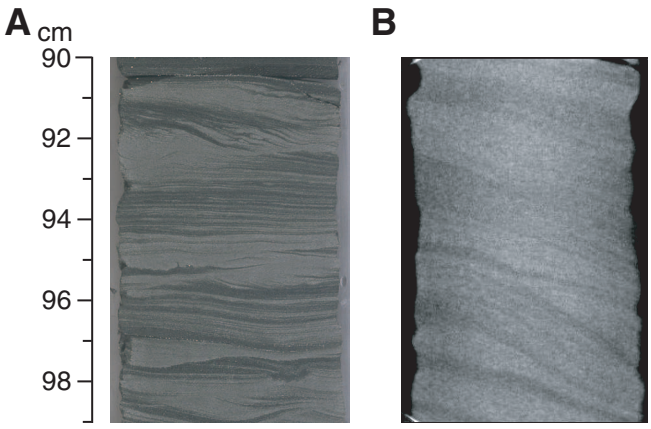

Figure F75. Close-up of descending cross lamination (120–125 cm) in a sandstone turbidite. This unusual structure may relate to progradation into a small seafloor depression during deposition from a turbidity current (Subunit 5B: interval 210-1276A-38R-5, 114–133 cm).

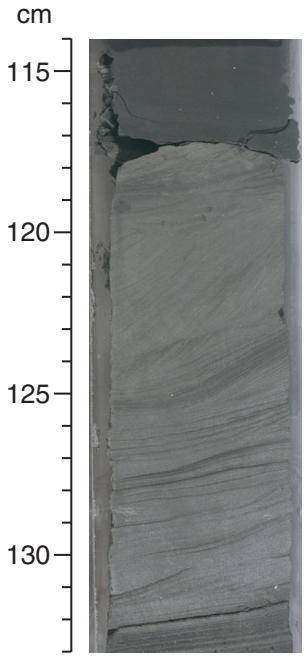

Figure F76. Close-up of fine sandstone interval of a graded fine sandstone → siltstone turbidite. Note the microflame structures (36.5 cm) that formed by syndepositional loading (Subunit 5B: interval 210-1276A-67R-5, 33–41 cm).

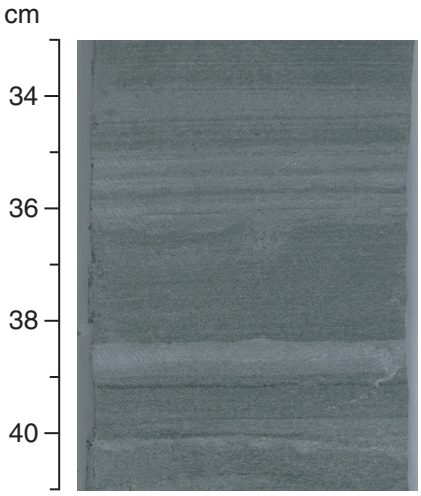

Figure F77. Close-up of granule-grade base of a turbidite overlain by a parallel-laminated sandstone division. Note the relatively well rounded grains and well-developed grading (Subunit 5B: interval 210-1276A-50R-4, 53–60 cm).

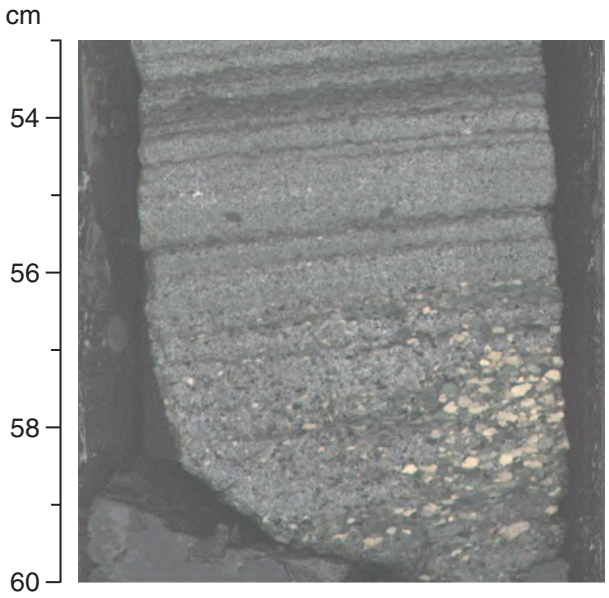

Figure F78. Coarse-grained sandstone turbidite with entrained mudstone rip-up clasts in a division of planar-laminated sandstone (71–77 cm) (Subunit 5B: interval 210-1276A-68R-3, 64–86 cm).

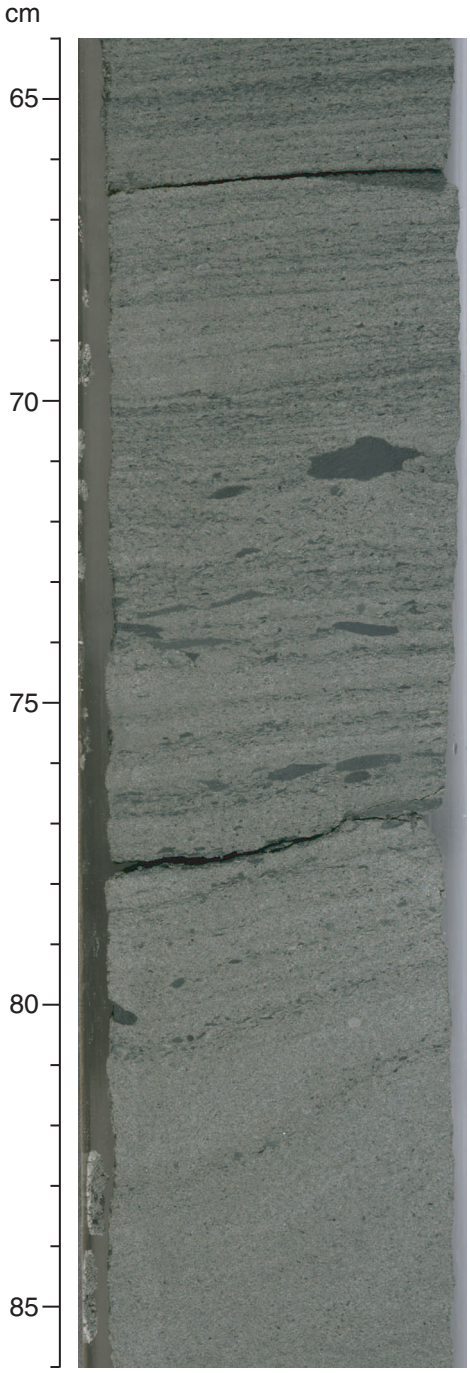

Figure F79. Close-up of part of a graded sandstone turbidite (44.5–63 cm) with scattered elongate mudstone rip-up clasts showing an upward decrease in grain size (Subunit 5B: interval 210-1276A-69R-2, 40–63 cm).

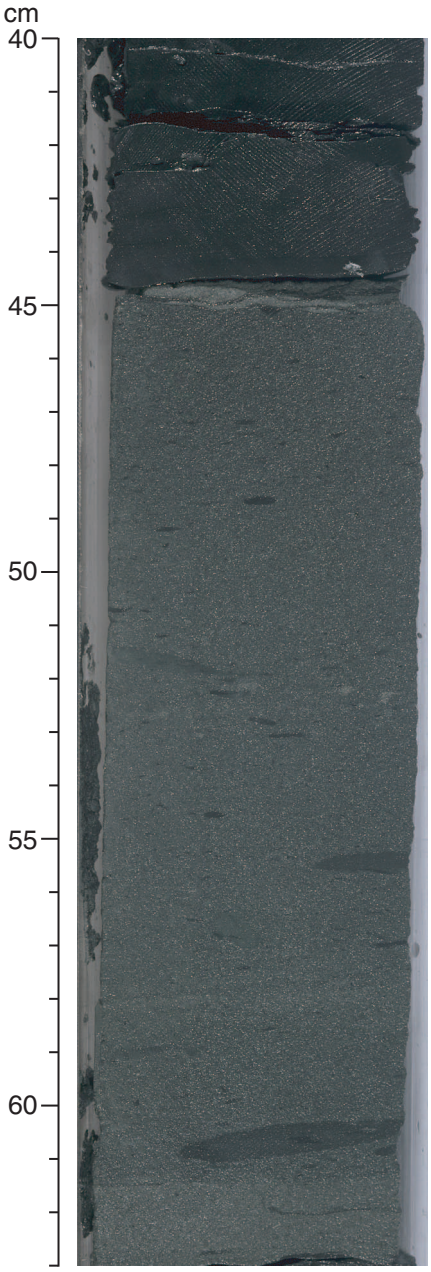

Figure F80. Close-up of very fine grained sandstone lamina with millimeter-sized, subrounded siltstone clasts. This is tentatively interpreted as the toe of a silty debris flow deposit, thicker examples of which are found in the upper part of underlying Subunit 5C (Subunit 5B: interval 210-1276A-62R-2, 102–107 cm).

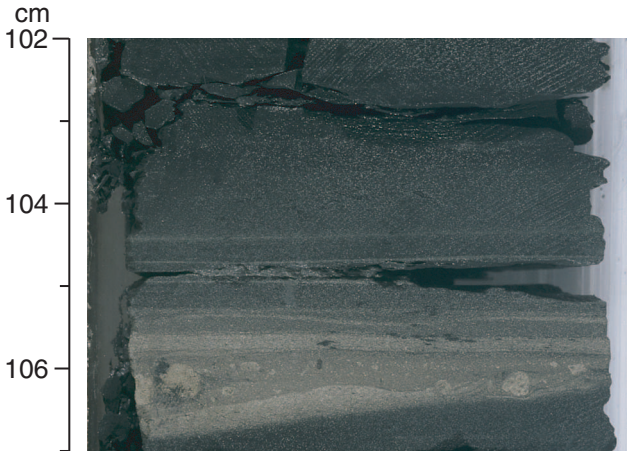

Figure F81. Close-up of laminae and very thin beds of fine-grained calcareous sandstone and siltstone in dark claystones. The thin intervals of fine sandstone/siltstone are interpreted as deposits from low-density turbidity currents (Subunit 5B: interval 210-1276A-40R-4, 124–131 cm).

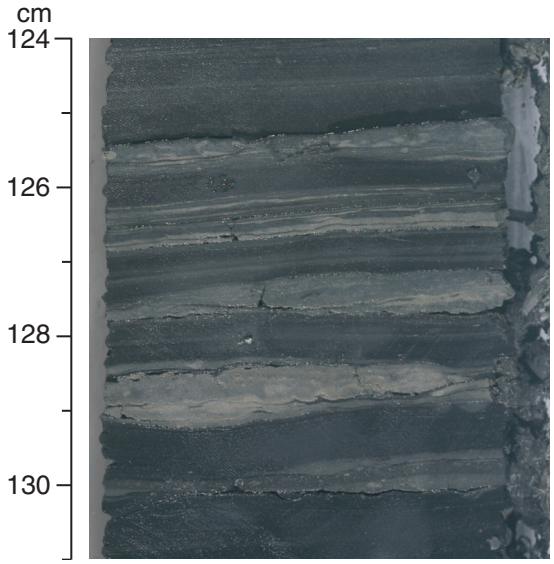

Figure F82. Close-up of a complex interval of turbidity-current deposition. Inclined laminae (99–102 cm) might record repeated deposition from low-density flows passing over a topographically irregular seafloor. The lenticular distorted interval above this (98–99 cm) may record the infill of local seabed relief. The interval from 86 to 98 cm is interpreted as a single sand → silt → mud turbidite, with a basal planar-laminated division (96–98 cm), followed by a climbing ripple division (90–96 cm), and then a convoluted division characterized by soft-sediment deformation (86–90 cm). A subsequent turbidity current deposited sand and silt above a scoured base at 86 cm. This interval as a whole illustrates a complex interplay between turbidity-current deposition and an inferred irregular seafloor topography (Subunit 5B: interval 210-1276A-72R-1, 80–103 cm).

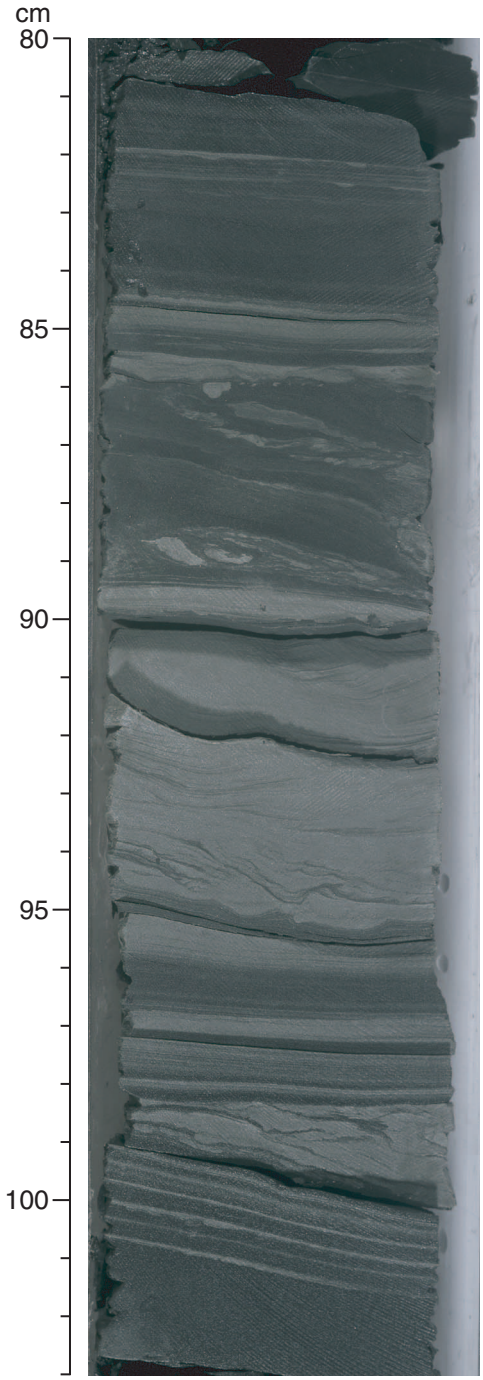

Figure F83. Photomicrograph of a silty sandstone in cross-polarized light to show components such as quartz (Q), biotite (B), and potassium feldspar (K) with cross-hatch twinning, as well as large enveloping crystals of carbonate (poikilotopic) cement (C; white where extinct) (Subunit 5B: Sample 210-1276A-54R-1, 63–66 cm).

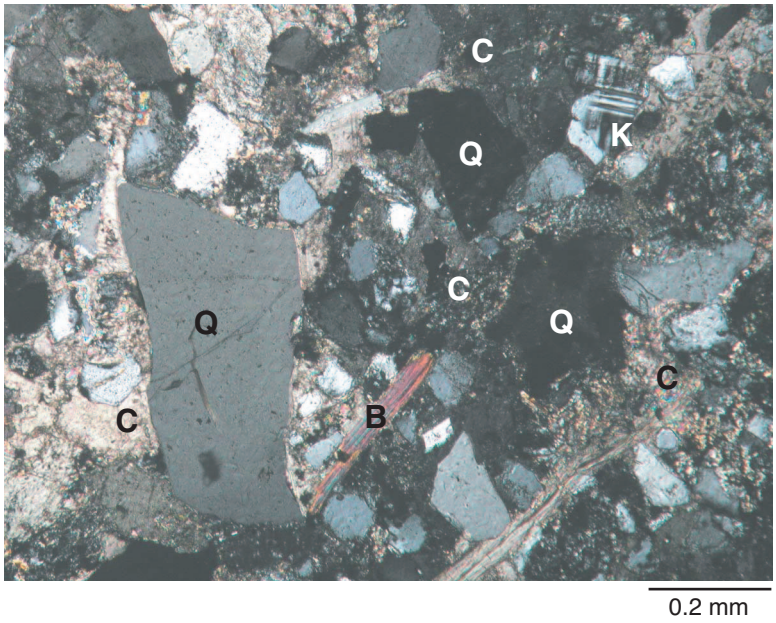

Figure F84. Low-magnification photomicrograph (plane-polarized light) of sandy siltstone with darker mudstone intraclasts (L) from Subunit 5B (Sample 210-1276A-69R-2, 50–53 cm). Bedding is vertically oriented in this view and outlined by the parallel alignment of the intraclasts.

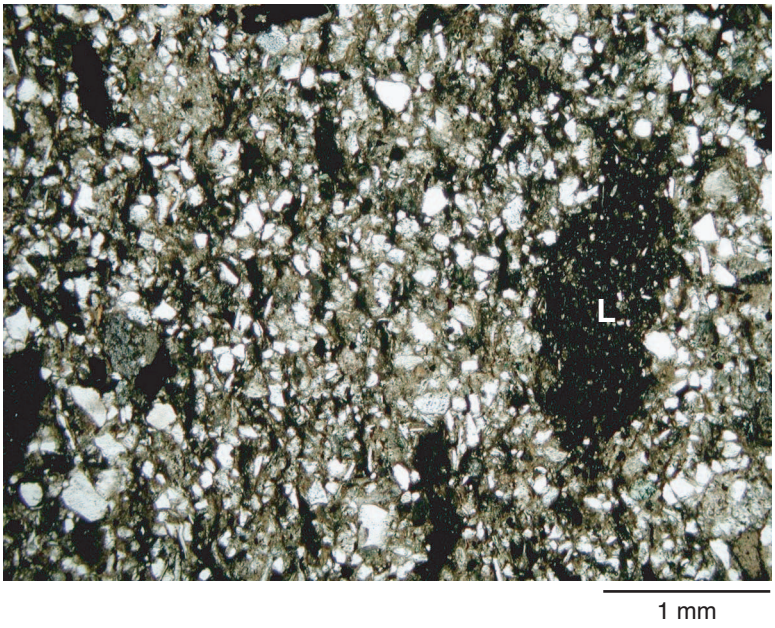

Figure F85. Photomicrograph of laminated terrigenous siltstone. The darker laminae are defined by micrite and fine platy components such as muscovite and biotite flakes (circled). Lighter laminae are dominated by quartz grains and carbonate cement. View in plane-polarized light (Subunit 5B: Sample 210-1276A-48R-3, 69–71 cm).

Figure F86. Photomicrograph of a grainstone in which calcareous grains are primarily smaller planktonic foraminifers (f) and reworked radiolarians (R), some with spines. The former are filled by colorless microspar, and the latter are filled and locally coated by darker micrite. Fine micrite (m) to microspar (S) between grains is likely siderite, according to XRD analyses of nearby sediments from this section (Subunit 5B: Sample 210-1276A-41R-2, 88–91 cm).

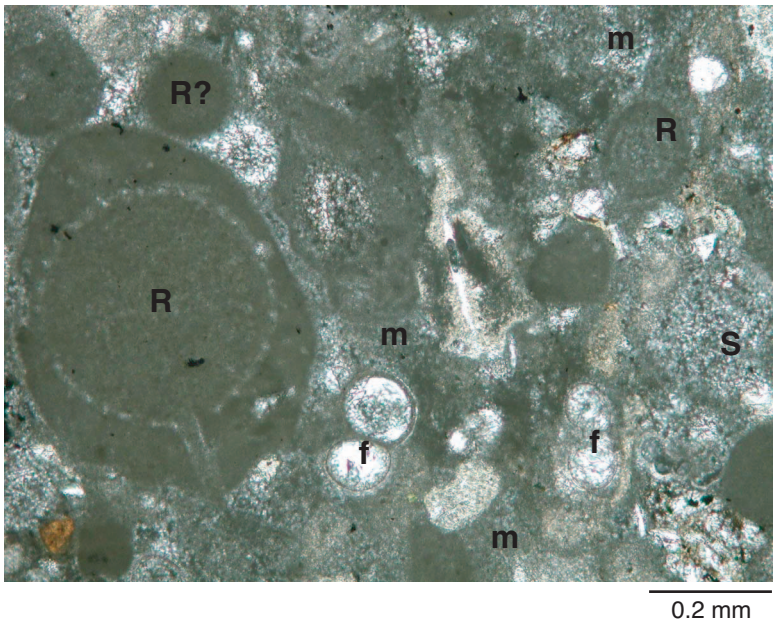

Figure F87. Close-up of massive mudstone with a fine sandstone/siltstone parting (74 cm), interpreted to be the product of a mud-rich, low-density turbidity current (Subunit 5C: interval 210-1276A-77R-2, 69–76 cm).

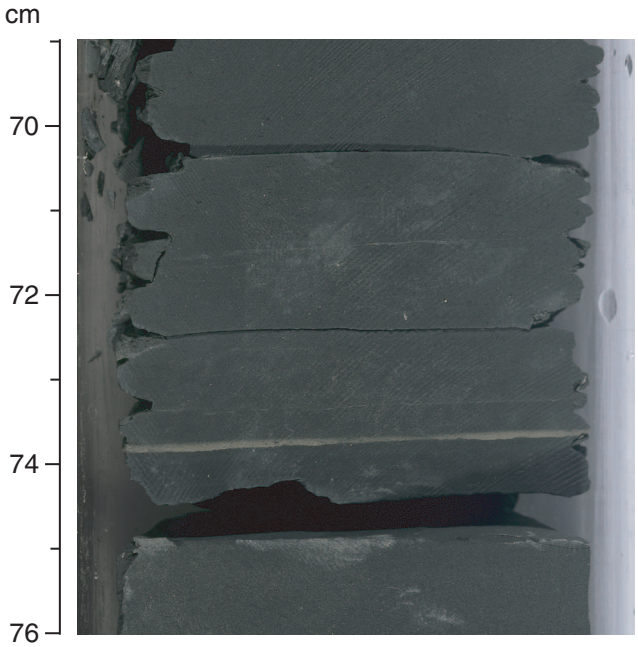

Figure F88. Repeated intervals of calcareous mudstones, each of which grades upward into a paler siltstone (<3 mm thick); these are interpreted to be the products of mud- and silt-rich, low-density turbidity currents (Subunit 5C: interval 210-1276A-77R-5, 98–106 cm).

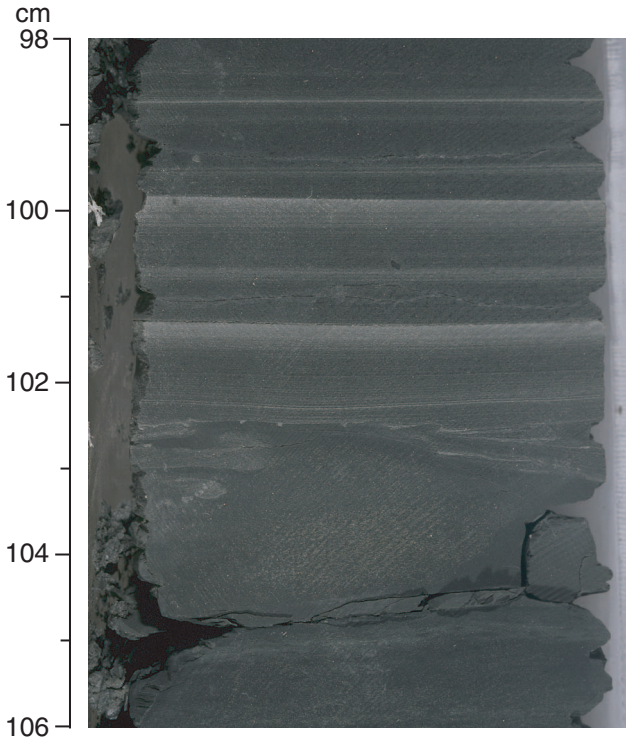

Figure F89. Close-up of finely laminated claystone, showing siltstone laminae, flame structures (41–42 cm), and tiny ripples or microload casts (39.5 cm). These sediments may represent deposits from low-density turbidity currents (Subunit 5C: interval 210-1276A-76R-2, 38–49 cm).

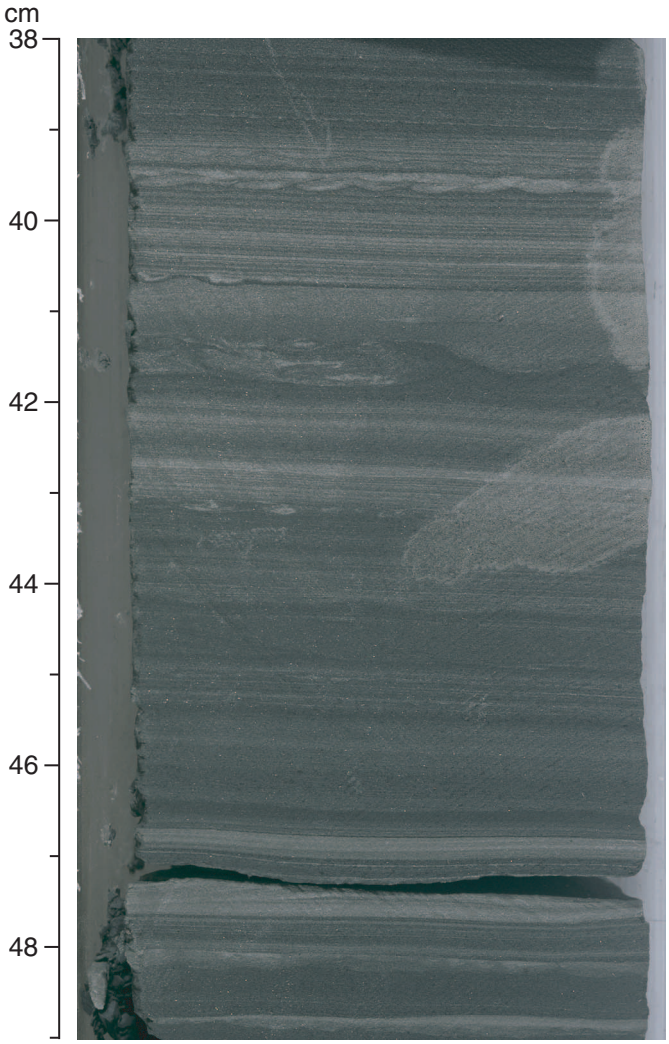

Figure F90. Close-up of one of the few black shales in Subunit 5C (95–104 cm); it passes transitionally into burrowed claystone above and below. This black shale was thermally altered in proximity to a diabase sill (Subunit 5C: interval 210-1276A-98R-1, 87–110 cm).

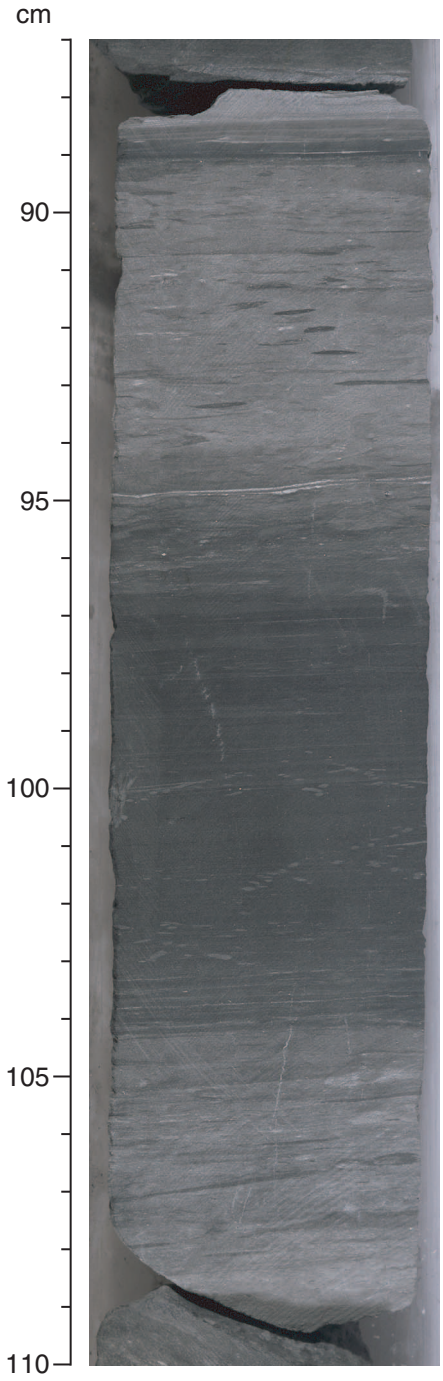

Figure F91. Close-up of massive silty sandstone containing dispersed sandstone clasts (11–13 cm) and interpreted as mass-flow deposits that characterize Subunit 5C (interval 210-1276A-77R-1, 3–19 cm).

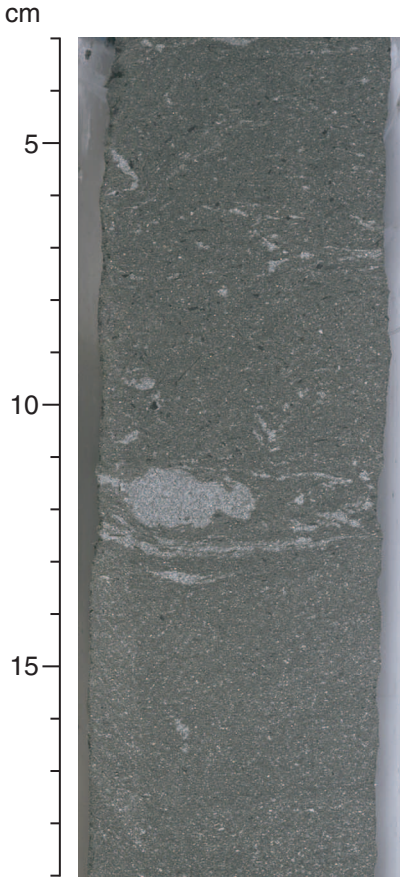

Figure F92. Close-up of silty sandstone, interpreted as a debris flow deposit, with "floating" large calcareous mudclast from 17 to 20 cm (Subunit 5C; interval 210-1276A-76R-3, 5–26 cm).

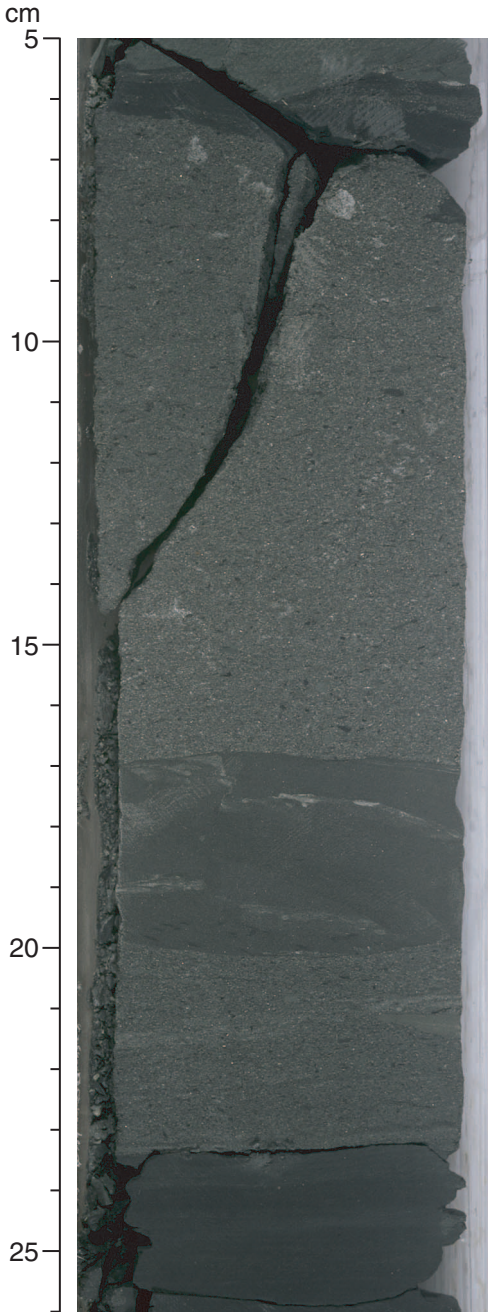

Figure F93. Close-up of claystones and thin-bedded lenticular siltstones affected by slumping and soft-sediment deformation (Subunit 5C: interval 210-1276A-75R-5, 50–73 cm).

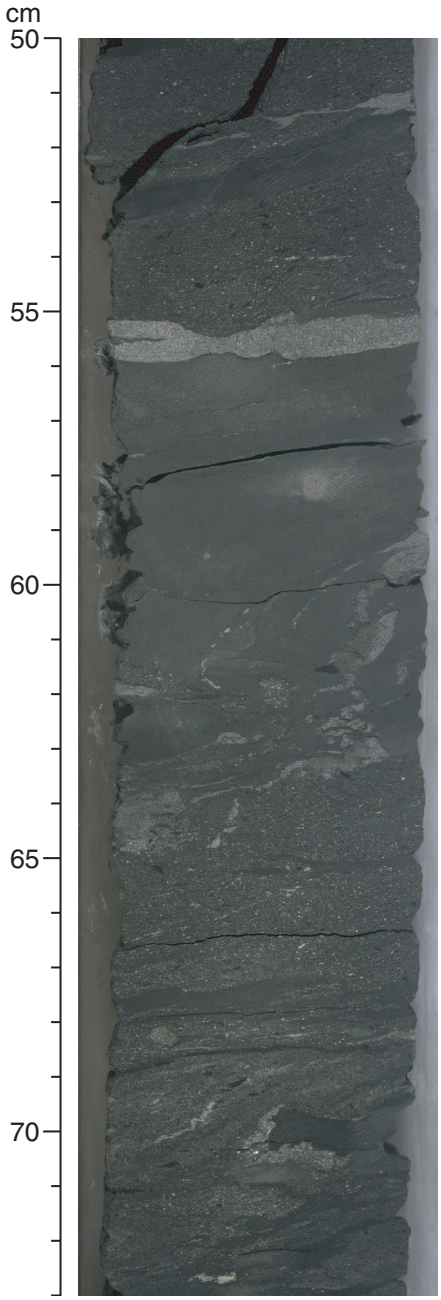

Figure F94. Close-up of middle part of a highly disorganized gravity-flow deposit showing parallel lamination (101–108 cm) passing upward into a convoluted and swirled interval (81–101 cm). Such flow features characterize Subunit 5C (interval 210-1276A-89R-6, 81–120 cm).

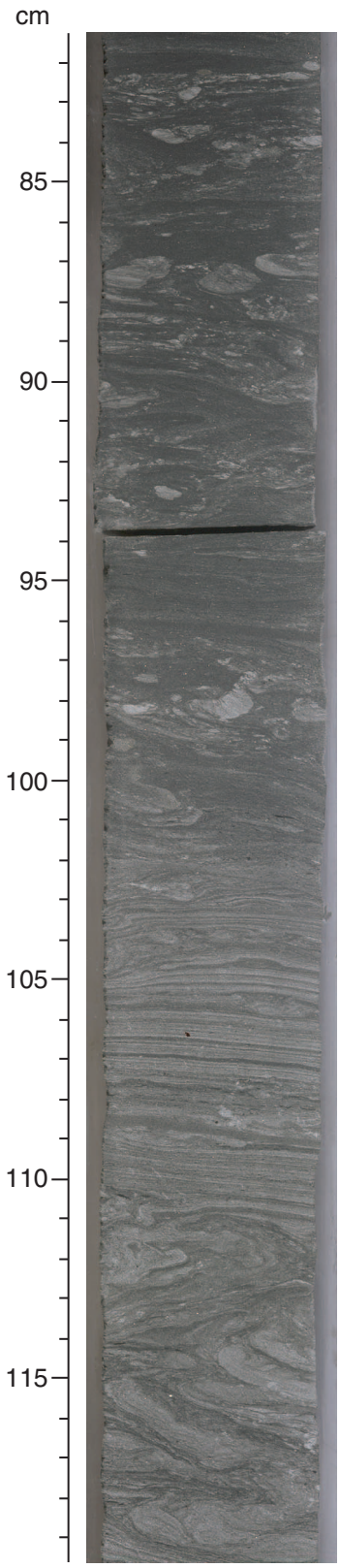

Figure F95. Close-up of sharp-based calcareous sandstone turbidite, grading upward from basal sandstone (133–135 cm) through a swirled and convolute laminated interval (113–133 cm), showing entrained deformed sandstone clasts near the top (115–117 cm) (Subunit 5C: interval 210-1276A-91R-4, 110–138 cm).

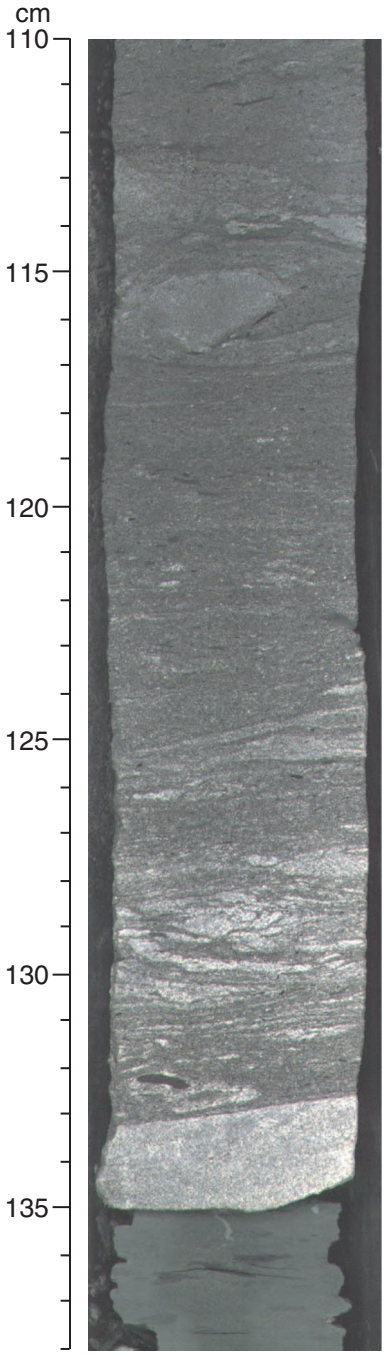

Figure F96. Close-up of a swirled interval in the middle part of a sandstone gravity-flow deposit. Note the soft-sediment folds toward the top and the ductile deformation throughout (Subunit 5C: interval 210-1276A-91R-4, 22–33 cm).

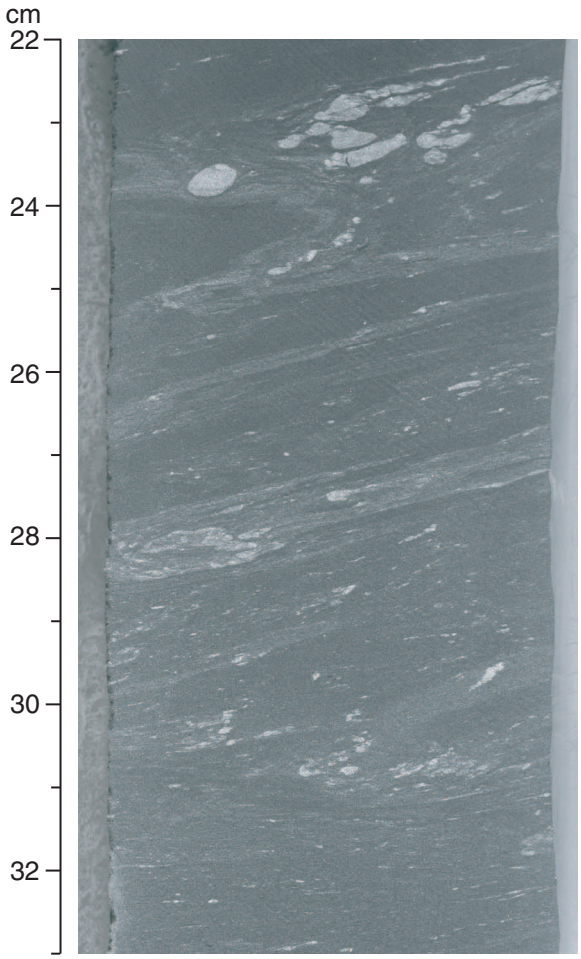

Figure F97. Close-up of the central part of a chaotic mudclast conglomerate. Note the range in color of the mudstone clasts and the variety of clast shapes (Subunit 5C: interval 210-1276A-93R-3, 70–97 cm).

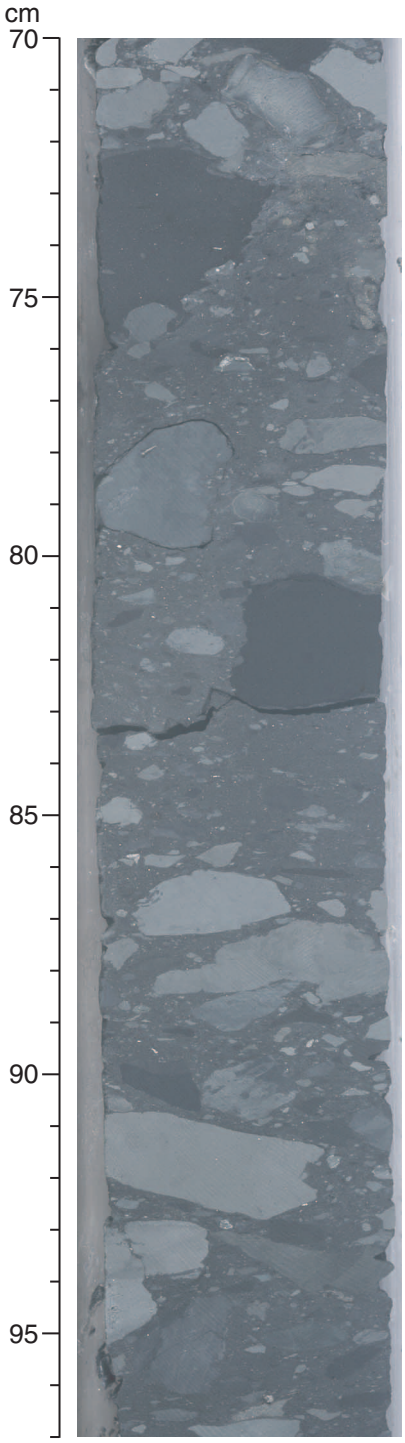

Figure F98. Close-up of the upper part and sharp upper contact of the mudclast conglomerate shown in Figure F97, p. 220. Note the plastic deformation in individual mudstone clasts (Subunit 5C: interval 210-1276A-93R-3, 28–48 cm).

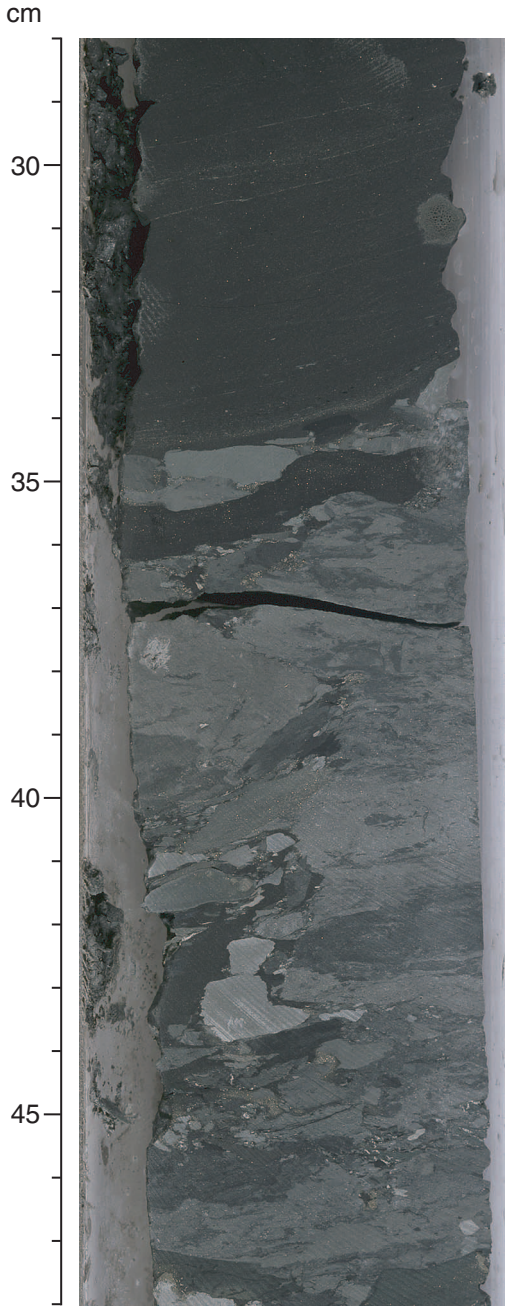

Figure F99. Close-up of a severely contorted interval of sandstone and mudstone, some of which may be intricately admixed, deformed clasts in a debris flow deposit (Subunit 5C: interval 210-1276A-94R-2, 90–108 cm).

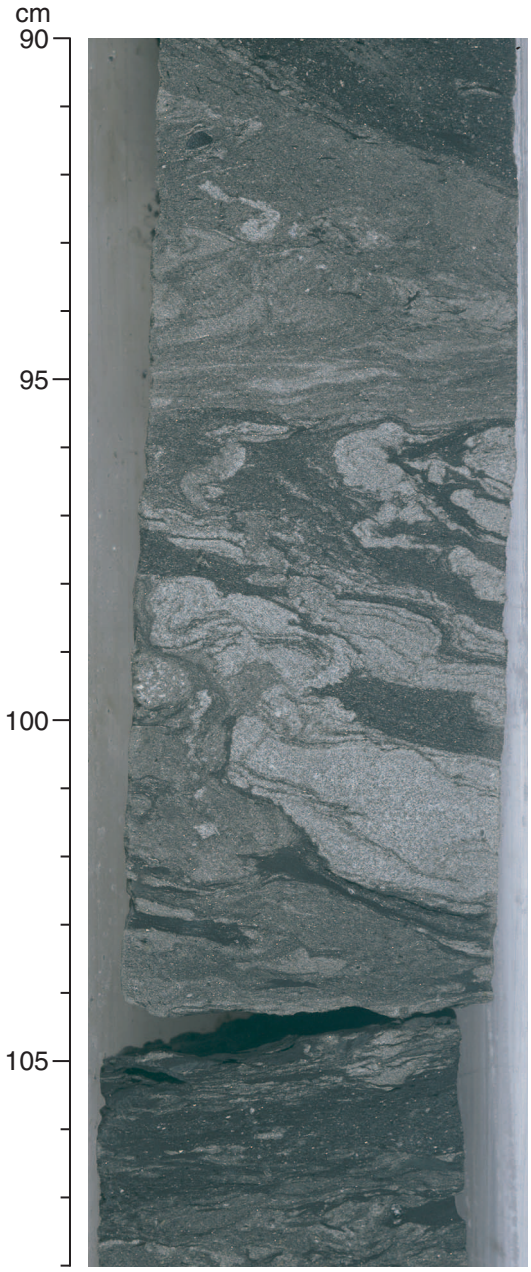

Figure F100. Photomicrographs of sandy siltstone in Subunit 5C under (**A**) plane-polarized light and (**B**) in cross-polarized light. Components are dominantly white angular quartz grains, biotite flakes (b), muscovite flakes (m and brightly birefringent grain), green glauconite, phyllite fragments (S), and an echinoid spine (E). These grains are surrounded by microcrystalline carbonate cement (Sample 210-1276A-81R-3, 64–67 cm).

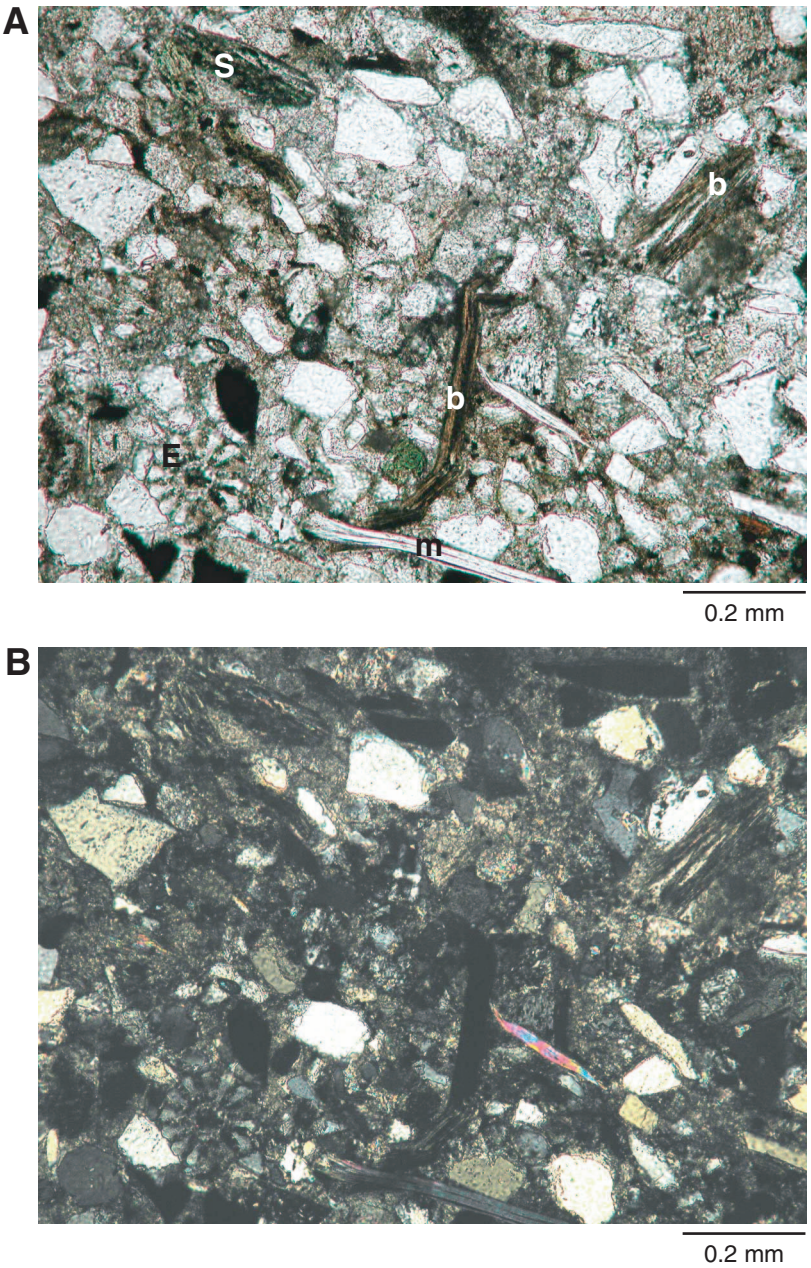

Figure F101. Photomicrograph of sandy siltstone from Subunit 5C viewed at high magnification (Sample 210-1276A-80R-3, 70–73 cm). Sand-sized microporous piece of plant matter (P) is surrounded by quartz (white grains) and biotite (b) set in a tan micritic matrix.

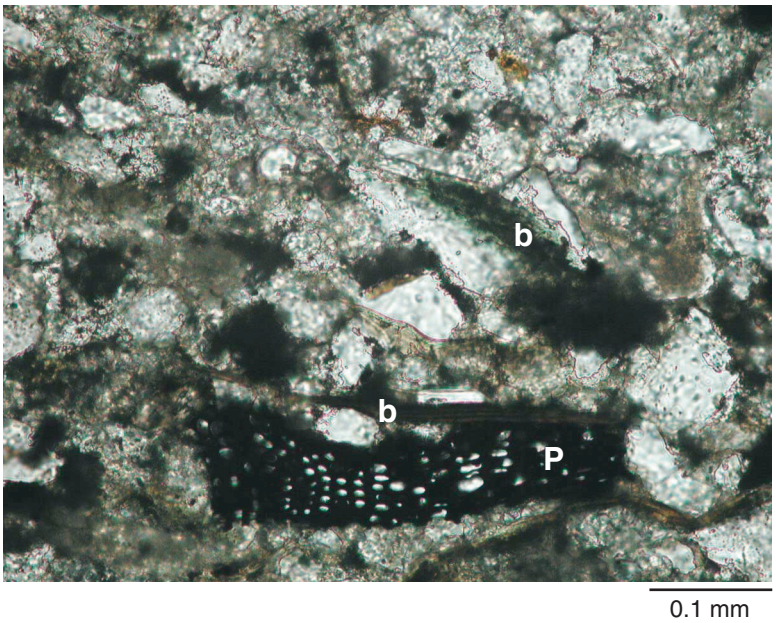

Figure F102. Sandstone turbidite showing planar lamination passing upward into convolute lamination (interval 210-1276A-89R-6, 115–150 cm).

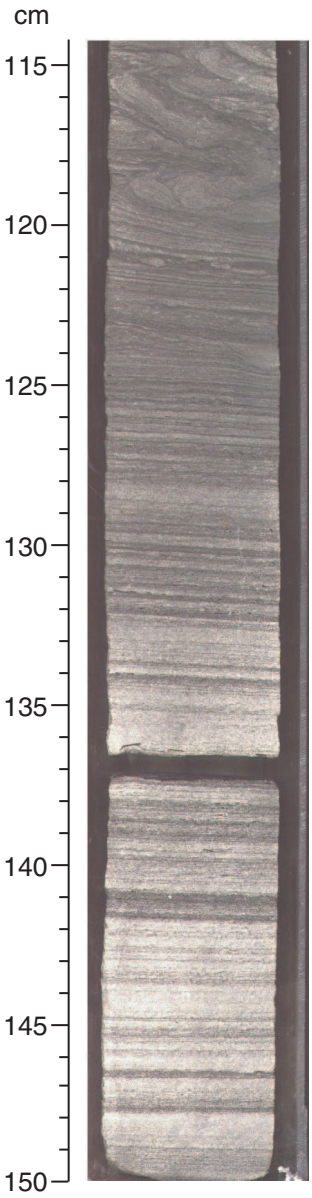

Figure F103. Photomicrograph, under plane-polarized light, of siltstone from just beneath the Subunit 5B/5C boundary. This unusual cross-laminated siltstone is probably an altered tuff. A relict grain that exhibits vesicular texture is circled. In cross-polarized light, this grain shows low birefringence, suggesting that it was glass that was altered to clay minerals. Surrounding white areas are authigenic carbonate, whereas darker material is low birefringent to isotropic; both are considered to be alteration products (Sample 210-1276A-75R-6, 37–40 cm).

Figure F104. Close-up of sandstone fill of burrows (87–93 cm) that were cemented by calcite spar relatively early in diagenesis while surrounding mud or clay remained plastic and was molded around the burrows (Subunit 5B: interval 210-1276A-37R-3, 87–98 cm).

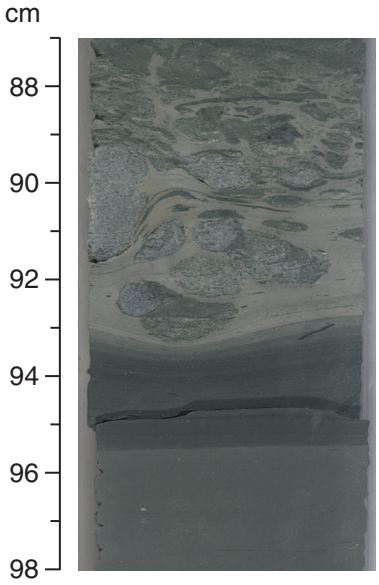

Figure F105. Close-up of lenticular sandstone showing irregular calcite cementation (21–25 cm), followed by differential compaction such that the laminae converge outside the cemented area (Subunit 5C: interval 210-1276A-81R-6, 18–28 cm).

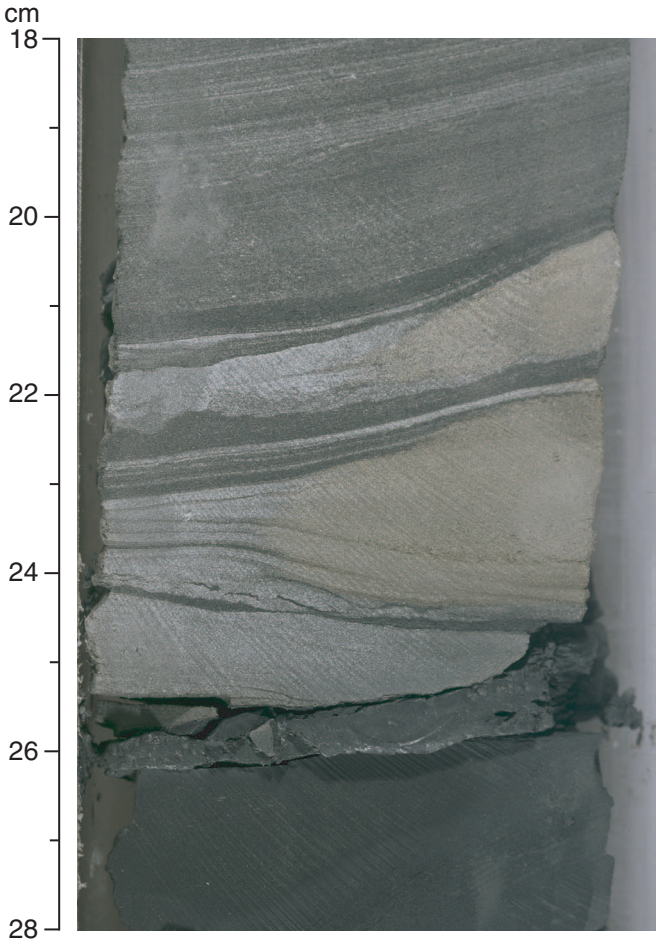

Figure F106. CT scan of calcareous sandstone showing bright spots. The bright spots may be calcite-spar cement (Subunit 5C: interval 210-1276A-79R-2, 99–107 cm).

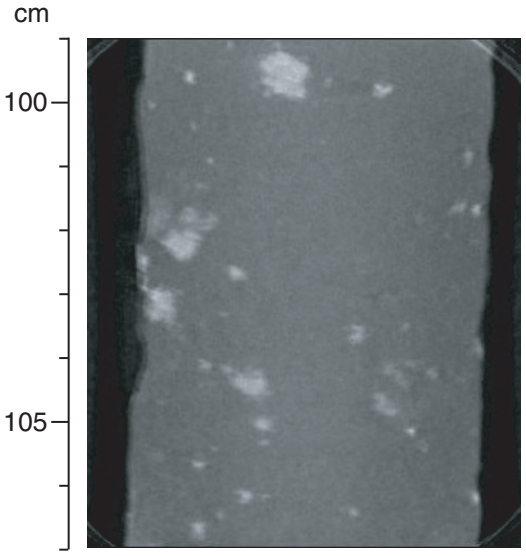

Figure F107. Comparison of CT scan and core photograph from the deformed top of a gravity-flow deposit. **A.** The white spots on the CT image, not clearly identifiable on the core photograph in B, are interpreted as pyrite concretions. **B.** Convolute lamination is apparent in the core photograph but is not visible on the CT scan in A (Subunit 5C: interval 210-1276A-89R-6, 91.5–99 cm). This interval is also shown in Figure F94, p. 217.

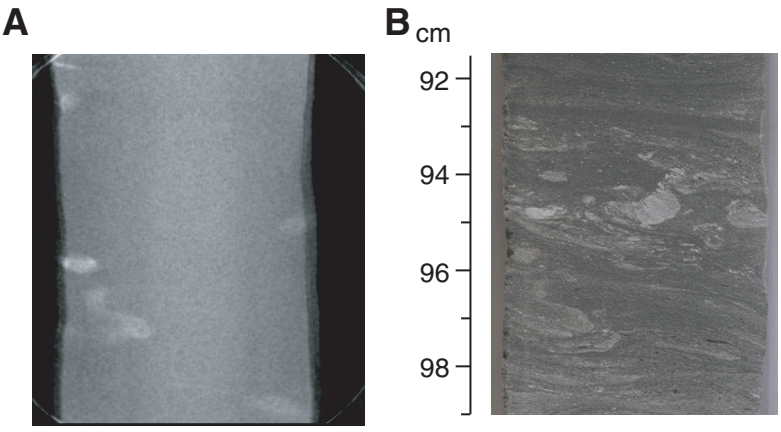

Figure F108. Close-up of irregular carbonate concretionary layers formed by replacement of mud or mudrock. These layers have a very high magnetic susceptibility and contain siderite, as determined by XRD analysis (Subunit 5B: interval 210-1276A-48R-3, 92–98 cm).

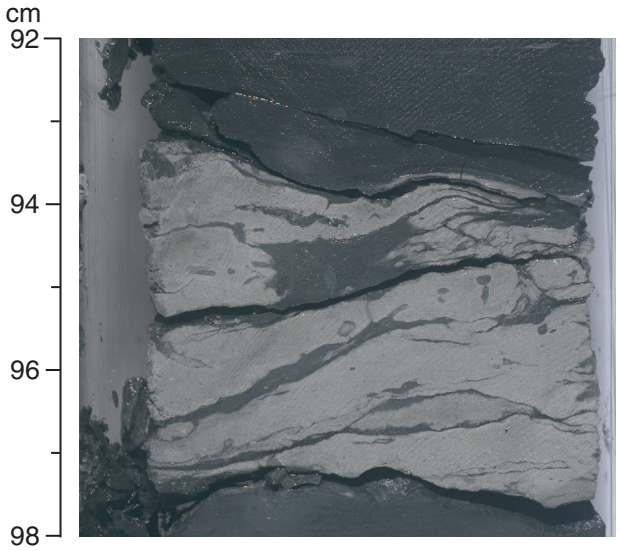

Figure F109. Close-up of dark noncalcareous claystone with a round nodule composed of peloidal grains (fecal pellets) that are organized concentrically around the edge. The nodule formed by early carbonate cementation of pelleted clay. See text for further discussion (Subunit 5B: interval 210-1276A-62R-6, 31–39 cm).

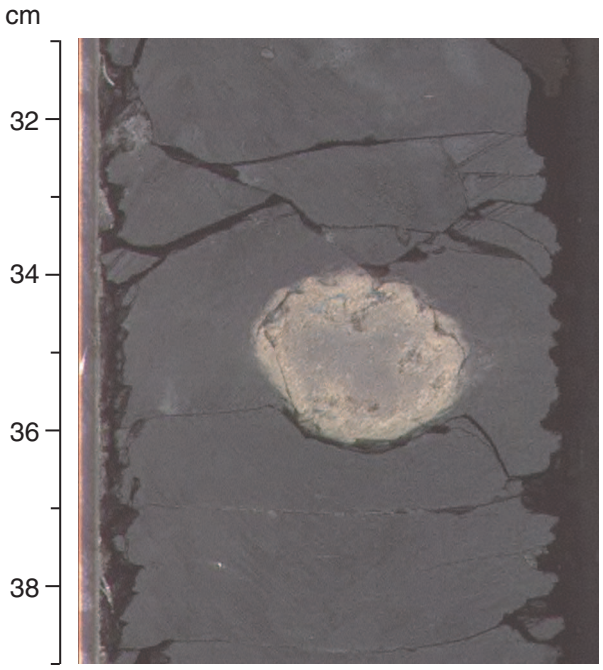

Figure F110. Photomicrograph of concretion in Subunit 5B mudstone under plane-polarized light. Vaguely pelleted mudstone with darker pellets (P) cemented by dolomicrite (m) is cut by a round, porous (s = pore spaces) burrow (lower center) partly filled with smaller pellets likely left by the burrowing organism. This concretion provides a glimpse of the original texture of the burrowed mudstones in this unit (Subunit 5B: Sample 210-1276A-60R-2, 25–27 cm).

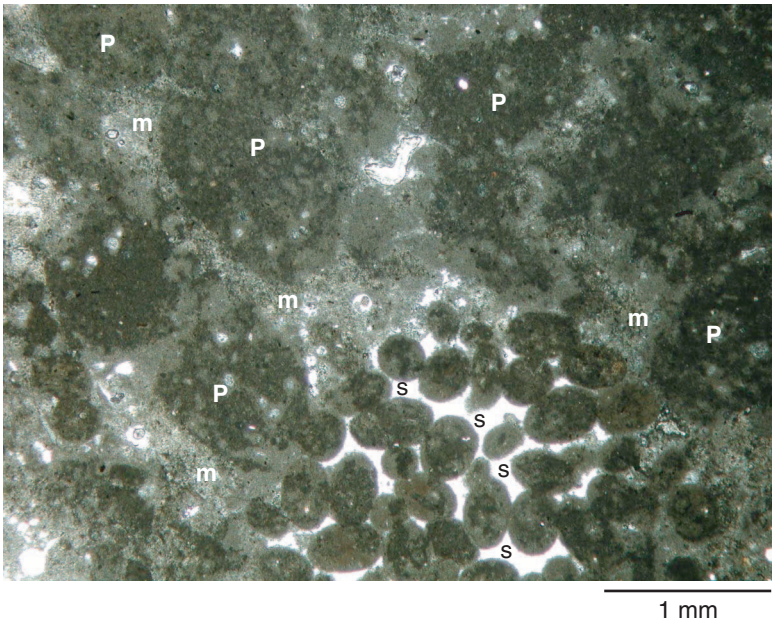

Figure F111. Close-up of finely laminated claystone with thin, diagenetically formed carbonate lenses (at 97 cm and 100 cm) and small granular bodies (94 cm) (Subunit 5B: interval 210-1276A-43R-1, 92–102 cm). See text for discussion.

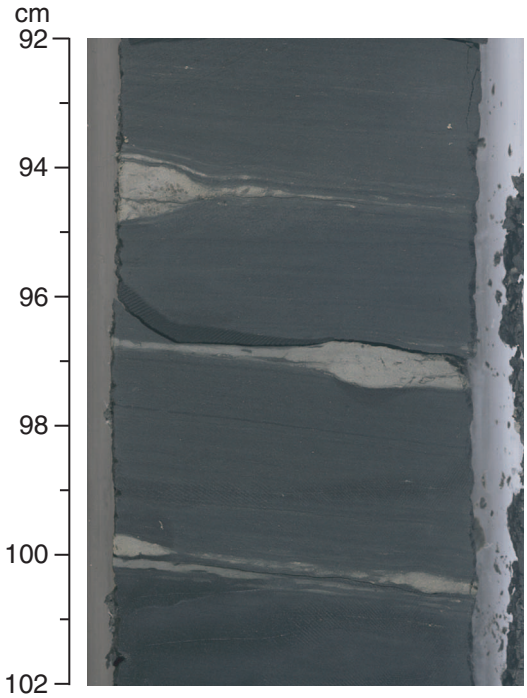

Figure F112. Close-up of very finely laminated mudstone with small, elongate, carbonate-rich microconcretions. These have a fine pelletal texture and may represent early diagenetic cementation of original sedimentary texture (Subunit 5B: interval 210-1276A-72R-5, 104–110 cm).

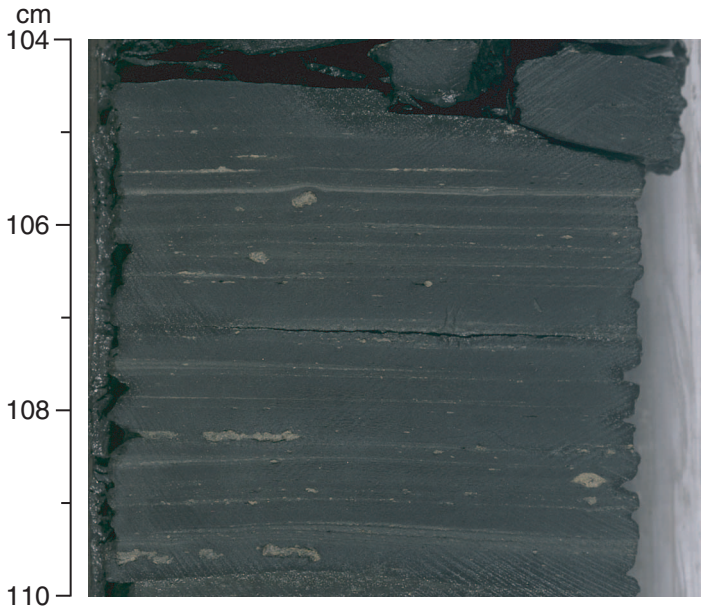

Figure F113. Close-up of septarian concretion in laminated claystone, showing slight deflection of laminae in the adjacent claystone. Note the steeply inclined septarian cracks filled with calcite spar (Subunit 5C: interval 210-1276A-76R-6, 94–110 cm).

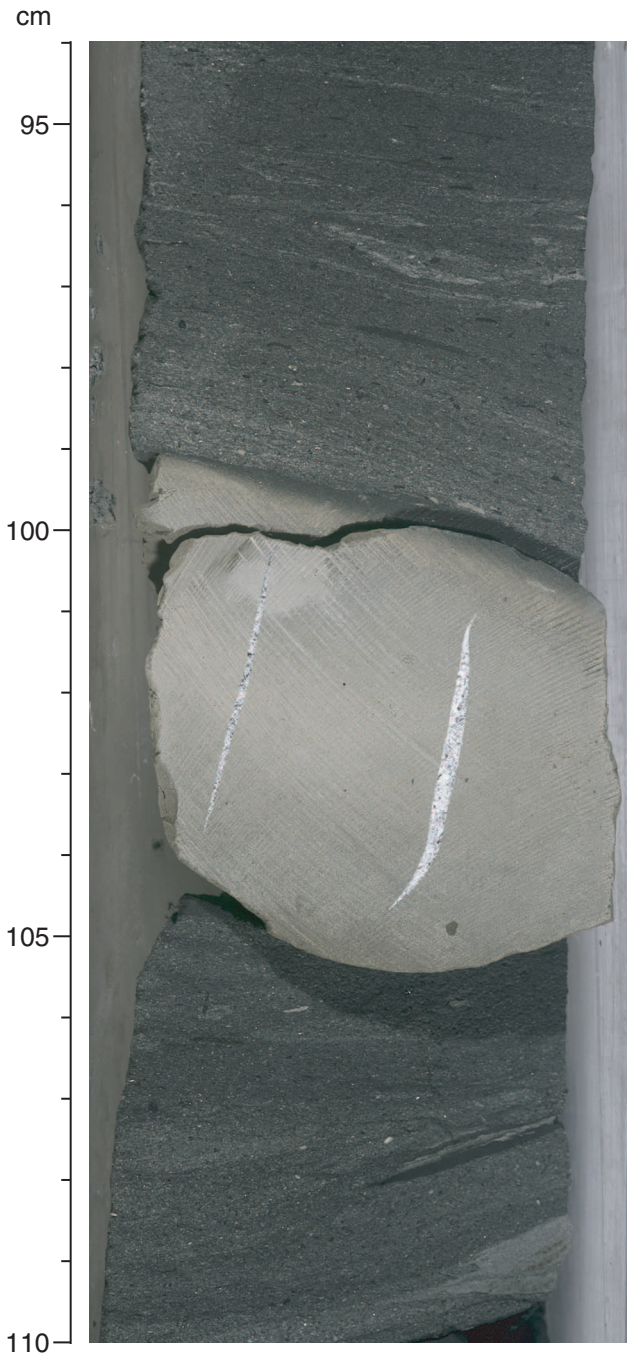

Figure F114. Low-angle range of X-ray powder diffractograms from dark green bioturbated "background" lithologies (mudrocks of variable carbonate content). The intensity bulge at ~14 Å is absent below 1241.26 mbsf, except in a sample of altered ash (Sample 210-1276A-89R-1, 20–21 cm; 1623.80 mbsf). Note the strong increase in the 7-Å diffraction peak (corresponding to chlorite and kaolinite) below 1321 mbsf. See text for discussion.

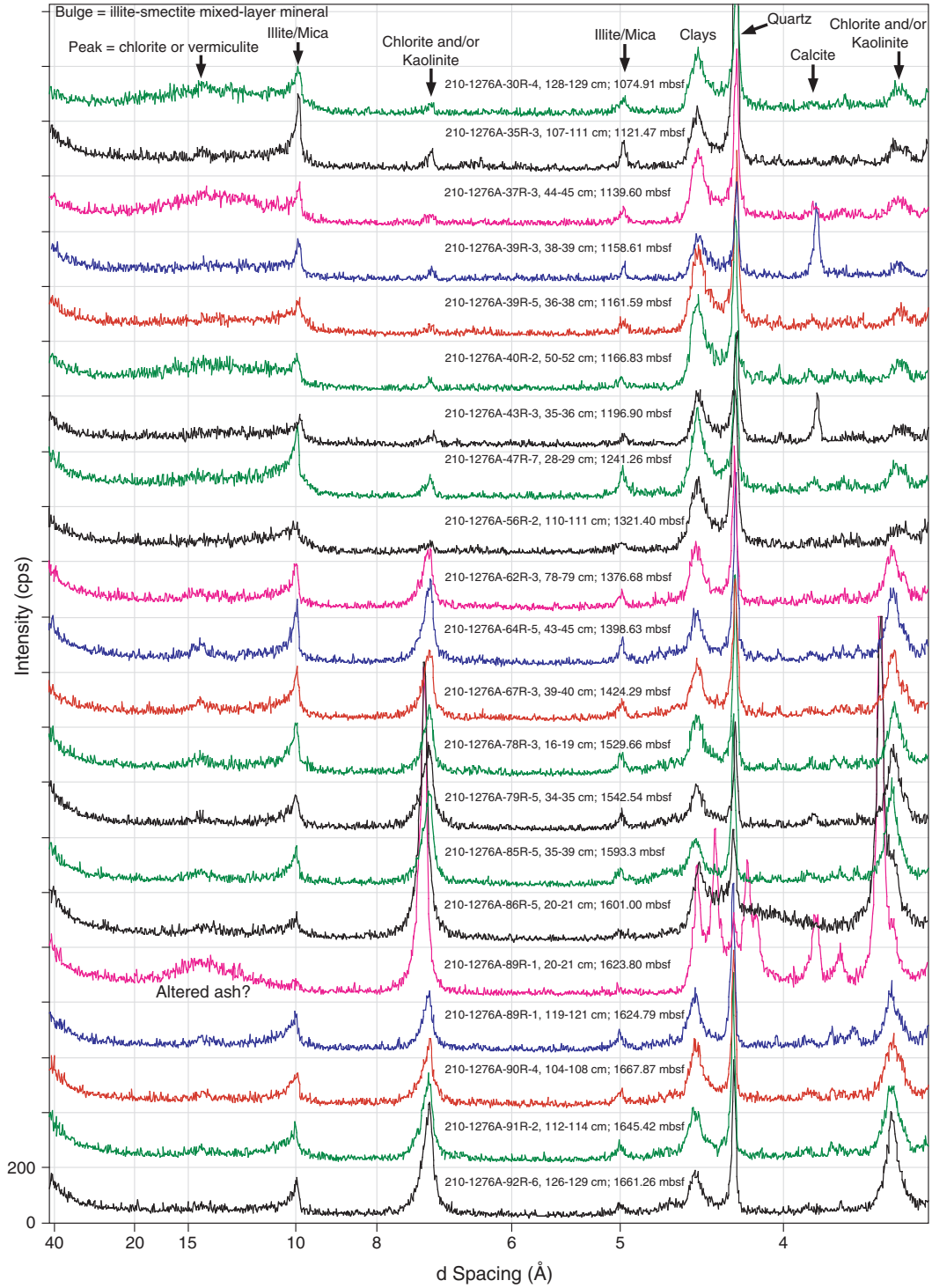

Figure F115. Comparison of a feature observed in a core photograph with CT scans (interval 210-1276A-87R-6, 18–27 cm). **A.** A porphyroblastic mudrock that is the top of a sandstone → mudstone turbidite. The patchy mineral growth relates to thermal and hydrothermal effects of nearby intrusion of diabase sill Subunit 5C1. The mineral growth appears to be mainly horizontal in the core photograph. **B.** CT scan of the same interval. Note that the secondary, patchy mineral growth is clearly visible, but the subvertical hydrothermal calcite vein seen in the core photograph (A) is not. In contrast to what is seen in the split-core photograph, the elongate crystals appear to have a near-random orientation. **C.** A horizontal slice of the same core interval viewed with IMAGEJ software. This image also suggests a near-random orientation of the porphyroblasts. Taken together, images B and C suggest little preferred orientation of these crystals.

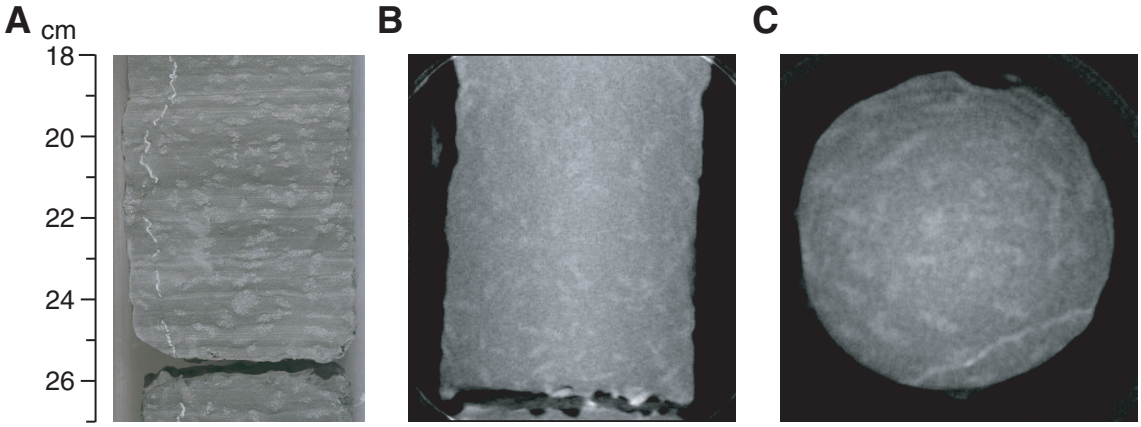

Figure F116. Close-up of porphyroblastic mudrock affected by sill intrusion near the base of Subunit 5C. The porphyroblasts are composed of quartz, albite, alkali feldspar, and magnesian chlorite based on XRD analysis. An original burrow sedimentary texture is recognizable, overprinted by thermal effects (contact metamorphism or hydrothermal alteration) (Subunit 5C: interval 210-1276A-98R-3, 5–14 cm).

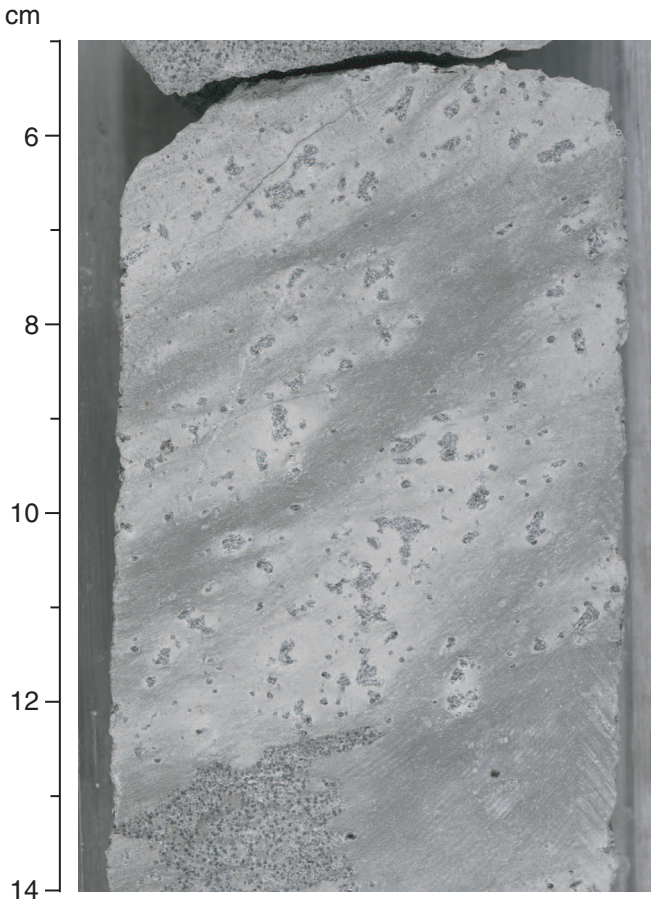

Figure F117. Close-up of hydrothermally altered sediment above a diabase sill in the lower part of Subunit 5C. The background sediment was originally burrowed mudrock (30–39 cm and 50–60 cm) and graded calcareous sandstone (40–50 cm). The sandstone has been strongly altered and replaced as noted in the text. The porous and permeable calcareous sandstone was probably the focus of hydrothermal fluid flow related to the sill intrusion (Subunit 5C: interval 210-1276A-98R-3, 30–60 cm).

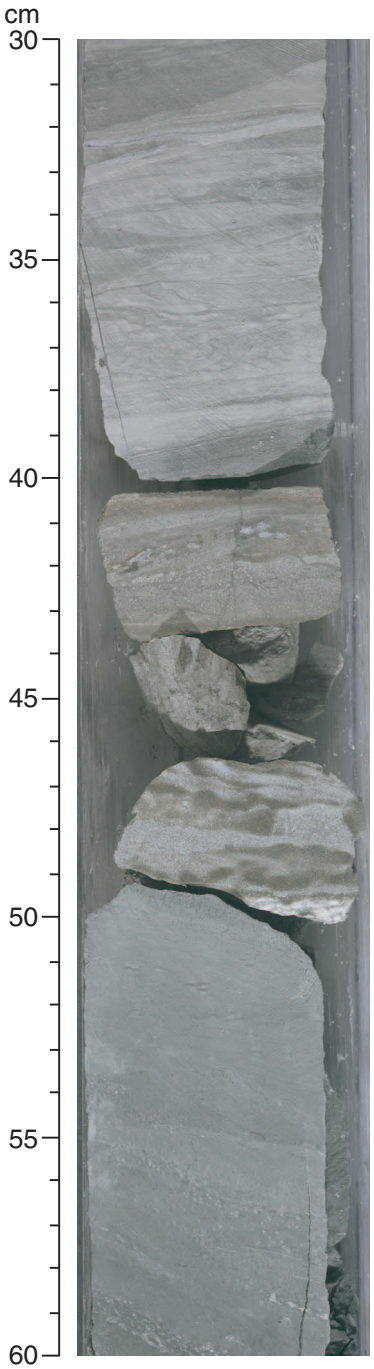

Figure F118. Simplified time-stratigraphic comparison of the lithostratigraphy of the Newfoundland and Iberia conjugate margins. The column at right summarizes the lithostratigraphy and formation names for the North American Basin (i.e., the western central North Atlantic) for comparison. Note that gravity-flow deposits dominate the successions cored at Site 1276 and the Iberia Abyssal Plain sites. Lithostratigraphic unit designations and unit thicknesses are given for each site, based on the site reports. TD = total depth.

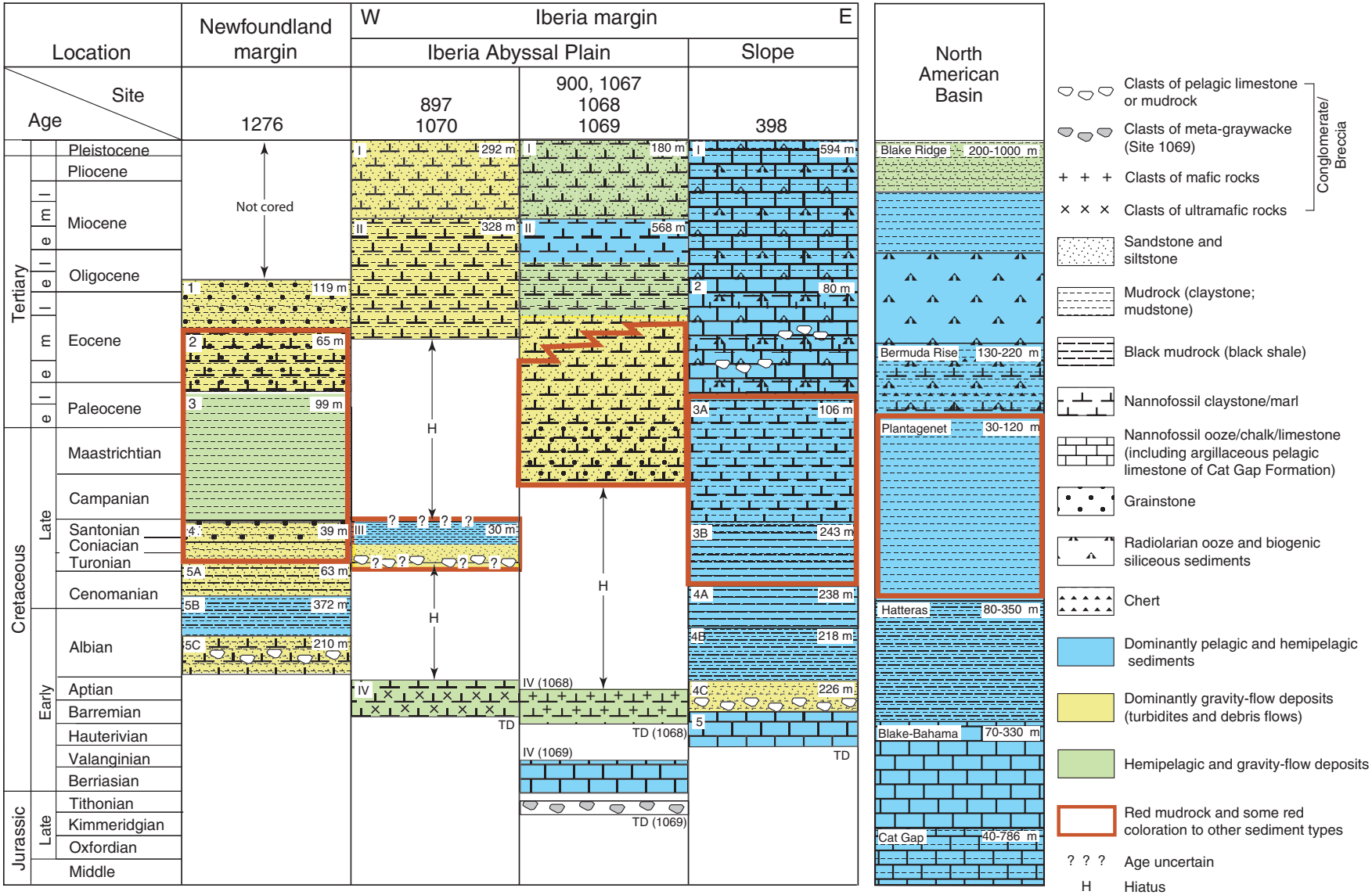

Figure F119. Photograph of the upper contact of the sill composing Subunit 5C1 (interval 210-1276A-87R-6, 40–85 cm [before cutting; depth of the contact changed slightly after cutting]).

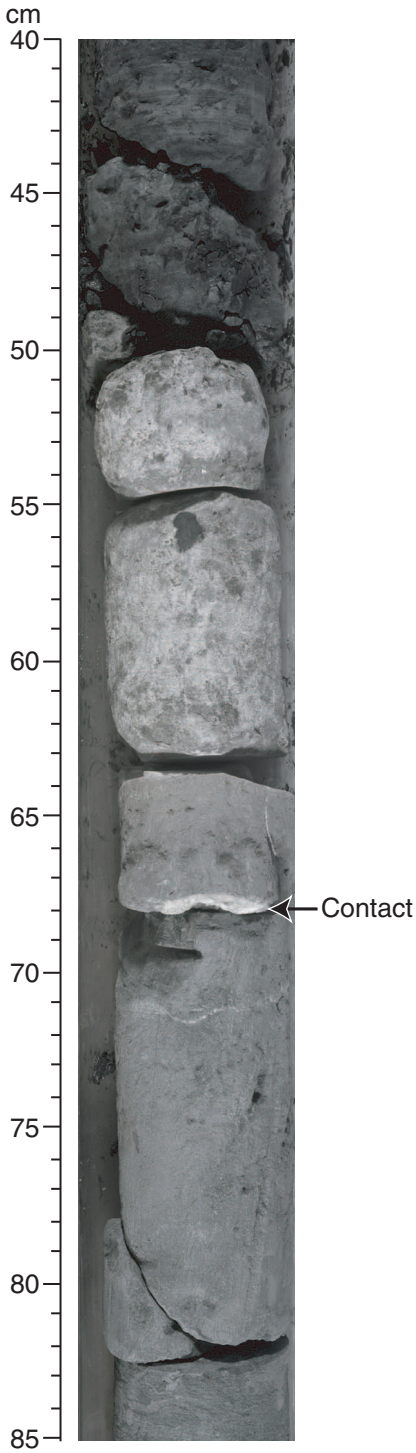

Figure F120. Summary of observations made on the upper sill, Subunit 5C1 (interval 210-1276A-87R-6, 72 cm, through 88R-7, 117 cm). Plag = plagioclase, cpx = clinopyroxene, mag = magnetite.

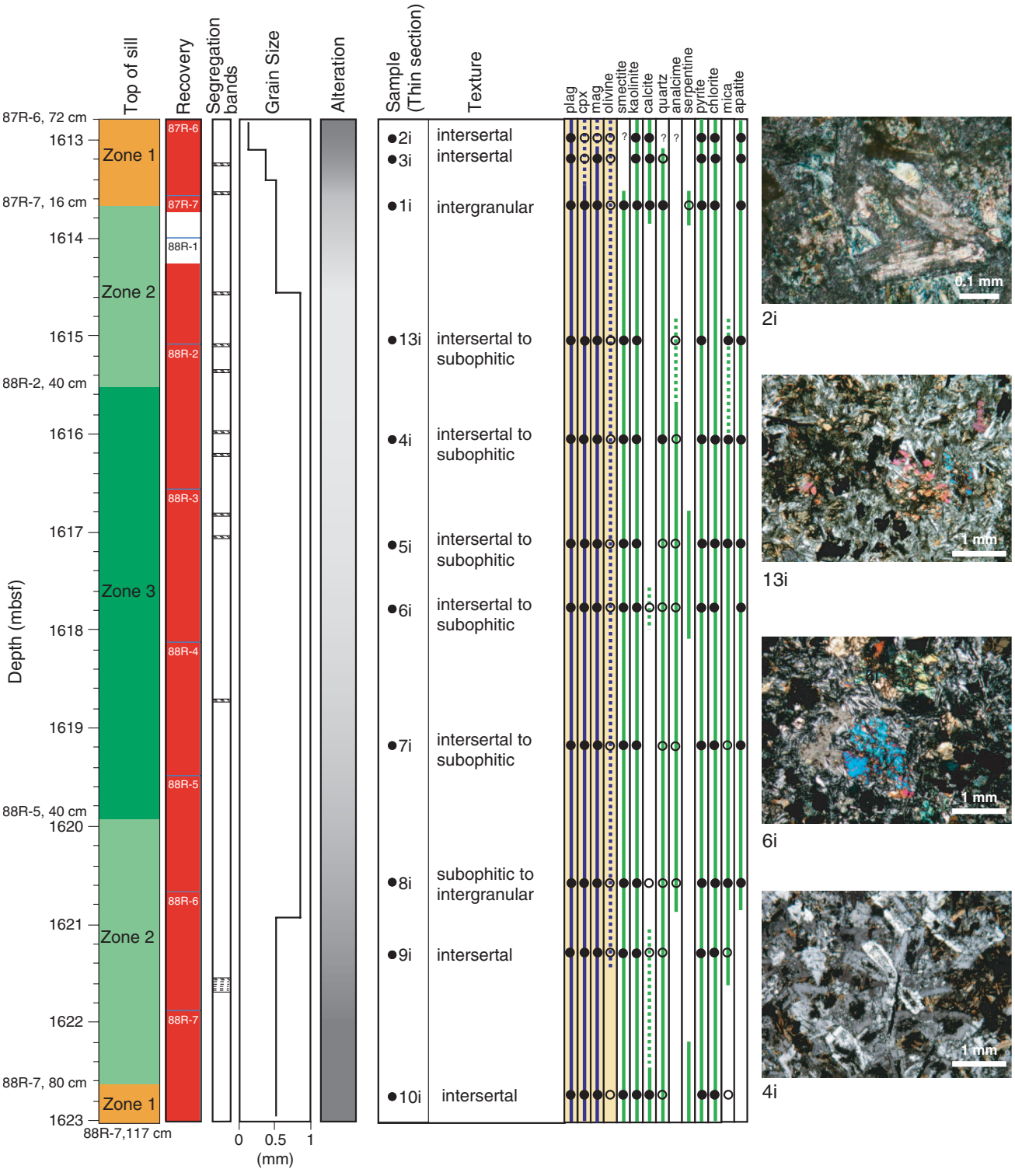

Figure F121. Close-up of calcareous siltstones (interval 210-1276A-87R-6, 2–38 cm) overlying the upper contact between the upper sill and the overlying sediments. Porphyroblasts increase in size downsection over the interval 210-1276A-87R-6, 6–55 cm. Note the folded subvertical vein.

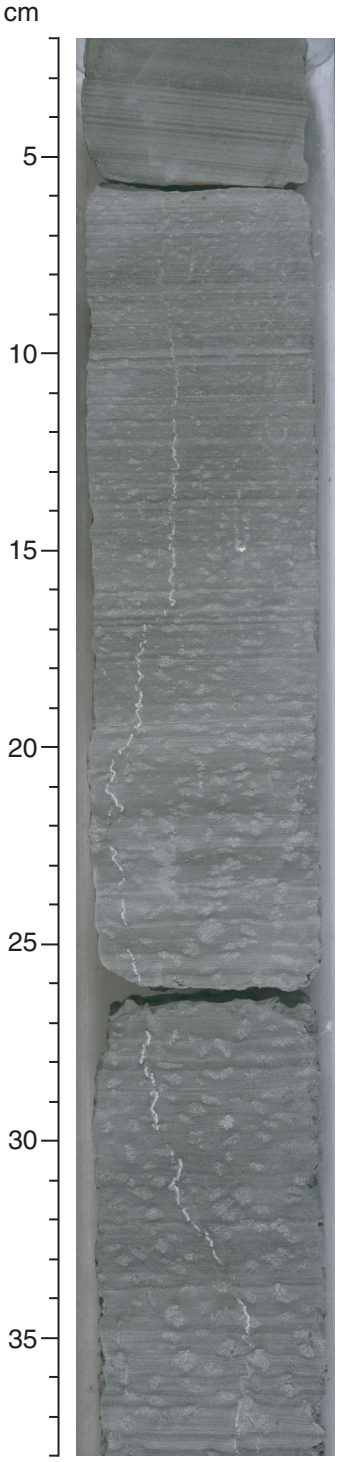

Figure F122. Close-up photograph of the lower contact between the upper sill (Subunit 5C1) and the underlying sediments (before cutting; depths changed slightly after cutting) (intervals 210-1276A-88R-7, 103–119 cm, through 88R-8, 0–7.5 cm).

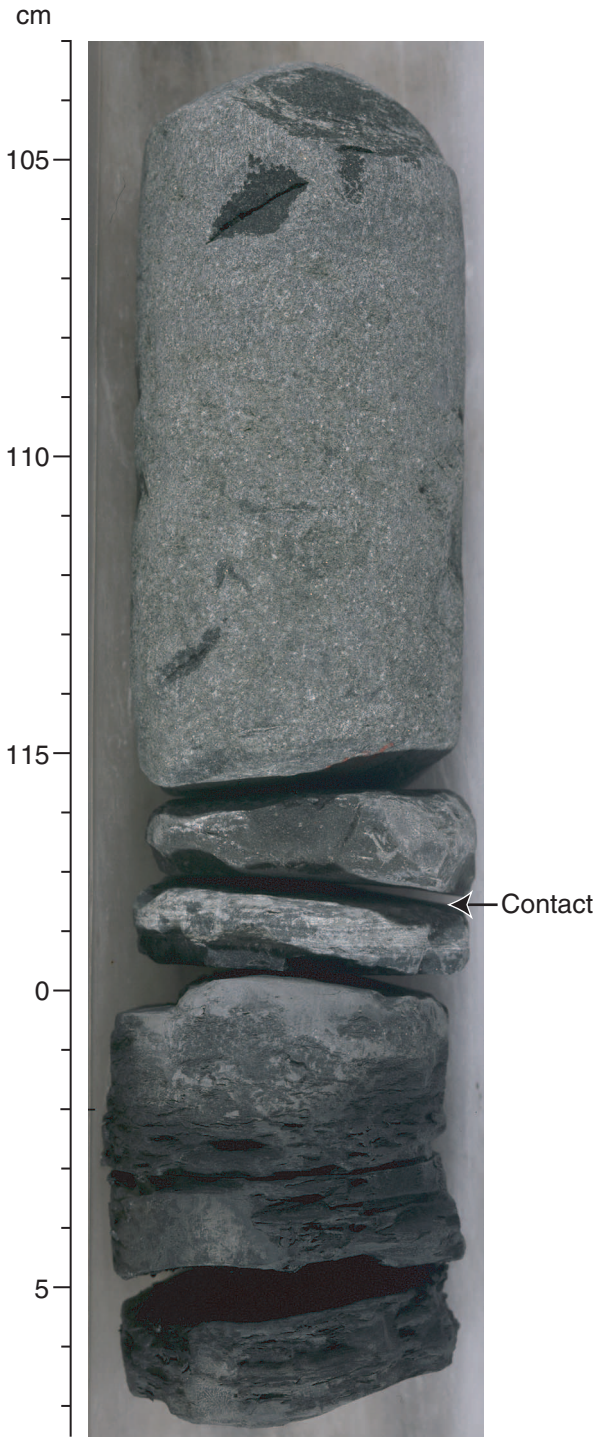

Figure F123. Thin section photomicrograph of a characteristic texture of zone 1. There is strong hydrothermal alteration that overprints a primary intersertal texture in the sample (Sample **210-1276A-87R-6, 86–89 cm**). **A.** Plane-polarized light. **B.** Cross-polarized light.

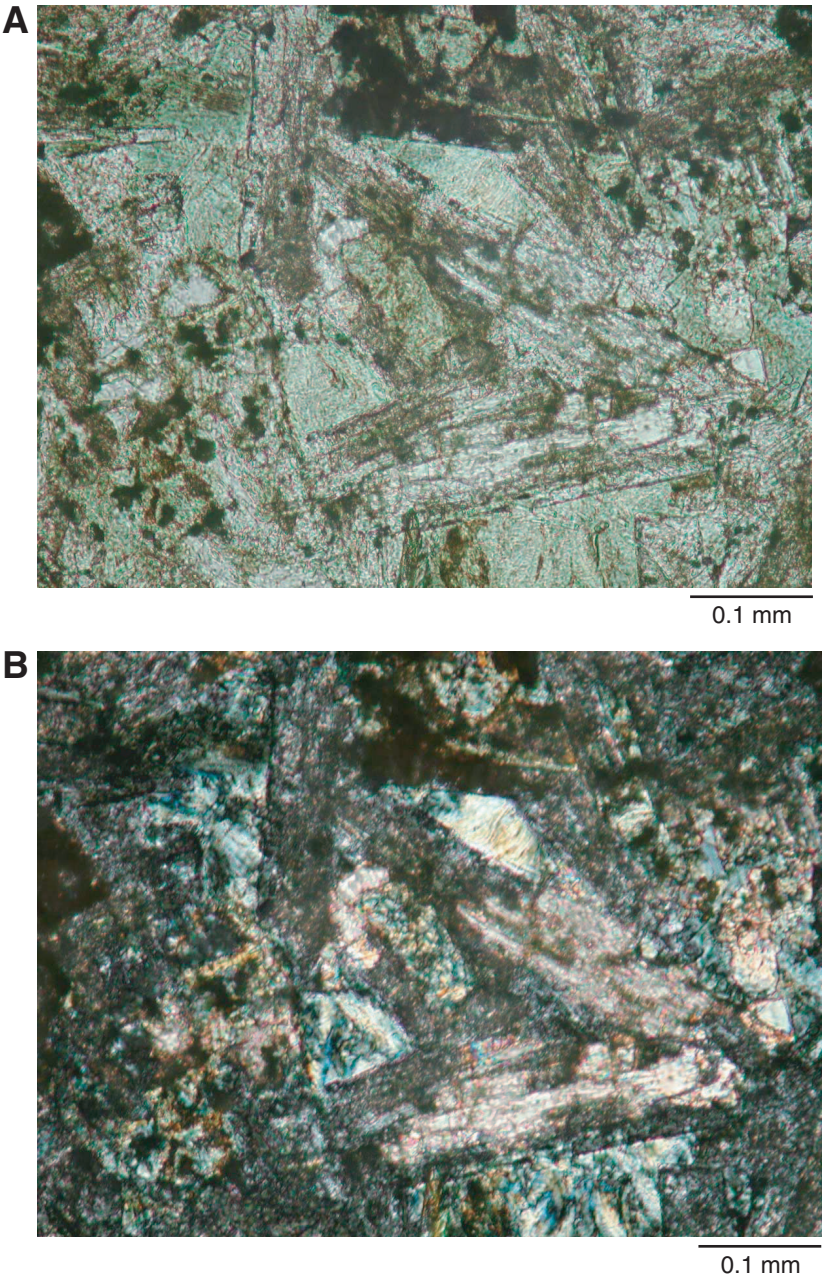

Figure F124. Thin section photomicrograph of a characteristic texture from zone 2 in the upper sill. Lath-shaped plagioclase crystals are enclosed in segregations of devitrified glass (intersertal texture), and other plagioclase lath-shaped crystals enclose augite minerals in an intergranular texture (Sample **210-1276A-88R-5, 104–109 cm**). **A.** Plane-polarized light. **B.** Cross-polarized light.

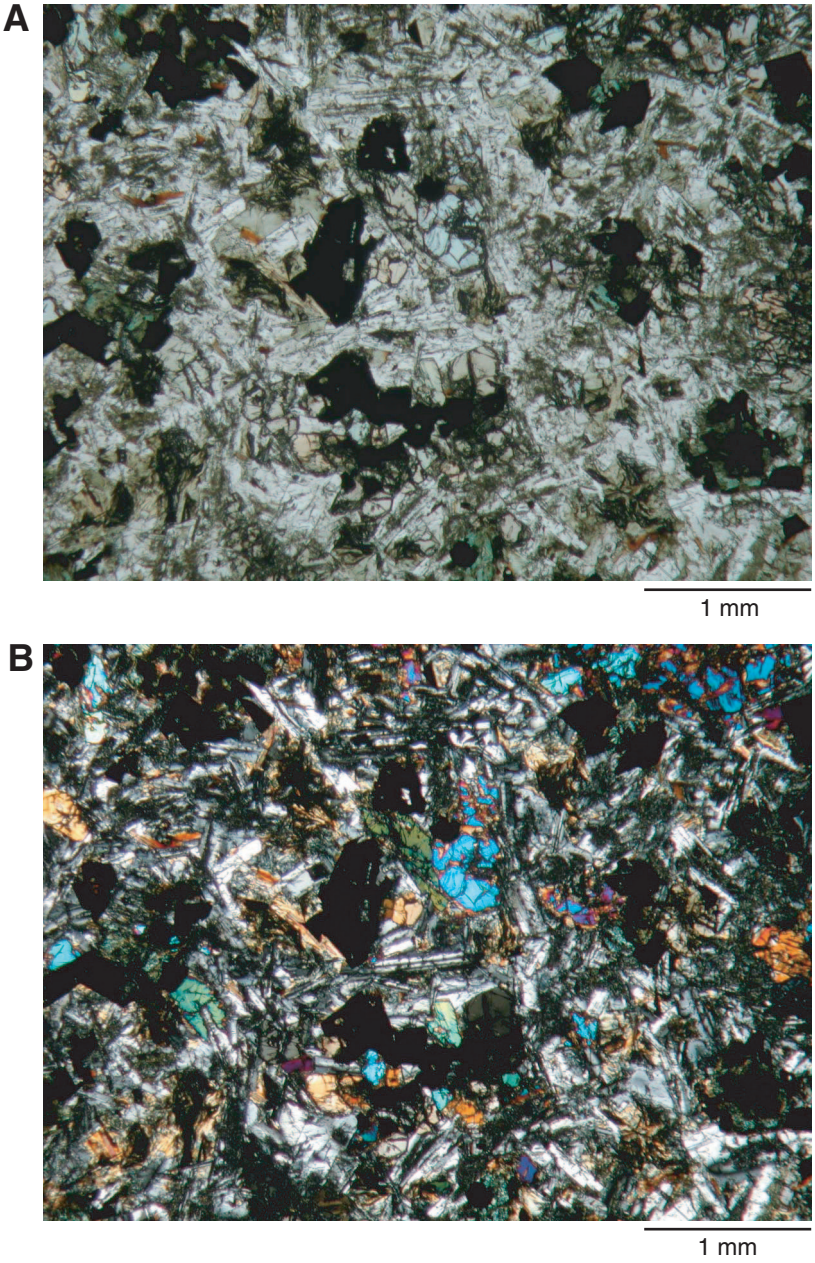

Figure F125. Close-up core photograph showing characteristic texture in zone 3 in the upper sill (interval 210-1276A-88R-2, 86–99 cm). The lighter band corresponds to a more differentiated segregation band, showing distinct (but not sharp) contacts with the host rock.

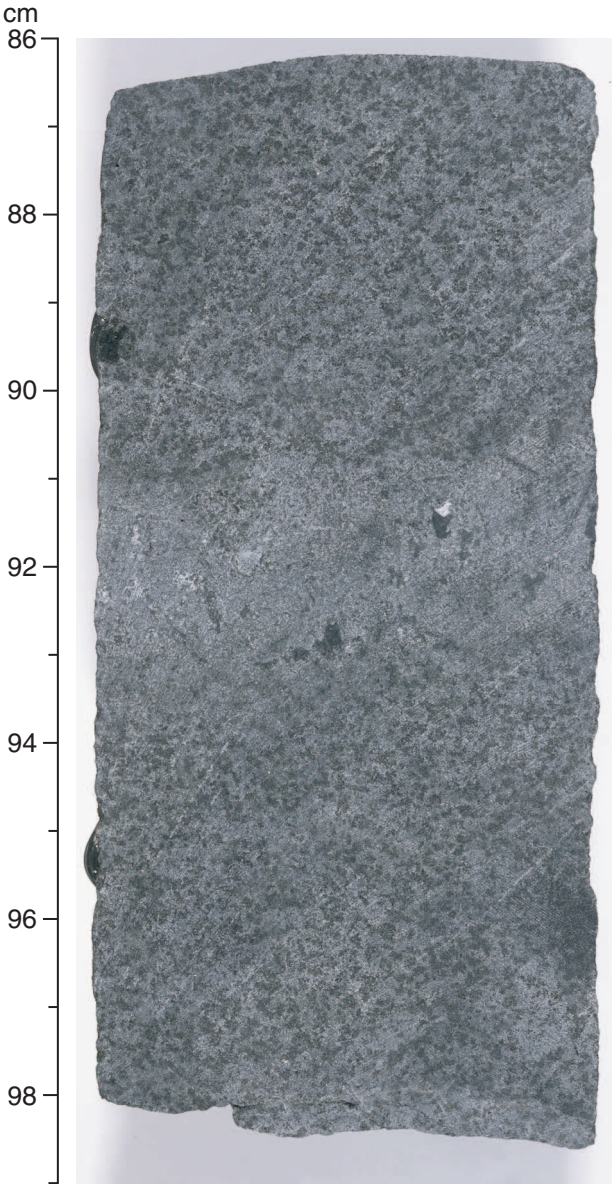

Figure F126. Core photograph showing characteristic texture in zone 3 of the upper sill (interval 210-1276A-88R-3, 85–100 cm). A characteristic patchy pattern distinguishes this zone from the remainder of the core.

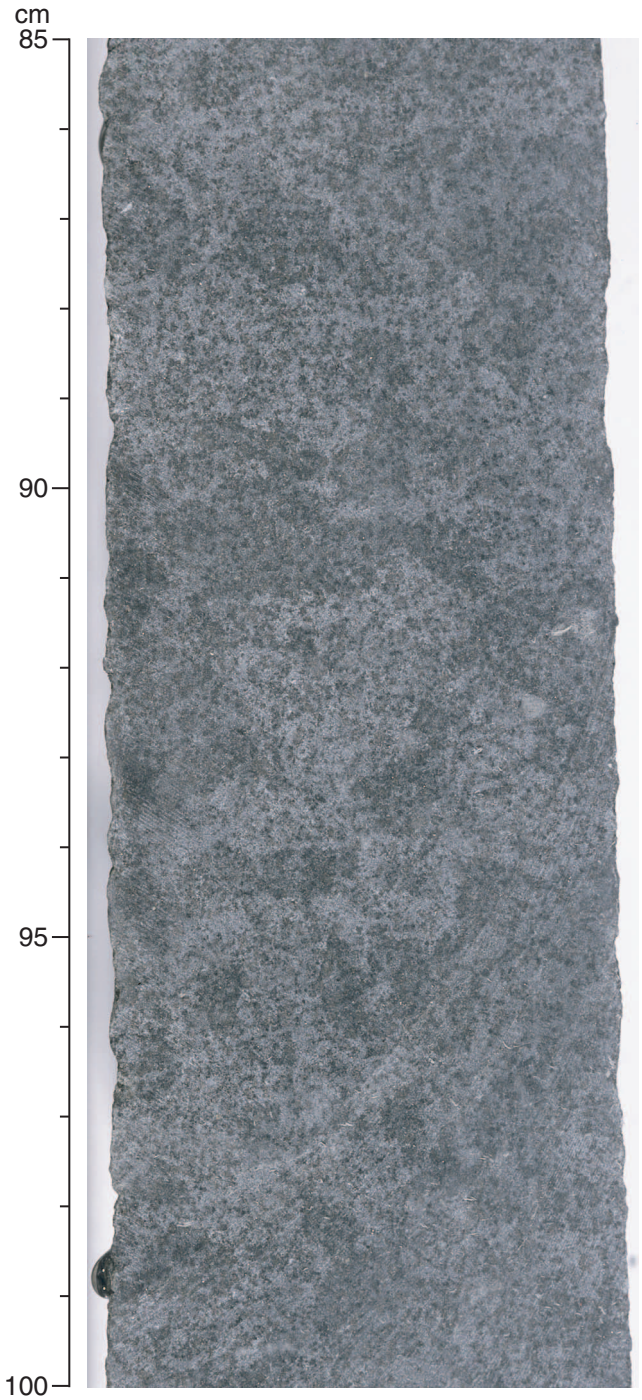

Figure F127. Thin section photomicrograph of zone 3 in the upper sill. Plagioclase laths are embedded in or penetrate the augite crystals (Sample 210-1276A-88R-3, 121–125 cm). **A.** Plane-polarized light. **B.** Cross-polarized light.

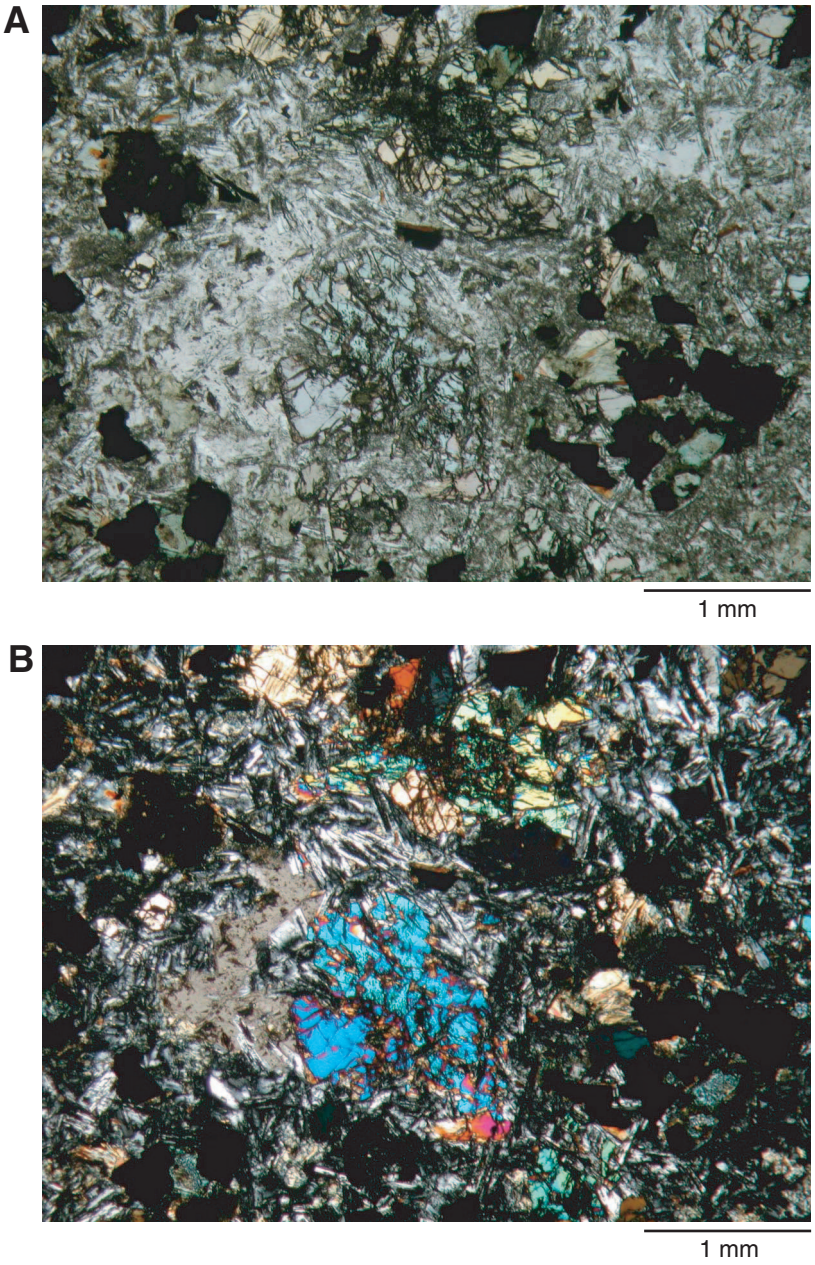

Figure F128. Variation diagrams showing major and trace elements plotted against SiO_2 and cross plots of immobile elements for the diabase of the upper sill from Site 1276.

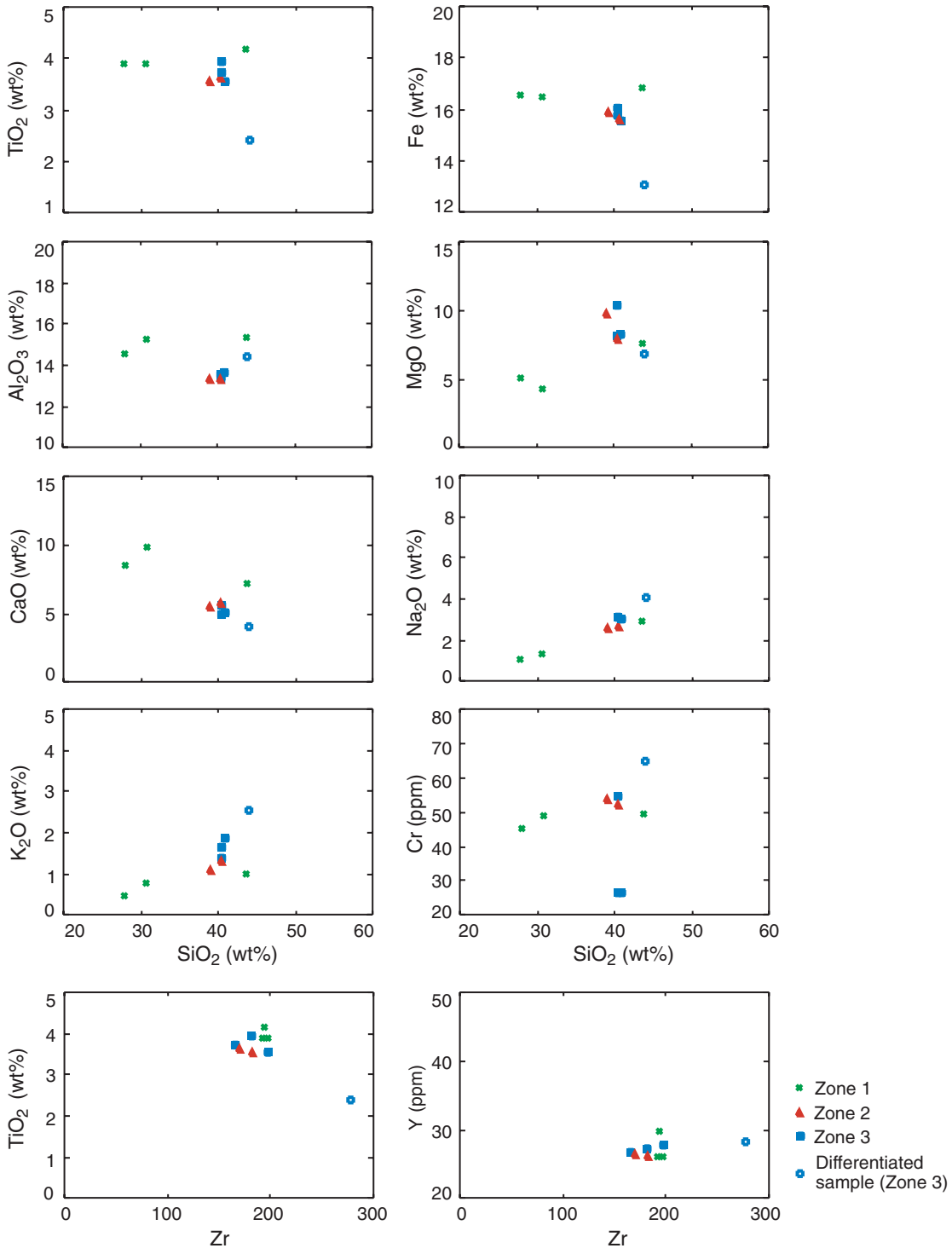

Figure F129. Composition of zone 2 and 3 igneous rocks from Site 1276 diabase sills plotted on the $Na_2O + K_2O$ vs. SiO_2 classification diagram of Le Bas et al. (1986). Note that the compositions were probably affected by hydrothermal alteration. See text for discussion.

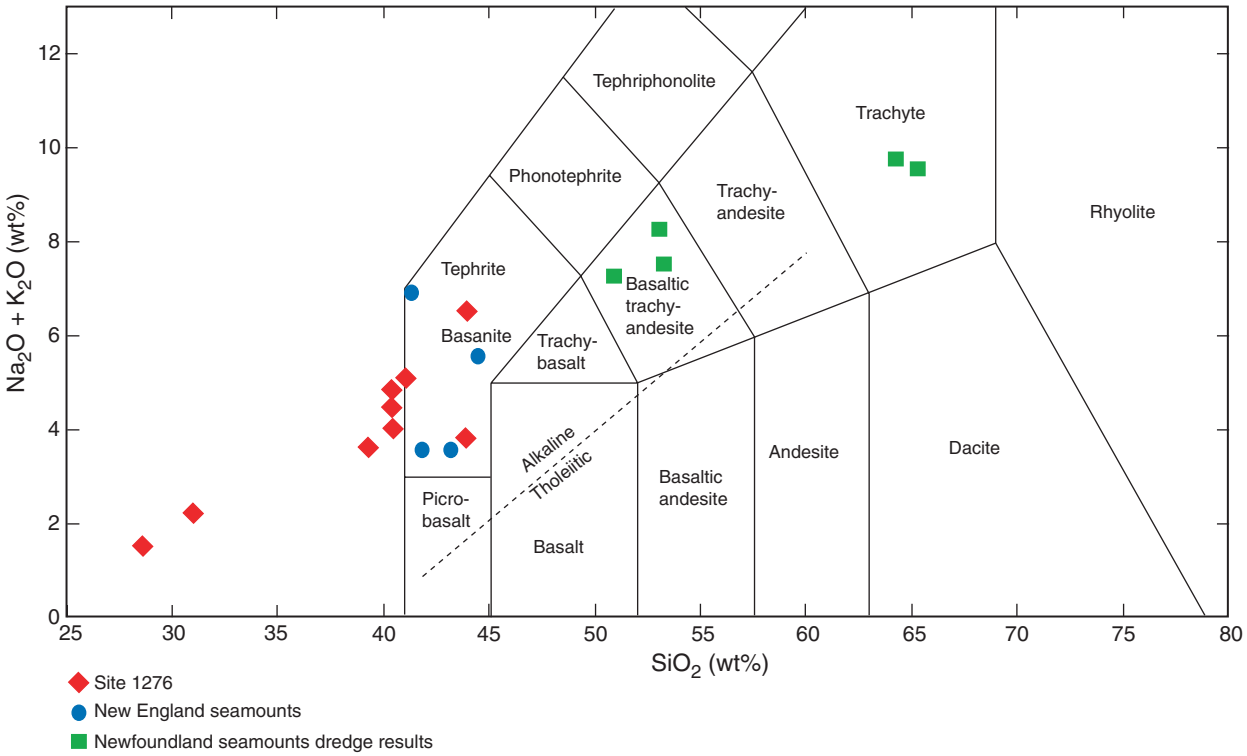

Figure F130. Stratigraphic relations between lower-sill units and intervening sediments. Photographs highlight key features; these are also shown in the accompanying line drawings. This figure also shows the recovery of the lower cores.

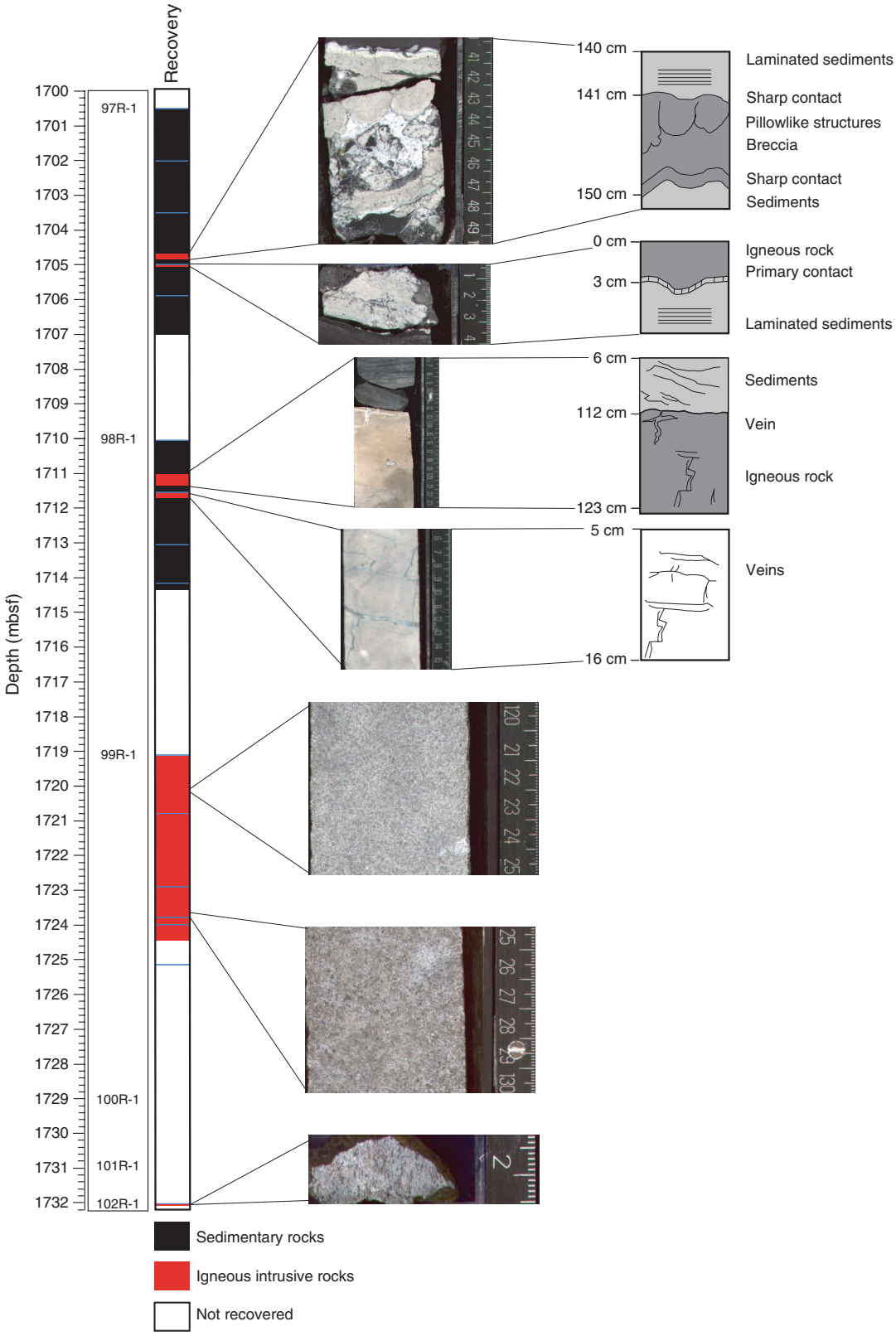

Figure F131. A. Close-up core photograph showing a small "breccia pipe" and sill/sediment contact in the lower sill complex (interval 210-1276A-97R-3, 138–150 cm). **B.** Thin section photomicrograph of the sill/sediment contact (plane-polarized light) (Sample 210-1276A-97R-3, 140.5 cm). C = contact, G = glassy matrix, S = sediment, V = vesicle.

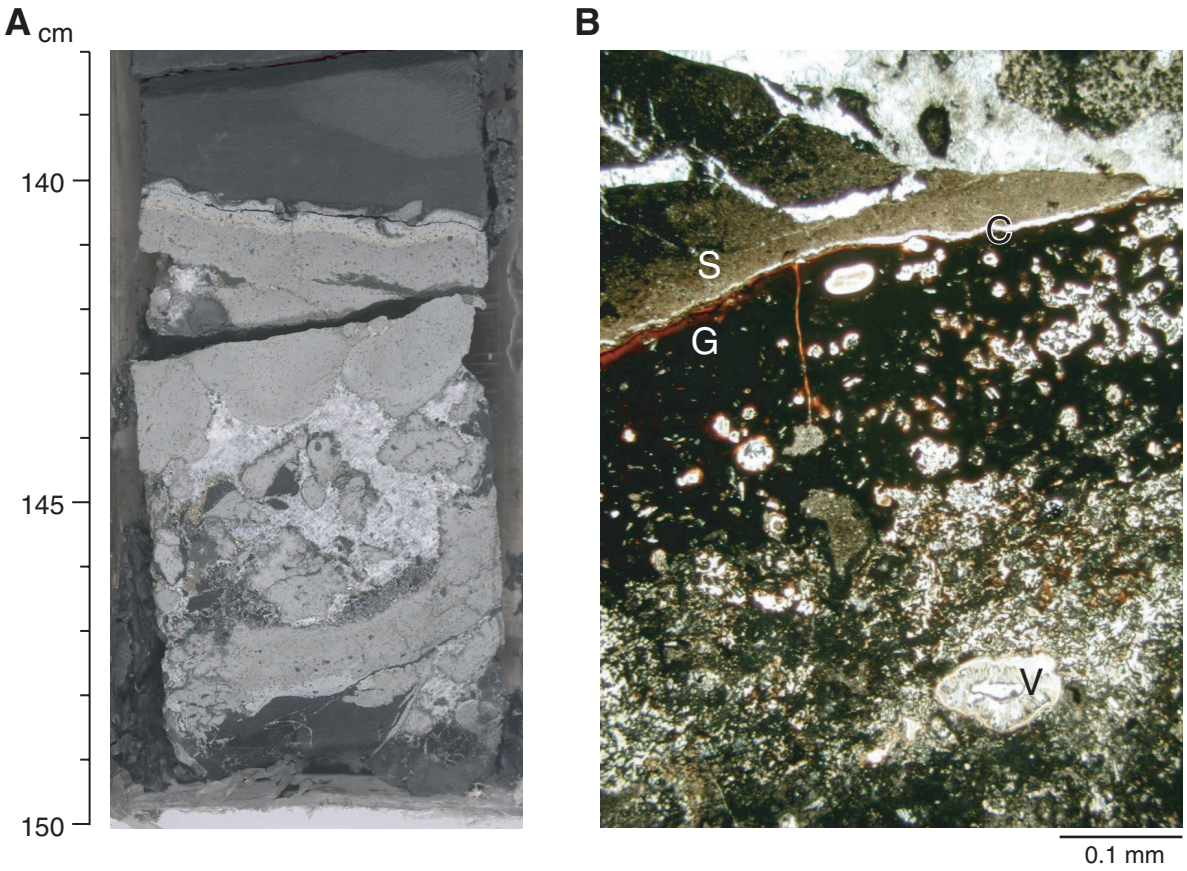

Figure F132. Thin section photomicrographs of the intrusive rocks in the lower section of the lower sill complex (Sample 210-1276A-99R-1, 123–126 cm). **A.** Plane-polarized light. **B.** Cross-polarized light.

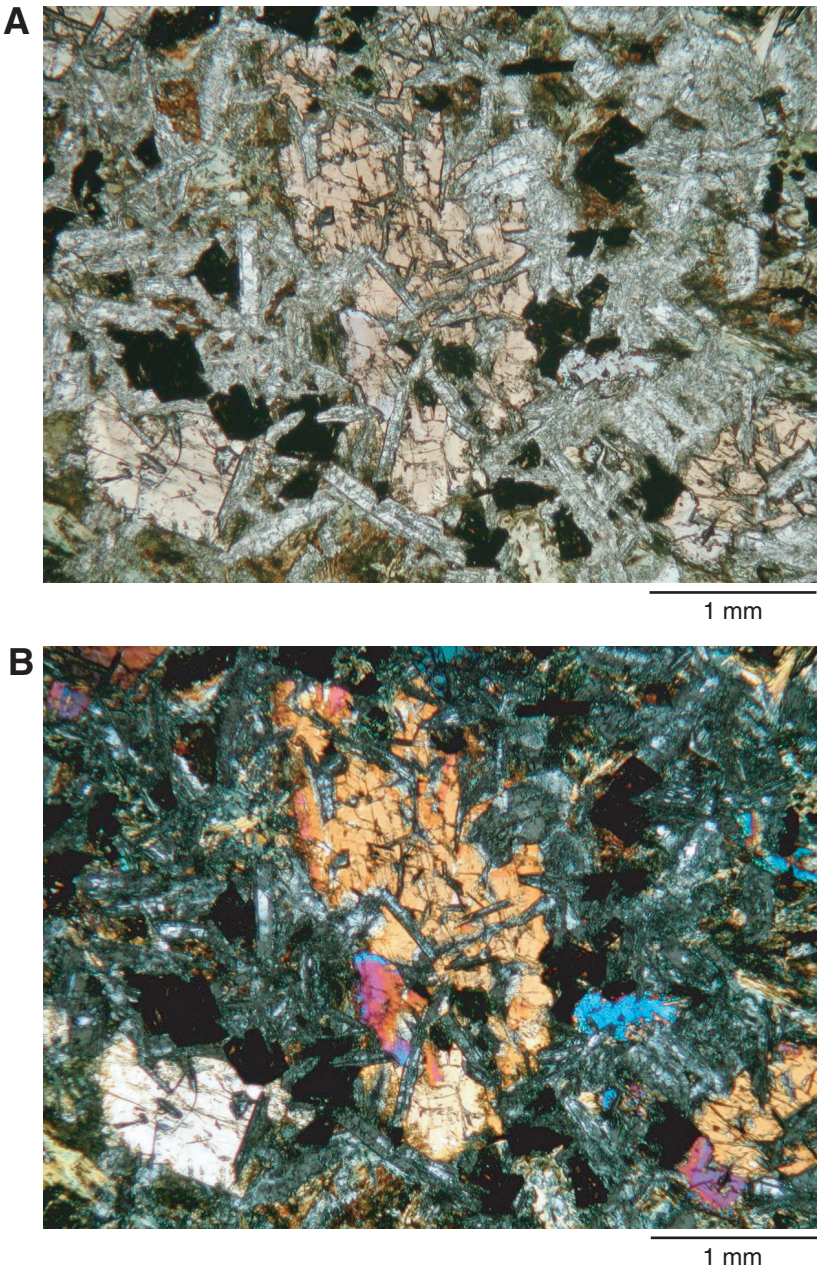

Figure F133. Apparent dip of sedimentary beds and distribution of deformation structures observed in cores at Site 1276.

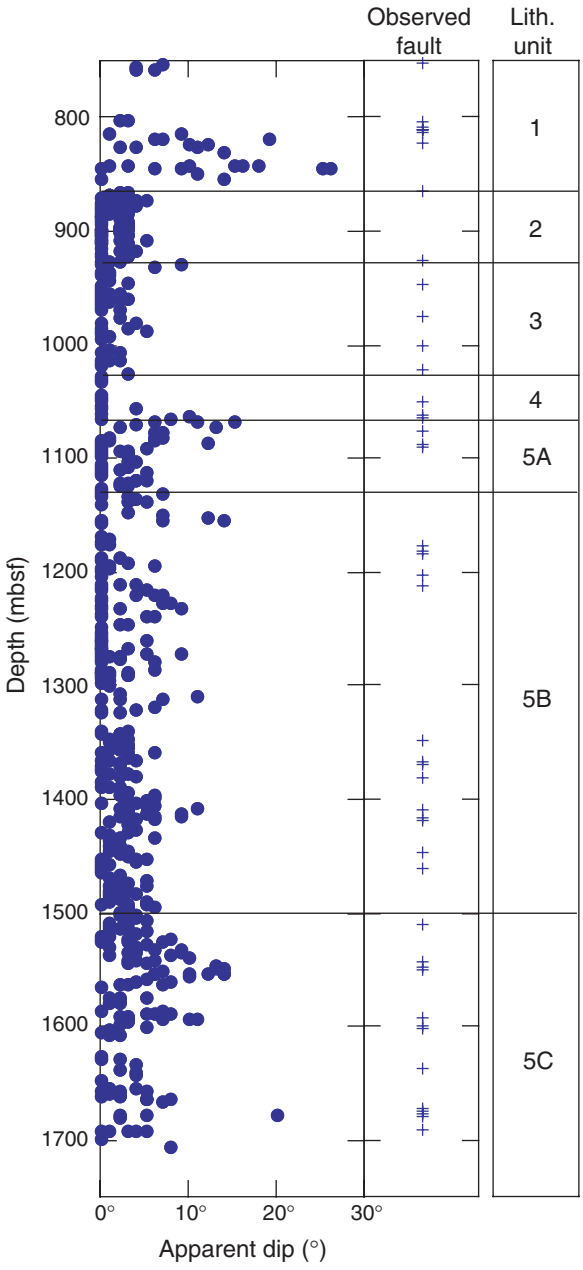

Figure F134. Close-up of several limbs of a chevron-type fold (interval 210-1276A-14R-2, 8–32 cm). Note that the fold axial planes are subhorizontal and subparallel to the overlying bedding plane.

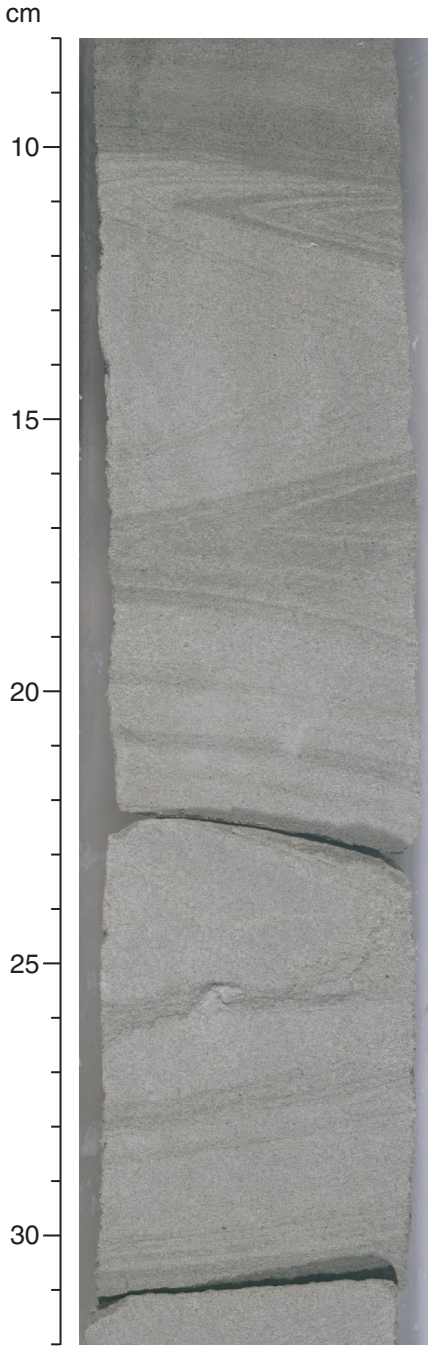

Figure F135. Close-up of a well-developed conjugate normal fault system forming a symmetric graben structure (interval 210-1276A-15R-2, 68–76 cm). The faults are marked by arrows.

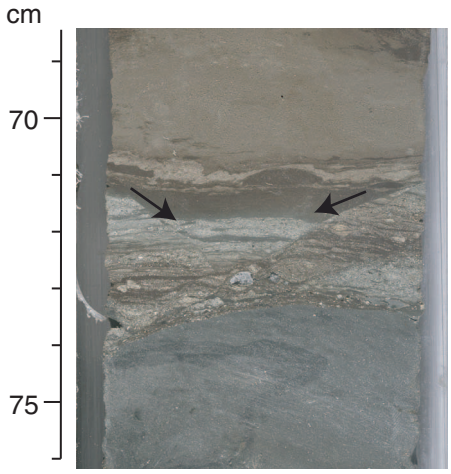

Figure F136. Close-up of a folded burrow (interval 210-1276A-17R-5, 83–88 cm). The folds show a subhorizontal fold axial plane and extension of the fold limbs parallel to this plane. This may be explained by compaction-related vertical shortening and horizontal elongation.

Figure F137. Close-up of stylolites in the sandy fraction of a calcareous turbidite (interval 210-1276A-21R-4, 125–132 cm).

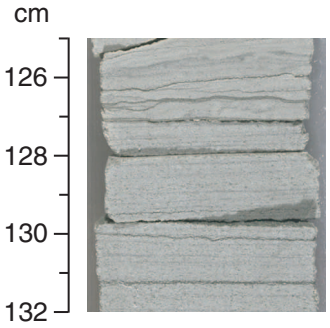

Figure F138. Close-up of a localized zone of ductile shearing in a bioturbated mudstone (interval 210-1276A-27R-3, 34–40 cm). The shear component is illustrated by asymmetric folds and elongated burrows that are aligned at a slightly oblique angle to the shear-zone boundaries.

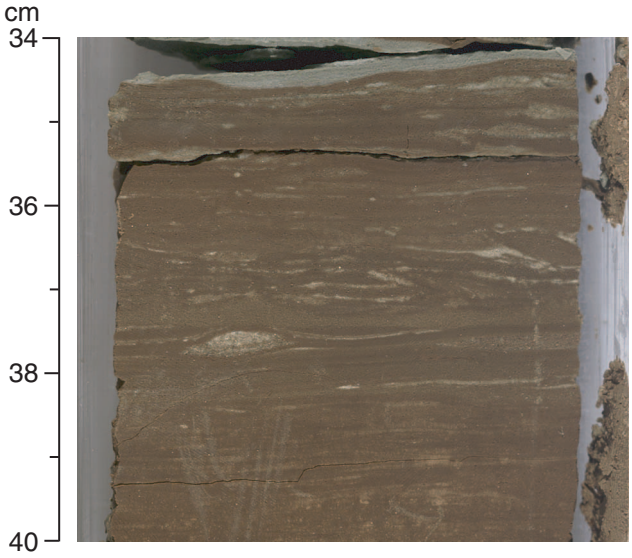

Figure F139. Close-up of a small reverse fault accommodating subhorizontal shortening in laminated siltstone (interval 210-1276A-94R-5, 20–27 cm).

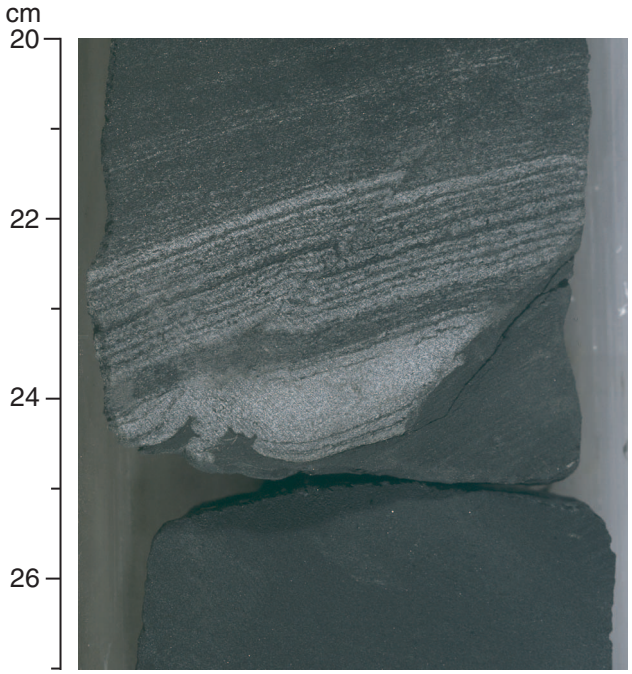

Figure F140. Summary of core recovery, lithology, and microfossil zones for Site 1276. (Continued on next two pages.)

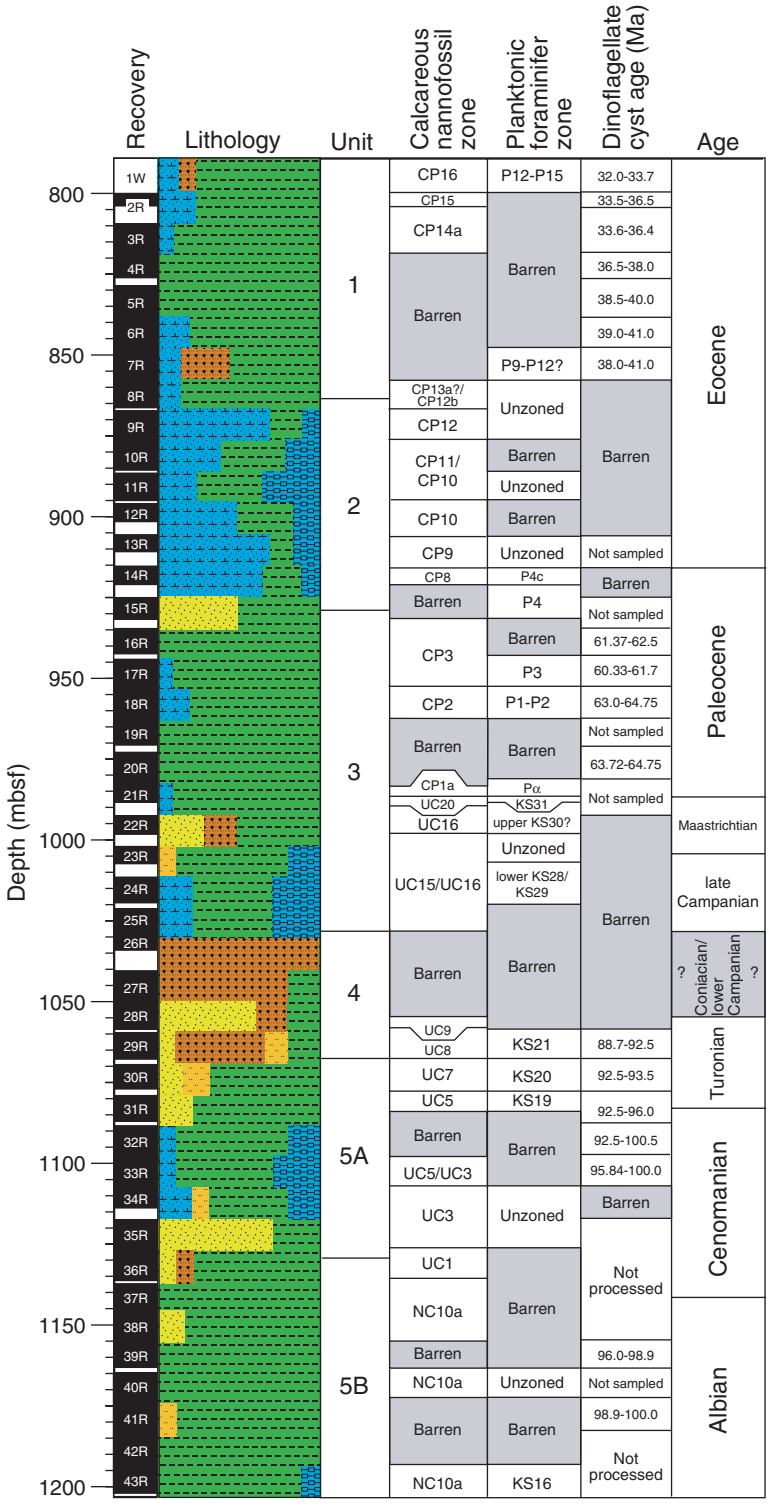

Figure F140 (continued).

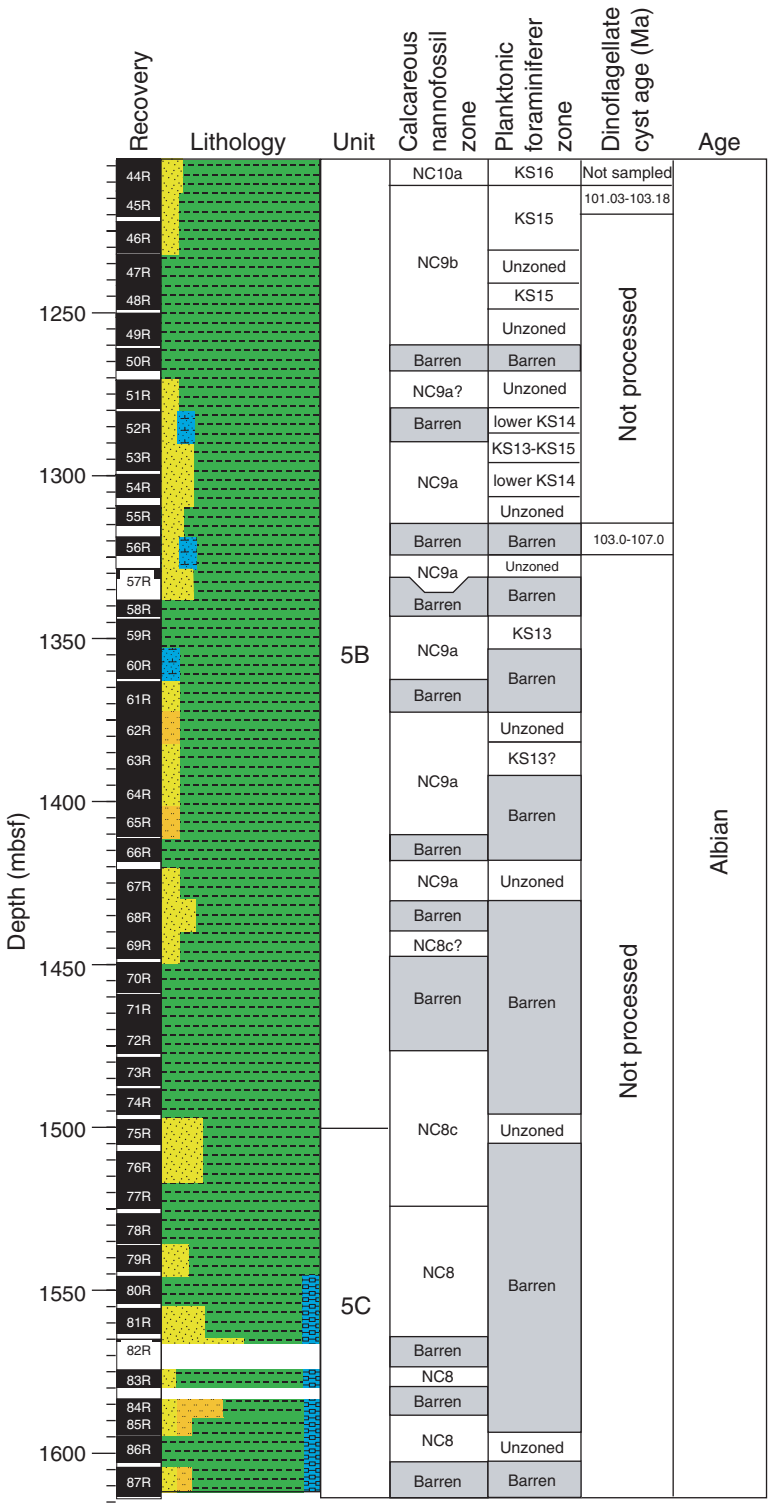

Figure F140 (continued).

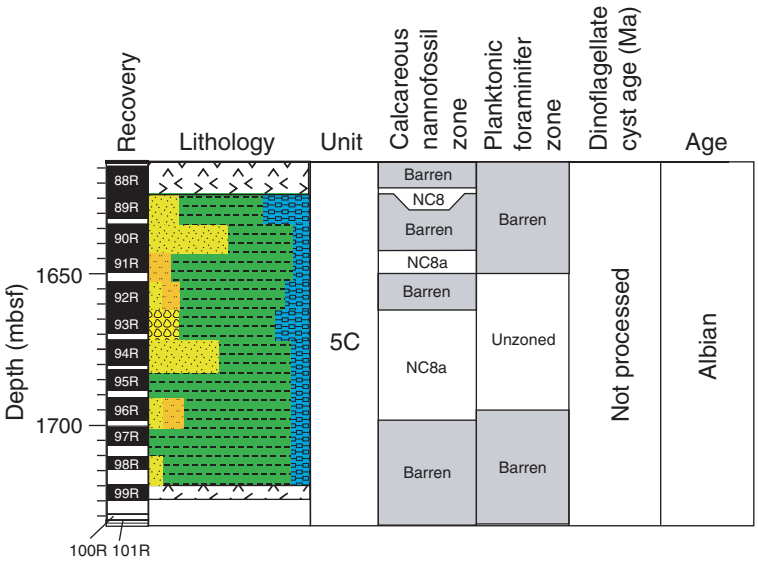

Figure F141. Age-depth plots based on first and last occurrence datums (FOs and LOs) of microfossils at ODP Site 1276 and DSDP Site 398. Dashed lines represent intervals in which no samples were analyzed, age-diagnostic datums are uncertain, or samples were found to be barren. Approximate sedimentation rates at Site 1276 are shown for straight-line segments through median depths of key calcareous nannofossil and palynomorph FOs and LOs. Datums used to construct age-depth plots at Site 1276 are listed in Table T12, p. 338; datums used to construct age-depth plots at Site 398 are listed in Table T13, p. 339.

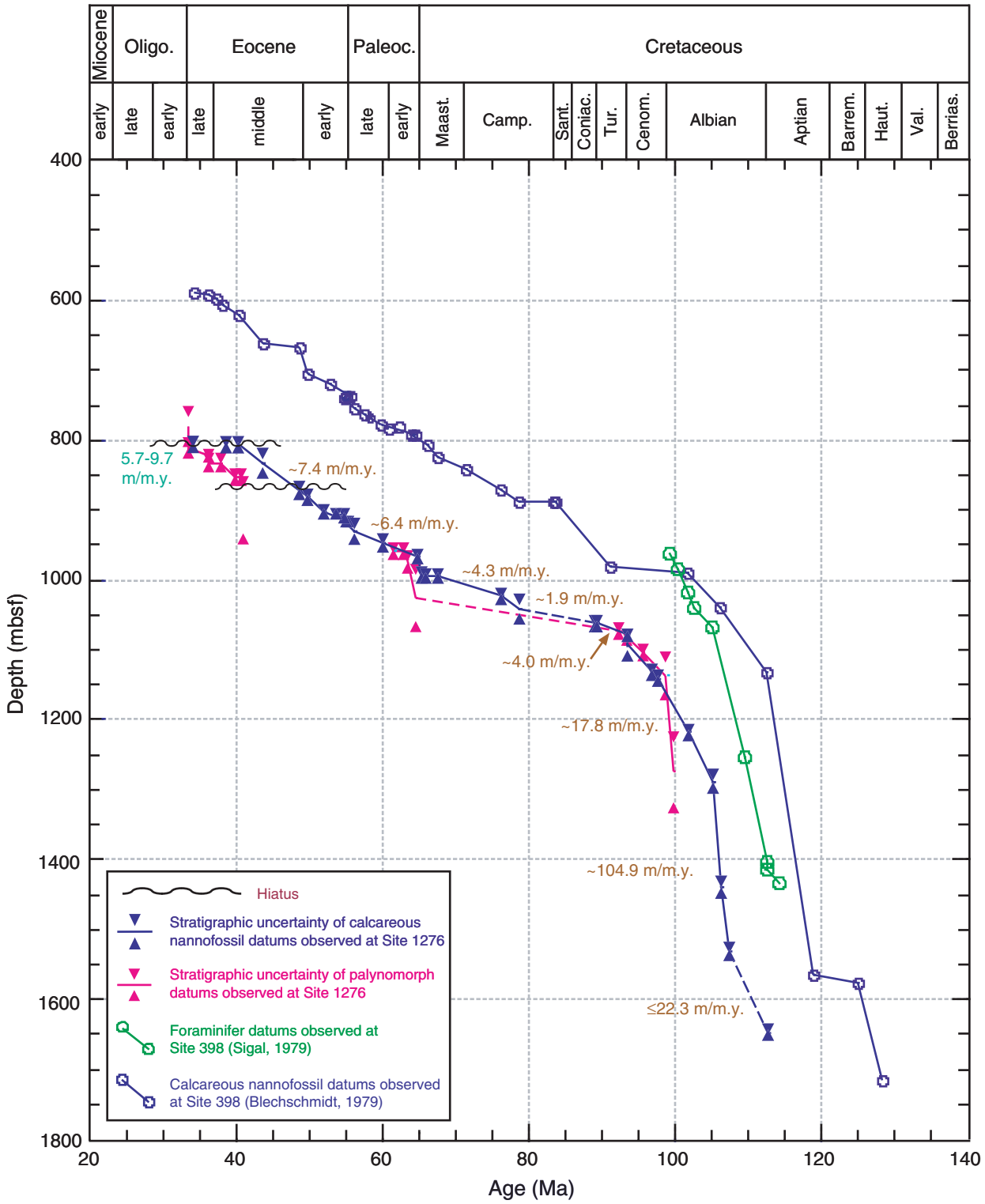

Figure F142. Age-depth plots based on first and last occurrences of microfossils at DSDP Site 398, and zonal boundary ages of microfossils observed at ODP Site 1276. Each set of opposing arrows represents the age of the biozone of one sample analyzed during shipboard operations at ODP Site 1276 (summarized on Table T7, p. 331). Ages of nannofossil and foraminifer datums in the Site 398 age-depth plot can be found in Tables T1, p. 58, T2, p. 60, T3, p. 62, T4, p. 63, and T5, p. 64, all in the "Explanatory Notes" chapter. Zonations used in estimating microfossil ages can be found in Figures F10, p. 51, and F11, p. 56, both in the "Explanatory Notes" chapter. Datums used to construct age-depth plots at Site 398 are listed in Table T13, p. 339.

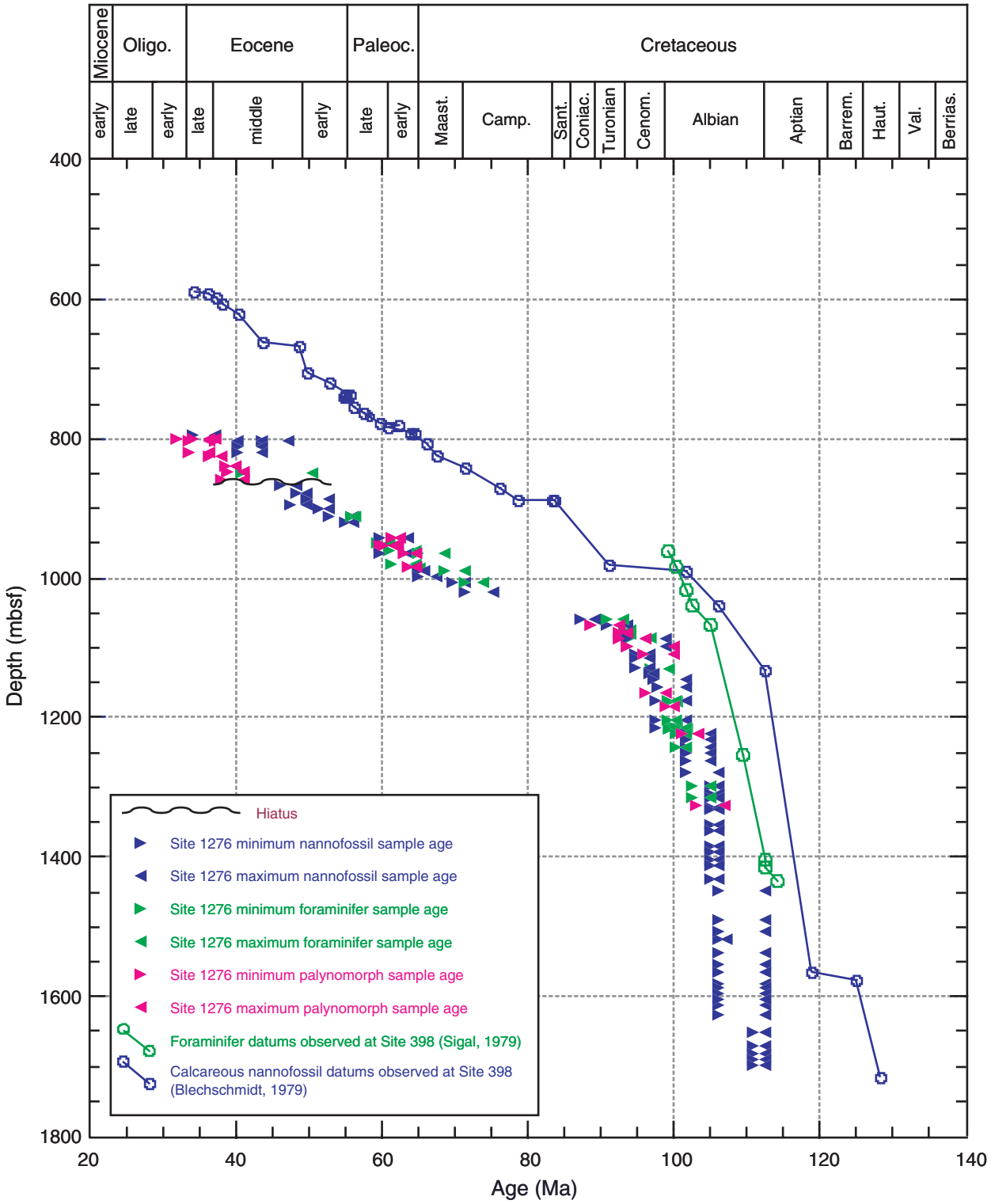

Figure F143. Measurements of magnetic susceptibility by AMST and natural remanent magnetization (NRM) intensity vs. depth for cores from Hole 1276A. Data for the two diabase sills in Subunit 5C are shown at expanded scale in Figures **F147,** p. 272, and **F148,** p. 273, respectively. For the lithologic key, see Fig. **F6,** p. 127.

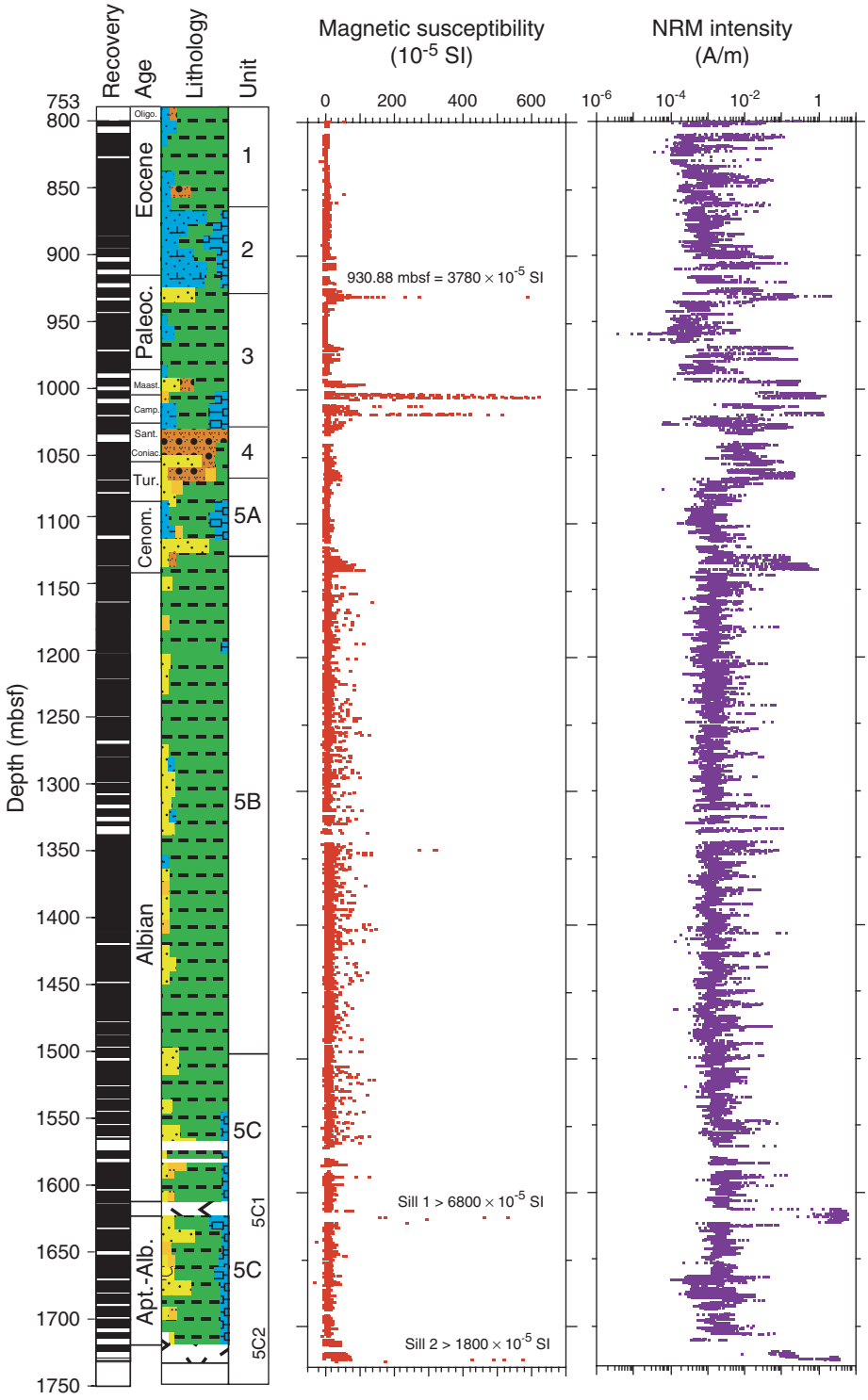

Figure F144. Remanent magnetization before and after 30-mT AF demagnetization, as a function of depth. (**A**) Inclination and (**B**) intensity of archive halves from Section 210-1276A-35R-5 are shown. The natural remanent magnetization (NRM) inclinations are biased toward high positive inclinations, suggesting that drilling-induced magnetization is present. AF demagnetization by 30 mT can effectively remove this drilling-induced magnetization, as indicated by the changes in inclination and intensity.

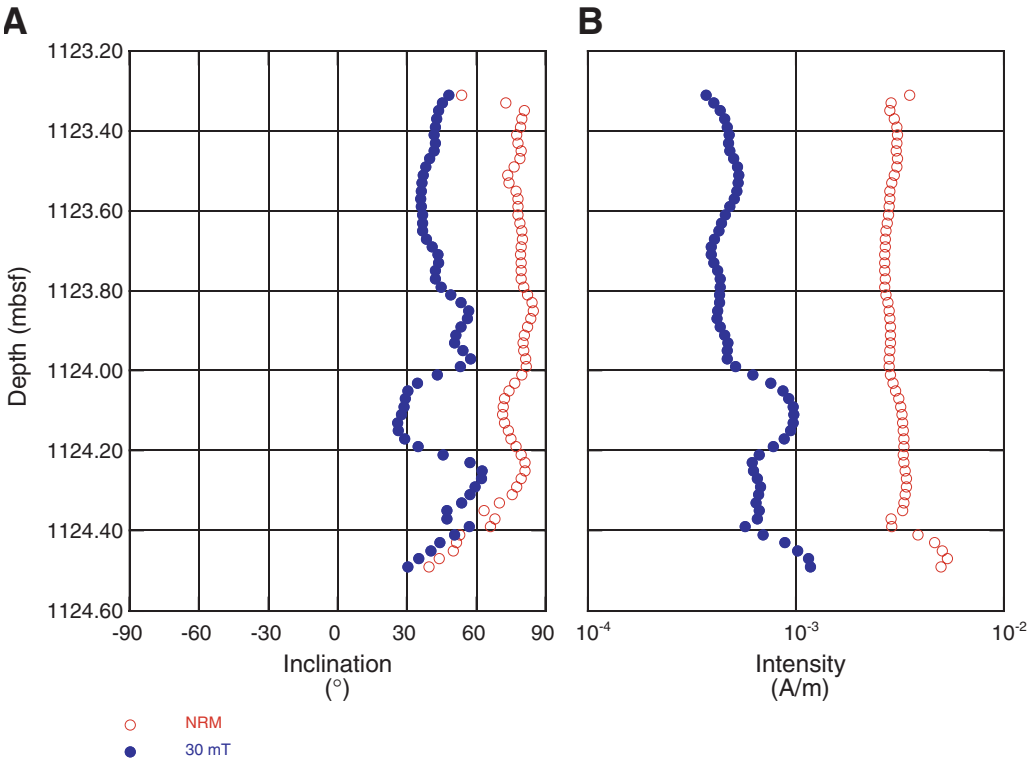

Figure F145. Examples of high-quality Zijderveld diagrams for sediments from (**A–C**) lithologic Units 2–4 and (**D**) Subunit 5B. These demonstrate the AF removal of a normal component of remagnetization caused either by drilling or by an overprint from the present geomagnetic field (A–C). The diagrams also show isolation of a more stable component that shows univectorial decay toward the origin of the vector plots (Zijderveld, 1967). An example of demagnetization behavior of a sample during thermal demagnetization is also illustrated (D). Open squares = vector endpoints projected onto the vertical plane, solid squares = vector endpoints projected onto the horizontal plane. These demagnetization behaviors are typical of the majority of samples from Unit 1 through Subunit 5B. NRM = natural remanent magnetization.

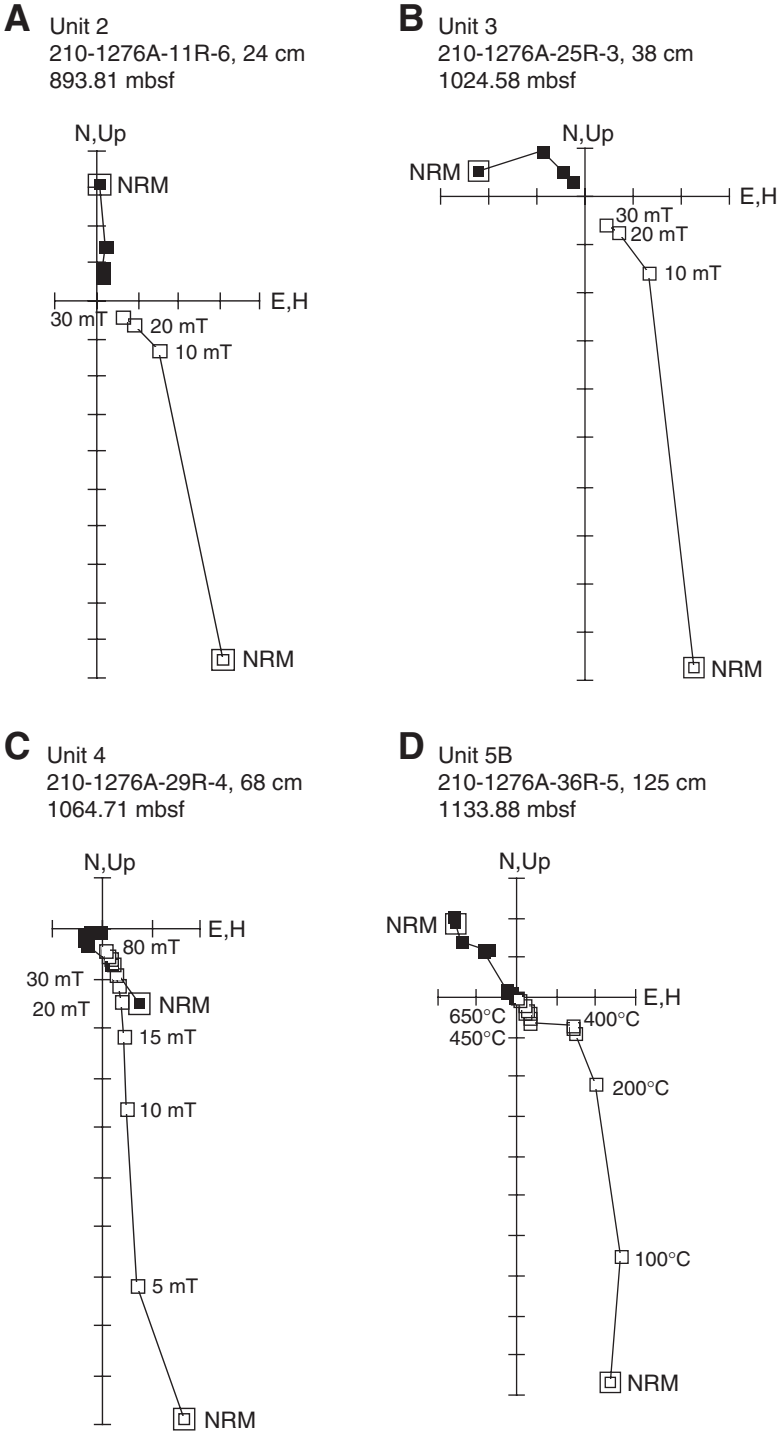

Figure F146. Measurements of (**A**) magnetic susceptibility and (**B**) remanent intensity before and after 30-mT AF demagnetization for Sections 210-1276A-33R-2 through 38R-3. Muddy sandstones from Sections 210-1276A-36R-1 through 36R-6 show high magnetization peaks. NRM = natural remanent magnetization.

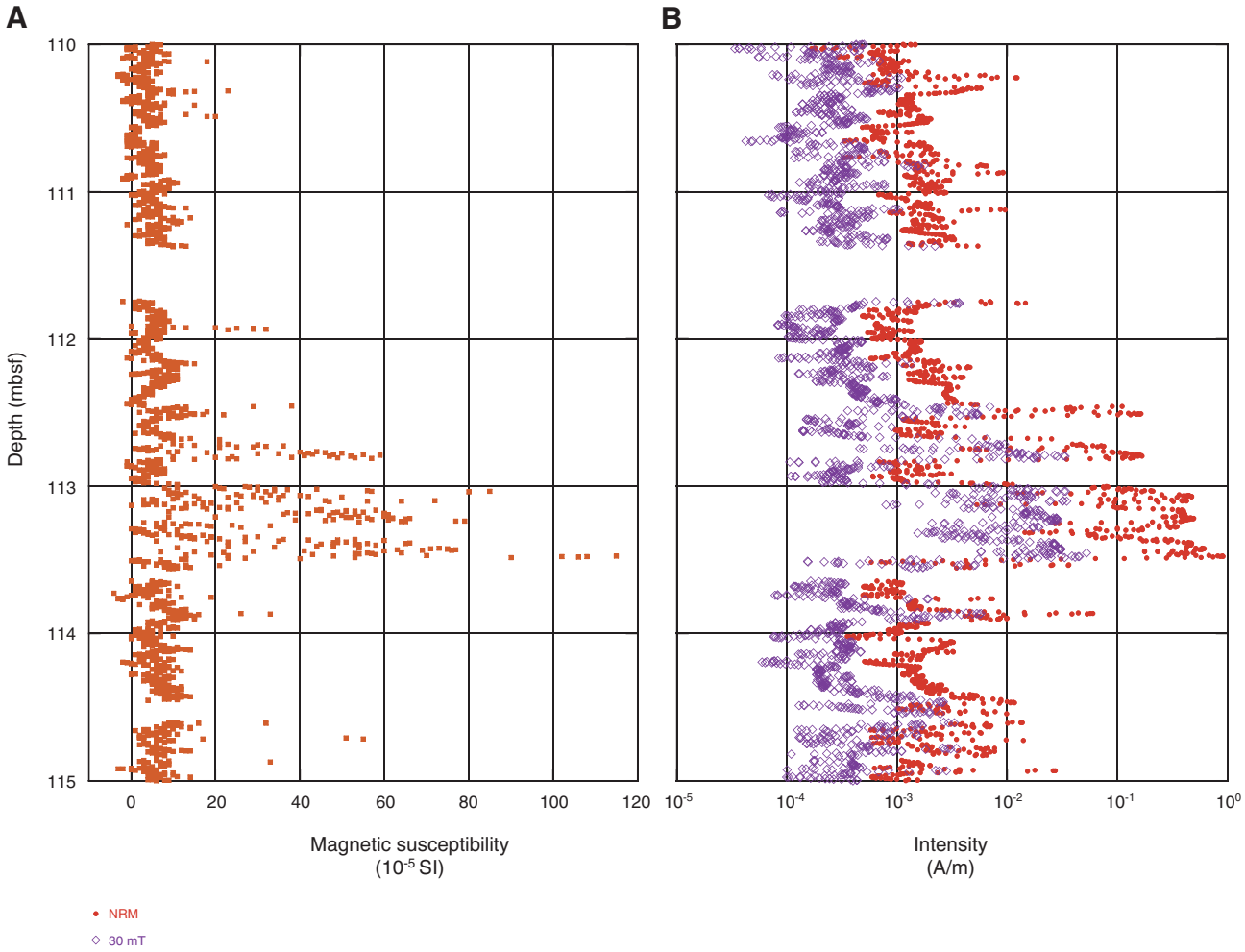

Figure F147. (**A**) Magnetic susceptibility by AMST and (**B, C**) intensity and inclination of the upper diabase sill (Sections 210-1276A-87R-6 through 88R-7 in Subunit 5C) before and after 20-mT AF demagnetization. NRM = natural remanent magnetization. For an explanation of the zonation of the sill, see Fig. **F120,** p. 243, and **"Igneous and Metamorphic Petrology,"** p. 64.

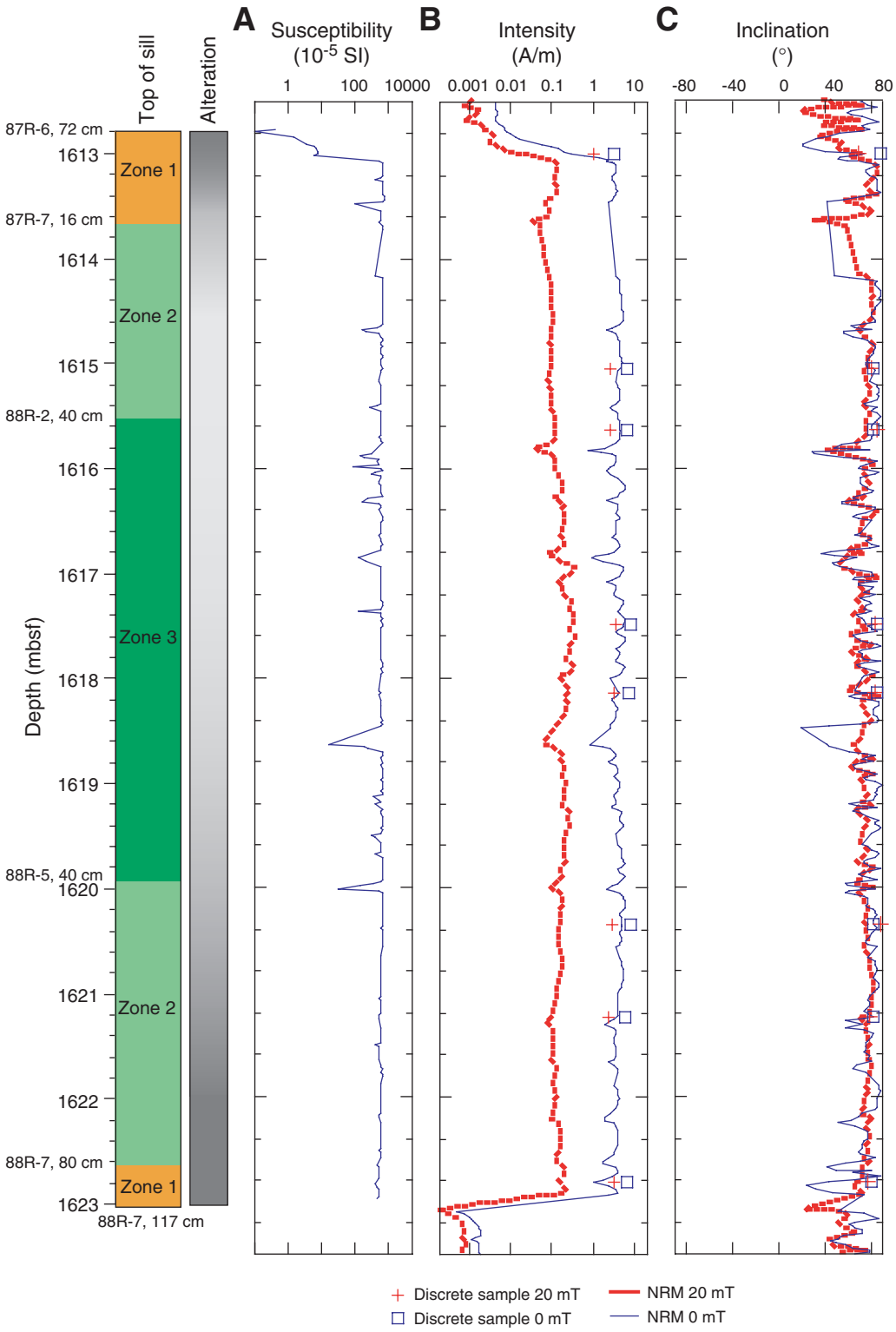

Figure F148. (**A**) Magnetic susceptibility by AMST and (**B**, **C**) intensity and inclination in the lower diabase sill (Sections 210-1276A-99R-1 through 99R-6 in Subunit 5C) before and after 20-mT AF demagnetization. NRM = natural remanent magnetization.

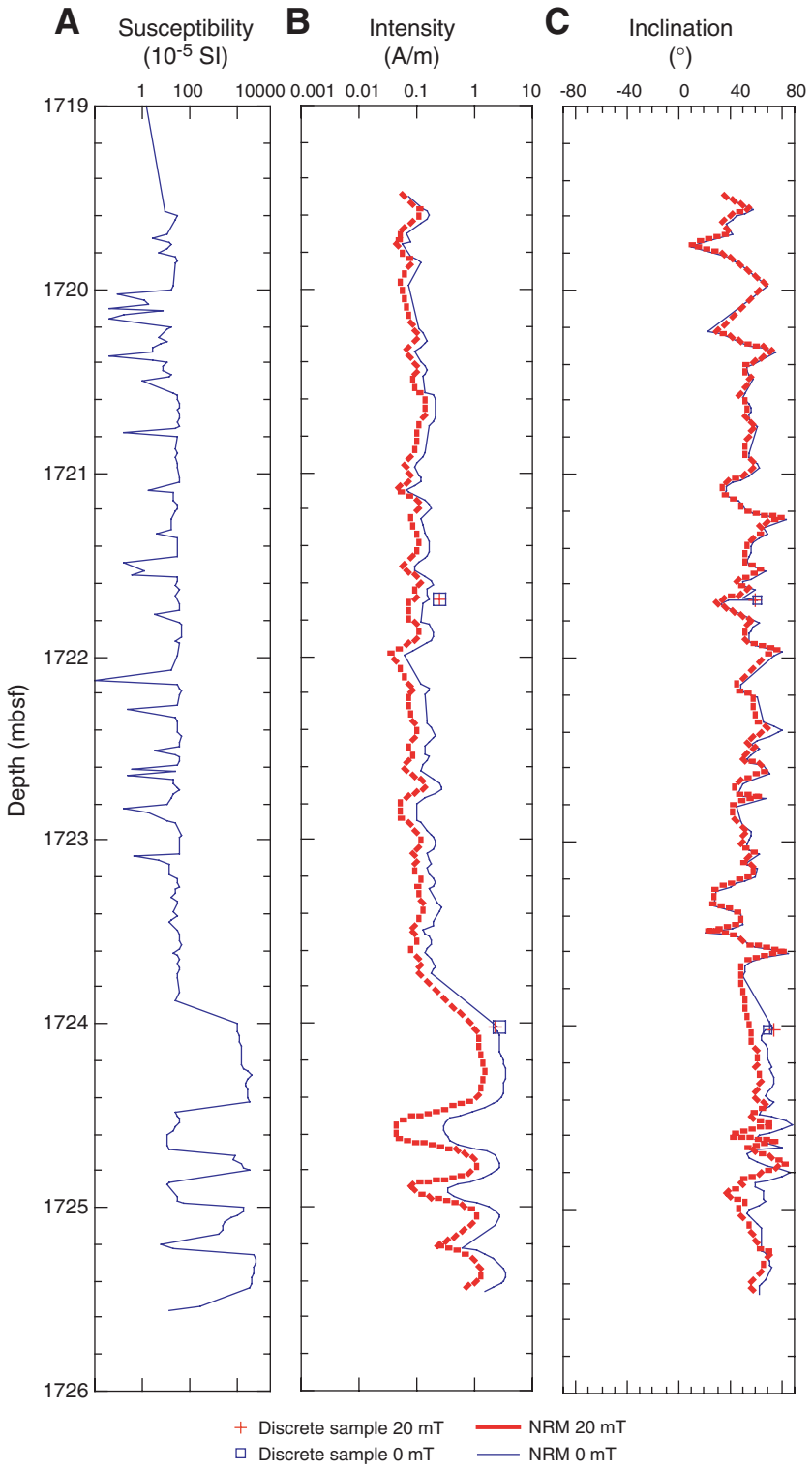

Figure F149. Zijderveld diagrams (Zijderveld, 1967) showing the results of AF demagnetization for diabase sills. (**A**) Sample 210-1276A-88R-4, 60 cm, from the upper sill and (**B**) Sample 210-1276A-99R-1, 126 cm, from the lower sill. Solid squares = projection of the magnetization vector endpoint on the horizontal plane, open squares = projection of the magnetization vector endpoints on the vertical plane. NRM = natural remanent magnetization.

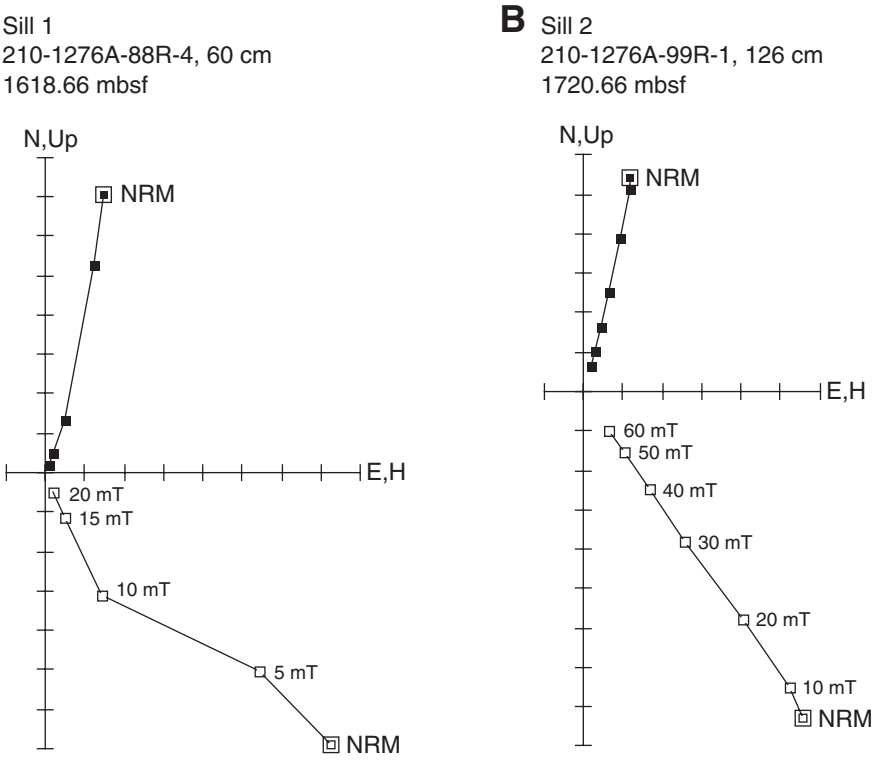

Figure F150. Remanent magnetization intensity (**A**) before and (**B**) after 20-mT AF demagnetization (Cores 210-1276A-58R through 68R). Even- and odd-numbered cores were retrieved by magnetic (i.e., conventional) and nonmagnetic rotary core barrels, respectively. NRM = natural remanent magnetization.

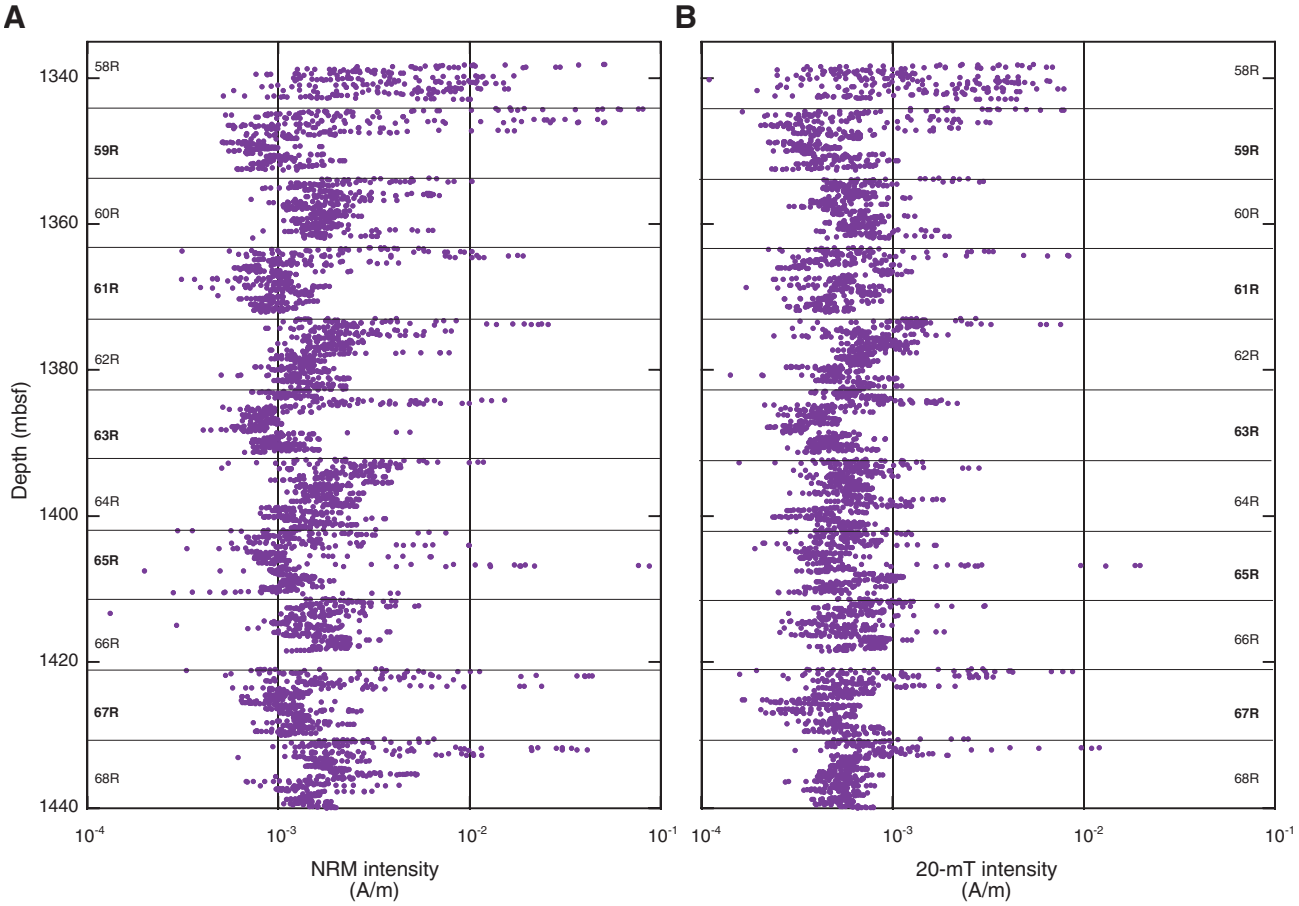

Figure F151. Inclination (**A**) before and (**B**) after 20-mT AF demagnetization (Cores 210-1276A-58R through 68R). Even- and odd-numbered cores were retrieved by magnetic (i.e., conventional) and nonmagnetic rotary core barrels, respectively. NRM = natural remanent magnetization.

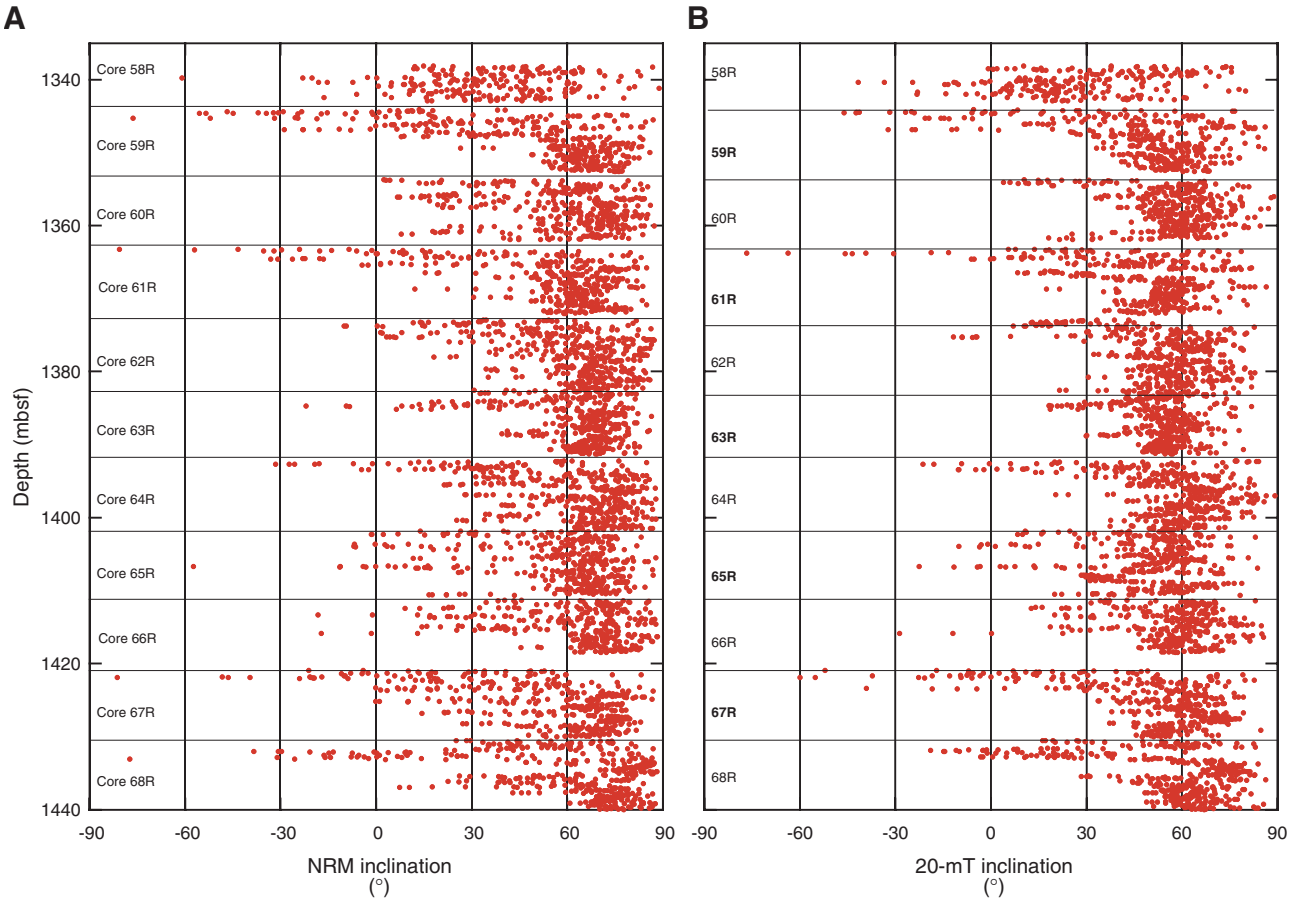

Figure F152. Downhole profiles of C_1 and C_2 concentrations and C_1/C_2 ratios, Hole 1276A.

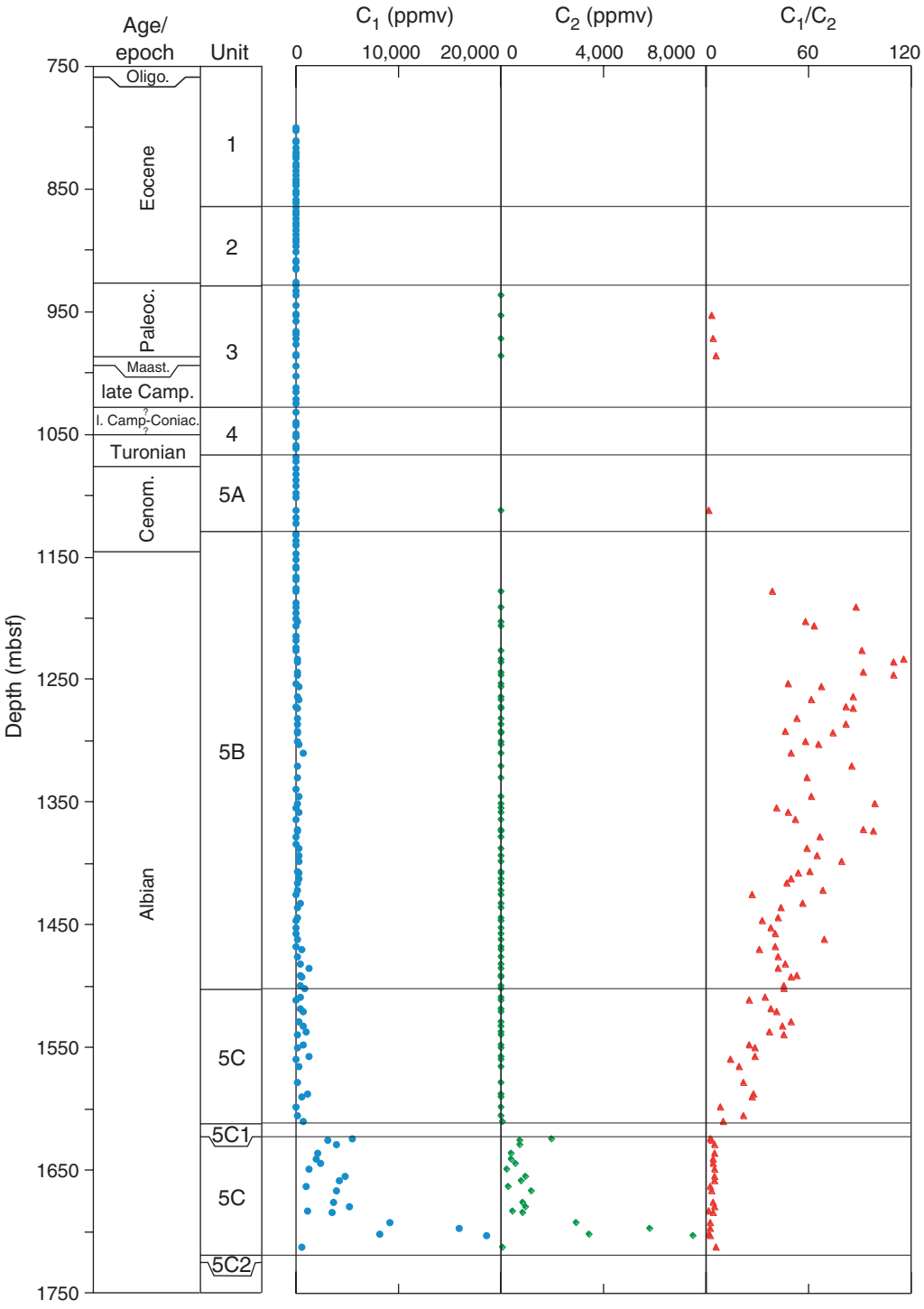

Figure F153. Comparison of C_1 and total organic carbon (TOC) profiles, Hole 1276A.

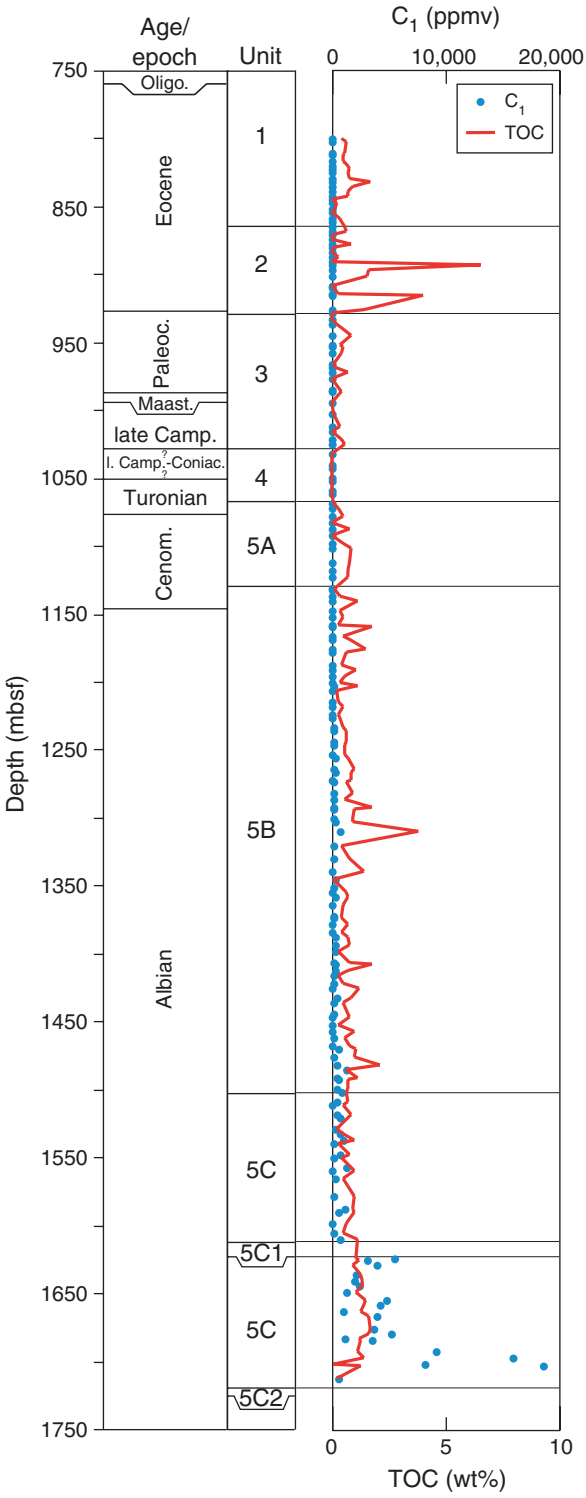

Figure F154. Downhole profiles of $CaCO_3$, total organic carbon (TOC) contents, and C/N ratios, Hole 1276A.

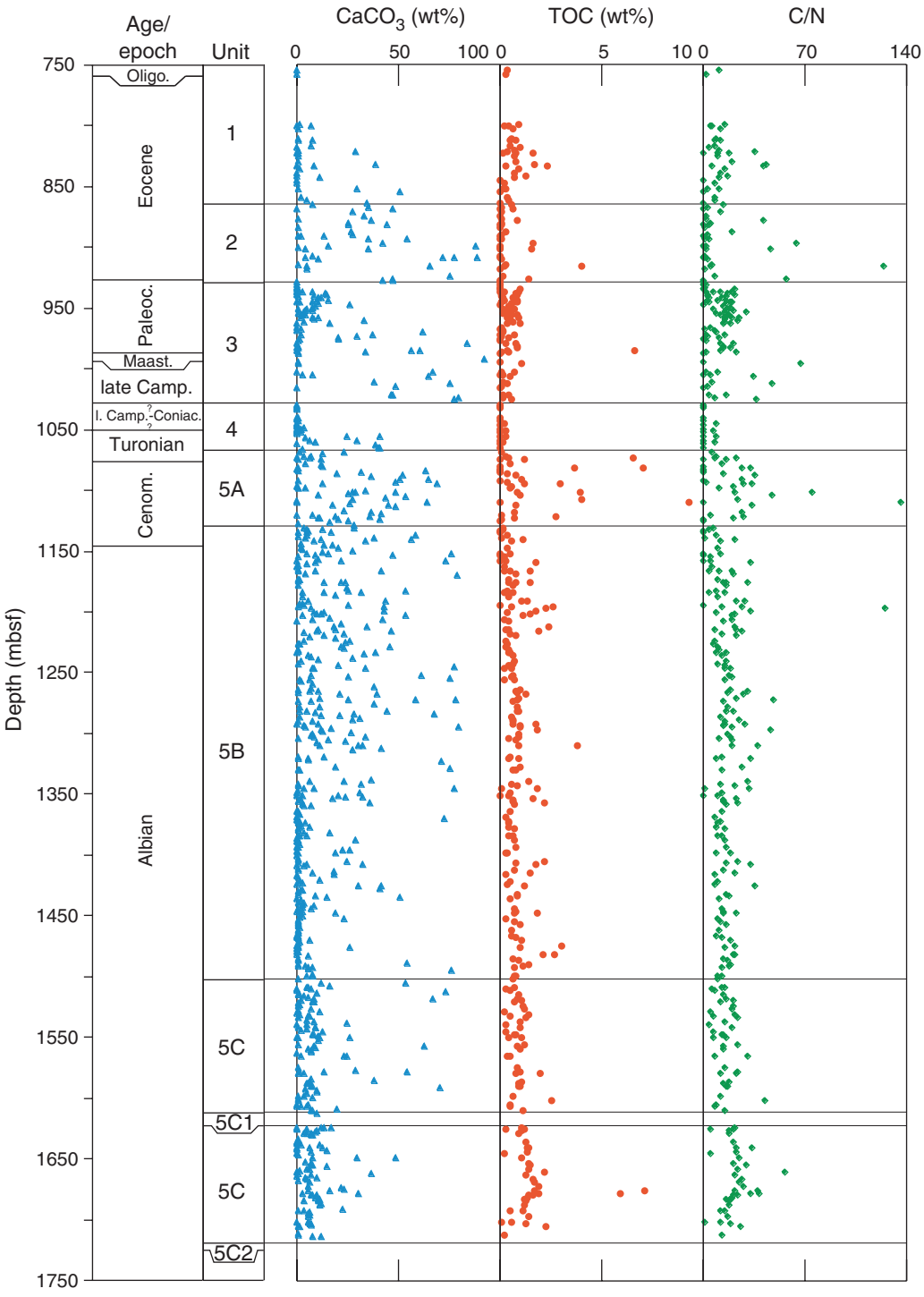

Figure F155. Downhole profile of total organic carbon (TOC) and Al concentrations, and Ba/Al, Ni/Al, Cr/Al, and V/Al ratios, Hole 1276A, with locations of possible Oceanic Anoxic Event (OAE) black shales. MCE = mid-Cenomanian event.

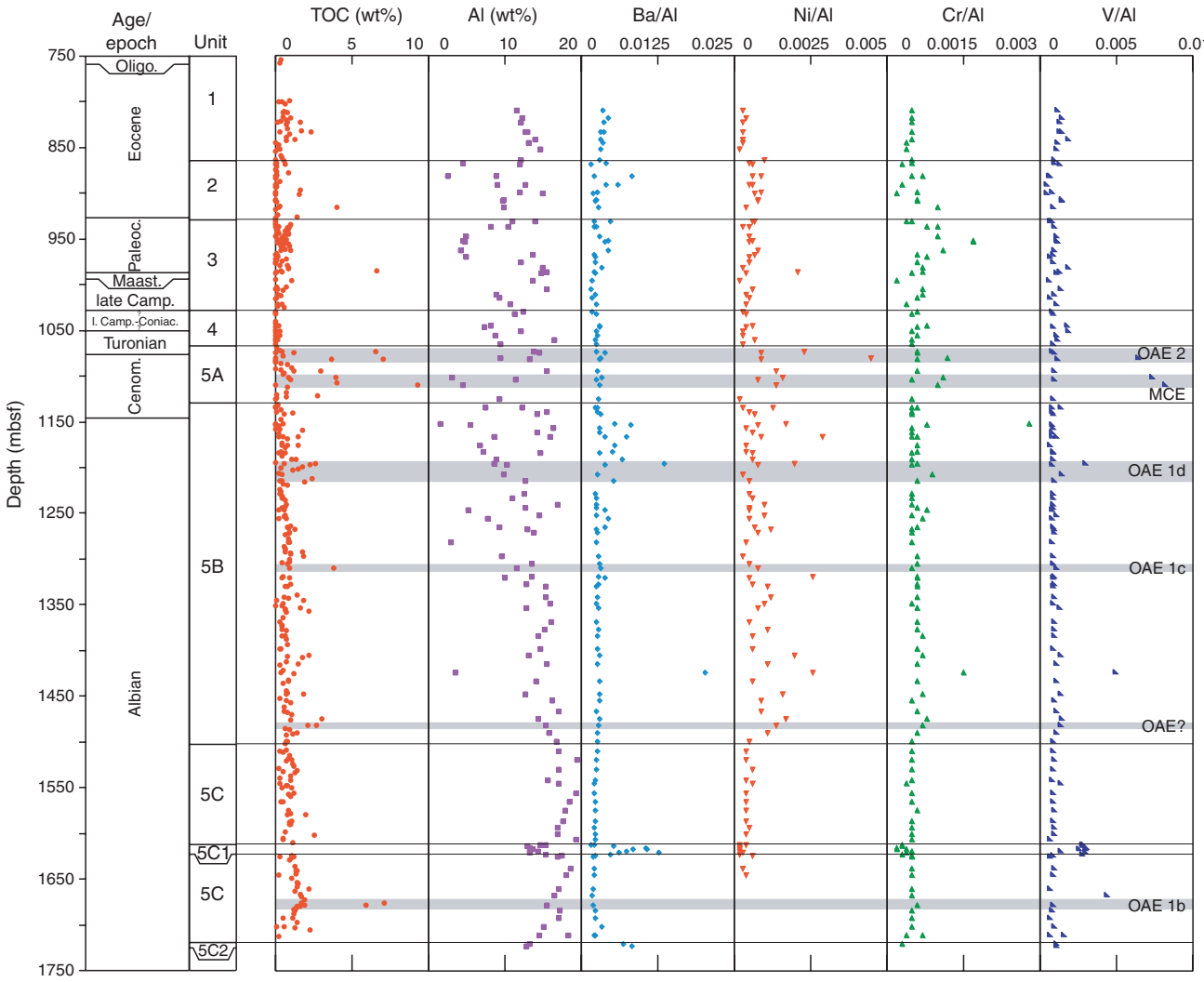

Figure F156. Downhole profiles of total organic carbon (TOC) contents and results from Rock-Eval pyrolysis in Hole 1276A, with locations of possible Oceanic Anoxic Event (OAE) black shales. HI = hydrogen index. MCE = mid-Cenomanian event.

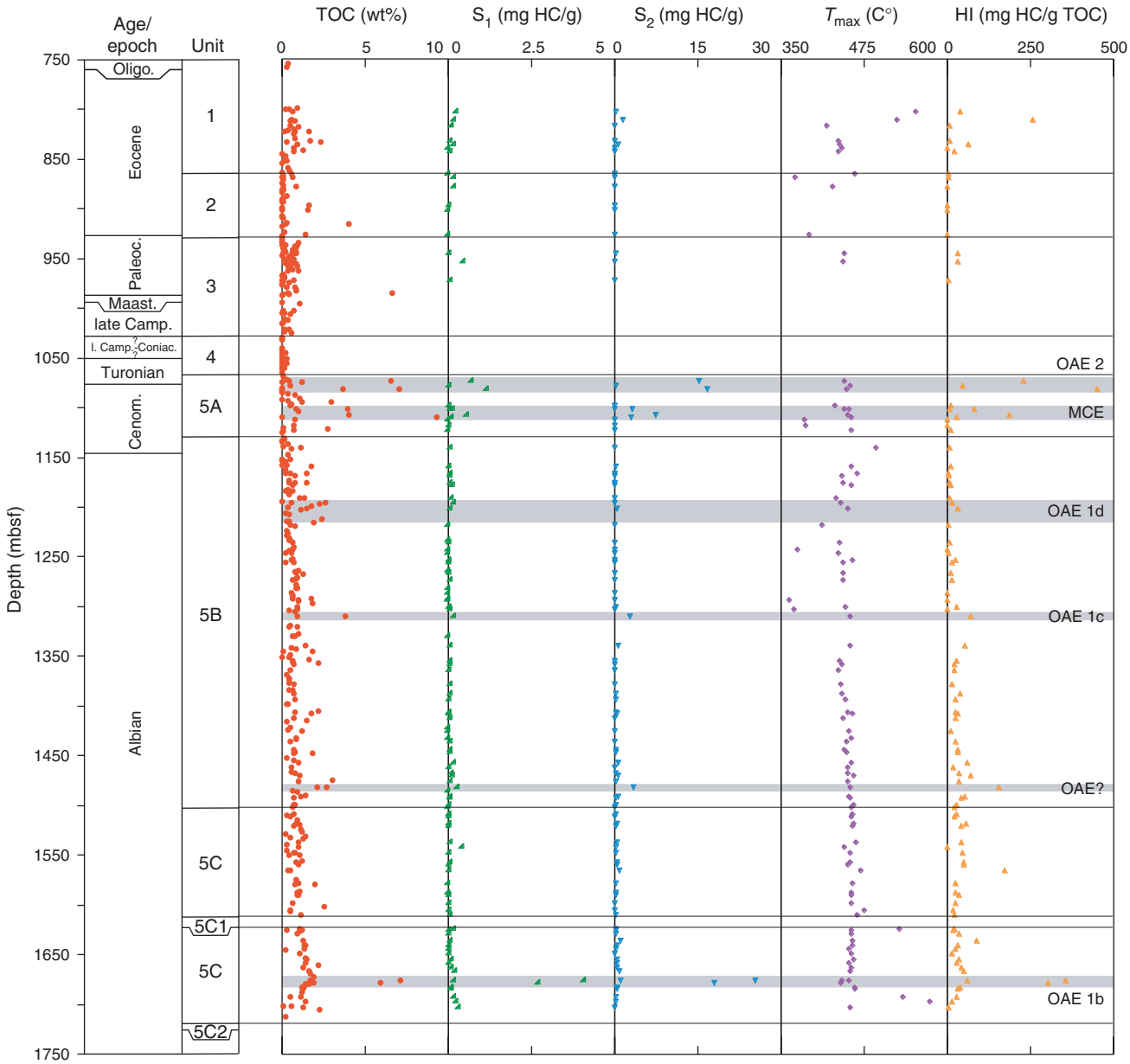

Figure F157. Comparison of Rock-Eval pyrolysis hydrogen index and T_{max} (modified from Wagner and Pletsch 2001). Only results from samples with total organic carbon (TOC) > 0.5 wt% and T_{max} < 500°C are included.

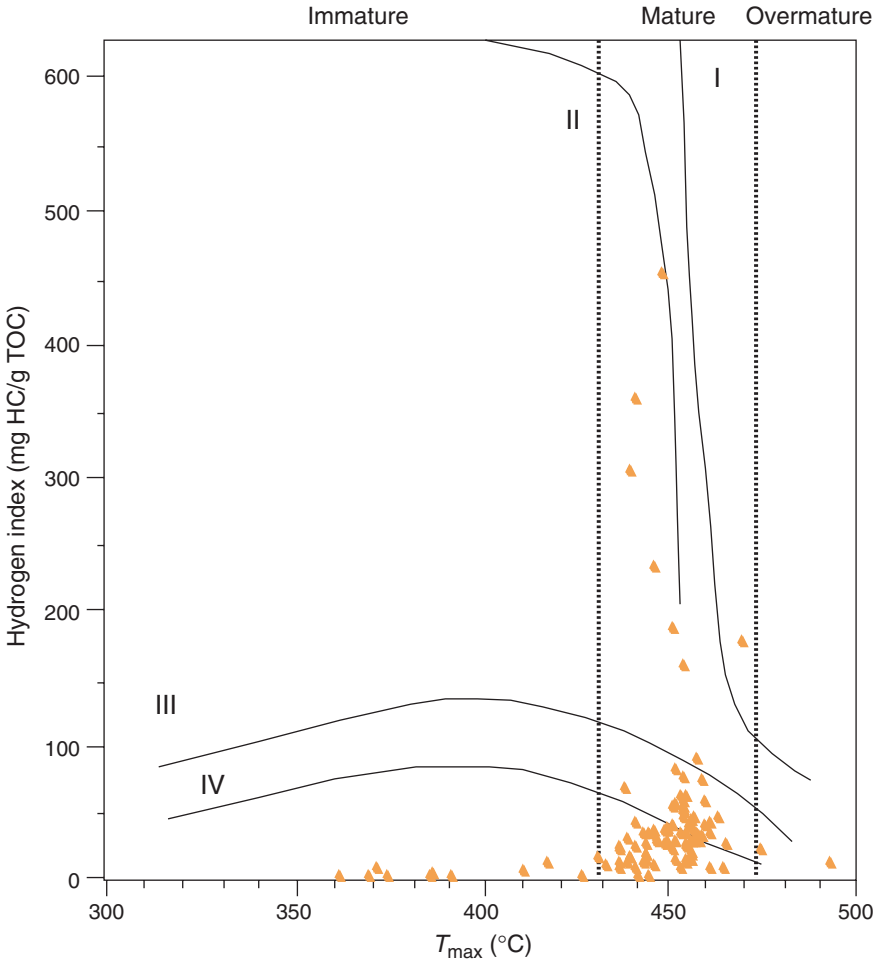

Figure F158. GRA bulk density (red dots) and MAD bulk density (blue dots) plotted next to core recovery and lithologic units. (Continued on next page.)

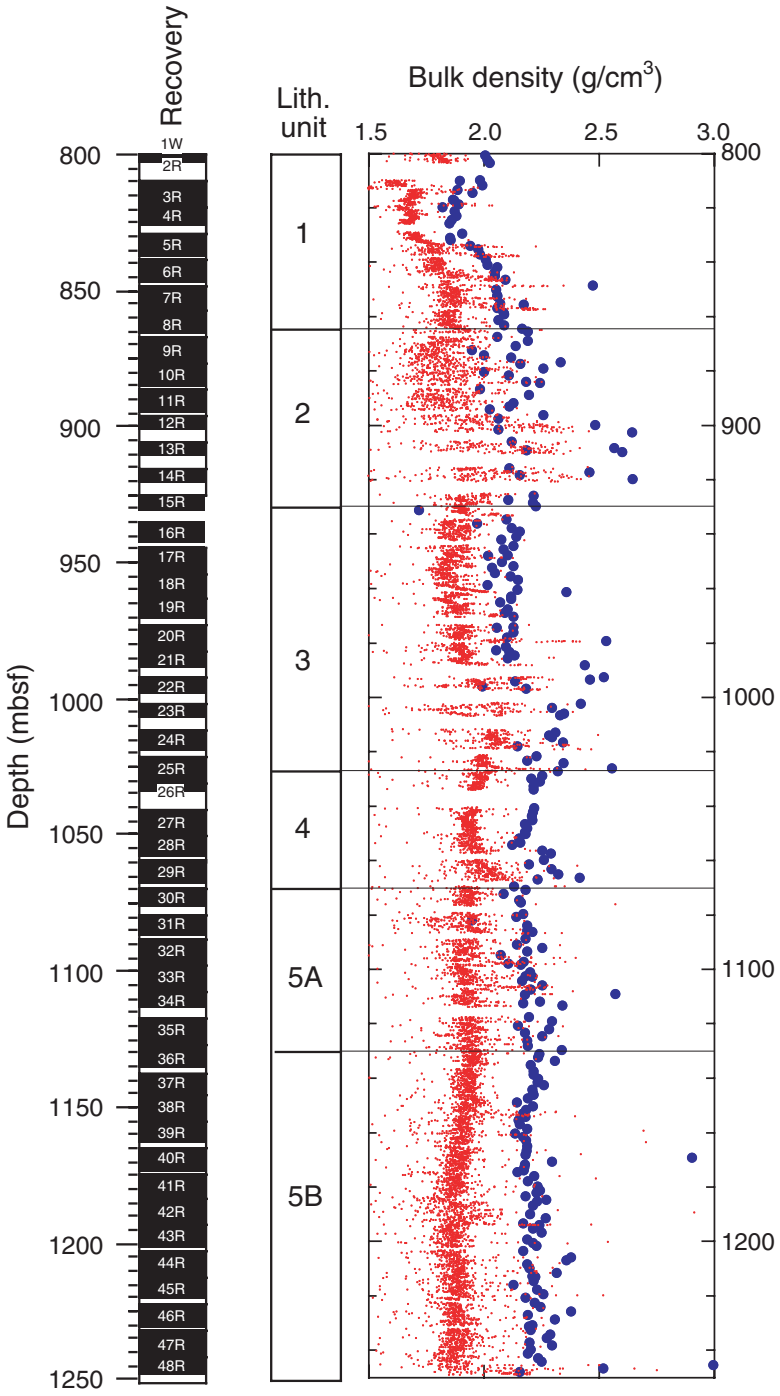

Figure F158 (continued).

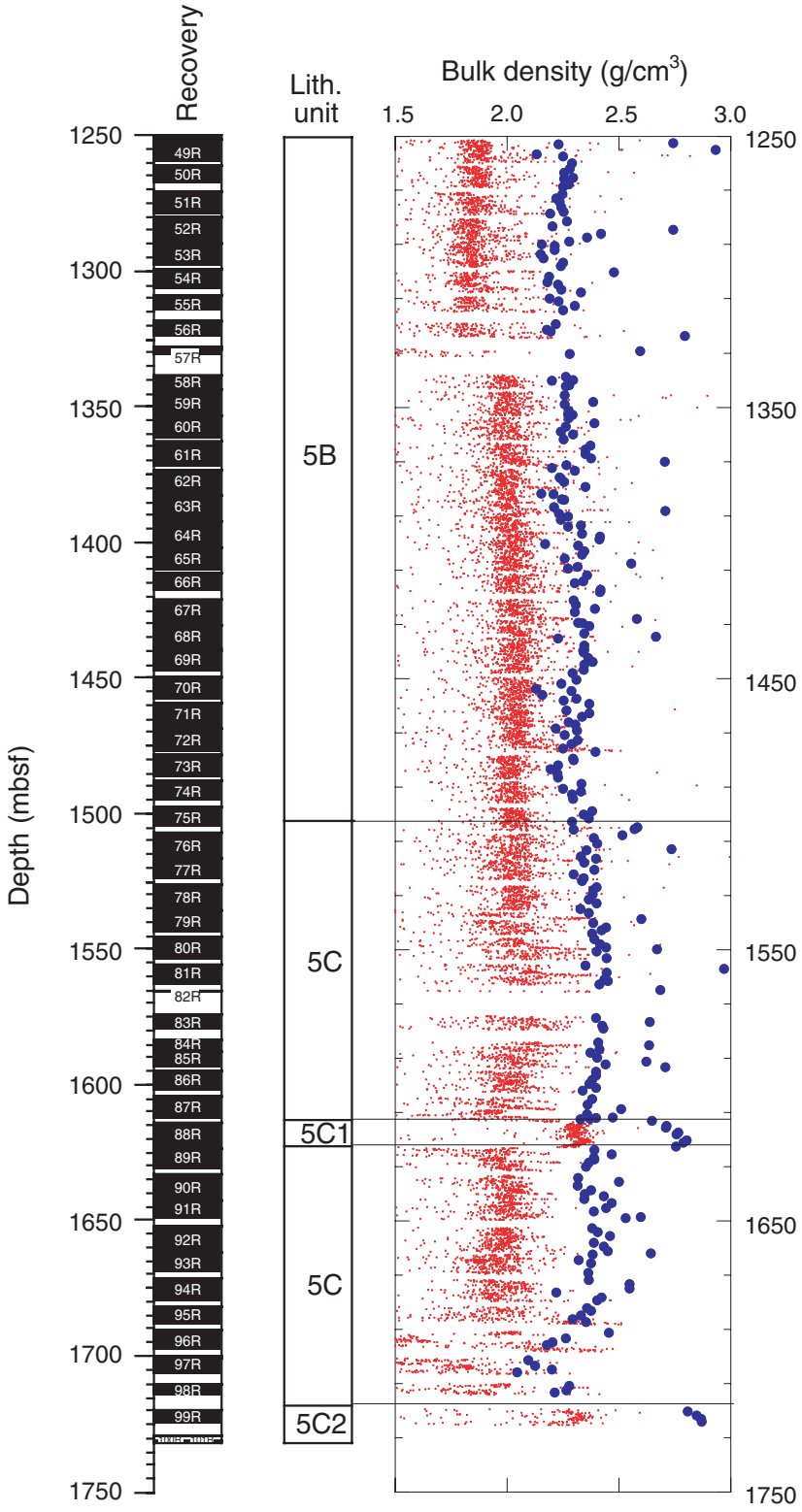

Figure F159. Bulk density, grain density, and porosity vs. depth, from MAD measurements. Lithologic symbols are defined in Figure F160, p. 287. (Continued on next page.)

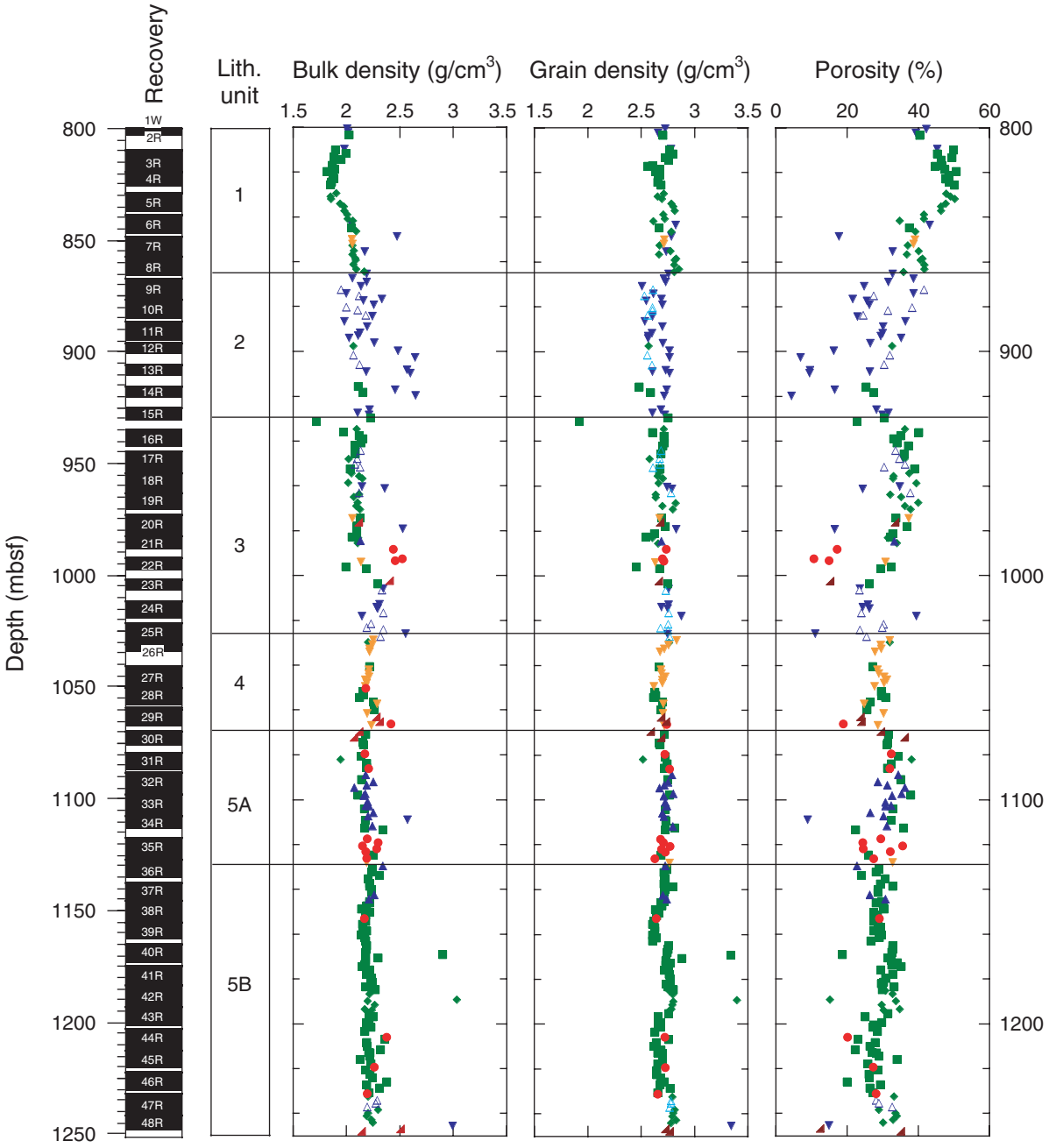

Figure F159 (continued).

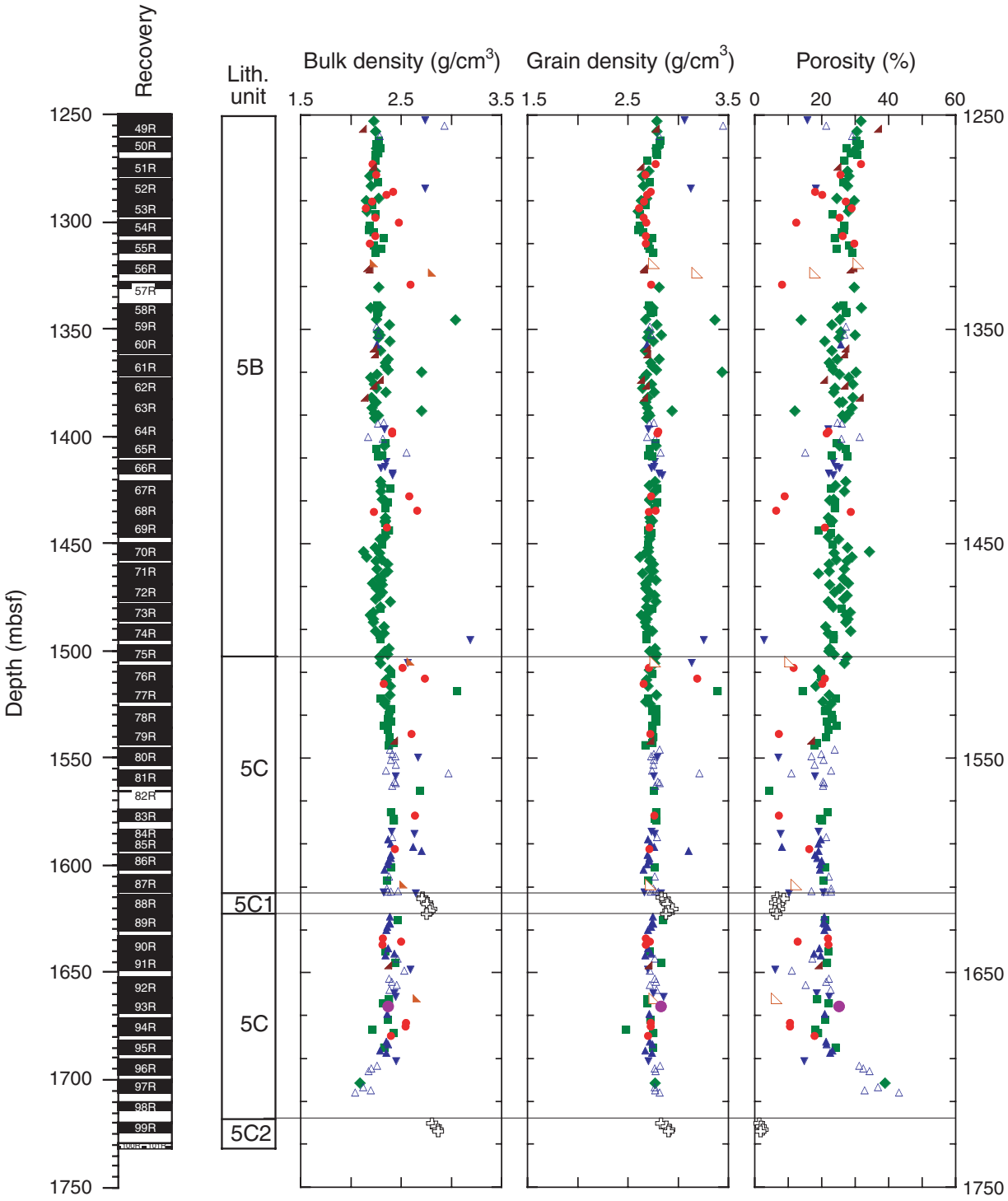

Figure F160. Symbols used for plotting physical property data according to major lithology in Figures F159, p. 285, F161, p. 288, F162A, p. 290, F162B, p. 291, F162C, p. 292, F162E, p. 294, F164, p. 297, and F167, p. 303. The lithologic identification of each sample was obtained by automated lookup from the AppleCORE barrel sheet database for Hole 1276A.

Figure F161. A. MAD porosity vs. depth. Best-fit (Athy's law) porosity vs. depth for the general lithologies recovered at Site 1276 (except carbonate/siderite concretions, well-lithified carbonate-cemented sandstones, and those sediments that are hornfels) are shown in blue. Lithologic symbols are defined in Figure F160, p. 287. (Continued on next page.)

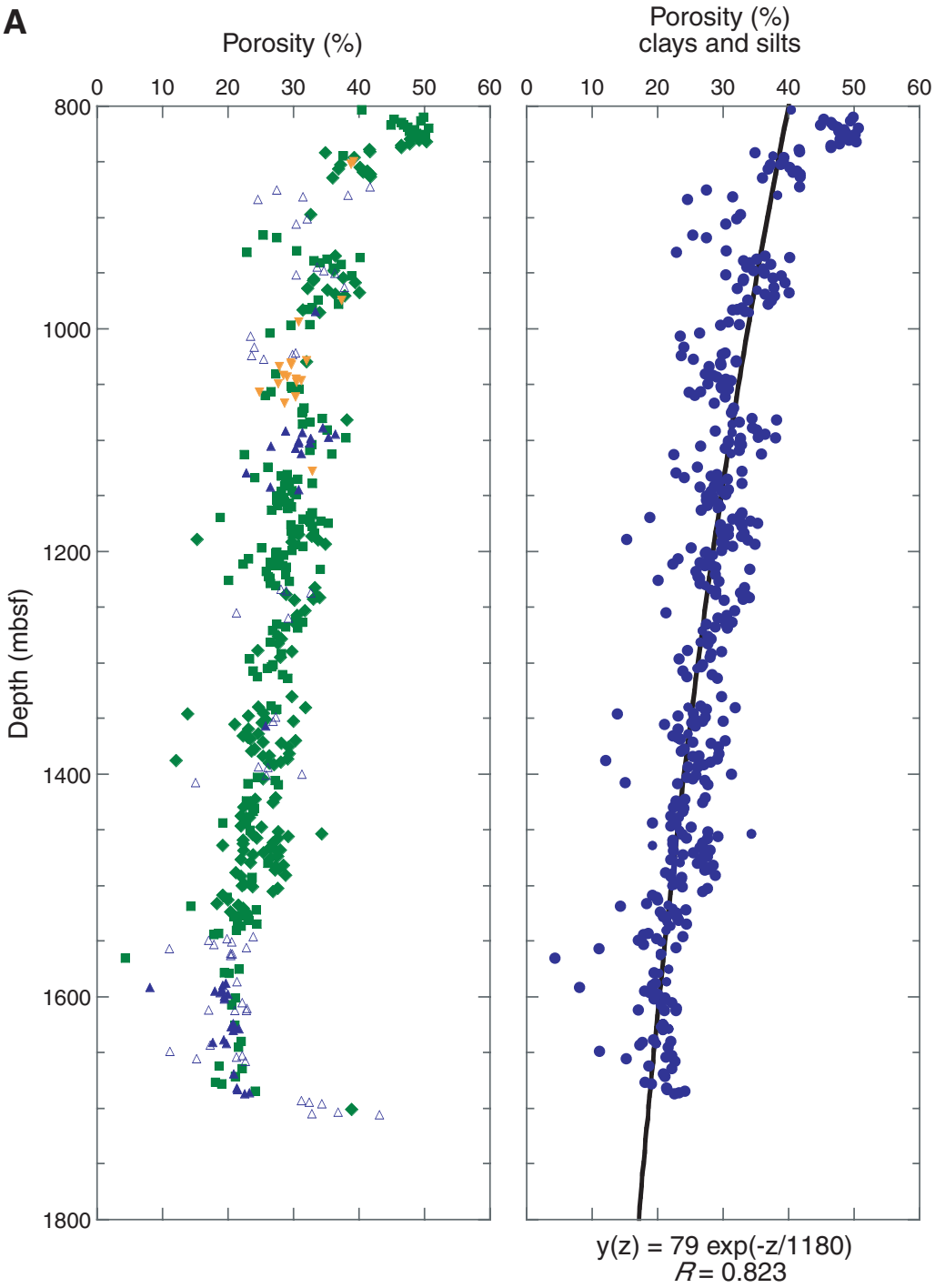

Figure F161 (continued). B. A schematic lithologic column, x-direction velocity, porosity, and methane (C_1) cross plots vs. depth for the lowermost 50 m of Site 1276 (1675–1725 mbsf). Right-hand border on lithologic column = relative degree of compaction. Black circles = shipboard measurements. Dashed red lines = best-fit lines for each respective data set. Mudst. = mudstone, calc. = calcareous.

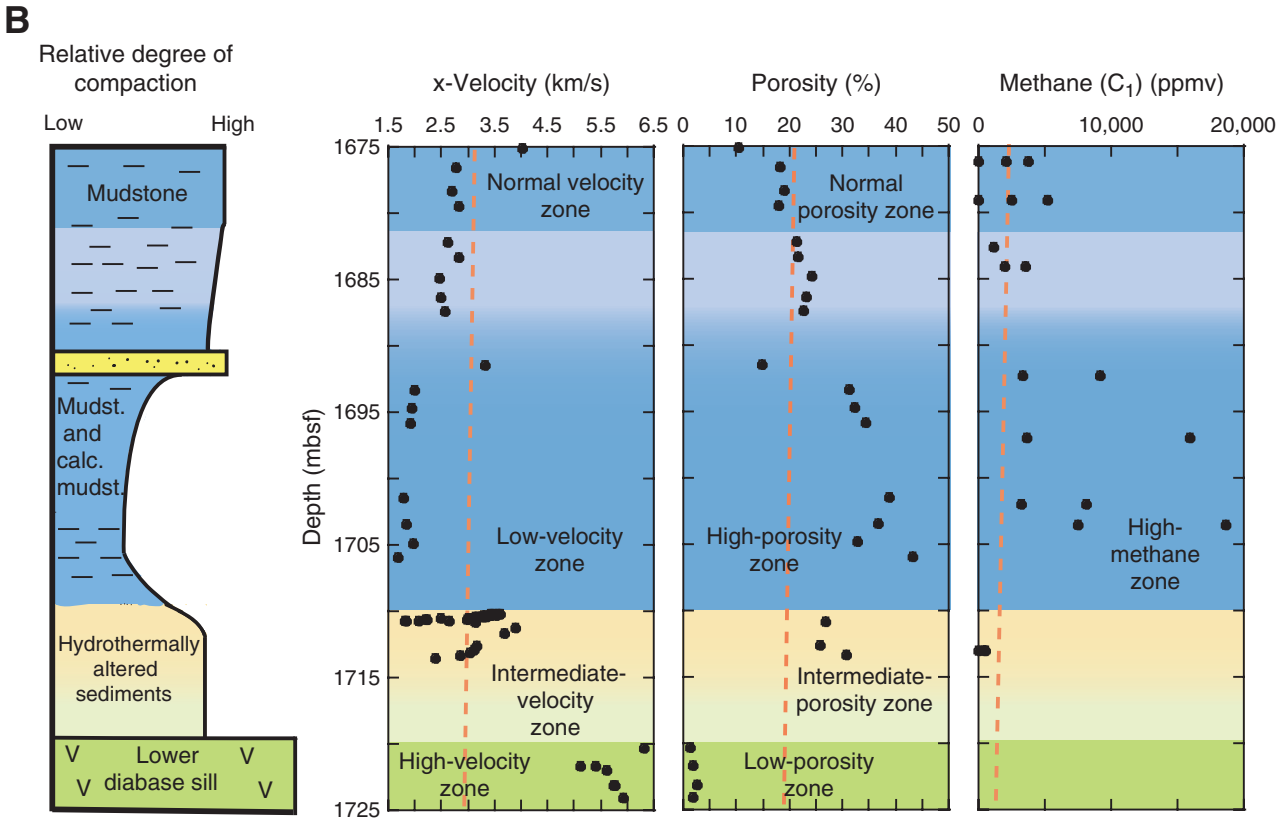

Figure F162. A. *P*-wave velocity (x-, y-, and z-directions) measured using the *P*-wave velocity sensor 3 contact probe system, plotted next to core recovery and lithologic units. Lithologic symbols are defined in Figure F160, p. 287. (Continued on next four pages.)

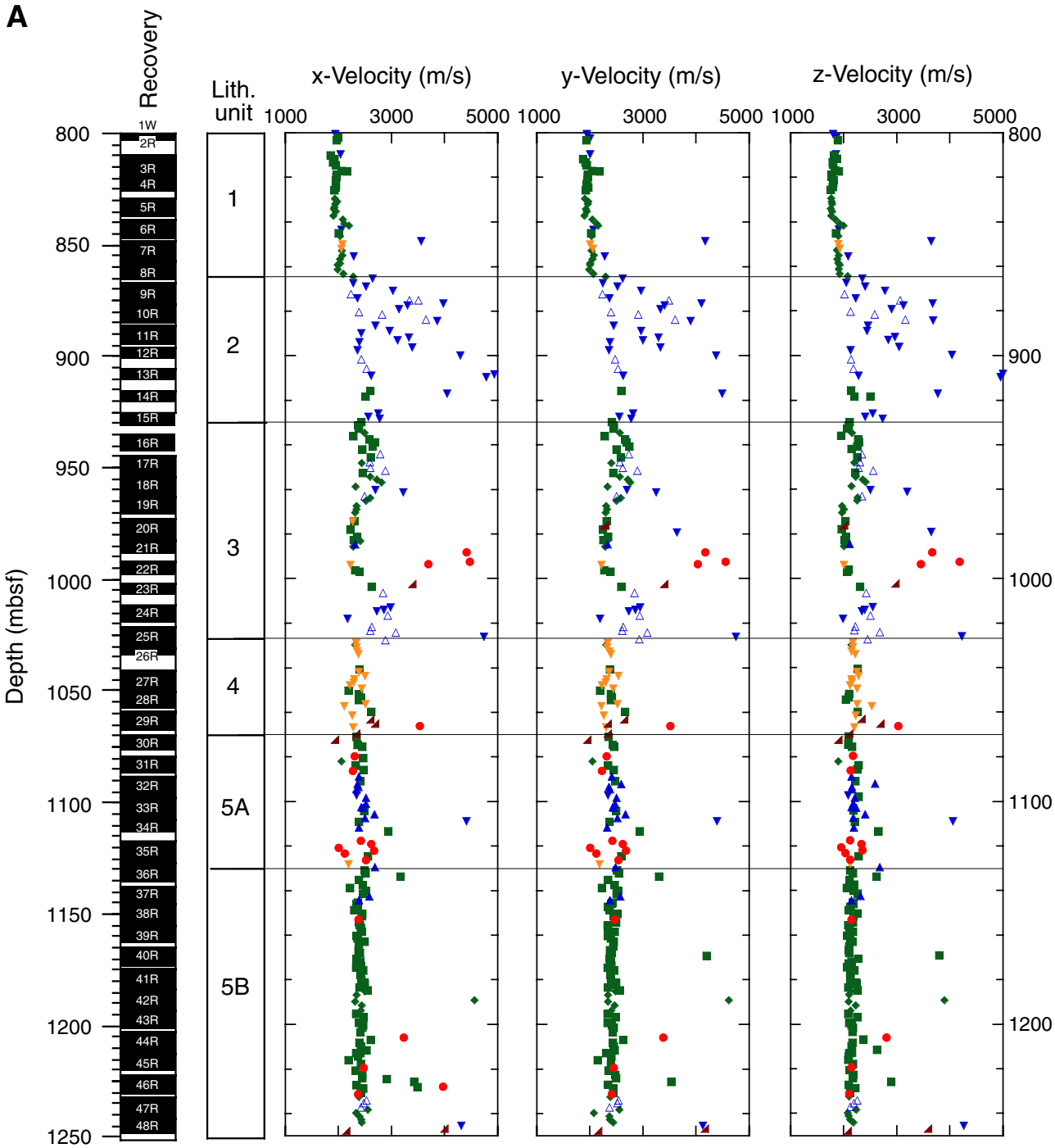

Figure F162 (continued). B. *P*-wave velocity (x-, y-, and z-directions) measured using the *P*-wave sensor 3 contact probe system, plotted next to core recovery and lithologic units. Lithologic symbols are defined in Figure F160, p. 287.

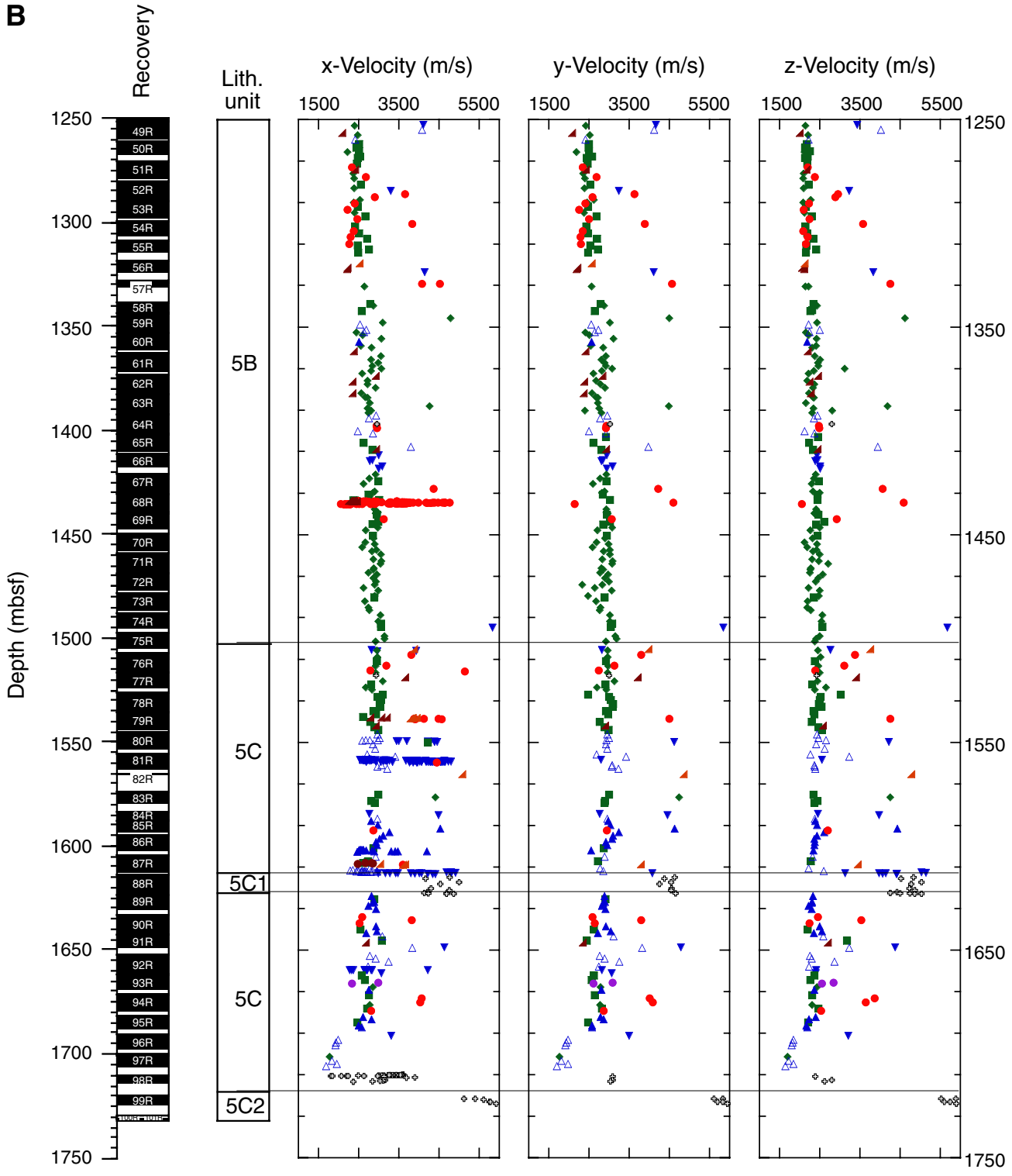

Figure F162 (continued). C. X-direction velocity measured at 2- to 10-cm spacing over turbidites in Sections 210-1276A-68R-3 and 68R-4, 79R-2, and 80R-3, respectively, plotted next to core photographs of these sections. The arrows on the section at left show the position of the last measurement downcore. $CaCO_3$ is also plotted, and it is indicated with black bars. Note the correlation between high concentrations of $CaCO_3$ and high velocity in fine-grained sandstones, suggesting that carbonate cementation may play a primary role in controlling velocity structure within turbidites. Lithologic symbols are defined in Figure F160, p. 287.

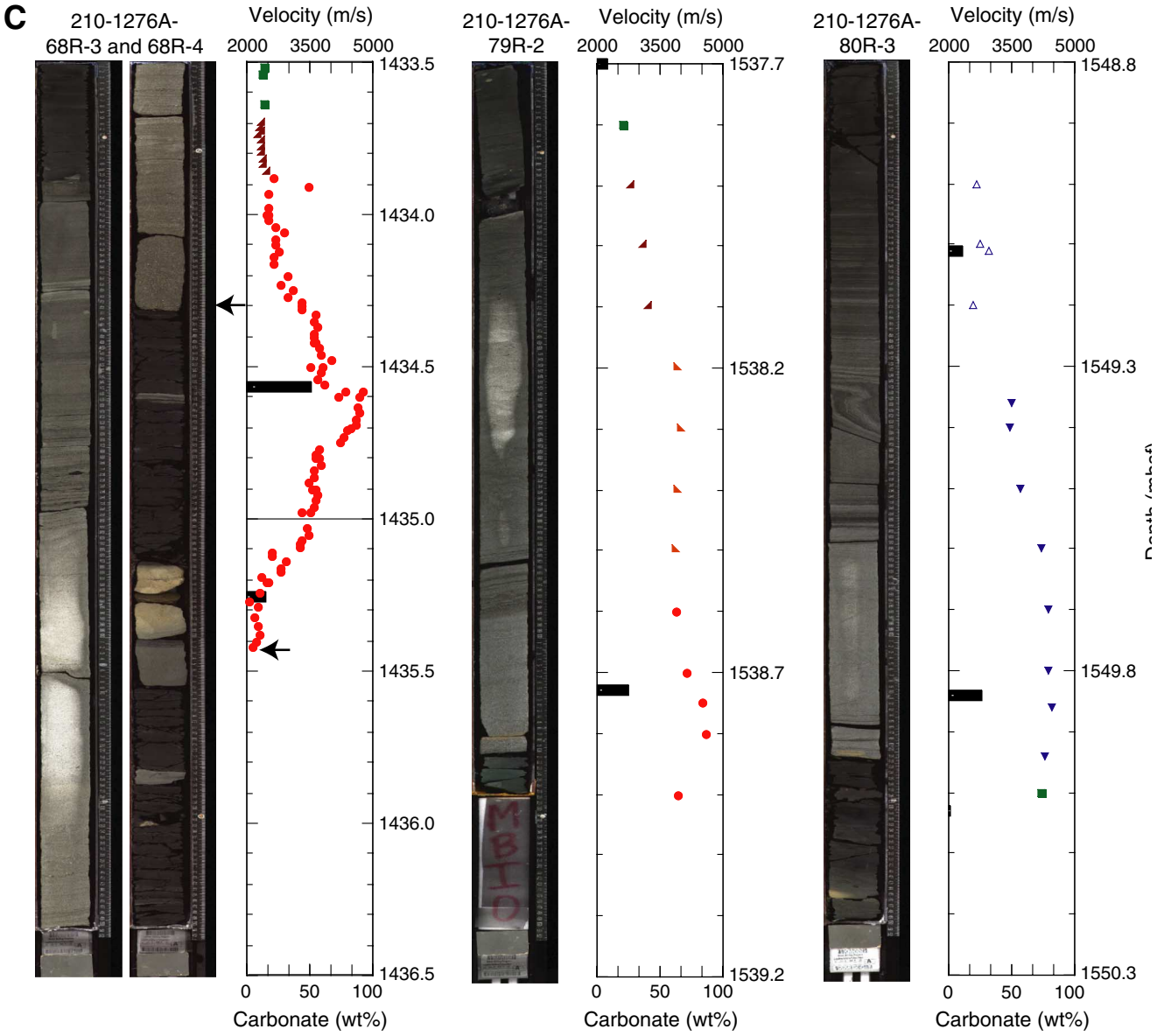

Figure F162 (continued). D. $CaCO_3$ percentage (red) vs. normalized x-direction velocity (black). The x-direction velocity has been normalized by subtracting the minimum x-direction velocity (1792 m/s) and dividing by the maximum velocity/100 (64 m/s) to give a normalized x-direction velocity range between 0 and 100 m/s. The $CaCO_3$ and normalized velocity curves are filtered to remove short-wavelength variations. Yellow shading highlights sections in which we judge the positive correlation to be strong. Orange shading locates the two diabase sills, in which we do not anticipate a correlation.

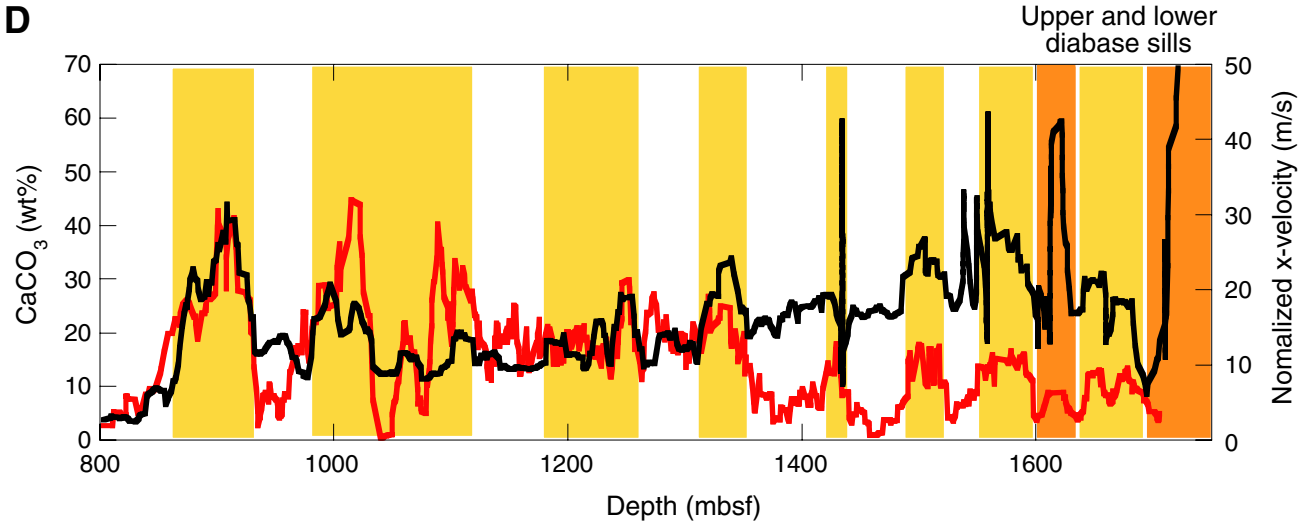

Figure F162 (continued). E. X-direction velocity measured at 2- to 10-cm spacing over the upper sill/sediment contact preserved in Section 210-1276A-87R-6. Measurements characterize the relatively unmetamorphosed porphyroblastic mudstones, a zone of intense contact metamorphism and the upper section of the sill itself. These measurements indicate that the transition from relatively low sedimentary velocity (2500 m/s) to diabase velocity (5000 m/s) occurs over a very short distance, creating a sharp velocity boundary. Lithologic symbols are defined in Figure F160, p. 287.

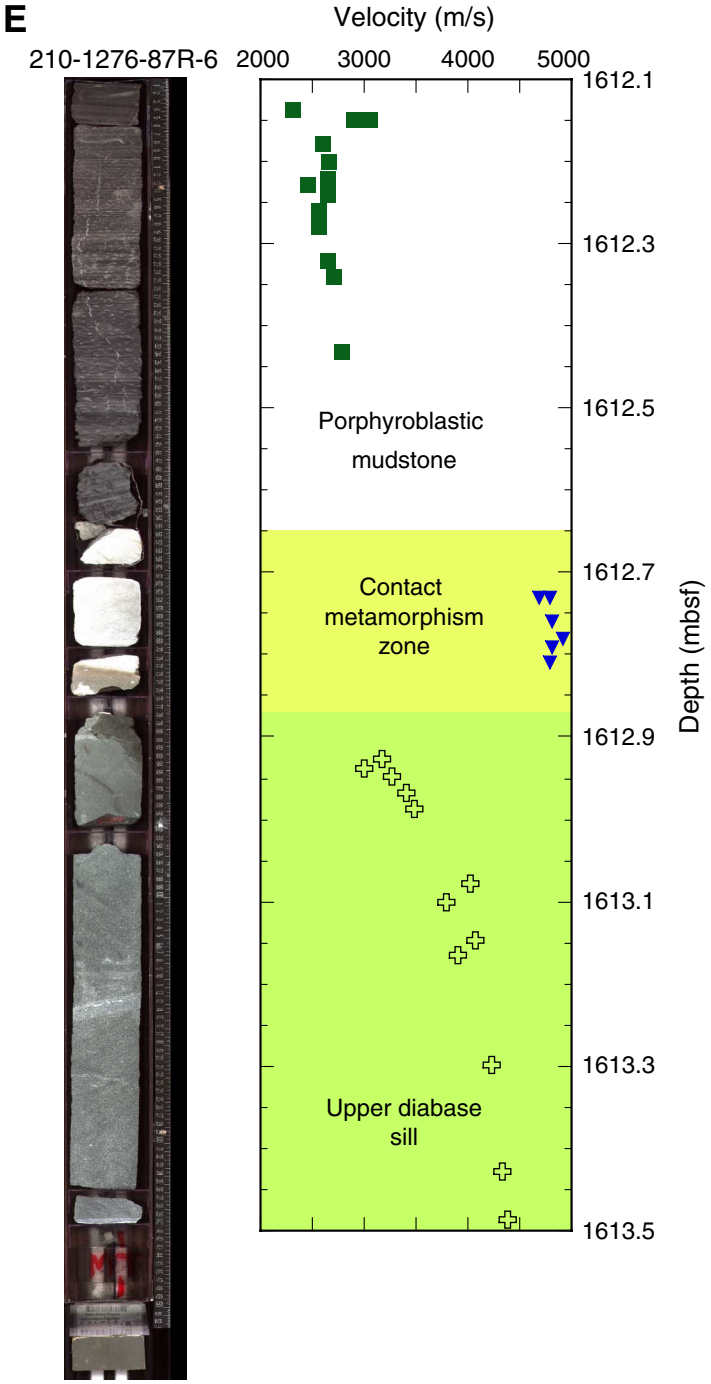

Figure F163. Velocity anisotropy vs. depth, plotted next to core recovery and lithologic units. Positive anisotropy corresponds to vertical velocity slower than horizontal velocity. (Continued on next page.)

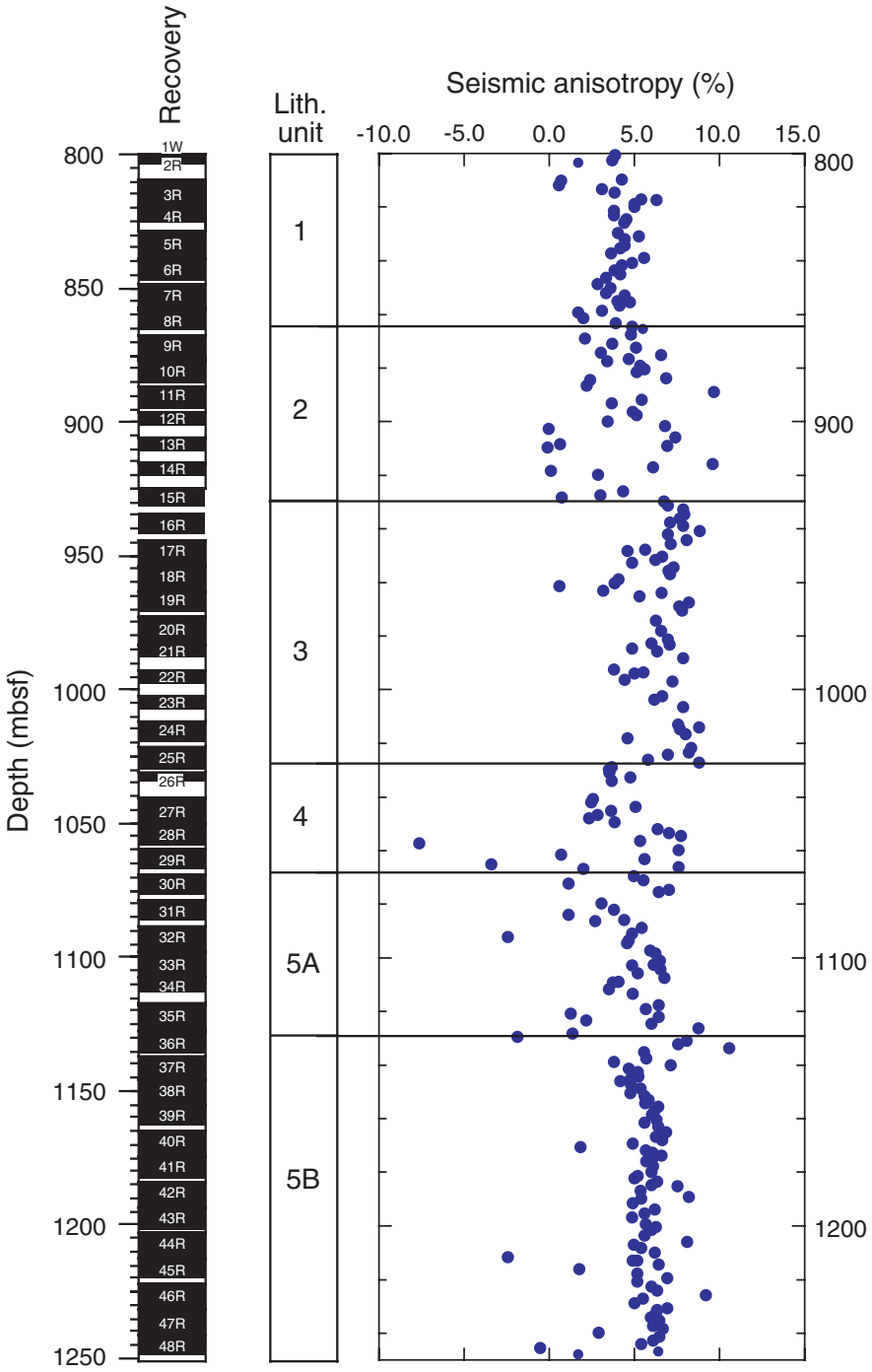

Figure F163 (continued).

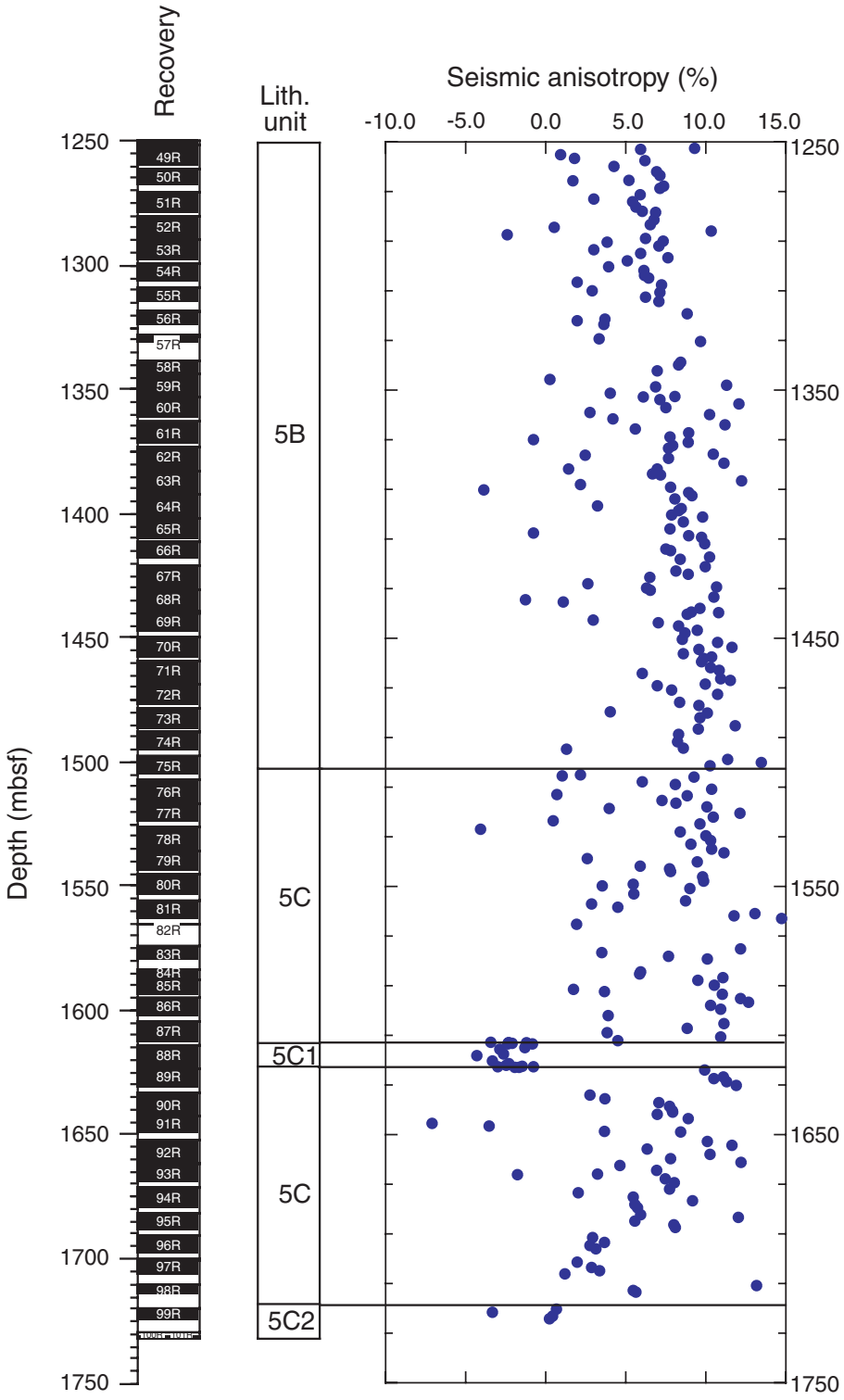

Figure F164. Thermal conductivity vs. depth, plotted next to core recovery and lithologic units. Lithologic symbols are defined in Figure F160, p. 287. (Continued on next page.)

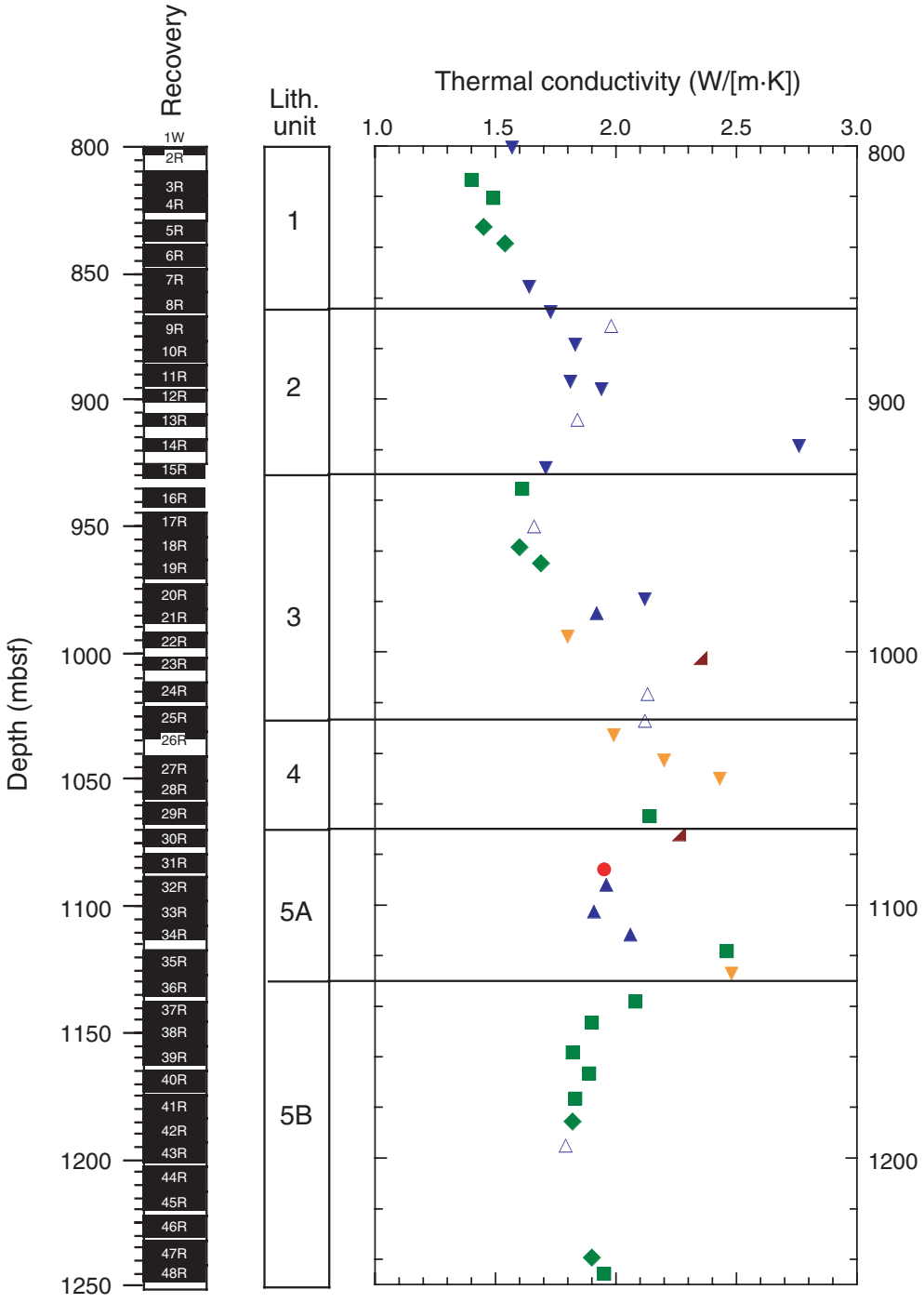

Figure F164 (continued).

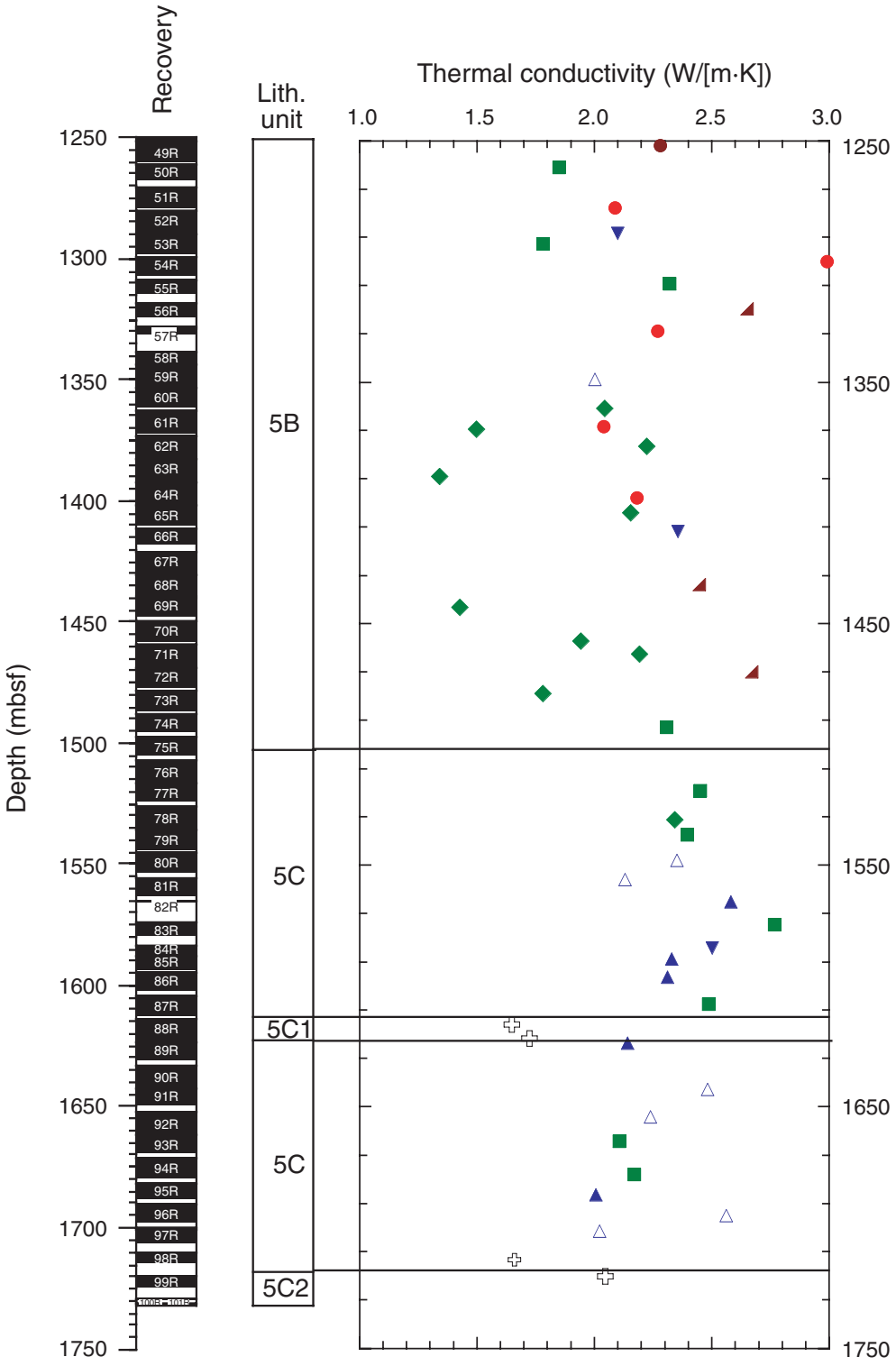

Figure F165. A, B. Natural gamma radiation (NGR) and magnetic susceptibility (MS) measured on the MST vs. depth, plotted next to core recovery and lithologic units. MS values plot offscale for the two sills (Subunits 5C1 and 5C2). For MS, values can be converted to SI units by multiplying by 0.66×10^{-5}. (Continued on next page.)

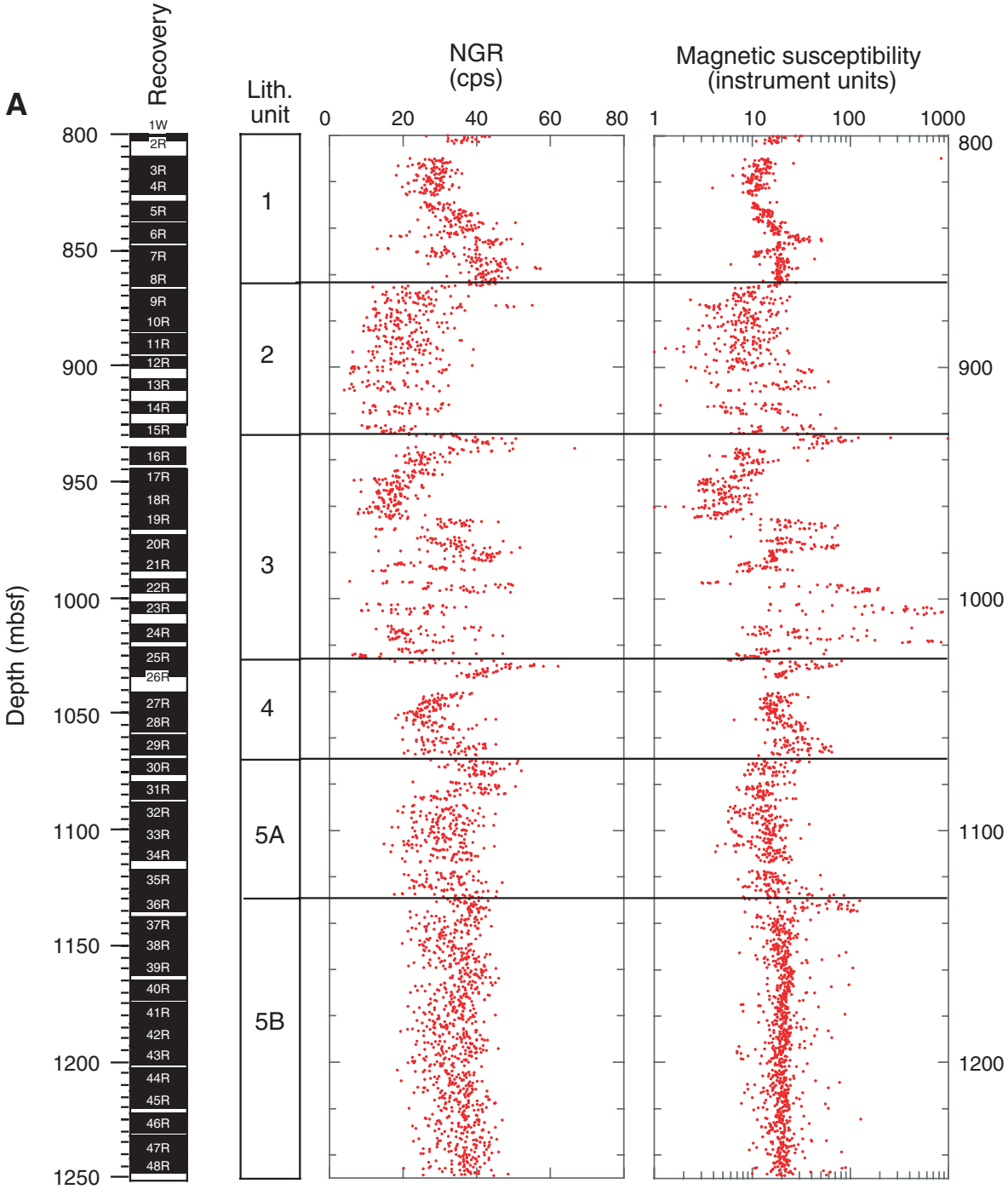

Figure F165 (continued).

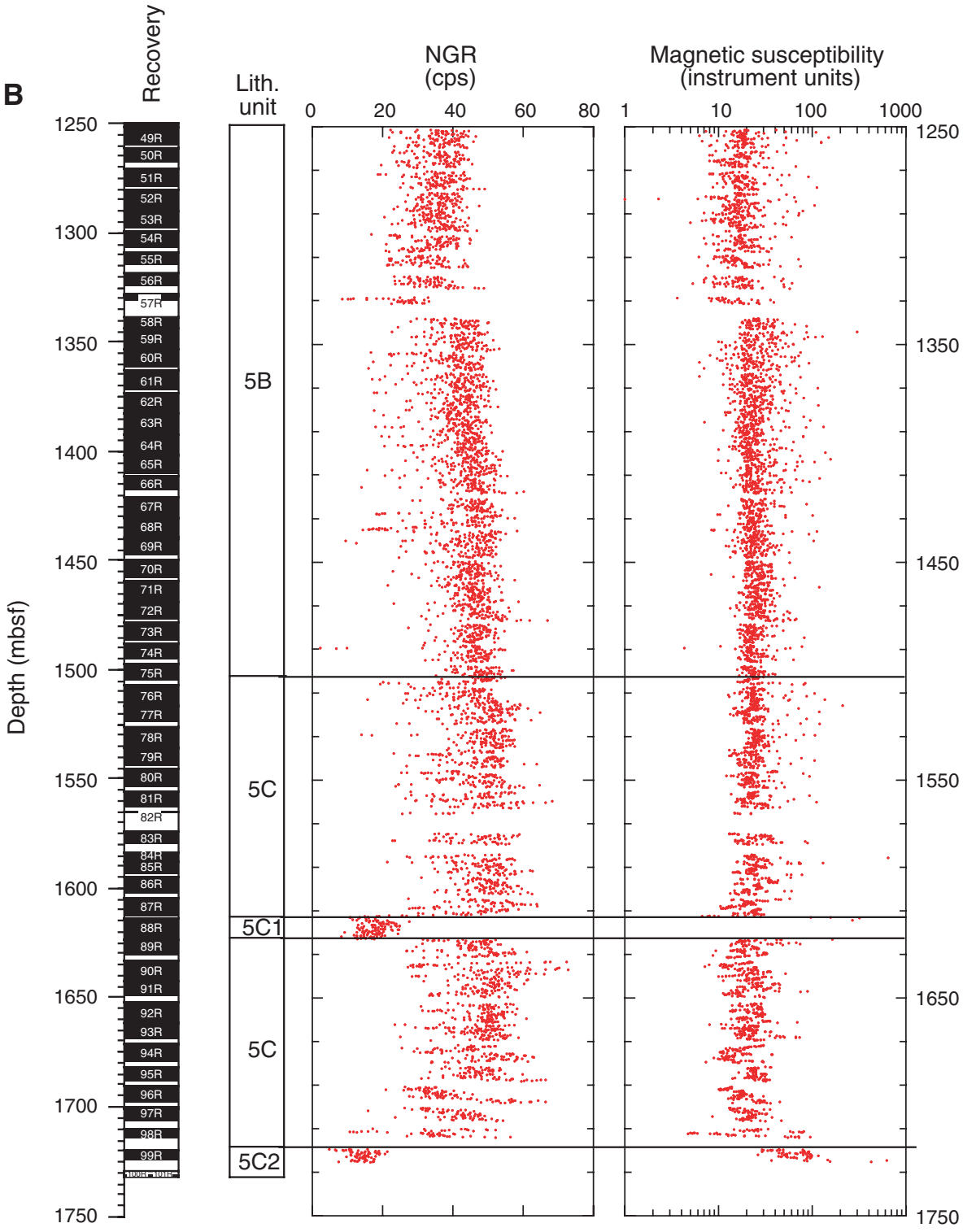

Figure F166. A, B. Natural gamma radiation (NGR) and magnetic susceptibility (MS), smoothed with 100-point running-average filter, vs. depth, plotted next to core recovery and lithologic units. MS values plot offscale for the two sills (Subunits 5C1 and 5C2). For MS, values can be converted to SI units by multiplying by 0.66×10^{-5}. (Continued on next page.)

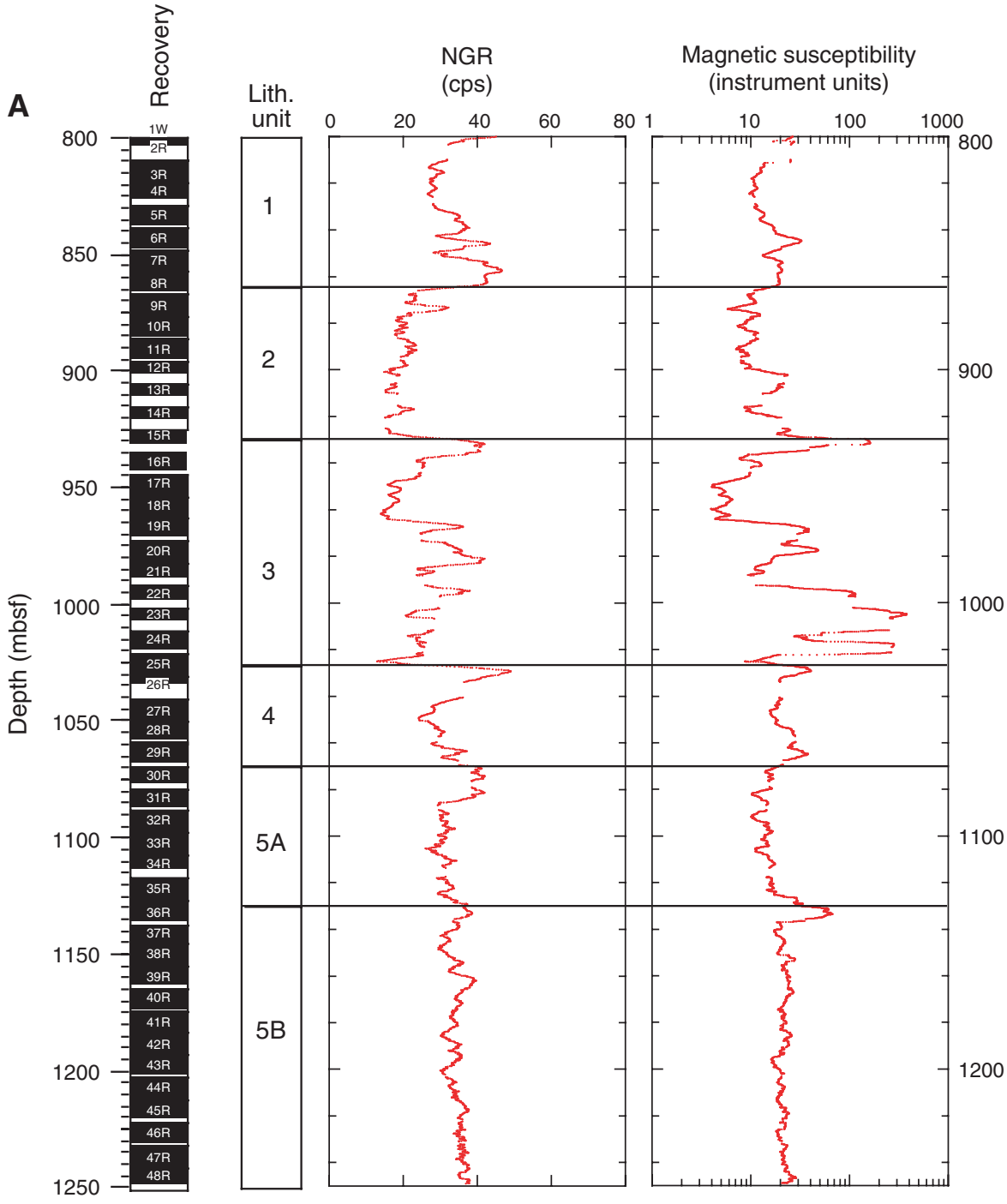

Figure F166 (continued).

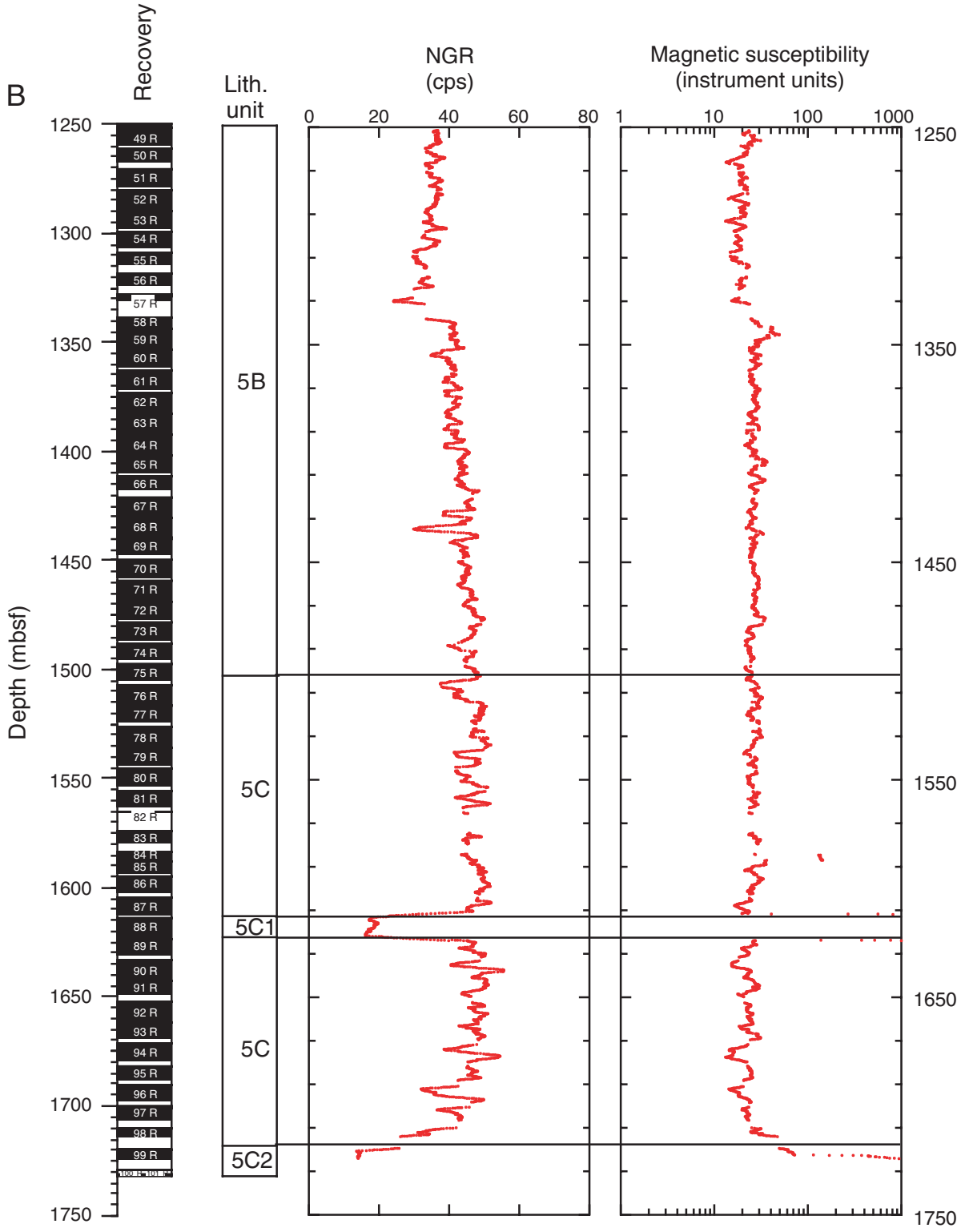

Figure F167. Digital core images (Core 210-1276A-68R) and associated natural gamma ray (NGR) values and x-direction velocity. Major sand-rich turbidites (red dots) are characterized by low NGR values, whereas clay-rich units (green squares and diamonds) correlate with high NGR values. The shape of the NGR response appears to be a function of grain size distribution within the upper part of the turbidite but not the base. In contrast, velocity probably is affected by both grain size and carbonate cementation. Lithologic symbols are defined in Figure F160, p. 287.

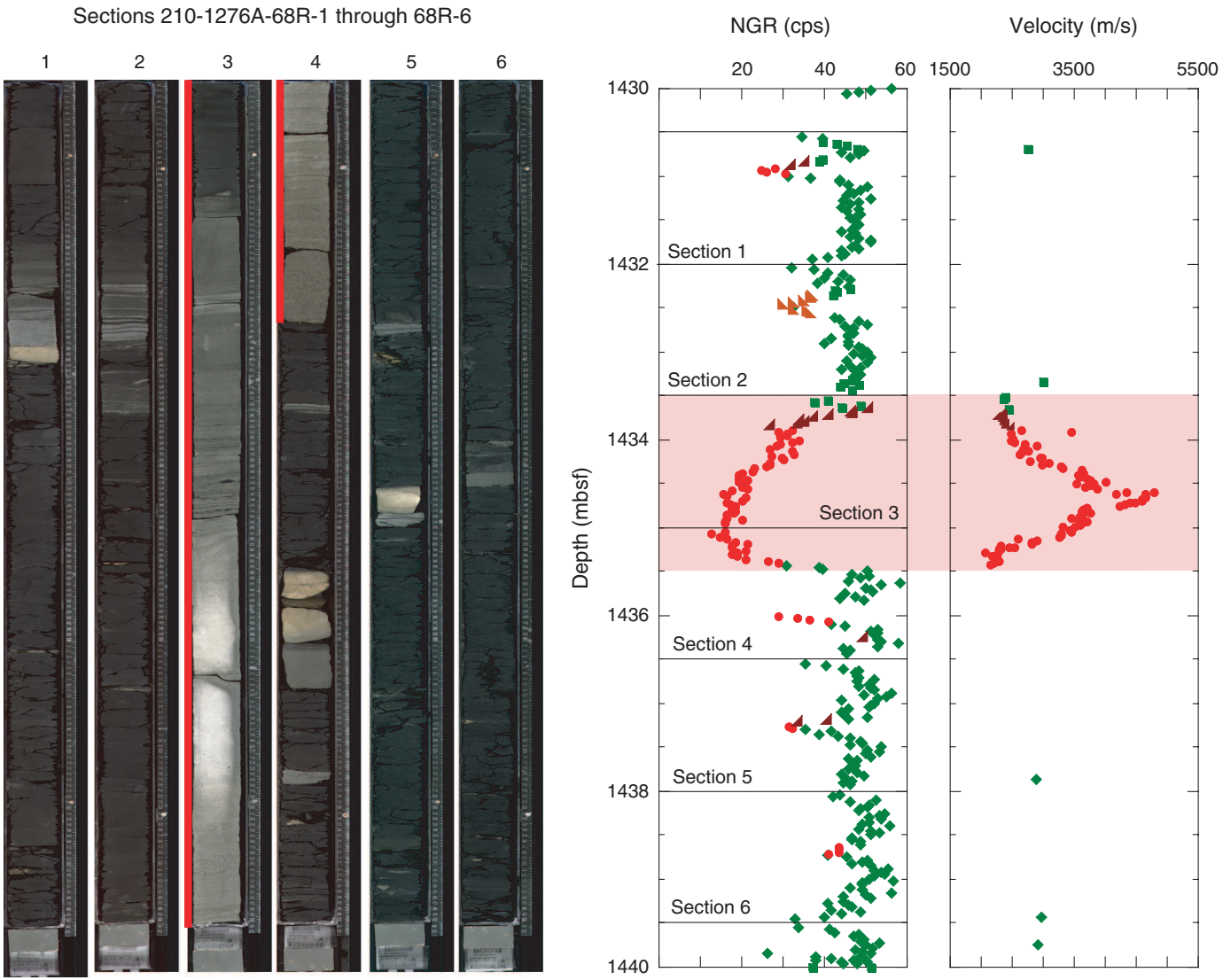

Figure F168. Digital core images and associated magnetic susceptibility (MS) measurements from the MST. Note strong correlation between MS peaks and light-colored siderite-rich intervals. (Continued on next page.)

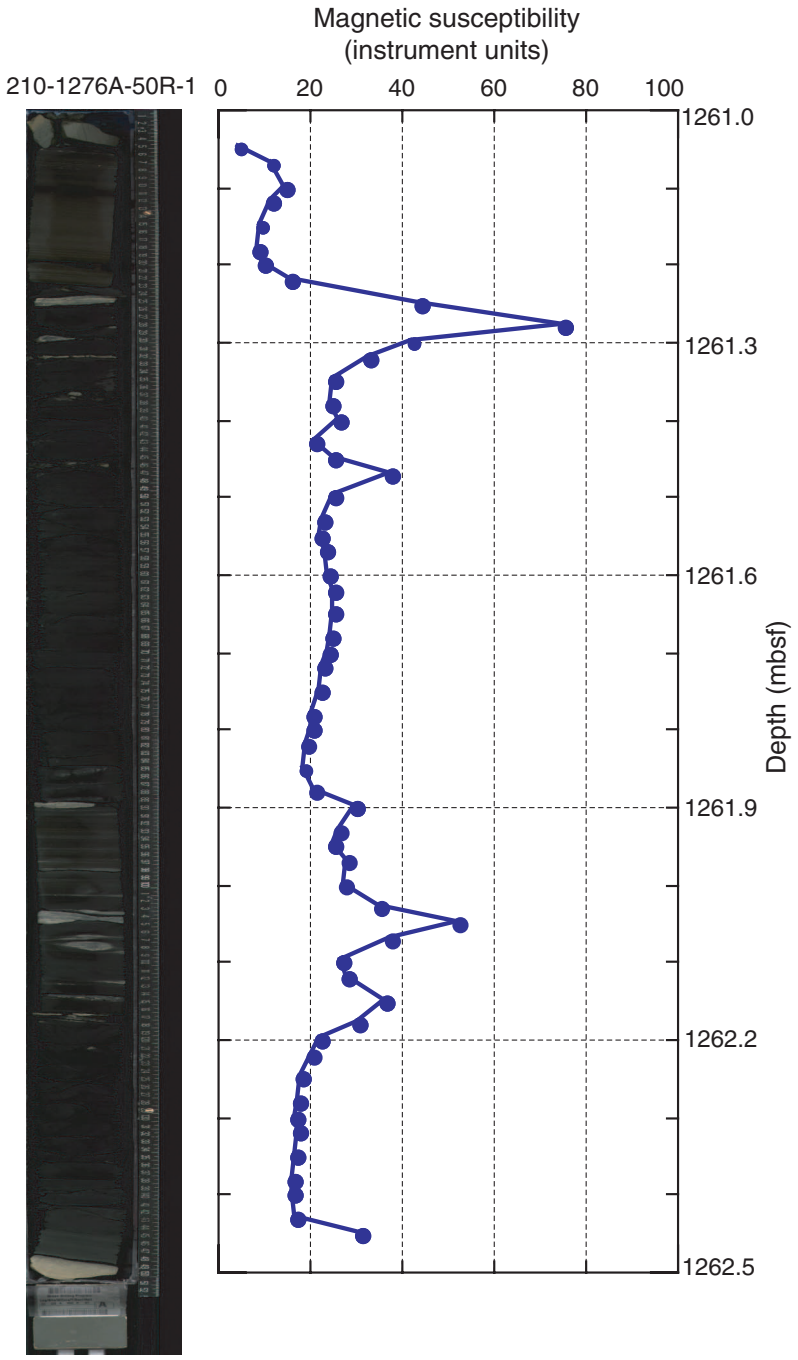

Figure F168 (continued).

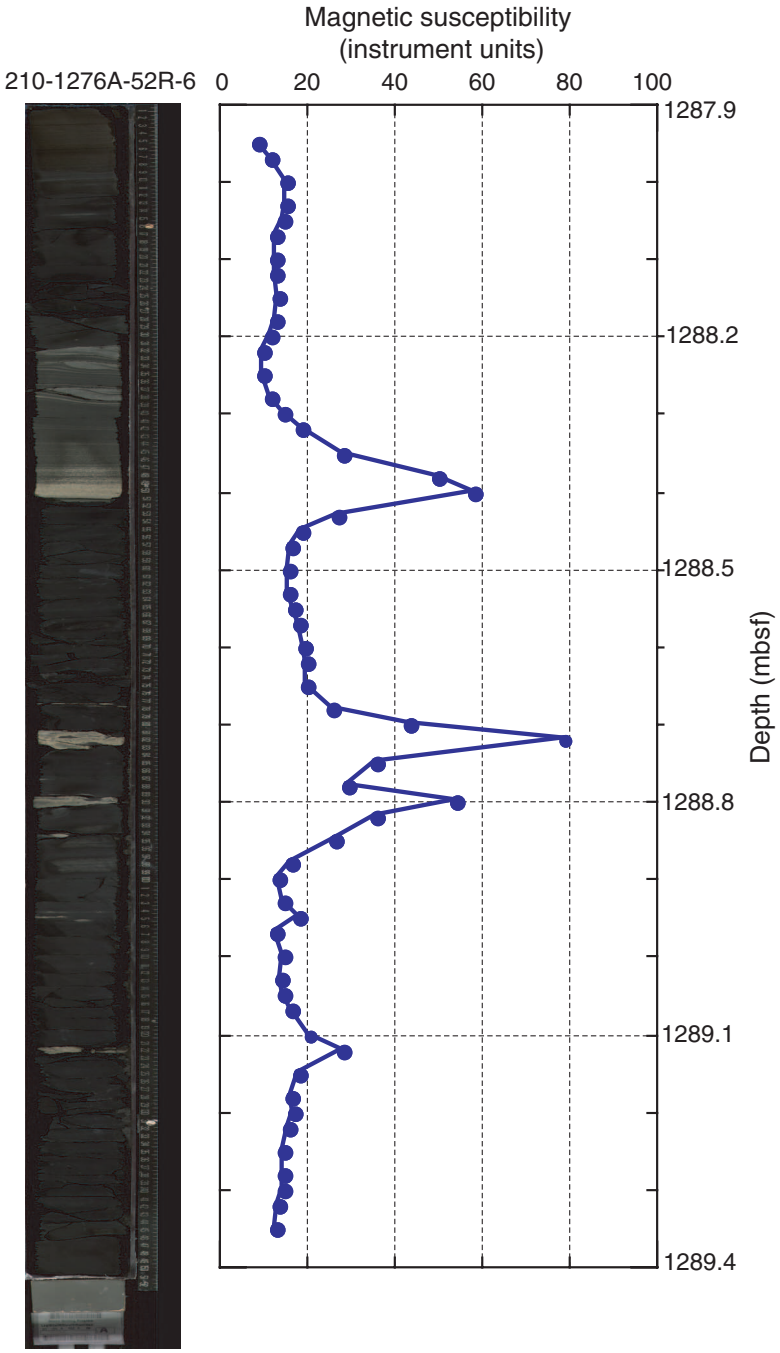

Figure F169. Digital core image of Section 210-1276A-87R-6 and magnetic susceptibility (MS) measurements from the MST. MS data are plotted on a log scale.

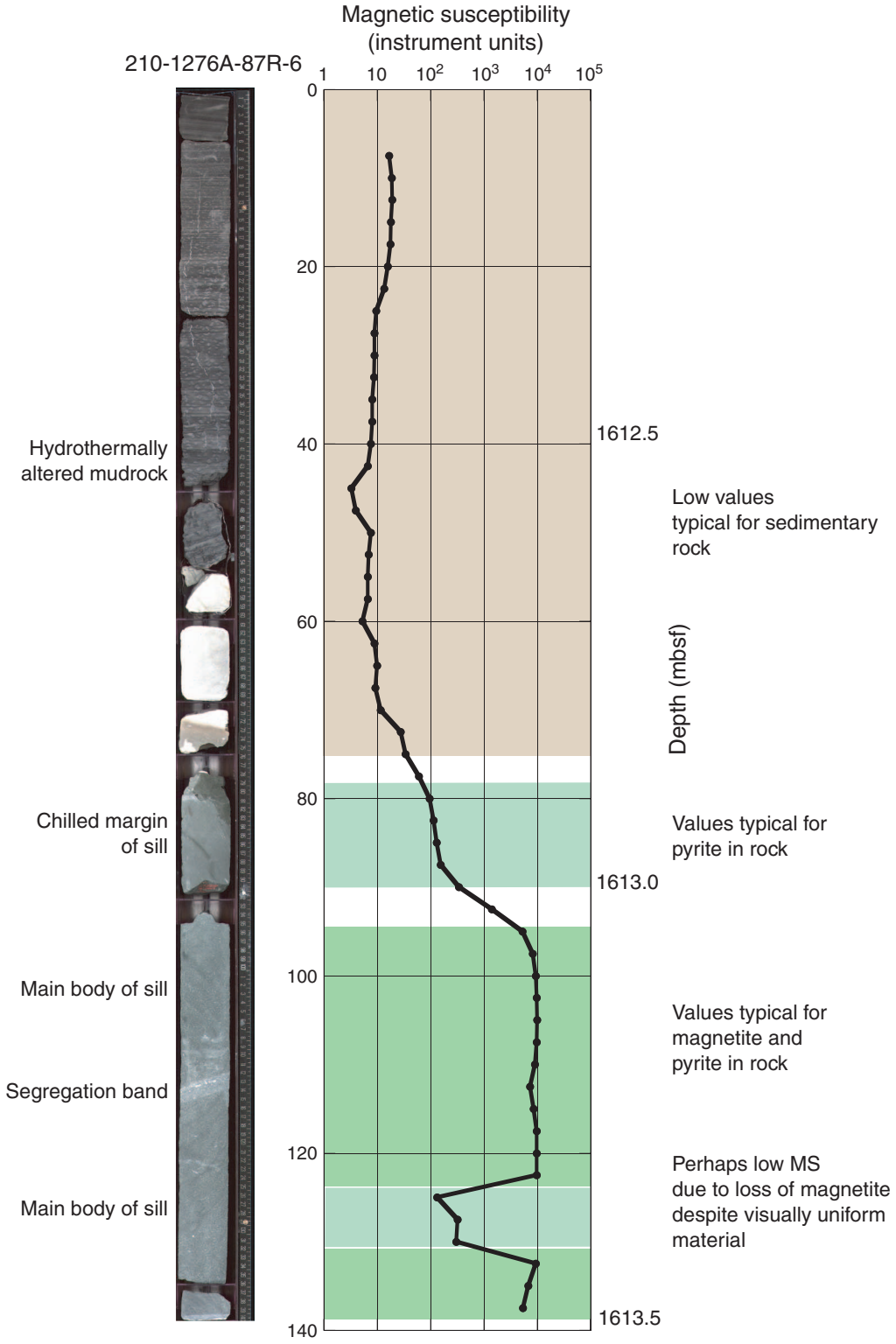

Figure F170. Sections of SCREECH seismic reflection profiles 2MCS and 303 where they cross at Site 1276. Positive reflection amplitudes are shown by red to yellow colors, and negative amplitudes are black or gray. The black line shows the location of the drill site and the estimated total depth to which it reached. For line locations, see Figure F6, p. 46, in the "Leg 210 Summary" chapter. CMP = common midpoint.

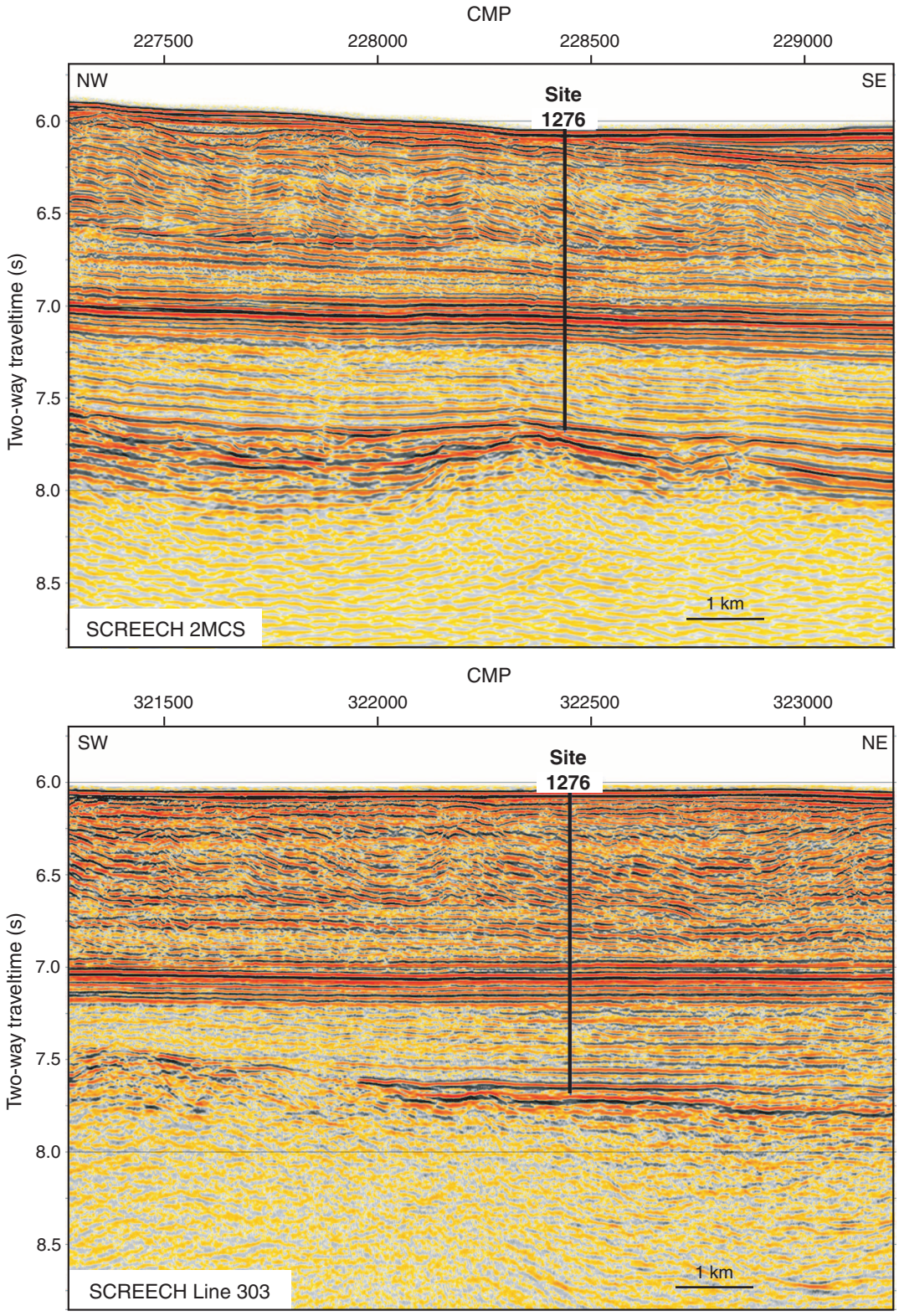

Figure F171. Horizontal (x and y) and vertical (z) compressional wave velocities measured on Site 1276 core samples.

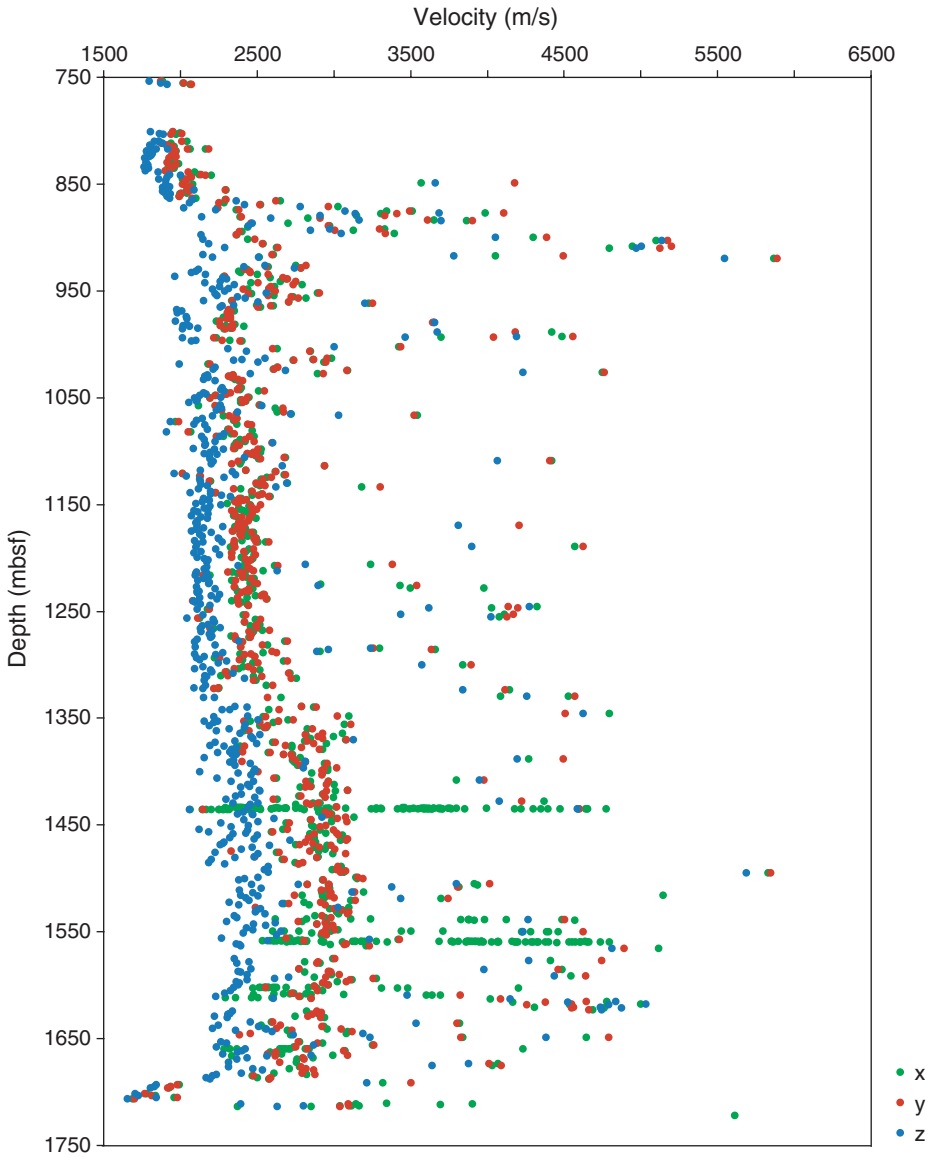

Figure F172. Time-depth relationship for the cored section at Site 1276, calculated using the z-component of velocity measured on cores. Zero two-way traveltime is set at the depth of our checkshot at 864 mbsf.

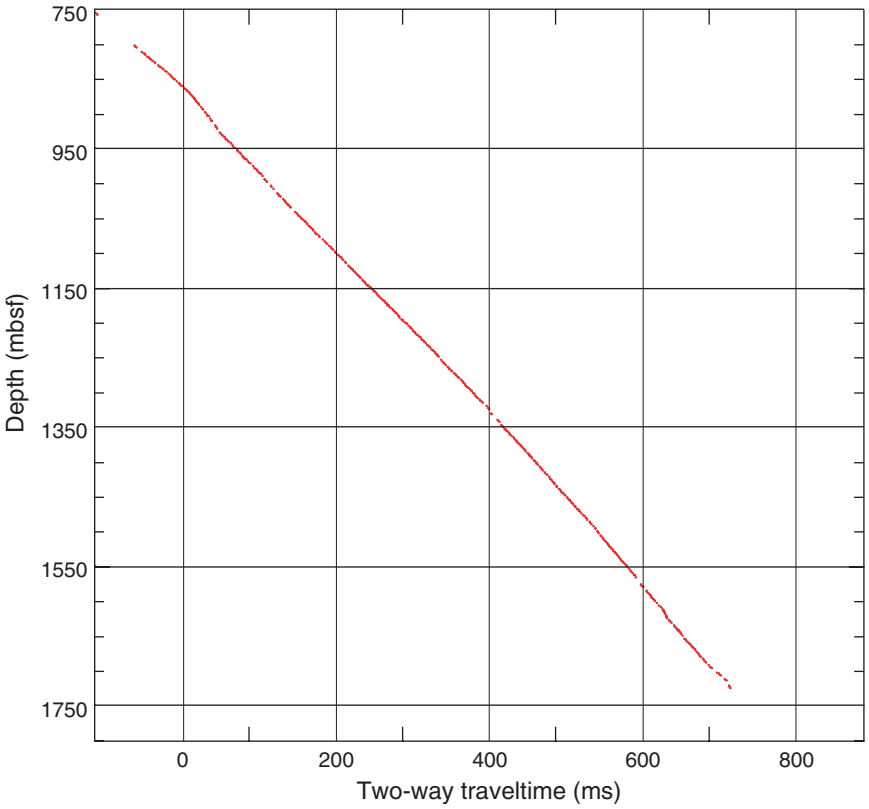

Figure F173. Histogram showing distribution of z-direction velocity measured on cores. Note that the vast majority of samples have velocity between 2100 and 2500 m/s. These velocities will dominate the time-depth conversion.

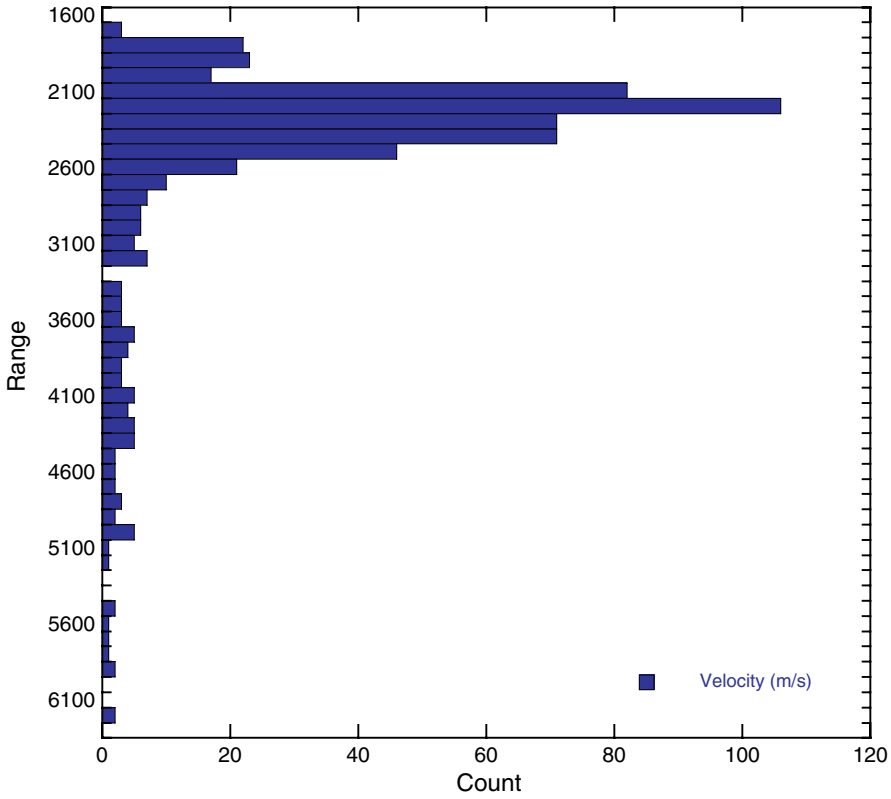

Figure F174. Comparison of synthetic seismograms to seismic reflection data from SCREECH line 2MCS. The synthetic seismograms are generated from reflection coefficients determined from z-component velocity and (**A**) GRA density and (**B**) MAD bulk density measured on cores. Positive amplitudes are shown by red to yellow colors, and negative amplitudes are black or gray. In the velocity/density column, velocity values are blue and density values are red. The break between lithologic Units 1 and 2 is inferred to correlate with the strong reflection at ~6.98 s in the SCREECH line 2MCS data and is aligned to this depth. The reflection-time scale is linear, and the depth scale (mbsf) is nonlinear.

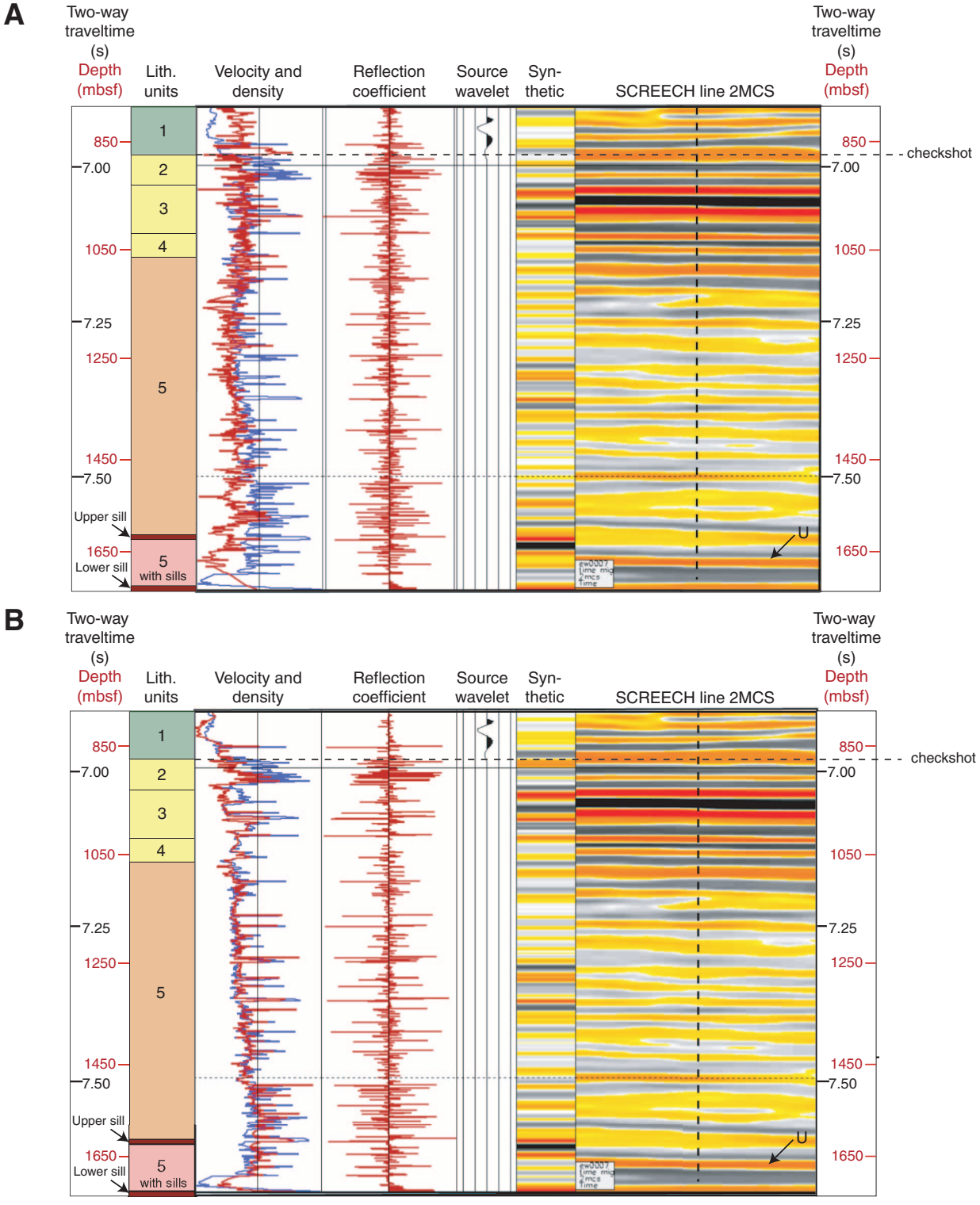

Figure F175. Color-coded interpretation of SCREECH line 2MCS reflection profile, split at Site 1276 to show the correlation of lithologic units with seismic reflection patterns. The top of interlayered sills and sediments at the base of Unit 5 is interpreted to correlate with the U reflection. CMP = common midpoint.

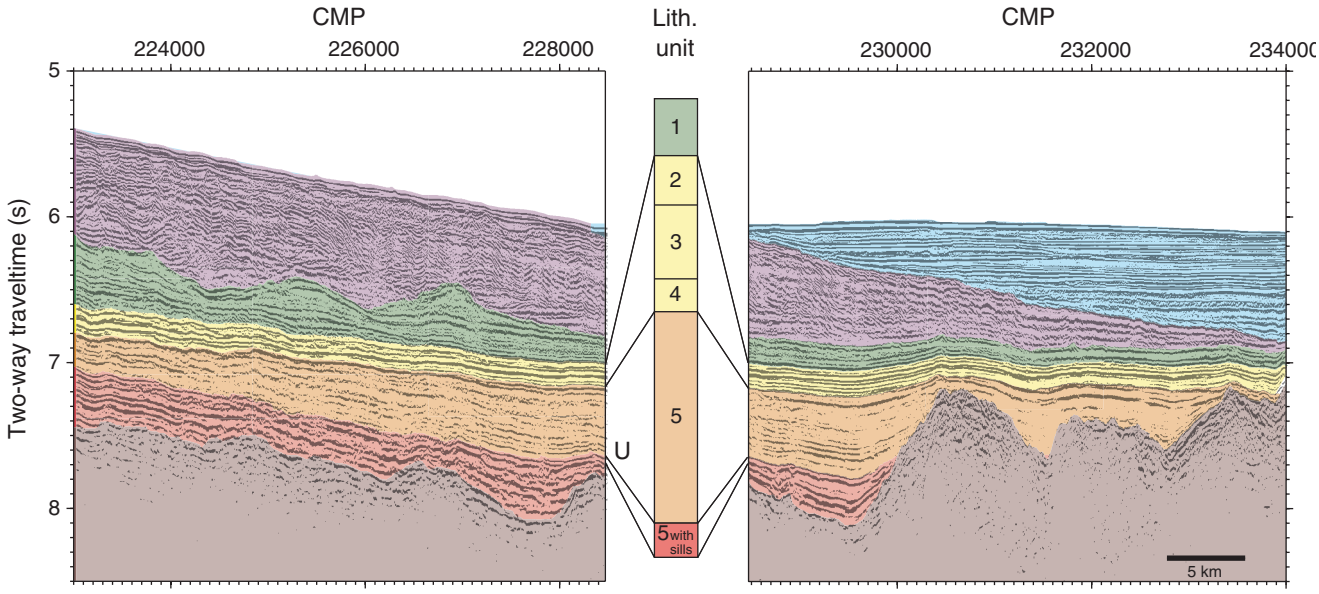

Figure F176. SCREECH line 2MCS. Red dashed line marks the base of lithologic Unit 4 from time-depth conversion, which corresponds to a seismic unconformity. CMP = common midpoint.

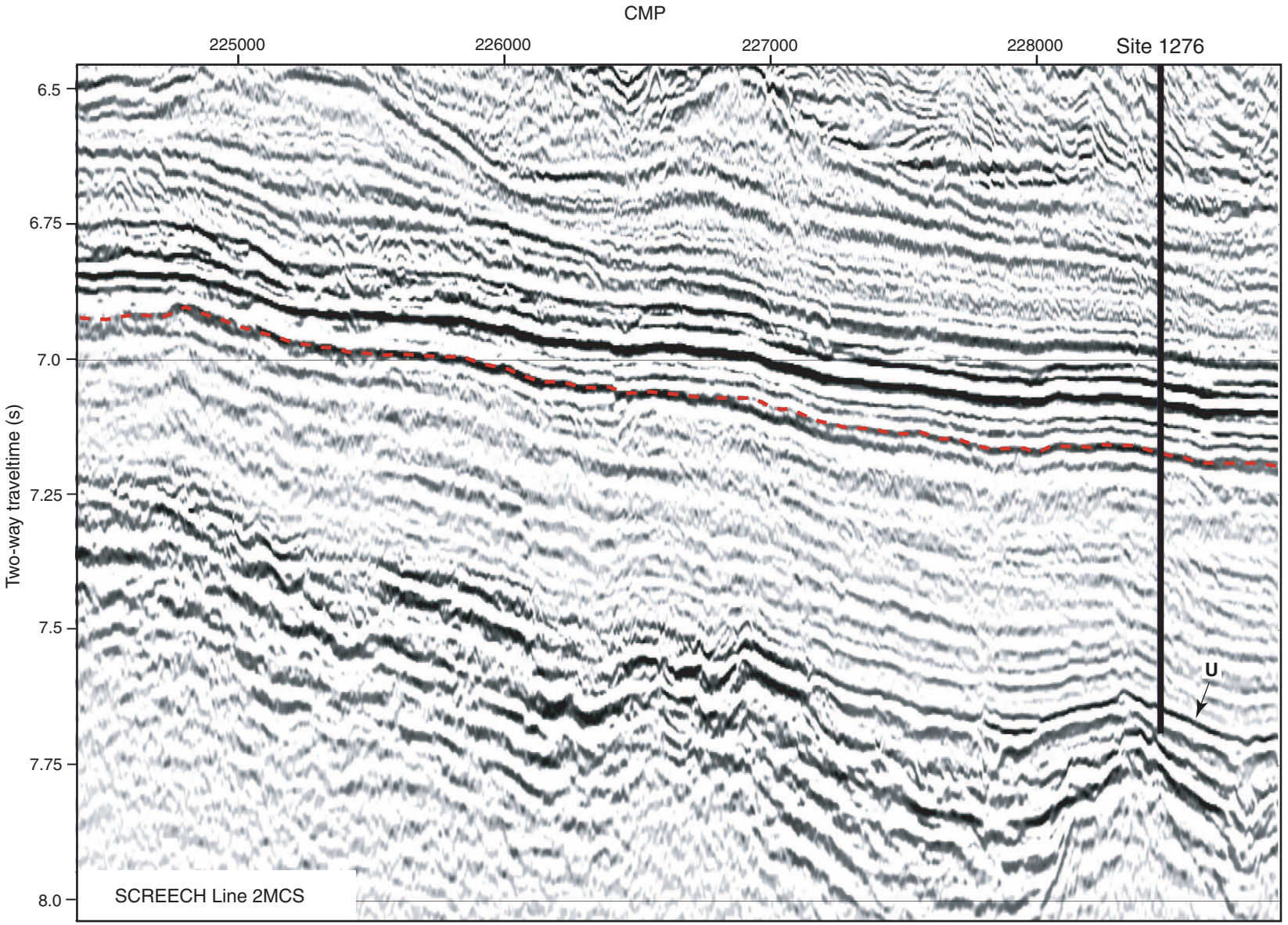

Table T1. Site 1276 Coring Summary. (See table note. Continued on next page.)

Hole: 1276A
Latitude: 45°24.3198′N
Longitude: 44°47.1496′W
Time on site: 1158.77 hr (0844 hr, 16 Jul–1530 hr, 2 Sep 2003)
Seafloor (drill pipe measurement from rig floor, mbrf): 4560
Distance between rig floor and sea level (m): 10.9
Water depth (drill pipe measurement from sea level, m): 4549.1
Total depth (from rig floor, mbrf): 6296.9
Total penetration (m): 1736.9
Total length of cored section (m): 936.9 (800.0–1736.9 mbsf)
Total core recovered (m): 790.35 (not including 6.37 m from wash Core 210-1276A-1W)
Core recovery (%): 84
Total number of cores: 103
Total number of drilled intervals: 3 (0–106.9, 106.9–753.0, and 753.0–800.0 mbsf)
Total length of drilled intervals without coring (m): 800

Core	Date (Aug 2003)	Local time (hr)	Depth (mbsf) Top	Depth (mbsf) Bottom	Length (m) Cored	Length (m) Recovered	Recovered (%)	Comment
210-1276A-								
			*****Drilled without coring from 0 to 106.9 mbsf*****					Install 20-in casing
			*****Drilled without coring from 106.9 to 753 mbsf*****					Install 16-in casing
1W	6	2355	*****Drilled without coring from 753 to 800 mbsf*****					Drill out rathole
2R	7	0235	800.0	809.5	9.5	3.74	39	Half nonmagnetic core barrel
3R	7	0455	809.5	819.2	9.7	9.94	102	Half nonmagnetic core barrel
4R	7	0705	819.2	828.8	9.6	6.82	71	Remote memory module for DSS; half nonmagnetic core barrel
5R	7	0910	828.8	838.4	9.6	9.45	98	Half nonmagnetic core barrel
6R	7	1120	838.4	848.0	9.6	9.17	95	Half nonmagnetic core barrel
7R	7	1325	848.0	857.6	9.6	9.92	103	Remote memory module for DSS; half nonmagnetic core barrel
8R	7	1530	857.6	867.2	9.6	8.73	90	Half nonmagnetic core barrel
9R	7	1915	867.2	876.8	9.6	9.91	103	Half nonmagnetic core barrel
10R	7	2230	876.8	886.4	9.6	8.67	90	Half nonmagnetic core barrel
11R	8	0140	886.4	896.0	9.6	8.54	88	Half nonmagnetic core barrel
12R	8	0715	896.0	905.7	9.7	6.90	71	Half nonmagnetic core barrel
13R	8	1035	905.7	915.3	9.6	5.07	52	Remote memory module for DSS; half nonmagnetic core barrel
14R	8	1350	915.3	925	9.7	5.68	58	Half nonmagnetic core barrel
15R	8	1555	925.0	934.5	9.5	8.57	90	Half nonmagnetic core barrel
16R	8	1810	934.5	944.1	9.6	7.83	81	Half nonmagnetic core barrel
17R	8	2055	944.1	953.8	9.7	9.61	99	Half nonmagnetic core barrel
18R	8	2335	953.8	963.5	9.7	9.84	101	Half nonmagnetic core barrel
19R	9	0145	963.5	973.1	9.6	7.20	75	Half nonmagnetic core barrel
20R	9	0415	973.1	982.7	9.6	9.92	103	Half nonmagnetic core barrel
21R	9	0645	982.7	992.4	9.7	5.72	58	Half nonmagnetic core barrel
22R	9	0940	992.4	1002.0	9.6	5.71	59	Remote memory module for DSS; half nonmagnetic core barrel
23R	9	1230	1002.0	1011.6	9.6	5.20	54	Half nonmagnetic core barrel
24R	9	1500	1011.6	1021.2	9.6	7.86	81	Remote memory module for DSS; half nonmagnetic core barrel
25R	9	1730	1021.2	1030.8	9.6	9.43	98	Half nonmagnetic core barrel
26R	9	2000	1030.8	1040.5	9.7	3.38	34	Half nonmagnetic core barrel
27R	9	2220	1040.5	1050.1	9.6	9.94	103	Half nonmagnetic core barrel
28R	10	0025	1050.1	1059.7	9.6	7.49	78	Half nonmagnetic core barrel
29R	10	0255	1059.7	1069.4	9.7	8.10	83	Remote memory module for DSS; half nonmagnetic core barrel
30R	10	0510	1069.4	1079	9.6	7.59	79	Half nonmagnetic core barrel
31R	10	0725	1079.0	1088.6	9.6	7.98	83	Half nonmagnetic core barrel
32R	10	0935	1088.6	1098.2	9.6	9.93	103	Half nonmagnetic core barrel
33R	10	1845	1098.2	1107.8	9.6	10.03	104	Half nonmagnetic core barrel
34R	10	2100	1107.8	1117.4	9.6	6.08	63	Half nonmagnetic core barrel
35R	10	2330	1117.4	1127.1	9.7	9.65	99	Half nonmagnetic core barrel
36R	11	0135	1127.1	1136.4	9.3	8.67	93	Half nonmagnetic core barrel
37R	11	0345	1136.4	1146.0	9.6	9.17	95	Half nonmagnetic core barrel
38R	11	0600	1146.0	1155.2	9.2	9.70	105	Half nonmagnetic core barrel
39R	11	0805	1155.2	1164.8	9.6	8.93	93	Half nonmagnetic core barrel
40R	11	1015	1164.8	1174.4	9.6	9.38	97	Half nonmagnetic core barrel
41R	11	1230	1174.4	1184.0	9.6	9.49	98	Half nonmagnetic core barrel
42R	11	1450	1184.0	1193.5	9.5	10.37	109	Half nonmagnetic core barrel
43R	11	1725	1193.5	1203.2	9.7	8.53	87	Half nonmagnetic core barrel
44R	11	2000	1203.2	1212.8	9.6	9.82	102	Half nonmagnetic core barrel

Table T1 (continued).

Core	Date (Aug 2003)	Local time (hr)	Depth (mbsf) Top	Depth (mbsf) Bottom	Length (m) Cored	Length (m) Recovered	Recovered (%)	Comment
45R	11	2215	1212.8	1222.4	9.6	8.90	92	Half nonmagnetic core barrel
46R	12	0030	1222.4	1232.0	9.6	9.24	96	Half nonmagnetic core barrel
47R	12	0250	1232.0	1241.7	9.7	9.70	100	Half nonmagnetic core barrel
48R	12	0510	1241.7	1251.4	9.7	7.46	76	Half nonmagnetic core barrel
49R	12	0745	1251.4	1261.0	9.6	8.78	91	Half nonmagnetic core barrel
50R	12	1015	1261.0	1270.7	9.7	8.08	83	Half nonmagnetic core barrel
51R	12	1300	1270.7	1280.4	9.7	8.56	88	Half nonmagnetic core barrel
52R	12	1550	1280.4	1290.0	9.6	9.83	102	Half nonmagnetic core barrel
53R	12	1900	1290.0	1299.6	9.6	8.52	88	Half nonmagnetic core barrel
54R	12	2140	1299.6	1309.2	9.6	8.30	86	Half nonmagnetic core barrel
55R	13	0045	1309.2	1318.8	9.6	5.93	61	Half nonmagnetic core barrel
56R	13	0315	1318.8	1328.5	9.7	5.96	61	Half nonmagnetic core barrel
57R	13	0605	1328.5	1338.1	9.6	3.07	31	Half nonmagnetic core barrel
58R	16	1545	1338.1	1344.1	6.0	5.15	85	
59R	16	1820	1344.1	1353.7	9.6	9.34	97	Full-length nonmagnetic core barrel
60R	16	2105	1353.7	1363.2	9.5	8.49	89	
61R	16	2350	1363.2	1372.9	9.7	9.68	99	Full-length nonmagnetic core barrel
62R	17	0225	1372.9	1382.5	9.6	9.74	101	
63R	17	0445	1382.5	1392.2	9.7	9.67	99	Full-length nonmagnetic core barrel
64R	17	0755	1392.2	1401.8	9.6	9.71	101	
65R	17	1020	1401.8	1411.3	9.5	9.09	95	Full-length nonmagnetic core barrel
66R	17	1330	1411.3	1420.9	9.6	7.46	77	
67R	17	1625	1420.9	1430.5	9.6	9.45	98	Full-length nonmagnetic core barrel
68R	17	1915	1430.5	1439.8	9.3	9.88	106	
69R	17	2215	1439.8	1449.5	9.7	8.31	85	Full-length nonmagnetic core barrel
70R	18	0120	1449.5	1459.2	9.7	9.38	96	
71R	18	0410	1459.2	1468.9	9.7	9.58	98	Full-length nonmagnetic core barrel
72R	18	0715	1468.9	1478.5	9.6	8.48	88	
73R	18	1025	1478.5	1488.1	9.6	8.79	91	Full-length nonmagnetic core barrel
74R	18	1340	1488.1	1497.7	9.6	7.93	82	
75R	18	1650	1497.7	1507.3	9.6	8.61	89	Full-length nonmagnetic core barrel
76R	18	2135	1507.3	1516.9	9.6	10.53	109	
77R	19	0145	1516.9	1526.5	9.6	8.05	83	Full-length nonmagnetic core barrel
78R	19	0525	1526.5	1536.2	9.7	9.05	93	
79R	19	1035	1536.2	1545.8	9.6	8.32	86	Full-length nonmagnetic core barrel
80R	19	1450	1545.8	1555.4	9.6	8.24	85	
81R	20	1840	1555.4	1565.0	9.6	7.85	81	Full-length nonmagnetic core barrel
82R	20	2340	1565.0	1574.5	9.5	0.94	9	
83R	21	0440	1574.5	1584.2	9.7	5.46	55	Full-length nonmagnetic core barrel
84R	21	0825	1584.2	1587.7	3.5	3.60	102	
85R	24	0205	1587.7	1594.8	7.1	6.37	89	Full-length nonmagnetic core barrel
86R	24	0745	1594.8	1604.5	9.7	8.22	84	
87R	24	1235	1604.5	1614.1	9.6	8.99	93	Full-length nonmagnetic core barrel
88R	24	1640	1614.1	1623.6	9.5	9.22	97	
89R	24	2150	1623.6	1633.3	9.7	8.23	84	Full-length nonmagnetic core barrel
90R	25	0230	1633.3	1642.8	9.5	9.15	96	
91R	25	0805	1642.8	1652.5	9.7	7.07	72	Full-length nonmagnetic core barrel
92R	25	1345	1652.5	1662.1	9.6	9.51	99	Tensor tool run for hole deviation: 7.43°
93R	25	1805	1662.1	1671.8	9.7	7.68	79	Full-length nonmagnetic core barrel
94R	25	2300	1671.8	1681.4	9.6	8.34	86	
95R	26	0400	1681.4	1690.9	9.5	7.17	75	Full-length nonmagnetic core barrel
96R	26	0830	1690.9	1700.5	9.6	7.64	79	
97R	26	1220	1700.5	1710.1	9.6	6.23	64	Full-length nonmagnetic core barrel
98R	26	1550	1710.1	1719.4	9.3	4.38	47	
99R	26	2120	1719.4	1729.1	9.7	5.36	55	Orientation and sequence unknown for Sections 5 and 6. These were recovered after Core 101R. Core found jammed in bit when bit was recovered on the rig floor. Full-length nonmagnetic core barrel
100R	27	0325	1729.1	1731.1	2.0	0.00	0	
101R	27	1715	1731.1	1732.1	1.0	0.00	0	Bit recovered with damage; lost cone and core pieces from Core 99R
102R	31	0445	1732.1	1732.9	0.8	0.02	2	Attempt to drill out broken drill bit cone and core
103R	31	1005	1732.9	1734.9	2.0	0.00	0	Attempt to drill out broken drill bit cone and core; deploy center bit
104R	31	2205	1734.9	1736.9	2.0	0.00	0	Deploy center bit three times; pipe stuck for 12 hr; free pipe, abandon hole
				Total:	936.9	790.35	84	

Note: DSS = Drilling Sensor Sub.

Table T2. Summary of lithostratigraphic units, Hole 1276A. (Continued on next page.)

Unit	Age	Core, section, interval (cm)	Depth (mbsf)	Thickness (m)	Lithology (major/*minor*)	Color (major/*minor*)
		210-1276A-				
1	middle Eocene to early Oligocene	1W-1, 0 through 8R-5, 113	Top = 753.00–794.13 Base = 864.73	70.6–111.73	Mudstone and claystone	Greenish gray, olive green, olive gray, to grayish olive
					Grainstone; muddy sandstone and sandy mudstone	*Olive gray to light olive gray; pale yellowish brown*
2	late Paleocene to middle Eocene	8R-5, 113 through 15R-3, 125	864.73–929.25	64.52	Grainstone and calcareous sandstone	Very light gray, greenish gray, light brown
					Marlstone	Reddish brown, grayish red, greenish gray
					Claystone and mudstone	Olive gray, moderate olive brown, moderate brown
3	early Campanian to late Paleocene	15R-3, 125 through 25R-5, 80	929.25–1028.00	98.75	Claystone and mudstone	Moderate brown, grayish green, light olive gray, greenish black
					Grainstone and calcareous sandstone	Yellowish gray, light greenish gray, olive gray, light olive gray, white, pale olive, light brown
					Marlstone	*Pale green to light brown*
					Calcareous siltstone	*Yellowish gray, light greenish gray, olive gray, light olive*
					Sandy mudstone	*Light olive gray, olive gray, moderate brown*
4	Turonian to late Santonian	25R-5, 80 through 29R-6, 62	1028.00–1067.24	39.24	Sandy mudstone and muddy sandstone	Brown and yellowish brown
					Sandstone	Brown to light brown
					Mudstone/*siltstone*	Light brown/*moderate brown*
5A	Cenomanian to Turonian	29R-6, 62 through 36R-2, 129	1067.24–1129.80	62.56	Claystone and mudstone/*calcareous sandstone*	Dark greenish gray, greenish gray moderate brown, greenish black, yellowish green, grayish black/*light olive gray, medium gray*
					Marlstone	*Light olive gray, greenish gray, grayish blue*
					Black shale	*Grayish black, dark gray, olive black*
					Grainstone	*Light olive gray, medium light gray, greenish gray, yellowish gray*
5B	Albian to Cenomanian	36R-2, 129 through 75R-3, 142	1129.80–1502.12	372.32	Claystone, mudstone, and calcareous mudstone/*sandstone and siltstone*	Dark greenish gray, moderate brown, greenish black, olive black, dark gray, olive gray/*light olive gray, medium gray*
					Black shale	*Grayish black, dark gray, olive black*
5C	?late Aptian to Albian	75R-3, 142 through 104R (unrecovered)	Top = 1502.12 Base = 1732.12–1736.9	234.78	Claystone and mudstone/*sandstone and siltstone*	Dark greenish gray, moderate brown, greenish black/*light olive gray, medium gray*
					Grainstone	*Light olive gray, medium light gray*
5C1	Albian or younger	87R-6, 72 through 88R-7, 117	1612.72–1623.00	10.3	Diabase sill	
5C	?late Aptian to Albian	Continuation of 5C (see above)	(see above)	(see above)	Continuation of 5C (see above)	
5C2	Albian or younger	99R, entire core through 104R (unrecovered)	Top = 1719.40 Base = 1732.12–1736.9	12.72–17.5	Diabase sill	

Table T2 (continued).

Unit	Age	Sedimentation rate (m/m.y.)	Physical processes
1	middle Eocene to early Oligocene	~7, but poorly constrained	Hemipelagic deposition (claystone) punctuated by deposition from turbidity currents and debris flows. Postdepositional folding, shearing, and extensional faulting.
2	late Paleocene to middle Eocene	~7	Hemipelagic deposition (claystone) punctuated by deposition from frequent turbidity currents (high proportion of graded beds).
3	early Campanian to late Paleocene	~1–8; lowest in Core 210-1276A-22R	Hemipelagic deposition (claystone) punctuated by deposition from mud-laden turbidity currents. Condensed interval of sandy mudstone in Core 210-1276A-22R with abundant *Zoophycos.*
4	Turonian to late Santonian	~2 or less	Slow accumulation of thinly interbedded sand and mud, in variable proportions, sufficiently slowly that burrowers completely homogenize the sediment; possible slow reworking of originally downslope-transported material by fluctuating bottom currents to produce coarsening–fining cycles.
5A	Cenomanian to Turonian	~2–15.0	Mud-dominated gravity-flow deposits (~80%) alternating with (1) bioturbated hemipelagic mudrocks and (2) periodic slow accumulation of carbon-rich muds from suspension with no bioturbation (due to anoxia).
5B	Albian to Cenomanian	~18–100	Hemipelagic bioturbated mudrock (~70%) punctuated by (1) mud-dominated gravity-flow deposits (~10%) and (2) periodic slow accumulation of carbon-rich muds from suspension with no bioturbation (due to anoxia).
5C	?late Aptian to Albian	~22–100	Mud-dominated gravity-flow deposits (~90%) alternating with (1) bioturbated hemipelagic mudrocks and (2) very rare accumulation of carbon-rich muds from suspension with no bioturbation (due to anoxia).
5C1	Albian or younger		Igneous intrusion
5C	?late Aptian to Albian	~22	Continuation of 5C (see above)
5C2	Albian or younger		Igneous intrusion

Table T3. Summary of XRD data, Hole 1276A. (See table notes. Continued on next four pages.) (N2)

Core, section, interval (cm)	Depth (mbsf)	Lith. unit	14 Å	10 Å	7 Å	Zeo	Gt	Opal	Qtz	KFs	Pl	Cc	Dol	Sd	Py	Others	D	M	Lithology
210-1276A-																			
4R-3, 54–55	822.74	1	2	2	1	0	0	3	4	0	2	0	1	0	2		X		Claystone
4R-4, 9–11	823.79	1	2	3	2	0	0	3	4	1	2	2	2	0	2	Hornblende	X		Claystone
5R-4, 20–21	833.50	1	2	2	2	0	0	2	4	1	2	3	2	0	2	Gypsum	X		Claystone
5R-4, 24–25	833.54	1	1	2	2	1	0	2	4	1	2	0	0	0	2		X		Claystone
6R-2, 44–44.5	840.34	1	1	2	1	2	0	1	4	1	2	0	0	0	2		X		Porcellanite with zeolite
6R-2, 44–44.5	840.34	1	1	2	2	3	1	0	4	1	2	1	0	0	2		X		Porcellanite with zeolite
6R-3, 59–60	841.99	1	1	2	2	0	0	0	4	2	2	0	0	0	1		X		Claystone
6R-6, 10–11	846.00	1	1	2	1	0	0	0	4	1	2	0	0	0	0	Hornblende	X		Claystone
7R-4, 35–35.5	852.85	1	1	2	2	0	0	0	4	1	2	0	0	0	1		X		Claystone
7R-4, 35–35.5	852.85	1	2	2	2	0	0	0	4	1	2	1	1	0	0	Chlorite, minor kaolinite	X		Claystone
8R-5, 116–117	864.76	2	2	2	1	1	0	0	4	1	2	0	0	0	1		X		Claystone
9R-1, 32–34	867.52	2	1	1	0	2	0	3	4	1	2	4	0	0	1		X		Siliceous marlstone
9R-2, 72–75	869.42	2	3	2	0	1	0	1	4	2	1	0	0	0	0		X		Claystone
10R-4, 101–105	882.28	2	3	0	0	1	0	1	4	1	1	4	1	0	1		X		Calcareous mudstone
10R-4, 109–113	882.36	2	1	2	0	2	0	3	4	1	1	4	0	0	0		X		Calcareous mudstone
11R-4, 1.5–4	890.91	2	3	0	0	2	0	1	4	0	1	4	0	0	1		X		Calcareous mudstone
11R-4, 122–125	892.12	2	3	0	0	3	1	0	4	1	1	0	1	0	0			X	Zeolitic claystone
12R-3, 30–31	899.30	2	2	2	0	2	2	0	3	2	2	4	0	0	1	Celadonite?	X		Calcareous mudstone
12R-4, 54–55	901.04	2	2	1	1	1	1	0	4	1	2	0	1	0	0	Palygorskite?	X		Mudstone
12R-4, 116–117	901.66	2	2	2	0	2	0	0	4	2	2	3	1	0	0	Palygorskite?	X		Mudstone
13R-2, 120–121	908.40	2	2	1	0	0	0	0	4	3	2	4	0	0	1		X		Claystone
13R-3, 9–10	908.79	2	2	1	0	0	1	0	4	1	2	3	2	0	1		X		Claystone
14R-1, 38–39	915.68	2	1	1	0	0	1	1	4	1	1	3	1	0	2		X		Calcareous claystone
15R-4, 20–22	929.70	3	2	1	0	0	0	0	4	1	1	0	0	0	1		X		Sandy mudstone
15R-4, 45–46	929.95	3	2	2	0	0	0	0	4	2	2	0	0	0	1	Biotite	X		Sandy mudstone
15R-5, 27–29	931.27	3	2	1	0	0	0	0	4	1	1	0	0	0	1	Palygorskite? subdued peaks	X		Claystone
15R-5, 40–41	931.40	3	2	1	0	0	0	1	4	0	0	0	0	0	0		X		Claystone with Mn oxides?
15R-5, 107–108	932.07	3	2	1	1	0	0	0	4	0	1	0	0	0	1		X		Mudstone
15R-6, 24–26	932.74	3	2	0	0	0	0	0	4	0	0	0	0	0	1		X		Mudstone
16R-2, 76–77	936.76	3	2	1	0	0	0	1	4	1	0	0	0	0	1		X		Mudstone
16R-2, 124–125	937.24	3	2	1	0	0	0	1	4	1	0	4	0	0	2		X		Claystone
17R-4, 21–25	948.12	3	1	1	0	0	0	0	4	3	1	4	0	0	1		X		Calcareous claystone
17R-7, 24–28	952.55	3	2	1	0	0	0	0	4	2	2	4	1	0	1		X		Claystone
18R-1, 31–35	954.11	3	1	1	0	0	0	0	4	1	1	3	0	0	2		X		Claystone
18R-7, 97–101	962.90	3	1	1	0	0	0	0	4	1	2	4	0	0	2		X		Calcareous claystone
19R-2, 103–104	965.96	3	0	0	0	0	0	0	2	0	1	4	0	0	0	Cc nonstoichiometric		X	Calcite vein
19R-3, 122–123	967.61	3	2	1	1	0	1	0	4	2	2	0	2	0	0		X		Claystone
19R-5, 100–101	970.17	3	1	1	1	0	0	0	3	1	1	4	0	0	0		X		Marlstone
20R-3, 90–92	976.74	3	2	1	1	0	0	0	4	1	2	1	2	0	2	Palygorskite?	X		Mudstone
20R-7, 59–62	982.21	3	2	2	2	0	0	0	4	1	2	0	1	0	2		X		Mudstone
21R-4, 26–28	987.22	3	2	2	2	1	0	0	4	1	3	0	0	0	0	Sanidine	X		Mudstone
21R-4, 63–64	987.59	3	2	2	2	0	0	0	4	1	2	0	0	0	2	No sanidine	X		Mudstone
22R-3, 90–91	996.30	3	2	0	0	0	0	0	3	2	3	4	0	0	0	Sanidine	X		Marlstone
23R-2, 108–109	1004.47	3	1	0	1	0	0	0	1	0	0	4	0	0	0			X	Calcite nodule
23R-2, 108–109	1004.47	3	0	0	0	0	0	0	2	0	0	4	0	0	0			X	Calcite nodule
23R-3, 68–72	1005.52	3	3	1	1	0	2	0	3	4	2	3	0	0	0	Microcline, hematite, glass?	X		Mudstone
23R-3, 68–72	1005.52	3	4	1	1	0	0	0	3	4	1	3	0	0	0	Microcline, glass?	X		Mudstone
23R-4, 79–80	1006.73	3	3	1	1	1	3	0	4	4	1	4	0	0	0	Microcline, hematite, glass?			Calcareous claystone

Table T3 (continued).

Core, section, interval (cm)	Depth (mbsf)	Lith. unit	14 Å	10 Å	7 Å	Zeo	Gt	Opal	Qtz	KFs	Pl	Cc	Dol	Sd	Py	Others	D	M	Lithology
23R-4, 79–80	1006.73	3	3	1	1	1	3	0	4	4	1	4	0	0	0	Microcline, hematite, glass?			Calcareous claystone
24R-1, 51–54	1012.11	3	1	2	2	0	0	0	4	2	2	4	0	0	1		X		Calcareous sandstone
24R-3, 80–84	1015.40	3	1	2	2	0	0	0	4	2	1	4	0	0	0		X		Marlstone
25R-2, 1–6	1022.71	3	1	2	2	0	0	0	4	2	1	4	0	0	0		X		Marlstone
25R-7, 24–30	1029.94	4	2	2	2	0	1	0	4	2	2	0	0	0	0	Biotite	X		Claystone
26R-2, 40–44.5	1032.66	4	2	2	1	0	0	0	4	2	2	0	0	0	2		X		Muddy sandstone
27R-3, 59–60	1044.00	4	0	0	0	0	0	0	3	0	0	0	0	0	0	Manganite, pyrolusite, cryptomelane?		X	Manganite nodule
27R-4, 29–31	1045.20	4	2	2	0	0	2	0	4	2	3	2	0	0	0	Hematite		X	Mudstone
27R-5, 70–72	1047.11	4	1	2	0	0	0	0	4	2	2	0	1	0	1		X		Mudstone
28R-2, 40–41	1052.00	4	1	2	0	0	0	0	4	2	1	0	1	0	2		X		Mudstone
28R-4, 141–142	1055.67	4	0	1	0	0	0	0	4	1	2	4	0	0	2		X		Marlstone
29R-2, 34–36	1061.48	4	2	2	0	0	2	0	4	3	3	3	0	0	2	Diaspore?	X		Muddy sandstone
29R-5, 10–12	1065.63	4	2	2	1	0	0	1	4	1	2	4	0	0	2		X		Nannofossil marlstone
30R-4, 78–79	1074.41	5A	2	2	2	0	0	0	4	1	2	0	2	0	2		X		Nannofossil mudstone
30R-4, 128–129	1074.91	5A	2	2	2	0	1	0	4	1	2	3	1	2	2		X		Mudstone
31R-2, 15–18	1080.65	5A	2	3	2	0	0	0	4	2	2	0	0	2	2		X		Mudstone
31R-2, 124–128	1081.74	5A	2	3	2	0	0	0	4	2	2	0	0	0	3	Vivianite? marcasite?	X		Mudstone with organic matter
32R-5, 23–27	1094.65	5A	0	2	0	0	0	0	3	2	2	4	0	0	3		X		Marlstone
33R-3, 91–95	1102.11	5A	2	3	1	0	0	0	3	1	0	4	0	0	3	Chlorite	X		Marlstone
33R-4, 133–137	1104.03	5A	2	3	2	0	0	0	4	2	2	3	0	1	1		X		Marlstone
34R-2, 94–98	1110.11	5A	2	2	1	0	0	0	3	1	1	4	0	0	3		X		Mudstone
34R-2, 94–98	1110.11	5A	2	2	1	0	0	0	3	1	1	4	0	0	3		X		Mudstone
34R-2, 102–106	1110.19	5A	2	3	2	0	0	0	4	2	3	0	0	0	1	Chlorite		X	Claystone
34R-2, 102–106	1110.19	5A	2	3	2	0	0	0	4	2	3	0	0	0	1	Chlorite		X	Claystone
35R-3, 107–111	1121.47	5A	1	2	2	0	0	0	4	2	2	1	2	2	0	Chlorite	X		Mudstone
35R-6, 57–61	1125.12	5A	2	2	2	0	0	0	4	2	2	4	0	2	2		X		Nannofossil marlstone
36R-5, 142–143	1134.05	5B	1	1	1	0	0	0	4	2	2	4	0	1	1			X	Calcite nodule
36R-6, 62–66	1134.75	5B	1	2	1	0	0	0	4	2	2	2	2	1	2		X		Mudstone
36R-6, 82–86	1134.95	5B	1	2	0	0	0	0	4	1	2	4	0	0	2		X		Muddy nannofossil limestone
37R-3, 44–45	1139.60	5B	2	1	2	0	0	0	4	2	2	4	2	2	1		X		Mudstone
37R-5, 26–27	1141.91	5B	1	2	1	0	1	0	3	1	2	4	4	4	1			X	Carbonate nodule
37R-5, 52–53	1142.17	5B	2	2	2	0	0	0	4	1	2	3	1	2	0		X		Mudstone
38R-5, 96–98	1152.40	5B	1	2	1	0	1	0	4	1	1	4	0	4	0			X	Carbonate nodule
38R-6, 96–98	1153.78	5B	0	2	1	0	0	0	4	2	2	4	0	3	1		X		Sandstone with carbonate cement
39R-2, 20–21	1156.90	5B	1	2	2	0	0	0	4	1	2	4	1	1	0		X		Black shale
39R-3, 38–39	1158.61	5B	1	2	2	0	1	0	4	1	2	4	0	2	1		X		Mudstone
39R-5, 36–38	1161.59	5B	1	2	2	0	1	0	4	2	2	0	2	2	1		X		Mudstone
40R-2, 50–52	1166.83	5B	2	2	2	0	1	0	4	2	2	0	2	2	1		X		Mudstone
41R-1, 113–117	1175.53	5B	2	2	2	0	1	0	4	2	2	4	2	2	2	Chlorite	X		Calcareous siltstone
41R-4, 23–24	1179.20	5B	1	2	1	0	0	0	3	2	2	3	0	4	1			X	Carbonate nodule
41R-6, 79–84	1182.84	5B	2	2	1	0	1	0	4	1	2	4	0	3	1		X		Siltstone with carbonate cement
42R-1, 4–8	1184.04	5B	2	2	2	0	1	0	4	2	2	4	1	2	1		X		Calcareous claystone
42R-4, 115–116	1189.31	5B	1	2	1	0	0	0	4	2	2	3	0	4	1			X	Siderite nodule
42R-6, 39–43	1191.59	5B	1	2	2	0	0	0	4	1	2	4	0	0	2		X		Marlstone
43R-2, 88–92	1195.91	5B	0	1	1	0	0	0	4	0	1	4	0	0	3		X		Marlstone
43R-3, 35–36	1196.90	5B	1	2	2	0	0	0	4	2	2	4	2	2	2		X		Calcareous mudstone
43R-5, 78–79	1200.25	5B	0	0	0	0	0	0	0	0	0	0	0	0	0	Barite		X	Barite nodule
44R-4, 27–28	1208.01	5B	0	0	0	0	0	0	0	0	0	0	0	0	0	Barite		X	Barite nodule
44R-4, 62–63	1208.36	5B	2	2	2	0	0	0	4	2	2	0	2	2	1		X		Mudstone

Table T3 (continued).

Core, section, interval (cm)	Depth (mbsf)	Lith. unit	14 Å	10 Å	7 Å	Zeo	Gt	Opal	Qtz	KFs	Pl	Cc	Dol	Sd	Py	Others	D	M	Lithology
46R-2, 52–53	1224.43	5B	0	1	0	0	0	0	3	1	1	3	0	4	2			X	Siderite nodule
46R-5, 105–106	1229.58	5B	1	2	2	0	0	0	4	2	2	4	0	2	1		X		Calcareous mudstone
47R-2, 66–69	1234.19	5B	1	2	2	0	0	0	4	2	2	4	0	2	2		X		Nannofossil marlstone
47R-3, 23–24	1235.27	5B	0	0	0	0	0	0	0	0	0	0	0	0	0	Barite		X	Barite nodule
47R-7, 28–29	1241.26	5B	2	2	2	0	1	0	4	1	2	2	0	2	1		X		Green mudstone at 32 cm
47R-7, 42–43	1241.40	5B	0	1	0	0	0	0	2	0	0	1	4	2	1			X	Dolomite nodule
48R-2, 90–92	1244.14	5B	1	2	2	0	0	0	4	2	2	4	1	2	1		X		Calcareous claystone at 88 cm
48R-4, 44–45	1246.76	5B	1	2	2	0	0	0	4	2	2	4	1	2	2			X	Siltstone with carbonate cement at 47 cm
49R-2, 6–11	1252.96	5B	2	2	2	0	0	0	4	2	2	3	2	2	2		X		Claystone
49R-4, 67–72	1256.57	5B	2	2	2	0	0	0	4	2	3	3	1	1	2	Chlorite	X		Siltstone
50R-4, 18–22	1265.68	5B	2	2	2	0	0	0	4	2	3	3	1	1	2	Chlorite	X		Siltstone
50R-6, 60–64.5	1268.58	5B	1	2	2	0	0	0	4	2	2	4	0	2	2		X		Calcareous claystone
51R-1, 60–63	1271.30	5B	2	2	2	0	0	0	4	2	2	4	0	2	2	Chlorite	X		Claystone with nannofossils
52R-2, 36–37	1282.26	5B	2	2	2	0	0	0	4	2	2	2	0	1	1	Chlorite	X		Mudstone
52R-3, 90–91	1284.30	5B	1	2	1	0	0	0	4	2	2	4	0	0	2		X		Calcareous mudstone
52R-4, 91–92	1285.81	5B	2	3	2	0	0	0	4	3	3	4	0	0	2	Chlorite	X		Calcareous siltstone
53R-5, 107–108	1297.01	5B	1	2	2	0	0	0	4	2	2	4	0	2	2		X		Calcareous mudstone
54R-4, 120–121	1305.30	5B	2	3	2	0	0	0	4	2	2	3	2	1	2	Brittle mica?	X		Mudstone
55R-2, 10–13	1310.80	5B	1	2	2	0	0	0	4	1	2	4	0	1	2		X		Nannofossil marlstone
55R-2, 21–22	1310.91	5B	0	1	1	0	0	0	3	1	1	3	0	4	2			X	Siderite nodule
56R-1, 118–120	1319.98	5B	1	2	2	0	0	0	4	2	2	3	0	2	2		X		Claystone
56R-2, 110–111	1321.40	5B	1	2	2	0	0	0	4	2	2	0	1	2	1		X		Mudstone
57R-1, 4–5	1328.54	5B	2	2	2	0	0	0	4	2	2	4	0	2	2		X		Calcareous mudstone
57R-2, 38–39	1330.38	5B	2	2	2	0	0	0	4	2	2	2	1	2	2		X		Claystone
58R-3, 68–72	1341.78	5B	2	2	3	0	0	0	4	2	2	0	0	2	1	Chlorite, kaolinite	X		Mudstone
59R-4, 103–107	1349.63	5B	2	3	3	0	0	0	4	1	2	2	1	2	2	Kaolinite	X		Claystone
60R-1, 18–19	1353.88	5B	1	2	2	0	0	0	4	1	2	3	0	2	2		X		Calcareous mudstone
61R-4, 119–120	1368.89	5B	2	3	3	0	0	0	4	2	3	0	2	2	0		X		Clay/mudstone
62R-3, 78–79	1376.68	5B	2	3	3	0	0	0	4	2	2	0	2	2	1		X		Mudstone
63R-1, 135–136	1383.85	5B	2	3	2	0	0	0	4	2	2	3	0	2	1		X		Claystone
64R-5, 43–44	1398.63	5B	2	3	3	0	0	0	4	1	2	0	2	2	0		X		Claystone
65R-3, 100–101	1405.80	5B	1	2	2	0	0	0	4	1	2	3	0	0	3		X		Claystone
66R-3, 42–43	1414.72	5B	2	3	3	0	0	0	4	2	3	3	1	1	3	12.4 Å	X		Claystone
67R-3, 39–40	1424.29	5B	2	3	3	0	0	0	4	2	2	0	2	2	0			X	Mudstone
68R-2, 137–141	1433.37	5B	2	3	3	0	0	0	4	2	3	3	3	0	2	2.8 Å	X		Calcareous mudstone
68R-4, 90–91	1435.90	5B	0	1	0	0	0	0	3	1	2	2	4	4	3	F-apatite		X	Carbonate nodule
69R-6, 55–56	1447.85	5B	1	2	2	0	0	0	4	1	2	3	3	1	3	2.96 Å	X		Calcareous claystone
70R-4, 49–50	1454.49	5B	2	3	3	0	0	0	4	2	2	1	0	0	0		X		Claystone
71R-6, 20–21	1466.90	5B	2	3	3	0	0	0	4	1	2	1	0	0	1		X		Claystone
72R-5, 79–80	1475.52	5B	2	3	2	0	0	0	4	1	2	1	0	0	1		X		Claystone
73R-3, 46–47	1481.96	5B	2	3	2	0	0	0	4	2	2	0	0	0	3	Chlorite	X		Mudstone
74R-2, 121–122	1490.81	5B	2	3	2	0	0	0	4	2	2	1	0	0	2		X		Claystone
76R-3, 45–46	1510.75	5C	2	3	3	0	0	0	4	2	3	0	2	2	0		X		Claystone
77R-2, 21–23	1518.61	5C	0	0	2	0	0	0	3	0	2	0	3	4	1			X	Siderite nodule
77R-2, 110–112	1519.50	5C	2	3	3	0	0	0	4	1	2	1	2	2	3		X		Claystone
78R-3, 16–19	1529.66	5C	2	3	3	0	0	0	4	1	3	1	2	0	0		X		Claystone
79R-5, 34–35	1542.54	5C	2	2	3	0	0	0	4	1	2	3	1	1	2		X		Calcareous claystone
80R-1, 28–29	1546.08	5C	2	2	3	0	0	0	4	1	2	3	0	2	2		X		Calcareous mudstone
81R-1, 37–40	1555.77	5C	2	3	3	0	0	0	4	2	3	2	2	2	2		X		Calcareous mudstone

Table T3 (continued).

Core, section, interval (cm)	Depth (mbsf)	Lith. unit	14 Å	10 Å	7 Å	Zeo	Gt	Opal	Qtz	KFs	Pl	Cc	Dol	Sd	Py	Others	D	M	Lithology
82R-1, 6–9	1565.06	5C	2	3	3	0	0	0	4	2	2	3	0	0	1		X		Claystone
83R-1, 62–63	1575.12	5C	2	3	3	0	0	0	4	2	2	0	0	0	1	C-V-S-ML	X		Mudstone
83R-3, 133–134	1578.83	5C	2	3	3	0	0	0	4	2	2	3	0	0	2	Cc nonstoichiometric		X	Nodular calcite with host sediment
84R-2, 114–115	1586.84	5C	2	3	3	0	0	0	4	2	2	3	0	0	2		X		Mudstone with nannofossils
85R-5, 31–32	1593.26	5C	2	2	4	0	0	2	4	1	2	0	1	0	0	Kaolinite		X	Claystone with kaolin blebs
85R-5, 35–39	1593.30	5C	2	2	3	0	0	0	4	2	2	1	1	0	1	Chlorite	X		Claystone
86R-2, 25–26	1596.55	5C	2	2	3	0	0	0	4	1	2	1	0	0	1	Chlorite	X		Calcareous mudstone
86R-5, 20–21	1601.00	5C	2	2	4	0	0	0	4	1	1	1	0	0	1	Kaolinite	X		Claystone
87R-2, 99–100	1606.99	5C	2	2	2	0	0	0	4	2	2	0	0	0	1	Kaolinite + chlorite	X		Mudstone
87R-2, 104–106	1607.04	5C	2	2	2	0	0	0	4	2	2	1	0	0	2	Kaolinite + chlorite	X		Mudstone
87R-6, 29–30	1612.40	5C1	2	1	3	0	0	0	4	2	4	4	0	0	2	Strong kaolinite, weaker chlorite		X	Poikiloblastic hornfels (altered siltstone)
87R-6, 85–86	1612.96	5C1	3	0	4	0	0	0	4	0	3	4	0	0	2	Cc nonstoichiometric		X	Altered sill
87R-6, 106–107	1613.17	5C1	2	0	3	0	0	0	2	2	3	4	0	0	1	Kaolinite + chlorite equal, apatite, magnetite		X	Altered sill
87R-7, 19–20	1613.70	5C1	3	1	3	0	0	0	4	0	4	3	0	0	2	Pyroxene, magnetite, chlorite, serpentine		X	Altered sill
88R-1, 92–93	1616.04	5C1	3	2	3	3	0	0	3	4	4	1	0	0	1	Analcite, augite, biotite		X	Altered sill
88R-3, 61–62	1617.17	5C1	3	2	3	3	0	0	2	4	4	1	0	0	1	Magnetite, analcite, augite, apatite, biotite		X	Altered sill
88R-3, 119–120	1617.75	5C1	2	2	2	2	0	0	2	4	4	1	0	1	2	No magnetite, analcite, augite, apatite		X	Altered sill
88R-4, 109–110	1619.15	5C1	2	2	2	3	0	0	2	4	4	0	0	0	0	Augite, analcite, mica		X	Altered sill
88R-5, 106–109	1620.59	5C1	3	2	3	2	0	0	2	4	3	1	0	2	2	Augite, apatite, analcite, biotite		X	Altered sill
88R-5, 106–109	1620.59	5C1	3	2	3	2	0	0	2	4	3	1	0	2	2	Augite, apatite, analcite, biotite		X	Altered sill
88R-6, 69–70	1621.31	5C1	3	2	2	0	0	0	3	4	4	1	0	1	1	Augite, ilmenite? pyrite, biotite		X	Altered sill
88R-7, 93–94	1622.76	5C1	3	1	2	0	0	0	3	4	4	3	0	1	2	Augite, magnetite, ilmenite? biotite		X	Altered sill
89R-1, 20–21	1623.80	5C	3	1	4	0	0	0	4	2	1	3	0	0	0	Cc nonstoichiometric		X	Altered ash?
89R-1, 119–121	1624.79	5C	2	3	3	0	0	0	4	2	3	0	0	0	2		X		Claystone
89R-2, 35–36	1625.45	5C	2	2	3	0	0	0	4	2	2	1	0	0	2	Chlorite	X		Claystone
90R-4, 104–108	1638.81	5C	2	2	3	0	0	0	4	2	2	1	0	0	1		X		Claystone
91R-2, 112–114	1645.42	5C	1	2	3	0	0	0	4	2	2	0	0	0	1		X		Mudstone
92R-5, 71–72	1659.21	5C	0	2	2	0	0	0	3	1	1	0	0	0	?	CaF-apatite		X	Phosphate nodule
92R-6, 126–129	1661.26	5C	1	2	3	0	0	0	4	2	1	0	0	0	2		X		Mudstone
93R-4, 127–130	1667.87	5C	2	2	3	0	0	0	4	2	2	0	0	0	2	Chlorite	X		Claystone
94R-5, 71–72	1678.30	5C	2	2	2	0	0	0	4	1	2	2	0	0	3	Chlorite	X		Mudstone
95R-3, 74–78	1684.80	5C	2	3	3	0	0	0	4	2	2	2	0	0	0	Chlorite	X		Mudstone
96R-1, 131–132	1692.21	5C	1	2	2	0	0	0	4	1	3	3	0	0	3		X		Mudstone
96R-CC, 9–10	1698.58	5C	2	3	3	0	0	0	4	2	3	2	0	0	1	Chlorite, mica	X		Mudstone, soft
97R-1, 84–85	1701.34	5C	1	0	3	0	0	0	4	0	0	4	0	0	2	Apatite		X	Calcareous siltstone with phosphate
97R-1, 96–102	1701.46	5C																	
97R-3, 142–143	1704.92	5C2	2	0	4	0	0	0	3	3	4	4	0	0	3			X	Minor vein
97R-3, 144–145	1704.94	5C2	2	1	3	0	0	0	2	3	4	4	0	0	2	Chlorite		X	Minor vein
98R-1, 76–77	1710.86	5C2	2	2	3	2	0	0	4	0	4	0	0	0	0	Analcite, chlorite		X	Aureole (altered sediments)
98R-1, 98–99	1711.08	5C2	2	3	3	2	0	0	4	0	4	0	0	1	1	Analcite, chlorite, olivine?		X	Aureole (altered sediments)
98R-1, 117–119	1711.27	5C2	3	0	3	0	0	0	4	2	4	0	0	0	1			X	Altered sill
98R-2, 113–114	1712.64	5C2	2	2	2	0	0	0	3	1	4	0	0	0	0			X	Aureole (altered sediments)
98R-2, 132–133	1712.83	5C2	2	3	2	0	0	0	3	2	4	3	0	0	1			X	Aureole (altered sediments)
98R-3, 6–9	1713.07	5C2	2	3	2	0	0	0	4	3	4	0	0	0	1	Mg-chlorite		X	Aureole (altered sediments)
98R-3, 47–49	1713.48	5C2	4	0	4	2	0	0	0	0	4	4	0	0	3	Analcite, sudoite		X	Aureole (altered sediments)
98R-3, 87–88	1713.88	5C2	3	0	3	0	0	0	0	3	2	4	0	0	0	Cc nonstoichiometric		X	Aureole (altered sediments)

Table T3 (continued).

Core, section, interval (cm)	Depth (mbsf)	Lith. unit	14 Å	10 Å	7 Å	Zeo	Gt	Opal	Qtz	KFs	Pl	Cc	Dol	Sd	Py	Others	D	M	Lithology
99R-1, 123–126	1720.63	5C2	2	0	2	3	0	0	2	4	4	0	0	0	0	Augite, analcite, Mg-analcite, serpentine, magnetite, ilmenite, Mg-chlorite		X	Altered sill
99R-3, 113–114	1723.42	5C2	3	1	3	3	0	0	2	3	4	0	0	0	0	Augite, analcite, Mg-analcite, serpentine, magnetite, ilmenite, Mg-chlorite		X	Altered sill

Notes: The main results are summarized in the text. Zeo = zeolite, Gt = goethite, Qtz = quartz, KFs = K feldspar, Pl = plagioclase, Cc = calcium carbonate, Dol = dolomite, Sd = siderite, Py = pyrite. C-V-S-ML = chlorite-vermiculite-smectite mixed-layer clay. D = dominant, M = minor. 0 = not detected, 1 = barely detectable, 2 = low intensity relative to the major peak in the sample, 3 = intermediate intensity relative to major peak, 4 = major peak or intensity similar to major peak.

Table T4. Major and trace element analyses determined by ICP-AES. (See table notes. Continued on next five pages.)

Core, section, interval (cm)	Depth (mbsf)	Run	LOI (wt%)	Major element oxide (wt%)										Trace element (ppm)						
				SiO_2	TiO_2	Al_2O_3	Fe_2O_3*	MnO	MgO	CaO	Na_2O	K_2O	P_2O_5	Zr	Y	Sr	Ni	Cr	V	Ba
210-1276A-																				
3R-2, 17–19	809.96	M-1	9.33	63.14	0.51	11.67	5.22	0.01	2.42	1.74	1.28	1.69	0.06	78.04	15.10	154.05	37.58	54.27	123.39	419.94
3R-8, 11–13	818.78	M-2	10.27	49.08	0.51	12.30	5.40	0.04	1.83	7.75	1.23	1.93	0.07	90.59	20.28	410.98	49.35	61.26	171.32	535.94
4R-4, 7–8	823.77	M-3	8.61	65.65	0.52	12.18	5.03	0.01	1.91	1.66	1.35	1.61	0.06	85.75	13.28	162.82	35.51	63.88	142.41	447.49
5R-4, 20–21	833.50	M-4	8.38	55.10	0.53	12.76	4.75	0.01	2.28	4.28	1.24	1.95	0.06	95.88	17.35	277.26	44.42	60.31	180.06	422.44
5R-4, 24–25	833.54	M-5	7.35	59.46	0.57	12.96	4.67	0.01	3.18	1.69	1.39	1.97	0.07	122.62	22.11	166.28	34.90	67.37	161.18	475.51
6R-3, 56–59	841.96	M-6	7.07	62.97	0.57	14.06	5.64	0.01	1.52	1.38	1.35	2.26	0.09	100.30	17.79	165.88	40.65	72.59	258.54	450.01
6R-6, 8–10	845.98	M-7	6.77	63.20	0.54	13.10	6.35	0.03	2.04	1.44	1.13	1.20	0.07	98.50	18.85	162.46	36.07	57.50	137.61	471.63
7R-4, 33–35	852.83	M-8	6.87	57.41	0.59	14.71	5.12	0.01	1.69	1.39	1.37	2.62	0.07	115.61	18.43	165.43	23.85	62.11	143.99	484.28
8R-5, 114–116	864.74	M-9	5.27	65.33	0.52	12.23	4.46	0.01	2.51	1.49	1.19	2.06	0.12	108.26	24.32	161.82	117.51	56.67	113.99	362.33
9R-1, 34–36	867.54	M-10	17.60	45.90	0.23	4.60	2.17	0.24	1.63	16.70	0.79	0.72	0.13	72.41	15.53	320.02	23.92	23.06	40.20	186.86
9R-2, 72–75	869.42	M-11	6.55	62.85	0.42	12.04	6.01	0.02	3.24	1.84	1.49	1.40	0.17	169.56	20.12	183.50	76.97	39.57	141.08	195.22
10R-4, 101–105	882.28	M-12	14.04	51.79	0.33	8.88	4.19	0.10	3.12	10.43	1.19	0.86	0.13	76.49	19.96	285.89	82.03	40.02	43.78	188.48
10R-4, 109–113	882.36	M-13	23.43	39.95	0.14	2.53	0.86	0.28	1.03	20.74	0.58	0.44	0.06	61.03	10.69	214.00	14.33	16.92	16.19	211.18
11R-4, 2–4	890.92	M-14	18.03	49.52	0.24	9.12	3.15	0.10	2.48	10.15	1.27	0.84	0.11	169.03	15.98	259.84	43.41	23.85	38.38	386.35
11R-4, 122–125	892.12	M-15	3.50	67.17	0.32	12.67	4.26	0.10	2.82	1.91	1.89	1.29	0.10	357.30	22.84	265.47	77.72	38.35	45.03	774.13
12R-3, 30–32	899.30	M-17	13.99	53.39	0.53	12.07	6.70	0.05	2.32	1.83	1.31	2.11	0.22	134.21	36.32	175.52	107.37	66.65	85.88	323.50
12R-4, 54–57	901.04	M-16	4.71	55.81	0.40	14.98	3.59	0.16	3.11	8.28	1.95	1.34	0.09	710.05	17.87	308.08	106.25	25.57	55.33	305.48
13R-2, 120–123	908.40	M-18	11.37	54.81	1.36	9.89	7.13	0.02	2.46	3.54	1.35	1.37	0.18	174.76	29.09	207.43	80.45	56.80	135.41	247.28
13R-3, 10–13	908.80	M-19	14.70	53.91	1.29	9.78	6.82	0.02	2.44	3.41	1.34	0.88	0.19	165.97	28.16	197.77	79.22	55.05	134.82	230.42
14R-1, 39–42	915.69	M-20	6.00	66.83	0.68	9.92	4.15	0.01	1.38	3.42	1.18	1.97	0.20	224.73	29.01	199.59	41.29	100.29	79.41	291.63
15R-5, 40–41	931.40	M-21	7.13	59.23	0.65	14.03	6.81	0.14	3.52	1.94	1.51	1.84	0.27	173.56	51.62	229.07	89.52	74.32	95.42	303.74
15R-5, 107–108	932.07	M-22	10.52	53.46	0.47	11.02	5.76	0.56	2.90	1.79	1.38	1.56	0.15	96.74	35.19	211.31	73.08	39.83	69.49	525.84
16R-2, 74–76	936.74	M-24	4.80	64.89	0.54	10.52	3.08	0.03	2.12	5.16	1.19	1.46	0.09	87.06	22.23	364.21	49.67	102.45	96.18	221.30
16R-2, 121–123	937.21	M-23	5.10	75.37	0.42	8.17	1.90	0.02	1.19	1.43	1.03	1.07	0.10	81.74	19.75	159.32	26.27	67.62	70.47	204.21
17R-4, 21–25	948.12	M-25	13.10	56.84	0.28	5.06	1.33	0.14	0.92	12.40	0.72	0.74	0.11	22.04	20.03	433.70	23.20	49.11	51.30	156.23
17R-7, 24–28	952.55	M-26	2.70	81.87	0.19	4.57	1.83	0.02	2.16	3.02	0.81	0.73	0.09	19.09	8.93	160.88	26.64	77.01	47.69	199.62
18R-1, 31–35	954.11	M-27	1.00	77.11	0.22	4.87	1.53	0.01	1.68	2.45	0.76	0.82	0.05	1.45	6.65	160.01	26.30	82.02	52.58	187.63
18R-7, 97–101	962.90	M-28	8.60	66.89	0.18	4.30	1.42	0.30		9.83	0.71	0.61	0.08	4.06	8.09	210.85	35.00	45.52	39.64	191.64
19R-3, 122–124	967.61	M-29	5.53	65.62	0.65	13.66	8.60	1.26	2.87	1.80	1.55	2.10	0.20	113.77	18.19	363.64	100.23	84.16	106.50	306.07
19R-5, 100–102	970.17	M-30	29.30	22.67	0.22	4.93	1.79	0.75	0.93	27.31	0.39	0.55	0.11	34.57	19.92	366.37	22.64	40.98	31.83	119.47
20R-3, 90–92	976.74	M-31	11.80	54.21	0.54	12.20	7.81	0.53	2.45	1.80	1.36	2.28	0.27	104.00	45.29	203.03	65.36	73.78	95.85	294.29
20R-7, 59–62	982.21	M-32	4.10	63.16	0.63	15.04	4.99	0.11	2.42	1.50	1.35	2.76	0.09	115.47	22.90	201.51	46.23	100.07	269.94	517.27
21R-4, 26–28	987.22	M-33	8.20	58.29	0.69	15.49	5.53	0.02	0.00	0.93	1.25	2.74	0.14	156.88	22.62	189.47	327.34	103.38	188.45	347.45
21R-4, 61–63	987.57	M-34	7.80	56.52	0.63	14.81	5.56	0.02	0.00	1.57	1.26	2.66	0.56	155.15	75.03	206.24	62.27	75.36	144.13	342.23
22R-3, 91–93	996.31	M-35	12.80	42.55	1.27	13.73	7.19	0.24	2.02	9.45	1.45	2.20	0.18	543.52	40.32	299.96	30.11	22.76	68.04	256.05
23R-3, 68–72	1005.52	M-36	9.08	41.62	3.01	15.52	11.94	0.12	2.63	3.05	1.52	2.91	0.50	258.68	36.64	250.51	90.75	110.62	200.25	259.87
24R-1, 51–54	1012.11	M-37	18.20	42.93	0.65	8.89	2.35	0.24	1.22	17.49	0.69	1.74	0.28	231.04	28.28	507.04	39.39	64.19	76.73	203.95
24R-3, 80–84	1015.40	M-38	25.44	26.89	0.40	9.40	3.07	0.24	1.10	22.84	0.58	1.43	0.10	66.39	15.02	413.12	46.94	51.91	58.83	172.63
25R-2, 1–6	1022.71	M-40	24.40	51.86	0.59	10.82	5.86	0.10	1.86	1.23	0.79	1.90	0.25	224.22	38.85	127.15	42.11	46.71	108.89	272.51
25R-7, 24–30	1029.94	M-39	4.70	36.90	0.63	12.44	4.29	0.21	1.57	29.18	0.82	1.93	0.10	83.33	22.59	1066.45	36.20	80.60	90.52	226.56
26R-2, 40–44	1032.66	M-41	5.90	61.33	0.71	11.33	5.05	0.05	2.38	1.71	1.18	2.25	0.12	286.69	26.78	173.21	47.77	59.32	87.37	297.99
27R-4, 29–31	1045.20	M-42	7.00	62.02	0.51	8.16	5.93	0.11	2.08	1.69	0.93	1.74	0.10	196.97	18.04	149.16	47.41	62.69	137.11	255.48
27R-5, 70–72	1047.11	M-43	2.50	79.83	0.51	7.40	3.21	0.04	1.65	1.34	0.90	1.47	0.06	236.13	17.21	141.13	30.97	45.39	62.49	226.18
28R-2, 40–43	1052.00	M-44	3.30	70.08	0.83	12.11	2.01	0.02	1.97	1.45	1.13	2.15	0.10	260.15	29.38	174.05	31.17	66.46	217.84	298.10
28R-4, 141–144	1055.67	M-45	14.20	42.08	0.63	8.73	4.66	0.11	2.15	12.90	0.84	1.58	0.09	194.79	20.08	226.28	29.79	56.71	88.94	245.06
29R-2, 34–38	1061.48	M-46	5.70	58.94	0.80	16.53	5.05	0.03	2.03	2.54	1.11	2.85	0.06	126.11	25.38	265.82	116.02	84.96	182.62	402.92
29R-5, 8–10	1065.61	M-47	21.20	34.24	0.54	9.48	5.44	0.29	1.06	19.91	0.76	1.66	0.07	115.08	20.92	504.88	28.28	50.09	77.77	245.15
30R-4, 78–80	1074.41	M-48	10.07	56.04	0.76	13.84	7.93	0.02	1.62	1.07	1.13	2.68	0.06	131.51	22.91	241.45	323.50	79.05	102.58	343.44
30R-4, 128–130	1074.91	M-49	4.80	53.98	0.79	14.55	6.05	0.01	2.10	4.70	1.16	2.58	0.04	130.69	24.06	421.61	135.66	88.08	137.03	569.50

Table T4. (continued).

Core, section, interval (cm)	Depth (mbsf)	Run	Carbon (wt%)			Color	Lithology
			$CaCO_3$	C_{tot}	C_{org}		
210-1276A-							
3R-2, 17–19	809.96	M-1					
3R-8, 11–13	818.78	M-2					
4R-4, 7–8	823.77	M-3	1.08	1.81	1.68	Olive gray	Claystone
5R-4, 20–21	833.50	M-4	8.41	3.36	2.35	Olive gray	Claystone
5R-4, 24–25	833.54	M-5	0.50	0.34	0.28	Grayish olive	Claystone
6R-3, 56–59	841.96	M-6	0.50	1.35	1.29	Olive gray	Claystone
6R-6, 8–10	845.98	M-7	0.58	0.11	0.04	Greenish gray	Claystone
7R-4, 33–35	852.83	M-8	0.83	0.44	0.34	Greenish gray	Claystone
8R-5, 114–116	864.74	M-9	35.15	0.13	0.00	Greenish gray	Claystone
9R-1, 34–36	867.54	M-10	35.57	4.36	0.09	Greenish gray	Siliceous marlstone
9R-2, 72–75	869.42	M-11	0.58	0.12	0.05	Dusky yellowish green	Claystone
10R-4, 101–105	882.28	M-12	25.41	3.18	0.13	Moderate brown	Calcareous mudstone
10R-4, 109–113	882.36	M-13	44.40	0.13	0.00	Pale olive	Calcareous mudstone
11R-4, 2–4	890.92	M-14	13.58	1.50	0.00	Light olive gray	Calcareous mudstone
11R-4, 122–125	892.12	M-15	0.75	0.08	0.00	Greenish gray	Zeolitic claystone
12R-3, 30–32	899.30	M-17	15.58	1.92	0.05	Greenish gray	Calcareous mudstone
12R-4, 54–57	901.04	M-16	0.92	0.13	0.02	Moderate reddish brown	Mudstone
13R-2, 120–123	908.40	M-18	7.83	0.97	0.03	Moderate reddish brown	Claystone
13R-3, 10–13	908.80	M-19	4.83	0.62	0.04	Moderate reddish brown	Claystone
14R-1, 39–42	915.69	M-20	5.00	0.81	0.21	Dark greenish gray	Calcareous claystone
15R-5, 40–41	931.40	M-21	0.42	0.06	0.01	Brownish black	Claystone with Mn oxides?
15R-5, 107–108	932.07	M-22	0.25	0.06	0.03	Moderate brown	Mudstone
16R-2, 74–76	936.74	M-24	0.50	0.12	0.06	Grayish green	Mudstone
16R-2, 121–123	937.21	M-23	8.00	1.90	0.94	Olive gray	Claystone
17R-4, 21–25	948.12	M-25	26.49	3.16	0.00	Light greenish gray	Calcareous claystone
17R-7, 24–28	952.55	M-26	4.42	1.15	0.62	Olive black	Claystone
18R-1, 31–35	954.11	M-27	3.67	0.87	0.43	Olive black	Claystone
18R-7, 97–101	962.90	M-28	16.58	2.38	0.39	Light olive gray	Calcareous claystone
19R-3, 122–124	967.61	M-29	2.33	0.33	0.05	Moderate brown	Claystone
19R-5, 100–102	970.17	M-30	62.06	7.63	0.18	Light brown	Marlstone
20R-3, 90–92	976.74	M-31	1.75	0.23	0.02	Moderate brown	Mudstone
20R-7, 59–62	982.21	M-32	0.75	0.99	0.90	Greenish black	Mudstone
21R-4, 26–28	987.22	M-33	0.92	0.18	0.07	Dusky green	Mudstone
21R-4, 61–63	987.57	M-34	0.83	0.11	0.01	Dark greenish gray	Mudstone
22R-3, 91–93	996.31	M-35				Moderate brown	Marlstone
23R-3, 68–72	1005.52	M-36	3.00	0.51	0.15	Moderate brown	Mudstone
24R-1, 51–54	1012.11	M-37	38.49	4.79	0.17	Pale olive	Calcareous sandstone
24R-3, 80–84	1015.40	M-38	49.06	5.99	0.10	Light olive gray	Marlstone
25R-2, 1–6	1022.71	M-40	47.31	5.82	0.14	Olive gray	Marlstone
25R-7, 24–30	1029.94	M-39	0.25	0.03	0.00	Moderate brown	Claystone
26R-2, 40–44	1032.66	M-41	0.42	0.02	0.00	Moderate brown	Muddy sandstone
27R-4, 29–31	1045.20	M-42	0.08	0.27	0.26	Light brown	Mudstone
27R-5, 70–72	1047.11	M-43	0.25	0.03	0.00	Light brown	Mudstone
28R-2, 40–43	1052.00	M-44	0.50	0.36	0.30	Medium dark gray	Mudstone
28R-4, 141–144	1055.67	M-45	40.90	5.23	0.32	Moderate brown	Marlstone
29R-2, 34–38	1061.48	M-46	9.41	1.31	0.18	Dark brown	Muddy sandstone
29R-5, 8–10	1065.61	M-47	41.40	4.71	0.00	Moderate brown	Nannofossil marlstone
30R-4, 78–80	1074.41	M-48	6.75	1.23	0.42		Nannofossil mudstone
30R-4, 128–130	1074.91	M-49	1.00	0.13	0.01	Dusky green	Mudstone

Table T4. (continued).

Core, section, interval (cm)	Depth (mbsf)	Run	LOI (wt%)	Major element oxide (wt%)										Trace element (ppm)						
				SiO_2	TiO_2	Al_2O_3	Fe_2O_3*	MnO	MgO	CaO	Na_2O	K_2O	P_2O_5	Zr	Y	Sr	Ni	Cr	V	Ba
31R-2, 15–18	1080.65	M-50	7.80	56.72	0.59	9.54	10.35	0.01	1.43	1.22	0.94	1.69	0.19	150.06	32.44	182.05	429.39	118.10	611.80	313.24
31R-2, 124–128	1081.74	M-51	14.20	56.66	0.76	13.29	4.50	0.01	0.00	0.77	0.97	2.46	0.06	184.44	29.68	160.52	122.20	78.85	145.01	395.89
32R-5, 23–27	1094.65	M-52	4.70	56.12	0.81	15.59	10.80	0.04	2.90	1.25	0.76	2.79	0.03	134.37	25.18	136.18	223.30	92.13	140.27	439.96
33R-3, 91–95	1102.11	M-53	30.59	19.03	0.15	3.22	2.10	0.79	0.77	28.36	0.32	0.33	0.10	17.87	30.47	339.04	51.46	36.78	234.49	109.13
33R-4, 133–137	1104.03	M-54	10.39	68.15	0.60	11.51	3.73	0.04	1.68	6.19	0.96	2.09	0.07	117.85	15.18	342.22	87.48	62.29	104.76	300.08
34R-2, 102–106	1110.19	M-56	30.92	18.90	0.21	4.61	2.25	0.64	0.87	28.06	0.32	0.43	0.05	30.62	25.29	325.81	63.34	45.50	371.50	143.30
35R-6, 57–61	1125.12	M-58	14.50	44.33	0.55	9.41	5.25	0.07	2.13	10.59	0.83	1.61	0.05	144.91	20.90	331.62	19.16	50.39	71.00	273.23
36R-6, 62–66	1134.75	M-59	7.70	50.70	0.77	12.25	8.31	1.28	2.11	4.48	1.04	2.43	0.13	179.70	28.91	273.21	39.42	62.57	81.44	291.36
36R-6, 82–86	1134.95	M-60	20.22	33.73	0.34	7.46	6.34	0.28	1.17	20.68	0.68	1.48	0.09	61.65	21.59	583.41	99.57	45.90	95.96	207.02
37R-3, 46–49	1139.62	M-61	4.21	69.32	0.81	15.58	7.06	0.02	2.25	1.69	1.20	2.78	0.08	159.12	16.76	273.70	74.58	75.06	103.05	416.51
37R-5, 54–57	1142.19	M-62	12.60	54.65	0.75	14.24	4.93	0.08	2.31	6.27	1.17	2.18	0.07	131.73	24.17	397.72	97.34	71.72	115.29	470.57
38R-5, 96–99	1152.40	M-63	32.16	5.48	0.10	1.64	33.34	19.84	3.43	8.68	0.19	0.15	0.07		21.38	122.23	28.20	45.31		91.08
38R-6, 96–98	1153.78	M-64	17.30	40.37	0.41	5.61	7.81	2.71	0.80	14.75	0.59	1.01	0.33	197.31	53.68	222.32	45.72	45.84	38.07	453.31
39R-2, 16–18	1156.86	M-65	6.10	67.92	0.81	16.34	5.65	0.02	2.14	3.92	1.29	2.83	0.06	154.41	16.46	351.35	66.88	80.97	131.04	511.23
39R-5, 36–38	1161.59	M-66	7.60	61.28	0.72	14.30	6.17	0.02	0.00	0.86	1.09	2.49	0.05	146.79	27.81	182.89	80.99	70.38	98.56	426.34
40R-2, 50–52	1166.83	M-67	0.60	63.30	0.85	16.02	5.79	0.02	2.60	1.78	1.26	2.92	0.07	160.79	27.48	199.01	138.13	82.03	111.88	628.84
40R-2, 80–83	1167.13	M-68	23.92	28.35	0.37	8.71	3.42	0.80	0.00	21.93	0.63	1.36	0.09	51.22	23.11	319.32	254.06	55.07	84.28	650.46
41R-1, 113–117	1175.53	M-69	9.40	59.48	0.66	6.88	2.19	0.44	1.12	11.12	0.82	1.46	0.01	273.33	29.60	188.96	27.03	39.58	44.27	379.08
41R-6, 79–84	1182.84	M-70	25.42	25.79	0.31	7.26	6.43	1.98	1.59	20.56	0.62	1.09	0.15	43.53	35.64	318.42	26.49	40.94	61.23	373.92
42R-1, 4–8	1184.04	M-71	10.40	48.22	0.73	14.66	5.60	0.05	2.02	6.73	1.08	2.58	0.06	109.48	25.03	372.61	87.11	73.60	113.70	459.70
42R-6, 39–43	1191.59	M-72	21.35	37.49	0.40	8.98	3.27	0.27	1.23	20.33	0.74	1.50	0.06	65.76	14.50	628.44	55.98	47.10	70.55	602.27
43R-2, 88–92	1195.91	M-73	22.58	26.61	0.35	8.62	5.02	0.34	0.56	21.34	0.66	1.14	0.10	47.45	28.57	311.69	175.65	49.66	251.08	1177.05
43R-3, 33–35	1196.88	M-74	16.30	45.59	0.53	10.37	4.49	0.62	1.33	10.74	0.82	1.87	0.07	74.12	22.07	400.75	80.52	51.65	76.69	414.97
44R-4, 60–63	1208.34	M-75	8.00	68.82	0.84	9.96	3.33	0.02	1.44	1.36	0.96	1.85	0.05	389.90	29.64	146.29	30.44	93.73	140.28	273.49
45R-2, 25–27	1214.58	M-76	14.70	46.10	0.66	12.70	4.92	0.35	1.54	8.30	0.93	2.37	0.10	99.05	23.94	378.83	69.80	70.78	113.22	684.11
46R-5, 105–106	1229.58	M-77	11.20	46.70	0.58	12.54	4.06	0.15	2.87	12.49	0.90	2.26	0.05	96.54	23.96	246.71	56.68	63.18	100.24	298.94
47R-2, 66–69	1234.19	M-78	17.50	37.27	0.57	11.08	4.17	0.21	1.31	16.29	0.78	1.84	0.13	76.19	25.00	488.34	65.44	54.01	88.50	284.14
47R-7, 28–31	1241.26	M-79	5.86	55.73	0.71	16.89	5.39	0.03	2.94	1.90	1.12	2.73	0.05	118.43	24.65	189.59	177.28	91.98	126.68	425.18
48R-2, 90–92	1244.14	M-80	12.80	46.82	0.58	12.70	5.64	0.45	1.63	8.41	0.85	2.34	0.07	96.19	24.58	340.09	60.72	72.22	103.49	312.71
48R-4, 42–44	1246.74	M-81	16.10	48.03	0.72	5.22	2.06	0.60	0.00	17.44	0.60	1.02	0.01	510.91	39.01	166.85	27.12	39.29	37.02	210.36
49R-2, 6–11	1252.96	M-82	7.80	54.09	0.65	14.62	5.20	0.05	1.86	4.40	1.03	2.38	0.08	99.86	24.28	289.20	139.15	74.74	142.90	372.88
49R-4, 67–72	1256.57	M-83	3.00	75.50	0.87	7.86	2.35	0.03	1.25	3.28	0.89	1.61	0.06	743.86	34.99	174.95	40.46	54.56	56.65	345.28
50R-4, 18–22	1265.68	M-84	0.50	72.76	0.80	9.31	3.48	0.06	1.91	3.46	0.95	1.94	0.10	513.76	29.80	171.73	67.52	59.25	72.77	373.01
50R-6, 60–64	1268.58	M-85	14.70	42.44	0.59	12.98	4.51	0.21	1.60	11.18	0.87	2.24	0.05	82.24	23.66	383.13	155.09	64.97	122.44	328.14
51R-1, 60–63	1271.30	M-86	6.90	55.52	0.57	13.85	5.35	0.10	2.53	8.02	0.90	2.39	0.07	87.57	27.97	217.34	113.21	72.32	129.33	376.68
52R-2, 36–39	1282.26	M-87	6.10	36.27	0.25	3.01	1.49	0.06	0.27	2.51	0.32	0.51	0.02	121.75	9.06	57.63	13.52	15.75	20.69	74.36
53R-5, 105–107	1296.99	M-88	12.90	64.07	0.75	9.57	3.40	0.01	1.10	0.72	0.89	1.73	0.06	356.32	24.71	138.97	33.43	53.73	78.85	280.23
54R-4, 121–123	1305.31	M-89	10.00	50.56	0.69	13.57	5.65	0.17	2.30	8.90	0.82	2.18	0.08	139.90	27.23	256.27	62.90	77.51	112.41	400.88
55R-2, 10–13	1310.80	M-90	15.10	42.27	0.50	11.66	3.86	0.35	1.47	15.51	0.78	2.11	0.07	78.39	26.56	255.34	89.50	62.53	112.51	367.60
56R-1, 118–120	1319.98	M-91	5.50	65.59	0.60	13.58	5.30	0.03	2.22	0.99	0.93	2.66	0.02	93.38	16.86	163.72	347.56	82.53	115.86	391.45
56R-2, 111–112	1321.41	M-92	5.94	66.47	0.89	10.03	3.49	0.04	2.00	3.40	0.94	1.84	0.08	440.76	31.46	170.65	51.96	55.49	75.73	390.39
57R-1, 3–4	1328.53	M-93	13.40	50.07	0.68	12.85	4.70	0.31	2.00	9.28	0.93	2.22	0.09	102.50	24.48	394.85	76.24	74.97	110.04	378.27
57R-2, 42–43	1330.42	M-94	6.90	55.02	0.70	15.42	8.21	0.04	2.19	1.31	0.92	2.90	0.05	101.81	24.74	195.55	172.34	89.54	121.36	399.13
58R-3, 68–72	1341.78	M-95	7.90	58.58	0.63	15.42	7.60	0.07	0.00	0.90	0.90	2.83	0.04	101.82	26.00	161.61	177.74	89.43	137.22	432.50
59R-4, 103–107	1349.63	M-96	6.70	52.94	0.67	16.04	12.19	0.06	1.92	1.36	0.77	2.44	0.05	113.21	23.49	145.85	163.63	80.33	133.54	423.49
60R-1, 19–21	1353.89	M-97	14.00	46.10	0.60	12.93	4.61	0.47	1.85	8.66	0.80	2.30	0.05	95.62	26.93	217.39	103.19	81.73	158.41	373.59
61R-4, 122–125	1368.92	M-98	4.36	69.96	0.78	16.17	8.51	0.03	2.38	1.27	0.96	2.66	0.04	162.47	16.59	187.63	88.20	90.74	142.99	424.93
62R-3, 78–80	1376.68	M-99	3.60	58.83	0.71	15.29	9.51	0.06	0.00	1.17	0.80	2.82	0.03	131.06	23.92	146.90	170.05	95.89	139.96	441.23
63R-1, 137–139	1383.87	M-100	7.31	53.52	0.65	14.42	6.49	0.07	2.50	3.60	0.85	2.83	0.06	108.65	24.22	217.50	82.77	93.80	129.20	407.30
64R-5, 38–42	1398.58	M-101	6.00	52.08	0.80	14.70	9.51	0.08	2.58	1.27	0.84	2.69	0.04	147.07	25.52	135.44	81.30	84.24	118.91	414.93

Table T4. (continued).

Core, section, interval (cm)	Depth (mbsf)	Run	Carbon (wt%)			Color	Lithology
			$CaCO_3$	C_{tot}	TOC		
31R-2, 15–18	1080.65	M-50	13.33	0.09	0.00		Mudstone
31R-2, 124–128	1081.74	M-51	0.67	3.78	3.70		Mudstone with organic matter
32R-5, 23–27	1094.65	M-52	69.47	9.60	1.26		Marlstone
33R-3, 91–95	1102.11	M-53	48.73	9.83	3.98		Marlstone
33R-4, 133–137	1104.03	M-54	10.66	2.30	1.02		Marlstone
34R-2, 102–106	1110.19	M-56	0.50	9.41	9.35		Mudstone
35R-6, 57–61	1125.12	M-58	25.41	3.07	0.02		Nannofossil marlstone
36R-6, 62–66	1134.75	M-59	5.58	0.69	0.02	Greenish gray	Mudstone
36R-6, 82–86	1134.95	M-60	17.24	2.03	0.00		Muddy nannofossil limestone
37R-3, 46–49	1139.62	M-61	4.58	0.62	0.07		Mudstone
37R-5, 54–57	1142.19	M-62	8.83	1.68	0.62		Mudstone
38R-5, 96–99	1152.40	M-63	76.47	9.07	0.00		Carbonate nodule
38R-6, 96–98	1153.78	M-64	47.48	5.44	0.00		Sandstone with carbonate cement
39R-2, 16–18	1156.86	M-65	11.08				Black shale
39R-5, 36–38	1161.59	M-66	0.67			Dusky green	Mudstone
40R-2, 50–52	1166.83	M-67	0.83	0.35	0.25	Dusky green	Mudstone
40R-2, 80–83	1167.13	M-68	42.15	6.54	1.48		
41R-1, 113–117	1175.53	M-69	22.32	3.15	0.47		Calcareous siltstone
41R-6, 79–84	1182.84	M-70	53.65	6.84	0.40		Siltstone with carbonate cement
42R-1, 4–8	1184.04	M-71	13.75	2.34	0.69		Calcareous claystone
42R-6, 39–43	1191.59	M-72	43.90	6.64	1.37		Marlstone
43R-2, 88–92	1195.91	M-73	43.15	7.79	2.61		Marlstone
43R-3, 33–35	1196.88	M-74	7.33	3.14	2.26	Dusky green	Calcareous mudstone
44R-4, 60–63	1208.34	M-75	0.42	0.53	0.48		Mudstone
45R-2, 25–27	1214.58	M-76	19.58	2.80	0.45		
46R-5, 105–106	1229.58	M-77	21.83	2.95	0.33		Calcareous mudstone
47R-2, 66–69	1234.19	M-78	38.90	5.11	0.44		Nannofossil marlstone
47R-7, 28–31	1241.26	M-79	2.42	1.04	0.75		Green mudstone at 32 cm
48R-2, 90–92	1244.14	M-80	20.74	2.96	0.47		Calcareous claystone at 88 cm
48R-4, 42–44	1246.74	M-81	34.15	4.37	0.27		Siltstone with carbonate cement at 47 cm
49R-2, 6–11	1252.96	M-82	7.25	1.54	0.67		Claystone
49R-4, 67–72	1256.57	M-83	6.75	1.06	0.25		Siltstone
50R-4, 18–22	1265.68	M-84	6.91	1.63	0.80		Siltstone
50R-6, 60–64	1268.58	M-85	21.16	3.84	1.30		Calcareous claystone
51R-1, 60–63	1271.30	M-86	11.50	2.34	0.96		Claystone with nannofossils
52R-2, 36–39	1282.26	M-87	1.92	1.10	0.87		Mudstone
53R-5, 105–107	1296.99	M-88	12.16	3.35	1.89		Calcareous mudstone
54R-4, 121–123	1305.31	M-89	15.66	2.67	0.79		Mudstone
55R-2, 10–13	1310.80	M-90	30.32	4.56	0.92		Nannofossil marlstone
56R-1, 118–120	1319.98	M-91	0.92	0.61	0.50		Claystone
56R-2, 111–112	1321.41	M-92	6.25	1.67	0.92	Dusky green	Mudstone
57R-1, 3–4	1328.53	M-93	19.33	3.30	0.98		Calcareous mudstone
57R-2, 42–43	1330.42	M-94	0.75	0.74	0.65		Claystone
58R-3, 68–72	1341.78	M-95	0.75	0.65	0.56		Mudstone
59R-4, 103–107	1349.63	M-96	0.58	0.62	0.55		Claystone
60R-1, 19–21	1353.89	M-97	17.66	3.76	1.64		Calcareous mudstone
61R-4, 122–125	1368.92	M-98	0.58	0.40	0.33		Clay/mudstone
62R-3, 78–80	1376.68	M-99	1.50	0.65	0.47	Dusky green	Mudstone
63R-1, 137–139	1383.87	M-100	5.33	1.27	0.63		Claystone
64R-5, 38–42	1398.58	M-101	0.67	0.43	0.35	Dark greenish gray	Claystone

Table T4. (continued).

Core, section, interval (cm)	Depth (mbsf)	Run	LOI (wt%)	Major element oxide (wt%)										Trace element (ppm)						
				SiO_2	TiO_2	Al_2O_3	Fe_2O_3*	MnO	MgO	CaO	Na_2O	K_2O	P_2O_5	Zr	Y	Sr	Ni	Cr	V	Ba
65R-3, 99–102	1405.79	M-102	10.50	43.84	0.59	13.12	5.37	3.30	0.00	8.64	0.81	2.30	0.12	104.15	40.18	197.29	266.09	91.47	175.02	388.55
66R-3, 39–42	1414.69	M-103	5.93	69.64	0.81	15.53	5.38	0.64	1.83	2.41	1.13	2.82	0.05	183.24	16.45	208.91	165.36	97.70	151.01	438.72
67R-3, 40–42	1424.30	M-104	30.95	17.97	0.21	3.57	2.42	0.78	0.60	29.51	0.14	0.25	0.05	21.57	18.90	778.59	91.12	52.62	174.67	725.96
68R-2, 137–141	1433.37	M-105	9.00	51.90	0.81	14.14	7.39	0.21	0.00	4.43	0.89	2.41	0.07	156.89	30.06	172.91	88.35	84.26	135.69	441.97
69R-6, 57–59	1447.87	M-106	20.30	41.75	0.60	12.80	5.41	1.36	0.00	5.07	0.74	2.24	0.16	103.47	35.51	166.11	200.50	91.88	163.70	383.43
70R-4, 51–53	1454.51	M-107	4.80	59.19	0.73	16.22	8.05	0.07	0.00	0.83	0.84	2.85	0.07	125.71	29.76	153.59	147.29	87.00	151.32	481.12
71R-6, 19–21	1466.89	M-108	2.40	68.82	0.81	17.07	7.92	0.05	2.46	1.34	0.95	3.22	0.04	136.04	16.41	186.08	159.92	96.28	172.25	441.94
72R-5, 80–83	1475.53	M-109	8.00	52.34	0.65	14.45	7.32	1.36	0.00	2.42	0.82	2.86	0.10	122.53	42.14	160.92	247.19	115.76	202.92	427.64
73R-3, 45–46	1481.95	M-110	9.70	51.12	0.68	15.41	7.63	0.03	0.00	0.83	0.92	2.70	0.05	127.79	31.32	152.03	220.11	105.67	198.17	454.38
74R-2, 120–122	1490.80	M-111	7.68	66.84	0.74	15.81	6.10	0.04	2.45	1.83	0.99	3.19	0.07	138.95	16.52	192.26	174.57	100.34	165.08	423.50
75R-2, 87–91	1500.07	M-112	6.60	54.51	0.85	16.83	7.46	0.08	0.00	2.70	0.77	2.88	0.10	131.78	26.77	162.10	79.20	86.85	139.51	465.42
76R-3, 46–47	1510.76	M-113	5.10	61.09	0.92	17.08	7.92	0.03	2.25	1.24	0.94	2.99	0.05	157.75	25.29	165.93	65.91	89.01	131.29	463.01
77R-2, 110–113	1519.50	M-114	3.80	60.28	1.04	19.48	6.23	0.03	2.00	1.32	0.88	3.31	0.09	169.88	26.63	152.38	84.64	104.74	182.44	487.65
78R-3, 16–19	1529.66	M-115	2.95	57.89	0.84	17.08	8.67	0.03	2.59	1.03	0.87	3.14	0.04	163.41	24.63	146.43	97.95	89.84	136.43	441.28
79R-5, 30–32	1542.50	M-116	8.06	45.29	0.80	15.73	13.69	0.09	2.39	5.35	0.63	2.40	0.05	157.79	24.66	165.01	55.85	76.03	117.05	369.00
80R-1, 30–33	1546.10	M-117	5.80	46.69	1.82	17.16	10.32	0.24	2.90	5.47	0.69	2.62	0.30	265.93	29.08	224.24	102.01	76.96	217.25	369.11
81R-1, 37–40	1555.77	M-118	7.80	61.72	0.95	19.35	5.67	0.02	1.31	1.06	0.61	2.64	0.05	148.89	16.12	97.57	78.60	102.07	150.78	399.98
82R-1, 6–9	1565.06	M-119	5.60	62.13	0.88	18.54	8.20	0.05	1.80	2.56	0.76	3.40	0.06	161.15	16.70	132.91	71.18	99.74	140.77	440.25
83R-1, 63–64	1575.13	M-120	4.80	52.53	0.96	17.96	8.56	0.03	1.92	1.01	0.74	3.08	0.05	165.37	26.04	111.77	79.27	101.89	165.39	423.80
84R-2, 114–116	1586.84	M-121	7.10	49.02	0.92	17.65	8.78	0.07	1.99	3.58	0.66	2.87	0.11	150.95	26.55	157.65	70.26	95.59	141.99	413.62
85R-5, 33–35	1593.28	M-122	4.67	50.89	0.81	16.92	13.44	0.05	2.31	1.73	0.66	2.73	0.05	165.32	26.92	101.14	85.20	82.68	144.74	375.92
86R-5, 28–30	1601.08	M-123	5.01	47.83	0.83	17.03	12.28	0.05	2.22	0.92	0.68	2.89	0.03	154.54	25.10	99.64	71.98	92.47	157.65	399.79
87R-2, 96–99	1606.96	M-124	4.94		0.62	19.38	5.59	0.11	0.95	1.19	0.03	4.90			22.50			96.94	123.98	439.62
87R-6, 86–89	1612.97	M-125	11.05	30.81	3.91	15.36	16.50	0.40	4.27	9.77	1.37	0.80	0.75	192.33	25.78	221.15	36.08	49.24	420.58	341.93
87R-6, 107–108	1613.18	M-126	12.84	28.06	3.89	14.64	16.52	0.30	5.04	8.47	1.07	0.50	0.76	197.08	25.91	180.24	57.09	45.48	416.89	255.00
87R-7, 19–20	1613.70	M-127	5.02	36.96	3.51	13.08	14.30	0.27	4.77	8.30	2.62	1.05	0.59	170.61	27.93	580.28	27.48	35.51	355.01	690.87
88R-2, 96–97	1616.08	M-128	3.35	40.45	3.93	13.35	16.05	0.35	10.38	4.95	3.14	1.65	0.73	181.68	27.20	344.62	22.21	26.74	401.79	1411.44
88R-3, 59–60	1617.15	M-129	3.41	40.94	3.55	13.67	15.52	0.33	8.20	5.09	3.04	1.87	0.70	197.69	27.72	302.25	22.97	26.73	341.45	1471.99
88R-3, 120–121	1617.76	M-130	3.81	40.49	3.71	13.52	15.74	0.35	8.16	5.61	3.12	1.37	0.69	165.38	26.62	310.88	30.72	54.69	396.84	1162.10
88R-4, 110–111	1619.16	M-131	4.06	43.96	2.41	14.38	13.11	0.23	6.79	4.07	4.10	2.54	0.69	279.68	28.22	242.24	33.90	65.24	191.27	1069.26
88R-5, 103–104	1620.56	M-132	2.53	40.40	3.63	13.34	15.65	0.32	8.00	5.78	2.70	1.35	0.64	168.75	26.39	423.33	40.08	52.42	383.42	1700.64
88R-6, 72–74	1621.34	M-133	2.65	38.98	3.55	13.34	15.92	0.31	9.86	5.40	2.57	1.13	0.71	181.44	26.24	474.66	40.93	53.96	380.38	835.31
88R-7, 92–93	1622.75	M-134	-6.01	43.87	4.17	15.43	16.79	0.33	7.53	7.16	2.90	1.03	0.77	194.42	29.55	635.86	35.74	49.82	416.33	745.31
89R-1, 117–119	1624.77	M-135	3.92	65.56	0.85	17.48	12.50	0.04	2.01	1.17	0.75	3.48	0.05	172.18	17.79	110.51	96.68	92.48	133.53	409.49
89R-2, 31–34	1625.41	M-136	4.51		0.90	16.89	14.65	0.07	1.76	1.15	0.03	3.81			22.14			79.70	105.02	345.01
90R-4, 104–108	1638.81	M-137	4.51	60.03	0.92	18.60	10.58	0.04	1.89	1.15	0.53	3.16	0.06	177.54	16.41	102.67	47.56	101.94	166.84	399.08
91R-2, 108–112	1645.38	M-138	4.14	63.35	0.90	18.06	10.90	0.04	1.87	1.16	0.62	2.92	0.04	175.90	17.39	103.90	77.95	94.83	148.19	389.77
92R-6, 126–129	1661.26	M-139	5.02		0.82	17.12	16.33	0.05	2.42	1.16	0.03	3.87			22.34			84.64	109.49	343.82
93R-4, 127–130	1667.87	M-140	4.71		0.47	16.47	17.37	0.06	2.52	1.16	0.31	4.41			18.67			85.93	715.11	296.38
94R-5, 71–75	1678.30	M-141	7.89		0.36	15.55	5.49	0.09	1.42	2.15	0.03	3.73			26.86			90.24	127.65	317.06
95R-3, 74–78	1684.80	M-142	4.72		0.74	17.20	7.61	0.10	1.60	1.86	0.02	4.33			23.18			88.28	123.46	401.60
96R-1, 131–134	1692.21	M-143	4.63		0.66	17.07	7.55	0.09	3.83	1.15	0.02	4.00			22.39			84.07	103.17	397.49
97R-1, 96–102	1701.46	M-144	3.59		0.57	15.18	6.53	0.13	9.37	1.19	0.03	3.69			21.76			74.82	139.67	537.55
98R-1, 96–98	1711.06	M-146	4.23		0.96	18.32	5.74	0.67	2.40	1.76	0.04	2.96			21.59			124.75	105.75	398.24
98R-1, 119–120	1711.29	M-145	5.59		2.71	14.55	14.16	0.34	9.20	1.93	0.03	1.50			36.90			57.47	216.24	341.93
99R-1, 120–122	1720.60	M-147	3.37		1.06	13.30	15.72	0.31	10.68	6.21	0.92	2.95			36.41			38.54	135.77	925.29
99R-3, 115–117	1723.44	M-148	2.58		1.07	12.83	14.77	0.31	10.75	6.90	0.93	3.16			36.38				130.41	1075.50

Notes: The main results are summarized in the text. Organic carbon (C_{org}) and carbonate carbon data usually obtained from same interval. In rare instances, interval differs by as much as 4 cm but lithology is the same. ICP-AES = inductively coupled plasma–atomic emission spectroscopy. LOI = loss on ignition. C_{tot} = total carbon, TOC = total organic carbon. * = all Fe as Fe_2O_3.

Table T4. (continued).

Core, section, interval (cm)	Depth (mbsf)	Run	Carbon (wt%)			Color	Lithology
			$CaCO_3$	C_{tot}	C_{org}		
65R-3, 99–102	1405.79	M-102	24.66	5.17	2.21		Claystone
66R-3, 39–42	1414.69	M-103	8.00	2.46	1.50		Claystone
67R-3, 40–42	1424.30	M-104	0.50	0.45	0.39	Dusky green	Mudstone
68R-2, 137–141	1433.37	M-105	9.41	2.00	0.87		Calcareous mudstone
69R-6, 57–59	1447.87	M-106	19.24	4.18	1.87		Calcareous claystone
70R-4, 51–53	1454.51	M-107	0.75	0.82	0.73		Claystone
71R-6, 19–21	1466.89	M-108	0.92	0.67	0.56		Claystone
72R-5, 80–83	1475.53	M-109	0.58	3.13	3.06		Claystone
73R-3, 45–46	1481.95	M-110	0.58	2.76	2.69		Mudstone
74R-2, 120–122	1490.80	M-111	1.00	1.54	1.42		Claystone
75R-2, 87–91	1500.07	M-112	5.58	1.49	0.82		
76R-3, 46–47	1510.76	M-113	0.58	0.39	0.32		Claystone
77R-2, 110–113	1519.50	M-114	2.25	1.37	1.10		Claystone
78R-3, 16–19	1529.66	M-115	0.50			Dusky green	Claystone
79R-5, 30–32	1542.50	M-116	9.41			Dusky green	Calcareous claystone
80R-1, 30–33	1546.10	M-117	12.91	1.87	0.32		Calcareous mudstone
81R-1, 37–40	1555.77	M-118	0.67	1.34	1.26		Calcareous mudstone
82R-1, 6–9	1565.06	M-119	2.42	0.64	0.35		Claystone
83R-1, 63–64	1575.13	M-120	0.67	0.93	0.85		Mudstone
84R-2, 114–116	1586.84	M-121	6.58	1.86	1.07		Mudstone with nannofossils
85R-5, 33–35	1593.28	M-122	10.08			Dusky green	Claystone
86R-5, 28–30	1601.08	M-123					
87R-2, 96–99	1606.96	M-124	0.08	0.52	0.51	Dark greenish gray	Mudstone
87R-6, 86–89	1612.97	M-125					Altered sill
87R-6, 107–108	1613.18	M-126					Altered sill
87R-7, 19–20	1613.70	M-127					Altered sill
88R-2, 96–97	1616.08	M-128					Altered sill
88R-3, 59–60	1617.15	M-129					Altered sill
88R-3, 120–121	1617.76	M-130					Altered sill
88R-4, 110–111	1619.16	M-131					Altered sill
88R-5, 103–104	1620.56	M-132					Altered sill
88R-6, 72–74	1621.34	M-133					Altered sill
88R-7, 92–93	1622.75	M-134					Altered sill
89R-1, 117–119	1624.77	M-135	0.50			Pale reddish brown	Claystone
89R-2, 31–34	1625.41	M-136	0.58			Dark greenish gray	Claystone
90R-4, 104–108	1638.81	M-137	2.33			Dusky green	Claystone
91R-2, 108–112	1645.38	M-138	0.50	0.30	0.24	Dusky green	Mudstone
92R-6, 126–129	1661.26	M-139	7.66	2.38	1.46	Dusky green	Mudstone
93R-4, 127–130	1667.87	M-140	0.67			Dusky green	Claystone
94R-5, 71–75	1678.30	M-141	2.92	2.30	1.95	Dark greenish gray	Mudstone
95R-3, 74–78	1684.80	M-142	3.67			Grayish green	Mudstone
96R-1, 131–134	1692.21	M-143	1.08	0.65	0.52	Dark gray	Mudstone
97R-1, 96–102	1701.46	M-144	0.17	0.64	0.62		
98R-1, 96–98	1711.06	M-146	0.75				Aureole (altered sediments)
98R-1, 119–120	1711.29	M-145					Altered sill
99R-1, 120–122	1720.60	M-147					Altered sill
99R-3, 115–117	1723.44	M-148					Altered sill

Table T5. Comparison of approximate sedimentation rates at DSDP and ODP sites on the Newfoundland and Iberia conjugate margins.

Site 1276 Unit	Age	Sedimentation rate (m/m.y.)			
		Site 1276	Site 897*	Sites 900† and 1068‡	Site 398**
1	middle Eocene to earliest Oligocene	7	11	17–18	~7–15
2	late Paleocene to middle Eocene	7	9	18	~5
3	base Campanian to late Paleocene	~1–8	—	11–18	~5
4	Turonian to top Santonian	<2	—	2–4	Not well dated
5A	Cenomanian to Turonian	2–15	—	—	Not well dated
5B	Albian to Cenomanian	~18–100	—	—	~30
5C	late Aptian(?)–Albian	~22–100	—	—	~50

Note: * = Shipboard Scientific Party (1994a), † = Shipboard Scientific Party (1994b), ‡ = Ladner and Wise (2001) and Shipboard Scientific Party (1998), ** = Shipboard Scientific Party (1979).

Table T6. ICP-AES major and trace element analysis of whole-rock samples from the upper sill and the lower sill complex, Hole 1276A.

Core, section interval (cm)	Depth (mbsf)	Major element oxide (wt%)										Trace element (ppm)							Bead LOI (wt%)
		SiO_2	TiO_2	Al_2O_3	Fe	MnO	MgO	CaO	Na_2O	K_2O	P_2O_5	Zr	Y	Sr	Ni	Cr	V	Ba	
210-1276A-																			
87R-6, 86–89	1612.97	30.81	3.91	15.36	16.50	0.40	4.27	9.77	1.37	0.80	0.75	192.33	25.78	221.15	36.08	49.24	420.58	341.93	11.05
87R-6, 107–108	1613.18	28.06	3.89	14.64	16.52	0.30	5.04	8.47	1.07	0.50	0.76	197.08	25.91	180.24	57.09	45.48	416.89	255.00	12.84
88R-2, 96–97	1616.08	40.45	3.93	13.35	16.05	0.35	10.38	4.95	3.14	1.65	0.73	181.68	27.20	344.62	22.21	26.74	401.79	1411.44	3.35
88R-3, 59–60	1617.15	40.94	3.55	13.67	15.52	0.33	8.20	5.09	3.04	1.87	0.70	197.69	27.72	302.25	22.97	26.73	341.45	1471.99	3.41
88R-3, 120–121	1617.76	40.49	3.71	13.52	15.74	0.35	8.16	5.61	3.12	1.37	0.69	165.38	26.62	310.88	30.72	54.69	396.84	1162.10	3.81
88R-4, 110–111	1619.16	43.96	2.41	14.38	13.11	0.23	6.79	4.07	4.10	2.54	0.69	279.68	28.22	242.24	33.90	65.24	191.27	1069.26	4.06
88R-5, 103–104	1620.56	40.40	3.63	13.34	15.65	0.32	8.00	5.78	2.70	1.35	0.64	168.75	26.39	423.33	40.08	52.42	383.42	1700.64	2.53
88R-6, 72–74	1621.34	38.98	3.55	13.34	15.92	0.31	9.86	5.40	2.57	1.13	0.71	181.44	26.24	474.66	40.93	53.96	380.38	835.31	2.65
88R-7, 92–97	1622.75	43.87	4.17	15.43	16.79	0.33	7.53	7.16	2.90	1.03	0.77	194.42	29.55	635.86	35.74	49.82	416.33	745.31	–6.01
99R-1, 120–122	1720.60		1.06	13.30	15.72	0.31	10.68	6.21	0.92	2.95			36.41			38.54	135.77	925.29	3.37
99R-3, 115–117	1723.44		1.07	12.83	14.77	0.31	10.75	6.90	0.93	3.16			36.38			–0.55	130.41	1075.50	2.58

Note: ICP-AES = inductively coupled plasma–atomic emission spectroscopy.

Table T7. Summary of paleontological observations for various lithologies, Hole 1276A. (This table is available in an **oversized format.**)

Table T8. Distribution of Cenozoic calcareous nannofossils, Hole 1276A. (Continued on next two pages.)

Lithologic unit	Zone	Epoch	Core, section, interval (cm)	Depth (mbsf)	Abundance	Preservation	Reworked Cretaceous species	*Blackites spinosus*	*Braarudosphaera bigelowii*	*Cruciplacolithus asymmetricus*	*Cyclicargolithus praebisectus*	*Campylosphaera dela*	*Chiasmolithus oamaroensis*	*Chiasmolithus altus*	*Chiasmolithus bidens*	*Chiasmolithus consuetus*	*Chiasmolithus danicus*	*Chiasmolithus grandis*	*Chiasmolithus solitus*	*Clausicoccus fenestratus*	*Clausicoccus obrutus*	*Clausicoccus subdistichus*	*Coccolithus formosus*	*Coccolithus pelagicus*	*Coccolithus subpertusus*	*Cruciplacolithus primus*	*Cruciplacolithus subrotundus*	*Cruciplacolithus tenuis*	*Cyclagelosphaera* cf. *reinhardtii*	*Cyclicargolithus floridanus*	*Discoaster barbadiensis*	*Discoaster binodosus*	*Discoaster diastypus*	*Discoaster deflandrei*	*Discoaster elegans*	*Discoaster kuepperi*	*Discoaster lodoensis*	*Discoaster mediosus*	*Discoaster multiradiatus*	*Discoaster nobilis*	*Discoaster tani nodifer*
			210-1276A-																																				
	CP16	latest Eocene	1W-4, 37 db	757.36	C	M		R					F	R									F																
	CP16	early Oligocene	1W-CC	759.19	C	M		R	R					R								R	F							F									
	CP15	late Eocene	2R-1, 144	801.44	C	M												R					C								F								r
	CP13		2R-2, 83 db	802.33	A	M			F		C							F	C												F								
	CP14	middle Eocene	2R-3, 36 db	803.36	A	M																	C	F						C									
	CP14b–CP15		2R-CC	803.51	A	M		C			C								R	F	C	C	C	C							R			R					
1	CP14a		3R-2, 51	810.30	A	G												R	F											C									
	CP14a		3R-CC	819.26	F	P																								R									
			4R-CC	825.90	B																																		
			5R-CC	838.15	B																																		
			6R-CC	847.40	B																																		
	CP12b	early–middle Eocene	7R-1, 43 db	848.43	A	M										F		R	F				R	C							R	R							
			7R-CC	857.68	B																																		
	CP12b–CP13		8R-CC	866.13	C	P	F	R				R							F		F		F	C						C	R								
	CP12a		9R-CC	876.92	R	P	F																	C						C	R					F	F		
	CP10/CP11	early Eocene	10R-CC	885.37	R	P	F																F	C	R						R		R			F	R		
	CP10/CP11		11R-CC	894.58	F	P																	F								R						F		
	CP10		12R-4, 55	901.05	F	P																															R		
2			12R-CC	902.69	B																																		
	CP9b	early Eocene	13R-1, 35	906.05	F	P																															C		
	CP9a		13R-1, 51	906.21	C	P																									C					F	C		
	CP9a		13R-1, 96	906.66	F	P																											F				C		
	CP9a		13R-CC	910.39	R	P																															C		
	CP9a		14R-1, 24–25	915.54	R	P																											R		R		R	C	R	
	CP8	late Paleocene	14R-1, 104–105	916.34	R	P																															F		
	CP8		14R-CC	920.64	C	P	F								F									C				F									A	R	
			15R-CC	933.33	B																																		
	CP3	early Paleocene	16R-CC	942.23	C	P	C			R							R						C	F			R	C											
	CP3		17R-CC	953.66	R	P	C										R						C	C	R			C											
	CP2/CP3		18R-CC	963.40	R	M	C										R						R		R			R											
3			19R-CC	970.55	B																																		
			20R-CC	982.82	B																																		
	CP1a		21R-2, 25–26	984.21	A	G	A																					F											
	CP1a		21R-3, 52	985.98	A	G	A																					F											
	CP1a		21R-4, 40–41	987.36	A	G	A																																

Notes: Total abundance: V = very abundant, A = abundant, C = common, F = few, R = rare, B = barren. Preservation: G = good, M = moderate, P = poor. Reworked specimens are denoted by lowercase letters. db = debris flow/turbidite; may contain older assemblages.

Table T8 (continued).

Lithologic unit	Zone	Epoch	Core, section, interval (cm)	Depth (mbsf)	Abundance	Preservation	*Discoaster saipanensis*	*Discoaster scrippsae*	*Discoaster sublodoensis*	*Ellipsolithus lajollaensis*	*Ellipsolithus macellus*	*Fasciculithus billi*	*Fasciculithus lilianae*	*Fasciculithus magnus*	*Fasciculithus schaubi*	*Fasciculithus tympaniformis*	*Fasciculithus ulii*	*Helicosphaera euphratis*	*Helicosphaera intermedia*	*Heliolithus kleinpellii*	*Isthmolithus recurvus*	*Lanternithus minutus*	*Lophodolithus nascens*	*Markalius astroporus*	*Markalius inversus*	*Micrantholithus concinnus*	*Micrantholithus entaster*	*Micula decussata*	*Nannotetrina fulgens*	*Neobiscutum parvulum*	*Neobiscutum romeinii*	*Neococcolithes dubius*	*Neocrepidolithus neocrassus*	*Pemma basquensis*	*Pemma papillatum*	*Placozygus sigmoides*	*Pontosphaera distincta*	*Pontosphaera macropora*	*Pontosphaera multipora*	*Pontosphaera scissura*	*Pontosphaera* sp.
			210-1276A-																																				
	CP16	latest Eocene	1W-4, 37 db	757.36	C	M	C											F			R	R											F	R			R		
	CP16	early Oligocene	1W-CC	759.19	C	M																											R							
	CP15	late Eocene	2R-1, 144	801.44	C	M																																		
	CP13		2R-2, 83 db	802.33	A	M												F															C	R						
	CP14	middle Eocene	2R-3, 36 db	803.36	A	M																																		
	CP14b–CP15		2R-CC	803.51	C	M												R				R			F											R	R			
1	CP14a		3R-2, 51	810.30	A	G																									F		F							F
	CP14a		3R-CC	819.26	F	P																																		
			4R-CC	825.90	B																																			
			5R-CC	838.15	B																																			
			6R-CC	847.40	B																																			
	CP12b–CP13	early–middle Eocene	7R-1, 43 db	848.43	A	M													R						R		f						F		R		R		
			7R-CC	857.68	B																																			
	CP12b		8R-CC	866.13	C	P		R	R	R	R																	?										R	F
	CP12a		9R-CC	876.92	R	P			R		R															R													
	CP10/CP11	early Eocene	10R-CC	885.37	R	P																	R																
	CP10/CP11		11R-CC	894.58	F	P												R							R														
	CP10		12R-4, 55	901.05	F	P																																		
2			12R-CC	902.69	B																																			
	CP9b	early Eocene	13R-1, 35	906.05	F	P																																		R
	CP9a		13R-1, 51	906.21	C	P																																		
	CP9a		13R-1, 96	906.66	F	P																																		
	CP9a		13R-CC	910.39	R	P																																		
	CP9a		14R-1, 24–25	915.54	R	P																																		
	CP8a	late Paleocene	14R-1, 104–105	916.34	R	P										R																							
	CP8		14R-CC	920.64	C	P				R			C		C	C				R				R															
			15R-CC	933.33	B																																			
	CP3	early Paleocene	16R-CC	942.23	C	P						F					R												R										
	CP3		17R-CC	953.66	R	P								R										R				f		R									
	CP2/CP3		18R-CC	963.40	R	M																														R				
3			19R-CC	970.55	B																																			
			20R-CC	982.82	B																																			
	CP1a		21R-2, 25–26	984.21	A	G																			F				A	A		F							
	CP1a		21R-3, 52	985.98	A	G																			F				A	A		F							
	CP1a		21R-4, 40–41	987.36	A	G																			F				A	A		F							

Table T8 (continued).

Lithologic unit	Zone	Epoch	Core, section, interval (cm)	Depth (mbsf)	Abundance	Preservation	*Prinsius bisulcus*	*Prinsius martini*	*Reticulofenestra bisecta*	*Reticulofenestra daviesi*	*Reticulofenestra dictyoda*	*Reticulofenestra hillae*	*Reticulofenestra reticulata*	*Reticulofenestra oamaroensis*	*Reticulofenestra* spp.	*Reticulofenestra umbilicus*	*Rhabdosphaera inflata*	*Rhomboaster cuspis*	*Rhomboaster* spp.	*Scyphosphaera* sp.	*Sphenolithus editus*	*Sphenolithus moriformis*	*Sphenolithus radians*	*Thoracosphaera operculata*	*Thoracosphaera* spp.	*Toweius callosus*	*Toweius eminens*	*Toweius occultatus*	*Toweius tovae*	*Tribrachiatus bramlettei*	*Tribrachiatus contortus*	*Tribrachiatus orthostylus*	*Zeugrhabdotus spiralis*	*Zygrhablithus bijugatus*
			210-1276A-																														
	CP16	latest Eocene	1W-4, 37 db	757.36	C	M							C			C						R											F
	CP16	early Oligocene	1W-CC	759.19	C	M			F	F			F	R		F																	R
	CP15	late Eocene	2R-1, 144	801.44	C	M			F				F	R		C																	
	CP13		2R-2, 83 db	802.33	A	M																											C
	CP14	middle Eocene	2R-3, 36 db	803.36	A	M										C																	C
	CP14b–CP15		2R-CC	803.51	C	M			R			F	F			C				R		C											R
1	CP14a		3R-2, 51	810.30	A	G					C										F	F											C
	CP14a		3R-CC	819.26	F	P										F																	
			4R-CC	825.90	B																												
			5R-CC	838.15	B																												
			6R-CC	847.40	B																												
	CP12b	early–middle Eocene	7R-1, 43 db	848.43	A	M											R					R											R
			7R-CC	857.68	B																												
	CP12b–CP13		8R-CC	866.13	C	P				R	R						F				R	F											
	CP12a		9R-CC	876.92	R	P	C	C			F											F						R					
	CP10/CP11	early Eocene	10R-CC	885.37	R	P									R							C	F								R		F
	CP10/CP11		11R-CC	894.58	F	P																F	R			R	R	F					R
	CP10		12R-4, 55	901.05	F	P																									F		
2			12R-CC	902.69	B																												
	CP9b	early Eocene	13R-1, 35	906.05	F	P																									R	F	
	CP9a		13R-1, 51	906.21	C	P																			R	R					F		
	CP9a		13R-1, 96	906.66	F	P												F	F			R								R	R		
	CP9a		13R-CC	910.39	R	P																											
	CP9a		14R-1, 24–25	915.54	R	P												F	F											R			
	CP8a	late Paleocene	14R-1, 104–105	916.34	R	P												R	R														
	CP8		14R-CC	920.64	C	P																			C	A							
			15R-CC	933.33	B																												
	CP3	early Paleocene	16R-CC	942.23	C	P	C																										
	CP3		17R-CC	953.66	R	P																		F									
	CP2/CP3		18R-CC	963.40	R	M																											
3			19R-CC	970.55	B																												
			20R-CC	982.82	B																												
	CP1a		21R-2, 25–26	984.21	A	G																			F							C	
	CP1a		21R-3, 52	985.98	A	G																			F							C	
	CP1a		21R-4, 40–41	987.36	A	G																			F							C	

Table T9. Distribution of Mesozoic calcareous nannofossils, Hole 1276A. (This table is available in an **oversized format.**)

Table T10. Distribution of benthic foraminifers, Hole 1276A. (This table is available in an **oversized format.**)

Table T11. Distribution of palynomorphs, Hole 1276A. (This table is available in an **oversized format.**)

Table T12. Calcareous nannofossil and dinoflagellate cyst (palynomorph) datums, Hole 1276A.

Biostratigraphic datum	Age (Ma)	Present		Absent		Median depth (mbsf)
		Depth (mbsf)	Core, section, interval (cm)	Depth (mbsf)	Core, section, interval (cm)	
Cenozoic nannofossils			210-1276A-		210-1276A-	
LO *Discoaster barbadiensis*	34.3	803.51	2R-CC	803.36	2R-3, 36	803.43
FO *Reticulofenestra bisecta*	38.0	803.51	2R-CC	810.30	3R-2, 51	806.91
LO *Chiasmolithus solitus*	40.4	810.30	3R-2, 51	803.51	2R-CC	806.91
FO *Reticulofenestra umbilicus*	43.7	819.26	3R-CC	848.43	7R-1, 43	833.85
FO *Rhabdosphaera inflata*	48.5	866.13	8R-CC	876.92	9R-CC	871.53
FO *Discoaster sublodoensis*	49.7	876.92	9R-CC	885.37	10R-CC	881.15
FO *Discoaster lodoensis*	52.85	901.05	12R-4, 55	906.21	13R-1, 51	903.63
FO *Tribrachiatus orthostylus*	53.6	906.05	13R-1, 35	906.21	13R-1, 51	906.13
FO *Tribrachiatus contortus*	54.7	906.66	13R-1, 96	910.39	13R-CC	908.53
FO *Discoaster diastypus*	55.0	915.54	14R-1, 24–25	916.34	14R-1, 104–105	915.94
LO *Fasciculithus tympaniformis*	55.3	916.34	14R-1, 104–105	915.54	14R-1, 24–25	915.94
FO *Discoaster multiradiatus*	56.2	920.64	14R-CC	942.23	16R-CC	931.44
FO *Fasciculithus ulii*	59.9	942.23	16R-CC	953.66	17R-CC	947.95
FO *Cruciplacolithus primus*	64.8	963.40	18R-CC	970.55	19R-CC	966.98
Mesozoic nannofossils						
FO *Micula prinsii*	65.4	988.32	21R-CC	997.41	22R-CC	992.87
FO *Nephrolithus frequens*	65.8	992.42	22R-1, 2	997.41	22R-CC	994.92
FO *Lithraphidites quadratus*	67.5	992.42	22R-1, 2	997.41	22R-CC	994.92
FO *Uniplanarius trifidus*	76.0	1019.07	24R-CC	1027.68	25R-5, 48–49	1023.38
FO *Ceratolithoides aculeus*	78.5	1027.68	25R-5, 48–49	1056.46	28R-5, 76–77	1042.07
FO *Lithastrinus septenarius*	89.3	1057.36	28R-CC	1067.61	29R-CC	1062.49
FO *Marthasterites furcatus*	89.3	1057.36	28R-CC	1067.61	29R-CC	1062.49
FO *Quadrum gartneri*	93.2	1076.64	30R-CC	1079.25	31R-1, 25–26	1077.95
FO *Lithraphidites acutus*	96.8	1126.87	35R-CC	1135.58	36R-CC	1131.23
FO *Corollithion kennedyi*	97.6	1135.58	36R-CC	1145.43	37R-CC	1140.51
FO *Eiffellithus turriseiffelii*	101.7	1212.91	44R-CC	1221.50	45R-CC	1217.21
FO *Eiffellithus monechiae*	105.0	1279.06	51R-CC	1298.19	53R-CC	1288.63
FO *Axopodorhabdus albianus*	106.1	1430.11	67R-CC	1447.96	69R-CC	1439.04
FO *Tranolithus orionatus*	107.3	1524.40	77R-CC	1535.45	78R-CC	1529.93
FO *Hayesites albiensis*	112.5	1642.40	90R-CC (uncertain)	1649.80	91R-CC	1646.10
Cenozoic dinoflagellate cysts						
LO *Lentinia serrata*	33.5	803.51	2R-CC	759.19	1R-CC	781.35
FO *Areoligera semicirculata*	33.7	759.19	1W-CC	803.51	2R-CC	781.35
LO *Hemiplacophora semilunifera*	33.6	819.26	3R-CC	803.51	2R-CC	811.39
FO *Hemiplacophora semilunifera*	36.4	819.26	3R-CC	825.90	4R-CC	822.58
FO *Enneadocysta pectiniformis*	36.5	825.90	4R-CC	838.15	5R-CC	832.03
LO *Cerebrocysta bartonensis*	38.0	838.15	5R-CC	825.90	4R-CC	832.03
FO *Lentinia serrata*	40.0	847.40	6R-CC	857.68	7R-CC	852.54
FO *Rhombodinium draco*	40.5	847.40	6R-CC	857.68	7R-CC	852.54
FO *Cordosphaeridium cantharellum*	40.8	847.40	6R-CC	857.68	7R-CC	852.54
FO *Cerebrocysta bartonensis*	41.0	857.68	7R-CC	942.23	16R-CC	899.96
FO *Alisocysta margarita*	61.7	953.66	17R-CC	963.40	18R-CC	958.53
LO *Oligosphaeridium pulcherrimum*	63.0	963.40	18R-CC	953.66	17R-CC	958.53
LO *Spongodinium delitiense*	63.7	982.82	20R-CC	963.40	18R-CC	973.11
FO *Damassadinium californicum*	64.8	982.82	20R-CC	1067.61	29R-CC	1025.22
Mesozoic dinoflagellate cysts						
LO *Litosphaeridium siphoniphorum*	93.8	1076.64	30R-CC	1067.61	29R-CC	1072.13
FO *Senoniasphaera rotundata alveolata*	93.1	1067.61	29R-CC	1076.64	30R-CC	1072.13
FO *Chatangiella verrucosa*	93.5	1076.64	30R-CC	1086.88	31R-CC	1081.76
LO *Ovoidinium verrucosum*	95.8	1107.76	33R-CC	1098.33	32R-CC	1103.05
FO *Xiphophoridium alatum*	98.0	1164.03	39R-CC	1107.76	33R-CC	1135.90
FO *Palaeohystrichophora infusorioides*	99.9	1221.50	45R-CC	1324.66	56R-CC	1273.08

Notes: LO = last occurrence, FO = first occurrence. Age references are found in Tables T1, p. 58, T3, p. 62, and T5, p. 64, all in the "Explanatory Notes" chapter.

Table T13. Calcareous nannofossil and foraminiferal datums, DSDP Site 398.

Core, section, interval (cm)	Biostratigraphic datum	Age (Ma)	Depth (mbsf)
Cenozoic nannofossils			
47B-398D-			
19-3, 94	LO *Discoaster saipanensis*	34.2	588.4
19-3, 94	LO *Discoaster barbadiensis*	34.3	588.4
19-CC	FO *Isthmolithus recurvus*	36.0	592.9
20-3, 40	LO *Chiasmolithus grandis*	37.1	597.4
21-3, 62	FO *Reticulofenestra bisecta*	38.0	607.1
22-5, 68	LO *Chiasmolithus solitus*	40.4	619.7
26-CC	FO *Reticulofenestra umbilicus*	43.7	660.5
27-5, 85	FO *Rhabdosphaera inflata*	48.5	667.4
31-CC	FO *Discoaster sublodoensis*	49.7	704.2
33-1, 107	FO *Discoaster lodoensis*	52.85	718.6
34-7, 22	FO *Campylosphaera eodela*	55.5	736.2
35-1, 66	FO *Discoaster diastypus*	55.0	737.2
35-3, 123	FO *Tribrachiatus contortus*	54.7	740.7
36-CC	FO *Discoaster multiradiatus*	56.2	755.5
37-CC	FO *Discoaster mohleri*	57.5	762.0
38-3, 66	FO *Heliolithus kleinpellii*	58.4	768.7
39-2, 121	FO *Chiasmolithus consuetus*	59.7	777.2
39-3, 44	FO *Fasciculithus tympaniformis*	59.7	777.9
39-4, 136	FO *Ellipsolithus macellus*	62.2	780.4
40-1, 7	FO *Chiasmolithus bidens*	60.7	784.1
40-CC	FO *Cruciplacolithus tenuis*	64.5	793.4
40-CC	FO *Chiasmolithus danicus*	63.8	793.4
Mesozoic nannofossils			
47B-398D-			
42-CC	FO *Micula murus*	66.2	806.9
44-1, 115	FO *Lithraphidites quadratus*	67.5	823.2
46-1, 85	LO *Uniplanarius trifidus*	71.3	841.9
48-CC	FO *Uniplanarius trifidus*	76.0	869.5
50-6, 10	FO *Ceratolithoides aculeus*	78.5	886.6
50-6, 10	FO *Aspidolithus parcus*	83.4	886.6
50-6, 10	FO *Arkhangelskiella cymbiformis*	83.5	886.6
59-6, 14	LO *Helenea chiastia*	91.0	981.6
60-CC	FO *Eiffellithus turriseiffelii*	101.7	988.2
65-5, 55	FO *Axopodorhabdus albianus*	106.1	1037.6
74-4, 121	FO *Hayesites albiensis*	112.5	1131.7
120-3, 13	FO *Eprolithus floralis*	119.0	1566.1
121-3, 101	LO *Calcicalathina oblongata*	125.1	1576.5
136-1, 68	LO *Cruciellipsis cuvillieri*	128.3	1715.7
Mesozoic foraminifers			
47B-398D-			
57-5, 8	FO *Rotalipora globotruncanoides*	99.1	961.0
60-1, 6	FO *Rotalipora appenninica*	100.4	983.6
63-4, 24	FO *Rotalipora ticinensis*	101.7	1016.7
65-5, 135	FO *Rotalipora subticinensis*	102.4	1038.4
68-5, 63	FO *Biticinella breggiensis*	105.0	1066.1
86-2, 38	FO *Ticinella primula* (cf.)	109.5	1251.4
103-2, 35	LO *Ticinella bejaouaensis*	112.4	1403.4
104-2, 11	LO *Planomalina cheniourensis*	112.6	1412.6
106-3, 26	FO *Ticinella bejaouaensis*	114.3	1433.3

Notes: FO = first occurrence, LO = last occurrence. Age references are found in Tables **T1,** p. 58, **T2,** p. 60, **T3,** p. 62, and **T4,** p. 63, all in the "Explanatory Notes" chapter. Datum occurrences are based on data recorded by Blechschmidt (1979) and Sigal (1979).

Table T14. ChRM direction, maximum angular deviation of PCA, NRM, magnetic susceptibility, and *Q* for selected diabase sill pieces, Hole 1276A. (See table notes. Continued on next page.)

Core, section, piece	Depth (mbsf)	Dec (°)	Inc (°)	MAD (°)	NRM (A/m)	*k* (10^{-5} SI)	*Q*
210-1276A-							
87R-6 (Piece 2A)	1612.77	48.00	56.20	0.6	7.46E-03	4	4.70
87R-6 (Piece 4A)	1612.91	297.00	43.00	1.9	5.76E-02	43	4.30
87R-6 (Piece 5A)	1613.43	169.10	74.30	1.7	2.80E+00	7120	0.99
87R-7 (Piece 1A)	1613.53	34.40	75.20	0.9	2.13E+00	5598	0.96
87R-7 (Piece 2A)	1613.69	3.70	57.20	1.4	2.37E+00	6810	0.88
88R-1 (Piece 2A)	1614.60	125.80	83.40	0.4	4.74E+00	6561	1.82
88R-2 (Piece 1A)	1615.38	108.00	74.80	0.9	3.47E+00	5588	1.57
88R-2 (Piece 3A)	1615.92	8.40	73.50	0.7	3.68E+00	5346	1.74
88R-2 (Piece 4A)	1616.08	243.90	75.30	2.2	3.32E+00	5950	1.41
88R-2 (Piece 4B)	1616.24	218.20	71.10	2.2	4.51E+00	5928	1.92
88R-2 (Piece 5A)	1616.36	332.00	65.30	1.3	4.05E+00	5635	1.82
88R-2 (Piece 6A)	1616.48	196.00	70.40	2.9	4.33E+00	6387	1.71
88R-3 (Piece 1A)	1616.64	143.70	77.70	1.2	3.33E+00	5250	1.60
88R-3 (Piece 2A)	1616.78	179.90	71.80	2.0	3.63E+00	5906	1.55
88R-3 (Piece 5A)	1616.98	356.20	68.20	1.8	5.41E+00	5763	2.37
88R-3 (Piece 6A)	1617.12	67.50	74.90	2.1	3.35E+00	5958	1.42
88R-3 (Piece 7A)	1617.28	37.30	76.80	1.3	5.37E+00	6413	2.12
88R-3 (Piece 8A)	1617.48	348.60	74.90	0.7	5.51E+00	6294	2.21
88R-3 (Piece 9A)	1617.62	19.60	70.50	1.7	5.67E+00	5782	2.48
88R-3 (Piece 10A)	1617.76	288.10	71.20	2.4	4.47E+00	5979	1.89
88R-3 (Piece 11A)	1617.90	349.80	72.90	1.7	5.58E+00	6668	2.11
88R-4 (Piece 1A)	1618.14	298.40	72.10	2.2	4.24E+00	5480	1.95
88R-4 (Piece 2A)	1618.34	59.00	82.30	2.2	3.59E+00	6126	1.48
88R-4 (Piece 8A)	1618.72	32.30	73.50	1.2	3.37E+00	6474	1.31
88R-4 (Piece 9A)	1618.86	304.10	70.70	2.0	3.78E+00	6374	1.50
88R-4 (Piece 10A)	1619.06	151.00	83.20	2.0	4.04E+00	6335	1.61
88R-4 (Piece 11A)	1619.28	319.40	73.20	2.0	4.66E+00	6141	1.92
88R-4 (Piece 12A)	1619.48	201.30	82.10	2.2	3.65E+00	6079	1.52
88R-5 (Piece 1A)	1619.61	54.50	79.10	1.7	4.39E+00	5700	1.95
88R-5 (Piece 1B)	1619.75	60.90	76.70	1.8	5.45E+00	6303	2.18
88R-5 (Piece 2A)	1619.91	312.70	80.20	2.1	5.35E+00	6392	2.11
88R-5 (Piece 3A)	1620.13	36.00	77.40	2.1	5.59E+00	6585	2.14
88R-5 (Piece 3B)	1620.43	50.70	81.10	1.3	4.53E+00	6272	1.82
88R-6 (Piece 1A)	1621.04	74.90	86.10	0.9	3.73E+00	5465	1.72
88R-6 (Piece 2A)	1621.40	91.20	82.90	1.6	3.34E+00	5468	1.54
88R-6 (Piece 3A)	1621.64	150.60	79.20	0.6	3.02E+00	5339	1.43
88R-7 (Piece 1A)	1621.92	211.80	81.80	0.9	3.71E+00	5963	1.57
88R-7 (Piece 2A)	1622.31	85.90	80.30	2.0	3.79E+00	5812	1.65
88R-7 (Piece 3A)	1622.67	52.10	73.00	1.6	3.39E+00	4993	1.71
88R-7 (Piece 5A)	1622.94	84.40	75.50	0.4	2.34E+00	4986	1.19
99R-1 (Piece 4A)	1719.60	221.30	44.10	0.1	1.66E–01	55	7.62
99R-1 (Piece 9A)	1719.84	69.10	43.40	0.3	1.12E–01	54	5.24
99R-1 (Piece 18A)	1720.30	24.90	56.00	0.2	1.39E–01	25	14.04
99R-1 (Piece 19A)	1720.44	68.80	52.50	0.3	1.46E–01	32	11.52
99R-1 (Piece 21A)	1720.64	15.50	55.50	0.2	2.14E–01	59	9.16
99R-2 (Piece 1A)	1720.89	153.60	52.20	0.3	1.41E–01	53	6.72
99R-2 (Piece 3A)	1721.05	192.70	40.40	0.3	1.15E–01	60	4.84
99R-2 (Piece 5A)	1721.19	269.70	49.90	0.2	1.78E–01	56	8.03
99R-2 (Piece 8A)	1721.39	161.40	54.00	0.1	1.70E–01	56	7.67
99R-2 (Piece 10A)	1721.59	118.70	48.40	0.2	1.78E–01	56	8.03
99R-2 (Piece 11A)	1721.69	265.00	37.00	0.4	4.84E–01	56	21.83
99R-2 (Piece 18A)	1722.19	99.40	48.80	0.3	1.65E–01	66	6.31
99R-3 (Piece 1A)	1722.37	183.50	58.50	1.1	1.56E–01	55	7.16
99R-3 (Piece 2A)	1722.55	273.40	49.40	0.3	1.63E–01	63	6.54
99R-3 (Piece 4A)	1722.75	147.30	48.70	0.6	2.14E–01	46	11.75
99R-3 (Piece 8A)	1723.01	120.00	50.10	0.4	2.07E–01	61	8.57
99R-3 (Piece 10A)	1723.23	224.60	44.70	0.1	2.09E–01	58	9.10
99R-3 (Piece 11A)	1723.35	355.70	27.00	0.4	2.22E–01	53	10.58
99R-3 (Piece 12A)	1723.45	270.50	49.80	0.4	1.99E–01	39	12.89
99R-3 (Piece 13A)	1723.55	36.80	52.20	0.3	1.80E–01	62	7.33
99R-3 (Piece 14A)	1723.77	215.70	50.30	0.2	8.95E–02	58	3.90
99R-5 (Piece 1A)	1723.98	7.60	50.40	2.9	1.34E+00	1050	3.22
99R-5 (Piece 2A)	1724.52	124.00	59.80	1.8	3.85E–01	60	16.21
99R-6 (Piece 1A)	1725.20	70.20	41.30	2.3	3.44E–01	46	18.89

Table T14 (continued).

Notes: ChRM = characteristic remanent magnetization, NRM = natural remanent magnetization, MAD = maximum angular deviation, PCA = principal component analysis, Dec = declination, Inc = inclination, *k* = magnetic susceptibility, *Q* = Königsberger ratio. A present-day field of 39.59 A/m at Site 1276 was used for *Q* calculations (see **"Paleomagnetism,"** p. 22, in the Explanatory Notes chapter).

Table T15. Concentrations of C_1 to C_6 hydrocarbons in headspace gas, Hole 1276A. (Continued on next two pages.)

Core, section, interval (cm)	Depth (mbsf)	C_1/C_2	C_1 (ppmv)	C_2 (ppmv)	$C_{2=}$ (ppmv)	C_3 (ppmv)	$C_{3=}$ (ppmv)	*i*-C_4 (ppmv)	*n*-C_4 (ppmv)	*i*-C_5 (ppmv)	*n*-C_5 (ppmv)	*i*-C_6 (ppmv)	*n*-C_6 (ppmv)
210-1276A-													
2R-2, 0–5	801.50		4.5										
2R-3, 0–5	803.00		7.4										
3R-3, 0–5	811.18		3.5										
3R-4, 0–5	812.68		3.2										
3R-7, 0–5	817.17		3.7										
4R-2, 0–5	820.70		5.2										
4R-4, 0–5	823.70		2.4										
4R-5, 0–5	825.20		5.3										
5R-2, 0–5	830.30		3.8										
5R-4, 0–5	833.30		3.3										
5R-6, 0–5	836.30		4.7										
6R-2, 0–5	839.90		3.1										
6R-4, 0–5	842.90		1.6										
6R-6, 0–5	845.90		4.1										
7R-1, 0–5	848.00		1.7										
7R-4, 0–5	852.50		2.9										
7R-6, 0–5	855.50		3.0										
8R-2, 0–5	859.10		1.8										
8R-4, 0–5	862.10		2.2										
8R-6, 0–5	865.10		2.0										
9R-2, 0–5	868.70		2.2										
9R-4, 0–5	871.70		1.6										
9R-6, 0–5	874.61		1.7										
10R-2, 0–5	878.30		1.8										
10R-4, 0–5	881.27		1.6										
10R-6, 0–5	884.11		1.7										
11R-2, 0–5	887.90		1.9										
11R-4, 0–5	890.90		1.6										
11R-6, 0–5	893.57		1.8										
12R-2, 0–5	897.50		1.9										
12R-5, 0–5	902.00		1.5										
13R-3, 0–5	908.70		1.7										
13R-4, 64–69	910.34		1.5										
14R-1, 0–1	915.30		1.5										
14R-2, 0–1	916.80		1.8										
15R-2, 0–1	926.50		2.2										
15R-4, 0–1	929.50		2.5										
16R-1, 0–1	934.50		1.7										
16R-3, 0–1	937.46	6.0	4.2	0.7									
17R-2, 0–1	945.36		2.7										
17R-7, 0–1	952.31		3.6										
18R-1, 0–1	953.80	3.8	3.8	1.0									
18R-5, 0–1	959.12		1.9										
19R-3, 0–1	966.39		3.3										
19R-5, 0–1	969.17		3.3										
20R-1, 0–1	973.10	4.8	2.9	0.6									
20R-4, 0–1	977.21		4.4										
21R-3, 0–1	985.46		3.9										
21R-4, 0–1	986.96	6.2	6.8	1.1									
22R-3, 0–1	995.40		3.1										
23R-2, 0–5	1,003.39		3.1										
24R-2, 0–1	1,013.10		1.6										
24R-4, 0–1	1,016.10		4.9										
25R-2, 0–1	1,022.70		2.7										
25R-4, 0–1	1,025.70		2.5										
26R-2, 0–1	1,032.26		1.7										
27R-1, 0–1	1,040.50		1.9										
27R-3, 0–1	1,043.41		2.2										
28R-1, 0–1	1,050.10		1.6										
28R-3, 0–1	1,052.91		1.8										
29R-1, 0–1	1,059.70		1.7										
29R-3, 0–1	1,062.53		1.8										
30R-1, 0–1	1,069.40		2.1										
30R-3, 0–1	1,072.13		2.4										
31R-1, 0–1	1,079.00		2.3										
31R-4, 0–1	1,083.39		2.5										
32R-1, 0–1	1,088.60		1.9										

Table T15 (continued).

Core, section, interval (cm)	Depth (mbsf)	C_1/C_2	C_1 (ppmv)	C_2 (ppmv)	$C_{2=}$ (ppmv)	C_3 (ppmv)	$C_{3=}$ (ppmv)	*i*-C_4 (ppmv)	*n*-C_4 (ppmv)	*i*-C_5 (ppmv)	*n*-C_5 (ppmv)	*i*-C_6 (ppmv)	*n*-C_6 (ppmv)
32R-4, 0–1	1,092.97		2.0										
33R-1, 0–1	1,098.20		2.2										
33R-4, 0–1	1,102.70		1.8										
34R-4, 0–1	1,112.13	2.2	2.6	1.2	1.0								
35R-2, 0–1	1,118.90		1.6										
35R-5, 0–1	1,123.25		1.8										
36R-4, 0–1	1,131.34		2.0										
36R-5, 0–1	1,132.63		3.5										
37R-2, 0–1	1,137.77		2.9										
37R-4, 0–1	1,140.51		2.2										
38R-3, 0–1	1,148.59		17.6										
38R-6, 0–1	1,152.82		6.4										
39R-3, 0–1	1,158.23		14.2										
39R-4, 0–1	1,159.71		18.5										
40R-2, 0–1	1,166.33		13.1										
40R-4, 0–2	1,169.36		54.2										
41R-2, 0–1	1,175.90		20.7										
41R-4, 0–1	1,178.97	39.4	47.3	1.2									
42R-4, 0–1	1,188.16		37.5										
42R-6, 0–1	1,191.20	88.1	79.3	0.9									
43R-3, 0–1	1,196.55		28.5										
43R-6, 0–1	1,201.00		6.9										
44R-1, 0–1	1,203.20	58.6	211.1	3.6									
44R-3, 0–1	1,206.20	63.4	63.4	1.0									
45R-2, 0–1	1,214.33		44.7										
45R-5, 0–1	1,218.92		10.1										
46R-1, 146–147	1,223.86		83.3										
46R-4, 0–1	1,226.99	91.3	82.2	0.9									
47R-2, 0–1	1,233.53	115.9	139.1	1.2									
47R-4, 0–1	1,236.57	110.4	165.6	1.5									
48R-2, 0–1	1,244.78	92.5	148.0	1.6									
48R-4, 0–1	1,246.32	110.2	143.3	1.3									
49R-3, 0–1	1,254.40	48.5	58.2	1.2									
49R-4, 0–1	1,255.90	67.7	284.3	4.2									
50R-3, 0–1	1,264.00	86.2	189.7	2.2									
50R-5, 0–1	1,267.00	61.7	277.8	4.5									
51R-2, 0–1	1,272.20	82.6	90.9	1.1									
51R-3, 0–1	1,273.70	86.8	147.5	1.7									
52R-2, 0–1	1,281.90	53.5	139.1	2.6									
52R-5, 0–1	1,286.40	82.5	214.5	2.6									
53R-2, 120–121	1,292.70	46.6	176.9	3.8									
53R-3, 131–132	1,294.31	74.6	201.4	2.7									
54R-2, 0–1	1,301.10	58.6	234.2	4.0									
54R-3, 0–1	1,302.60	66.4	311.9	4.7									
55R-2, 0–1	1,310.70	50.4	705.4	14.0		*7.9*							
56R-2, 0–1	1,320.30	86.1	232.5	2.7									
57R-2, 0–1	1,330.00	59.3	171.9	2.9									
58R-2, 0–1	1,339.60		1.4										
59R-2, 0–1	1,345.60	61.8	271.7	4.4									
59R-6, 0–1	1,351.62	99.6	199.2	2.0									
60R-2, 0–1	1,355.20	41.6	91.5	2.2									
60R-4, 0–1	1,358.10	48.7	282.5	5.8									
61R-2, 0–1	1,364.70	52.6	57.9	1.1									
61R-7, 52–53	1,372.62	92.8	222.8	2.4									
62R-2, 0–1	1,374.40	98.6	256.4	2.6									
62R-5, 0–1	1,378.90	66.8	86.8	1.3									
63R-2, 0–1	1,384.00		37.3										
63R-5, 0–1	1,388.50	59.8	281.0	4.7									
64R-2, 0–1	1,393.70	65.8	289.4	4.4									
64R-5, 0–1	1,398.20	79.8	311.1	3.9									
65R-4, 0–1	1,406.30	61.3	233.1	3.8									
65R-5, 0–1	1,407.80	54.3	347.6	6.4									
66R-2, 0–1	1,412.80	50.3	386.9	7.7									
66R-4, 0–1	1,415.80	48.0	177.4	3.7									
67R-2, 0–1	1,422.40	68.6	219.5	3.2									
67R-4, 0–1	1,425.40	27.4	79.5	2.9	1.1								
68R-2, 0–1	1,432.00	57.0	410.4	7.2									
68R-5, 0–1	1,436.50	44.2	145.8	3.3									
69R-4, 0–1	1,444.30	42.9	210.0	4.9									

Table T15 (continued).

Core, section, interval (cm)	Depth (mbsf)	C_1/C_2	C_1 (ppmv)	C_2 (ppmv)	$C_{2=}$ (ppmv)	C_3 (ppmv)	$C_{3=}$ (ppmv)	*i*-C_4 (ppmv)	*n*-C_4 (ppmv)	*i*-C_5 (ppmv)	*n*-C_5 (ppmv)	*i*-C_6 (ppmv)	*n*-C_6 (ppmv)
69R-6, 0–1	1,447.30	32.9	42.7	1.3									
70R-3, 0–1	1,452.50	38.4	80.6	2.1									
70R-6, 0–1	1,457.00	40.9	81.8	2.0									
71R-3, 0–1	1,462.20	70.0	252.1	3.6									
71R-7, 0–1	1,467.91	40.7	122.2	3.0									
72R-2, 0–1	1,470.40	31.5	554.0	17.6		9.2		7.2	3.1	3.7			
72R-6, 0–1	1,476.23	42.8	248.1	5.8				2.0					
73R-3, 0–1	1,481.50	46.6	489.4	10.5				3.4	1.6	1.8			
73R-6, 0–1	1,486.00	42.5	1,326.6	31.2		12.3		10.4	4.2	6.3	1.5		
74R-3, 0–1	1,491.10	53.9	474.0	8.8				2.2		1.3			
74R-4, 0–1	1,492.60	50.4	655.7	13.0		4.4		3.3		2.0			
75R-2, 0–1	1,499.20	46.1	515.9	11.2				2.9	1.4	1.6			
75R-4, 0–1	1,502.20	46.0	919.4	20.0		6.7		4.3	2.0	2.6			
76R-2, 0–1	1,508.80	34.8	434.9	12.5				3.3	1.5	2.1			
76R-4, 0–1	1,511.80	26.0	46.8	1.8									
77R-2, 0–1	1,518.40	38.6	416.5	10.8				3.0		1.6			
77R4, 0–1	1,521.40	42.1	733.1	17.4				3.7	1.5	1.8			
78R-3, 0–1	1,529.50	50.5	338.0	6.7				1.8					
78R-5, 0–1	1,532.50	44.9	705.1	15.7				3.2	1.4	1.5			
79R-2, 0–1	1,537.70	37.9	1,112.9	29.4		5.6		5.0	1.9	2.2			
79R-3, 0–1	1,539.20	45.7	191.8	4.2									
80R-2, 0–1	1,547.30	26.1	719.5	27.6		6.5		4.0	1.6	2.1			
80R-4, 0–1	1,550.30	29.4	253.2	8.6									
81R-2, 0–1	1,556.90	29.4	1,353.2	46.0		8.6	10.0	6.4	2.4		2.6		
81R-3, 139–140	1,559.79	15.1	88.8	5.9				1.4					
82R-1, 0–1	1,565.00	19.8	306.5	15.5			2.6	1.8					
83R-4, 0–1	1,579.00	22.4	257.1	11.5			5.3	3.3			1.2		
84R-3, 0–1	1,587.20	28.4	1,123.0	39.6		5.1	7.0	4.3	1.9		1.4		
85R-3, 0–1	1,590.70	27.3	603.6	22.1			4.2	2.7					
86R-3, 0–1	1,597.80	9.1	61.6	6.8			2.1	1.4					
87R-2, 0–1	1,606.00	22.0	250.5	11.4			3.0	2.1					
87R-5, 0–1	1,610.58	10.2	751.9	74.0		14.8	14.4	8.7	3.6		3.4		
88R-8, 97–98	1,624.01	2.7	5,484.4	2,014.4		296.8	168.6	11.9	26.1	3.2	5.5		
89R-2, 0–1	1,625.10	4.0	3,107.0	771.4		103.8	91.5	8.5	14.3	1.4	3.4		
89R-5, 0–1	1,628.64	5.3	4,035.1	761.2		86.7	52.7	4.5	8.3		1.6		
90R-3, 0–1	1,636.27	5.2	2,224.3	431.0		50.9	52.2	4.8	9.2		2.1		
90R-6, 0–1	1,640.77	4.9	1,995.7	411.9		48.8	53.0	5.1	9.6		2.3		
91R-2, 0–1	1,644.30	4.2	2,471.0	582.8		76.5	75.3	7.6	12.8	1.5	3.3		
91R-5, 0–1	1,648.80	5.1	1,391.8	272.5		26.8	32.2	3.0	5.2		1.2		
92R-3, 0–1	1,655.50	5.0	4,777.9	956.0		102.9	96.7	7.8	13.1	1.6	2.9		
92R-5, 0–1	1,658.50	5.5	4,315.3	787.7		82.2	61.2	5.5	8.5		2.1		
93R-2, 0–1	1,663.60	3.2	1,069.8	331.7		43.3	35.2	3.6	6.0		1.4		
93R-4, 0–1	1,666.60	3.4	4,021.7	1,192.2		142.7	88.8	7.4	12.5	1.4	2.8		
94R-4, 0–1	1,676.15	4.4	3,784.9	854.6		96.6	94.4	7.9	12.6	2.0	3.3		1.8
94R-6, 0–1	1,679.09	5.4	5,233.7	967.6		96.7	89.5	6.6	10.3	1.5	2.1		
95R-2, 0–1	1,682.56	2.4	1,153.1	480.0		59.1	75.7	5.0	8.2		1.3		
95R-3, 0–1	1,684.06	4.2	3,578.2	843.9		100.5	99.5	6.5	11.6	1.5	2.0		
96R-2, 0–1	1,692.33	3.1	9,149.7	2,956.8		339.2	257.6	16.9	33.0	2.7	3.3		
96R-5, 0–1	1,696.95	2.8	15,962.9	5,801.8		602.3	256.7	15.6	25.3	1.7	2.1		
97R-2, 0–1	1,702.00	2.4	8,173.7	3,442.1		535.2	300.0	18.7	31.6		1.3		
97R-3, 0–1	1,703.50	2.5	18,668.6	7,501.1		1,416.8	657.0	73.2	101.9	2.6	5.9		1.2
98R-3, 0–1	1,713.01	5.9	556.3	94.6		9.1	9.8		1.4				

Table T16. Inorganic carbon and carbonate content, Hole 1276A. (Continued on next three pages.)

Core, section, interval (cm)	Depth (mbsf)	Inorganic carbon (wt%)	$CaCO_3$ (wt%)
210-1276A-			
1W-2, 110–111	755.59	0.07	0.58
1W-5, 0–1	758.49	0.07	0.58
2R-1, 45–46	800.45	0.21	1.75
2R-1, 84–85	800.84	0.07	0.58
2R-2, 0–5	801.50	0.86	7.16
2R-3, 0–5	803.00	0.08	0.67
3R-3, 0–5	811.18	0.10	0.83
3R-3, 133–134	812.51	0.08	0.67
3R-4, 0–5	812.68	0.96	8.00
3R-7, 0–5	817.17	0.86	7.16
3R-8, 17–18	818.84	0.07	0.58
4R-2, 0–5	820.70	0.14	1.17
4R-3, 39–40	822.59	3.49	29.07
4R-3, 53–54	822.73	0.06	0.50
4R-4, 0–5	823.70	0.16	1.33
4R-4, 8–9	823.78	0.13	1.08
4R-5, 0–5	825.20	0.11	0.92
5R-2, 0–5	830.30	0.09	0.75
5R-4, 0–5	833.30	4.65	38.74
5R-4, 20–21	833.50	1.01	8.41
5R-4, 24–25	833.54	0.06	0.50
5R-6, 0–5	836.30	0.17	1.42
6R-2, 0–5	839.90	0.05	0.42
6R-3, 59–60	841.99	0.06	0.50
6R-4, 0–5	842.90	1.35	11.25
6R-6, 0–5	845.90	0.07	0.58
7R-1, 0–5	848.00	0.07	0.58
7R-4, 0–5	852.50	3.58	29.82
7R-4, 35–36	852.85	0.10	0.83
7R-6, 0–5	855.50	6.13	51.06
8R-2, 0–5	859.10	0.32	2.67
8R-4, 0–5	862.10	0.66	5.50
8R-5, 116–117	864.76	4.22	35.15
8R-6, 0–5	865.10	0.96	8.00
9R-1, 32–34	867.52	4.27	35.57
9R-2, 0–5	868.70	5.73	47.73
9R-2, 72–75	869.42	0.07	0.58
9R-4, 0–5	871.70	3.35	27.91
9R-6, 0–5	874.61	4.04	33.65
10R-1, 21–22	877.01	0.08	0.67
10R-2, 0–5	878.30	4.46	37.15
10R-4, 0–5	881.27	3.06	25.49
10R-4, 101–105	882.28	3.05	25.41
10R-4, 109–113	882.36	5.33	44.40
10R-6, 0–5	884.11	0.10	0.83
11R-2, 0–5	887.90	3.21	26.74
11R-3, 71–72	890.11	3.37	28.07
11R-4, 0–5	890.90	0.31	2.58
11R-4, 2–4	890.92	1.63	13.58
11R-4, 122–125	892.12	0.09	0.75
11R-6, 0–5	893.57	6.56	54.65
11R-6, 60–61	894.17	4.25	35.40
12R-2, 0–5	897.50	5.09	42.40
12R-3, 30–31	899.30	1.87	15.58
12R-3, 82–83	899.82	10.64	88.63
12R-4, 54–55	901.04	0.11	0.92
12R-4, 116–117	901.66	0.54	4.50
12R-5, 0–5	902.00	4.28	35.65
13R-2, 120–121	908.40	0.94	7.83
13R-2, 129–130	908.49	9.36	77.97
13R-3, 0–5	908.70	8.63	71.89
13R-3, 7–8	908.77	10.72	89.30
13R-3, 9–10	908.79	0.58	4.83
13R-4, 64–69	910.34	1.30	10.83
14R-1, 0–1	915.30	0.11	0.92
14R-1, 38–39	915.68	0.60	5.00
14R-2, 0–1	916.80	7.90	65.81
14R-3, 8–9	918.38	0.61	5.08
15R-1, 0–1	925.00	9.06	75.47
15R-2, 0–1	926.50	5.71	47.56
15R-2, 105–106	927.55	5.71	47.56
15R-3, 52–53	928.52	5.09	42.40
15R-4, 0–1	929.50	0.06	0.50
15R-5, 40–41	931.40	0.05	0.42
15R-5, 107–108	932.07	0.03	0.25
16R-1, 0–1	934.50	0.05	0.42
16R-1, 68–69	935.18	0.04	0.33
16R-1, 103–104	935.53	0.16	1.33
16R-2, 77–78	936.77	0.06	0.50
16R-2, 124–125	937.24	0.96	8.00
16R-3, 0–1	937.46	0.06	0.50
16R-3, 22–23	937.68	0.36	3.00
16R-3, 128–129	938.74	1.76	14.66
16R-4, 38–39	939.34	1.85	15.41
16R-4, 107–108	940.03	0.07	0.58
16R-5, 73–74	941.18	0.09	0.75
16R-5, 110–111	941.55	1.02	8.50
16R-6, 21–22	941.94	1.31	10.91
16R-CC, 9–10	942.32	1.48	12.33
17R-1, 47–48	944.57	1.87	15.58
17R-1, 77–78	944.87	1.23	10.25
17R-1, 108–109	945.18	0.07	0.58
17R-2, 0–1	945.36	0.98	8.16
17R-2, 46–47	945.82	0.99	8.25
17R-2, 73–74	946.09	0.21	1.75
17R-3, 23–24	947.11	1.31	10.91
17R-4, 21–25	948.12	3.18	26.49
17R-4, 106–107	948.97	1.12	9.33
17R-5, 39–40	949.81	0.94	7.83
17R-6, 25–26	951.18	0.09	0.75
17R-6, 69–70	951.62	0.64	5.33
17R-7, 0–1	952.31	0.94	7.83
17R-7, 24–28	952.55	0.53	4.42
18R-1, 0–1	953.80	0.47	3.92
18R-1, 31–35	954.11	0.44	3.67
18R-1, 125–126	955.05	0.09	0.75
18R-2, 99–100	956.18	0.36	3.00
18R-3, 1–2	956.45	0.55	4.58
18R-3, 9–10	956.53	0.28	2.33
18R-4, 4–5	957.98	1.29	10.75
18R-4, 54–55	958.48	0.33	2.75
18R-5, 0–1	959.12	0.99	8.25
18R-5, 17–18	959.29	1.05	8.75
18R-6, 56–57	960.99	4.00	33.32
18R-6, 129–130	961.72	0.44	3.67
18R-7, 97–101	962.90	1.99	16.58
18R-7, 139–140	963.32	0.07	0.58
19R-3, 0–1	966.39	0.06	0.50
19R-3, 122–123	967.61	0.28	2.33
19R-5, 0–1	969.17	0.06	0.50
19R-5, 100–101	970.17	7.45	62.06
20R-1, 0–1	973.10	0.25	2.08
20R-1, 23–24	973.33	4.49	37.40
20R-1, 114–115	974.24	3.58	29.82
20R-2, 50–51	974.95	2.46	20.49
20R-3, 29–31	976.13	2.49	20.74
20R-3, 90–92	976.74	0.21	1.75
20R-4, 0–1	977.21	0.10	0.83
20R-5, 62–64	979.33	10.12	84.30
20R-5, 133–135	980.04	0.05	0.42
20R-7, 59–62	982.21	0.09	0.75
20R-7, 106–107	982.68	0.07	0.58
21R-1, 53–54	983.23	0.12	1.00
21R-2, 123–124	985.19	0.06	0.50
21R-3, 0–1	985.46	6.78	56.48
21R-3, 15–16	985.61	7.32	60.98
21R-4, 0–1	986.96	4.08	33.99
21R-4, 25–26	987.21	0.11	0.92
21R-4, 63–64	987.59	0.10	0.83
22R-1, 11–12	992.51	11.15	92.88
22R-3, 0–1	995.40	0.08	0.67
22R-3, 72–73	996.12	0.08	0.67
23R-1, 70–71	1002.70	8.04	66.97
23R-2, 0–5	1003.39	0.02	0.17
23R-3, 68–72	1005.52	0.36	3.00
23R-4, 10–11	1006.04	0.98	8.16
23R-4, 57–58	1006.51	7.80	64.97
24R-1, 51–54	1012.11	4.62	38.49
24R-2, 0–1	1013.10	9.11	75.89
24R-3, 80–84	1015.40	5.89	49.06
24R-4, 0–1	1016.10	0.06	0.50
25R-2, 0–1	1022.70	5.59	46.57
25R-2, 1–6	1022.71	5.68	47.31
25R-3, 1–2	1024.21	9.56	79.64
25R-4, 0–1	1025.70	9.36	77.97
25R-7, 24–30	1029.94	0.03	0.25
26R-1, 23–24	1031.03	0.04	0.33
26R-2, 0–1	1032.26	0.06	0.50
26R-2, 40–45	1032.66	0.05	0.42
26R-3, 72–73	1033.98	0.06	0.50
27R-1, 0–1	1040.50	0.10	0.83
27R-1, 18–19	1040.68	0.02	0.17
27R-2, 13–14	1042.10	0.05	0.42
27R-3, 0–1	1043.41	0.08	0.67
27R-4, 29–31	1045.20	0.01	0.08
27R-5, 25–26	1046.66	0.03	0.25
27R-5, 70–72	1047.11	0.03	0.25
27R-6, 8–9	1047.95	0.01	0.08
27R-7, 13–14	1049.50	0.49	4.08
28R-1, 0–1	1050.10	0.06	0.50
28R-1, 13–14	1050.23	0.26	2.17
28R-2, 40–41	1052.00	0.06	0.50
28R-3, 0–1	1052.91	0.25	2.08
28R-3, 47–48	1053.38	0.03	0.25
28R-4, 10–11	1054.36	0.05	0.42
28R-4, 141–142	1055.67	4.91	40.90
28R-5, 19–20	1055.89	3.03	25.24
28R-6, 63–63	1057.29	0.53	4.42
29R-1, 0–1	1059.70	0.81	6.75
29R-1, 16–17	1059.86	3.55	29.57
29R-2, 36–38	1061.50	1.13	9.41
29R-3, 0–1	1062.53	0.02	0.17
29R-3, 63–64	1063.16	4.71	39.23
29R-4, 116–118	1065.19	4.85	40.40
29R-5, 11–12	1065.64	4.97	41.40
29R-6, 33–35	1066.95	0.39	3.25
30R-1, 0–1	1069.40	0.21	1.75
30R-1, 18–19	1069.58	2.79	23.24
30R-2, 11–12	1070.87	1.53	12.75
30R-3, 0–1	1072.13	0.88	7.33
30R-3, 12–13	1072.25	0.43	3.58
30R-4, 47–48	1074.10	0.06	0.50
30R-4, 78–79	1074.41	0.81	6.75
30R-4, 115–116	1074.78	0.16	1.33
30R-4, 128–129	1074.91	0.12	1.00
30R-5, 33–34	1075.46	1.46	12.16
31R-1, 0–1	1079.00	0.58	4.83
31R-1, 65–66	1079.65	1.50	12.50
31R-2, 15–18	1080.65	1.60	13.33
31R-2, 124–128	1081.74	0.08	0.67
31R-3, 51–52	1082.46	0.10	0.83
31R-4, 0–1	1083.39	0.05	0.42
31R-4, 48–49	1083.87	7.64	63.64

Table T16 (continued).

Core, section, interval (cm)	Depth (mbsf)	Inorganic carbon (wt%)	$CaCO_3$ (wt%)
31R-4, 54–55	1083.93	0.10	0.83
31R-5, 97–98	1085.86	3.83	31.90
31R-6, 32–33	1086.25	2.38	19.83
32R-1, 0–1	1088.60	6.29	52.40
32R-1, 30–31	1088.90	4.43	36.90
32R-2, 83–84	1090.93	7.83	65.22
32R-3, 48–49	1092.08	6.12	50.98
32R-4, 0–1	1092.97	0.15	1.25
32R-4, 57–58	1093.54	5.87	48.90
32R-5, 23–27	1094.65	8.34	69.47
32R-5, 45–46	1094.87	1.55	12.91
32R-7, 30–31	1097.72	0.06	0.50
32R-7, 49–50	1097.91	0.08	0.67
33R-1, 0–1	1098.20	0.52	4.33
33R-1, 16–17	1098.36	0.13	1.08
33R-2, 138–139	1101.08	4.08	33.99
33R-3, 91–95	1102.11	5.85	48.73
33R-3, 139–140	1102.59	3.36	27.99
33R-4, 0–1	1102.70	3.51	29.24
33R-4, 19–20	1102.89	3.10	25.82
33R-4, 133–137	1104.03	1.28	10.66
33R-6, 13–14	1105.83	6.47	53.90
33R-7, 14–15	1107.34	5.26	43.82
33R-CC, 46–47	1108.22	3.35	27.91
34R-2, 10–11	1109.27	0.06	0.50
34R-2, 94–98	1110.11	7.77	64.72
34R-2, 102–106	1110.19	0.06	0.50
34R-3, 112–113	1111.79	3.20	26.66
34R-4, 0–1	1112.13	5.44	45.32
34R-4, 43–44	1112.56	2.14	17.83
34R-5, 36–37	1113.40	5.84	48.65
35R-1, 21–22	1117.61	2.79	23.24
35R-2, 0–1	1118.90	4.47	37.24
35R-2, 21–22	1119.11	5.03	41.90
35R-3, 31–32	1120.71	0.95	7.91
35R-3, 107–111	1121.47	0.03	0.25
35R-4, 20–21	1121.95	4.32	35.99
35R-4, 64–65	1122.39	2.30	19.16
35R-5, 0–1	1123.25	1.36	11.33
35R-5, 6–7	1123.31	1.34	11.16
35R-6, 9–10	1124.64	2.45	20.41
35R-6, 31–32	1124.86	4.93	41.07
35R-6, 57–61	1125.12	3.05	25.41
35R-7, 22–23	1126.26	1.99	16.58
36R-1, 109–110	1128.19	0.08	0.67
36R-2, 110–112	1129.61	3.43	28.57
36R-3, 108–110	1131.07	3.39	28.24
36R-4, 0–1	1131.34	0.45	3.75
36R-4, 103–105	1132.37	1.58	13.16
36R-5, 0–1	1132.63	0.65	5.42
36R-5, 103–105	1133.66	0.74	6.16
36R-6, 62–66	1134.75	0.67	5.58
36R-6, 82–86	1134.95	2.07	17.24
36R-6, 111–112	1135.24	0.13	1.08
37R-1, 104–106	1137.44	7.03	58.56
37R-2, 0–1	1137.77	0.67	5.58
37R-2, 106–108	1138.83	0.10	0.83
37R-3, 45–46	1139.61	0.55	4.58
37R-3, 99–100	1140.15	4.62	38.49
37R-4, 0–1	1140.51	1.44	12.00
37R-4, 91–92	1141.42	6.84	56.98
37R-5, 53–54	1142.18	1.06	8.83
37R-5, 88–89	1142.53	4.10	34.15
37R-6, 126–127	1144.32	0.27	2.25
37R-7, 81–82	1145.39	1.64	13.66
38R-1, 7–8	1146.07	2.14	17.83
38R-2, 2–3	1147.35	0.28	2.33
38R-3, 0–1	1148.59	2.51	20.91
38R-3, 24–25	1148.83	0.41	3.42
38R-4, 18–19	1150.32	3.35	27.91
38R-5, 13–14	1151.57	1.58	13.16
38R-5, 96–98	1152.40	9.18	76.47
38R-6, 0–1	1152.82	1.90	15.83
38R-6, 20–21	1153.02	0.63	5.25
38R-6, 96–98	1153.78	5.70	47.48
38R-7, 9–10	1154.30	1.12	9.33
39R-1, 32–33	1155.52	0.08	0.67
39R-2, 20–21	1156.90	1.33	11.08
39R-3, 0	1158.23	0.07	0.58
39R-3, 36–37	1158.59	2.68	22.32
39R-3, 92–93	1159.15	8.85	73.72
39R-4, 0–1	1159.71	1.12	9.33
39R-4, 64–65	1160.35	0.65	5.42
39R-5, 36–38	1161.59	0.08	0.67
39R-6, 21–22	1162.96	0.06	0.50
40R-1, 32–33	1165.12	0.12	1.00
40R-2, 0–1	1166.33	1.15	9.58
40R-2, 50–52	1166.83	0.10	0.83
40R-2, 80–83	1167.13	5.06	42.15
40R-4, 0–1	1169.36	0.55	4.58
40R-4, 122–123	1170.58	9.51	79.22
40R-7, 30–31	1173.77	0.17	1.42
40R-CC, 0–1	1174.29	0.09	0.75
41R-1, 13–14	1174.53	0.10	0.83
41R-1, 113–117	1175.53	2.68	22.32
41R-1, 146–147	1175.86	1.62	13.50
41R-2, 0–1	1175.90	2.88	23.99
41R-4, 0–1	1178.97	0.12	1.00
41R-5, 86–87	1181.37	2.97	24.74
41R-6, 79–84	1182.84	6.44	53.65
41R-7, 41–42	1183.53	3.06	25.49
41R-CC, 19–20	1184.15	0.40	3.33
42R-1, 4–8	1184.04	1.65	13.75
42R-1, 82–84	1184.82	3.85	32.07
42R-3, 2–4	1186.77	2.30	19.16
42R-4, 0–1	1188.16	0.34	2.83
42R-6, 0–1	1191.20	0.71	5.91
42R-6, 39–43	1191.59	5.27	43.90
42R-7, 74–76	1193.47	0.24	2.00
42R-CC, 26–27	1194.51	0.44	3.67
43R-1, 46–49	1193.96	0.35	2.92
43R-2, 34–36	1195.37	3.10	25.82
43R-2, 88–92	1195.91	5.18	43.15
43R-3, 0–1	1196.55	0.16	1.33
43R-3, 31–32	1196.86	0.88	7.33
43R-4, 146–147	1199.41	5.17	43.07
43R-5, 104–106	1200.51	1.67	13.91
43R-6, 0–1	1201.00	1.08	9.00
43R-6, 57–59	1201.57	1.19	9.91
43R-CC, 4–5	1202.34	1.45	12.08
44R-1, 0–1	1203.20	6.45	53.73
44R-1, 33–35	1203.53	0.36	3.00
44R-2, 123–125	1205.96	1.98	16.49
44R-3, 0–1	1206.20	0.94	7.83
44R-3, 71–72	1206.91	5.07	42.23
44R-4, 60–62	1208.34	0.05	0.42
44R-5, 69–71	1209.97	2.65	22.08
44R-7, 61–63	1212.97	4.17	34.74
45R-1, 8–9	1212.88	2.24	18.66
45R-2, 0–1	1214.33	1.33	11.08
45R-2, 25–26	1214.58	2.35	19.58
45R-3, 42–43	1216.28	1.26	10.50
45R-3, 53–54	1216.39	5.59	46.57
45R-4, 22–24	1217.61	0.44	3.67
45R-5, 0–1	1218.92	2.86	23.82
45R-5, 45–46	1219.37	1.61	13.41
45R-6, 28–29	1220.73	0.78	6.50
46R-1, 23–24	1222.63	2.28	18.99
46R-1, 146–147	1223.86	0.45	3.75
46R-2, 23–24	1224.14	3.18	26.49
46R-3, 43–44	1225.88	2.94	24.49
46R-4, 0–1	1226.99	0.09	0.75
46R-4, 15–16	1227.14	0.24	2.00
46R-5, 27–28	1228.80	5.53	46.07
46R-5, 105–106	1229.58	2.62	21.83
46R-6, 74–75	1230.81	2.82	23.49
46R-7, 15–16	1231.26	0.11	0.92
47R-1, 55–57	1232.55	0.12	1.00
47R-2, 0–1	1233.53	0.05	0.42
47R-2, 64–66	1234.17	4.67	38.90
47R-3, 39–41	1235.43	4.03	33.57
47R-4, 0–1	1236.57	0.71	5.91
47R-4, 66–68	1237.23	0.84	7.00
47R-5, 28–30	1238.39	3.29	27.41
47R-6, 21–23	1239.86	1.29	10.75
47R-7, 31–33	1241.29	0.29	2.42
48R-1, 115–116	1242.85	0.14	1.17
48R-2, 0–1	1243.24	0.10	0.83
48R-2, 89–90	1244.13	2.49	20.74
48R-3, 70–71	1245.48	9.31	77.55
48R-4, 0–1	1246.32	1.03	8.58
48R-4, 11–12	1246.43	0.99	8.25
48R-4, 44–45	1246.76	4.10	34.15
49R-1, 117–118	1252.57	7.41	61.73
49R-2, 6–11	1252.96	0.87	7.25
49R-3, 0–1	1254.40	3.10	25.82
49R-3, 65–66	1255.05	9.07	75.55
49R-4, 0–1	1255.90	0.19	1.58
49R-4, 67–72	1256.57	0.81	6.75
49R-5, 19–20	1257.59	0.26	2.17
49R-6, 91–92	1259.81	1.00	8.33
50R-1, 100–101	1262.00	4.60	38.32
50R-2, 103–104	1263.53	0.84	7.00
50R-3, 0–1	1264.00	0.14	1.17
50R-3, 139–140	1265.39	1.32	11.00
50R-4, 18–22	1265.68	0.83	6.91
50R-5, 0–1	1267.00	0.10	0.83
50R-5, 86–88	1267.86	4.75	39.57
50R-6, 60–65	1268.58	2.54	21.16
51R-1, 58–60	1271.28	1.38	11.50
51R-2, 0–1	1272.20	7.08	58.98
51R-2, 77–79	1272.97	3.04	25.32
51R-2, 91–92	1273.11	9.39	78.22
51R-3, 0–1	1273.70	0.13	1.08
51R-3, 41–43	1274.11	0.85	7.08
51R-4, 103–105	1276.23	4.63	38.57
51R-5, 114–116	1277.84	1.35	11.25
51R-6, 25–27	1278.45	0.21	1.75
52R-1, 100–101	1281.40	5.37	44.73
52R-2, 0–1	1281.90	0.61	5.08
52R-2, 36–37	1282.26	0.23	1.92
52R-2, 125–126	1283.15	1.13	9.41
52R-3, 90–91	1284.30	3.42	28.49
52R-3, 106–107	1284.46	8.17	68.06
52R-4, 91–92	1285.81	2.54	21.16
52R-4, 100–101	1285.90	1.44	12.00
52R-5, 0–1	1286.40	0.18	1.50
52R-5, 100–101	1287.40	3.78	31.49
52R-6, 97–98	1288.87	3.37	28.07
52R-7, 57–58	1289.97	0.15	1.25
53R-1, 46–48	1290.46	0.97	8.08
53R-2, 47–49	1291.97	0.05	0.42
53R-2, 120–121	1292.70	1.28	10.66
53R-3, 131–132	1294.31	0.44	3.67

Table T16 (continued).

Core, section, interval (cm)	Depth (mbsf)	Inorganic carbon (wt%)	$CaCO_3$ (wt%)
53R-4, 26–27	1294.70	9.63	80.22
53R-4, 54–56	1294.98	0.54	4.50
53R-5, 58–60	1296.52	2.04	16.99
53R-5, 107–108	1297.01	1.46	12.16
53R-6, 50–52	1297.94	1.57	13.08
54R-1, 70–71	1300.30	3.28	27.32
54R-2, 0–1	1301.10	0.98	8.16
54R-2, 67–69	1301.77	0.91	7.58
54R-3, 0–1	1302.60	4.09	34.07
54R-3, 118–120	1303.78	1.01	8.41
54R-4, 70–71	1304.80	0.08	0.67
54R-4, 120–121	1305.30	1.88	15.66
54R-5, 93–94	1306.53	2.93	24.41
54R-6, 51–52	1307.52	1.24	10.33
55R-1, 70–73	1309.90	1.43	11.91
55R-2, 0–1	1310.70	3.89	32.40
55R-2, 10–13	1310.80	3.64	30.32
55R-3, 39–41	1312.59	5.05	42.07
55R-4, 50–52	1314.20	3.31	27.57
56R-1, 33–34	1319.13	1.61	13.41
56R-1, 118–120	1319.98	0.11	0.92
56R-2, 0–1	1320.30	0.10	0.83
56R-2, 109–110	1321.39	0.75	6.25
56R-3, 30–31	1322.10	0.70	5.83
56R-4, 30–31	1323.60	8.60	71.64
57R-1, 4–5	1328.54	2.32	19.33
57R-1, 74–75	1329.24	9.06	75.47
57R-2, 0–1	1330.00	0.22	1.83
57R-2, 38–39	1330.38	0.09	0.75
58R-1, 69–70	1338.79	4.42	36.82
58R-2, 0–1	1339.60	2.84	23.66
58R-2, 26–27	1339.86	0.81	6.75
58R-3, 68–72	1341.78	0.09	0.75
58R-4, 11–12	1342.21	3.85	32.07
58R-CC, 22–23	1343.24	0.10	0.83
59R-1, 134–135	1345.44	0.47	3.92
59R-2, 0–1	1345.60	1.06	8.83
59R-2, 7–8	1345.67	9.30	77.47
59R-3, 85–86	1347.95	0.12	1.00
59R-4, 18–19	1348.78	3.75	31.24
59R-4, 103–107	1349.63	0.07	0.58
59R-5, 119–120	1351.29	0.36	3.00
59R-6, 0–1	1351.62	0.07	0.58
59R-6, 10–11	1351.72	2.48	20.66
59R-6, 87–88	1352.49	2.95	24.57
59R-7, 4–5	1352.70	3.89	32.40
60R-1, 18–19	1353.88	2.12	17.66
60R-2, 0–1	1355.20	0.31	2.58
60R-2, 52–54	1355.72	0.09	0.75
60R-3, 40–42	1357.10	4.32	35.99
60R-4, 0–1	1358.10	0.35	2.92
60R-4, 86–88	1358.96	0.45	3.75
60R-5, 31–33	1359.91	0.50	4.17
60R-5, 59–61	1360.19	0.84	7.00
61R-1, 84–85	1364.04	0.07	0.58
61R-2, 0–1	1364.70	0.12	1.00
61R-2, 90–91	1365.60	0.11	0.92
61R-3, 104–105	1367.24	0.17	1.42
61R-4, 119–120	1368.89	0.07	0.58
61R-5, 79–81	1369.99	8.72	72.64
61R-6, 45–46	1371.15	0.07	0.58
61R-7, 34–36	1372.44	0.08	0.67
61R-7, 52–53	1372.62	0.20	1.67
62R-1, 53–54	1373.43	0.57	4.75
62R-2, 0–1	1374.40	0.16	1.33
62R-2, 133–134	1375.73	0.32	2.67
62R-3, 78–79	1376.68	0.18	1.50
62R-4, 10–11	1377.50	0.76	6.33
62R-5, 0–1	1378.90	0.09	0.75
62R-5, 48–49	1379.38	0.09	0.75
62R-6, 134–136	1381.74	1.99	16.58
62R-7, 8–9	1381.93	0.43	3.58
63R-1, 135–136	1383.85	0.64	5.33
63R-2, 0–1	1384.00	0.19	1.58
63R-2, 7–8	1384.07	0.14	1.17
63R-3, 119–120	1386.69	0.07	0.58
63R-4, 110–111	1388.10	3.48	28.99
63R-5, 0–1	1388.50	0.10	0.83
63R-5, 72–73	1389.22	0.07	0.58
63R-6, 22–23	1390.22	0.16	1.33
63R-7, 5–6	1391.40	0.19	1.58
64R-1, 134–135	1393.54	0.07	0.58
64R-2, 0–1	1393.70	0.06	0.50
64R-2, 23–24	1393.93	0.09	0.75
64R-3, 77–78	1395.97	3.13	26.07
64R-3, 146–147	1396.66	2.74	22.82
64R-4, 102–103	1397.72	0.06	0.50
64R-5, 0–1	1398.20	2.35	19.58
64R-5, 44–45	1398.64	0.08	0.67
64R-6, 57–58	1400.27	0.05	0.42
64R-7, 24–25	1400.94	0.07	0.58
65R-1, 128–129	1403.08	0.09	0.75
65R-2, 104–105	1404.34	0.11	0.92
65R-3, 99–100	1405.79	2.96	24.66
65R-4, 0–1	1406.30	0.08	0.67
65R-4, 129–130	1407.59	3.96	32.99
65R-5, 0–1	1407.80	0.64	5.33
65R-5, 104–105	1408.84	0.42	3.50
65R-6, 4–5	1409.34	0.06	0.50
66R-1, 50–52	1411.80	0.09	0.75
66R-2, 0–1	1412.80	0.10	0.83
66R-2, 130–132	1414.10	2.27	18.91
66R-3, 44–45	1414.74	0.96	8.00
66R-4, 0–1	1415.80	2.26	18.83
66R-4, 141–142	1417.21	0.05	0.42
66R-5, 78–80	1418.08	0.12	1.00
67R-1, 21–22	1421.11	1.35	11.25
67R-2, 0–1	1422.40	0.17	1.42
67R-2, 42–43	1422.82	0.34	2.83
67R-3, 36–37	1424.26	0.06	0.50
67R-4, 0–1	1425.40	5.03	41.90
67R-5, 104–105	1427.94	4.94	41.15
67R-6, 91–92	1429.31	0.26	2.17
67R-7, 32–33	1429.72	0.37	3.08
68R-1, 17–18	1430.67	0.16	1.33
68R-2, 0–1	1432.00	0.10	0.83
68R-2, 137–141	1433.37	1.13	9.41
68R-3, 107–108	1434.57	6.14	51.15
68R-4, 26–27	1435.26	1.83	15.24
68R-5, 0–1	1436.50	0.07	0.58
68R-5, 135–136	1437.85	0.30	2.50
68R-6, 143–144	1439.43	0.44	3.67
68R-7, 24–25	1439.74	0.12	1.00
69R-1, 62–63	1440.42	0.40	3.33
69R-2, 123–125	1442.53	1.02	8.50
69R-3, 100–101	1443.80	0.34	2.83
69R-4, 0–1	1444.30	0.12	1.00
69R-4, 65–66	1444.95	0.87	7.25
69R-5, 93–94	1446.73	0.05	0.42
69R-6, 0–1	1447.30	0.39	3.25
69R-6, 55–56	1447.85	2.31	19.24
69R-CC, 14–15	1448.10	0.17	1.42
70R-1, 101–102	1450.51	0.38	3.17
70R-2, 85–86	1451.85	0.17	1.42
70R-3, 0–1	1452.50	2.83	23.57
70R-3, 122–123	1453.72	0.12	1.00
70R-4, 48–49	1454.48	0.09	0.75
70R-5, 62–63	1456.12	0.11	0.92
70R-6, 0–1	1457.00	0.15	1.25
70R-6, 45–46	1457.45	0.10	0.83
70R-7, 15–16	1458.05	0.13	1.08
71R-1, 26–27	1459.46	0.18	1.50
71R-2, 108–109	1461.78	0.08	0.67
71R-3, 0–1	1462.20	0.09	0.75
71R-3, 62–63	1462.82	0.08	0.67
71R-4, 33–34	1464.03	0.08	0.67
71R-5, 104–105	1466.24	0.06	0.50
71R-6, 20–21	1466.90	0.11	0.92
71R-7, 0–1	1467.91	0.11	0.92
71R-7, 49–50	1468.40	0.05	0.42
72R-1, 24–25	1469.14	0.13	1.08
72R-2, 0–1	1470.40	0.77	6.41
72R-2, 44–46	1470.84	0.24	2.00
72R-3, 79–80	1472.69	0.09	0.75
72R-4, 89–90	1474.29	0.09	0.75
72R-5, 78–79	1475.51	0.07	0.58
72R-5, 104–105	1475.77	3.18	26.49
72R-6, 0–1	1476.23	0.13	1.08
72R-6, 78–80	1477.01	0.06	0.50
73R-1, 111–112	1479.61	0.08	0.67
73R-2, 13–14	1480.13	0.06	0.50
73R-3, 0–1	1481.50	0.06	0.50
73R-3, 46–47	1481.96	0.07	0.58
73R-4, 31–32	1483.31	0.68	5.66
73R-5, 69–70	1485.19	0.16	1.33
73R-6, 0–1	1486.00	0.11	0.92
73R-6, 49–50	1486.49	0.09	0.75
74R-1, 70–71	1488.80	6.57	54.73
74R-2, 117–118	1490.77	0.12	1.00
74R-3, 0–1	1491.10	0.08	0.67
74R-3, 62–64	1491.72	0.57	4.75
74R-4, 0–1	1492.60	0.69	5.75
74R-4, 18–19	1492.78	0.94	7.83
74R-5, 21–22	1494.31	0.73	6.08
74R-5, 72–74	1494.82	9.16	76.30
75R-1, 127–128	1498.97	0.94	7.83
75R-2, 0–1	1499.20	0.94	7.83
75R-2, 87–91	1500.07	0.67	5.58
75R-3, 81–82	1501.51	0.08	0.67
75R-4, 0–1	1502.20	0.11	0.92
75R-6, 29–30	1505.49	6.44	53.65
75R-6, 62–63	1505.82	1.47	12.25
76R-1, 53–55	1507.83	1.99	16.58
76R-2, 0–1	1508.80	0.69	5.75
76R-2, 15–17	1508.95	0.67	5.58
76R-3, 45–46	1510.75	0.07	0.58
76R-3, 51–53	1510.81	0.88	7.33
76R-4, 0–1	1511.80	0.04	0.33
76R-4, 120–122	1513.00	8.84	73.64
76R-5, 13–15	1513.43	1.20	10.00
76R-6, 41–42	1515.21	0.08	0.67
76R-6, 66–68	1515.46	0.22	1.83
76R-7, 32–34	1516.40	0.48	4.00
77R-1, 97–98	1517.87	0.74	6.16
77R-2, 0–1	1518.40	1.05	8.75
77R-2, 21–23	1518.61	8.08	67.31
77R-2, 110–112	1519.50	0.27	2.25
77R-3, 69–71	1520.59	0.97	8.08
77R-4, 0–1	1521.40	1.07	8.91
77R-5, 71–73	1522.12	0.08	0.67
77R-4, 0–1	1523.61	0.20	1.67
77R-6, 38–39	1524.78	0.11	0.92
78R-1, 52–53	1527.02	0.88	7.33
78R-2, 3–5	1528.03	0.10	0.83

Table T16 (continued).

Core, section, interval (cm)	Depth (mbsf)	Inorganic carbon (wt%)	$CaCO_3$ (wt%)
78R-3, 0–1	1529.50	1.37	11.41
78R-3, 16–19	1529.66	0.06	0.50
78R-4, 58–59	1531.58	0.21	1.75
78R-5, 0–1	1532.50	0.68	5.66
78R-5, 45–47	1532.95	0.79	6.58
78R-5, 96–97	1533.46	0.10	0.83
79R-1, 27–28	1536.47	0.63	5.25
79R-2, 0–1	1537.70	1.04	8.66
79R-2, 103–104	1538.73	3.01	25.07
79R-3, 0–1	1539.20	0.05	0.42
79R-3, 97–98	1540.17	0.66	5.50
79R-4, 108–109	1541.78	1.15	9.58
79R-4, 131–132	1542.01	0.08	0.67
79R-5, 34–35	1542.54	1.13	9.41
79R-5, 67–68	1542.87	0.64	5.33
79R-3, 0–1	1543.99	0.27	2.25
80R-1, 29–30	1546.09	1.55	12.91
80R-2, 0–1	1547.30	1.04	8.66
80R-2, 70–72	1548.00	0.96	8.00
80R-3, 31–33	1549.11	1.31	10.91
80R-3, 104–106	1549.84	3.19	26.57
80R-3, 123–124	1550.03	0.12	1.00
80R-4, 0–1	1550.30	0.06	0.50
80R-4, 51–53	1550.81	1.40	11.66
80R-6, 29–31	1553.09	1.33	11.08
81R-1, 37–40	1555.77	0.08	0.67
81R-2, 0–1	1556.90	1.02	8.50
81R-2, 14–15	1557.04	7.55	62.89
81R-3, 3–4	1558.43	1.16	9.66
81R-3, 139–140	1559.79	0.74	6.16
81R-4, 120–122	1561.00	0.90	7.50
81R-5, 48–50	1561.71	0.88	7.33
81R-6, 67–68	1562.79	0.07	0.58
82R-1, 0–1	1565.00	2.82	23.49
82R-1, 6–9	1565.06	0.29	2.42
82R-1, 32–34	1565.32	2.96	24.66
82R-1, 64–65	1575.14	0.08	0.67
82R-2, 64–65	1576.64	3.53	29.41
82R-3, 67–68	1578.17	0.23	1.92
82R-3, 133–134	1578.83	6.56	54.65
83R-4, 0–1	1579.00	1.68	13.99
83R-4, 16–17	1579.16	0.44	3.67
83R-4, 42–43	1579.42	0.11	0.92
84R-1, 24–25	1584.44	0.90	7.50
84R-1, 105–106	1585.25	4.62	38.49
84R-2, 114–115	1586.84	0.79	6.58
84R-3, 0–1	1587.20	0.75	6.25
85R-1, 22–23	1587.92	0.65	5.42
85R-2, 60–61	1589.80	0.98	8.16
85R-3, 0–1	1590.70	0.92	7.66
85R-3, 71–72	1591.41	8.52	70.97
85R-4, 96–97	1592.41	0.52	4.33
85R-5, 35–39	1593.30	1.21	10.08
86R-1, 25–26	1595.05	1.23	10.25
86R-2, 23–24	1596.53	0.63	5.25
86R-3, 0–1	1597.80	0.42	3.50
86R-3, 16–17	1597.96	0.10	0.83
86R-4, 17–18	1599.47	0.98	8.16
86R-5, 19–20	1600.99	0.09	0.75
86R-6, 23–24	1602.03	0.16	1.33
87R-1, 58–60	1605.08	0.73	6.08
87R-2, 0–1	1606.00	0.07	0.58
87R-2, 100–101	1607.00	0.01	0.08
87R-2, 104–106	1607.04	0.61	5.08
87R-2, 118–120	1607.18	0.29	2.42
87R-2, 120–121	1607.20	0.29	2.42
87R-3, 136–138	1608.90	2.41	20.08
87R-5, 0–1	1610.58	0.93	7.75
87R-5, 6–8	1610.64	0.88	7.33
87R-5, 143–145	1612.01	1.18	9.83
88R-8, 96–97	1624.00	1.51	12.58
89R-1, 34–35	1623.94	1.65	13.75
89R-1, 35–36	1623.95	2.05	17.08
89R-1, 119–121	1624.79	0.06	0.50
89R-2, 0–1	1625.10	0.60	5.00
89R-2, 35–36	1625.45	0.07	0.58
89R-2, 36–37	1625.46	0.05	0.42
89R-3, 13–14	1626.73	1.20	10.00
89R-4, 3–4	1627.34	1.18	9.83
89R-4, 5–6	1627.36	1.10	9.16
89R-5, 0–1	1628.64	0.92	7.66
89R-5, 3–4	1628.67	0.63	5.25
89R-5, 6–7	1628.70	0.47	3.92
89R-6, 3–4	1630.17	0.88	7.33
89R-6, 5–6	1630.19	0.94	7.83
90R-1, 82–83	1634.12	0.12	1.00
90R-2, 84–85	1635.64	0.09	0.75
90R-3, 0–1	1636.27	0.07	0.58
90R-3, 87–88	1637.14	0.06	0.50
90R-4, 79–80	1638.56	1.37	11.41
90R-4, 104–108	1638.81	0.28	2.33
90R-5, 96–97	1640.23	0.05	0.42
90R-6, 0–1	1640.77	0.76	6.33
90R-6, 26–27	1641.03	1.53	12.75
90R-7, 21–22	1641.88	0.05	0.42
91R-1, 60–62	1643.40	1.85	15.41
91R-2, 0–1	1644.30	0.84	7.00
91R-2, 112–114	1645.42	0.06	0.50
91R-3, 74–76	1646.54	0.12	1.00
91R-4, 133–135	1648.63	3.55	29.57
91R-5, 0–1	1648.80	0.97	8.08
91R-5, 17–19	1648.97	5.91	49.23
92R-1, 23–25	1652.73	0.50	4.17
92R-1, 130–132	1653.80	0.92	7.66
92R-2, 24–25	1654.24	0.95	7.91
92R-3, 0–1	1655.50	0.89	7.41
92R-3, 21–22	1655.71	1.79	14.91
92R-4, 97–98	1657.97	0.78	6.50
92R-5, 0–1	1658.50	0.67	5.58
92R-5, 112–113	1659.62	0.19	1.58
92R-6, 126–129	1661.26	0.05	0.42
92R-CC, 46–47	1661.94	4.46	37.15
93R-1, 29–31	1662.39	0.12	1.00
93R-2, 0–1	1663.60	0.88	7.33
93R-2, 83–85	1664.43	0.04	0.33
93R-3, 65–68	1665.75	1.20	10.00
93R-3, 96–99	1666.06	0.53	4.42
93R-4, 0–1	1666.60	0.60	5.00
93R-4, 127–130	1667.87	0.08	0.67
93R-5, 115–117	1669.25	0.78	6.50
94R-1, 8–9	1671.88	0.68	5.66
94R-2, 14–15	1673.40	2.69	22.41
94R-3, 47–48	1675.12	2.86	23.82
94R-4, 0–1	1676.15	0.71	5.91
94R-4, 31–32	1676.46	1.95	16.24
94R-5, 36–37	1677.95	3.64	30.32
94R-5, 71–72	1678.30	0.35	2.92
94R-6, 0–1	1679.09	0.89	7.41
94R-6, 34–35	1679.43	1.20	10.00
94R-CC, 23–24	1680.13	0.99	8.25
95R-1, 78–79	1682.18	1.14	9.50
95R-2, 0–1	1682.56	1.32	11.00
95R-2, 77–78	1683.33	1.36	11.33
95R-3, 0–1	1684.06	1.33	11.08
95R-3, 78–80	1684.84	0.44	3.67
95R-4, 75–76	1686.31	1.45	12.08
95R-5, 43–44	1687.39	1.40	11.66
96R-1, 53–55	1691.43	2.72	22.66
96R-1, 132–133	1692.22	0.13	1.08
96R-2, 0–1	1692.33	0.49	4.08
96R-2, 99–101	1693.32	0.77	6.41
96R-3, 79–81	1694.66	0.71	5.91
96R-4, 44–46	1695.85	0.77	6.41
96R-5, 0–1	1696.95	0.75	6.25
97R-1, 96–102	1701.46	0.02	0.17
97R-2, 0–1	1702.00	0.72	6.00
97R-2, 145–146	1703.45	0.86	7.16
97R-3, 0–1	1703.50	0.83	6.91
97R-3, 135–136	1704.85	0.89	7.41
97R-4, 55–56	1705.55	0.15	1.25
97R-5, 10–11	1705.98	0.22	1.83
98R-1, 76–77	1710.86	0.12	1.00
98R-1, 98–99	1711.08	0.09	0.75
98R-3, 0–1	1713.01	0.15	1.25
98R-3, 45–46	1713.46	0.98	8.16
98R-3, 87–88	1713.88	1.50	12.50

Table T17. Carbon, nitrogen, and hydrogen results, Hole 1276A. (Continued on next three pages.)

Core, section, interval (cm)	Depth (mbsf)	Organic carbon (wt%)	Nitrogen (wt%)	Hydrogen (wt%)	C/N (atomic)
210-1276A-					
1W-2, 110–111	755.59	0.4	0.0	0.8	11.2
1W-5, 0–1	758.49	0.3	0.2	0.8	1.9
2R-1, 45–46	800.45	0.9	0.1	0.8	14.9
2R-1, 84–85	800.84	0.2	0.0	0.9	5.9
2R-2, 0–5	801.50	0.5	0.1	1.0	5.7
2R-3, 0–5	803.00	0.7	0.1	1.1	12.1
3R-3, 0–5	811.18	0.6	0.1	1.1	9.3
3R-3, 133–134	812.51	0.8	0.1	1.0	12.3
3R-4, 0–5	812.68	0.5	0.1	1.0	8.1
3R-7, 0–5	817.17	0.5	0.1	1.0	8.3
3R-8, 17–18	818.84	1.0	0.3	0.9	4.5
4R-2, 0–5	820.70	0.7	0.1	1.4	11.0
4R-3, 39–40	822.59	0.4	0.0	0.3	36.4
4R-3, 53–54	822.73	0.1	5.2	1.1	0.0
4R-4, 0–5	823.70	0.8	0.1	1.1	10.6
4R-4, 8–9	823.78	1.7	0.1	0.0	18.1
4R-5, 0–5	825.20	0.8	0.1	1.1	10.0
5R-2, 0–5	830.30	0.8	0.0	1.2	19.7
5R-4, 0–5	833.30	1.7	0.0	0.4	44.2
5R-4, 20–21	833.50	2.3	0.1	0.0	41.6
5R-4, 24–25	833.54	0.3	0.1	1.2	6.1
5R-6, 0–5	836.30	1.0	0.1	1.3	15.3
6R-2, 0–5	839.90	0.7	0.1	1.4	12.4
6R-3, 59–60	841.99	1.3	0.1	0.0	17.2
6R-4, 0–5	842.90	0.7	0.1	1.1	11.6
6R-6, 0–5	845.90	0.0	0.1	1.2	0.8
7R-1, 0–5	848.00	0.2	0.0	1.3	8.2
7R-4, 0–5	852.50	0.2	0.1	0.9	3.3
7R-4, 35–36	852.85	0.3	0.0	0.0	11.1
7R-6, 0–5	855.50	0.0	0.1	0.5	0.6
8R-2, 0–5	859.10	0.4	0.1	1.0	8.6
8R-4, 0–5	862.10	0.4	0.1	0.9	8.5
8R-5, 116–117	864.76	0.0	0.0	0.9	0.0
8R-6, 0–5	865.10	0.6	0.0	0.8	14.6
9R-1, 32–34	867.52	0.1	0.0	0.4	3.2
9R-2, 0–5	868.70	0.6	2.8	0.2	0.3
9R-2, 72–75	869.42	0.1	0.1	1.0	0.6
9R-4, 0–5	871.70	0.1	0.0	0.3	12.1
9R-6, 0–5	874.61	0.0	0.0	0.4	2.2
10R-1, 21–22	877.01	0.1	0.0	1.1	2.6
10R-2, 0–5	878.30	0.9	0.0	0.2	42.0
10R-4, 0–5	881.27	0.1	0.0	0.9	5.2
10R-4, 101–105	882.28	0.1	0.0	0.7	4.4
10R-4, 109–113	882.36	0.0	0.0	1.3	0.0
10R-6, 0–5	884.11	0.0	0.0	0.0	1.0
11R-2, 0–5	887.90	0.3	0.0	0.9	19.9
11R-3, 71–72	890.11	0.1	0.0	0.7	3.5
11R-4, 0–5	890.90	0.0	0.1	1.3	0.3
11R-4, 2–4	890.92	0.0	0.0	1.1	0.0
11R-4, 122–125	892.12	0.0	0.0	1.3	0.0
11R-6, 0–5	893.57	0.0	0.0	0.3	1.4
11R-6, 60–61	894.17	0.1	0.0	0.5	4.5
12R-2, 0–5	897.50	1.6	0.0	0.6	64.3
12R-3, 30–31	899.30	0.1	0.0	1.3	2.1
12R-3, 82–83	899.82	0.0	0.1	0.4	0.0
12R-4, 54–55	901.04	0.0	0.0	1.2	1.0
12R-4, 116–117	901.66	0.0	0.0	1.1	2.8
12R-5, 0–5	902.00	1.6	0.0	0.6	46.9
13R-2, 120–121	908.40	0.0	0.0	1.1	1.5
13R-2, 129–130	908.49	0.0	0.0	0.2	0.0
13R-3, 0–5	908.70	0.0	0.0	0.5	0.0
13R-3, 7–8	908.77	0.0	0.0	0.0	0.0
13R-3, 9–10	908.79	0.0	0.0	1.2	1.6
13R-4, 64–69	910.34	0.1	0.0	1.0	3.3
14R-1, 0–1	915.30	0.3	0.1	1.1	6.5
14R-1, 38–39	915.68	0.2	0.0	0.8	5.6
14R-2, 0–1	916.80	4.1	0.0	0.2	124.9
14R-3, 8–9	918.38	0.1	0.0	0.9	1.5
15R-1, 0–1	925.00	0.1	0.0	0.1	8.8
15R-2, 0–1	926.50	1.5	0.0	0.3	57.4
15R-3, 52–53	928.52	0.0	0.0	0.1	0.0
15R-4, 0–1	929.50	0.0	0.0	1.3	0.0
15R-5, 40–41	931.40	0.0	0.0	1.5	0.3
15R-5, 107–108	932.07	0.0	0.0	1.4	2.2
16R-1, 0–1	934.50	0.1	0.0	0.0	1.3
16R-1, 68–69	935.18	1.0	0.1	1.1	21.7
16R-1, 103–104	935.53	0.0	0.0	1.0	0.0
16R-2, 77–78	936.77	0.1	0.0	0.9	2.1
16R-2, 124–125	937.24	0.9	0.1	1.0	20.0
16R-3, 0–1	937.46	0.3	0.0	0.9	11.8
16R-3, 22–23	937.68	0.3	0.0	0.9	7.0
16R-3, 128–129	938.74	0.8	0.1	0.8	16.8
16R-4, 38–39	939.34	0.9	0.0	0.9	22.0
16R-4, 107–108	940.03	0.1	0.0	1.0	3.7
16R-5, 73–74	941.18	0.1	0.0	0.9	3.0
16R-5, 110–111	941.55	0.8	0.1	0.8	15.8
16R-6, 21–22	941.94	0.7	0.1	0.7	13.4
16R-CC, 9–10	942.32	0.2	0.1	0.9	4.3
17R-1, 47–48	944.57	0.9	0.1	1.0	16.6
17R-1, 77–78	944.87	0.3	0.0	0.7	10.7
17R-1, 108–109	945.18	0.1	0.0	1.0	2.6
17R-2, 0–1	945.36	0.8	0.1	0.9	19.7
17R-2, 46–47	945.82	0.8	0.0	0.7	19.3
17R-2, 73–74	946.09	0.1	0.0	0.8	4.7
17R-3, 23–24	947.11	0.6	0.0	0.7	16.2
17R-4, 21–25	948.12	0.0	0.0	0.4	0.0
17R-4, 106–107	948.97	0.4	0.0	0.7	14.0
17R-5, 39–40	949.81	0.6	0.0	0.6	19.0
17R-6, 25–26	951.18	0.2	0.0	0.8	6.8
17R-6, 69–70	951.62	0.7	0.1	0.5	17.2
17R-7, 0–1	952.31	0.4	0.0	0.5	20.9
17R-7, 24–28	952.55	0.6	0.0	0.4	16.2
18R-1, 0–1	953.80	0.5	0.0	0.5	29.6
18R-1, 31–35	954.11	0.4	0.0	0.6	15.1
18R-1, 125–126	955.05	0.2	0.0	0.6	8.8
18R-2, 99–100	956.18	0.5	0.1	0.6	12.1
18R-3, 1–2	956.45	0.8	0.1	0.8	18.6
18R-3, 9–10	956.53	0.6	0.0	0.6	17.1
18R-4, 4–5	957.98	0.9	0.1	0.6	19.9
18R-4, 54–55	958.48	0.4	0.0	0.5	15.1
18R-5, 0–1	959.12	0.4	0.0	0.6	24.6
18R-5, 17–18	959.29	0.6	0.0	0.5	15.1
18R-6, 56–57	960.99	0.5	0.0	0.3	24.5
18R-6, 129–130	961.72	0.6	0.0	0.5	15.6
18R-7, 97–101	962.90	0.4	0.0	0.4	13.9
18R-7, 139–140	963.32	1.0	0.1	0.8	19.0
19R-3, 0–1	966.39	0.1	0.0	1.2	5.5
19R-3, 122–123	967.61	0.1	0.0	1.3	1.7
19R-5, 0–1	969.17	0.1	0.0	1.2	8.4
19R-5, 100–101	970.17	0.2	0.0	0.4	8.9
20R-1, 0–1	973.10	0.7	0.1	0.9	15.0
20R-1, 23–24	973.33	0.1	0.0	0.8	2.8
20R-1, 114–115	974.24	0.1	0.0	0.8	3.5
20R-2, 50–51	974.95	0.4	0.0	1.0	11.2
20R-3, 29–31	976.13	0.0	0.0	1.0	1.6
20R-3, 90–92	976.74	0.0	0.0	1.3	0.7
20R-4, 0–1	977.21	0.1	0.0	1.3	1.9
20R-5, 62–64	979.33	0.3	0.0	0.1	21.1
20R-5, 133–135	980.04	0.8	0.1	1.2	12.4
20R-7, 59–62	982.21	0.9	0.1	1.2	13.8
20R-7, 106–107	982.68	0.9	0.1	1.3	19.0
21R-1, 53–54	983.23	0.9	0.1	1.0	14.6
21R-2, 123–124	985.19	6.7	0.0	0.5	
21R-3, 0–1	985.46	0.4	0.0	0.5	12.0
21R-4, 0–1	986.96	0.5	0.0	0.9	23.2

Table T17 (continued).

Core, section, interval (cm)	Depth (mbsf)	Organic carbon (wt%)	Nitrogen (wt%)	Hydrogen (wt%)	C/N (atomic)
21R-4, 25–26	987.21	0.1	0.0	1.2	1.9
21R-4, 63–64	987.59	0.0	0.0	1.0	0.4
22R-3, 0–1	995.40	0.0	0.0	1.4	0.0
22R-3, 72–73	996.12	1.1	0.0	1.2	67.9
23R-1, 70–71	1002.70	0.7	0.1	0.3	10.5
23R-2, 0–5	1003.39	0.1	0.0	1.2	2.0
23R-3, 68–72	1005.52	0.1	0.0	1.4	5.8
23R-4, 10–11	1006.04	0.0	0.0	1.2	0.2
23R-4, 57–58	1006.51	0.5	0.0	0.3	35.3
24R-1, 51–54	1012.11	0.2	0.0	0.4	6.1
24R-2, 0–1	1013.10	0.4	0.0	0.2	47.4
24R-3, 80–84	1015.40	0.1	0.0	0.6	3.7
24R-4, 0–1	1016.10	0.0	0.0	1.3	0.7
25R-2, 0–1	1022.70	0.4	0.0	0.7	15.9
25R-2, 1–6	1022.71	0.1	0.0	0.6	4.5
25R-3, 1–2	1024.21	0.1	0.0	0.1	7.9
25R-4, 0–1	1025.70	0.6	0.0	0.2	36.7
25R-7, 24–30	1029.94	0.0	0.0	0.8	0.0
26R-1, 23–24	1031.03	0.0	0.0	0.9	0.1
26R-2, 0–1	1032.26	0.0	0.0	0.9	0.0
26R-2, 40–45	1032.66	0.0	0.1	0.8	0.0
27R-1, 0–1	1040.50	0.0	0.0	0.6	0.0
27R-3, 0–1	1043.41	0.0	0.0	0.7	0.0
27R-4, 29–31	1045.20	0.3	0.0	0.7	9.6
27R-5, 70–72	1047.11	0.0	0.4	0.5	0.0
28R-1, 0–1	1050.10	0.0	0.0	0.8	0.0
28R-2, 40–41	1052.00	0.3	0.0	0.9	7.4
28R-3, 0–1	1052.91	0.0	0.0	0.4	0.0
28R-4, 141–142	1055.67	0.3	0.0	0.5	9.4
28R-5, 19–20	1055.89	0.0	0.0	0.7	0.0
29R-1, 0–1	1059.70	0.0	0.0	0.5	0.0
29R-2, 36–38	1061.50	0.2	0.0	0.3	8.2
29R-3, 0–1	1062.53	0.0	0.0	1.0	0.7
29R-5, 11–12	1065.64	0.0	0.0	0.5	0.0
30R-1, 0–1	1069.40	0.1	0.0	0.4	6.5
30R-3, 0–1	1072.13	0.3	0.0	0.5	9.7
30R-4, 47–48	1074.10	6.6	0.3	1.5	22.7
30R-4, 78–79	1074.41	0.4	0.1	1.0	8.8
30R-4, 115–116	1074.78	1.2	0.1	1.0	16.4
30R-4, 128–129	1074.91	0.0	0.1	1.1	0.1
31R-1, 0–1	1079.00	0.5	0.0	0.5	13.6
31R-2, 15–18	1080.65	0.0	0.0	0.8	0.0
31R-2, 124–128	1081.74	3.7	0.2	1.0	27.2
31R-3, 51–52	1082.46	7.1	0.3	1.5	32.6
31R-4, 0–1	1083.39	0.0	0.0	0.4	0.0
31R-4, 48–49	1083.87	0.0	0.2	1.3	0.0
31R-5, 97–98	1085.86	0.0	4.2	0.5	0.0
31R-6, 32–33	1086.25	0.4	0.0	0.5	14.4
32R-1, 0–1	1088.60	0.8	0.0	0.1	36.2
32R-2, 83–84	1090.93	1.1	0.0	0.3	26.7
32R-4, 0–1	1092.97	0.0	0.0	1.4	0.1
32R-4, 57–58	1093.54	0.4	0.2	0.4	2.4
32R-5, 23–27	1094.65	1.3	0.1	0.3	27.8
32R-5, 45–46	1094.87	3.0	0.1	0.9	34.3
32R-7, 30–31	1097.72	0.6	0.0	0.9	21.2
33R-1, 0–1	1098.20	0.5	0.1	0.8	11.1
33R-3, 91–95	1102.11	4.0	0.1	0.3	75.0
33R-4, 0–1	1102.70	0.9	0.0	0.5	21.8
33R-4, 133–137	1104.03	1.0	0.0	0.8	47.7
33R-CC, 46–47	1108.22	4.1	0.2	1.0	24.2
34R-2, 94–98	1110.11	0.0	0.0	0.7	0.0
34R-2, 102–106	1110.19	9.4	0.1	0.4	136.8
34R-4, 0–1	1112.13	0.8	0.0	0.3	33.8
35R-2, 0–1	1118.90	0.7	0.0	0.5	27.5
35R-3, 107–111	1121.47	0.1	0.0	0.7	4.9
35R-4, 64–65	1122.39	2.8	0.1	1.0	28.1
35R-5, 0–1	1123.25	0.8	0.0	0.6	21.1
35R-6, 31–32	1124.86	0.1	0.2	0.3	0.5
35R-6, 57–61	1125.12	0.0	0.0	0.6	0.6
36R-4, 0–1	1131.34	0.2	0.0	0.4	6.9
36R-5, 0–1	1132.63	0.2	0.0	0.4	4.7
36R-5, 103–105	1133.66	0.0	0.0	0.6	0.0
36R-6, 62–66	1134.75	0.0	0.0	1.0	0.6
36R-6, 82–86	1134.95	0.0	0.0	0.6	0.0
37R-2, 0–1	1137.77	0.4	0.0	1.0	9.3
37R-3, 45–46	1139.61	0.1	0.1	1.1	1.6
37R-4, 0–1	1140.51	1.1	0.1	0.8	22.0
37R-5, 53–54	1142.18	0.6	0.1	1.2	12.1
38R-3, 0–1	1148.59	0.3	0.0	0.7	9.8
38R-5, 96–98	1152.40	0.0	0.0	0.1	0.0
38R-6, 0–1	1152.82	0.5	0.0	0.8	12.4
38R-6, 96–98	1153.78	0.0	0.0	0.3	0.0
39R-1, 32–33	1155.52	0.2	0.1	1.0	5.5
39R-3, 0	1158.23	0.3	0.1	1.0	5.6
39R-3, 92–93	1159.15	0.0	0.0	0.1	0.0
39R-4, 0–1	1159.71	1.8	0.1	0.8	32.9
39R-6, 21–22	1162.96	0.3	0.0	1.0	6.4
40R-2, 0–1	1166.33	0.6	0.1	1.1	11.5
40R-2, 50–52	1166.83	0.2	0.1	0.8	4.3
40R-2, 80–83	1167.13	1.5	0.1	0.6	20.6
40R-4, 0–1	1169.36	0.8	0.0	1.1	20.7
40R-CC, 0–1	1174.29	0.5	0.1	0.9	10.0
41R-1, 113–117	1175.53	0.5	0.0	0.2	16.3
41R-1, 146–147	1175.86	0.8	0.1	0.9	14.5
41R-2, 0–1	1175.90	1.5	0.1	1.0	31.0
41R-4, 0–1	1178.97	0.6	0.0	0.9	16.3
41R-6, 79–84	1182.84	0.4	0.0	0.4	9.5
41R-CC, 19–20	1184.15	0.2	0.1	1.0	4.3
42R-1, 4–8	1184.04	0.7	0.1	1.1	15.6
42R-4, 0–1	1188.16	0.4	0.0	0.9	10.6
42R-6, 0–1	1191.20	1.1	0.1	0.9	23.2
42R-6, 39–43	1191.59	1.4	0.1	0.7	29.2
42R-CC, 26–27	1194.51	0.0	0.1	1.0	0.8
43R-2, 88–92	1195.91	2.6	0.1	0.8	27.5
43R-3, 0–1	1196.55	0.6	0.1	1.0	13.3
43R-3, 31–32	1196.86	2.3	0.0	0.7	
43R-4, 146–147	1199.41	1.8	0.1	0.7	33.1
43R-6, 0–1	1201.00	0.4	0.0	1.0	9.4
43R-CC, 4–5	1202.34	1.5	0.1	1.1	21.9
44R-1, 0–1	1203.20	1.1	0.1	0.5	19.7
44R-3, 0–1	1206.20	0.3	0.0	0.2	19.8
44R-4, 60–62	1208.34	0.5	0.0	0.5	14.5
44R-7, 61–63	1212.97	2.4	0.1	1.0	21.8
45R-2, 0–1	1214.33	0.3	0.0	0.8	22.8
45R-2, 25–26	1214.58	0.5	0.1	0.7	7.9
45R-3, 53–54	1216.39	2.0	0.1	0.6	26.7
45R-5, 0–1	1218.92	0.5	0.0	0.8	13.6
45R-5, 45–46	1219.37	0.8	0.0	0.8	22.6
46R-1, 146–147	1223.86	0.3	0.0	1.1	7.9
46R-4, 0–1	1226.99	0.4	0.1	1.1	7.7
46R-5, 105–106	1229.58	0.3	0.0	0.7	10.5
46R-7, 15–16	1231.26	0.5	0.0	0.9	11.2
47R-2, 0–1	1233.53	0.5	0.1	1.1	9.3
47R-2, 64–66	1234.17	0.4	0.0	0.5	15.9
47R-4, 0–1	1236.57	0.6	0.1	1.0	13.7
47R-7, 31–33	1241.29	0.7	0.1	0.9	16.2
48R-2, 0–1	1243.24	0.6	0.1	1.1	10.6
48R-2, 89–90	1244.13	0.5	0.0	0.7	15.3
48R-4, 0–1	1246.32	0.6	0.0	1.1	14.8
48R-4, 44–45	1246.76	0.3	0.0	0.2	19.4
49R-2, 6–11	1252.96	0.7	0.0	0.8	17.7
49R-3, 0–1	1254.40	0.6	0.0	0.3	20.1
49R-4, 0–1	1255.90	0.7	0.1	1.2	14.9
49R-4, 67–72	1256.57	0.2	0.0	0.2	15.2
50R-3, 0–1	1264.00	1.0	0.1	1.2	18.9
50R-4, 18–22	1265.68	0.8	0.0	0.4	31.1

Table T17 (continued).

Core, section, interval (cm)	Depth (mbsf)	Organic carbon (wt%)	Nitrogen (wt%)	Hydrogen (wt%)	C/N (atomic)
50R-5, 0–1	1267.00	0.9	0.1	1.2	17.4
50R-6, 60–65	1268.58	1.3	0.1	0.8	27.6
51R-1, 58–60	1271.28	1.0	0.0	0.7	22.9
51R-2, 0–1	1272.20	0.9	0.0	0.1	49.0
51R-3, 0–1	1273.70	0.7	0.1	1.0	13.9
51R-6, 25–27	1278.45	0.8	0.1	0.9	17.6
52R-2, 0–1	1281.90	0.9	0.1	1.0	16.3
52R-2, 36–37	1282.26	0.9	0.0	0.9	20.7
52R-5, 0–1	1286.40	0.6	0.1	1.0	12.2
52R-6, 97–98	1288.87	0.7	0.0	0.6	24.6
52R-7, 57–58	1289.97	0.7	0.1	0.9	15.7
53R-2, 47–49	1291.97	0.7	0.1	0.8	14.9
53R-2, 120–121	1292.70	1.8	0.1	1.1	28.5
53R-3, 131–132	1294.31	1.0	0.1	1.0	14.6
53R-4, 54–56	1294.98	1.0	0.1	0.9	20.4
53R-5, 107–108	1297.01	1.9	0.0	0.7	47.1
54R-2, 0–1	1301.10	0.9	0.1	1.0	17.0
54R-3, 0–1	1302.60	0.9	0.1	0.7	19.4
54R-4, 70–71	1304.80	0.4	0.0	0.8	10.9
54R-4, 120–121	1305.30	0.8	0.0	0.7	20.1
55R-2, 0–1	1310.70	3.8	0.1	0.8	38.0
55R-2, 10–13	1310.80	0.9	0.1	0.6	19.9
56R-1, 118–120	1319.98	0.5	0.0	0.7	12.8
56R-2, 0–1	1320.30	0.4	0.1	1.0	9.6
56R-2, 109–110	1321.39	0.9	0.0	0.5	32.8
57R-1, 4–5	1328.54	1.0	0.0	0.7	27.2
57R-2, 0–1	1330.00	0.8	0.1	1.1	12.9
57R-2, 38–39	1330.38	0.6	0.1	0.9	13.5
58R-2, 0–1	1339.60	1.4	0.1	0.9	31.4
58R-3, 68–72	1341.78	0.6	0.1	1.0	12.0
58R-CC, 22–23	1343.24	0.9	0.0	1.1	22.1
59R-1, 134–135	1345.44	1.9	0.1	1.1	31.9
59R-2, 0–1	1345.60	0.1	0.1	1.0	1.7
59R-4, 103–107	1349.63	0.5	0.0	1.0	13.3
59R-6, 0–1	1351.62	0.4	0.0	0.9	10.1
59R-6, 10–11	1351.72	0.0	0.0	1.1	0.0
60R-1, 18–19	1353.88	1.6	0.1	1.0	23.4
60R-2, 0–1	1355.20	0.6	0.1	1.1	14.0
60R-2, 52–54	1355.72	0.6	0.1	1.0	14.2
60R-3, 40–42	1357.10	2.2	0.1	0.8	23.6
60R-4, 0–1	1358.10	0.7	0.1	1.2	16.3
61R-2, 0–1	1364.70	0.5	0.1	1.1	12.8
61R-4, 119–120	1368.89	0.3	0.0	0.9	8.5
61R-7, 52–53	1372.62	0.5	0.0	1.1	12.1
62R-2, 0–1	1374.40	0.5	0.1	1.1	10.5
62R-3, 78–79	1376.68	0.5	0.1	0.9	9.6
62R-5, 0–1	1378.90	0.7	0.1	1.0	15.1
63R-1, 135–136	1383.85	0.6	0.1	0.9	13.5
63R-2, 0–1	1384.00	0.4	0.1	1.0	10.0
63R-5, 0–1	1388.50	0.7	0.1	1.2	15.7
64R-2, 0–1	1393.70	0.8	0.1	1.2	15.8
64R-5, 0–1	1398.20	0.3	0.0	0.2	19.5
64R-5, 44–45	1398.64	0.3	0.0	0.8	8.8
65R-3, 99–100	1405.79	2.2	0.1	0.9	23.9
65R-4, 0–1	1406.30	0.8	0.1	1.2	15.9
65R-5, 0–1	1407.80	1.8	0.1	1.1	33.3
66R-2, 0–1	1412.80	0.7	0.1	1.1	14.6
66R-3, 44–45	1414.74	1.5	0.1	0.9	22.3
66R-4, 0–1	1415.80	0.3	0.0	0.9	8.1
67R-2, 0–1	1422.40	0.5	0.1	1.1	10.3
67R-3, 36–37	1424.26	0.4	0.1	0.8	8.2
67R-4, 0–1	1425.40	1.2	0.0	0.5	35.6
68R-2, 0–1	1432.00	0.9	0.1	1.1	16.0
68R-2, 137–141	1433.37	0.9	0.1	0.7	17.8
68R-5, 0–1	1436.50	0.5	0.1	1.1	10.9
69R-4, 0–1	1444.30	0.7	0.1	1.1	13.4
69R-6, 0–1	1447.30	0.8	0.1	1.1	14.7
69R-6, 55–56	1447.85	1.9	0.1	0.8	22.8
69R-CC, 14–15	1448.10	0.7	0.1	1.1	14.3
70R-3, 0–1	1452.50	0.3	0.0	0.3	9.9
70R-4, 48–49	1454.48	0.7	0.1	0.9	12.2
70R-6, 0–1	1457.00	1.0	0.1	1.0	16.1
71R-3, 0–1	1462.20	0.6	0.1	0.9	11.0
71R-6, 20–21	1466.90	0.6	0.1	0.9	9.5
71R-7, 0–1	1467.91	0.8	0.1	0.9	12.9
72R-2, 0–1	1470.40	1.1	0.1	0.8	18.7
72R-5, 78–79	1475.51	3.1	0.2	1.2	21.7
72R-6, 0–1	1476.23	1.0	0.1	0.9	15.5
73R-3, 0–1	1481.50	2.2	0.1	1.1	21.6
73R-3, 46–47	1481.96	2.7	0.1	1.0	22.0
73R-6, 0–1	1486.00	0.6	0.1	1.1	14.0
73R-6, 49–50	1486.49	0.9	0.1	0.9	17.0
74R-2, 117–118	1490.77	1.4	0.1	1.0	19.4
74R-3, 0–1	1491.10	1.2	0.1	1.1	18.2
74R-4, 0–1	1492.60	0.7	0.1	0.9	13.1
75R-2, 0–1	1499.20	0.8	0.1	0.8	9.9
75R-2, 87–91	1500.07	0.8	0.1	0.8	13.5
75R-4, 0–1	1502.20	0.6	0.1	0.9	10.2
76R-2, 0–1	1508.80	0.8	0.1	0.8	13.1
76R-2, 15–17	1508.95	0.7	0.1	0.7	15.0
76R-3, 45–46	1510.75	0.3	0.1	0.7	6.1
76R-4, 0–1	1511.80	0.5	0.1	1.0	8.7
76R-6, 41–42	1515.21	0.9	0.1	0.9	14.3
77R-2, 0–1	1518.40	0.9	0.1	0.6	16.6
77R-2, 110–112	1519.50	1.1	0.1	0.8	21.4
77R-4, 0–1	1521.40	0.7	0.1	0.8	12.0
77R-6, 38–39	1524.78	1.2	0.1	0.8	21.1
78R-1, 52–53	1527.02	1.2	0.1	0.8	20.5
78R-3, 0–1	1529.50	0.3	0.1	1.1	5.6
78R-4, 58–59	1531.58	1.5	0.1	0.9	22.2
78R-5, 0–1	1532.50	0.5	0.1	0.8	7.5
78R-5, 96–97	1533.46	1.3	0.1	0.9	23.9
79R-2, 0–1	1537.70	1.0	0.1	0.8	14.8
79R-3, 0–1	1539.20	0.3	0.1	0.8	4.6
79R-4, 131–132	1542.01	1.0	0.1	0.9	19.9
80R-1, 29–30	1546.09	0.3	0.1	1.0	7.5
80R-2, 0–1	1547.30	0.8	0.1	0.8	12.9
80R-2, 70–72	1548.00	0.8	0.1	0.8	13.7
80R-3, 123–124	1550.03	1.1	0.1	0.9	16.5
80R-4, 0–1	1550.30	0.4	0.1	0.9	7.6
81R-1, 37–40	1555.77	1.3	0.1	0.9	24.2
81R-2, 0–1	1556.90	0.9	0.1	0.9	14.0
81R-3, 139–140	1559.79	1.0	0.1	0.9	14.4
82R-1, 0–1	1565.00	0.5	0.0	0.2	30.7
82R-1, 6–9	1565.06	0.4	0.0	0.8	8.4
82R-1, 64–65	1575.14	0.8	0.1	0.9	15.3
83R-4, 0–1	1579.00	1.1	0.1	0.5	23.7
83R-4, 16–17	1579.16	0.8	0.1	0.8	12.0
83R-4, 42–43	1579.42	2.0	0.1	1.0	22.8
84R-2, 114–115	1586.84	1.1	0.1	0.8	17.9
84R-3, 0–1	1587.20	0.9	0.1	0.8	14.1
85R-2, 60–61	1589.80	1.0	0.1	0.8	17.2
85R-3, 0–1	1590.70	1.0	0.1	0.9	16.5
86R-3, 0–1	1597.80	0.6	0.1	0.8	12.3
86R-6, 23–24	1602.03	2.6	0.1	0.7	42.6
87R-2, 0–1	1606.00	0.5	0.1	0.8	9.8
87R-2, 100–101	1607.00	0.5	0.1	0.9	8.6
87R-5, 0–1	1610.58	1.2	0.1	0.8	15.3
88R-8, 96–97	1624.00	1.1	0.1	0.7	21.8
89R-2, 0–1	1625.10	1.3	0.1	0.9	20.9
89R-2, 36–37	1625.46	0.3	0.1	0.9	5.2
89R-3, 13–14	1626.73	1.1	0.1	0.8	18.5
89R-5, 0–1	1628.64	0.9	0.1	0.9	17.9
90R-3, 0–1	1636.27	1.3	0.1	1.0	21.4
90R-6, 0–1	1640.77	1.4	0.1	0.9	22.9
90R-6, 26–27	1641.03	1.4	0.1	0.8	33.8

Table T17 (continued).

Core, section, interval (cm)	Depth (mbsf)	Organic carbon (wt%)	Nitrogen (wt%)	Hydrogen (wt%)	C/N (atomic)
91R-2, 0–1	1644.30	1.4	0.1	0.8	22.7
91R-2, 112–114	1645.42	0.2	0.1	0.9	5.6
91R-5, 0–1	1648.80	1.1	0.1	0.6	24.8
92R-1, 130–132	1653.80	1.5	0.1	0.9	21.3
92R-3, 0–1	1655.50	1.5	0.1	0.7	30.0
92R-5, 0–1	1658.50	1.4	0.1	0.9	23.9
92R-6, 126–129	1661.26	2.2	0.0	1.2	56.9
93R-2, 0–1	1663.60	1.3	0.1	0.8	22.2
93R-4, 0–1	1666.60	1.6	0.1	0.8	27.2
93R-5, 115–117	1669.25	1.7	0.1	0.9	24.8
94R-1, 8–9	1671.88	2.0	0.1	0.9	28.2
94R-4, 0–1	1676.15	1.7	0.1	0.8	22.2
94R-4, 31–32	1676.46	7.1	0.2	1.5	37.9
94R-5, 36–37	1677.95	5.9	0.2	1.1	38.5
94R-5, 71–72	1678.30	2.0	0.1	0.7	32.6
94R-6, 0–1	1679.09	1.7	0.1	0.8	24.3
94R-CC, 23–24	1680.13	1.4	0.1	0.9	21.0
95R-1, 78–79	1682.18	1.4	0.1	0.9	20.5
95R-2, 0–1	1682.56	1.2	0.1	0.8	16.1
95R-2, 77–78	1683.33	1.3	0.1	0.9	19.3
95R-3, 0–1	1684.06	1.3	0.1	0.8	18.6
95R-5, 43–44	1687.39	1.2	0.1	0.8	17.8
96R-1, 132–133	1692.22	0.5	0.1	0.8	12.0
96R-2, 0–1	1692.33	1.2	0.1	0.8	15.3
96R-5, 0–1	1696.95	1.4	0.1	0.7	16.8
97R-1, 96–102	1701.46	0.6	0.1	0.5	12.1
97R-2, 0–1	1702.00	0.1	0.1	0.6	1.3
97R-3, 0–1	1703.50	1.3	0.1	0.5	19.0
97R-4, 55–56	1705.55	2.3	0.1	0.5	26.4
98R-3, 0–1	1713.01	0.2	0.0	0.1	13.5

Table T18. Organic carbon and Rock-Eval pyrolysis results, Hole 1276A. (See table notes. Continued on next two pages.)

Core, section, interval (cm)	Depth (mbsf)	TOC (wt%)	S_1 (mg HC/g)	S_2 (mg HC/g)	T_{max} (°C)	PI	HI (mg HC/g TOC)
210-1276A-							
2R-2, 0–5	801.50	0.5	0.2	0.1	428	0.5	31
2R-3, 0–5	803.00	0.7	0.3	0.3	554	0.5	41
3R-3, 0–5	811.18	0.6	0.2	1.5	526	0.1	257
3R-4, 0–5	812.68	0.5	0.4	0.4	575	0.5	74
3R-7, 0–5	817.17	0.5	0.1	0.1	419	0.7	10
4R-2, 0–5	820.70	0.7					
4R-4, 0–5	823.70	0.8					
4R-5, 0–5	825.20	0.8					
5R-2, 0–5	830.30	0.8					
5R-4, 0–5	833.30	1.7	0.1	0.2	438	0.3	10
5R-6, 0–5	836.30	1.0	0.2	0.6	439	0.2	66
6R-2, 0–5	839.90	0.7	0.0	0.0	443	0.7	0
6R-4, 0–5	842.90	0.7	0.1	0.2	438	0.3	21
6R-6, 0–5	845.90	0.0	0.0	0.4	603	0.1	866
7R-1, 0–5	848.00	0.2	0.0			1.0	0
7R-4, 0–5	852.50	0.2	0.1	0.1	426	0.5	52
7R-6, 0–5	855.50	0.0	0.1	0.2	443	0.4	452
8R-2, 0–5	859.10	0.4	0.1	0.1	429	0.4	23
8R-4, 0–5	862.10	0.4	0.1	0.1	429	0.4	20
8R-6, 0–5	865.10	0.6	0.0	0.0	462	0.4	6
9R-2, 0–5	868.70	0.6	0.2	0.0	373	0.8	5
9R-4, 0–5	871.70	0.1	0.0	0.0	370	0.9	2
9R-6, 0–5	874.61	0.0	0.2	0.0		0.9	47
10R-2, 0–5	878.30	0.9	0.2	0.0	428	1.0	0
10R-4, 0–5	881.27	0.1	0.0			1.0	
10R-6, 0–5	884.11	0.0	0.0	0.0		0.7	11
11R-2, 0–5	887.90	0.3	0.1	0.0	508	0.9	3
11R-4, 0–5	890.90	0.0	0.0			1.0	
12R-2, 0–5	897.50	1.6	0.1	0.0		0.6	2
12R-5, 0–5	902.00	1.6	0.0	0.0		0.8	0
13R-3, 0–5	908.70	0.0	0.0			1.0	
13R-4, 64–69	910.34	0.1	0.0	0.0	471	0.5	39
14R-1, 0–1	915.30	0.3	0.1	0.1	431	0.4	38
14R-2, 0–1	916.80	4.1	0.0	0.1	452	0.3	2
15R-2, 0–1	926.50	1.5	0.0	0.0	393	0.7	1
15R-4, 0–1	929.50	0.0	0.0			1.0	
16R-1, 0–1	934.50	0.1	0.0	0.0		0.5	10
16R-3, 0–1	937.46	0.3	0.0			1.0	
16R-CC, 9–10	942.32	0.2	0.1	0.2	445	0.4	116
17R-2, 0–1	945.36	0.8	0.0	0.3	446	0.1	32
17R-7, 0–1	952.31	0.4	0.0	0.0	442	0.7	4
18R-1, 0–1	953.80	0.5	0.5	0.2	444	0.7	32
18R-5, 0–1	959.12	0.4	0.2	0.1	443	0.7	19
19R-3, 0–1	966.39	0.1	0.1	0.0		0.7	42
19R-5, 0–1	969.17	0.1	0.0	0.0		0.8	4
20R-1, 0–1	973.10	0.7	0.1	0.0		0.7	4
20R-4, 0–1	977.21	0.1	0.1	0.0		0.7	50
21R-3, 0–1	985.46	0.4	0.0	0.0		0.7	3
21R-4, 0–1	986.96	0.5	0.0	0.0		0.7	3
22R-3, 0–1	995.40	0.0	0.1	0.0	590	0.7	
23R-2, 0–5	1003.39	0.1	0.0	0.0	474	0.7	22
24R-2, 0–1	1013.10	0.4	0.1	0.0	407	0.8	3
24R-4, 0–1	1016.10	0.0	0.1	0.1	504	0.6	173
25R-2, 0–1	1022.70	0.4	0.0	0.0	443	0.8	2
25R-4, 0–1	1025.70	0.6	0.0	0.0	401	0.6	4
26R-2, 0–1	1032.26	0.0	0.0	0.0	492	0.5	
27R-1, 0–1	1040.50	0.0	0.0			1.0	
27R-3, 0–1	1043.41	0.0	0.1	0.1	522	0.4	
28R-1, 0–1	1050.10	0.0	0.0	0.0	579	0.5	
28R-3, 0–1	1052.91	0.0	0.0	0.1	586	0.4	
29R-1, 0–1	1059.70	0.0	0.0	0.0	360	0.9	
29R-3, 0–1	1062.53	0.0	0.0	0.1	513	0.2	433
30R-1, 0–1	1069.40	0.1	0.0	0.0	430	0.4	9
30R-3, 0–1	1072.13	0.3	0.0	0.0	427	0.3	17
30R-4, 47–48	1074.10	6.6	0.7	15.2	447	0.0	231
31R-1, 0–1	1079.00	0.5	0.1	0.3	455	0.2	49
31R-2, 124–128	1081.74	3.7	1.2	16.7	449	0.1	452

Table T18 (continued).

Core, section, interval (cm)	Depth (mbsf)	TOC (wt%)	S_1 (mg HC/g)	S_2 (mg HC/g)	T_{max} (°C)	PI	HI (mg HC/g TOC)
31R-4, 0–1	1083.39	0.0	0.0	0.0	505	0.4	
32R-1, 0–1	1088.60	7.1	0.0	0.1	461	0.2	2
32R-4, 0–1	1092.97	0.0	0.0	0.1	600	0.2	6950
33R-1, 0–1	1098.20	0.5	0.1	0.1	432	0.5	13
33R-3, 91–95	1102.11	4.0	0.2	3.2	453	0.0	81
33R-4, 0–1	1102.70	0.9	0.1	0.1	447	0.5	8
33R-CC, 46–47	1108.22	4.1	0.6	7.6	452	0.1	187
34R-2, 102–106	1110.19	9.4	0.1	2.9	456	0.0	31
34R-4, 0–1	1112.13	0.8	0.0	0.0	387	1.0	0
35R-2, 0–1	1118.90	0.7	0.0	0.0	388	0.9	1
35R-5, 0–1	1123.25	0.8	0.0	0.1	456	0.2	11
36R-4, 0–1	1131.34	0.2	0.1	0.0	465	0.9	5
36R-5, 0–1	1132.63	0.2	0.0	0.0	372	0.9	2
37R-2, 0–1	1137.77	0.4	0.1	0.0	394	0.8	7
37R-4, 0–1	1140.51	1.1	0.1	0.1	494	0.4	10
38R-3, 0–1	1148.59	0.3	0.0	0.0	428	0.5	7
38R-6, 0–1	1152.82	0.5	0.1	0.0	451	0.6	9
39R-3, 0–1	1158.23	0.3	0.1	0.1	577	0.4	33
39R-4, 0–1	1159.71	1.8	0.0	0.2	456	0.2	13
40R-2, 0–1	1166.33	0.6	0.1	0.0	466	0.7	5
40R-4, 0–1	1169.36	0.8	0.1	0.0	442	0.6	6
41R-2, 0–1	1175.90	1.5	0.1	0.2	444	0.3	10
41R-4, 0–1	1178.97	0.6	0.2	0.1	457	0.7	11
41R-CC, 19–20	1184.15	0.2	0.1	0.0	444	0.8	18
42R-4, 0–1	1188.16	0.4	0.1	0.1	459	0.6	15
42R-6, 0–1	1191.20	1.1	0.1	0.1	434	0.5	8
42R-CC, 26–27	1194.51	0.0	0.1	0.1	568	0.7	130
43R-3, 0–1	1196.55	0.6	0.2	0.1	441	0.7	14
43R-6, 0–1	1201.00	0.4	0.1	0.0	443	0.6	12
43R-CC, 4–5	1202.34	1.5	0.1	0.5	451	0.1	34
44R-1, 0–1	1203.20	1.1	0.0	0.7	456	0.1	62
44R-3, 0–1	1206.20	0.3	0.0	0.0	453	0.4	17
45R-2, 0–1	1214.33	0.3	0.0	0.0	449	0.3	14
45R-5, 0–1	1218.92	0.5	0.0	0.0	412	0.5	4
46R-1, 146–147	1223.86	0.3	0.0	0.0	397	0.4	10
46R-4, 0–1	1226.99	0.4	0.0			1.0	
47R-2, 0–1	1233.53	0.5	0.0			1.0	
47R-4, 0–1	1236.57	0.6	0.0	0.1	440	0.4	9
48R-2, 0–1	1243.24	0.6	0.0	0.0	376	0.6	0
48R-4, 0–1	1246.32	0.6	0.0	0.0	438	0.3	6
49R-3, 0–1	1254.40	0.6	0.0	0.2	458	0.2	27
49R-4, 0–1	1255.90	0.7	0.0	0.1	445	0.3	16
50R-3, 0–1	1264.00	1.0	0.0			1.0	
50R-5, 0–1	1267.00	0.9	0.1	0.1	445	0.3	12
51R-2, 0–1	1272.20	0.9	0.0	0.0	470	0.4	5
51R-3, 0–1	1273.70	0.7	0.1	0.1	445	0.4	17
52R-2, 0–1	1281.90	0.9	0.0			1.0	
52R-5, 0–1	1286.40	0.6	0.0	0.0		0.6	1
53R-2, 120–121	1292.70	1.8	0.0			1.0	
53R-3, 131–132	1294.31	1.0	0.0	0.0	363	0.7	1
54R-2, 0–1	1301.10	0.9	0.0	0.3	448	0.2	28
54R-3, 0–1	1302.60	0.9	0.1	0.0	371	1.0	0
55R-2, 0–1	1310.70	3.8	0.2	2.8	455	0.1	73
56R-2, 0–1	1320.30	0.4	0.0	0.0	443	0.5	11
57R-2, 0–1	1330.00	0.8	0.0			1.0	
58R-2, 0–1	1339.60	1.4	0.1	0.8	455	0.1	55
59R-2, 0–1	1345.60	0.1	0.1	0.2	447	0.3	199
59R-6, 0–1	1351.62	0.4	0.1	0.1	441	0.4	23
60R-2, 0–1	1355.20	0.6	0.1	0.2	440	0.3	29
60R-4, 0–1	1358.10	0.7	0.1	0.2	442	0.3	22
61R-2, 0–1	1364.70	0.5	0.0	0.1	438	0.2	
61R-7, 52–53	1372.62	0.5	0.0			1.0	
62R-2, 0–1	1374.40	0.5		0.0		0.0	
62R-5, 0–1	1378.90	0.7	0.1	0.1	441	0.4	
63R-2, 0–1	1384.00	0.4	0.0	0.1	437	0.3	
63R-5, 0–1	1388.50	0.7	0.1	0.3	442	0.2	
64R-2, 0–1	1393.70	0.8	0.1	0.2	448	0.2	26
64R-5, 0–1	1398.20	0.3	0.0	0.1	457	0.2	26
65R-4, 0–1	1406.30	0.8	0.0	0.2	451	0.2	25

Table T18 (continued).

Core, section, interval (cm)	Depth (mbsf)	TOC (wt%)	S_1 (mg HC/g)	S_2 (mg HC/g)	T_{max} (°C)	PI	HI (mg HC/g TOC)
65R-5, 0–1	1407.80	1.8	0.0	0.6	458	0.1	33
66R-2, 0–1	1412.80	0.7	0.1	0.2	445	0.4	24
66R-4, 0–1	1415.80	0.3	0.0	0.1	449	0.2	38
67R-2, 0–1	1422.40	0.5	0.0			1.0	
67R-4, 0–1	1425.40	1.2	0.0	0.2	453	0.2	13
68R-2, 0–1	1432.00	0.9	0.0		456	1.0	
68R-5, 0–1	1436.50	0.5	0.1	0.1	450	0.3	25
69R-4, 0–1	1444.30	0.7	0.1	0.2	447	0.3	34
69R-6, 0–1	1447.30	0.8	0.1	0.3	450	0.3	34
70R-3, 0–1	1452.50	0.3	0.1	0.3	461	0.2	99
70R-6, 0–1	1457.00	1.0	0.2	0.6	456	0.2	61
71R-3, 0–1	1462.20	0.6	0.0	0.1	452	0.3	20
71R-7, 0–1	1467.91	0.8	0.1	0.3	452	0.3	38
72R-2, 0–1	1470.40	1.1	0.1	0.8	460	0.2	72
72R-6, 0–1	1476.23	1.0	0.1	0.4	451	0.2	37
73R-3, 0–1	1481.50	2.2	0.3	3.4	455	0.1	158
73R-6, 0–1	1486.00	0.6	0.0			1.0	
74R-3, 0–1	1491.10	1.2	0.1	0.6	453	0.1	54
74R-4, 0–1	1492.60	0.7	0.1	0.3	455	0.2	45
75R-2, 0–1	1499.20	0.8	0.0	0.2	460	0.2	29
75R-4, 0–1	1502.20	0.6	0.0	0.1	456	0.2	23
76R-2, 0–1	1508.80	0.8	0.1	0.2	459	0.2	29
76R-4, 0–1	1511.80	0.5	0.0	0.1	456	0.2	24
77R-2, 0–1	1518.40	0.9	0.1	0.5	461	0.1	56
77R4, 0–1	1521.40	0.7	0.1	0.3	458	0.1	44
78R-3, 0–1	1529.50	0.3	0.0	0.1	453	0.2	49
78R-5, 0–1	1532.50	0.5	0.1	0.2	457	0.3	31
79R-2, 0–1	1537.70	1.0	0.1	0.4	464	0.1	44
79R-3, 0–1	1539.20	0.3	0.1	0.1	560	0.4	34
79R-4, 131–132	1542.01	1.0	0.4	0.3	445	0.6	28
80R-2, 0–1	1547.30	0.8	0.1	0.4	455	0.1	49
80R-4, 0–1	1550.30	0.4	0.1	0.1	471	0.3	30
81R-2, 0–1	1556.90	0.9	0.1	0.4	455	0.1	51
81R-3, 139–140	1559.79	1.0	0.1	0.5	452	0.1	51
82R-1, 0–1	1565.00	0.5	0.0	0.9	471	0.0	176
83R-4, 0–1	1579.00	1.1	0.0	0.3	459	0.1	27
84R-3, 0–1	1587.20	0.9	0.0	0.2	457	0.1	26
85R-3, 0–1	1590.70	1.0	0.0	0.4	456	0.1	38
86R-3, 0–1	1597.80	0.6	0.0	0.2	457	0.2	26
87R-2, 0–1	1606.00	0.5	0.0	0.1	475	0.3	20
87R-5, 0–1	1610.58	1.2	0.1	0.3	466	0.3	24
88R-8, 97–98	1624.00	1.1	0.2	0.3	528	0.4	23
89R-2, 0–1	1625.10	1.3	0.1	0.2	457	0.2	18
89R-5, 0–1	1628.64	0.9	0.0	0.3	457	0.1	36
90R-3, 0–1	1636.27	1.3	0.1	1.1	458	0.1	89
90R-6, 0–1	1640.77	1.4	0.0	0.4	458	0.1	32
91R-2, 0–1	1644.30	1.4	0.0	0.4	453	0.1	27
91R-5, 0–1	1648.80	1.1	0.1	0.2	457	0.2	16
92R-3, 0–1	1655.50	1.5	0.1	0.6	461	0.2	38
92R-5, 0–1	1658.50	1.4	0.1	0.4	454	0.1	31
93R-2, 0–1	1663.60	1.3	0.1	0.6	457	0.2	42
93R-4, 0–1	1666.60	1.6	0.2	0.8	455	0.2	52
94R-4, 0–1	1676.15	1.7	0.2	1.0	454	0.2	61
94R-4, 31–32	1676.46	7.1	4.1	25.4	442	0.1	357
94R-5, 36–37	1677.95	5.9	2.7	18.0	441	0.1	304
94R-6, 0–1	1679.09	1.7	0.2	0.9	458	0.2	52
95R-2, 0–1	1682.56	1.7	0.1	0.5	462	0.2	29
95R-3, 0–1	1684.06	1.3	0.1	0.4	462	0.2	32
96R-2, 0–1	1692.33	1.2	0.2	0.4	534	0.4	30
96R-5, 0–1	1696.95	1.4	0.3	0.2	575	0.5	15
97R-2, 0–1	1702.00	0.1	0.2	0.1	593	0.8	71
97R-3, 0–1	1703.50	1.3	0.3	0.1	454	0.8	6
98R-3, 0–1	1713.01	0.2	0.1	0.0	475	0.8	6

Notes: TOC = total organic carbon. S_1 = volatile hydrocarbons, S_2 = pyrolysis hydrocarbons. PI = production index = $S_1/(S_1+S_2)$, HI = hydrogen index = $S_2/TOC \times 100$.

Table T19. Sulfate concentrations in interstitial water, Hole 1276A.

Core, section, interval (cm)	Depth (mbsf)	Sulfate (mM)	Salinity
210-1276A-			
2R-1, 130–140	801.30	5.14	28.00
3R-6, 140–150	817.07	3.22	27.50

Table T20. Predicted two-way traveltimes of contacts between lithologic units, Site 1276.

Lithologic contact	Depth (mbsf)	Predicted two-way traveltime (s)
Unit 1/2	864.8	6.982
Unit 2/3	929.2	7.03
Unit 3/4	1029.5	7.108
Unit 4/Subunit 5A	1069.4	7.147
Subunit 5A/5B	1129.8	7.201
Subunit 5B/5C	1502.1	7.516
Top of first sill	1612.8	7.598
Top of second sill	1719.4	7.681

Note: Based on laboratory measurements of sediment velocities below the lithologic Unit 1/2 contact. The Unit 1/2 contact is interpreted to correlate with the strong reflection in SCREECH line 2MCS data at 6.98 s.

CHAPTER NOTE*

N1. Williams, G.L., Boessenkool, K.P., Brinkhuis, H., Pearce, M.A., Fensome, R.A., and Weegink, J.W., unpubl. data. Upper Cretaceous–Neogene dinoflagellate cyst course: morphology, stratigraphy and (paleo)ecology [Urbino, Italy, 4–8 June, 2001].

N2. 19 October 2004—In Table T3 under the column labeled Others, the term "palygonite" incorrectly appears. In each instance it was replaced with palygorskite.

*Dates reflect file corrections or revisions.